Advances in Materials Science and Engineering

Progress in Road Materials and Structures 2021

Lead Guest Editor: Meng Guo
Guest Editors: Bo Li, Chundi Si, Yongjie Ding, Yongsheng Yao, and Qiao Dong

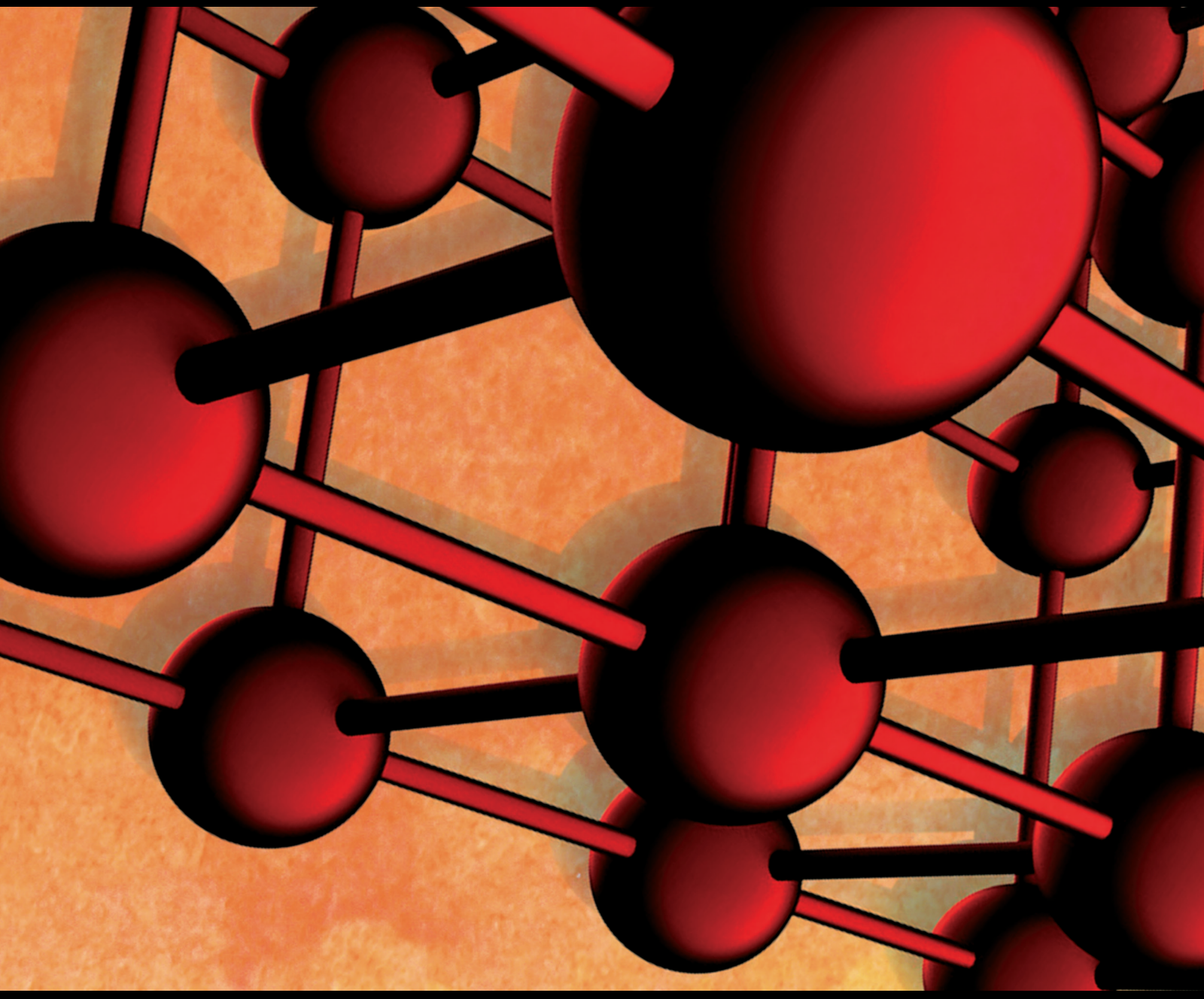

Progress in Road Materials and Structures 2021

Advances in Materials Science and Engineering

Progress in Road Materials and Structures 2021

Lead Guest Editor: Meng Guo
Guest Editors: Bo Li, Chundi Si, Yongjie Ding, Yongsheng Yao, and Qiao Dong

Contents

Contents

Hindawi
Advances in Materials Science and Engineering
Volume 2022, Article ID 6360301, 12 pages
https://doi.org/10.1155/2022/6360301

Research Article

Characteristics of Pavement Cement Concrete Incorporating Steel Slag Powder

Erbu Tian,[1,2] **Yamin Liu**,[3] **Xianpeng Cheng**,[4] **and Wuhua Zeng**[1,2]

[1]*School of Civil Engineering, Sanming University, Sanming 365004, China*
[2]*Key Laboratory of Engineering Material & Structure Reinforcement in Fujian Province, Sanming 365004, China*
[3]*Key Laboratory for Special Area Highway Engineering of Ministry of Education, Chang'an University, Xi'an 710064, China*
[4]*Xi'an University of Finance and Economics, Xi'an 710100, China*

Correspondence should be addressed to Erbu Tian; testb@fjsmu.edu.cn

Received 16 August 2021; Revised 23 March 2022; Accepted 6 May 2022; Published 27 June 2022

Academic Editor: Bo Li

After thermal braising and magnetic separation, steel slag is often ground into steel slag powder (SSP), which contains active silica (SiO_2) and can be used as a cementitious material to replace part of the cement and applied in concrete. However, there have been relatively few studies on the influence of SSP on the performance of pavement cement concrete (PCC). In this paper, SSP was used as an admixture to replace part of the cement in the cement paste, cement mortar, and PCC, to investigate the effect of SSP on the fluidity of SSP-cement slurry, the mechanical properties, and the durability of PCC. Results showed that SSP can lead to the secondary hydration reaction with $Ca(OH)_2$ in the cement paste and affect the hydration products, morphology, pore characteristics, and strength of the cement paste. When the SSP mixing amount was less than 20% and up to 1.3% superplasticizer was added, the fluidity of the cement slurry could be optimized. For the samples with the SSP mixing amount of less than 20%, the concrete compressive strengths were greater than 50 MPa, and the flexural strengths were greater than 5.0 MPa. As the SSP mixing amount increased, concrete displayed a better anticarbonization performance. Finally, using 15% SSP, the best performance in terms of the concrete antipermeability (chloride ion diffusion coefficient and electric flux) and frost resistance was achieved.

1. Introduction

Steel slag (SS) is one of the typical industrial wastes in steel production, characterized by abundant free calcium/magnesium oxide, low cementitious properties, and high heavy metal contents. While manufacturing one ton of steel, 130 ~ 200 kg SS is produced as byproducts [1, 2]. In 2020, the amount of SS was estimated to be between 180 and 270 million tons globally [3]. The SS disposal in the landfill without applying is obviously wasteful and would also cause pollution to the environment.

Recently, many studies have focused on using SS as an ecofriendly material, particularly as a cementitious material. Usually, the SS comprise 45%–60% calcium oxide (CaO), 10%–15% silicon dioxide (SiO_2), 7%–20% iron trioxide (Fe_2O_3), 3%–13% magnesium oxide (MgO), 1%–8% manganese oxide (MnO), 1%–7% aluminum oxide (Al_2O_3), and phosphorous pentoxide 1%–4% (P_2O_5) [4, 5]. The SSs contain the same mineral compositions as cement, such as C_3S, C_2S, C_4AF, and C_2F, which are potential mineral admixtures in the cement or concrete industry [4, 6, 7]. After thermal braising and magnetic separation, the substances that affect the SS stability (free CaO and MgO) are greatly reduced, and the difficulty in grinding due to a large amount of iron minerals is solved [8, 9].

SS is frequently utilized as asphalt pavement material on highways for its high strength. In this respect, Morisson [10] used SS to prepare the mixture of 50% SS, 39% stream sand, 3% fly ash, and 8% asphalt cement, which could render service at places with no heavy truck traffic for longer than 10 years without structural deformation. Moreover, the SS is also employed as the railway ballast, leading to three essential effects, i.e., spreading vertical loads, providing elasticity to the rails, and preventing plant growth [11]. In research by Palankar et al. [12], SS was exploited in concrete instead of 50% coarse aggregate to improve the compressive

Table 1: Chemical compositions of the cement and SSP (%).

Samples	CaO	SiO_2	Al_2O_3	Fe_2O_3	MgO	MnO	P_2O_5	SO_3	Na_2O_{eq}	Loss
Cement	56.11	23.46	7.93	3.46	3.15	–	–	3.49	0.72	2.31
SSP	44.57	18.11	7.26	19.01	4.17	2.55	1.87	–	0.29	1.38

$Na_2O_{eq} = Na_2O + 0.685\ K_2O$.

strength, with the best results being about 60 MPa (very similar to the reference sample). In addition, the water absorption value increased, depending on the slag porosity.

SS is often ground into steel slag powder (SSP), and SSP can be used as a cost effective waste product in concrete [13] or an active additive in the secondary hydration reaction [14, 15]. Li et al. [16] used SSP to replace 10% of cement by mass, and the results showed that compressive strength was reduced with increasing the SSP mixing amount. SSP could also control the hydration process in high-performance concrete, although its early age strength was low.

SSP can also be utilized as an active admixture due to its filling characteristics and pozzolan activity. Li et al. [17] studied the effect of SSP on the low-temperature fracture performance of asphalt materials. Jiao et al. [18] found that SSP could improve the thermal conductivity of SSP asphalt concrete. Chaurand et al. [19] reused SSP as an aggregate for road constructions.

The iron content of the cement clinker affects the flexural strength of the cement, which is lower than that of the steel slag. It is unclear if SSP addition to the cement increases the flexural strength of the cement and improves the flexural performance of pavement cement concrete (PCC). The production of one ton of cement produces 765 kg CO_2, and the production of one ton of SSP produces 86 kg CO_2 [20]. If feasible, SSP will help reduce the amount of the cement in PCC and carbon emissions from pavement engineering, which is crucial.

In this paper, SSP was used as an admixture to replace a part of the cement in cement paste, cement mortar, and PCC, to study the influence of SSP on the fluidity of SSP-cement slurry, and the mechanical properties and durability of PCC.

2. Materials and Methods

2.1. Raw Materials. The ordinary Portland cement was used, with a specific surface area of 340 $m^2\ kg^{-1}$, and the strength grade of 42.5, and the technical indicators of cement were compiled according to ASTM C150/C150M-2012. Table 1 shows the chemical compositions of cement and SSP. The X-ray diffraction (XRD) pattern of the SSP is demonstrated in Figure 1. SSP produced by Fujian Sangang (Group) Co., Ltd. has been heat-simmered and magnetically separated, possessing a specific surface area of 456 kg m^{-2}.

After the heat-simmering and magnetic separation, the chemical compositions of SSP were dicalcium silicate (C_2S), tricalcium silicate (C_3S), calcium hydroxide ($Ca(OH)_2$), hydration calcium silicate (C–S–H), RO phase, silicon dioxide (SiO_2), calcium aluminum garnet ($Ca_2A_{l2}Si_3O_{12}$), calcium magnesium silicate (C-M-S), and iron aluminum calcium phase ($Ca_2(Fe, Al)_2O_5$), which are similar to those of

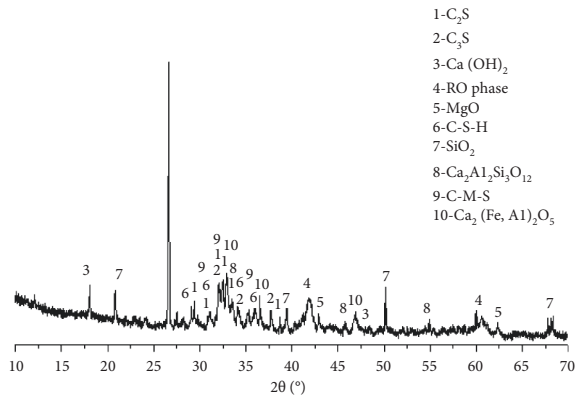

Figure 1: The XRD pattern of the steel slag.

cement. However, the formation temperature of SS was higher than that of the Portland cement clinker, so SS was also called overburned Portland cement [21]. The physical morphology of SSP is shown in Figure 2, in which the continuity of the particle size distribution of SSP was poor, and the SSP shape was irregular, comprising irregular quadrilateral, amorphous, and spherical. The contents of Mg, Mn, and Fe, shown as 1, 6, 9, and 10 marks in Figure 2, were relatively higher, showing that these SSP particles were RO phase, while the particle size of the similar cement clinker in SSP was smaller.

The coarse aggregate that was crushed basalt between 5 and 25 mm came from local quarries. The fine aggregate was natural river sand, smaller than 5 mm. The superplasticizer produced by Shandong Tengwei New Building Materials Co., Ltd. was used to achieve the desired workability for all cement slurry and concrete mixtures. All materials met the requirements of the related ASTM standards.

2.2. Mixture Design. SSP was used to replace some cement as the cementitious material. In this paper, the effects of three amounts of SSP (10, 15, and 20% by the weight of both SSP and cement) on the cement paste properties were investigated.

The details of the mixture design of the cement paste fluidity are shown in Table 2. The dose of superplasticizer was 0.4%, 0.6%, 0.8%, 0.9%, 1.0%, 1.1%, 1.2%, 1.3%, 1.4%, and 1.5% by the weight of cementitious material (both SSP and cement).

The details of the mixture design of the cement mortar are shown in Table 3.

The details of the mixture design of concrete are shown in Table 4. The dose of superplasticizer was 1.3% by the weight of cementitious material (both SSP and cement).

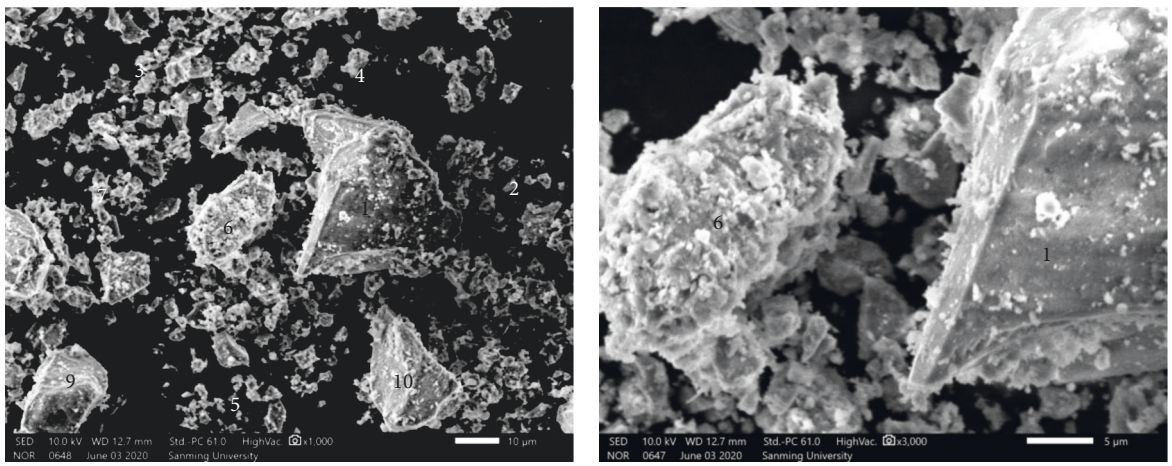

(a) (b)

Figure 2: Particle morphology of SSP. (a) Magnify 1000 times. (b) Magnify 3000 times.

Table 2: Mix proportions of the fluidity of cement paste.

Samples	Mix proportion (g)		Superplasticizer (%)										
	Cement	SSP											
C-P (100 : 0)	300	0	0	0.4	0.6	0.8	0.9	1.0	1.1	1.2	1.3	1.4	1.5
C-P (90 : 10)	270	30	0	0.4	0.6	0.8	0.9	1.0	1.1	1.2	1.3	1.4	1.5
C-P (85 : 15)	255	45	0	0.4	0.6	0.8	0.9	1.0	1.1	1.2	1.3	1.4	1.5
C-P (80 : 20)	240	60	0	0.4	0.6	0.8	0.9	1.0	1.1	1.2	1.3	1.4	1.5

Note. C-P (100 : 0) is the standard sample without SSP; the last number (C-P(80 : 20)) refers to the percentage of SSP in cementitious material (both SSP and cement), and so on.

Table 3: Mix proportions of cement mortar (g).

Samples	Cement	SSP	Water	Standard sand
CM-0	450	-	225	1350
CM-10	405	45		
CM-15	382.5	67.5		
CM-20	360	90		

Note. CM-0 is the standard sample without SSP; the number (CM-20) refers to the percentage of SSP in cementitious material (both SSP and cement), and so on.

Table 4: Mix proportions of concrete ($kg * m^{-3}$).

Samples	Cement	SSP	Water	Sand	Coarse aggregate	Superplasticizer
C-0	390	-	144	597	1269	5.07
C-10	351	39				
C-15	331.5	58.5				
C-20	312	78				

Note. C-0 is the standard sample without SSP; the number (C-20) refers to the percentage of SSP in cementitious material (both SSP and cement), and so on.

2.3. Test Methods

2.3.1. The Test Method of Cement Paste Fluidity. When SSP was added, first, the SSP and cement must have been mixed and stirred slowly for 30 s, and then 105 g water was added to test the cement paste fluidity according to ASTM C 311-2000.

2.3.2. The Test Methods of Cement Paste Hydration Properties. The pastes were cast in plastic sealed tubes after preparation, in case of water loss and carbonization, and were then cured at a temperature of 20°C ± 1°C. Hardened pastes were extracted and then immersed in absolute alcohol to prevent further hydration at testing ages. The samples were dried before testing using an electric vacuum drying oven.

(1) XRD Analysis. The Delong-7 X diffractometer manufactured in Germany was used to determine the mineral phases of the hydration products at the ages of 7, 28, and 180 d. The main technical parameters of the instrument are

as follows: tube voltage 0–60 kV, tube current 0–80 mA, the mode of continuous scanning, scanning speed 5°/min, and 2θ in the range (10°–80°).

(2) Morphology Analysis. The XL30 ESEM manufactured by FEI in the Netherlands was used to analyze the micromorphology of the cement paste under a high vacuum at the ages of 3, 7, 28, and 180 d. The accelerating voltage was 15–20 kV, and the working distance was 10 mm. A magnification of 2000 was selected for the analyses. The energy dispersive spectrometer was used to analyze the chemical elements of hydration products of the cement paste under a high vacuum at the ages of 3, 28, and 180 d.

(3) Pore Analysis. The pore characteristics of paste at the ages of 180 d were determined by dynamic nitrogen adsorption using the 3H-2000PS Beishide Instrument according to ASTM D 4365-2013.

2.3.3. The Test Method of Cement Mortar Strength. The standard sand of the cement mortar was consistent with the requirements of 5.1.3 in ISO 679: 2009. When the cement mortar would be mixed, the cement and SSP were added to the mixing pot together. Cement mortars of 40 mm × 40 mm × 160 mm were cast, then covered with the mold and placed on a horizontal shelf in a humidity curing box for curing for 24 hours, and removed the mold. Then, they were put in the water with a temperature of 20°C ± 1°C. The cement mortar strength tests were conducted in accordance with ASTM C 109/C 109M-2001 at the ages of 3, 7, 28, and 180 d.

2.3.4. The Test Method of Concrete Strength. Specimens of 150 mm × 150 mm × 150 mm and 150 mm × 150 mm × 550 mm were cast. Specimens were cured in a room with a temperature of 20°C ± 2°C and relative humidity of higher than 95%. The compressive strength and flexural strength of concrete were measured in accordance with ASTM C 293-2002 at the ages of 7 d and 28 d.

2.3.5. The Test Methods of Concrete Durability

(1) Chloride Ion Permeability. The concrete chloride ion permeability was tested at the age of 28 d and evaluated by measuring the current passing through the concrete, according to ASTM C 1202.

(2) Carbonation Resistance. Specimens of 100 mm × 100 mm × 100 mm were cast, and at the age of 26 d, the specimens were taken out of the standard curing condition and baked at 60°C for 48 hours and then were placed in a chamber with a temperature of 20°C ± 2°C, relative humidity of 70% ± 5% and a carbon dioxide concentration of 20% ± 3% for accelerated carbonation according to the ASTM C 1202. The carbonation depths of the specimens were tested after accelerated carbonation for 3, 7, and 28 d. Finally, the carbonation depth of concrete incorporating SSP could be calculated by

$$\overline{d_t} = \frac{1}{n}\sum_{i=1}^{n} d_i, \tag{1}$$

where $\overline{d}_t$ = average carbonization depth (mm); d_i = carbonization depth of a measuring point; n = total number of measuring points.

(3) Frost Resistance. The preparation procedure and size of the specimens in this test were consistent with the carbonization test. The difference was the curing method of the specimens. Before testing according to the ASTM C 1202, the specimens were cured for 24 days in standard conditions. Subsequently, the specimens were soaked for 4 days in water at 20°C ± 2°C, and the water surface was at least 20 mm higher than the specimens. A freeze-thaw cycle test was performed after curing. The mass loss of the specimens per 50 freeze-thaw cycles was recorded. Once the mass loss exceeded 5%, the test was terminated.

3. Results and Discussion

3.1. The Fluidity of Cement Paste. Figure 3 shows the fluidity changing curves with the increase of superplasticizer amount, when the SSP mixing amounts were 0%, 10%, 15%, and 20% (20 wt.% of both cement and SSP), respectively. Regardless of the SSP mixing amount, the fluidity of the cement paste increased with the increase in the superplasticizer amount and eventually leveled out. When the SSP mixing amounts were 0%, 10%, 15%, and 20%, the mixing amounts of superplasticizer that reached the maximum fluidity of the cement paste were significantly different, 3.0, 3.6, 3.9, and 3.9 g, respectively. It shows that as the SSP mixing amount increases, the fluidity of the slurry is decreased, mainly because the specific surface area of SSP is greater than that of cement. The SSP was finer than cement, and the water attraction was greater. More hydrophobic functional groups were needed to disperse the SSP particles, so a higher superplasticizer amount must have been added. The mixing amount of SSP was within 20%, and the superplasticizer amount in subsequent tests was 3.9 g (that is, 1.3% of the mass of the cementitious material) to ensure that the test could reach the maximum fluidity.

3.2. The Hydration Properties of Cement Paste

3.2.1. XRD Analysis. Figure 4 shows XRD patterns of cement paste with ages of 7, 28, and 180 d, when the mixing amount of SSP was 20%. According to the analysis results shown in Figure 4, the main minerals in the paste were hydrated C–S–H gel and $Ca(OH)_2$, residual minerals and the RO phase of SSP, and some unreacted gelling mineral silicates. Compared with the XRD pattern of the age of 7 d, the peaks of silicon oxide and calcium hydroxide for ages of 28 d and 180 d generally tend to decreased. This is due to the fact that the amorphous SiO_2 with lattice defects, which is the active SiO_2, reacts with $Ca(OH)_2$ in the solution for

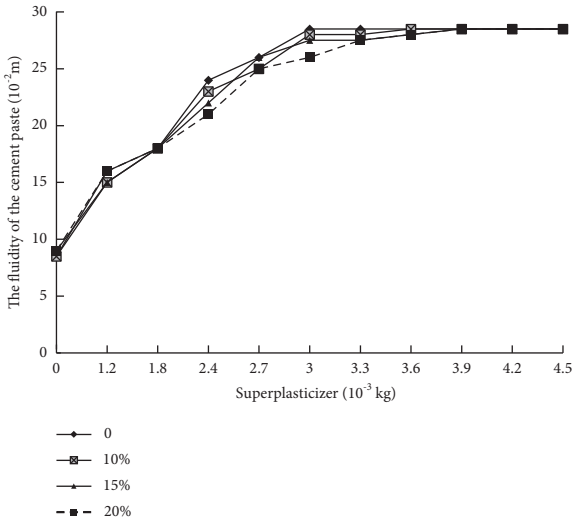

Figure 3: The fluidity change of the cement paste with the superplasticizer amount.

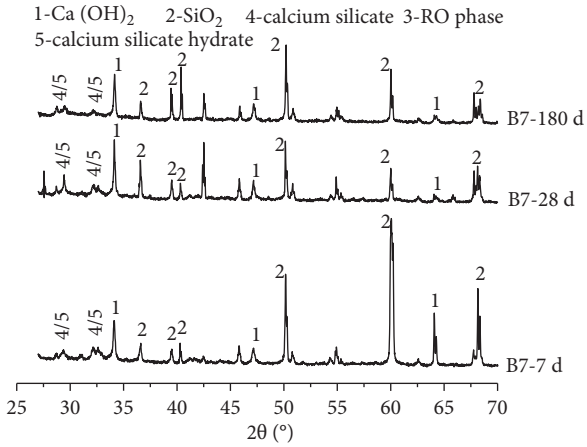

Figure 4: XRD patterns of the cement paste with 20% SSP.

secondary hydration. The secondary hydration is specifically a cement paste mixed with SSP. It provides an alkaline environment during the cement hydration, which can stimulate the activity of SSP and accelerate the generation rate of SSP hydration products. When the concentration of calcium hydroxide in the slurry reaches a certain level, it will react with the active SiO_2 to produce C–S–H.

3.2.2. Morphology Analysis. Figures 5–7 show the microscopic morphology images of cement pastes with ages of 3, 28, and 180 d, respectively, when the mixing amount of SSP was 20%, and the energy spectrum analysis of the corresponding regions is also displayed. Figure 5(a) demonstrates that there were more hydration products, and unhydrated particles were encapsulated by the hydration products. Figures 5(b) and 5(d) of the energy spectrum analysis chart show that the main chemical components of the regions Spc_3d_B2-4 and Spc_3d_B2-6 were O, Si, Al, and Ca, which should be unhydrated gelling components, calcium aluminum garnet ($Ca_2Al_2Si_3O_{12}$). Figure 7(d) of the energy spectrum analysis chart also indicates that the main chemical components of the area Spc_180d_B7-3 were O, Si, Al, and Ca. Whether in the early or later stage of hydration, $Ca_2Al_2Si_3O_{12}$ was formed in the micromorphology of the SSP-cement paste. It can be seen that the $Ca_2Al_2Si_3O_{12}$, with a smooth surface and large-particle size, was not easy to hydrate.

Figures 6(a) and 6(c) had a higher gel amount in the hardened paste than Figures 5(a) and 5(c), respectively, with an age of 180 d, and the paste structure was very dense. From Figures 7(a) and 7(c), it can be observed that there were particles with a complete shape, which were embedded between the gel-like hydration products, but there were weak connections between some larger particles and the surrounding hydration products. Most of the particles with smooth a surface and large-particle sizes were the RO phase of the SSP. The energy spectrum analysis in Figures 7(b) and 7(f) also shows that the components of the area Spc_180d_B7-1 and the area Spc_180d_B7-4 were O and Mg, which belong to the RO phase. Geiseler et al. [22] revealed that the hydration reaction ability of the RO phase depends on its composition. When the MgO content in the RO phase is sufficient, this RO phase type will have certain hydration activity. Two RO phases can be found in Figures 6 and 7; one type is shown in Figures 7(a) and 7(e), in which the RO phases were larger, and the RO phase surface was smooth since they did not participate in the chemical reaction. The other type is shown in Figure 6(a), in which the RO phases were relatively small and the RO phase surface was rough. The RO phase size was about 5 um and a chemical reaction occurred on the RO phase surface. The energy spectrum analysis results are shown in Figures 6(b) and 6(d). The area Spc_28d_B7-2 mainly contained O and Mg, and the area Spc_28d_B7-3 mostly comprised O, Si, and Ca. There was C–S–H gel on the RO phase, indicating that the RO phase had begun to undergo the hydration reaction. Therefore, the RO phase with a small particle size, in addition to being active due to the high content of MgO and participating in the hydration reaction, can also fill the pores left by water consumption or loss in the hardened paste, and play a role in filling microaggregates. Due to its smooth surface and weak bonding with the surrounding gel, the RO phase with a larger particle size may form a weak link in the hardened paste.

Figures 8(a) and 8(b) show the microscopic morphology of cement paste with 20% SSP at the age of 7 d. It can be clearly seen from Figure 8(b) that hexagonal plate-like crystals with regular shapes were formed, named calcium aluminate hydrate, which was in a metastable state at room temperature, also commonly known as cubic hydrogarnet (C_3AH_6). According to Bensted and Barnes [23], C_3AH_6 can be obtained in two ways: one is produced by CA hydration reaction at a temperature higher than 60°C, and the other is produced by mayenite ($C_{12}A_7$) hydration at room temperature to produce C_3AH_6 and C_2AH_8. Figure 8(a) shows that there was a large amount of calcium aluminate hydrate and "catkins" hydration products, and a crack can be clearly seen, indicating that the strength of the hydration products in this state was low.

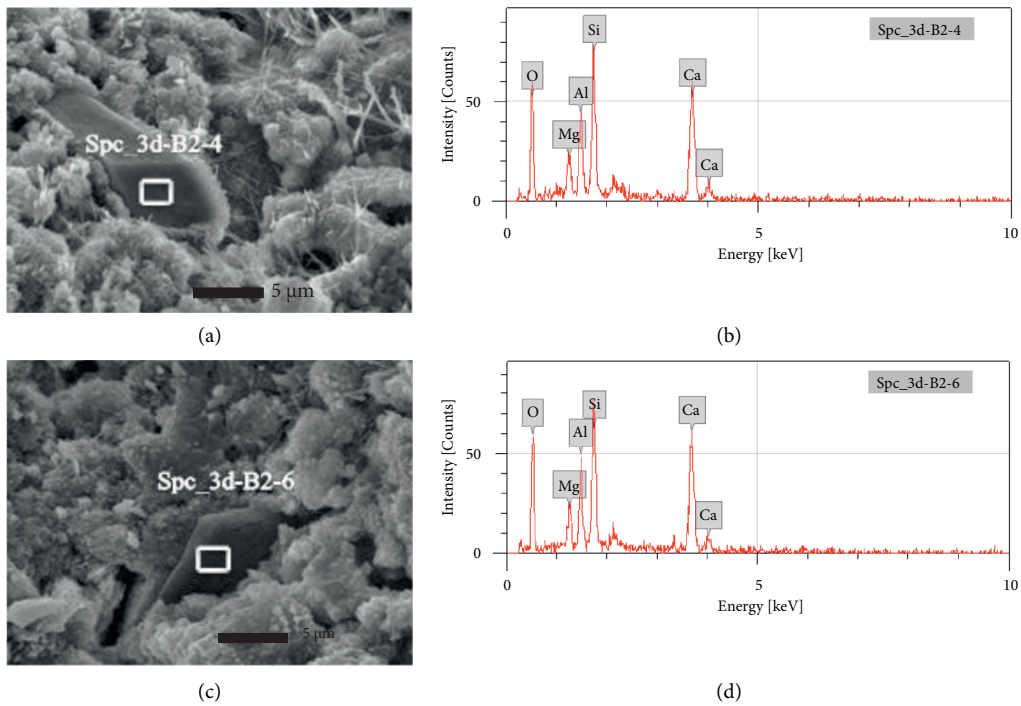

Figure 5: SSP-cement hydration microscopic morphology and energy spectrum analysis with the age of 3 d: (a) hydration microstructure with age of 3 d, (b) energy spectrum analysis of area Spc_3d_B2-4, (c) hydration microstructure with age of 3 d, and (d) energy spectrum analysis of area Spc_3d_B2-6.

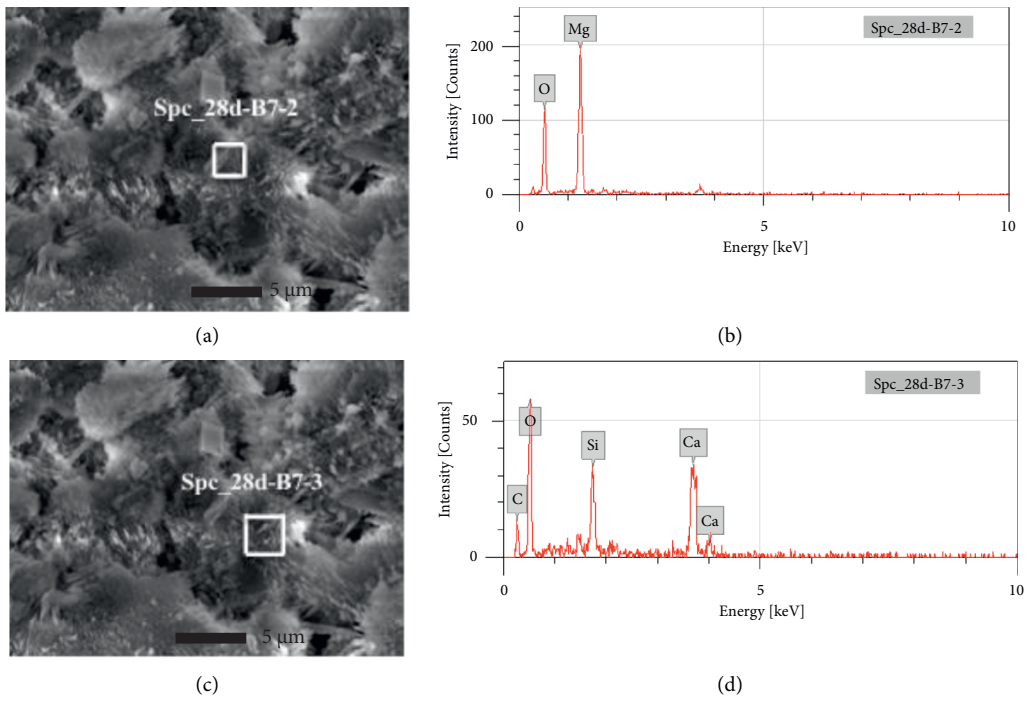

Figure 6: SSP-cement hydration microscopic morphology and energy spectrum analysis with the age of 28 d: (a) hydration microstructure with age of 28 d, (b) energy spectrum analysis of area Spc_28d_B7-2, (c) hydration microstructure with age of 28 d, and (d) energy spectrum analysis of area Spc_28d_B7-3.

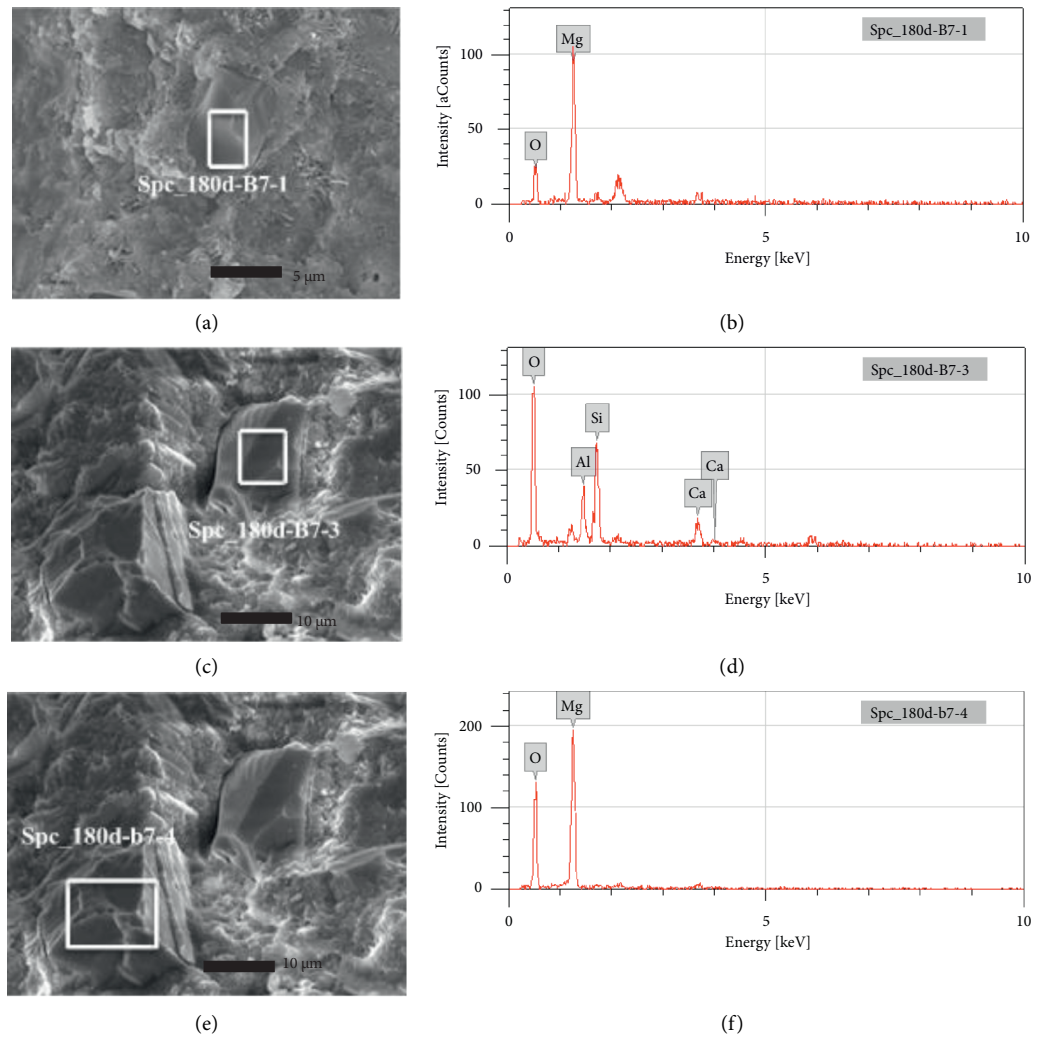

Figure 7: SSP-cement hydration microscopic morphology and energy spectrum analysis with the age of 180 d, (a) hydration microstructure with age of 180 d, (b) energy spectrum analysis of area Spc_180d_B7-1, (c) hydration microstructure with age of 180 d, (d) energy spectrum analysis of area Spc_180d_B7-3, (e) hydration microstructure with age of 180 d, and (f) energy spectrum analysis of area Spc_180d_B7-4.

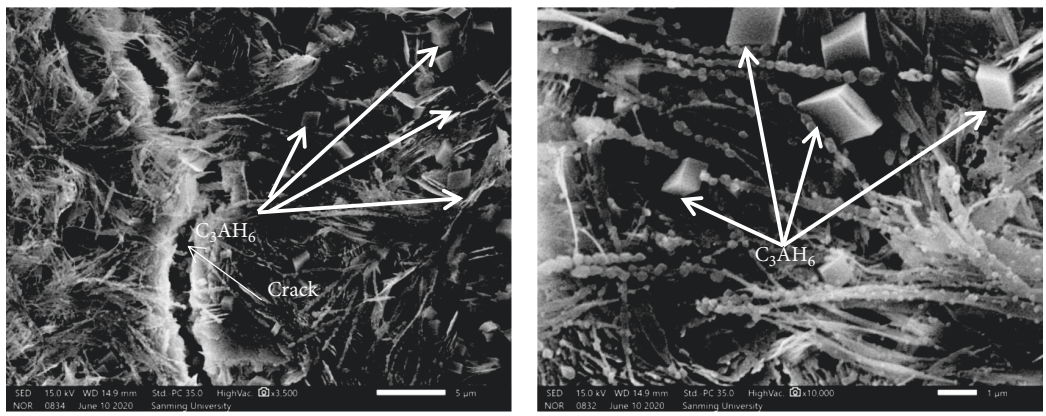

Figure 8: SSP-cement hydration microscopic morphology with the age of 7 d: (a) magnify 3500 times and (b) magnify 10000 times.

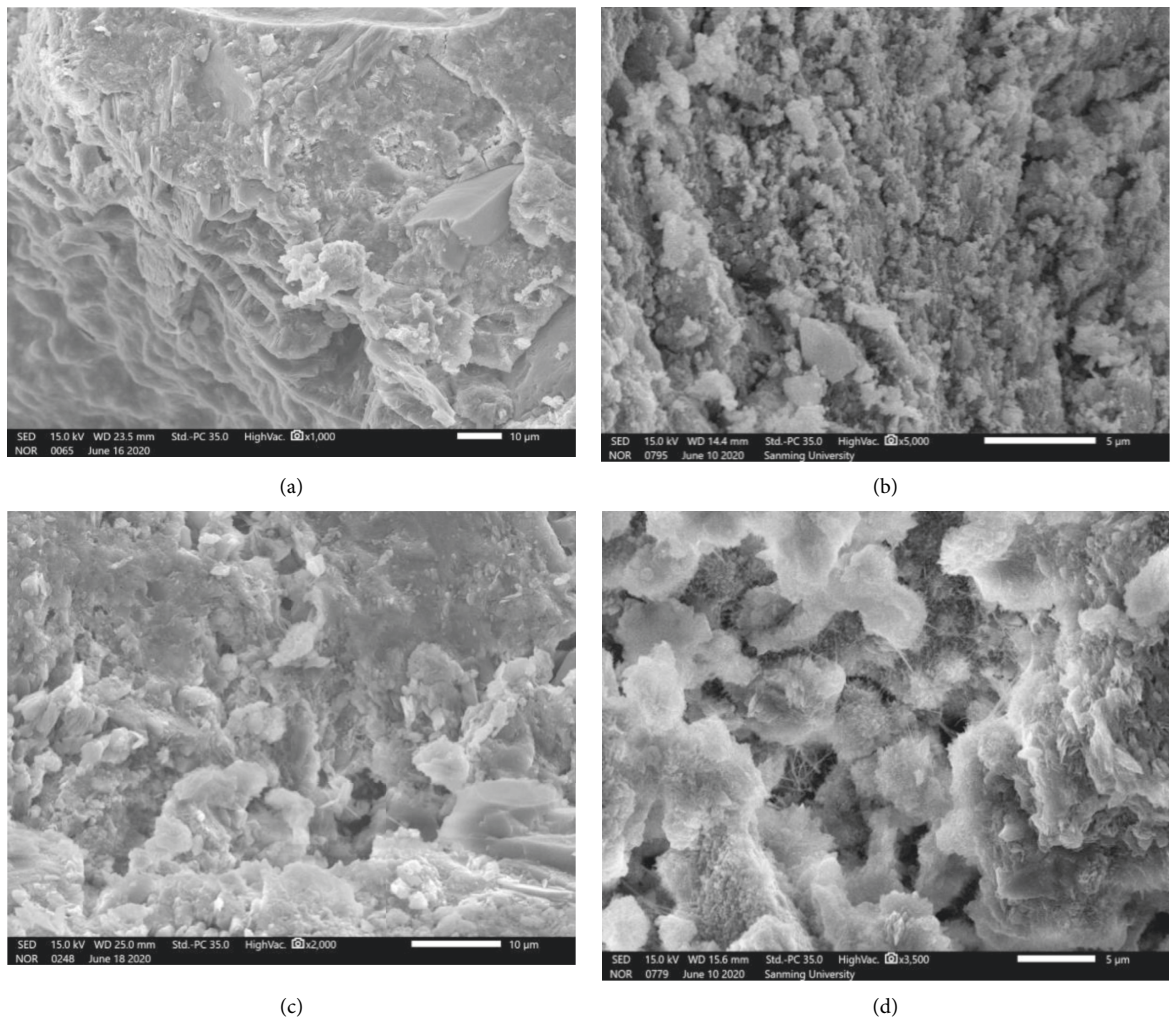

Figure 9: The microscopic morphology with the age of 7 d, (a) 0% steel slag powder mixed amount, 15% steel slag powder mixed amount, (b) 10% steel slag powder mixed amount, (c) 15% steel slag powder mixed amount, and (d) 20% steel slag powder mixed amount.

Figures 9(a)–9(d) demonstrate the microscopic morphology of the hardened cement paste with different SSP mixing amounts at the age of 7 d. The hydration products of the paste were very different. Figure 9(a) displays the plain cement (C-0) without SSP. Its hydration products of C–S–H gel and C-H phase were more, and the structures were very dense, and the pores were less. Figure 9(b) shows the microscopic morphology of the cement paste containing 10% SSP. Its hydration products formed a stable microstructure with fewer pores and a higher density, and the C–S–H gel was connected as a whole. Figure 9(d) shows the microscopic morphology of the cement paste containing 20% SSP, with fewer hydration products, no prismatic $Ca(OH)_2$, loose structure, many pores, and poor compactness. The strength test results of the paste with SSP also showed the corresponding characteristics. The strength of the mortar decreased with the increase of the SSP mixing amounts, and when the mixing amount was 20%, the strength of the mortar sand was further decreased. It can be seen that an increase in the SSP mixing amount could increase the pores of the hardened paste, resulting in a poorly compact structure, which is not effective in enhancing the paste strength.

3.2.3. Pore Analysis. Studies [24, 25] have shown that the pore size distribution can significantly affect the mechanical properties of hardened cement pastes. There are different types according to the aperture size. Gel pores are connected pores of gel particles with a pore diameter of less than 10 nm, which are harmless. Transition pores are regarded as pores between external hydration products, with a pore diameter between 10 and 50 nm, which are less harmful pores. Capillary pores are the original water-filled spaces that are not filled by hydration products, and their size is greater than 100 nm, which are harmful pores. Table 5 shows the ratio of the pore size distribution of cement paste at the age of 180 d. SSP greatly changed the pore size distribution ratio. Because the SSP particles are finer than cement, they could fill the capillary pores. Moreover, SSP participated in the secondary hydration reaction and improved the transition pores.

Table 5: The ratio of the pore size distribution (%).

Samples	Pore size					
	<10 nm	10–20 nm	20–50 nm	50–100 nm	100–200 nm	>200 nm
C-0	12.24	19.19	35.95	16.31	13.51	2.79
C-10	15.61	20.11	34.15	19	11.13	0
C-15	23.99	19.89	35.21	13.21	8.7	0
C-20	18.31	11.15	26.75	19.29	21.35	3.15

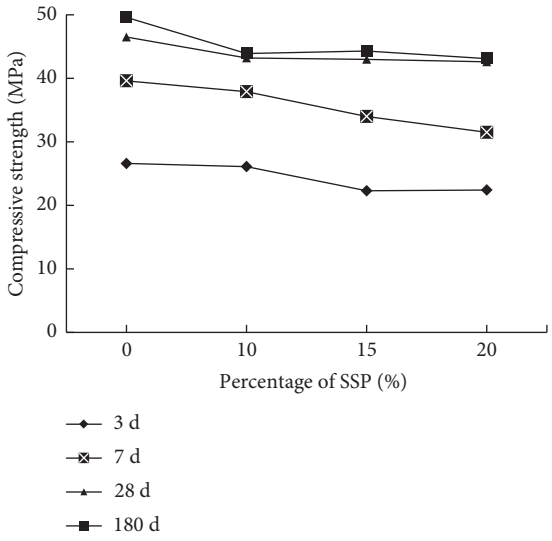

Figure 10: The compressive strength of mortar.

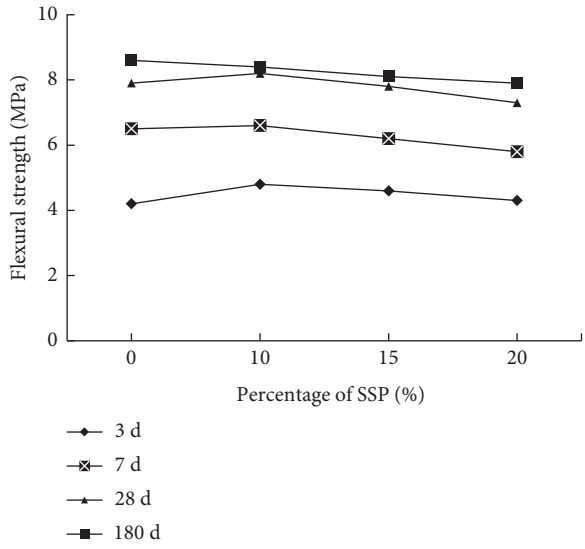

Figure 11: The flexural strength of mortar.

3.3. Strength

3.3.1. The Strength of Cement Mortar. Figures 10 and 11 plot the effect of the SSP mixing amount on the compressive and flexural strengths of cement mortars. It can be seen from Figures 10 and 11 that the longer the age, the higher the curve position, indicating the increase in the curing time, the compressive, and flexural strength of cement mortar. However, for the same curing time, with increasing the SSP mixing amount, the compressive and flexural strengths of cement mortar fluctuated in a small range, but the overall trend was downward. When the curing time was from 7 d to 180 d, with raising the SSP mixing amount, the overall compressive strength and flexural strength of cement mortar increased greatly, indicating that during the age from 28 d to 180 d, SSP participated in the secondary hydration reaction, and increased the compressive and flexural strength of the cement mortar.

3.3.2. The Strength of Concrete

(1) Flexural Strength. It can be seen from Figure 12 that when the standard curing age was 7 d, the flexural strengths of concrete mixed with SSP were lower than that of the C-0 concrete, and as the SSP mixing amounts increased, the flexural strengths gradually decreased, but the flexural strengths of each group were greater than 3.5 MPa, which meets the index requirements of the PCC flexural strength. As the curing age reached 28 d, the flexural strengths became greater than 5.0 MPa, reaching the specification requirements, and with the increase of the SSP mixing amounts, the flexural strengths of the concrete gradually decreased.

(2) Compressive Strength. Figure 13 shows that independent of the SSP addition amount, the compressive strengths of concrete increased with elongating the curing age. As the SSP mixing amounts increased, the compressive strengths of concrete showed a slightly decreasing trend. The compressive strengths of the SSP concrete increased rapidly in the later stage, mainly because the SSP participated in the secondary hydration reaction. In different curing ages, the concretes with 20% SSP showed higher compressive strengths, and when the curing age was 28 d, the compressive strengths of the different SSP mixing amounts reached more than 50 MPa, meeting the PCC specification requirements. It shows that the influence of the single SSP addition on the later compressive strength of concrete is small.

3.4. Durability

3.4.1. Chloride Ion Permeability. Table 6 shows the results of chloride ion permeability of the concretes. According to ASTM C1202, the grade of chloride ion permeability is "low" when the electric flux is between 1000 and 2000°C, and the grade is "moderate" when the electric flux is between 2000 and 4000 C. The permeability grades of C-0, C-10, and C-20 were medium, but the permeability grade of C-15 was low,

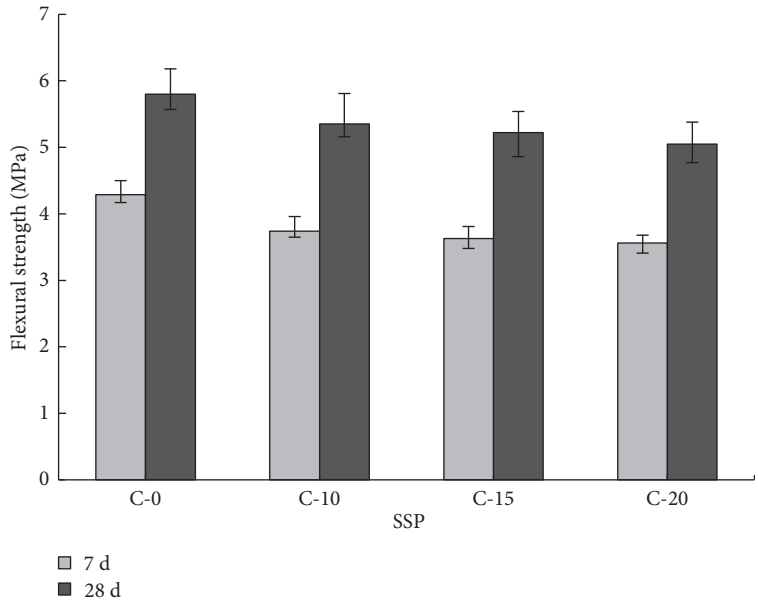

Figure 12: The flexural strength.

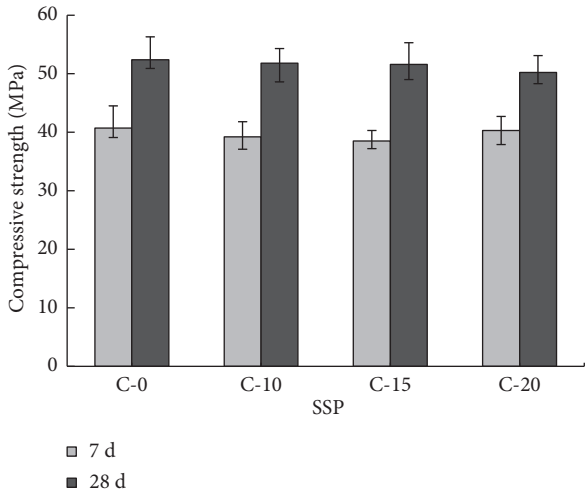

Figure 13: The compressive strength.

which was the lowest electric flux and the smallest chloride ion diffusion coefficient. Electric flux and chloride ion diffusion coefficients gradually decreased with the SSP mixing amount and then increased. When the SSP mixing amount was 15%, the two were the lowest. With increasing the SSP mixing amount, more and more SSP participated in the secondary hydration reaction, and the produced C–S–H gel could block the diffusion channel, improving the pore size distribution and geometric shape of the concrete pores; both the electric flux and the chloride ion diffusion coefficients were reduced. When the SSP mixing amount reached 15%, the electric flux was the lowest, and the chloride ion diffusion coefficient was the smallest. Combined with mechanical test results in Figures 12 and 13, it can be seen that an appropriate amount of SSP is beneficial in improving the pore structure of the concrete, increasing the concrete density, reducing the permeability, and improving the antipermeability performance of the concrete.

3.4.2. Carbonation Resistance. Figure 14 shows the carbonization depths of concrete with different mixing amounts of SSP and different carbonization times of 3, 7, and 28 d. The results show that as the mixing amounts of SSP increase, the anticarbonization effects of concrete are better. As the carbonization times increase, the overall carbonization depths of the concrete gradually increase, and the carbonization depths of the concrete with 0% and 10% SSP increase rapidly after carbonization for 7 d, while the increases are not much for concrete with 15% and 20% SSP. These results show that the $Ca(OH)_2$ produced by cement hydration have a secondary reaction with SSP, which reduces the $Ca(OH)_2$ production in the concrete and produces the C–S–H gel, and the SSP also fills the concrete pores and improves the pore size distribution and geometric shape of the concrete pores, and blocks some channels of concrete carbonization and reduces the chance of carbonization.

3.4.3. Frost Resistance. Table 7 shows the results of the weight and strength loss of concrete after freezing and thawing. After 100 freeze-thaw cycles, some shedding signs were found on the C-0 surface. After the 104th freeze-thaw cycle of the C-0, the mass loss reached 12%, and the strength dropped sharply by 36%. After 100 freeze-thaw cycles, the mass loss measurement and compressive strength test of C-0, C-10, C-15, and C-20 were performed. The results are given in Table 7, which show that before the freeze-thaw test, the apparent density of the C-15 concrete was the highest, and after 100 freeze-thaw cycles, the concrete with 15% SSP had the least mass loss and the lowest compressive strength loss. SSPs not only participated in the secondary hydration reaction but also had a filling effect, making the concrete

Table 6: The chloride ion permeability of concrete.

Samples	SSP	Electric flux (C)	Evaluation standard for the chloride ion permeability		Cl-diffusion coefficient (10^{-9} cm^2 s^{-1})
			Evaluation standard	Chloride ion permeability	
C-0	0	2444.2	2000–4000	Moderate	13.78
C-10	10%	2040.1	2000–4000	Moderate	12.61
C-15	15%	1877.91	2000–4000	Low	11.82
C-20	20%	2961.05	2000–4000	Moderate	17.15

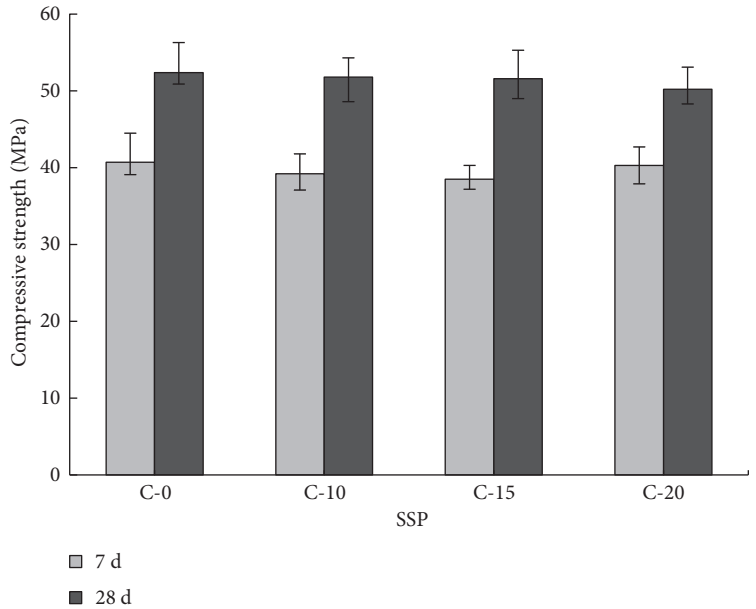

Figure 14: Carbonation depth of concrete.

Table 7: The weight and strength loss of concrete after freezing and thawing.

Samples	Mass (kg)			Compressive strength (MPa)		
	Before	After	Mass loss	Before	After	Strength loss
C-0	2.413	2.398	0.015	52.4	48.5	3.9
C-10	2.419	2.412	0.007	51.8	48.6	3.2
C-15	2.426	2.422	0.004	51.6	50	1.6
C-20	2.416	2.408	0.008	50.2	46.6	3.6

Note. The "Before" of compressive strength is the compressive strength of concrete at the age of 28 d, which is the 28 d compressive strength of Figure 13.

denser. The capillary channels of the concrete were filled with the C–S–H gel, and the products of the secondary hydration reaction made the pore size of the SSP-cement slurry smaller with fewer connecting holes. So, the water entering probability could be greatly reduced, decreasing the destroying chance of the concrete structure.

4. Conclusion

The SSP which possesses active SiO_2 can lead to the secondary hydration reaction with $Ca(OH)_2$ in the cement paste and affects the hydration products, morphology, pore characteristics, and strength of the cement paste.

When the mixing amount of SSP was less than 20% and the superplasticizer was added by 1.3% of the mass of the cementitious material, the fluidity of the cement slurry reached the maximum.

Within 20% SSP mixing amount, the concrete compressive strengths were greater than 50 MPa, and the flexural strengths were greater than 5.0 MPa, meeting the PCC specification requirements.

With increasing the SSP mixing amount, the concrete with a better anticarbonization performance was obtained. When the SSP mixing amount was 15%, the concrete antipermeability (chloride ion diffusion coefficient and electric flux) and frost resistance were the best.

Data Availability

The processed data required to reproduce these findings cannot be shared at this time as the data also form part of an ongoing study.

Conflicts of Interest

The authors declare that they have no conflicts of interest.

Acknowledgments

This work was supported by the Department of Science and Technology, Fujian Province, China (no. 2019Y0044). The authors thank Yuezong Lian and Haixin Kang for providing the steel slag sample.

References

[1] A. M. Rashad, "A synopsis manual about recycling steel slag as a cementitious material," *Journal of Materials Research and Technology*, vol. 8, no. 5, pp. 4940–4955, 2019.

[2] Q. Song, M.-Z. Guo, L. Wang, and T.-C. Ling, "Use of steel slag as sustainable construction materials: a review of accelerated carbonation treatment," *Resources, Conservation and Recycling*, vol. 173, Article ID 105740, 2021.

[3] U.S. Geological Survey, "Mineral commodity summaries 2021," *Mineral Commodity Summaries*, 2021.

[4] S. Liu and L. Li, "Influence of fineness on the cementitious properties of steel slag," *Journal of Thermal Analysis and Calorimetry*, vol. 117, no. 2, pp. 629–634, 2014.

[5] C. Shi, "Steel slag — its production, processing, characteristics, and cementitious properties," *Journal of Materials in Civil Engineering*, vol. 16, no. 3, pp. 230–236, 2005.

[6] J. N. Murphy, *Recycling Steel Slag as a Cement Additive*, University of British Columbia, Vancouver, Canada, 1961, http://circle.ubc.ca/handle/2429/4326.

[7] J. Li, Q. Yu, J. Wei, and T. Zhang, "Structural characteristics and hydration kinetics of modified steel slag," *Cement and Concrete Research*, vol. 41, no. 3, pp. 324–329, 2011.

[8] Z. Chen, R. Li, and J. Liu, "Preparation and properties of carbonated steel slag used in cement cementitious materials," *Construction and Building Materials*, vol. 283, no. 2, Article ID 122667, 2021.

[9] Y. Kong, P. Wang, and S. Liu, "Microwave pre-curing of Portland cement-steel slag powder composite for its hydration properties," *Construction and Building Materials*, vol. 189, no. 20, pp. 1093–1104, 2018.

[10] O. Gencel, O. Karadag, O. H. Oren, and T. Bilir, "Steel slag and its applications in cement and concrete technology: a review," *Construction and Building Materials*, vol. 283, Article ID 122783, 2021.

[11] P. K. Chamling, S. Haldar, and S. Patra, "Physico-chemical and mechanical characterization of steel slag as railway ballast," *Indian Geotechnical Journal*, vol. 50, no. 2, pp. 267–275, 2020.

[12] N. Palankar, A. U. Ravi Shankar, and B. M. Mithun, "Durability studies on eco-friendly concrete mixes incorporating steel slag as coarse aggregates," *Journal of Cleaner Production*, vol. 129, no. 15, pp. 437–448, 2016.

[13] C. M. Kansal and R. Goyal, "Analysing mechanical properties of concrete with nano silica, silica fume and steel slag," *Materials Today: Proceedings*, vol. 45, no. 94, pp. 4520–4525, 2021.

[14] F. Han and Z. Zhang, "Properties of 5-Year-Old concrete Containing Steel Slag Powder," *Powder Technology*, vol. 334, pp. 27–35, 2018.

[15] G. Liu, K. Schollbach, P. Li, and H. Brouwers, "Valorization of converter steel slag into eco-friendly ultra-high performance concrete by ambient CO2 pre-treatment," *Construction and Building Materials*, vol. 280, no. 7, Article ID 122580, 2021.

[16] Y. F. Li, Y. Yao, and L. Wang, "Recycling of industrial waste and performance of steel slag green concrete," *Journal of Central South University of Technology*, vol. 16, no. 5, pp. 768–773, 2009.

[17] Q. Li, Y. Qiu, A. Rahman, and H. Ding, "Application of steel slag powder to enhance the low-temperature fracture properties of asphalt mastic and its corresponding mechanism," *Journal of Cleaner Production*, vol. 184, no. 20, pp. 21–31, 2018.

[18] W. Jiao, A. Sha, Z. Liu et al., "Study on thermal properties of steel slag asphalt concrete for snow-melting pavement," *Journal of Cleaner Production*, vol. 277, no. 6, p. 123574, 2020.

[19] P. Chaurand, J. Rose, V. Briois et al., "Environmental impacts of steel slag reused in road construction: a crystallographic and molecular (XANES) approach," *Journal of Hazardous Materials*, vol. 139, no. 3, pp. 537–542, 2007.

[20] E. U.-B. R. E. F. Ceramics, "Integrated Pollution Prevention and Control(IPPC)Reference Document on Best Available Techniques in the Ceramic Manufacturing Industry," 2005, https://eippcb.jrc.es/pages/FActivities.htm.

[21] T. Zhang, Q. Yu, J. Wei, J. Li, and P. Zhang, "Preparation of high performance blended cements and reclamation of iron concentrate from basic oxygen furnace steel slag," *Resources, Conservation and Recycling*, vol. 56, no. 1, pp. 48–55, 2011.

[22] J. Geiseler, H. Kollo, and G. E. Lang, "Influence of blast furnace cements on durability of concrete structures," *ACI Materials Journal*, vol. 92, no. 3, pp. 252–257, 1995, https://www.researchgate.net/publication/279897880.

[23] N. R. Buenfeld, J. Bensted and P. Barnes, "Structure and performance of cements," *Engineering Structures*, Spon Press, vol. 251, p. 565, 2nd edition, 2002.

[24] S.-C. Kou, C.-S. Poon, and M. Etxeberria, "Influence of recycled aggregates on long term mechanical properties and pore size distribution of concrete," *Cement and Concrete Composites*, vol. 33, no. 2, pp. 286–291, 2011.

[25] A. Guerrero, S. Goñi, A. Maćias, and M. Luxan, "Mechanical properties, pore size distribution, and pore solution of fly ash-belite cement mortars," *Cement and Concrete Research*, vol. 29, no. 11, pp. 1753–1758, 1999.

Hindawi
Advances in Materials Science and Engineering
Volume 2022, Article ID 1844556, 10 pages
https://doi.org/10.1155/2022/1844556

Research Article

Study on Damage of the OGFC Mixture Based on Characteristics of Void Distribution

Teng Xu-qiu, Zhao Dongdong, and Zhang Fuqiang

College of Civil Engineering, LanZhou JiaoTong University, Box 15, Lanzhou, Gansu, China

Correspondence should be addressed to Teng Xu-qiu; tengxuqiu@mail.lzjtu.cn

Received 18 November 2021; Revised 25 February 2022; Accepted 26 February 2022; Published 24 May 2022

Academic Editor: Andrea Petrella

The void distribution characteristics of the drainage asphalt mixture have a certain influence on its durability. In this paper, X-ray CT technology and digital image processing technology are used to study the void distribution characteristics of three different graded asphalt mixtures, and the void ratio, void quantity, void equivalent diameter, and void fractal dimension of drainage asphalt mixtures are determined. On this basis, the damage characteristics of the asphalt mixture are analyzed with the split strength as the index, and the relationship between the void fractal dimension and the split strength is established. The relationship between the void diameter and the durability of the OGFC mixture is determined by the influence of the void diameter on the void fractal dimension. The results show that the void distribution characteristics of the OGFC mixture have a significant impact on its durability. The void larger than 3 mm in OGFC asphalt mixture has a greater impact on the durability of asphalt mixture. Even if the void ratio of different OGFC mixtures is relatively close, its durability is also very different. The difference in durability is mainly due to the difference of the void structure and the proportion of the number of large voids above 5 mm.

1. Introduction

With the development of computer technology and digital image processing technology, it is possible to obtain the internal structure of the asphalt mixture [1–6]. Digital image processing (DIP) is used to extract interesting objectives, so the influence of microstructure on asphalt mixture can be investigated [7–14]. Using digital image processing technology, researchers can process slice images taken by CT scans or high-definition cameras and distinguish the materials according to the different CT values and colors on the images, so as to obtain a clear and detailed structure diagram. It can provide reference for studying its internal structure characteristics and distribution law. Many researchers have applied nondestructive evaluation by using X-ray computed tomography (CT) to assess civil engineering materials [15, 16]. The internal structure and voids distribution of the asphalt mixture were achieved by X-ray CT [17, 18]; Masad.2002 [19–21].

Masad et al. quantitatively analyzed the effect of the compaction method on the internal structure of asphalt mixture samples by using digital camera technology and CT technology. By changing the conditions of rotary compaction to make it close to the level of on-site compaction, the compaction effect was finally evaluated. The results show that different compaction methods lead to different internal void distribution rules in the asphalt mixture, and the void ratio at the upper and lower ends of the asphalt mixture specimen is greater than the void ratio in the middle [18]; Masad et al. [22, 23]. Torres et al. studied the effect of pore distribution in HMA on its water permeability by CT scanning technology [24]. They found that Lognormal and Weibull distribution models can effectively fit the relationship between pores and water permeability, and a better correlation between connected pores and water permeability has been found. Through CT scanning and image processing of specimens with the same volume parameters such as VCA and VMA, Xu et al. [25] found that with different internal pore distributions of the specimens, the permeability and moisture damage were also different. Therefore, the pore distribution parameter as the evaluation index of water stability is more sensitive than the traditional volume parameter. Zhang Jialin used CT technology to analyze the horizontal and vertical void ratio, void equivalent diameter, void fractal dimension, and other parameters of

asphalt mixture specimens [26]. The research results showed that the void equivalent diameter was mainly distributed between 3 mm and 9 mm. The transverse percentage of voids of the mixture specimen is greater than the longitudinal percentage of voids, that is, the transverse drainage capacity is better than the longitudinal drainage capacity. Wu Wenliang of the South China University of Technology processed the CT slices of the asphalt mixture samples to obtain digital images that could characterize the void characteristics of the asphalt mixture and analyzed the plane and spatial distribution characteristics of the asphalt mixture [27].

In summary, many research studies have been conducted on the internal structure or loss of performance of the asphalt mixture in the past decades, but few studies have paid attention to comprehensive consideration of the relationship between void structure and performance evolution of the OGFC mixture from the meso and macro levels. Therefore, this paper uses CT scanning technology to explain the difference of indirect tensile strength of OGFC mixtures with different void structures, so as to realize a multiscale characterization of the damage characteristics of the OGFC mixtures. Finally, the relationship between void fractal dimension and splitting strength of OGFC mixture is established, and the void characteristics of the OGFC mixture with serious damage are determined.

2. Materials and Methods

2.1. Sample Preparation. In order to study the void distribution characteristics of the asphalt mixture, the drainage asphalt mixture (OGFC-13) with large void characteristics was selected as the research object, and the specimen was molded by the Marshall method. The specimen size was $\Phi 101.6\,\text{mm} \times 63.5\,\text{mm}$. The volumetric method was used to determine the void ratio of the asphalt mixture specimen and calculate the connected void ratio of the asphalt mixture specimen.

2.2. Materials. The coarse and fine aggregates used in this research were all basalt, and the ore powder was milled from limestone. The rubber asphalt was used as the binder, and fiber was mixed into the OGFC-13 mixture. The technical indicators of the raw materials are shown in Tables 1–4.

2.3. Mineral Material Grading Design. Since the percentage of voids of OGFC is closely related to the pass rate of the 2.36 mm sieve, the target percentage of voids of OGFC is controlled by adjusting the pass rate of the aggregate at the 2.36 mm sieve. First the gradation is determined according to the median value of the gradation recommended by the specification OGFC-1, then OGFC-2 and OGFC-3 are close to the upper and lower limits of the recommended gradation specifications. The pass rate of the three groups of mixture grading in each sieve is shown in Table 5.

2.4. Void Ratio and Connected Void Ratio Calculation. Table 6 shows the calculation results of the void ratio and connected void ratio of the three OGFC mixtures.

3. Results and Discussion

The void distribution characteristics of asphalt mixture specimens are affected by many factors such as molding method, aggregate gradation, uniformity of reclaiming, and molding temperature. This study intends to investigate the distribution of void ratio and void quantity at different heights of OGFC specimens, the void gradation and void fractal dimension of different gradation asphalt mixtures, and the distribution of void equivalent diameters at the cross section of the specimen. The void distribution characteristics of OGFC materials are studied.

3.1. Percentage of Void Distribution. According to the results of CT scanning, the gray threshold value T_1 of the CT scanning image is adjusted first, and then the gray value of pixels on the image is normalized. The gray value greater than T_1 is set to 255, and the gray value less than T_1 is set to zero. The result of image processing after binarization is shown in Figure 1, based on which the number of voids and void ratio of each two-dimensional slice can be determined.

Using MATLAB program to count the scanning slices of OGFC mixture, the total number of pixels in the circular part in Figure 1 is 32679, and the total number of pixels in the black part outside the circle is 12475. The difference between the sum of black pixels in the entire quadrilateral and the black pixels outside the circle is the number of black pixels in the circle, and the ratio of the difference to the total number of pixels in the circle is the void ratio of the scan slice. It can also determine the percentage of voids of the entire specimen.

It can be seen from Figure 2 that the percentage of voids of the OGFC mixture shows a C-type distribution along the height of sample. The void ratio decreases from both ends to the middle. The percentage of voids at both ends of the test sample is larger because the interpolating effect on the mixture causes more coarse aggregate and less fine aggregate at the end of the test simple when the test sample is formed. The measured percentage of voids values and the calculated percentage of voids values from image statistics of OGFC-1~OGFC-3 are shown in Table 7. The CT scan interval used in this study is 0.5 mm. It can be seen that the void ratio calculated from the scanned image is very close to the measured void ratio from Table 7.

Masad found that the void ratio at the upper and lower ends of the asphalt mixture specimen is greater than the void ratio in the middle [18, 23, 28]. This means that the distribution of void ratio along the height of sample for the normal asphalt mixes studied by Masad is basically the same as that of the OGFC mixtures.

3.2. Number of Void Distribution. The void distribution inside the asphalt mixture has a great influence on the performance of the asphalt mixture. In this paper, with the help of Image-Pro Plus's image processing and analysis functions, the number of voids, equivalent diameter distribution of voids, and void fractal dimensions in different gradation types of OGFC mixture samples are counted in

Table 1: Properties of coarse aggregate.

Test items		Test method	Unit	Normative value	Measured value
Polished stone value		T0312	BPN	≥38	58
Content of needle or plate	>9.5 mm	T0312	%	≤15	12.3
	<9.5 mm	T0312	%	≤20	16.4
Water absorption		T0304	%	≤3.0	1.7
Apparent density		T0304	$g{\cdot}cm^{-3}$	≥2.50	2.734
Crushing value		T0316	%	≤28	18.9
Adhesion		T0316	Level	≥4	4
Los Angeles wear value		T0317	%	≤30	15.3

Table 2: Properties of fine aggregate.

Test items	Test method	Unit	Normative value	Measured value
Sand equivalent	T0334	%	≥50	63.9
Angularity	T0345	s	≥30	36.1
Apparent density	T0328	g·cm-3	≥2.450	2.771
Methylene blue value	T0349	g·kg	—	20
Mud content(<0.075 mm)	T0333	%	<5.0	2.79
Robustness (>0.3 mm)	T0340	%	—	12.0

Table 3: Properties of rubber asphalt.

Test items		Test method	Unit	Normative value	Measured value
Penetration at 25°C		T 0604	0.1 mm	40~80	61
Ductility at 5°C		T 0605	cm	>10	17.3
Thin film oven test	Ductility at 5°C	T0605	cm	≥5	15.9
	Penetration ratio at 25°C	T0604	%	≥60	94.8
	Quality loss	T0609	%	≤±0.1	0.2
Elastic recovery		T0615	%	>55	71.5
Rotational viscosity at 180°C		T0625	Pa.s	1.0~4.0	1.64

Table 4: Properties of mineral powder.

Test items		Test method	Unit	Normative value	Measured value
Plasticity index		T0354	-	<4	3.6
Apparent density		T0352	$g{\cdot}cm^{-3}$	≥2.5	2.679
Stability		T0355	-	Measured	No change in color after heating
Hydrophilic coefficient		T0353	-	<1	0.6
Exterior		-	-	No clumps	No clumps
Particle size range	<0.6 mm	T0351	%	90–100	100
	<0.3 mm		%	75–100	95.2
	<0.075 mm		%	100	85.9

Table 5: Gradation composition.

Composite gradation	Passing percentage of each sieve (%)									
	16	13.2	9.5	4.75	2.36	1.18	0.6	0.3	0.15	0.075
OGFC-1	100	94.1	70.2	21.0	16.4	12.2	8.0	5.9	5.1	4.5
OGFC-2	100	92.5	62.4	18.7	14.8	11.2	7.6	5.8	5.1	4.5
OGFC-3	100	91.5	61.4	16.8	13.1	10.1	7.1	5.6	5.0	4.4
Upper limit of gradation	100	100	80	30	22	18	15	12	8	6
Median gradation	100	95	70	21	16	12	9.5	7.5	6	4
Lower limit of gradation	100	90	60	12	10	6	4	3	4	2

Table 6: OGFC mixture's percentage of voids and connected percentage of voids (%).

Specimen number	1		2		3		4	
Void category	Percentage of voids	Connected percentage of voids	Percentage of voids	Connected percentage of voids	Percentage of voids	Connected percentage of voids	Percentage of voids	Connected percentage of voids
OGFC-1	20.4	14.0	19.0	15.2	20.6	14.9	21.6	17.0
OGFC-2	20.3	15.8	21.3	17.6	20.6	15.8	21.5	18.0
OGFC-3	22.8	19.9	23.0	20.2	23.9	21.9	23.9	21.2

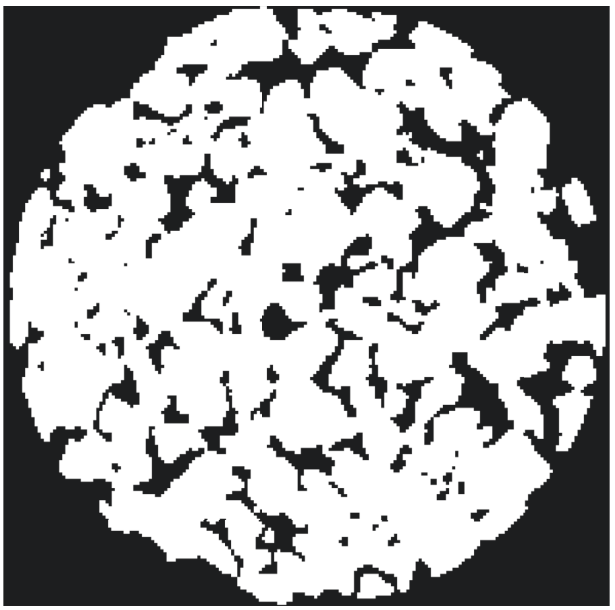

Figure 1: Binarization diagram of a bituminous mixture sample.

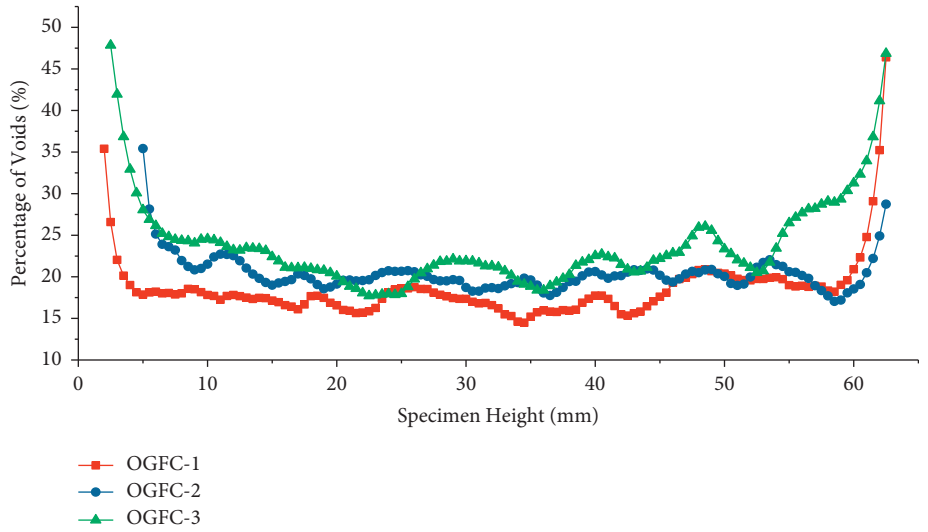

Figure 2: Percentage of void distribution along the height of the specimen.

Table 7: Measured percentage of voids and calculated percentage of voids.

Gradation	Measured percentage of voids	Calculated percentage of voids	Difference
OGFC-1	19.0	18.6	0.4
OGFC-2	20.3	20.4	0.1
OGFC-3	23.9	23.8	0.1

batches. The change in the number of voids along the height of the specimen is shown in Figure 3.

It can be seen from Figure 3 that the number of voids in the OGFC mixture shows a convex distribution along the height of samples. The number of voids increases from both ends to the middle. The number of voids at both ends of the test samples is small, while the number of voids in the middle is relatively large. Combining with the percentage of void distribution of Figure 2, it can be seen that the void volume at both ends of the specimen is large and the number is small, while the void volume in the middle of the specimen is small and the number is large.

3.3. Void Equivalent Diameter Distribution. The equivalent diameter of the void can represent the size of the void inside the asphalt mixture. The distribution law can be clarified by counting the size distribution of the equivalent diameter. By comparing and analyzing the void equivalent diameter distribution curves of different grades of OGFC mixtures, the durability of OGFC mixtures with different grades could be evaluated. The distribution of the equivalent diameter of the voids of OGFC-1~OGFC-3 mixtures is shown in Figures 4–7.

From Figures 4–6, it can be seen that the distribution range of the equivalent diameter of OGFC mixture voids is roughly between 0 and 10 mm, and most of the voids are distributed in the range of 1~4 mm, accounting for about 70%. The results are very close to those of [29]. Their research results shows voids with 0~4 mm equivalent aperture account for the largest proportion in the open-graded asphalt mixture. The space of 0~1 mm accounts for about 10%, and the space of more than 4 mm is about 20%. This part of the large void is mainly distributed on the surface of the asphalt mixture specimens. In the OGFC-1 and OGFC-2 mixture samples, the voids of 1 to 2 mm are the most prevalent, and their proportions reach 32.5% and 29%, respectively. In OGFC-3, the void of 2 to 3 mm is the most common, accounting for 23%. It can be seen from Figure 7 that the air-diameter frequency distribution functions of OGFC-1 and OGFC-2 mixtures are relatively close, and they are basically the same in the range of 1 to 5 mm. OGFC-2 has a wider range of void diameter distribution than OGFC-1, but the excess part occupies a smaller proportion and is mostly distributed on the surface of the specimen. The OGFC-3 mixture has more voids larger than 3 mm, so the durability order is OGFC-2>OGFC-1>OGFC-3. In summary, combined with the measured interconnected void fraction in Table 3, the drainage capacity order is: OGFC-3>OGFC-2>OGFC-1. Taking a comprehensive consideration, it is more reasonable to select OGFC-2 gradation.

3.4. Void Gradation Analysis. In this paper, the void gradation is the size distribution of the equivalent diameter of the void and mainly refers to the distribution ratio of the void diameter of different sizes. Under the combined action of internal and external causes, as the skeleton structure of asphalt mixture changes, its void distribution will be affected, and the void gradation will also change. Figure 8 shows the void gradation diagram of OGFC-1~OGFC-3 mixture samples.

It can be seen from Figure 8 that the overall size distribution of the void diameter is: OGFC-1 < OGFC-2 < OGFC-3. As the optimal gradation of OGFC-2, its gradation is close to the S-type distribution, that is, most of the voids are concentrated in the middle of the void diameter range, and there are fewer particularly large and small voids.

3.5. Void Fractal Dimension. In order to characterize the complexity of the void structure of OGFC mixture, the fractal dimension in fractal geometry is introduced to illustrate the structural characteristics of the void. Commonly used methods of geometric fractal dimensions are the number box method [30], the variable size method, and the small island method. In this paper, the box-counting method is used to study the characteristics of the gap fractal dimension. This method is commonly used to calculate the fractal dimension of complex irregular graphics, and a square box with a variable length of r is used to cover the fractal dimension of the graphics. Due to the irregularity of the covered graphics, there are often many holes and cracks that are not covered or part of it is covered. Count the number of these nonempty boxes, and record the number of nonempty boxes as $N(r)$, and then reduce the size of the box, and then calculate the new $N(r)$. When $r \longrightarrow 0$, the fractal dimension defined by the box method is obtained as follows:

$$D_0 = -\lim_{T \longrightarrow 0} \frac{\lg N(r)}{\lg r}. \quad (1)$$

In practical applications, a series of r and $N(r)$ can be obtained first, and then a straight line can be determined in the double logarithmic coordinate lgN-lgr, and the slope is D_0. Figure 9 shows the fractal dimensions of four different rules and smoothness graphs.

An OGFC mixture sample has more than 130 CT slices. In order to obtain the fractal dimension of the entire specimen, first obtain the void fractal dimension of each slice, and then calculate the average value to obtain the void fractal dimension of the entire specimen. The calculation formula is shown in (2), and the fractal dimension of OGFC1~OGFC3 mixture is shown in Figure 10.

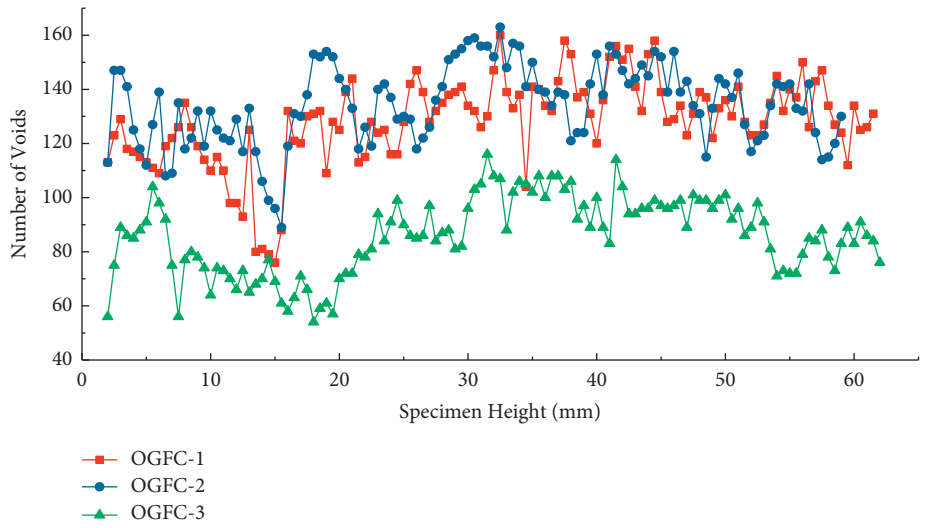

Figure 3: Distribution of the number of voids along the height of the specimen.

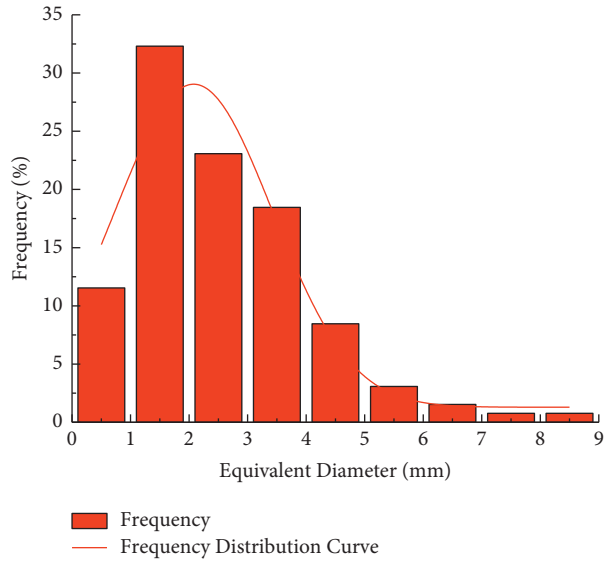

Figure 4: Equivalent diameter of OGFC-1.

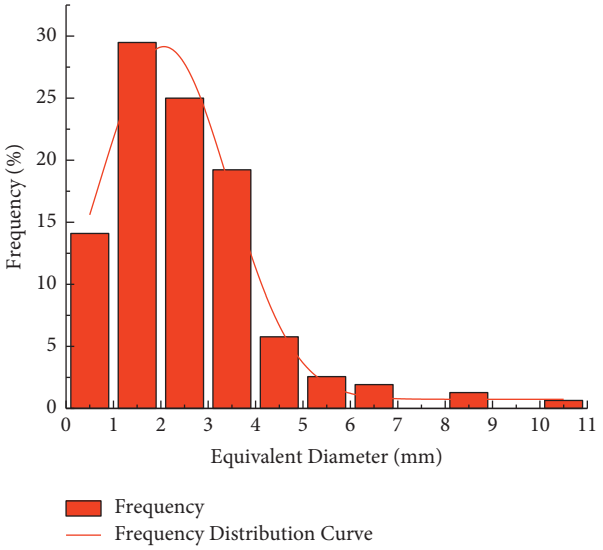

Figure 5: Equivalent diameter of OGFC-2.

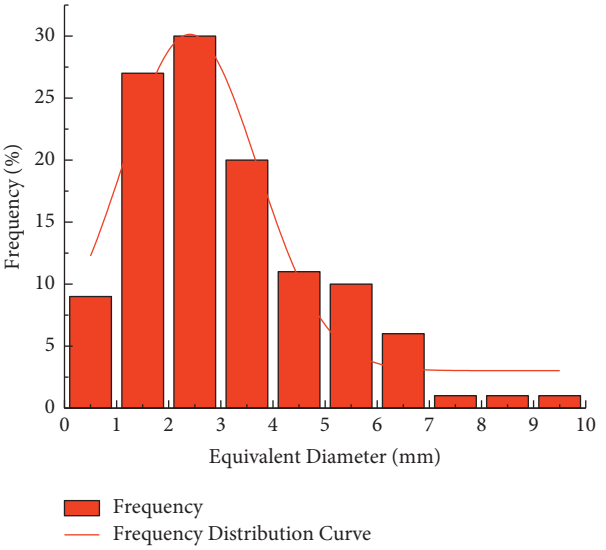

Figure 6: Equivalent diameter of OGFC-3.

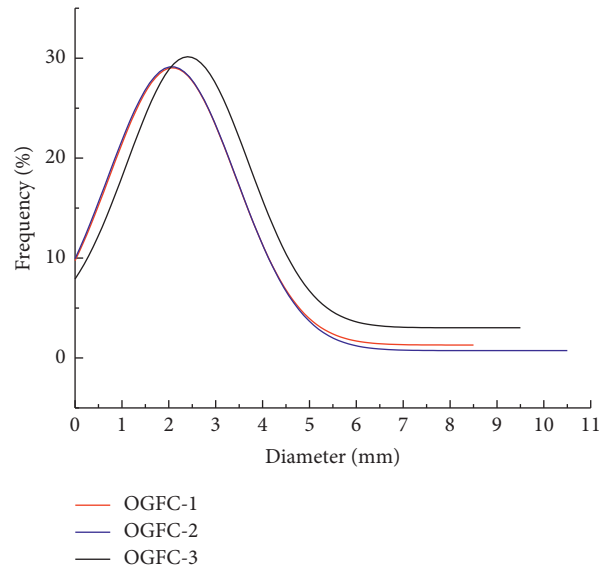

Figure 7: Frequency distribution function of the void diameter of three kinds of specimens.

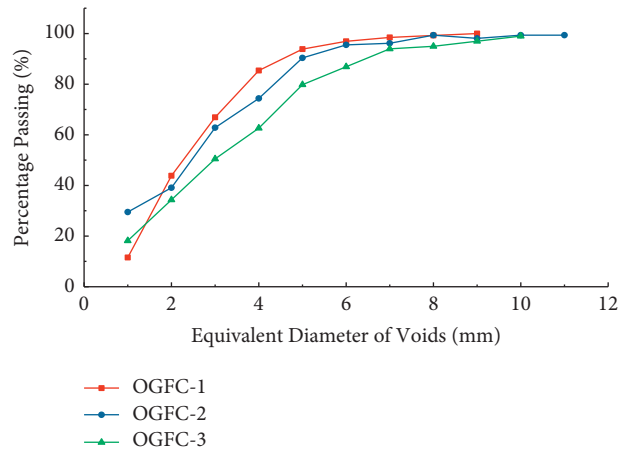

Figure 8: Void gradation diagram.

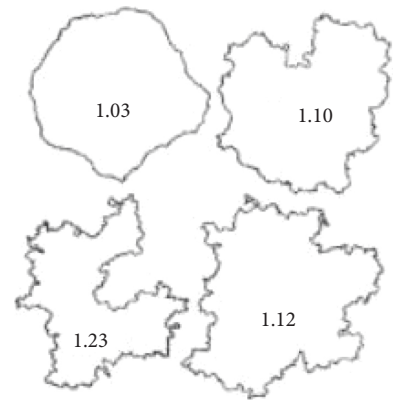

Figure 9: Fractal dimensions of four different rules and smoothness graphs.

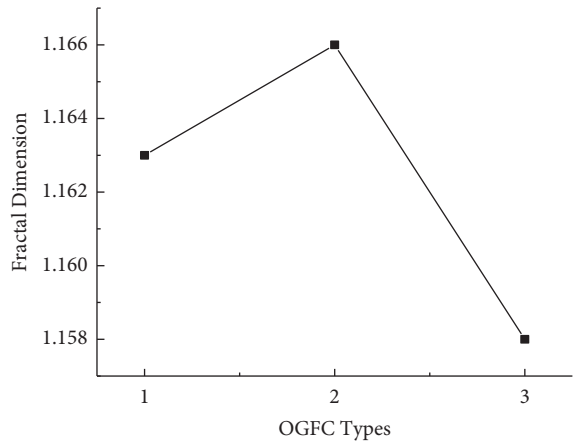

Figure 10: Fractal dimension distribution of different types of OGFC.

Table 8: Splitting strength of different gradation specimens.

Gradation	Percentage of voids	Void fractal dimension	Number of voids	Splitting strength (MPa)
OGFC-3	23.9	1.58	86	0.49
OGFC-1	19.0	1.63	128	0.64
OGFC-2	20.3	1.66	134	0.71

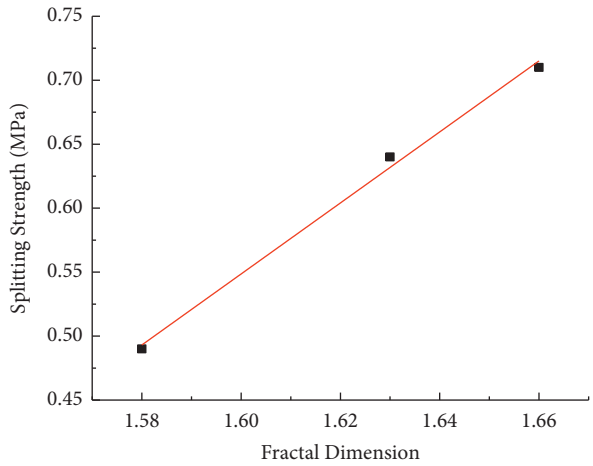

Figure 11: Relationship between the splitting strength and void fractal dimension.

$$D = \frac{\sum_{i=0}^{n} D_i}{n}, \tag{2}$$

where D is the fractal dimension of voids in the asphalt mixture and n is the number of CT image slices of the asphalt mixture.

3.6. Influence of Void Distribution Characteristics on Splitting Strength of Asphalt Mixture. The splitting strength of OGFC mixture is closely related to the void distribution. Related research shows that the splitting strength can indirectly reflect the ability of asphalt mixture to resist fatigue damage and water damage. In this paper, we will study the effect of void distribution characteristics on the splitting strength of OGFC mixture according to the void ratio, void fractal dimension, void number, and void equivalent diameter obtained above. In this paper, three gradations of OGFC-1, OGFC-2, and OGFC-3 were molded to measure the splitting tensile strength. Some of the measurement results are shown in Table 8.

It can be seen from Table 8 that the porosity of the OGFC-2 specimen is greater than that of the OGFC-1 specimen, but its splitting strength is higher. It can be seen that the splitting strength of the asphalt mixture increases with the increase of the void fractal dimension. It shows that there are certain shortcomings in evaluating the durability of OGFC mixtures by porosity index. When the porosity of the mixture is close, the splitting strength of the asphalt mixture is not only related to the porosity but also to its void structure, and the fractal dimension of the void can more effectively characterize the durability of the OGFC mixture specimen. The relationship between the fractal dimension of the void and the splitting strength is shown in Figure 11.

Fitting the relationship between the fractal dimension of the gap and the splitting strength, the relationship between the two is shown in (3):

$$R_T = -3.892 + 2.776D. \tag{3}$$

Here, R_T is the splitting strength and D is fractal dimension of voids.

The correlation coefficient of (3) is 0.996. Since $R_T > 0$, the value range of D is 1.4~2.

The study found that the main reason for the difference in the fractal dimension of voids is the proportion of voids larger than 3 mm in the asphalt mixture. Combining Figures 4–6, it can be seen that in the OGFC-1, OGFC-2, and OGFC-3 specimens, the proportions of the voids greater than 3 mm are 33%, 32%, and 37%, respectively. The data of this research show that the proportion of the voids larger than 3 mm is larger, the

fractal dimension of the voids is smaller. Therefore, the proportion of the voids larger than 3 mm has a great influence on the strength of OFGC mixture.

4. Conclusions

This paper uses CT technology to obtain the image information of the OGFC mixture specimen. On this basis, the void distribution characteristics of the OGFC mixture specimen are analyzed, and the corresponding relationship between the void distribution characteristics and the OGFC mixture damage is determined. The main conclusions are as follows:

(i) Based on MATLAB programming, calculating the void ratio by the number of pixels is an effective method, and the calculated void ratio is very close to the measured void ratio.

(ii) The internal voids of the OGFC mixture are unevenly distributed along the height of the specimen. The void ratio at both ends of the specimen is relatively large and gradually decreases from both ends to the middle. That is, the two ends of the mixture are distributed with a small number of large voids, and the middle is a large number of small voids.

(iii) The Gauss-Amp function was used to establish the frequency distribution function of the equivalent void diameter of the OGFC mixture, and the frequency distribution histogram of the equivalent void diameter was compared to determine that OGFC-2 was the best gradation.

(iv) Based on fractal geometry, the corresponding relationship between the void fractal dimension and splitting strength of OGFC mixture is established. The splitting strength increases with the increase of the void fractal dimension.

(v) The voids in the OGFC mixture with an equivalent diameter greater than 3 mm have a great influence on its splitting strength.

(vi) There is a positive linear relationship between the number of voids and the splitting strength. OGFC mixtures with more voids and relatively uniform void diameter distribution have better durability.

Data Availability

The data used to support the findings of this are available on request from the corresponding author.

Conflicts of Interest

The authors declare that they have no conflicts of interest.

References

[1] J. Zhang, "Research on asphalt mixture microstructure analysis method based on digital image processing technology," *Department of Road and Traffic Engineering*, Doctoral dissertation, Tongji University, Shanghai, China, 2000.

[2] L. I. Zhi, "Analysis of volume composition characteristics of asphalt mixture based on digital image processing technology," *Road and Railway Construction*, Doctoral Dissertation, Harbin Institute of Technology, Harbin, China, 2002.

[3] Q. Yao, "Research on Asphalt Mixture Composition Characteristics Based on Digital Image Processing Technology," Master's Thesis, Changan University, Xi'an, China, 2004.

[4] C. Wang, "Research on Asphalt Mixture Gradation Detection Technology Based on Digital Image," Master's Thesis, Changan University, Xi'an, China, 2007.

[5] Q. Zhang, Y. Bai, and D. Liang, "CT image entropy analysis for influences of moisture on asphalt mixtures," *J. Highway*, vol. 52, no. 4, pp. 158–161, 2007.

[6] Y. Hong, "Application and Research of Digital Image in Asphalt Mixture," Master's Thesis, Chongqing Jiaotong University, Chongqing, China, 2008.

[7] A. K. Apeagyei, J. R. A. Grenfell, and G. D. Airey, "Observation of reversible moisture damage in asphalt mixtures," *Construction and Building Materials*, vol. 60, pp. 73–80, 2014.

[8] D. L. Presti, N. A. Hassan, R. Khan, and G. Airey, "Reclaimed asphalt test specimen preparation assisted by image analysis," *Journal of Materials in Civil Engineering*, vol. 27, no. 8, 2014.

[9] M. Mohajeri, A. A. A. Molenaar, and M. F. C. V. D. Ven, "Experimental study into the fundamental understanding of blending between reclaimed asphalt binder and virgin bitumen using nanoindentation and nano-computed tomography," *Road Materials and Pavement Design*, vol. 15, no. 2, pp. 372–384, 2014.

[10] Z. A. Arega, A. Bhasin, and T. D. Kesel, "Influence of extended aging on the properties of asphalt composites produced using hot and warm mix methods," *Construction and Building Materials*, vol. 44, pp. 168–174, 2013.

[11] D. Braz, R. C. Barroso, R. T. Lopes, and L. M. G. Motta, "Crack detection in asphaltic mixtures by computed tomography," *NDT & E International*, vol. 44, no. 2, pp. 195–201, 2011.

[12] A. Moriyoshi, N. Takahashi, O. Ikeda, M. Kawashima, and T. Akabane, "Strain distribution in asphalt mixtures during the wheel tracking test at high temperatures," *Construction and Building Materials*, vol. 40, pp. 1128–1135, 2013.

[13] P. Liu, J. Hu, D. Wang et al., "Modelling and evaluation of aggregate morphology on asphalt compression behavior," *Construction and Building Materials*, vol. 133, pp. 196–208, 2017.

[14] J. Hu, P. Liu, and B. Steinauer, "A study on fatigue damage of asphalt mixture under different compaction using 3D-microstructural characteristics," *Journal of Frontiers of Structural and Civil Engineering*, vol. 11, pp. 1–9, 2017.

[15] J. Desrues, G. Viggiani, and P. Bésuelle, *X-ray Tomography as a Tool for Micromechanical Investigations of Cement and Mortar*, Wiley, NJ, USA, 2010.

[16] Y. M. Su, N. Hossiney, and M. Tia, "The analysis of air voids in concrete specimen using X-ray computed tomography," in *Nondestructive Characterization for Composite Materials,Aerospace Engineering, Civil Infrastructure, and Homeland Security*, T. Y. Yu, A. L. Gyekenyesi, P. J. Shull, A. A. Diaz, and H. F. Wu, Eds., SPIE, Bellingham, WA, USA, 2013.

[17] A. T. Papagiannakis, A. Abbas, and E. Masad, "Micromechanical analysis of viscoelastic properties of asphalt concretes, bituminous paving mixtures," *Materiales de Construcción*, vol. 1789, pp. 113–120, 2002.

[18] E. Masad, B. Muhunthan, N. Shashidhar, and T. Harman, "Internal structure characterization of asphalt concrete using image analysis," *Journal of Computing in Civil Engineering*, vol. 13, no. 2, pp. 88–95, 1999.

[19] M. Eyad and N. Somadevan, "Finite-element analysis of influence of localized strain distribution on asphalt mix properties," *Journal of Engineering Mechanics*, vol. 128, no. 10, pp. 1105–1114, 2002.

[20] E. Masad and J. Button, "Implications of experimental measurements and analyses of the internal structure of hot-mix asphalt," *Transportation Research Record: Journal of the Transportation Research Board*, vol. 1891, no. 1, pp. 212–220, 2004.

[21] E. Masad, A. Castelblanco, and B. Birgisson, "Effects of air void size distribution, pore pressure, and bond energy on moisture damage," *Journal of Testing and Evaluation*, vol. 34, no. 1, pp. 15–23, 2006.

[22] E. Masad and V. K. Jandhyala, "Characterization of air void distribution in asphalt mixes using X-ray computed tomography," *Journal of Materials in Civil Engineering*, vol. 14, no. 3, pp. 122–129, 2002.

[23] M. Eyad and J. W. Button, "Unified imaging approach for measuring aggregate angularity and texture," *J. Computer-Aided Civil and Infrastructure Engineering*, vol. 15, no. 4, pp. 273–280, 2010.

[24] A. C. Torres, *Probabilistic Analysis of Air Void Structure and its Relationship to Permeability and Moisture Damage of Hot Mix Asphalt*, Texas A&M University, Collage Station, TX, U.S.A, 2006.

[25] H. Xu, F. Chen, X. Yao, and Y. Tan, "Micro-scale moisture distribution and hydrologically active pores in partially saturated asphalt mixtures by X-ray computed tomography," *Construction and Building Materials*, vol. 160, pp. 653–667, 2018.

[26] J. Zhang, *Research on Characterization of Air Void Distribution and its fine Description in Porous Drainage Asphalt Mixture*, Chang'an University, Xi'an, China, 2008.

[27] L. Wen, *Research on Digital Image Processing Technology and Probability Statistics Method of Asphalt Mixture*, South China University of Technology, Guangzhou, China, 2009.

[28] E. Masad, L. Tashman, N. Somedavan, and D. Little, "Micromechanics-based analysis of stiffness anisotropy in asphalt mixtures," *Journal of Materials in Civil Engineering*, vol. 14, no. 5, pp. 374–383, 2002.

[29] G. Xu, "Characterization of air voids distribution in the open-graded asphalt mixture based on 2D image analysis," *Journal of Applied Sciences*, vol. 9, pp. 1–15, 2019.

[30] H. Xin, *Fractal Theory and Applications*, University of Science and Technology of China Press, Hefei, China, 1993.

Hindawi
Advances in Materials Science and Engineering
Volume 2022, Article ID 2425976, 9 pages
https://doi.org/10.1155/2022/2425976

Research Article

Analysis of Natural Aging Behavior of Asphalt Binder in Cold and Arid Region

Shanglin Song,[1,2,3] Meichen Liang,[4] Fujin Hou,[5] Honggang Gao,[3] Yufeng Bi,[6] Haixing Zhang,[7] and Meng Guo[4]

[1]*National Center for Materials Service Safety, University of Science and Technology Beijing, Beijing 100083, China*
[2]*Scientific Observation and Research Base of Transport Industry of Long Term Performance of Highway Infrastructure in Northwest Cold and Arid Regions, Gansu 736200, China*
[3]*Gansu Henglu Traffic Survey and Design Institute Co.,Ltd, Gansu 730030, China*
[4]*The Key Laboratory of Urban Security and Disaster Engineering of Ministry of Education, Beijing University of Technology, Beijing 100124, China*
[5]*Shandong Hi-Speed Construction Management Group Co.,LTD, Jinan 250001, China*
[6]*Shandong Provincial Communications Planning and Design Institute Group Co.,LTD, Jinan 250101, China*
[7]*China Communications Construction Company First Highway Bureau Southwest Engineering Co.,Ltd, Sichuan 610000, China*

Correspondence should be addressed to Meng Guo; gm@bjut.edu.cn

Received 17 November 2021; Accepted 17 March 2022; Published 29 March 2022

Academic Editor: Alicia E. Ares

With extremely bad climate and poor geographical environment in cold and arid region, the deterioration and failure of road materials are serious. In order to analyze the characteristics of natural aging behavior of asphalt binder in cold and arid region, the experiments were carried out based on the exposure field test base. The multiscale characterization of virgin asphalt under different natural aging conditions was carried out by means of macromechanical analysis and microchemical composition analysis. The results showed that the effects of natural aging and laboratory simulated aging on asphalt binder properties were similar. There was little effect on the performance of asphalt binder after natural aging one year. The effect of natural aging on asphalt binder in one year was similar to that of laboratory short-term aging. However, the strong UV radiation was a great challenge for asphalt pavement in Northwest China. Wind, dust, rain, and other factors have little effect on asphalt binder aging. Affected by the natural environment, macromolecular structures such as oxygen-containing polar functional groups will form in asphalt binder. The molecular weight of asphalt binder was increased, and the internal molecules of asphalt binder were subjected to large internal friction resistance in the process of movement. The macroscopic physical properties and road performance of asphalt binder become poor.

1. Introduction

Northwest China accounts for 42% of China's national area and is a typical cold and arid region in natural regionalization [1]. With extremely bad climate and poor geographical environment, the service life of the asphalt pavement is far lower than the design life [2]. Most areas of Northwest China belong to arid and semiarid climate, with an average rainfall of 45.3 mm and evaporation of 3410.6 mm. The total sunshine hours in the whole year are 3360 hours, the average maximum temperature is 24.9°C, and the average minimum temperature is −10.4°C. The annual average temperature difference exceeds 30°C, and the freezing and thawing days exceed 100 days. It is also affected by complex deterioration factors, such as strong wind, saline soil, and strong ultraviolet (UV) radiation. Asphalt pavement is exposed to the complex environment for a long time. The aging and failure of road materials are serious. The aging of asphalt binder affects asphalt pavement in many ways and makes it embrittle, of reduced damage tolerance and less

durable [3]. It caused the asphalt mixture to become excessively hard and brittle and susceptible to disintegration and fatigue cracking at low temperatures [4, 5]. As a result, the environmental factors easily accelerate the road diseases, such as cracking, loosening, and disintegration [6]. It will greatly reduce the service life of asphalt pavement. The service life of asphalt pavement is greatly reduced, which brings great challenges to pavement maintenance. The deterioration of the properties of the pavement materials during the service life of asphalt pavement is one of the main reasons for the pavement diseases [7]. Asphalt binder is a kind of high-efficiency binder, which plays an important role in bonding the constituent materials of asphalt mixture. The properties of asphalt binder play a decisive role in the quality and durability of asphalt mixture [8, 9].

The accelerated simulated aging test in the laboratory generally requires some forced aging of asphalt binder to enlarge the natural environmental factors. Generally speaking, the aging conditions are more severe than the external effects, so as to obtain a large amount of data in a short time. Based on laboratory accelerated simulated aging test, the studies have made it clear that asphalt binder will gradually undergo oxidation and aging under the effect of the external environment. Then, it becomes hard and brittle, and the bonding ability decreases, which will significantly reduce the performance of asphalt pavement [9–11]. A large number of studies have clarified the effect of aging on the macroproperties of asphalt binder samples. However, asphalt has about 105–106 different molecular types, and its chemical composition is very complex [12–14]. The changes of chemical composition of aged asphalt binder samples were also explored, but the internal aging process of asphalt binder was not clear. For example, Ruan et al. [15] found that aging further hardened the asphalt binder. It increased the viscosity but reduced ductility. Xu et al. [16] found that after aging, the rheological properties of asphalt binder decreased significantly. The complex modulus increased, but the phase angle decreased. Liu et al. [17] found that after aging, the low-temperature crack resistance decreased, but the high-temperature rutting resistance improved. The rutting factor of asphalt binder increased by 4.5 times, and the creep rate at −18°C was 3 times that of unaged asphalt binder.

The research has also explored the effect of aging on the chemical composition of asphalt binder. Under the conditions of high temperature, oxygen, and UV radiation, the light components of asphalt binder will evaporate, and the light components will change to heavy components. The polar functional groups will increase, and the average molecular weight will increase [18]. For example, Guo et al. [19] used Corbett separation method to separate the asphalt binder under different aging conditions. With the deepening of aging degree, the proportion of aromatics gradually decreased, the proportion of asphaltenes gradually increased, and there was no obvious change in saturates and resins content. It was because in the short-term aging process, more aromatics were transformed into resins, and relatively less resins were transformed into asphaltenes. Menapace et al. [6] believed that chemical reactions such as addition will occur after asphalt binder aging to generate long-chain compounds, and aromatics and colloids will be transformed into asphaltenes. Xing et al. [20] studied the changes of functional groups of asphalt binder before and after aging by atomic force microscope infrared spectroscopy. The results showed that the contents of carbonyl and sulfoxide groups increased. Relying on the accelerated aging simulation test of asphalt binder, researchers have carried out more research on the macro- and microproperties changes in the aging process asphalt binder. It will be used as a reference for studying the natural aging behavior of asphalt binder.

Due to the comprehensive effects of complex natural environment, such as weathering, cold, UV radiation, and chemical corrosion, asphalt binder has extremely complex aging behavior. Compared with other mild climate region, the aging behavior characteristics of asphalt binder under natural conditions in cold and dry areas are more obvious. Compared with the accelerated simulated aging test, the environmental factors of simulated aging test are relatively single. For example, the short-term aging simulates the aging of asphalt binder during pavement construction through the action of 163°C high temperature and oxygen. The long-term aging simulates the aging of asphalt binder during pavement service with 2.1 MPa pressure and 100°C high temperature. The photooxidative aging simulates the exposure of asphalt binder to UV radiation through the UV irradiation of high-pressure mercury lamp aging due to the action of oxygen [21]. The interaction and coupling effects of various factors are not considered, and the effects of such as rainfall, acid-base, and various chemical media are ignored. The simulation results are different from the actual service environment of asphalt pavement. The special environmental characteristics of cold and arid region play a role in accelerating aging and weakening the disadvantage of too long exposure test cycle of natural environment. The research results can clarify the impact of different natural environmental parameters on the service properties of asphalt binder in cold and dry region and then carry out targeted transformation and upgrading of asphalt binder to adapt to the road environment in cold and arid region. In addition, the natural aging data cannot be achieved under laboratory conditions, and the research results can effectively solve the problem of inconsistency between the test data and the actual data. It can be used to optimize the accelerated aging device in the laboratory and greatly improve the evaluation parameters related to the aging properties of road materials in Northwest China.

The objectives of this research are to explore the effects of different natural environmental parameters on the service properties of asphalt binder in cold and arid region and to analyze the characteristics of natural aging behavior of asphalt binder. In this study, combined with the complex climate environment in Northwest China, the experiments were carried out based on the exposure field test base. The multiscale characterization of virgin asphalt binder under different aging conditions was carried out by means of macromechanical analysis and microchemical composition analysis. The effect of natural aging on the macroproperties of virgin asphalt binder was qualitatively analyzed based on rheological properties. The effect of natural aging on the

chemical composition of virgin asphalt binder was analyzed based on chemical functional group and average molecular weight. The effects of different natural environmental factors on asphalt binder aging performance in cold and arid region were studied and analyzed. The evolution law of asphalt binder natural aging in cold and arid region was revealed. It is of great significance to the evaluation of aging performance and the improvement of antiaging performance of road materials in cold and arid region.

2. Materials and Test Methods

2.1. Experimental Materials. Virgin asphalt binder was used for relevant research, and a 90# virgin asphalt binder form Karamay was selected as the test sample.

2.2. Laboratory Ageing. As shown in Figure 1, the asphalt binder was put into the rolling thin film oven (RTFOT). The aging temperature was set to 163°C, and the aging time was 75 min. The short-term aged asphalt binder was obtained. Then, the short-term aged asphalt binder was put into pressure aging vessel (PAV). The aging temperature was set to 100°C, and the pressure was set to 2.1 MPa. After aging for 20 h, long-term aging asphalt binder was obtained.

2.3. Natural Aging Test of Asphalt Binder in Exposed Field. As shown in Figure 2, the natural aging test of asphalt binder was carried out based on the natural exposure site in the northwest cold and arid region with typical climate, such as strong UV radiation, large temperature difference, extreme drought, cold strong wind, and so on. According to the data of a meteorological station in Dunhuang city in 2020, the maximum temperature in summer is 48°C. The maximum temperature of asphalt pavement will reach 80°C. The monthly average daily ultraviolet radiation is 184.33 (J/cm^2·d). The average annual rainfall is less than 50 mm. The unaged asphalt binder sample was naturally aged in the exposure field. The film thickness of the asphalt binder sample was 3.18 mm, and the aging cycle of the test sample was 1 year. The asphalt binder sample shown in Figure (a) was directly exposed to the natural environment. The asphalt binder was aged under the comprehensive effect of the natural environment, which was recorded as all-weather (All) aging. The asphalt binder sample shown in Figure (b) was covered by an opaque plate. The asphalt binder was naturally aged to isolate UV radiation, water, wind, dust, and other factors, which was recorded as thermal oxygen (TO) aging. The asphalt binder sample shown in Figure (c) was covered with transparent plate. The asphalt binder was aged to isolate water, wind, dust, and other factors, which was recorded as thermal oxygen-+UV (TO + UV) aging. The asphalt binder samples after natural aging were shown in Figure 3.

2.4. Test Methods

2.4.1. Macroproperties Characterization of Asphalt Binder. In this study, DSR-2 produced by TA company from American was used to evaluate the macroproperties of asphalt binder samples. The parallel plates with diameter of 25 mm and thickness of 1 mm were selected. The temperature was 35°C, 45°C, and 55°C. 0.015% strain control mode was selected in the test, and the scanning frequency was from 0.1 rad/s to 100 rad/s. Based on 45°C, the complex modulus frequency curve and phase angle frequency curve at each temperature were translated according to the time-temperature superposition principle. The complex modulus master curve was obtained to characterize the viscoelastic properties of different kinds of asphalt binders.

Parallel plates with diameter of 25 mm and thickness of 1 mm were selected. The frequency was set at 10 rad/s, and the strain was set at 1%. The test took 46°C as the starting temperature, and the temperature raised automatically every 6°C, and finally raised to 82°C. The curves of rutting factor ($G*/\sin\delta$) with temperature were obtained. The curve varying with temperature was used to characterize the high-temperature rutting resistance of different kinds of asphalt binders.

Parallel plates with diameter of 4 mm and thickness of 1 mm were selected. The angular frequency range was 0.1–100 rad/s, and the temperatures were −18°C, −12°C, and −6°C. The loss modulus and storage modulus of asphalt binder samples were measured, and then, the stiffness modulus S and creep rate m of asphalt binder samples at −6°C, −12°C, and −18°C were calculated to characterize the low-temperature cracking resistance of asphalt binder.

2.4.2. Microproperties Characterization of Asphalt Binder. Spectrum II infrared spectrometer produced by American PE company was selected for the test. The resolution is 0.5 cm^{-1}, the scanning times are 32, and the wave number is 4000–500 cm^{-1}. The asphalt binder sample was heated to flow in a 135°C oven and then evenly applied to the test bench for testing. The atlas of asphalt binder samples was obtained and analyzed by OMNIC software.

The Waters 515-717-2410 GPC System gel chromatograph was selected, and the refractive index detector-Waters 2410 was used for the test. The polystyrene standard sample (PS) was used as the calibration method to calculate the molecular weight. The peak molecular weight range of polystyrene standard sample is 1.62–2300000. A total of 14 PS standard sample points were used to fit the molecular weight calibration curve. In the test, the asphalt binder sample was prepared with the concentration of 10–15 mg/ml, and THF was used as the mobile phase. The leaching rate was 1 ml/min, and the average molecular weight was obtained.

3. Results and Discussion

3.1. Effect of Natural Aging on the Rheological Properties of Asphalt Binder. Asphalt binder is a kind of viscoelastic material, which is solid at room temperature and low temperature and viscous liquid at high temperature. The service properties of asphalt binder are not only affected by temperature but also related to loading rate, load size, and loading time. The conventional test methods of asphalt

(a) (b)

Figure 1: Aging instrument for asphalt binder. (a) RTFOT. (b) PAV.

(a) (b) (c)

Figure 2: The natural aging test of asphalt binder. (a) All; (b) TO; (c) TO + UV.

(a) (b) (c)

Figure 3: The asphalt binder sample after natural aging. (a) All; (b) TO; (c) TO + UV.

binder have defects in studying the viscoelastic properties of asphalt binder. At present, the rheological method is widely used to characterize the viscoelastic properties of asphalt binder [22]. SHRP plans in United States use dynamic shear rheometer to evaluate the rheological properties of asphalt binder in the road properties specification of asphalt binder. It can also objectively reflect the high-temperature performance, low-temperature performance, and fatigue performance of asphalt binder.

3.1.1. The Effect of Natural Aging Based on Viscoelastic Properties. In order to study the effect of natural aging on viscoelastic properties of asphalt binder, dynamic shear rheological tests were carried out on virgin asphalt binder samples. According to the time-temperature equivalence principle, the complex modulus curve at each temperature can be translated along the horizontal direction to obtain the complex modulus master curve based on the reference temperature (45°C in this test). It can represent the rheological characteristics of asphalt binder at a wider frequency (wider temperature range), as shown in Figure 4.

It can be seen from Figure 4 that the complex modulus master curve of virgin asphalt binder increases obviously after aging in different ways. It showed that the modulus of asphalt binder increased after aging. The viscous component in asphalt binder decreased, but the elastic component increased. The asphalt binder hardened and became brittle, resulting in the enhancement of deformation resistance and the weakening of viscoelastic properties. It can be seen from Figure 4 that the natural aging of the three modes improved the complex modulus of asphalt binder. However, the increased degree was similar to that of short-term aging. It indicated that natural aging had little effect on the viscoelastic properties of asphalt binder.

In comparison, all-weather aging and thermal oxygen + UV aging had a greater impact on asphalt binder than thermal oxygen aging. The effect of thermal oxygen aging on

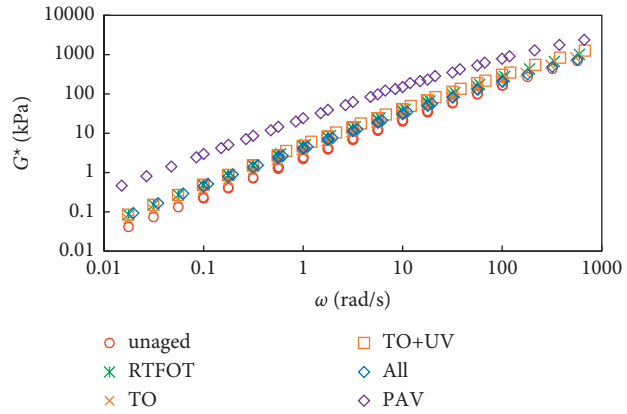

Figure 4: Master curve of complex modulus of asphalt binder before and after aging.

asphalt binder was less than that of short-term aging in laboratory. At low frequency (high temperature), the complex modulus of asphalt binder aged by the all-weather aging and thermal oxygen + UV aging increased relatively greatly. At high frequency (low temperature), the increase in thermal oxygen + UV aging was the most obvious, which was almost close to the long-term aging asphalt binder in the laboratory. It can be seen that UV radiation had a great impact on asphalt binder in cold and arid region. The experimental data also showed that the effects of laboratory short-term aging on viscoelastic properties of asphalt binder were matched to natural aging for one year in cold and arid region.

3.1.2. The Effect of Natural Aging Based on High-Temperature Properties. In order to study the effect of natural aging on the high-temperature properties of asphalt binder, the dynamic shear rheological test of virgin asphalt binder samples was carried out to obtain the rutting factor ($G*/\sin\delta$). Rutting factor reflects the dynamic rheological properties and permanent deformation resistance of asphalt binder. It is used as the evaluation index of high-temperature rutting resistance of asphalt binder in American Superpave Asphalt Performance specification. The rutting factor was larger, and the asphalt binder flow deformation capacity was smaller at the same temperature. At high temperature, the rutting resistance was stronger. The variation curve of rutting factor with temperature was shown in Figure 5.

It can be seen from Figure 5 that with the increase in temperature, the asphalt binder became soft, and the rutting resistance decreases gradually. After aging in different ways, the rutting factor of virgin asphalt binder increased obviously at the same temperature. It can be seen that the aging effect made the asphalt binder harden, the flow deformation became smaller, and the rutting resistance at high temperature was also improved. Compared with the long-term aging in the laboratory, it can be found that the increased rutting factor of asphalt binder samples aged for one year was small, and its effect of the high-temperature properties of asphalt binder was also small. It indicated that natural aging had little effect on the high-temperature properties of asphalt binder.

The rutting factor of thermal oxygen aged asphalt binder was less than that of laboratory short-term aged samples at the same temperature. It showed that the effect of thermal oxygen aging on asphalt binder was small. In comparison, all-weather aging had the greater impact on asphalt binder. It can be seen that the addition of UV radiation, wind, and dust had a great effect on the high-temperature properties of asphalt binder. Among them, the effect of all-weather aging on asphalt binder aging high-temperature performance was similar to that of thermal oxygen + UV aging. However, they were much greater than that of thermal oxygen aging. It can be seen that UV radiation contributes greatly to asphalt binder aging in cold and arid region. The experimental data also showed that the effects of laboratory short-term aging on high-temperature performance of asphalt binder were lower to natural aging for one year in cold and arid region.

3.1.3. The Effect of Natural Aging Based on Low-Temperature Properties. Asphalt binder will harden obviously at low temperature, which was characterized by Hooke elastomer. At low temperature, the asphalt binder will deform at the moment of stress application. The stiffness modulus S is used in Superpave to reflect the flexibility of asphalt binder. At low temperature, the greater the stiffness modulus of asphalt binder, that is, the smaller the creep compliance, the worse its deformation adaptability, and the smaller the allowable deformation. Under the action of external force or when the temperature continues to decrease, the greater the stress change of asphalt binder due to shrinkage strain, the worse the low-temperature crack resistance. The creep rate m was used to reflect the relaxation capacity of asphalt binder under stress. The greater the value of m, the greater the deformation capacity, and the stronger the relaxation capacity. Asphalt binder often had good low-temperature crack resistance. The test results are shown in Figure 6.

Comparing the data in Figures 6(a) and 6(b), it can be seen that under the three test temperatures, the stiffness modulus S of virgin asphalt binder after aging increased, the creep rate m value decreased. The results show that aging reduced the flexibility of virgin asphalt binder at low temperature and improved the possibility of low-temperature cracking. On the whole, natural aging had a great impact on the low-temperature performance of asphalt binder. The effect of natural aging on asphalt binder in different ways was greater than that of short-term aging. Thermal oxygen + UV aging and all-weather aging have the greatest impact on the aging of asphalt binder. It was close to the S value and m value of long-term aging.

At −6°C, the effect of different aging methods on asphalt binder at low temperature was as follows: long-term aging > all-weather aging > thermal oxygen + UV aging > hermal oxygen aging > short-term aging. It can be seen that with the increase in environmental factors, the natural aging degree of asphalt binder gradually increased, but it was still less than the effect degree of long-term aging. At −12°C, the effect of aging methods on the low-temperature

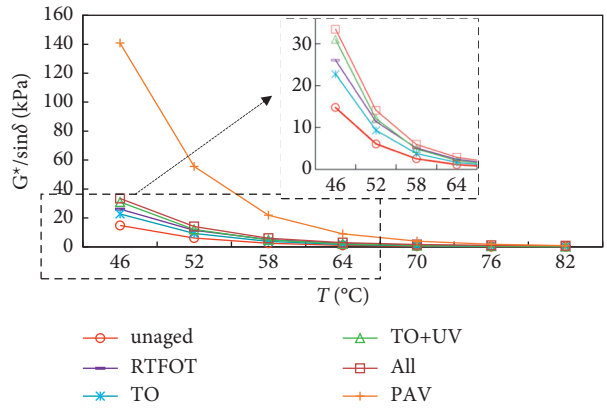

Figure 5: The variation curve of rutting factor with temperature of asphalt binder before and after aging.

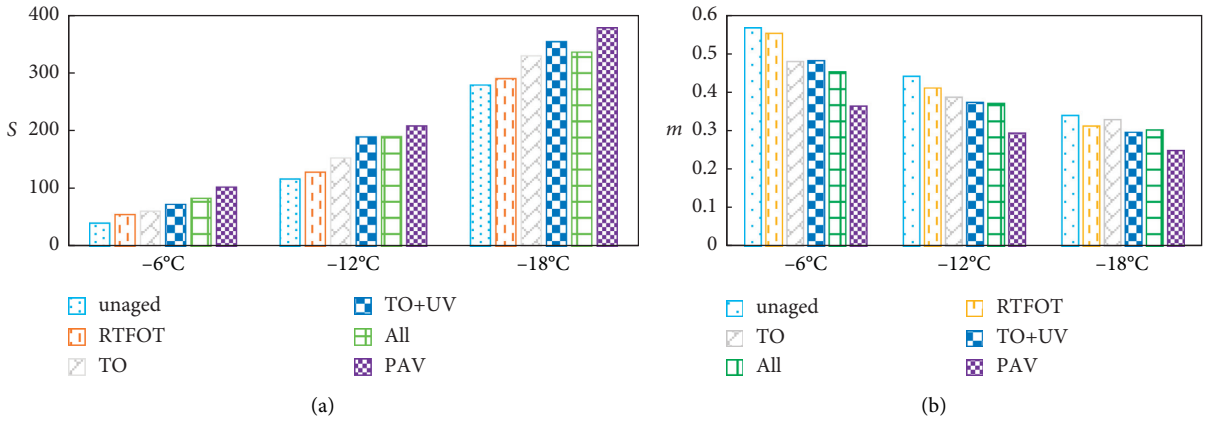

Figure 6: The stiffness modulus and creep rate of asphalt binder before and after aging. (a) Stiffness modulus *S*. (b) Creep rate *m*.

properties of asphalt binder was similar to that at −6°C. However, at this temperature, the effect of thermal oxygen + UV aging on asphalt binder was the same as that of all-weather aging. At −18°C, the effect degree of thermal oxygen + UV aging was greater than that of all-weather aging. It can be seen that with the decrease in temperature, the effect of wind, dust, rain, and other factors will gradually reduce the aging degree of asphalt binder. It was related to covering the all-weather aging surface, reducing the contact area between the asphalt binder and the external environment, and reducing the aging of asphalt binder by oxygen and UV radiation. It also showed the great effect of UV radiation on the properties of asphalt binder in cold and arid region.

In conclusion, the impact of natural aging on the properties of asphalt binder is similar to that of laboratory simulated aging, which will reduce the viscoelastic properties of asphalt binder and increase the risk of low-temperature cracking. The deformation resistance of asphalt binder was enhanced, and the rutting resistance at high temperature was improved. However, one year of natural aging had little effect on the aging degree of asphalt binder. Among them, the thermal oxygen aging degree of asphalt binder was the smallest, which was similar to that of short-term aging degree. It indicated that the factors such as large temperature difference and high temperature in Northwest China have a certain effect on asphalt binder aging, but the effect range was small. The natural aging degree of thermal oxygen + UV aging asphalt binder was large, and the deepening of UV aging degree of asphalt binder can be obviously felt. Strong UV radiation is a great challenge for asphalt pavement in Northwest China. Rain, wind, and dust have little effect on asphalt binder aging. They even cover the all-weather aging surface, reducing the contact area between the asphalt binder and the external environment. The aging of asphalt binder by oxygen and UV radiation was reduced.

3.2. Effect of Natural Aging on the Chemical Composition of Asphalt Binder

3.2.1. The Effect of Natural Aging Based on Functional Group. FTIR is a rapid method to analyze the information of functional groups in organic materials. It can judge whether there is a certain type of functional group in the molecule according to the wave number, peak shape, intensity, and quantity of the spectrum in the scanned sample spectrum. Then, the different types of functional groups in asphalt binder are evaluated. FTIR was used to analyze the functional group information of virgin asphalt binder undergoing different aging modes. The results were shown in Figure 7.

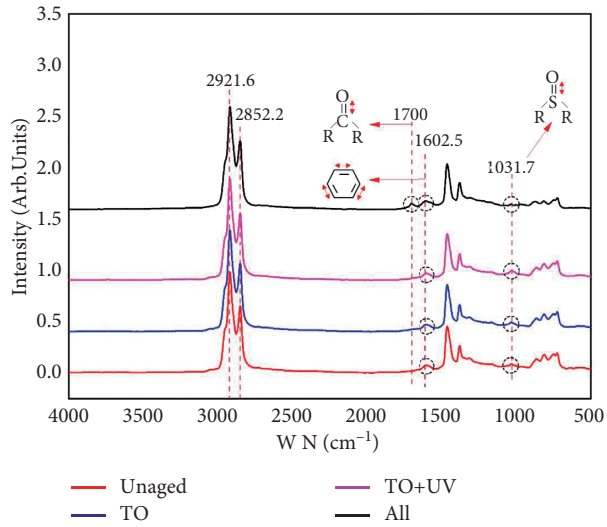

Figure 7: FTIR spectrum of asphalt binder before and after natural aging.

As shown in Figure 7, the unaged virgin asphalt binder contained a variety of characteristic peaks, including the antisymmetric stretching vibration peak of methylene (-CH2-) of 2920 cm^{-1}, the symmetrical stretching vibration peak of methylene (-CH2-) of 2850 cm^{-1}, the C–H plane stretching vibration peak in methyl (C–CH3) of 1460 cm^{-1}, the C–H plane stretching vibration peak in –CH2-, and the -CH3 symmetrical variable angle absorption peak of 1376 cm^{-1}. All these showed that asphalt binder is mainly composed of alkanes. The absorption peak near 1600 cm^{-1} is partly caused by the skeleton vibration of benzene ring. Therefore, it can be judged that there are aromatic compounds in asphalt binder. The carbonyl absorption peak is between 1800 and 1650 cm^{-1}. The absorption peak of sulfoxide group is near 1030 cm^{-1}. Carbonyl group and sulfoxide group were often used to characterize the aging of asphalt binder [23].

It can be found that the characteristic absorption peaks of asphalt binder before and after aging were roughly unchanged by comparing the unaged asphalt binder and natural aged asphalt binder. There were strong absorption peaks in the wave number range of 2852–2958 cm^{-1}, and there was no change in the height of the peak before and after aging. It showed that aging has little effect on alkanes, such as C–H, C–CH3 and C–CH2- in asphalt binder. According to Lambert-Beer law, the absorption peak intensity of functional groups was directly proportional to their concentration. The carbonyl characteristic peak of all-weather aged asphalt binder appeared at 1700 cm^{-1}. There was no obvious absorption peak in other natural aging asphalt binder samples. It can be found from 1600 cm^{-1} that the absorption peak of all-weather aged asphalt binder and thermal oxygen + UV aged asphalt binder was slightly higher than that of unaged asphalt binder. It showed that aging will increase the content of aromatic rings in asphalt binder. On the whole, although natural aging had little effect on the functional group composition of virgin asphalt binder, it still increased the content of polar functional groups. The content of carbonyl and sulfoxide increased obviously after the addition of UV radiation. It showed that the virgin asphalt binder will absorb oxygen during natural aging and generate oxygen-containing polar functional groups, such as carbonyl and sulfoxide.

3.2.2. The Effect of Natural Aging Based on Average Molecular Weight. According to different statistical average methods, the average molecular weight can be calculated as follows.

$$
\begin{aligned}
M_n &= \frac{\sum N_i M_i}{\sum N_i} = \frac{\sum W_i}{\sum W_i / M_i} \\
M_w &= \frac{\sum N_i M_i^2}{\sum N_i M_i} = \frac{\sum W_i M_i}{\sum W_i} \\
M_Z &= \frac{\sum N_i M_i^3}{\sum N_i M_i^2} = \frac{\sum W_i M_i^2}{\sum W_i} \\
D &= \frac{M_w}{M_n},
\end{aligned}
\tag{1}
$$

where M_n = average molecular weight calculated by molecular number; M_W = average molecular weight calculated by molecular weight; M_Z = average molecular weight calculated by Z-value; M_i = average molecular weight; N_i = molecular number; W_i = molecular weight; D = polydispersity index.

The average molecular weight of virgin asphalt binder samples with different aging methods were shown in Table 1.

It can be seen from Table 1 that the values of the average molecular weight calculated by different statistical methods of asphalt binder samples were increased after natural aging. From the perspective of Mn, thermal oxygen + UV aging had the greatest impact on asphalt binder samples. However, from the perspective of Mn, MZ, and D, the effect of different aging conditions on asphalt binder aging was as follows: All weather aging > thermal oxygen + UV aging > thermal oxygen aging. It showed that the molecular weight of asphalt binder increased after natural aging, which also complicated the internal ring structure of asphalt binder. In comparison,

Table 1: The average molecular weight of asphalt binder samples.

Samples	M_n	M_w	M_z	D
Unaged	385	1163	2945	3.0208
TO	506	1255	2813	2.4802
TO + UV	524	1488	3923	2.8397
All	474	1684	4060	3.4770

Table 2: The effect degree of different natural aging methods on the properties of asphalt binder.

Properties	Effect
Viscoelastic properties	TO + UV > all > TO
High-temperature performance	All > TO + UV > TO
Stiffness modulus at −6°C	All > TO + UV > TO
Stiffness modulus at −12°C	All = TO + UV > TO
Stiffness modulus at −18°C	All > TO + UV > TO
Functional group	All > TO + UV > TO
M_n	TO + UV > TO > all
M_w	All > TO + UV > TO

thermal oxygen aging had little effect on asphalt binder. The effect of thermal oxygen + UV aging on asphalt binder is relatively large, which is similar to that of all-weather aging. It can be seen that the addition of UV radiation had a great impact on asphalt binder.

3.2.3. The Effect of Natural Aging on Asphalt Binder. The effect degree of different natural aging methods on the macro- and microproperties of asphalt binder was shown in Table 2.

As shown in Table 2, different natural aging methods had similar effects on the macro- and microproperties of asphalt binder at the same aging time. It showed that the aging degree increases with the increase of aging factors, but the action of wind, dust, and rain had antiaging effect on asphalt binder. They can cover the all-weather aging surface, reducing the contact area between the asphalt binder and the external environment.

Functional groups were formed by oxygen absorption during natural aging of asphalt binder. There were permanent dipoles between polar functional groups and electrostatic forces between them during movement. It can accelerate the addition and association of small molecules and produce more macromolecules or larger molecules. The intermolecular force was enhanced, and the molecular weight of the material was increased. The molecular weight of materials was closely related to their properties [24]. The movement of molecules in substances with large molecular weight was subject to large internal friction resistance. The free movement between molecules will be limited, it was not easy to move, and the overall modulus of the material will be high. At high temperature, the internal molecular movement of aging asphalt binder requires more energy, and the high-temperature performance will be increased. At low temperature, the internal molecules of asphalt binder were not easy to move, the asphalt binder was hard and brittle, and the low-temperature performance was poor.

4. Conclusion

Combined with the complex climate environment in the cold and arid region of Northwest China, the effect of natural aging on the macro- and microproperties of virgin asphalt binder was analyzed. It was comprehensively analyzed by means of macromechanical analysis and microchemical composition characterization. The evolution law of asphalt binder natural aging in cold and arid region was revealed. The main conclusions of this study were as follows:

(1) The effects of natural aging and laboratory simulated aging on asphalt binder properties are similar. The aging degree of natural aging on asphalt binder in one year is similar to that of laboratory short-term aging. It will reduce the viscoelastic properties of asphalt binder, increase the risk of low-temperature cracking, and enhance the deformation resistance of asphalt binder.

(2) There was little effect on the aging performance of asphalt binder after natural aging one year. The aging degree of asphalt binder was obviously deepened by UV radiation in Northwest China. Strong UV radiation was a great challenge for asphalt pavement in Northwest China. Wind, dust, rain, and other factors have little effect on asphalt binder aging.

(3) Affected by the natural environment, macromolecular structures such as oxygen-containing polar functional groups will form in asphalt binder. The molecular weight of asphalt binder was increased, and the internal molecules of asphalt binder were subjected to large internal friction resistance in the process of movement. The macroscopic physical properties and road performance of asphalt binder become poor.

(4) Finally, it is worth noting that the natural environment will give a great effect on asphalt pavement, and further studies should be conducted to evaluate the effect of natural environment on the aging performance of asphalt mixture and pavement structure.

Data Availability

The data used to support the findings of this study are included within the article.

Conflicts of Interest

The authors declare that they have no conflict of interest.

Acknowledgments

This study was funded by National Natural Science Foundation of China (51808016, 52078018), Young Elite Scientists Sponsorship Program by China Association for Science and Technology (2018QNRC001) and Science and Technology Project of Gansu Province (20YF3GA007, 21JR7RA786, 21YF5GA041).

References

[1] C. S. Wang, Z. J. Fan, and S. C. Dong, "Eco-economical regionalization-a case study of the northwest," *Acta Ecologica Sinica*, vol. 25, no. 7, pp. 1804–1810, 2005.

[2] Y. Zhang, C. Zhao, and W. S. Li, "Study on evaluation model for the asphalt pavement diseases of expressway," *Journal of Inner Mongolia Agricultural University*, vol. 02, pp. 103–106, 2006.

[3] O. Sirin, D. K. Paul, and E. Kassem, "State of the art study on aging of asphalt mixtures and use of antioxidant additives," *Advances in Civil Engineering*, vol. 2018, Article ID 3428961, 2018.

[4] E. Rahmani, M. K. Darabi, D. N. Little, and E. A. Masad, "Constitutive modeling of coupled aging-viscoelastic response of asphalt concrete," *Construction and Building Materials*, vol. 131, pp. 1–15, 2017.

[5] S. Spadoni, A. Graziani, and F. Canestrari, "Laboratory and field investigation of grouted macadam for semi-flexible pavements," *Case Studies in Construction Materials*, vol. 16, 2022.

[6] I. Menapace and E. Masad, "Evolution of the microstructure of unmodified and polymer modified asphalt binders with aging in an accelerated weathering tester," *Journal of Microscopy*, vol. 263, no. 3, pp. 341–356, 2016.

[7] S. Weigel and D. Stephan, "Relationships between the chemistry and the physical properties of bitumen," *Road Materials and Pavement Design*, vol. 19, no. 7-8, pp. 1636–1650, 2018.

[8] S. Anjan kumar and A. Veeraragavan, "Dynamic mechanical characterization of asphalt concrete mixes with modified asphalt binders," *Materials Science and Engineering: A*, vol. 528, no. 21, pp. 6445–6454, 2011.

[9] H Alexander, R Quintant, and F Alberto, "Influence of the Bogotá environmental conditions on the mechanical behavior of an asphalt mixture," *Revista de la Facultad de Ingenieria*, vol. 24, no. 4, pp. 195–207, 2011.

[10] M. Guo, X. Liu, Y. Jiao, Y. Tan, and D. Luo, "Rheological characterization of reversibility between aging and rejuvenation of common modified asphalt binders," *Construction and Building Materials*, vol. 301, no. 6, Article ID 124077, 2021.

[11] M. Guo, H. Liu, Y. Jiao et al., "Effect of WMA-RAP technology on pavement performance of asphalt Mixture: A state-of-the-art review," *Journal of Cleaner Production*, vol. 266, Article ID 121704, 2020.

[12] K. Zhao, Y. Wang, and F. Li, "Influence of ageing conditions on the chemical property changes of asphalt binders," *Road Materials and Pavement Design*, vol. 22, no. 3, pp. 653–681, 2021.

[13] J. C. Petersen, "Chemical composition of asphalt as related to asphalt durability: State of the art," *Transportation Research Record Journal of the Transportation Research Board*, vol. 999, pp. 13–30, 1984.

[14] M. Guo, M. Liang, Y. Fu, A. Sreeram, and A. Bhasin, "Average molecular structure models of unaged asphalt binder fractions," *Materials and Structures*, vol. 54, no. 4, p. 173, 2021.

[15] Y. Ruan, R. R. Davison, and C. J. Glover, "Oxidation and viscosity hardening of polymer-modified asphalts," *Energy & Fuels*, vol. 17, no. 4, pp. 991–998, 2003.

[16] S. Xu, J. Yu, C. Hu, D. Qin, and L. Xue, "Laboratory evaluation of rejuvenation effect of reactive rejuvenator on aged SBS modified bitumen," *Materials and Structures*, vol. 50, no. 6, p. 233, 2017.

[17] G. Liu, T. Yang, J. Li, Y. Jia, Y. Zhao, and J. Zhang, "Effects of aging on rheological properties of asphalt materials and asphalt-filler interaction ability," *Construction and Building Materials*, vol. 168, pp. 501–511, 2018.

[18] Y. T. Qi and F. X. Wang, "Study and evaluation of aging performance of petroleum asphalts and their constituents during oxygen absorption. III. average molecular structure parameter changes," *Petroleum Science and Technology*, vol. 22, no. 3-4, pp. 275–286, 2004.

[19] M. Guo, M. Liang, A. Sreeram, A. Bhasin, and D. Luo, "Characterisation of rejuvenation of various modified asphalt binders based on simplified chromatographic techniques," *International Journal of Pavement Engineering*, vol. 2, pp. 1–11, 2021.

[20] C. Xing, L. Liu, Y. Cui, and D. Ding, "Analysis of base bitumen chemical composition and aging behaviors via atomic force microscopy-based infrared spectroscopy," *Fuel*, vol. 264, Article ID 116845, 2020.

[21] H. Liu, Z. Zhang, J. Xie, Z. Gui, N. Li, and Y. Xu, "Analysis of OMMT strengthened UV aging-resistance of Sasobit/SBS modified asphalt: Its preparation, characterization and mechanism," *Journal of Cleaner Production*, vol. 315, Article ID 128139, 2021.

[22] I. Marek, C. Małgorzata, and M. Grzegorz, "Viscoelastic properties of polymer modified bitumen in warm mix asphalt technology in terms of ageing," *Procedia Engineering*, vol. 172, pp. 401–408, 2017.

[23] X. Cao, H. Wang, X. Cao, W. Sun, H. Zhu, and B. Tang, "Investigation of rheological and chemical properties asphalt binder rejuvenated with waste vegetable oil," *Construction and Building Materials*, vol. 180, pp. 455–463, 2018.

[24] D. A. Netzel and T. F. Turner, "NMR characterization of size exclusion chromatographic fractions from asphalt," *Petroleum Science and Technology*, vol. 26, no. 12, pp. 1369–1380, 2008.

Hindawi
Advances in Materials Science and Engineering
Volume 2022, Article ID 5722752, 8 pages
https://doi.org/10.1155/2022/5722752

Research Article

Analysis of Coupling Effect and Heavy Load of High-Temperature Stability of Asphalt Mixture

Lu Bai,[1] **Yong-sheng Zhang**,[2] **and Dai-song Luo**[2]

[1]*School of Civil Engineering, Xuchang University, Xuchang 461000, China*
[2]*China Academy of Transportation Science, Beijing 100029, China*

Correspondence should be addressed to Lu Bai; lubai526@126.com

Received 14 October 2021; Revised 9 February 2022; Accepted 21 February 2022; Published 14 March 2022

Academic Editor: Chundi Si

To study the variation in the high-temperature stability of asphalt mixtures under extreme high temperature and heavy load, rut tests and analyses were carried out with both the APA (asphalt pavement analyzer) test and CLWT (Chinese wheel load test). In this paper, the relationship model between the dynamic stability of asphalt mixtures and the temperature, load, and binder viscosity is established; this model provides a method for evaluating the temperature stability of asphalt mixtures under nonstandard temperature conditions. The results revealed that the dynamic viscosity of an SBS-modified asphalt binder showed an exponential relationship with temperatures varying from 55°C to 70°C. Under a temperature condition from 55°C to 70°C and a pressure of 0.7 MPa, the dynamic stability of the asphalt mixture increased linearly with increasing temperature. The dynamic stability of the asphalt mixture exhibited a temperature inflection point at 65°C, and the decay rate was increased. The APA test results, which were used to evaluate the anti-rutting performance of the asphalt mixture on the basis of the ratio of the rutting depth difference to action times from 6000 to 8000, showed a good correlation with the CLWT test results. With a high temperature of 65°C and the pressure increasing from 0.7 MPa to 1.3 MPa, the dynamic stability of the asphalt mixture exhibited exponential decay. The variation laws of dynamic stability with temperature, load, and asphalt binder viscosity were revealed by complex logarithmic variation.

1. Introduction

Rutting not only influences the appearance and smoothness of the pavement of a road surface but also causes discomfort and potential safety hazards to road users; these problems are mainly the results of deformations in asphalt mixtures under high temperatures and heavy traffic loads. According to investigations, the temperature in the pavement structure layer in most areas of southern China exceeds 65°C [1]. Therefore, to study the performance of high anti-rutting asphalt mixtures, it is necessary to analyze the variation law of the dynamic stability of the asphalt mixtures with temperature. It has been shown that the rutting depth increased by approximately 1.8 times when the temperature was increased by 5°C from 40°C to 60°C, and the rutting depth increased by roughly the same multiple as the axle load [2]. Li Xi analyzed the influence of the true coupling of temperature and load on the rutting of asphalt pavement and concluded that the dynamic stability of the asphalt mixture as obtained by the Marshall method dropped suddenly at 60°C, and the maximum reduction rate of the dynamic stability of the asphalt mixture obtained by the rotary testing machine method (GTM) appeared at 70°C [3]. Sun and others carried out rutting tests with a wheel rutting tester for AC-20 under different temperatures from 40°C to 70°C and wheel pressures and confirmed that wheel pressure and temperature had a significant effect on the rutting resistance of asphalt mixtures [4]. Using new rutting test equipment with changing wheel speed and load to simulate the influences of overload and temperature (loading time) on asphalt mixtures, Jiang Li found that increasing the load time was equivalent to raising the experimental temperature and that using the temperature conditions in the specification to verify the high-temperature stability of asphalt mixtures for

uphill sections with long and large longitudinal slopes was unreasonable [5]. Through a simple performance dynamic modulus test (SPT), a standard rutting test, a Hamburg rutting test, a French rutting test, and an asphalt pavement analyzer rutting test, Sheng Li evaluated the rutting resistance of asphalt mixtures in the middle and lower courses of three semirigid base asphalt pavements of a full-scale test track road in Beijing, China, and concluded that the APA rutting test was the optimal testing method for evaluating the rutting performance of semirigid base asphalt pavements [6]. By simulating nano-ZnO modifier and improving the physical properties of asphalt with the molecular dynamics simulation technology, Manman Su found that nano-ZnO particles increased the bulk modulus, shear modulus, and elastic modulus of asphalt system and improved the high-temperature performance of asphalt [7]. Wang and others studied the rutting resistance of pouring semiflexible pavement under different loads and temperatures and put forward the stability correction index to evaluate the rutting resistance of it [8]. With the increase of tire contact pressure from 0.7 MPa to 1.5 MPa, the maximum deformation of the conventional asphalt pavement was 60% higher than that of high modulus asphalt concrete (HMAC) pavement; therefore, a heavy load is more harmful to the conventional pavement structure [9].

Meanwhile, the index used for evaluating the high-temperature performance and performance under heavy loads of GAC in hot regions still needs to be discussed. Li Zhi developed a design method for the gradation of asphalt mixtures under heavy loads and confirmed that this modification of gradation was successful in resisting rutting [4]. F P. Pramesti utilized a four-point bending test to predict fatigue cracking of GAC and developed a new calibration factor to describe the fatigue life of GAC mixtures [10, 11]. Based on this method, Zhang Yongsheng suggested that the index for evaluating the high-temperature performance and performance under heavy loads of GAC used in the Wu Shen Expressway in Guangdong Province should be reconsidered [12]. According to the test results obtained under conditions of different temperatures and loads and the two synchronous conditions, Shi Liwan analyzed the developing rules and established the relationship between the rutting evaluation index and test conditions [13]. By analyzing the influence of high viscosity additive dosage on key property indices, Li and others recommended appropriate dosage and dynamic viscosity standards aimed at different temperatures and load conditions and found a double-logarithmic relation of dynamic stability with dynamic viscosity [14]. Dai and others analyzed the sensitivity of dynamic creep permanent deformation parameters to dynamic stability and concluded that the viscosity coefficient η_1 was positively correlated with the change of dynamic stability(DS) and most sensitive to DS [15]. By establishing the rutting prediction formula across different months and analyzing indoor rutting tests of different types of asphalt mixtures under different temperatures, Li and others analyzed the rutting development on an asphalt pavement under the distribution of pavement temperature field and the actual traffic load and the coupling effect of temperature and load [3]. To evaluate the deformation resistance of modified asphalt mixture under high temperature and heavy load, Ji and others carried out the triaxial repeated load test on two asphalt mixtures under multi-temperature (50°C, 60°C, and 70°C) and multi-load (0.7, 0.8, 0.9, and 1.0 MPa) conditions and proposed two indices, the flow number and nonlinear fitting index, which had negative and positive correlation with temperature and load, respectively [16].

In the above studies, many researchers have suggested establishing the relationship between the DS and viscosity of asphalt binders, temperature, or load. However, an evaluation index to describe the relationship between the DS and viscosity of asphalt binders, temperature, and load is in demand because it can be used to evaluate the anti-rutting performance of asphalt mixtures under nonstandard high-temperature and heavy-load conditions. First, CLWTs and APA tests were conducted at different temperatures to determine the crucial temperature of the anti-rutting performance of GAC mixtures. Then, the correlation between the results from the CLWT and APA test was confirmed. The relationship between DS and the viscosity of asphalt mixtures as well as traffic loads was also examined. Finally, the fitting results of DS were confirmed based on the temperature, traffic loads, and viscosity of modified asphalt used in GAC mixtures.

2. Test Programme

2.1. Gradation Design of Asphalt Mixture. It has been shown that the viscosity was an indicator of asphalt binder viscosity, and it was used to reflect the degree of friction damping of molecules in fluid against molecules flowing temporarily. The viscosity of asphalt binder at 60°C was generally considered to reflect the heat resistance of the binder in the high-temperature season, but it was shown that the temperature of asphalt pavement in China reached nearly 70°C. Therefore, it is necessary to perform experiments to establish the relationship between the viscosity of SBS and temperature.

To imitate the temperature in southern areas of China, such as Guangdong Province, the experimental temperatures were set as 55°C, 57°C, 60°C, 63°C, 65°C, 67°C, and 70°C. The modified asphalt tested was SBS (I-D). The equipment used for the test was the widely used vacuum capillary viscometer tester (VCVT) utilized in previous research [17]. Note that three different models of specimens were used in this experiment. The results of the viscosity of SBS (I-D) in relation to temperature are shown in Table 1.

The relationship between the temperature and viscosity of modified asphalt can be described by

$$\eta = 6 \times 10^7 \times e^{(-0.12T)}, \quad R^2 = 0.9615, \tag{1}$$

where η is the viscosity of asphalt binder (Pa · s) and $R^2 = 0.9615$.

The aggregate of the asphalt mixture was limestone which was acquired from the Renhua area of Guangdong Province, and the design results of the asphalt mixture gradation GAC-20C are shown in Table 2.

Table 1: Viscosity of SBS-modified asphalt binder at different temperatures.

Temperature (°C)	Type of capillary	Average viscosity (Pa · s)
70	200	11219
67	200	23491
65	200	29950
63	200	31896
60	400	35533
57	400	67943
55	800	83750

Table 2: Design results of the GAC-20C gradation.

	Mass percentage (%) through the following sieve holes (mm)											
Sieve holes (mm)	26.5	19	16	13.2	9.5	4.75	2.36	1.18	0.6	0.3	0.15	0.075
Mass percentage (%)	100	97.5	84.5	73	56	36	28	20	16	12	8	5

2.2. Rutting Test. The rutting tests based on the Chinese load wheel test (CLWT) and asphalt pavement analyzer (APA) were as follows [18–20].

2.2.1. CLWT for Rutting. The CLWT has been widely used to verify the high-temperature stability of asphalt mixtures. To imitate the high temperature in southern areas of China, such as Guangdong Province, the experimental temperatures were set as 55°C, 57°C, 60°C, 63°C, 65°C, 67°C, and 70°C. The sizes of the specimens used for the CLWT were 300 mm × 300 mm×50 mm cuboids, which were compacted by the wheel-grind method with an air void of 4.5%. The rutting test was performed after maintaining the specimens at a specific experimental temperature for no less than 6 hours. The rutting speed back and forth was set at 42 times/min, and the loading pressure was set as 0.7 MPa. The ratio of loading times to rutting deformation at 45 min and 60 min was chosen as the dynamic stability (DS). The DS was chosen as the index to evaluate the anti-rutting performance of the asphalt mixtures. The value of DS is calculated according to

$$DS = \frac{(t_2 - t_1) \times N}{d_2 - d_1} \times c_1 \times c_2, \quad (2)$$

where d_1 represents deformation at 45 min (mm), d_2 represents deformation at 60 min (mm), N represents loading times (42 times/min), c_1 represents modifying coefficient for the size of the specimen (1.0 was selected here), c_2 represents modifying coefficient for the type of experimenting equipment (1.0 was selected here), $t_1 = 45$ min, and $t_2 = 60$ min.

The results of the test under different temperatures are summarized in Table 3.

A linear function was generated to fit the relationships between DS and experimental temperature. The function and the coefficient are presented in the following equation:

$$DS = a_1 T + b_1, \quad (3)$$

where a_1 is −590.17, b_1 is 44328, and R^2 is 0.9929.

The linear relationship between DS and experimental temperature is shown in Figure 1.

Table 3: Results of the CLWT.

Temperature (°C)	55	57	60	63	65	67	70
DS (times/mm)	12230	10734	8491	6929	5887	4843	3276

It is obvious that DS decreases remarkably as the experimental temperature increases. The percentage decrease in DS is shown in Figure 2.

When the test temperature is between 55°C and 65°C, the DS of the asphalt mixture decreases by 30.57% and 30.67% for every 5°C increase in temperature. When the test temperature increased from 65°C to 70°C, the DS of the asphalt mixture sharply decreased by 44.35%. It was indicated that 65°C was the temperature inflection point of the dynamic stability of the asphalt mixture. When the pavement temperature exceeds 65°C, the dynamic stability of the asphalt mixture decreases sharply. Under loading, asphalt pavement is more prone to deformation.

2.2.2. APA Test. The sizes of the specimens used for the APA test were φ150 mm × 75 mm cylinders, which were formed by a Superpave gyratory compactor (SGC) with an air void of 4.5%. Specimens were maintained for 2 hours at the APA test temperature of 55°C, 57°C, 60°C, 63°C, 65°C, 67°C, or 70°C after 2 hours at normal temperature. The loading pressure of the experimental tire was 45 kg (101.5 lbs). The number of loading times was set as 8000. The initial pressure in the rubber tube was set as 0.7 MPa (100 psi). The loading speed back and forth was set as 42 times/min to be in accordance with the CLWT. The ratio of loading times to deformation of 6000 times and 8000 times was defined as dynamic stability in the APA test, which was referred to as DS1. The value of DS1 is calculated according to the following equation:

$$DS_1 = \frac{N_2 - N_1}{d_2' - d_1'}, \quad (4)$$

where d_1' represents deformation when loaded 6000 times (mm), d_2' represents deformation when loaded 8000 times (mm), N_1 represents loading times (6000), and N_2 represents loading times (8000).

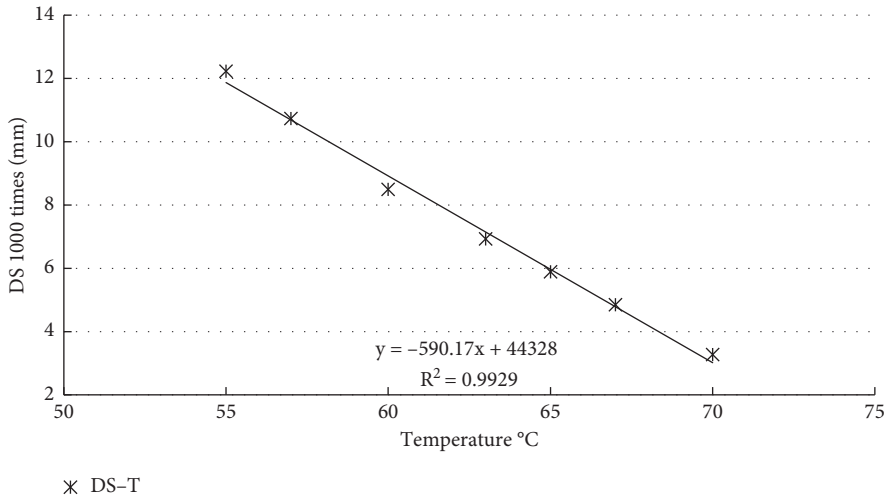

Figure 1: Relationship between DS and experimental temperature.

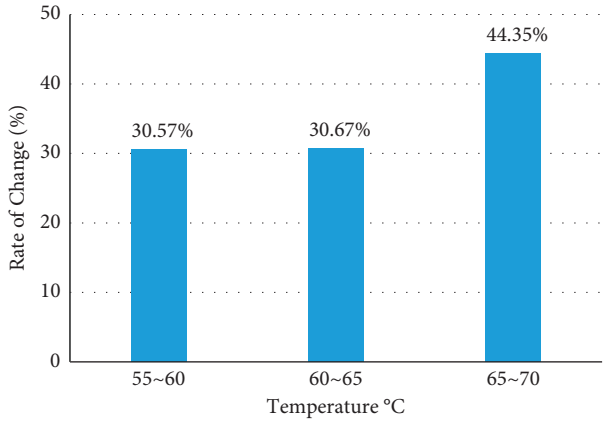

Figure 2: Percentage decrease in DS caused by the increase in temperature.

The results of DS_1 according to the experimental temperature are shown in Table 4.

The data from Table 4 show that the result obtained from the APA test is similar to that from the CLWT. A linear function was also generated to fit the relationship between DS1 and the experimental temperature. The function and the coefficient are presented in the following equation:

$$DS_1 = a_2 T + b_2, \tag{5}$$

where a_2 is −527.08, b_2 is 40185, and R^2 is 0.9939.

The linear relationship between DS_1 and the experimental temperature is drawn in Figure 3.

With the increase of pavement temperature field temperature, the viscosity of asphalt binder decreases, which results in the decline of adhesion between asphalt and aggregate and the decline of the resistance to deformation of asphalt mixture. It is obvious that DS decreases remarkably as the experimental temperature increases. The percentage decrease of DS_1 is shown in Figure 4. When the test temperature is between 55°C and 65°C, the DS_1 of the asphalt mixture decreases by 28.40% and 29.15% for every 5°C increase in temperature. When the test temperature increased from 65°C to 70°C, the DS_1 of the asphalt mixture sharply decreased by 39.15%. It was indicated that 65°C was the temperature inflection point of the dynamic stability of the asphalt mixture.

Table 4: Results of the APA test.

Temperature (°C)	55	57	60	63	65	67	70
DS_1 (times/mm)	11494	10181	8230	6791	5831	4910	3527

2.2.3. Correlations between APA Test and CLWT. To determine the anti-rutting performance of GAC mixtures under high temperature and high loading pressure, other experiments measuring the viscosity and DS under high loading pressure of asphalt mixtures need to be performed. However, only the APA test can be used to conduct the latter experiments. Therefore, the correlations between the results from the CLWT and APA test were conducted to determine whether the APA test experiments can replace the CLWT to determine the anti-rutting performance of GAC mixtures. Based on correlation analysis with Microsoft Office Excel, the relationships between the results from the two rutting tests were examined. The fitting function is shown in (6), while Figure 5 shows the two DS-temperature curves.

$$Y = 0.8926X + 600.04, \tag{6}$$

where R^2 is 0.9999.

The results of the two tests have good correlations with each other, so it is reasonable to perform rutting tests using APA to evaluate the anti-rutting performance of GAC mixtures under different temperatures and loading pressures. The following experiments are based on this assumption.

2.2.4. Experiments on Loading Pressures. Experiments aiming to evaluate the anti-rutting performance of GAC mixtures under heavy loading pressures were performed. The size of the specimens was the same as that used in APA

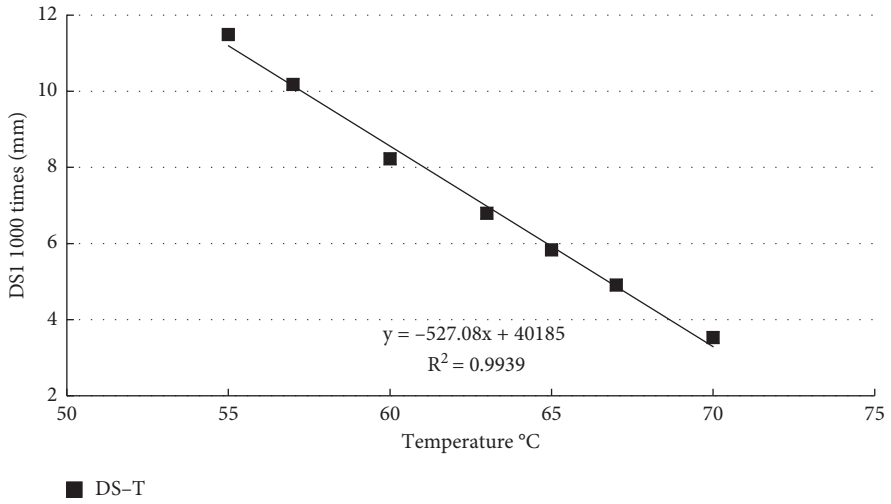

Figure 3: Relationship between DS_1 and experimental temperature.

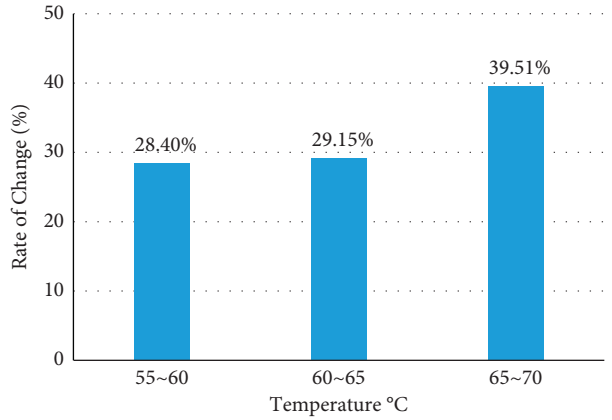

Figure 4: Percentage decrease in DS_1 caused by the increase in temperature.

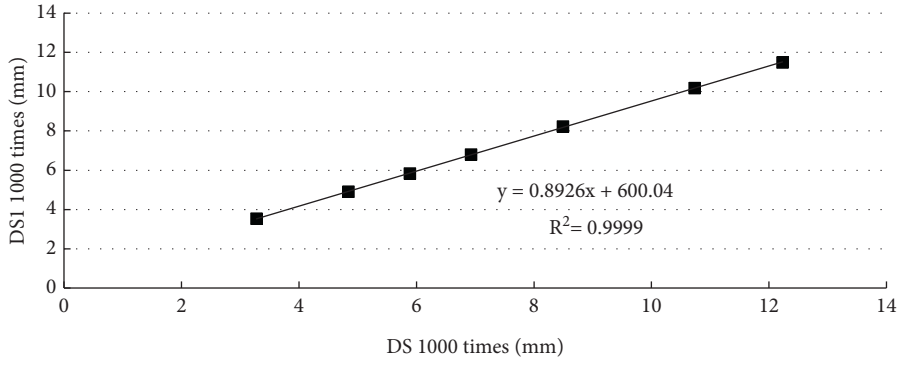

Figure 5: DS-temperature curves of the two tests.

in previous experiments. Four groups of tests were conducted with 3 specimens in each group. To imitate a heavy loading pressure, the pressures of the experiments were set as 0.7 MPa, 0.8 MPa, 0.9 MPa, 1.0 MPa, 1.1 MPa, 1.2 MPa, and 1.3 MPa, while the temperature was set as 65°C [1]. Note that 0.7 MPa is the standard axle load set in the specifications (JTG E20-2011) [21]. The number of loading times was 8000, and the loading speed was the same [22]. Table 5 shows the DS results under different loading pressures.

The relationship between DS and loading pressure can be fitted with

Table 5: Relationship between loading pressures and DS.

Loading P (MPa)	0.7	0.8	0.9	1	1.1	1.2	1.3
DS (times/mm)	5831	4210	3057	2485	1789	1460	1194

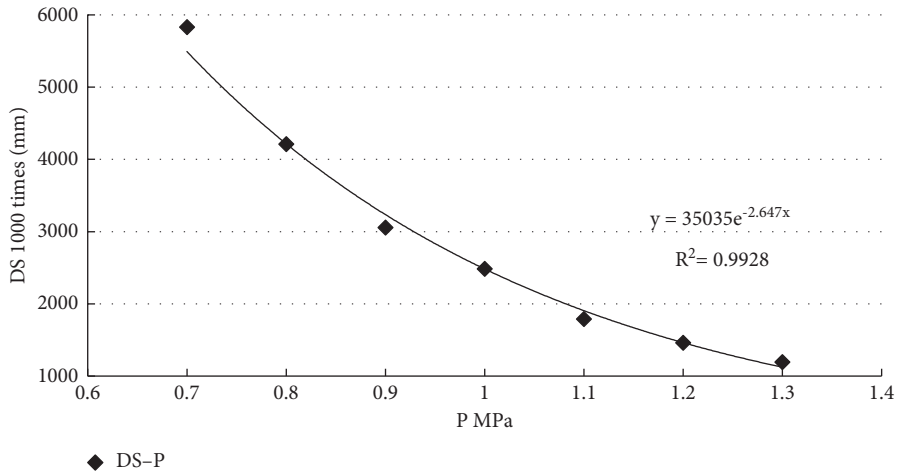

Figure 6: Relationship between loading pressures and DS.

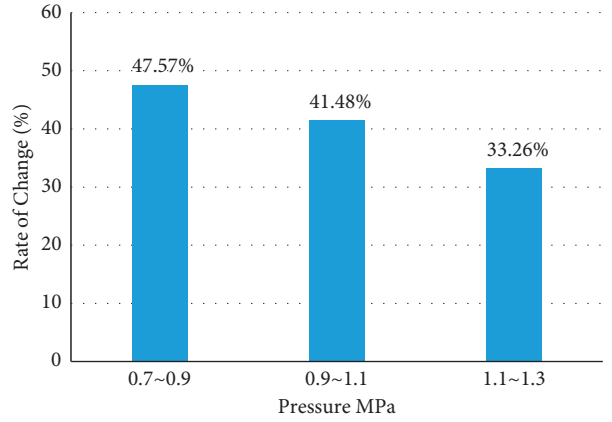

Figure 7: Percentage decrease in DS according to the increase in loading pressure.

$$DS = a_4 e^{-2.647P} + b_4, \quad (7)$$

where $a_4 = 35035$ and $R^2 = 0.9928$.

The DS-loading pressure curve is shown in Figure 6.

It can be seen from Figure 7 that when increasing the loading pressure from 0.7 MPa to 1.3 MPa by 0.2 MPa each time, the decrease in DS is 47.57%, 41.48%, and 33.26%, respectively. When compared with the drop in DS due to the increase in experimental temperature, it was concluded that the drop in DS of GAC mixtures mainly results from the rise in temperature (5°C each time), and the rise caused by changes in temperature is much less than that caused by the rise in loading pressure (0.2 MPa each time).

2.3. Influence of Asphalt Viscosity on DS of Asphalt Mixtures. It has been shown that the viscosity of the binder decreases and the strength of the asphalt mixture weakens with increasing pavement temperature. The results of the rutting test were combined with the results shown in Table 2 to determine the relationship between DS and the viscosity of modified asphalt. The results of the CLWT and APA test are shown in Figures 8(a) and 8(b).

It can be indicated from the two curves that the dynamic stability changes in the same trend with the change of asphalt viscosity. With the increase of temperature, the viscosity of asphalt and the dynamic stability of asphalt mixture decreases. The relationship between DS and the viscosity of modified asphalt can be described by

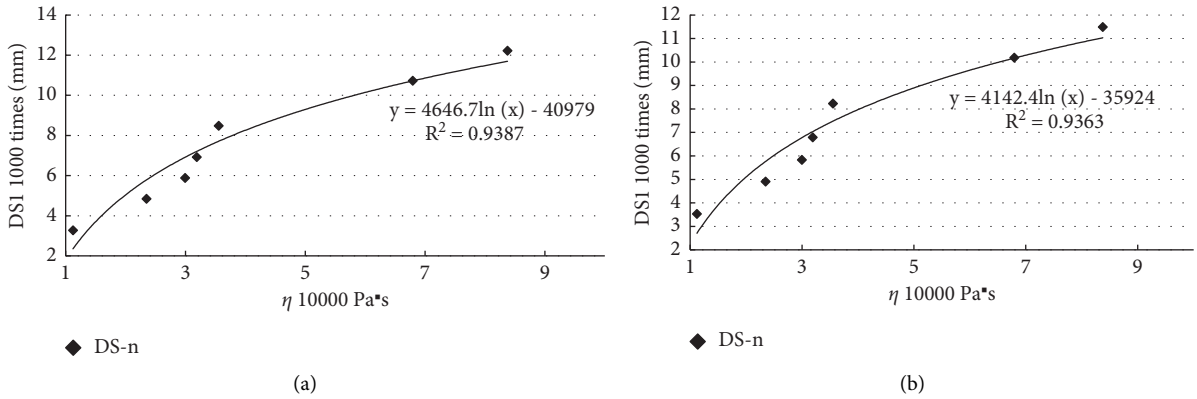

Figure 8: Relationship between DS and modified asphalt. (a) CLWT. (b) APA test.

$$DS = a_3 \ln(\eta) + b_3. \tag{8}$$

For the CLWT:

$$\begin{aligned} a_3 &= 4646.7, \\ b_3 &= -40979, \\ R^2 &= 0.9387. \end{aligned} \tag{9}$$

For the APA test:

$$\begin{aligned} a_3 &= 4142.4, \\ b_3 &= -35924, \\ R^2 &= 0.9363. \end{aligned} \tag{10}$$

2.4. High-Temperature Stability of Asphalt Mixtures under Coupling Action. Based on the fitting method referred to in previous studies [23], the relationship between the DS of GAC mixtures and the temperature, viscosity, and loading pressures is shown in (11) based on data from Tables 2–5:

$$\ln(DS) = a_4 \ln(T) + b_4 \ln(c_4 P + d_4) + m \ln \ln(\eta) + n, \tag{11}$$

where $a_4 = -3.0343$, $b_4 = -2.4358$, $c_4 = 0.2699$, $d_4 = -0.0124$, $m = 2.3732$, $n = 11.5707$, and $R^2 = 0.8312$.

The anti-rutting performance of the mixtures was related to dynamic stability. The higher the dynamic stability of the asphalt mixture is, the stronger the anti-rutting performance is. In this paper, the relationship between dynamic stability and different high temperatures, loads, and viscosities of asphalt binder is established, which will be used to determine the dynamic stability of asphalt mixtures under nonstandard conditions, and the coefficients in (11) are determined by using the experimental data of dynamic stability of different mixtures under the conditions of standard temperature, load, and viscosity.

3. Conclusions

In this paper, experiments were conducted to evaluate the anti-rutting performance of GAC mixtures under high temperature and heavy traffic loads. Tests based on both the CLWT and APA test were performed, and the results from these two tests were compared. The conclusions are drawn as follows:

(1) The results from both rutting tests suggest that the anti-rutting performance of GAC mixtures decreases remarkably when increasing the temperature or loading pressure. The results of the correlation analysis indicate that the APA test can replace the CLWT to evaluate anti-rutting performance. There is a good correlation between the two rutting test results.

(2) The comparison of the influences of temperature and loading pressure on DS suggests that the drop in DS resulting from an increase in temperature by 5°C is much larger than that resulting from an increase in loading pressure by 0.2 MPa.

(3) The dynamic stability of the asphalt mixture exhibited a temperature inflection point at 65°C, and the decay rate increased.

(4) Under the influence of high temperature, heavy load, and binder viscosity, the dynamic stability of asphalt mixtures was characterized by complex logarithmic variation.

Data Availability

The data used to support the findings of this study are available from the corresponding author upon request.

Conflicts of Interest

The authors declare that they have no conflicts of interest regarding the publication of this study.

Acknowledgments

This study was supported by the Science and Technology Project of Science and Technology Department of Henan Province (grant no. 202102310582), Key Scientific Research Project of Xuchang University (grant no. 2021ZD005), and Horizontal Project of Xuchang University in 2021

(2021HX146). The authors are grateful for the financial support.

References

[1] F. Chen and S. Meng, "Experimental study on anti-rutting accelerated loading of asphalt pavement," *Journal of China and Foreign Highway*, vol. 131, no. 3, pp. 77–81, 2011.

[2] X. Ji, *Study on Standard of High Temperature Performance of Asphalt Mixture in Gansu Province Based on the Full-Scale ALF Test*, Chang'an University, Xi'an, China, 2011.

[3] X. Li, X. Wang, N. Fang, and X. Wang, "Rutting prediction of asphalt pavement based on actual coupling of temperature and load," *Journal of Chang'an University (Natural Science Edition)*, vol. 38, no. 5, pp. 67–75, 2018.

[4] J. Sun, Z. Chen, and T. Xiao, "Effect of wheel pressure and temperature on rut resistance of AC-20 asphalt mixture," *Journal of Chongqing Jianzhu University*, vol. 31, no. 1, pp. 48–50, 2012.

[5] J. Li and E.-h. Yan, "Influence of loading time on high-temperature stability of asphalt mixtures," *Journal of Highway and Transportation Research and Development*, vol. 8, no. 3, pp. 7–12, 2014.

[6] S. Li, M. Fan, L. Xu, W. Tian, H. Yu, and K. Xu, "Rutting performance of semi-rigid base pavement in RIOHTrack and laboratory evaluation," *Frntiers in materials (structural materials)*, vol. 7, Article ID 590604, 2021.

[7] M. Su, C. Si, and H. Zhang, "Molecular dynamics study on influence of Nano-ZnO/SBS on physical properties and molecular structure of asphalt binder," *Journal of Chongqing Jianzhu University*, vol. 40, no. 11, pp. 118–127, 2021.

[8] T. Wang, C. Li, and H. Peng, "Research on rutting resistance of pouring semi - flexible pavement," *Northern Communications*, vol. 9, pp. 43–46, 2021.

[9] C. Si, H. Cao, E. Chen et al., "Dynamic response analysis of rutting resistance performance of high modulus asphalt Concrete pavement," *Applied Sciences*, vol. 8, no. 12, p. 2701, 2018.

[10] F. P. Pramesti, A. A. A. Molenaar, and M. F. C. van de Ven, "The prediction of fatigue life based on four point bending test," *Procedia Engineering*, vol. 54, pp. 851–862, 2013.

[11] F. P. Pramesti, A. A. A. Molenaar, and M. F. C. van de Ven, "Fatigue Cracking of Gravel Asphalt Concrete: Cumulative Damage Determination," *7th RILEM International Conference On Cracking In Pavements*, pp. 739–749, Springer, Dordrecht, Netherlands, 2012.

[12] Y. Zhang, *Research on Asphalt tructPavement Sure Design of WuShen Expressway in Guang Dong Province*, Research Institute of Highway M.O.T, Beijing, China, 2015.

[13] L. Shi, D. Wang, and R. Wu, "Common effects of temperature and load on total thickness rutting of asphalt pavement," *Journal of Huazhong University of Science and Technology (Nature Science Edition)*, vol. 41, no. 11, pp. 37–40, 2013.

[14] J. Li, Y. Li, and M. Li, "Dynamic viscosity standard of high viscosity modified asphalt considering temperature and load coupling effect," *IOP Conference Series: Materials Science and Engineering*, vol. 1075, no. 1, 2021.

[15] W. Dai, R. Hao, and Y. Li, "Sensitivity analysis of creep parameters of hydrophobic nano-silica modified asphalt mixture to dynamic stability," *Materials reports*, vol. 34, no. S1, pp. 237–240, 2020.

[16] J. Ji, L. Chen, and Z. Suo, "Effect of high temperature and heavy load on deformation resistance of DCLR modified asphalt mixture," *Journal of Traffic and Transportation Engineering*, vol. 19, no. 1, pp. 1–8, 2019.

[17] L. Li, H. Geng, and Y. Sun, "Evaluation method and indicator for viscosity of high-viscosity asphalt," *Journal of Building Materials*, vol. 13, no. 3, pp. 352–356, 2010.

[18] H. Chen, Y. Zhou, and B. Wang, "Dynamic mechanics performance of aged SBS modified asphalt," *Journal of Chang'an University (Natural Science Edition)*, vol. 29, no. 1, pp. 1–5, 2009.

[19] H. Wang, H. Tan, and J. Zhang, "Effects of molding shape and air void of asphalt mixture specimen on APA rutting tests," *Journal of Southeast University (Natural Science Edition)*, vol. 46, no. 3, pp. 589–593, 2016.

[20] Q. Zhang, X. Wei, and J. Xu, "Stability analysis for cellular neural networks with variable delays," *Chaos, Solitons & Fractals*, vol. 28, no. 2, pp. 331–336, 2006.

[21] Industry Standard of the People's Republic of China, *JTG E20-2011, Standard Test Methods of Bitumen and Bituminous Mixtures for Highway Engineering*, People's Communications Press, Beijing, China, 2011.

[22] M. Chen, Z. Xu, and Q. Huang, "Experimental study on rutting resistance of asphalt mixture based on heavy load," *Journal of Highway and Transportation Research and Development*, vol. 6, pp. 92–94, 2006.

[23] D. Cao, Q. Liu, and G. Tang, *Porous Asphalt Pavement*, People's Communications Press, Beijing, China, 2010.

Hindawi
Advances in Materials Science and Engineering
Volume 2022, Article ID 5302142, 15 pages
https://doi.org/10.1155/2022/5302142

Research Article

Research and Evaluation on Dynamic Response Characteristics of Various Pavement Structures

Meng Guo[1], **Fujin Hou**[2], **Shuaixiang Zhang**[1], **Xu Li**[3], **Yunliang Li**[3] and **Yufeng Bi**[4]

[1]*The Key Laboratory of Urban Security and Disaster Engineering of Ministry of Education, Beijing University of Technology, Beijing 100124, China*
[2]*Shandong Hi-Speed Construction Management Group Co. Ltd, Jinan 250001, China*
[3]*School of Transportation Science and Engineering, Harbin Institute of Technology, Harbin 150090, China*
[4]*Shandong Provincial Communications Planning and Design Institute Group Co. Ltd, Jinan 250101, China*

Correspondence should be addressed to Shuaixiang Zhang; zhangsx@emails.bjut.edu.cn

Received 18 November 2021; Accepted 15 February 2022; Published 11 March 2022

Academic Editor: Abílio De Jesus

In order to comprehensively analyze the dynamic response of full-depth asphalt pavement under moving load, a three-dimensional model of pavement structure and dynamic load moving zone are established based on ABAQUS finite element software. Based on the time history curves of different structures, the stress-strain states at the bottom of each structural layer in different structures under moving load are analyzed. The results show that the stress, strain, and shear stress of the middle layer of full-depth pavement are smaller than those of semirigid base pavement, and rutting is closely related to the deformation of this layer. The dynamic response results of the same structure at different speeds are similar, but the increase of the maximum speed will increase the shear stress at the bottom of the layer, and the road is more prone to longitudinal crack.

1. Introduction

In recent years, in order to deal with various overload and heavy load pavement conditions in the future, more and more countries begin to study the design and use of asphalt stabilized macadam flexible base in permanent roads, and the full-depth pavement structure has attracted a lot of attention. This kind of pavement can deal with road cracks and other problems depth by easily and quickly treating the surface wearing course. It does not need large-scale repair in the process of realizing the service function for a long time [1–3] and has its unique advantages in combating the reduction of service life caused by fatigue [4, 5].

In the design method of semirigid base course pavement based on classical pavement structure, the design method of the static load instead of vehicle dynamic load cannot reflect the real-time stress state of pavement structure, resulting in cracks, pits, ruts, and other damage phenomena of semirigid base course asphalt pavement before reaching the design service life [6–9]. Therefore, whether for full-depth pavement or semirigid base pavement, it is very necessary to accurately analyze the dynamic response of pavement under vehicle load.

Most of the early studies on the dynamic response of pavement structure under the moving load of heavy vehicles used analytical and experimental methods. In recent ten years, with the advent of the high-performance computer, various numerical methods have become a very effective tool to simulate pavement dynamics and play a more and more important role. There are two commonly used numerical methods: one is to directly use the numerical method to obtain the numerical solution of dynamic response, that is, to directly discretize the difficult partial differential equations and boundary conditions into a series of algebraic equations, and convert the mathematical analysis of continuous functions into a large number of normalized discrete values for calculation. For example, Yang et al. [10] used the Galerkin method to study the dynamic response of double-layer plate on Kelvin foundation under the coupling of vehicle and pavement and analyzed the influence of vehicle

parameters on pavement vibration. The second is the finite element method. The finite element method is a popular numerical simulation method at home and abroad. Its advantage is that it can adapt to complex geometry and boundary conditions and is suitable for solving linear and nonlinear, homogeneous, and heterogeneous problems [11, 12]. Siddharthan et al. [13] proposed a model for analyzing the strain response of pavement under real wheel load based on the finite layer theory. This model can consider the dynamic change of tire grounding pressure, the complex distribution form of grounding pressure, and vehicle speed and viscoelastic properties of materials and compiled a 3D-move finite element program on this basis.

Wu and Shen [14] combined the finite element method with Newmark integral to gradually solve the motion equation and studied the dynamic response of rigid pavement under moving single degree of freedom vehicle load. Yang et al. [15] studied the dynamic response of a three-dimensional-layered foundation under train load by using the combination of three-dimensional finite element and infinite element. Hou et al. [16] applied the three-dimensional finite element method to calculate the deformation and stress of the plate on Winkler foundation under moving point load, analyzed the natural frequency and critical speed of the plate, and discussed the effects of load moving speed, plate material parameters, and foundation parameters on the deflection and stress of the plate. Li [17] established a layered three-dimensional finite element model of semirigid pavement with ANSYS as the calculation tool, studied the stress and strain distribution characteristics of semirigid pavement under vehicle moving load, and analyzed the effects of driving speed, load, and wheel braking on pavement dynamic response. Shu and Qian [18] and Shan et al. [19] studied the dynamic characteristics of pavement structure based on ADINA and ABAQUS, respectively. Pei et al. [20] established the three-dimensional finite element model of asphalt pavement under different axle types through field investigation and studied the dynamic response of asphalt pavement under different axle load distribution conditions such as single rear axle, double rear axle, and three rear axles, respectively. Liu et al. [21] analyzed the dynamic response law of asphalt pavement structure under moving load by establishing the three-dimensional finite element model of pavement structure and compiling DLOAD and UTRACLOAD subroutines. Dong et al. [22] established the finite element model of asphalt pavement based on the assumption of transverse isotropy of materials and compared and analyzed the dynamic responses of isotropic and transverse isotropic models under moving load. Huang et al. [23] analyzed the influence of structural parameters on the dynamic response of asphalt pavement and analyzed the sensitivity of pavement structural parameters in combination with an orthogonal test. Considering the random characteristics of pavement roughness, Li et al. [24] obtained the random dynamic load sequence of four degrees of freedom vehicles acting on the pavement, developed the moving random load subroutine VDLOAD based on the secondary development platform of ABAQUS finite element software, and established the finite element dynamic analysis model of the asphalt pavement structure. Based on the model, the dynamic response of asphalt pavement structure under vehicle pavement interaction is studied. Peng et al. [25] imported the humidity field values into ABAQUS through MATLAB, indicating that the distribution of moisture content of subgrade significantly affects the resilient modulus distribution of subgrade and critical response of pavement structures. Li et al. [26] proposed a constitutive model of subgrade soils to incorporate soil suction and octahedral shear stress, and the model can be applied to analyze the fatigue cracking of both subgrade and surface layers.

The objective of this research is to reveal the dynamic response law of full-depth asphalt pavement under moving load and compare it with the performance of the traditional semirigid base pavement. Five typical pavement structures are selected, including full-depth asphalt pavement and semirigid base asphalt pavement. The three-dimensional model and dynamic load model are constructed based on ABAQUS. Through the setting of the load moving belt, the subroutine is written to realize the application of moving load, and the differences of the dynamic response of different structures are analyzed. Finally, by changing the parameters of the load-related subroutine and changing the load moving speed, the variation laws of the dynamic response of five structures under different speeds are studied.

2. Establishment of the Dynamic Response Model

2.1. Pavement Structures. In order to analyze the influence of pavement structure on dynamic response, comparing the performance difference between full-depth asphalt pavement and general semirigid base asphalt pavement, five different pavement structure types are selected [27], as shown in Table 1. Structures I, II, and III in the foundation are full-depth asphalt pavement, and structures IV and V are semirigid base asphalt pavement. The thickness and materials of each structural layer of the five pavement structures are shown in Figure 1 [27], and the values of material parameters are shown in Table 1.

2.2. Finite Element Model. In ABAQUS software, dynamic load simulation can be realized by setting load steps and load conditions, so as to be closer to the situation when the structure is used on the real road. With the development of finite element technology, the research community has done some research on the dynamic response of multilayer pavement under moving load, but most of them focus on the research of two-dimensional models [28–30].

In the static load analysis, the two-dimensional model can reduce the model scale and reduce the grid elements to improve the operation speed and save time. However, in the dynamic load analysis, because the vehicle driving is a dynamic process, the mechanical response at a certain position of the pavement structure changes with time, so the three-dimensional modeling analysis is needed. The current road design method generally simplifies the vehicle load into the

Table 1: Relevant parameters of various pavement materials.

Material name	Elastic modulus (MPa)	Poisson's ratio
SMA-13	1500	0.25
AC-13	1450	0.25
AC-20	1400	0.25
AC-25	1350	0.25
ATB-25	1200	0.40
Lime-ash soil	800	0.35
Cement-stabilized macadam	1600	0.25
Low content cement-stabilized macadam	1300	0.25
Modified soil	400	0.40
Soil	50	0.40

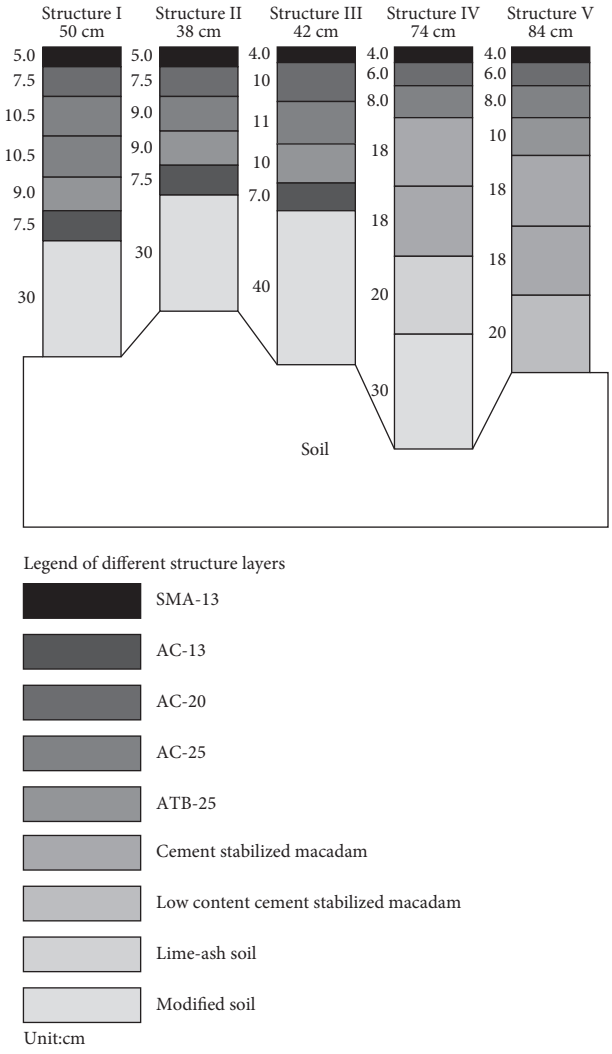

Figure 1: Pavement structure and materials.

static load. In fact, when the car is driving on the road, the road surface is affected by complex vertical and horizontal forces [31–33]. In order to simplify the problem, it is assumed that the vehicle wheel load is a vertically uniformly distributed rectangular load when the vehicle is running normally. In the braking section, it is assumed that the vehicle wheel load is uniformly distributed vertical and horizontal rectangular load.

In the calculation process, in order to realize the movement of the load, first set the load moving belt along the load moving direction. The transverse width of the moving belt along the road is the same as the applied uniformly distributed load width, and the longitudinal length of the moving belt along the road is the driving distance of the wheel load. Then, the load moving belt is subdivided into many small rectangles. As shown in Figure 2, the length of

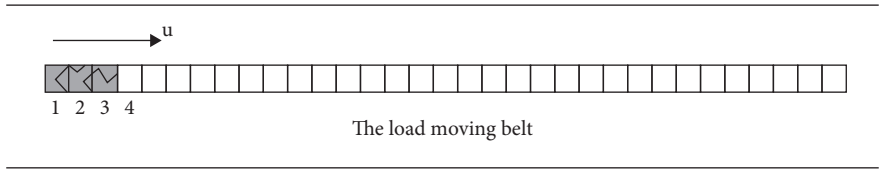

Figure 2: Load moving belt.

the small rectangle depends on the calculation accuracy and can be one third of the wheel load length.

In the initial state of wheel load, it occupies the area of three small rectangles 1, 2, and 3 in the figure. In the moving process, the load moves forward gradually along the moving belt. By setting multiple load steps, at the end of each load step, the load moves forward by a small rectangular area as a whole. For example, at the end of the first load step, the load occupies 2, 3, and 4. At the same time, in order to improve the calculation accuracy, multiple load substeps are set in each load step. For example, the middle load substep of the first load step gradually reduces the load on area 1, while the load on area 4 gradually increases, which develops in turn to achieve the effect of load movement. The moving speed of the load can be achieved by setting the time size of each load step. Since the ABAQUS foundation load setting is difficult to meet the above requirements, it is proposed to use the loading subroutine to realize the moving load. The user subroutine is written by the user according to the corresponding interface provided by ABAQUS and FORTRAN syntax. According to the needs of the problem studied, this paper compiles the subroutine VDLOAD for applying moving load. The moving speed of the load can be realized by the time of the load step in the subroutine.

The realization of dynamic load requires the establishment of a three-dimensional finite element model of the pavement structure. The cross section of the model pavement is 4 m in the transverse direction, 3 m in the depth, and 6 m in the moving direction of the load. The pavement structure is completely continuous with the five structures mentioned above. In order to reduce the influence of boundary conditions on the internal mechanical response law of pavement structure during loading, the load is applied at 1.5 m–4.5 m in the Z direction of the upper surface of the model. The boundary condition is that the bottom is completely fixed, the displacement in the X direction is constrained on both sides of the pavement section structure, and the displacement in the Z direction is constrained before and after. The model and boundary conditions are shown in Figure 3. The upper surface of the model is the application of the load moving belt. The small rectangle on the moving belt is divided directly on the model, and then, the mesh is divided [34]. In order to facilitate calculation convergence, the grid is set more densely at the surface layer and load moving zone, while the grid at the lower soil foundation is larger. The element type adopts c3d8r, namely, eight-node linear hexahedron element, reduced integral, and hourglass control. There are 56160 units in the model, and the meshing results are shown in Figure 4.

3. Results and Discussion

3.1. Time History Curve of Each Structure. Considering the vertical uniformly distributed load, the selected calculation point of stress is the special center point directly below the wheel load. The road surface, the bottom of upper layer, the bottom of middle layer, the bottom of lower layer, the bottom of ATB layer, the bottom of AC-13 layer, and the bottom of the modified soil layer are selected, respectively, to obtain the time history curves of vertical displacement, stress, strain, and shear stress of five structures, as shown in Figure 5. Among them, due to the setting of the load step, when the load moves to the center of the model, the time is about 0.0475 s, and there are slight differences before and after different structures, which can be seen in the resulting diagram.

Through the above curve, the changes of various indexes of the selected pavement structure in the process of dynamic load can be analyzed. According to the curve change, when the time history curve time reaches about 0.04 s, the slope in the time history curve increases significantly. The reason is that the load enters the area near the center point of the model at about 0.04 s, and the load in this area has a more direct influence on the internal mechanical changes of each structural layer.

For vertical displacement, the displacement value of the road surface is the largest in each time period, and the subsequent curves of each layer gradually decrease with the increase of layer depth.

The change of vertical stress is similar to vertical displacement. When the load moves to the center, the value of vertical stress gradually increases, the change value increases near 0.04~0.06 s, and the vertical stress of each layer reaches the maximum at 0.05 s.

The variation law of vertical micro strain in each layer is slightly different. With the increase of time, the vertical micro strain at the road surface, upper layer bottom, and middle layer bottom first increases positively, decreases rapidly, and becomes negative when it reaches 0.04 s, and the image is symmetrical about the time median. The other four-layer curves first increase in the negative direction to the peak value and then decrease with the increase of time.

The longitudinal shear stress of each layer first increases with time, rapidly increases to the peak near 0.04 s, decreases to 0 at 0.05 s, and then rapidly increases to the peak in the opposite direction. The curve trend is symmetrical about the midpoint of time.

For the transverse shear stress, the change trend of time history curve of each layer is the same, which first increases

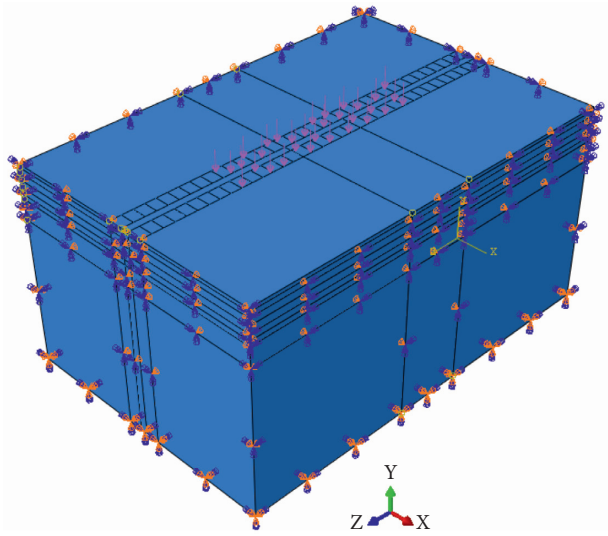

Figure 3: 3D model and boundary conditions.

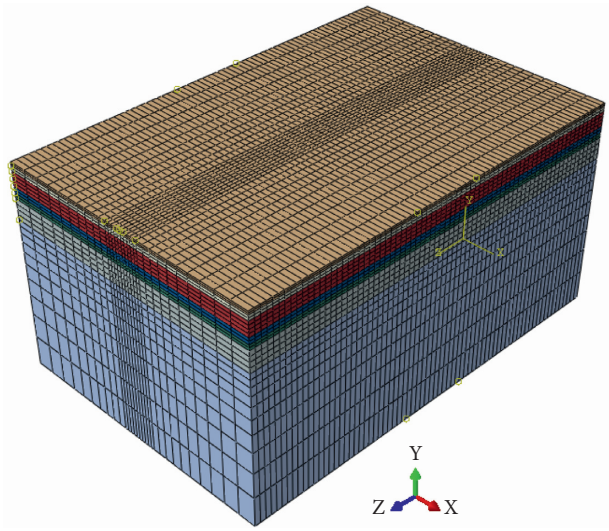

Figure 4: Grid division of the 3D model.

to the peak and then decreases, and the transverse shear stress at the bottom of the lower layer is the largest.

According to the above conclusions, the same analysis is made for the remaining four structures, and the data are extracted to obtain the time history curves of each index of the other four structures at the above positions, as shown in Figures 6–9, which are analyzed, respectively.

Comparing the time history curves of structure I and structure II, the overall law is roughly similar, but the values of each index are quite different. Compared with structure I, the maximum value of vertical displacement, vertical strain, and transverse shear stress of structure II increases, while the maximum value of vertical stress decreases, and the longitudinal shear stress changes little.

It can be seen that, compared with the first two structures, the vertical displacement time history curve of structure III has better symmetry. The vertical displacement value is also small, and the mechanical response under dynamic load is more stable. In general, the distribution of the selected indexes of the first three structures is similar, and the time history curves of the three full-depth structures have little difference.

Structure IV and structure V are two traditional semirigid structures used as the control group. Their structures are different from the first three. Cement-stabilized macadam semirigid structure layers are set at the bottom of the ATB layer. Different structures make the internal index values of the five structures have great differences. The vertical displacement value of the latter two semirigid structures decreases obviously, and the fluctuation of stress and strain also decreases. However, for structure IV and structure V, the indexes of the bottom of the middle surface layer are larger than the first three full-depth structures. Among the selected structural layers, the upper layer of each structure is quite different from the middle layer. According to other studies, the stress state of these two structural layers is relatively severe, which is the main embodiment of structural change. Because the road surface bears load directly, the values of other indicators are generally large except shear stress. Through the above analysis, it can be found that although the time history curve law of each index of each structure is different, it is not intuitive. The numerical differences need to be more intuitive compared in the follow-up research.

3.2. Numerical Comparison of Time History Curves of Various Structures. In order to study the different dynamic response laws among the five structures, it is necessary to compare the time history curves and index variation curves with the depth of different structures to study their variation laws. The analysis of the variation law of time history curves of different structures is reflected in the previous section. This section mainly analyzes the above results from the numerical point of view. According to the time history curve in the previous section, the maximum values of vertical displacement, vertical stress, strain, and longitudinal shear stress inside the structure appear on the road surface, and the maximum value of transverse shear stress generally appears at the bottom of the lower layer. Therefore, the time history curves of the five structures are compared according to the location of the maximum index, and the time history curves of each index on the same layer of the five structures are obtained as shown in Figure 10.

In order to more intuitively compare the different index values of the five structures in the same layer, the five pavement structures are now sorted according to different indexes. The smaller the serial number, the smaller the index value, as shown in Table 2.

In general, the semirigid base pavement has better bearing capacity under dynamic load. For the vertical displacement of road surface, the performance of full-depth asphalt pavement is worse than that of semirigid base pavement, which will be reflected as a rutting problem in practical engineering. Therefore, for full-depth pavement, a high modulus asphalt mixture should be used to reduce this adverse effect. In addition, the full-depth asphalt pavement

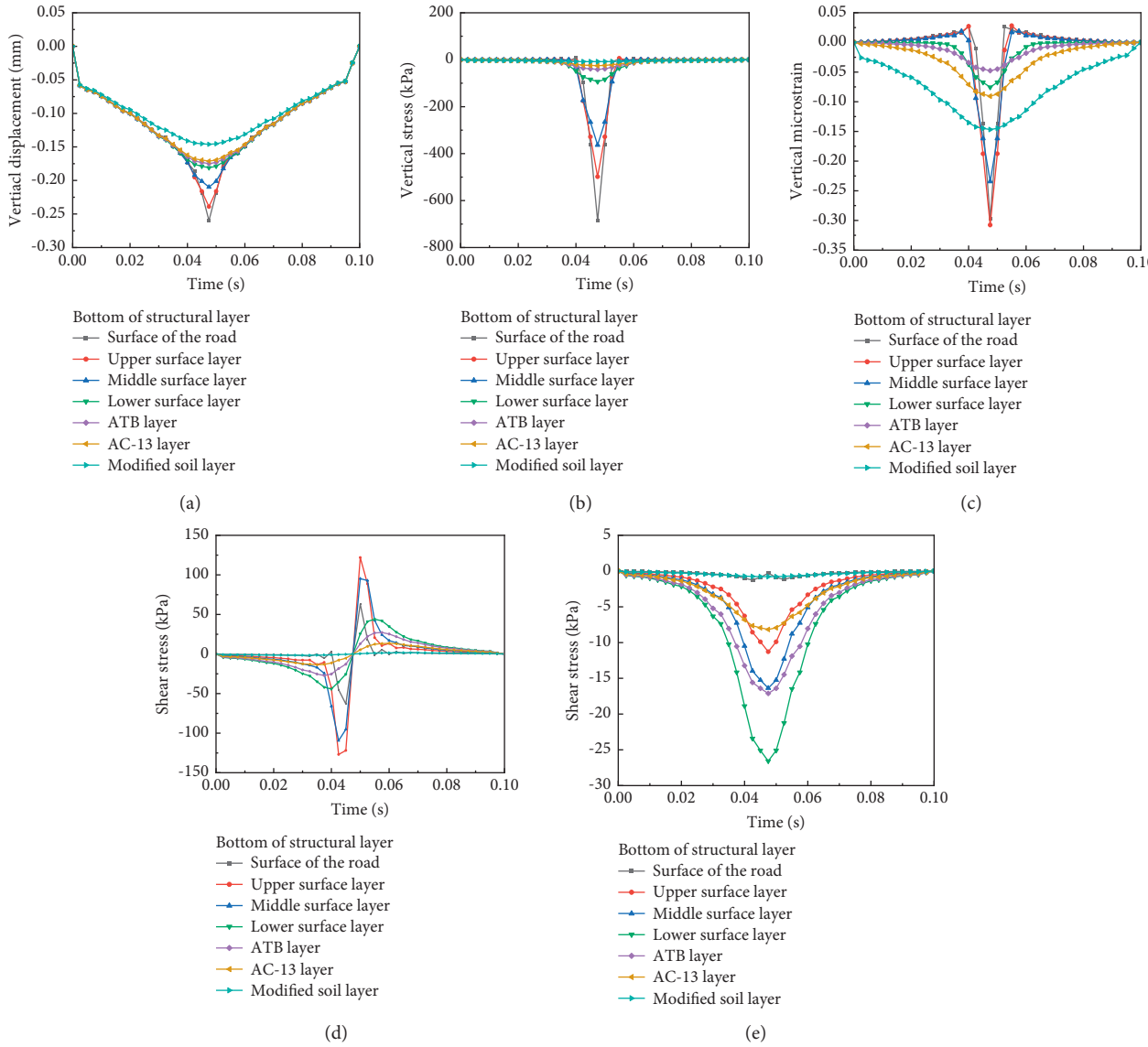

Figure 5: Time history curve of (a) vertical displacement, (b) vertical stress, (c) vertical micro strain, (d) longitudinal shear stress, and (e) transverse shear stress at each layer of structure I.

produces greater transverse shear stress under dynamic load, which means that the bottom of the lower layer is more prone to cracking. Therefore, it is necessary to set up a stress-absorbing layer to dissipate the internal stress in the design of full-depth asphalt pavement.

3.3. Dynamic Response of Full-Depth Pavement at Different Moving Load Speeds. In the actual use of pavement structure, the vehicle speed is often different, so it is necessary to analyze the dynamic response of pavement structure at different speeds. Structure I is selected for corresponding research. Referring to the current regulations of speed limit on expressways, it is assumed that cars are traveling at a uniform speed of 60 km/h, 72 km/h, 84 km/h, 96 km/h, 108 km/h, and 120 km/h, respectively, and then, the corresponding loads advance 1.67 m, 2 m, 2.33 m, 2.67 m, 3 m, and 3.33 m, respectively, within 0.1 s. According to the grid size, the number of grids occupied by the load within 0.1 s is 10, 12, 14, 16, 18, and 20, respectively. The simulation calculation is carried out for structure I, and the time history curves at different speeds and the curves with depth are obtained, as shown in Figures 11 and 12.

According to Figure 11, the vertical displacement of the road surface in the structure decreases with the increase of speed. When the speed is low, the vertical displacement of the road surface is large, which is also in line with the law of practical experience. As the load moves to the center, the vertical displacement of the selected point first increases, decreases near the center, and then increases; after selecting the position, the vertical displacement decreases slightly and then increases, and finally, the load moves back to the selected point, and the vertical displacement also decreases. The change of load speed basically has no effect on the

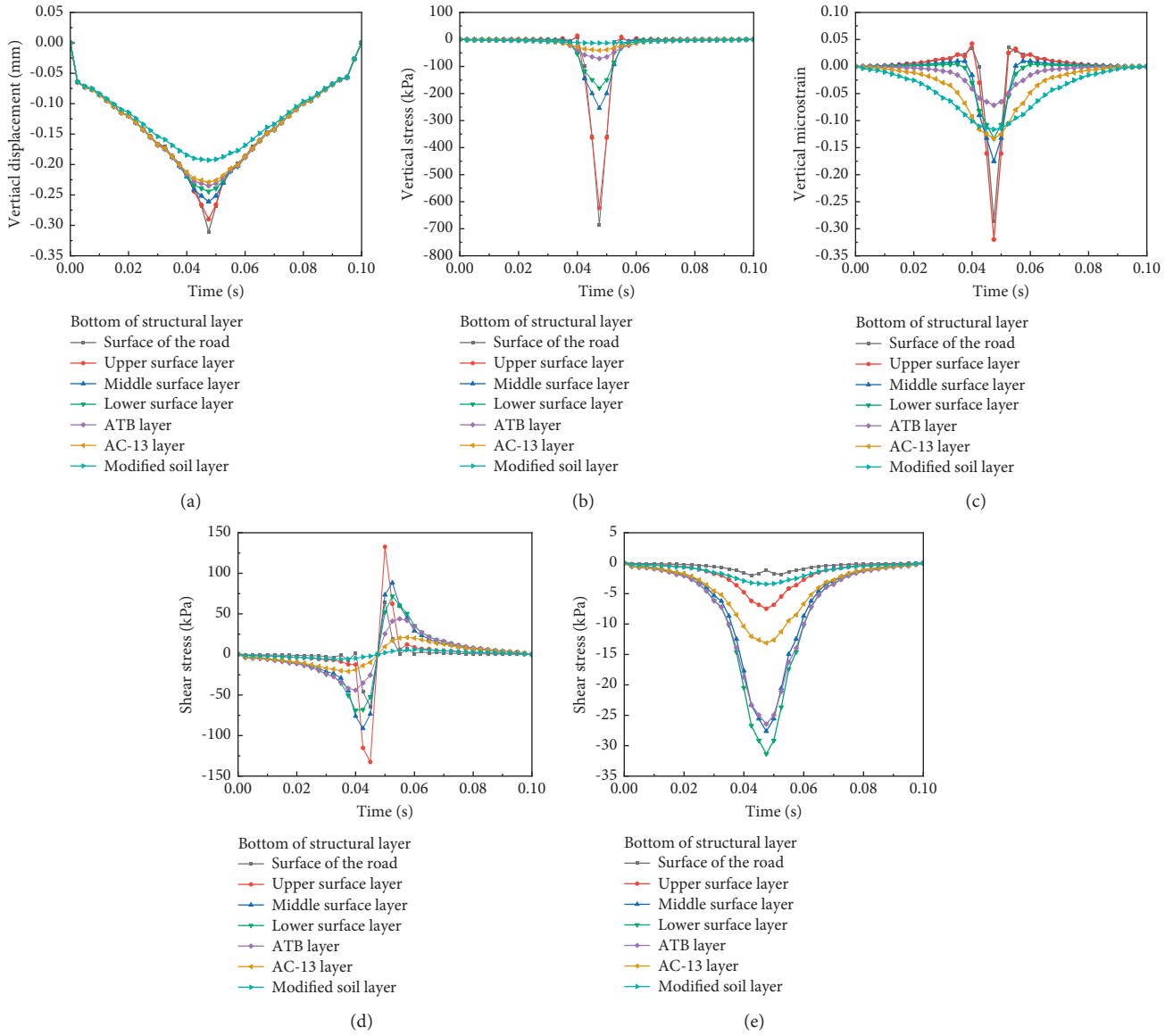

Figure 6: Time history curve of (a) vertical displacement, (b) vertical stress, (c) vertical micro strain, (d) longitudinal shear stress, and (e) transverse shear stress at each layer of structure II.

vertical stress and vertical strain of the road surface. The curve heights of different speeds coincide, and the values are similar, but the time to reach the maximum value is slightly different. This is the reason for the analysis step, not the effect of speed. The regularity of the longitudinal shear stress time history curve of road surface under different speeds is not obvious. Due to the large fluctuation of shear stress, the maximum value changes little with the speed, and the shear stress value is large at 72 km/h, 96 km/h, and 108 km/h. For the longitudinal shear stress, the value increases with the increase of speed. When the speed is 120 km/h, the longitudinal shear stress reaches 120 kPa.

Figure 12 shows the change of each index with depth on the taken path at different speeds. It can be seen from the figure that on the selected path, the vertical displacement increases with the increase of load speed, and the variation laws of different speed curves are basically the same. When the depth reaches 3 m, the vertical displacement of each curve is 0. The coincidence degree of vertical stress curve with depth under different speeds is higher, and the stress with high speed is slightly larger. The vertical micro strain increases with depth in the upper layer, then decreases with depth, and fluctuates after entering the base layer, which is consistent with the above law. With the increase of velocity, the maximum value of vertical micro strain decreases slightly, but the difference between the maximum value and the minimum value is less than 5%. Because the longitudinal shear stress fluctuates with depth at the selected position, it is difficult to compare its maximum value, but the overall law is similar. The variation law of transverse shear stress with depth under different speeds is the same, which increases with depth in the upper layer, and then decreases with depth.

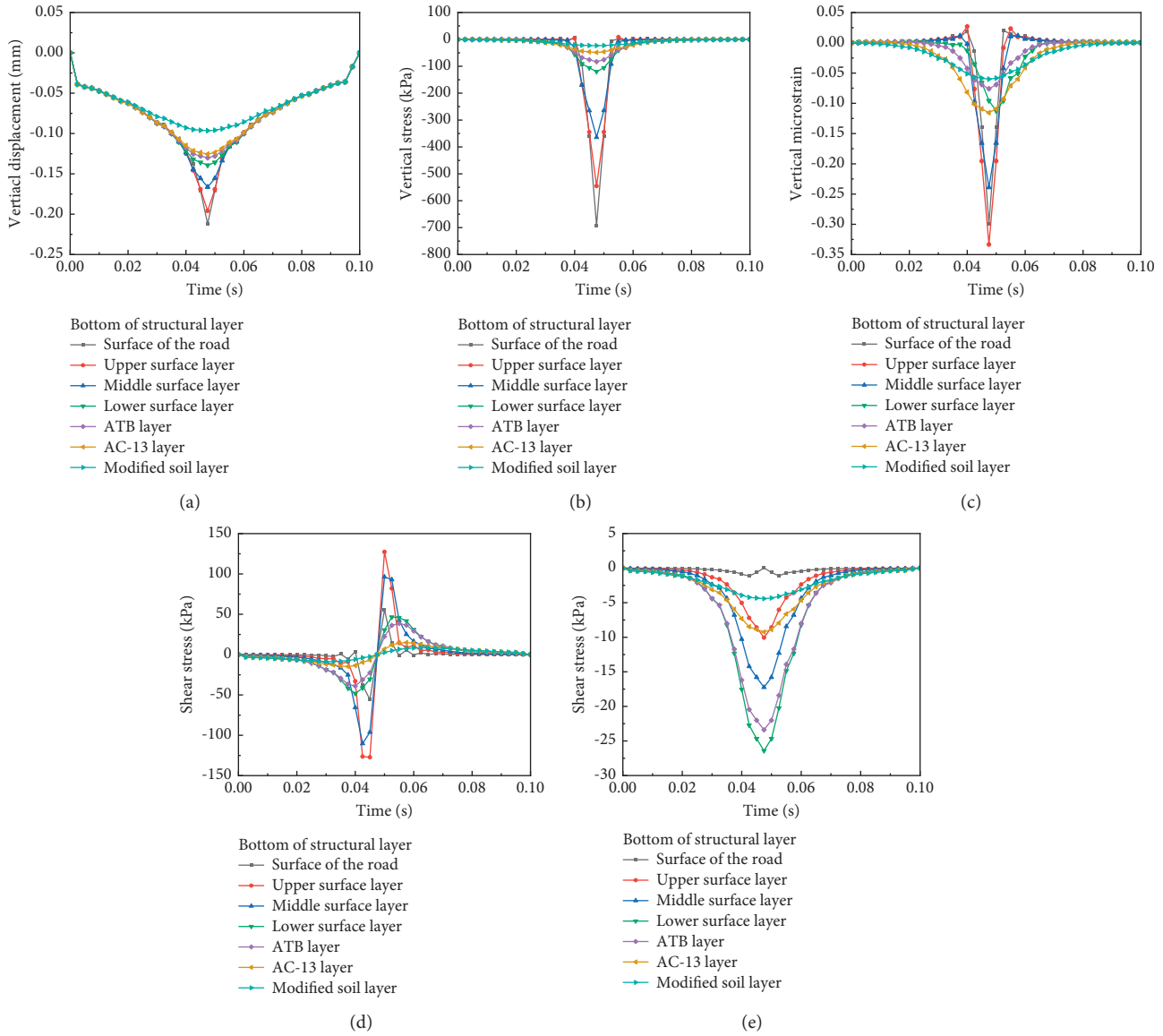

Figure 7: Time history curve of (a) vertical displacement, (b) vertical stress, (c) vertical micro strain, (d) longitudinal shear stress, and (e) transverse shear stress at each layer of structure III.

When the depth is 3 m, the value of each curve is 0. According to the maximum value at the bottom of the upper layer, the value of transverse shear stress increases with the increase of velocity.

According to the above conclusions, the increase of speed will increase the vertical displacement at the wheel load action point, but for the whole structure, the increase of speed will reduce the vertical displacement at other positions in the process. The vertical stress-strain and longitudinal shear stress change little and can be ignored. However, the increase of speed increases the transverse shear stress of the pavement. It can be considered that the transverse tensile

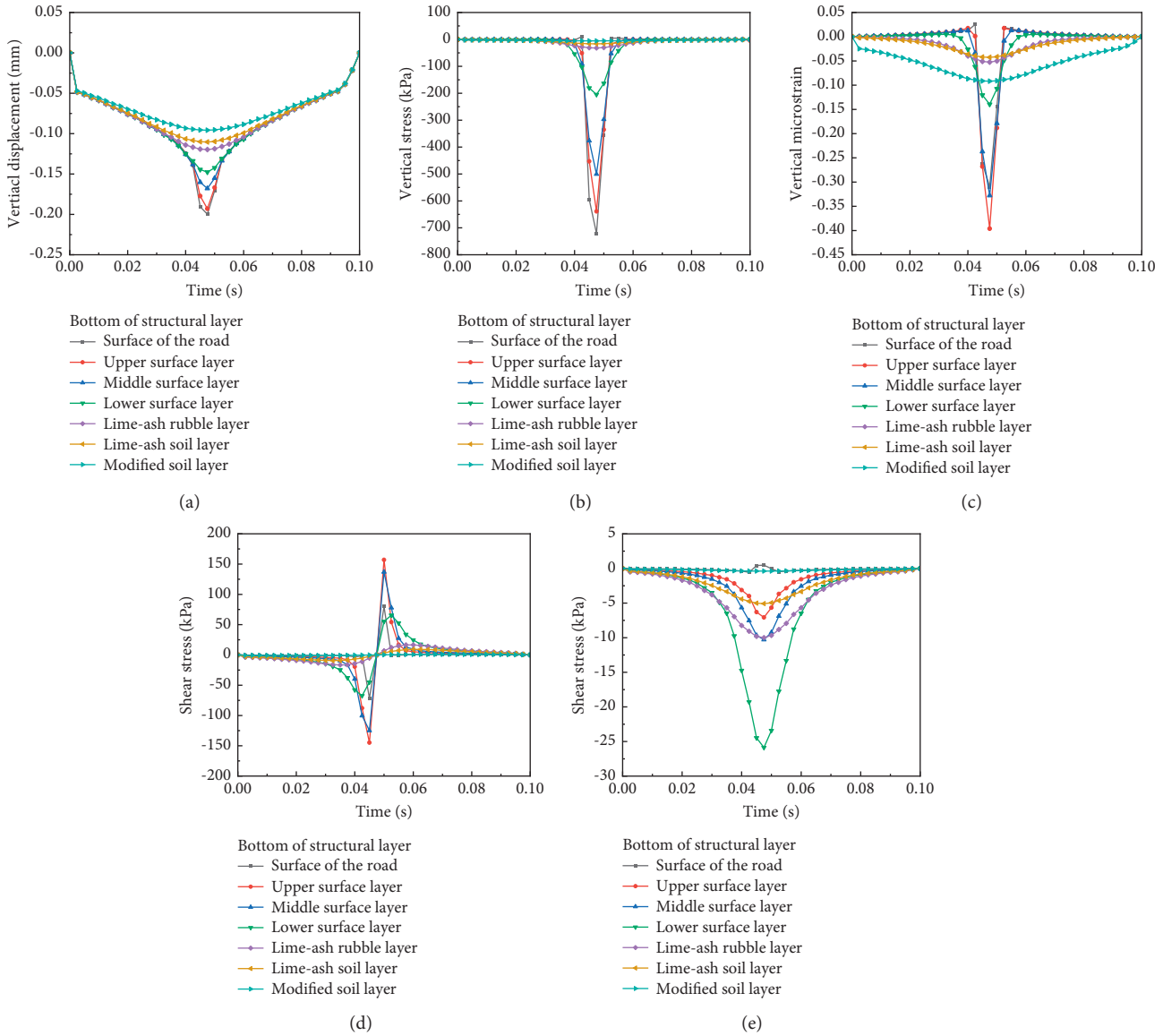

Figure 8: Time history curve of (a) vertical displacement, (b) vertical stress, (c) vertical micro strain, (d) longitudinal shear stress, and (e) transverse shear stress at each layer of structure IV.

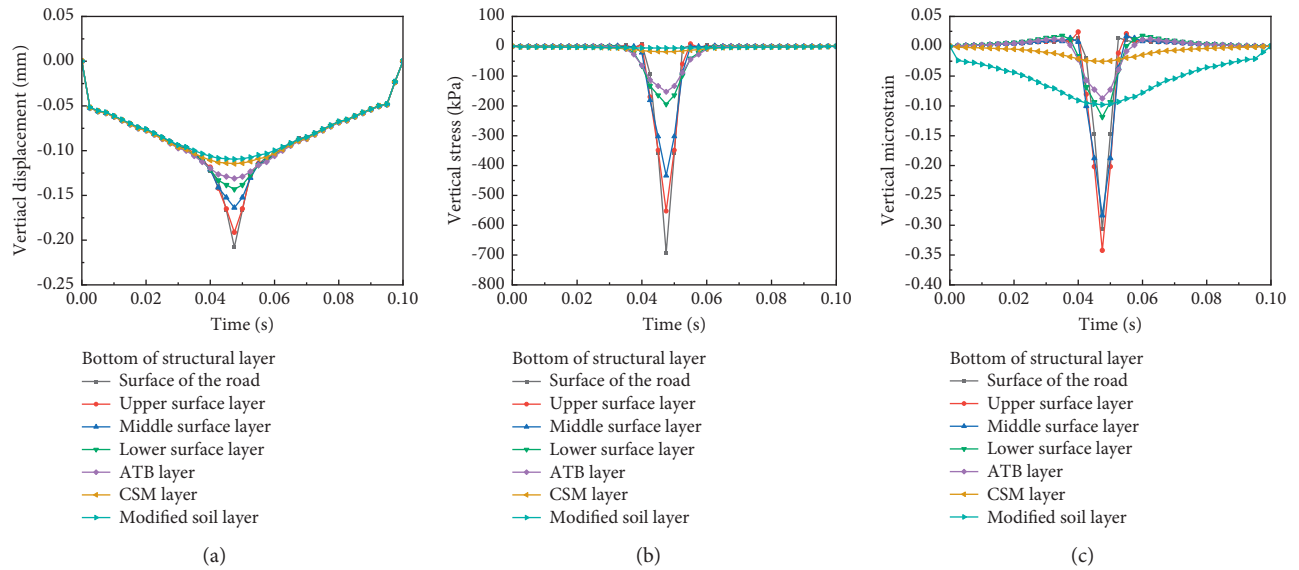

Figure 9: Continued.

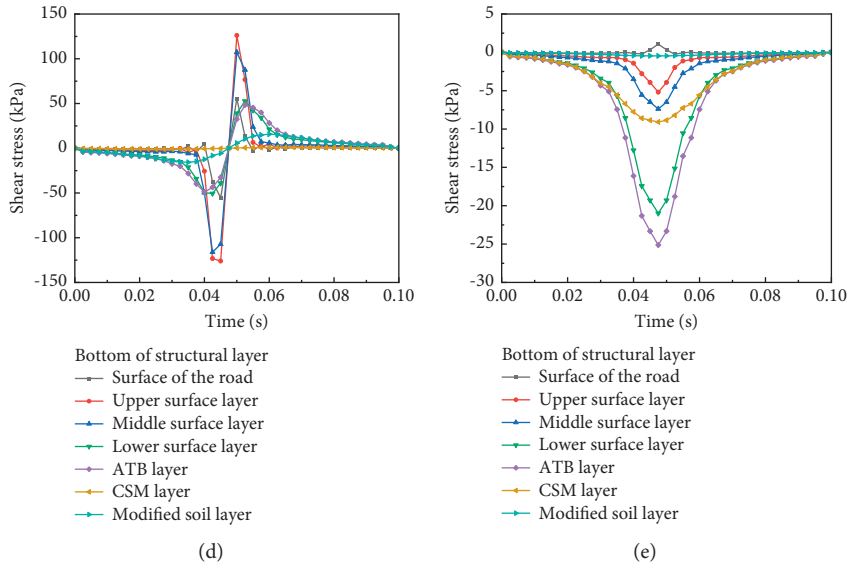

Figure 9: Time history curve of (a) vertical displacement, (b) vertical stress, (c) vertical micro strain, (d) longitudinal shear stress, and (e) transverse shear stress at each layer of structure V.

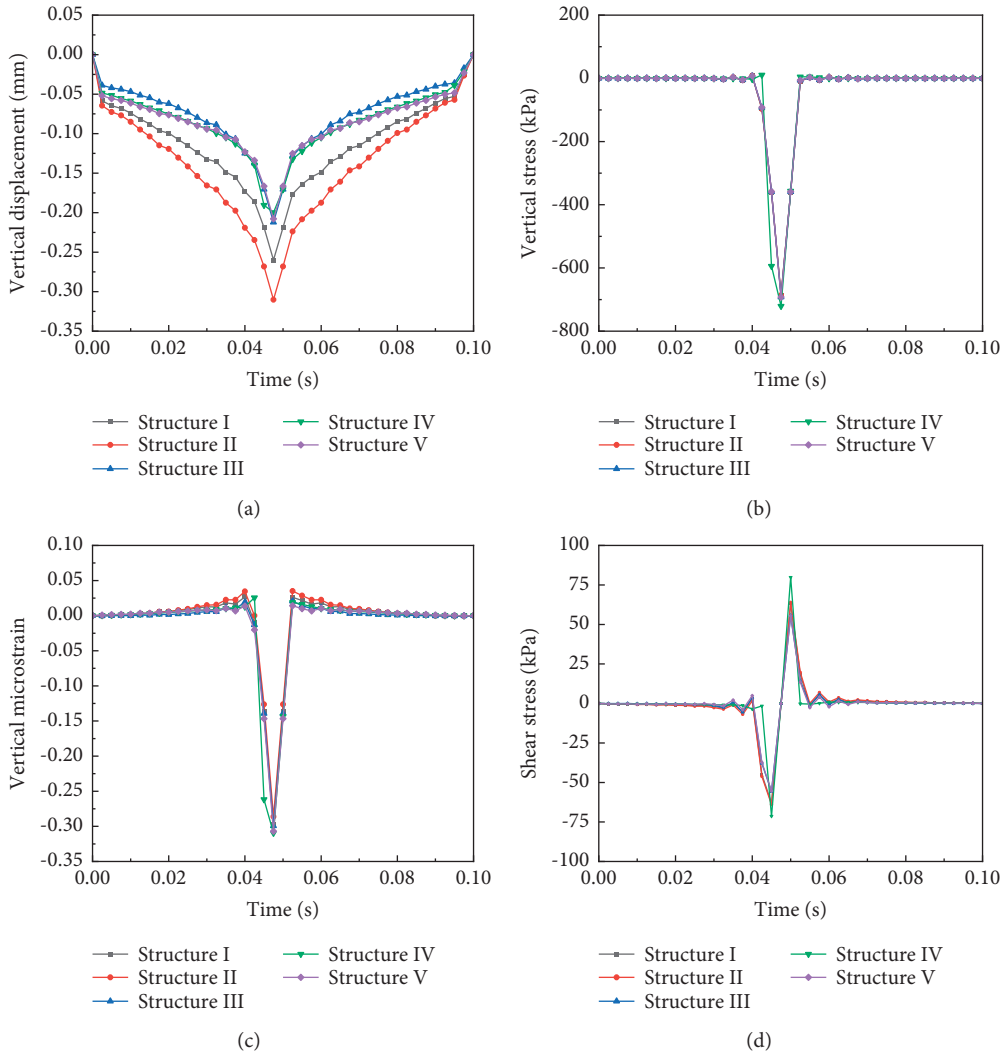

Figure 10: Continued.

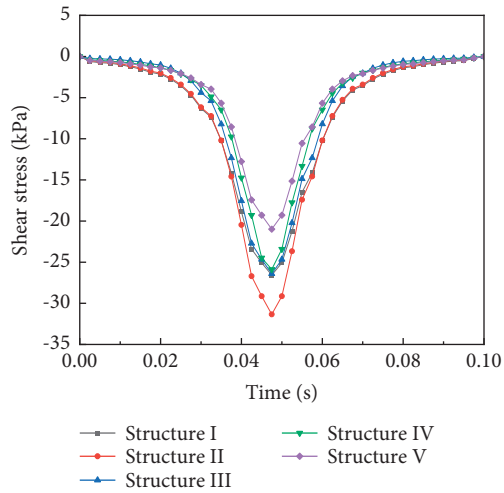

(e)

Figure 10: Time history curve of each index of five structures. (a) Time history curve of vertical displacement of the road surface. (b) Time history curve of vertical stress of road surface. (c) Time history curve of the vertical micro strain of road surface. (d) Time history curve of longitudinal shear stress of road surface. (e) Time history curve of transverse shear stress at the bottom of the lower surface layer.

Table 2: Ranking of indicators of five structures.

	Full-depth asphalt pavement			Semirigid base pavement	
	I	II	III	IV	V
Vertical displacement	4	5	3	1	2
Vertical micro strain	4	1	3	5	2
Longitudinal shear stress	3	4	2	5	1
Transverse shear stress	4	5	3	2	1

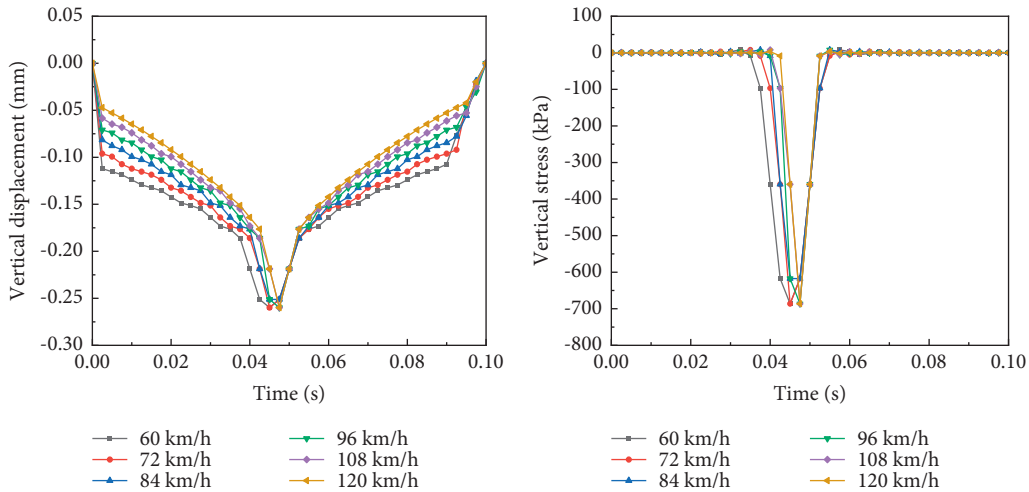

(a) (b)

Figure 11: Continued.

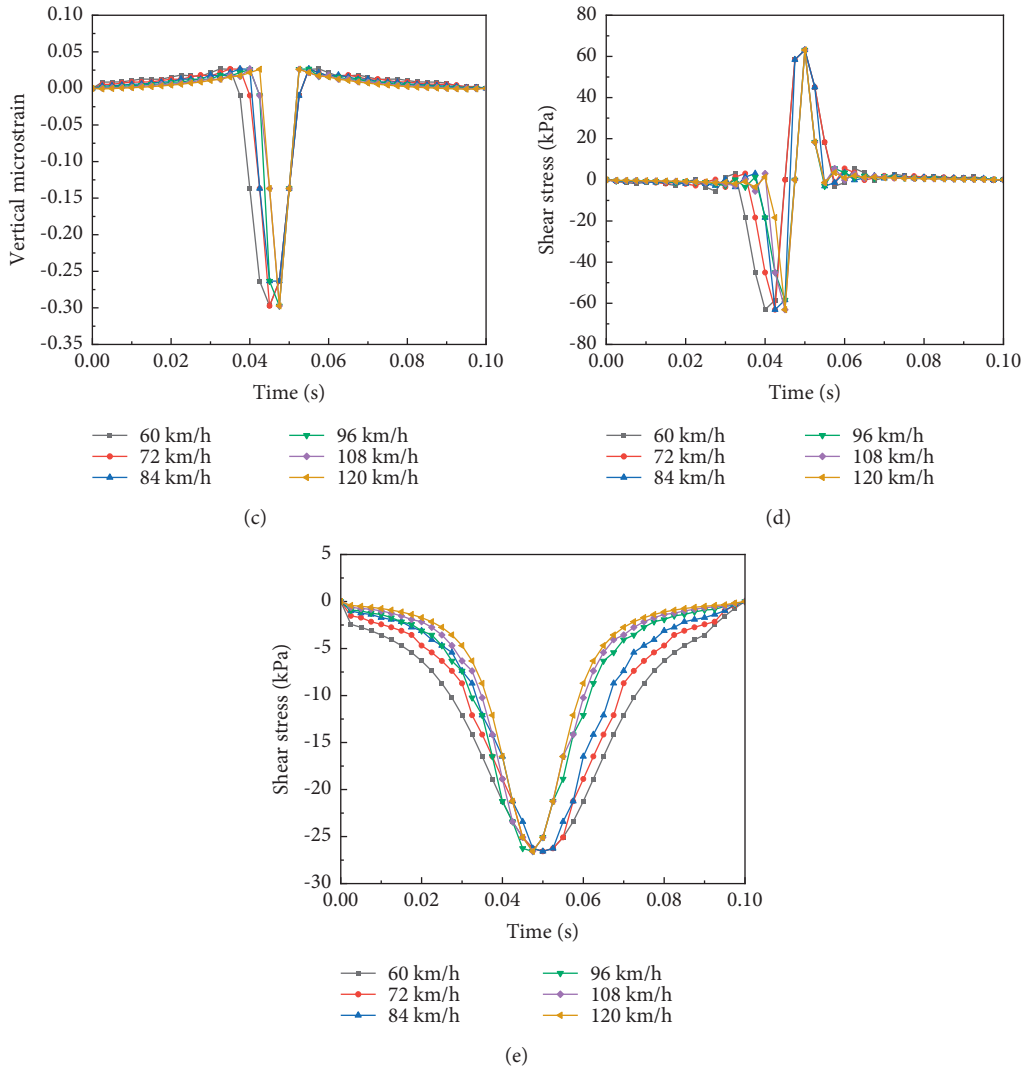

Figure 11: Time history curve of each index of structure I. (a) Time history curve of vertical displacement of road meter at different speeds. (b) Time history curve of vertical stress of road surface at different speeds. (c) Vertical micro strain time history curves of road meters at different speeds. (d) Time history curve of longitudinal shear stress of road surface at different speeds. (e) Time history curve of transverse shear stress at layer under different speeds.

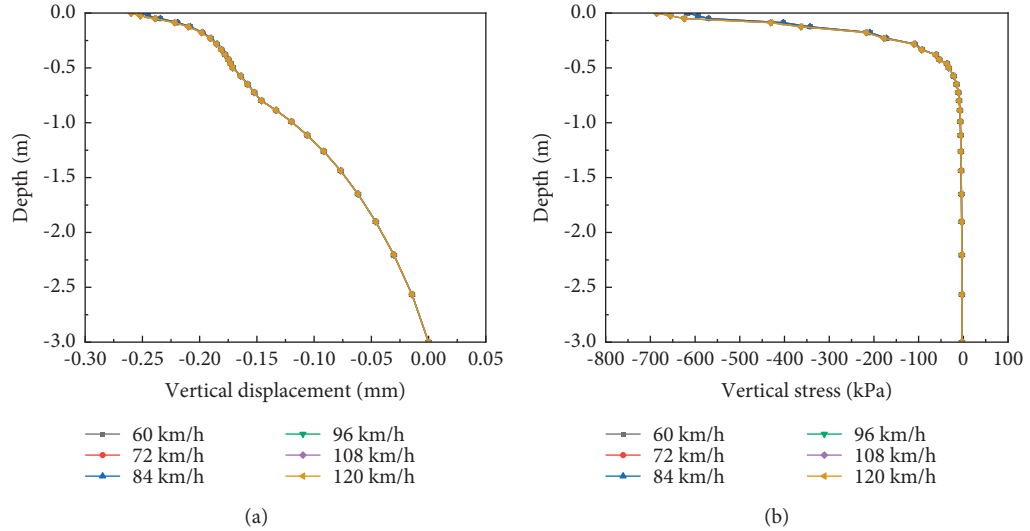

Figure 12: Continued.

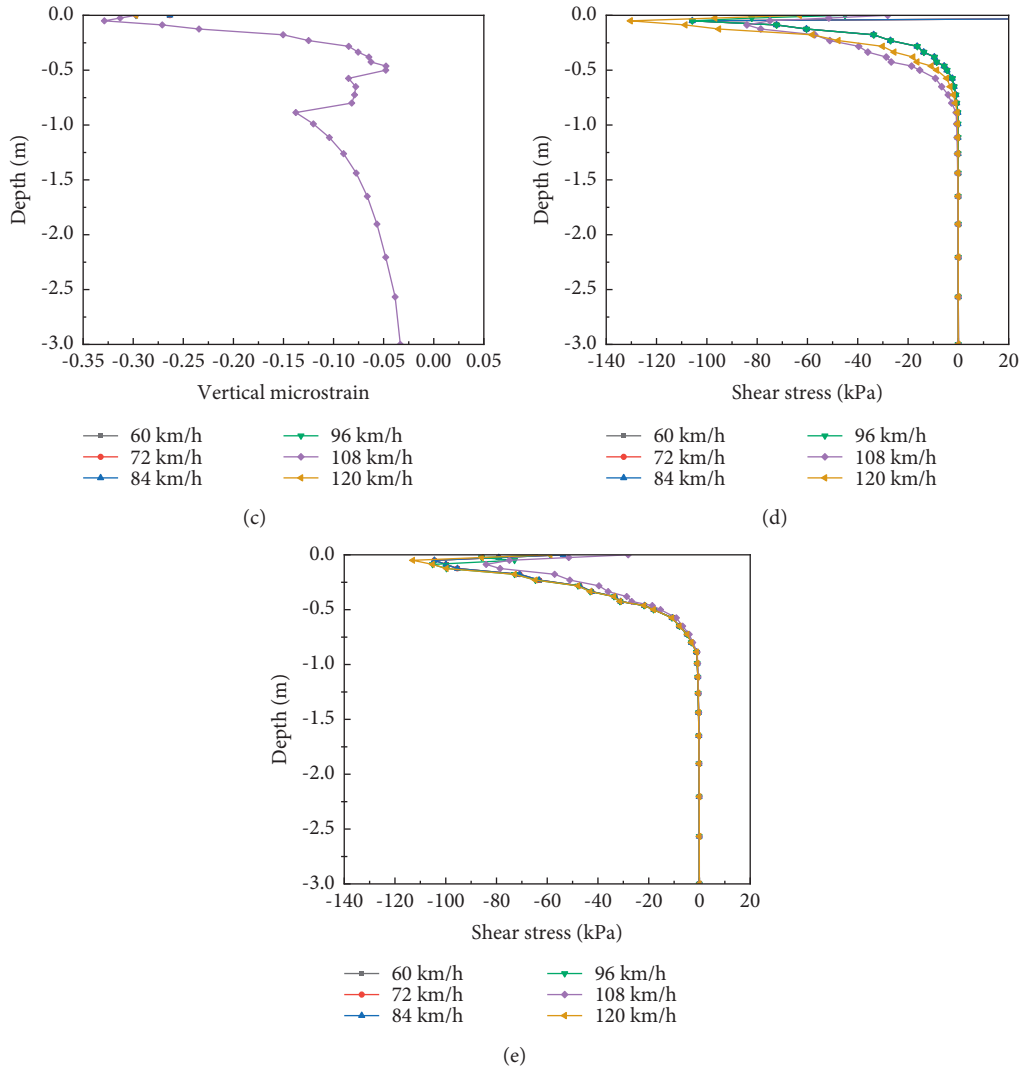

Figure 12: (a) Variation of vertical displacement with depth at different speeds. (b) Variation of vertical stress with depth at different speeds. (c) Variation of vertical micro strain with depth at different speeds. (d) Variation of longitudinal shear stress with depth at different speeds. (e) Variation of transverse shear stress with depth at different speeds.

stress at the bottom of each layer increases, which means that the pavement is more prone to longitudinal cracks.

4. Conclusion

(1) In the time history curve analysis of different positions of each structural layer, compared with full-depth asphalt pavement, the vertical displacement of the road surface of the semirigid base pavement is significantly reduced, and the stress-strain fluctuation is also small. However, for the middle surface layer, the displacement, vertical stress, and shear stress of semirigid base pavement are greater than those of full-depth pavement, which is also the embodiment of full-depth pavement in reducing rutting disease in dynamic response.

(2) In the comparison of time history curves of different structures, the vertical stress and strain of the five structures have little difference, and the transverse shear stress at bottom of the upper layer of full-depth pavement is greater than that of semirigid base pavement. Full-depth asphalt pavement should pay more attention to the cracking resistance of the upper layer mixture, which will directly affect the pavement performance and surface life.

(3) In the dynamic response analysis under different vehicle speeds, the vertical displacement of the road surface is large when the speed is low, which is

related to the load action time. The increase of speed will be accompanied by the increase of transverse shear stress at the bottom of the structural layer, and the pavement is more prone to longitudinal crack. The crack development can be restrained by setting a stress-absorbing layer in the pavement structure.

(4) The bearing capacity of semirigid base pavement is better, but the longitudinal shear stress in structure IV is the worst, which also indicates that the bottom of the pavement is prone to cracking. Combined with the shrinkage cracking of the base layer, it is detrimental to the pavement life. The full-depth pavement needs to consider the thickness and material design of each structural layer to make up for the bearing capacity defects and obtain longer service life. In practical application, the selection of pavement structure should take traffic conditions and service life into consideration.

Data Availability

The data used to support the findings of this study are included within the article.

Conflicts of Interest

The authors declare that they have no conflicts of interest.

Acknowledgments

This study was supported by the National Natural Science Foundation of China (51808016 and 52078018) and the Transportation Science and Technology Project of Shandong Province (2020B25).

References

[1] D. M. Mrawra and J. Luca, "Thermal properties and transient temperature response of full-depth asphalt pavements," *Transportation Research Record-series*, vol. 1809, pp. 160–171, 2002.

[2] H. Ceylan, A. Guclu, E. Tutumluer, and M. R. Thompson, "Backcalculation of full-depth asphalt pavement layer moduli considering nonlinear stress-dependent subgrade behavior," *International Journal of Pavement Engineering*, vol. 6, no. 3, pp. 171–182, 2005.

[3] O. Pekcan, E. Tutumluer, and J. Ghaboussi, "SOFTSYS for backcalculation of full-depth asphalt pavement layer moduli," *Erol Tutulumluer*, vol. 1, pp. 679–687, 2009.

[4] E. Kassem, L. Walubita, T. Scullion, E. Masad, and A. Wimsatt, "Evaluation of full-depth asphalt pavement construction using X-ray computed tomography and ground penetrating radar," *Journal of Performance of Constructed Facilities*, vol. 22, no. 6, pp. 408–416, 2008.

[5] L. Johanneck and S. Dai, "Responses and performance of stabilized full-depth reclaimed pavements at the Minnesota road research facility," *Transportation Research Record*, vol. 2368, pp. 114–125, 2013.

[6] A. Braham, "Comparing life-cycle cost analysis of full-depth reclamation versus traditional pavement maintenance and rehabilitation strategies," *Transportation Research Record*, vol. 2573, pp. 49–59, 2016.

[7] Y. D. Wang, J. Jeong, and Y. R. Kim, "Comparison of treatment timing between aggregate base and full-depth asphalt roads," *Journal of Transportation Engineering Part B-Pavements*, vol. 146, no. 4, 2020.

[8] M. Guo, H. Liu, Y. Jiao et al., "Effect of WMA-RAP technology on pavement performance of asphalt mixture: a state-of-the-art review," *Journal of Cleaner Production*, vol. 266, Article ID 121704, 2020.

[9] X. Yan, P. An, W. Wu, L. Wang, and J. Wei, "feasibility study on application of full depth asphalt pavement in national trunk road," *6th International Conference on Environmental Science and Civil Engineering*, vol. 455, 2020.

[10] S. P. Yang, L. S. L. Y. Engineering, S. R. Institute, S. Li, and Y. Lu, "Dynamics of vehicle-pavement coupled system based on a revised flexible roller contact tire model," *Science in China(Series E:Technological Sciences)*, vol. 52, 2009.

[11] Y. S. Yao, J. Li, J. J. Ni, C. Liang, and A. Zhang, "Effects of gravel content and shape on shear behaviour of soil-rock mixture: experiment and DEM modelling," *Computers and Geotechnics*, vol. 141, 2022.

[12] J. H. Zhang, H. S. Fan, S. P. Zhang, and J. Zheng, "Time-domain elasto-dynamic model of a transversely isotropic, layered road structure system with rigid substratum under a FWD load," *Road Materials and Pavement Design*, 2021.

[13] R. V. Siddharthan, P. E. Sebaaly, M. El-Desouky, D. Strand, and D. Huft, "Heavy off-road vehicle tire-pavement interactions and response," *Journal of Transportation Engineering*, vol. 131, no. 3, pp. 239–247, 2005.

[14] C.-P. Wu and P.-A. Shen, "Dynamic analysis of concrete pavements subjected to moving loads," *Journal of Transportation Engineering*, vol. 122, no. 5, pp. 367–373, 1996.

[15] Y. B. Yang, H. H. Hung, and D. W. Chang, "Train-induced wave propagation in layered soils using finite/infinite element simulation," *Soil Dynamics and Earthquake Engineering*, vol. 23, no. 4, pp. 263–278, 2003.

[16] Y. Hou, S. P. Sun, and Z. Y. Guo, "Dynamic response sensitivity analysis of plate on elastic foundation subjected to moving point loads," *Journal of Tongji University*, vol. 1, pp. 31–35, 2003.

[17] X. Y. Li, *Finite Analysis of Concrete Bridge Deck Pavement at Coupling Effect*, Dalian University of Technology, Dalian, Liaoning, China, 2012.

[18] F. M. Shu and Z. D. Qian, "Analysis on dynamic response of asphalt pavement under moving load," *Journal of Transportation Engineering and Information*, vol. 5, no. 3, pp. 90–95, 2007.

[19] J. S. Shan, X. M. Huang, and G. Y. Liao, "Dynamic response analysis of pavement structure under moving load," *Journal of Highway and Transportation Research and Development*, vol. 24, no. 1, pp. 10–13, 2007.

[20] J. Z. Pei, H. Wu, Y. Chen, and B. Wang, "Dynamic response characteristics of asphalt pavement under multi-axle moving load," *China Journal of Highway and Transport*, vol. 24, no. 5, pp. 30–35, 2011.

[21] X. Y. Liu, C. J. Shi, and S. J. Chen, "A theory research of asphalt pavement dynamic response under vehicle random stimulation," *Applied Mechanics and Materials*, vol. 105, no. 6, pp. 13–19, 2011.

[22] Z. J. Dong, M. H. Liu, H. Zheng, and X. Gong, "Dynamic mechanical analysis of asphalt pavement based on cross-isotropic properties," *China Journal of Highway and Transport*, vol. 25, no. 5, pp. 18–23, 2012.

[23] B. Huang, Y. Wu, C. F. Ai, and Z. F. Zhou, "Influence of structural parameters on dynamic response of asphalt pavement," *Journal of Highway and Transportation Research and Development*, vol. 30, no. 9, pp. 8–12, 2013.

[24] Q. Li, J. Q. Liu, and H. Liu, "Random dynamic response analysis of asphalt pavement based on the vehicle-pavement interaction," *Applied Mechanics and Materials*, vol. 744-746, pp. 1288–1297, 2015.

[25] J. H. Peng, J. H. Zhang, J. Li, J. Yao, and A. Zhang, "Modeling humidity and stress-dependent subgrade soils in flexible pavements," *Computers and Geotechnics*, vol. 120, 2020.

[26] J. Li, J. L. Zheng, Y. S. Yao, J. Zheng, and J. Peng, "Numerical method of flexible pavement considering moisture and stress sensitivity of subgrade soils," *Advances in Civil Engineering*, vol. 2019, Article ID 7091210, 10 pages, 2019.

[27] F. J. Hou, T. Li, X. Li, Y. Li, and M. Guo, "Research on the anti-reflective cracking performance of a full-depth asphalt pavement," *Sustainability*, vol. 13, 2021.

[28] J. Y. Liu, L. J. Zhang, B. Kou, and P. Shen, "The environment-friendly high-elasticity asphalt mixture using as stress absorbing layer," *Advanced Materials Research*, vol. 490-495, pp. 3753–3761, 2012.

[29] C. Baek, "Performance evaluation of fiber-reinforced, stress relief asphalt layers to suppress reflective cracks," *Applied Sciences*, vol. 10, no. 21, p. 7701, 2020.

[30] J. Z. Tan, J. G. Wei, C. Pan, and K. X. Huang, "Shear stress calculation of rubber asphalt overlay and stress-absorbing layer," in *Proceedings of the 2016 International Conference on Civil, Architecture and Environmental Engineering*, pp. 189–193, CRC Press/Balkema, Taipei, Taiwan, 2016.

[31] R. Pan and Y. M. Li, "Effect of warm mix rubber modified asphalt mixture as stress absorbing layer on anti-crack performance in cold region[J]," *Construction and Building Materials*, vol. 251, 2020.

[32] K. Emad, W. Lubinda, S. Tom, M. Eyad, and W. Andrew, "Evaluation of full-depth asphalt pavement construction using X-ray computed tomography and ground penetrating radar," *Journal of Performance of Constructed Facilities*, vol. 22, no. 6, pp. 408–416, 2008.

[33] J. Luke and D. Shongtao, "Responses and performance of stabilized full-depth reclaimed pavements at the Minnesota road research facility," *Transportation Research Record*, vol. 2368, no. 1, pp. 114–125, 2013.

[34] B. Andrew, "Comparing life-cycle cost analysis of full-depth reclamation versus traditional pavement maintenance and rehabilitation strategies," *Transportation Research Record*, vol. 2573, no. 1, pp. 49–59, 2016.

Hindawi
Advances in Materials Science and Engineering
Volume 2022, Article ID 5043729, 16 pages
https://doi.org/10.1155/2022/5043729

Research Article

Automated Particle Shape Identification and Quantification for DEM Simulation of Rockfill Materials in Subgrade Construction

Hao Bai,[1,2] Xiangyu Hu,[3] Ruidong Li,[3] Fei Chen,[2,4] and Zhiyong Liao[1,2]

[1]*Sichuan Expressway Construction & Development Group Co.,LTD., Chengdu 610041, China*
[2]*Shudao Investment Group Co.,Ltd., Chengdu 610041, China*
[3]*Department of Civil and Environmental Engineering, The Hong Kong Polytechnic University, Hung Hom, Kowloon, Hong Kong, China*
[4]*Sichuan Intelligent High-Speed Technology Co.,Ltd, Chengdu 610000, China*

Correspondence should be addressed to Xiangyu Hu; huxiangyu233@outlook.com

Received 13 June 2021; Revised 23 October 2021; Accepted 23 November 2021; Published 4 March 2022

Academic Editor: Qiao Dong

Rockfill materials, conducted by impermeable stone, are frequently used in subgrade construction projects. The irregularity and variability of particle shape are demonstrated to affect the mechanical properties of rockfill subgrade, such as void ratio and coordination number. This study first identifies the subgrade rockfill particle contour by machine learning algorithms, including AdaBoost, Cascade, and sliding windows. Then, the shape evaluation indexes of length flatness, edge angle, and roughness are quantified, and the statistical analysis of each index is presented. In addition, the discrete element method (DEM) simulation is implemented on the compaction of rockfill subgrade to explore the impact of roundness on characteristics of particles. Finally, the macroanalysis on the void ratio and cumulative settlement and the microanalysis on particle coordination number, rotation momentum, and displacement are studied. The results illustrate that roundness has a significant effect on the mechanical characteristics of subgrade rockfill materials. With the increase of rolling passes, the porosity of packing decreases, whereas the settlement increases gradually. The change rate starts fast and ends slowly.

1. Introduction

Rockfill materials have excellent engineering characteristics such as good compaction, strong water permeability, high filling density, high shear strength, small subsidence and deformation, high bearing capacity, and not easy to liquefy under the action of seismic load. Rockfill materials are applied in construction fields frequently for their excellent characteristics [1], meeting the requirements of in situ materials. In subgrade engineering, rockfill is mostly used, and it can make full use of local natural materials and adapt to different geological conditions.

The rockfill material method is relatively simple and possesses good seismic performance. Also, the evaluation of seismic reliability is an essential factor that needs to be considered. Zhang et al. evaluated geometric anisotropy modeling and shear behavior of graded crushed rocks [2]. There is research showing the seismic reliability of rockfill in hydraulic engineering under stochastic earthquake excitation considering the strain-softening behavior of rockfill materials. A new and efficient methodology that combines generalized probability density evolution method (GPDEM) with a spectral representation-random function method is presented to assess the seismic reliability [3].

To calculate the properties and state of rockfill materials more accurately, numerical simulation is a popular tool to make further research on rockfill materials [4]. For example, Li et al. researched by considering moisture and stress sensitivity of subgrade soils [5]. Hui et al. investigated the fracture evolution of asphalt mixture compared with acoustic emission [6]. The research found that particle breakage has some significant effects on the behavior of granular materials, and the shear strength and compressibility are also included. Raisianzadeh et al. [7] conducted a micromechanical study on particle

breakage in 2D angular rockfill materials under biaxial compression loading using a combined DEM and extended finite element method (XFEM) approach. Song et al. [8] investigated the skeleton behaviors of open-graded friction courses using DEM. Zhou et al. [9] presented simulating tri-axial compression tests on numerical samples reveals the relationships among the micromechanical parameters and macroscopic response of rockfill materials.

In engineering, the identification and quantification of particles help to realize the needs of material classification and risk prediction, intelligent construction and management, and computer deep learning. To explore the effect of particle shape, Li et al. simulated three dimensions of aggregate and asphalt mixture using parameterized shape and size gradation [10]. And Ma et al. used another discrete method by a microscopic modeling approach to simplify the discrete element's shape by introducing irregular convex polyhedrons to reproduce the geometry-dependent behavior of rockfills [11]. In addition, in the research of Zhou et al., the deformable DEM was employed to study the effect of particle shape on the macroscopic mechanical behavior of rockfill materials [9], indicating that the particle shape has a significant impact on the macroscopic response of rockfill. On top of that, Nie et al. [12] explored the impacts of Fourier-based particle shape on the macro-mesoscopic shear responses of rockfill materials by numerical biaxial compression tests. However, these works on the impact of particle shape are limited, since most of them were conducted by numerical tests, which is time-consuming and expensive. Furthermore, the complete particle shape is not extracted and processed.

The previous methods have achieved the identification of particles to a certain extent, but they have not studied the effects of particle size and shape in depth. In this study, the rockfill particle contour is firstly extracted based on machine learning algorithms such as AdaBoost, Cascade, and sliding windows. Then, the shape evaluation indexes are quantified and the statistical analysis of each index is presented. In addition, the DEM simulation is implemented on the deformation and compaction of rockfill. Based on the simulation, the macroanalysis on void ratio and cumulative settlement is given. Finally, the microanalysis on particle coordination number, rotation momentum, and displacement is studied. Overall, this study lays a foundation for further research on the effect of particle shape and size of rockfill.

2. Automated Shape Identification

In this study, low-precision photography equipment (such as mobile phones and digital cameras) is used to obtain multiple subgrade rockfill materials images to save time and cost, considering the characteristics of the large number and low-precision requirements of rockfill material samples, as shown in Figure 1. The target of this study is to extract the irregular shape of subgrade rockfill materials.

Due to the simplicity, high precision, and high computational efficiency of the algorithm, the improved Viola–Jones algorithm [13] is used to automatically identify subgrade rockfill particles.

2.1. Training Set Preparation. Firstly, the most common shape of subgrade rockfill particles is considered. All the images containing a particle have an aspect ratio of 1 : 1. About 1206 pictures of these rockfill particles are taken, and then, some of these particles are cropped and zoomed as a training dataset for the model. Each cropped image is a small square in the original image. Among them, the images containing the complete outline of the subgrade rockfill particle are marked as positive images, and the other images are marked as negative images. All the cropped images have a size of 32×32 pixels. Taking these images as input data, the computer can train the model and learn to obtain Haar-Like features [14]. Then, the feature results are stored in the classifier. The sample images are shown in Figure 2.

2.2. Scaling and Rotation of Training Images. Mostly, the aspect ratio of subgrade rockfill particles is 1 : 1 to 2 : 1. Therefore, for particles beyond this range of ratio, it is difficult to collect a large amount of image data by photographing. However, there exist some real rockfill particles with a high aspect ratio, so the classifier is expected to detect these particles as well. Therefore, a new method of acquiring a large number of images is needed. In this study, to quickly obtain a large number of slender rockfill particle images that can be used for training, a stretching method is used to digitally stretch the existing images with an aspect ratio of 1 : 1 [10]. By adjusting the size of the previous 1 : 1 training image (32×32 pixels), 1.5 : 1 training image (48×32 pixels), 2 : 1 training image (64×32 pixels), 3 : 1 training image (96×32 pixels), and 4 : 1 training images (128×32 pixels) can be obtained.

The aspect ratio of most railway subgrade rockfill particles is 1 : 1 to 2 : 1. Therefore, for rockfill that is not in this ratio, it is difficult to collect a large amount of image data by shooting. However, these high aspect ratio rockfill particles are real, so the classifier also needs to detect this rockfill. Therefore, we need a new method of acquiring a large number of images. To quickly obtain a large number of slender rockfill particle images that can be used for training, this article digitally stretches the existing images with a rockfill aspect ratio of 1 : 1 [15] by adjusting the size of the previous 1 : 1 training image (32×32 pixels), 1.5 : 1 training image (48×32 pixels), 2 : 1 training image (64×32 pixels), 3 : 1 training image (96×32 pixels) and 4 : 1 training images (128×32 pixels), as shown in Figure 3.

In addition, to recognize slender subgrade rockfill particles in any direction, the original image is rotated counterclockwise in 15° increments, as shown in Figure 4. For each rotated image, the sliding window scans the entire image in turn. The sliding window method may not be able to detect some subgrade rockfill particles due to the oblique placement of these particles. However, if the image is rotated, these particles will be converted to the vertical direction, which is easy to identify. After rotating the image by 15°, 30°, 45°, 60°, 75°, 90°, 105°, 120°, 135°, 150°, and 165°, 13 rotated images can be obtained. Figure 4 shows a simple example of 0°, 30°, and 60°.

Figure 1: Schematic of subgrade rockfill particles.

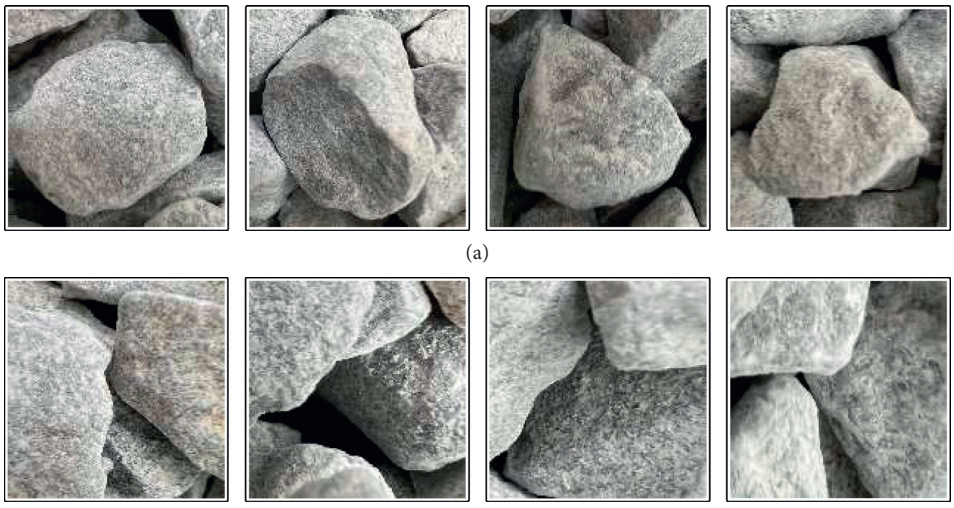

Figure 2: (a) Samples of positive images; (b) samples of negative images.

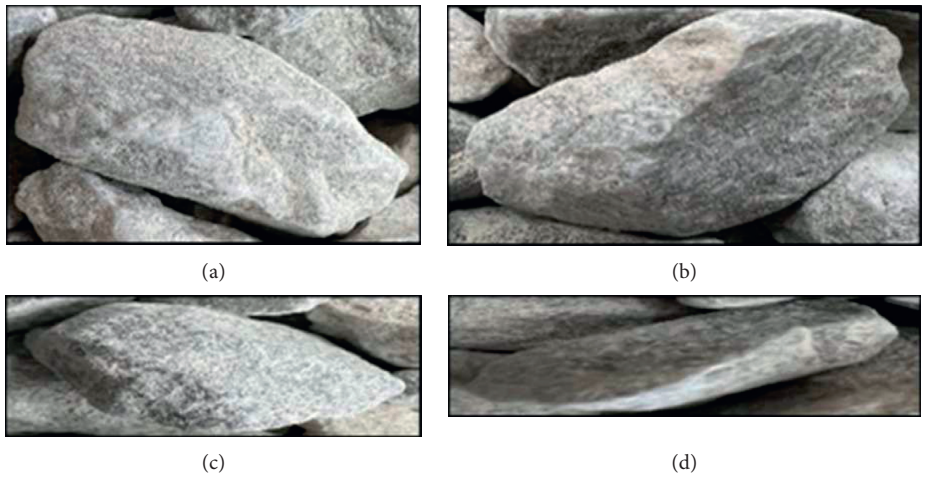

Figure 3: Schematic of stretching images: (a) 1.5 : 1 image; (b) 2 : 1 image; (c) 3 : 1 image; (d) 4 : 1 image.

Then, all the results of these images are merged. In each image, if a subgrade rockfill particle is successfully identified, a bounding box is added. Then, all bounding boxes will be superimposed when merging. However, due to the rotation, the same rockfill particle will generate some different bounding boxes. Thus, the image is rotated to the 0° position,

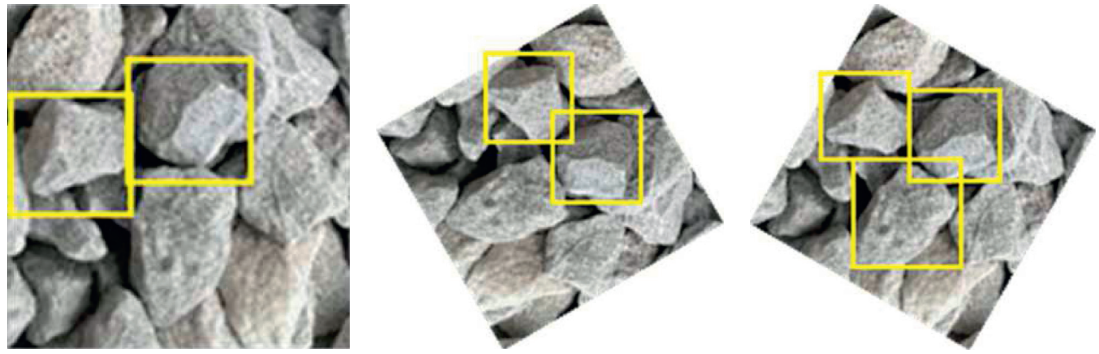

(a) (b) (c)

Figure 4: Schematic of rotation: (a) 0°; (b) 30°; (c) 60°.

which is equivalent to only rotating the sliding window. Then, the bounding box with the smallest area is selected as the final bounding box of this rockfill particle, as shown in Figure 5.

2.3. AdaBoost and Cascade Classifier. All the labeled images are used to train the model to obtain the feature difference between the positive and negative images in a dataset. Firstly, AdaBoost and Cascade methods [16] are used. Then, through the sliding window method [17], the subgrade rockfill particles can be successfully identified.

AdaBoost is a classification algorithm that can integrate some weak classifiers into a strong classifier. This strong classifier can be used in the Cascade method. The classifier is used to test an instance, and each classifier f_t will output the probability distribution of two classes of positive or negative. These probabilities are combined in proportion to the relevant multipliers. The detailed algorithm is shown in Figure 6.

The training process of the Cascade method is divided into multiple stages. At each stage, a strong classifier is trained through the AdaBoost algorithm. In addition, three parameters need to be set in advance: the number of stages s, the detection rate d, and the false positive rate f, where d represents the minimum percentage of correct detections and f represents the maximum percentage of negative images that are incorrectly identified as positive. In each stage, it is necessary to search for the smallest T in AdaBoost algorithm, so that the detection rate of the strong classifier $C(x)$ trained by AdaBoost is greater than d and the false positive rate is less than f.

In the hypothetical example of Figure 7, 100 positive images and 100 negative images are used as input data. The original parameters of each stage are $s = 3$, $d = 0.99$, and $f = 0.25$. Then, in each stage, a strong classifier with appropriate T is trained through AdaBoost, with the value of T 3, 10, and 35, respectively. In the first stage, the model has 200 input images, and the classifier meets the requirements that the detection rate is greater than d and the false positive rate is less than f. Then, the second stage is similarly performed. In stage 3, the total detection rate $D = d^3 = 0.97$ and the false positive rate $F = f^3 = 0.015$ can be obtained.

2.4. Identifying Particles Based on the Sliding Window Method. Through the previously obtained classifier, images containing real particles can be obtained. The next task is to identify the complete contour of subgrade rockfill particles. Given a new image of rockfill particles, at each scanning position, the area in the sliding window is input to the detector using a sliding window algorithm. The detector will find and extract features in the window area of the image. Based on these features, the classifier finally determines whether the image is a positive image or a negative image. If it is a positive image, a bounding box is added to the scanning position to identify it as an area containing complete outline particles. The specific instructions are as follows.

Since the smallest pixel of the particle is about 50×50, a 50×50 sliding window is first used to scan the entire image. In each window, the crop image is input to the classifier. Since the previous classifiers are trained based on 32×32 images, cropped images larger than 32×32 should be scaled to 32×32, and the $C_1(x)$ classifier in the Cascade algorithm is tested. If the output is positive, move to stage 2 of the Cascade method. Otherwise, the negative images are rejected, and the sliding window will move to the next position by 1 pixel. If the cropped image successfully passes all s classifiers, it will be a positive image containing the complete contour rockfill particles with a high probability. Then, the sliding window at this position is marked as the bounding box of the particle. Next, continue to move the sliding window until the entire image is scanned. The moving increment of the sliding window in the horizontal direction and the vertical direction is 1 pixel, and the moving path is shown in Figure 8(a).

When the 50×50 sliding window successfully scans the entire image, we add 5 pixels to the size of the sliding window in both horizontal and vertical directions, as shown in Figure 8(b). The previous sliding process is repeated until the sliding window expands to the maximum size of 300×300 pixels. Since most of the cropped images will be classified as negative images and rejected, only a small number of images can successfully pass all s classifiers, so the algorithm has high computational efficiency.

Note that when the sliding window is large enough, several movements of the sliding window may contain the

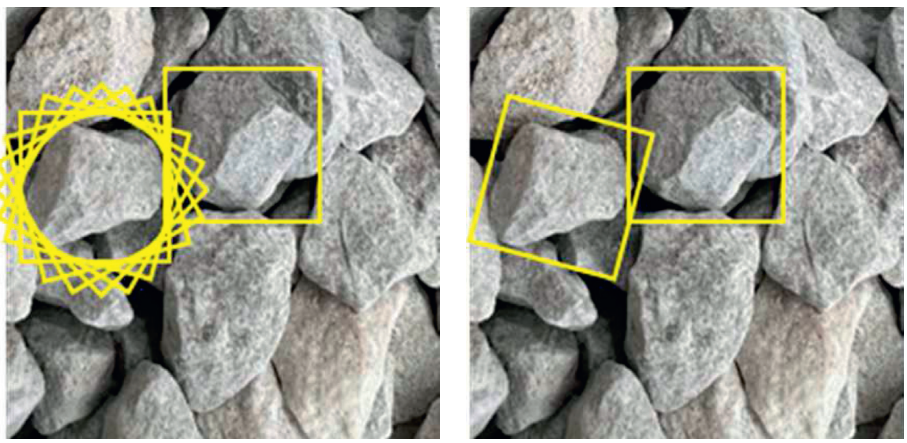

(a) (b)

Figure 5: (a) The merges results of all rotation; (b) the average window of particles.

Algorithm 1 Adaboost

1: Set weight $w_i = 1/n$, i=1,2,....,n

2: for $t = 1,2,....,\ T$ do:

3: Obtain classifier f_t by learning method(decision tree) and training data

4: $err_t \leftarrow \sum_{i:f_t(x_i)\neq y_i} w_i$

5: if $0<err_t<0.5$, for all i:

6: $w_i = \begin{cases} w_i & if\ f_t(x_i) = y_i \\ w_i \cdot \dfrac{1-err_t}{err_t} & if\ f_t(x_i) \neq y_i \end{cases}$

7: Otherwise, algorithm terminates.

8: fot all i, $w_i \leftarrow w_i / \sum_{i=1}^{n} w_i$ (Normalization)

9: Return classifier $f(x) = \sum_{t=1}^{T} \log\left(\dfrac{1-err_t}{err_t}\right) f_t$

Figure 6: AdaBoost algorithm.

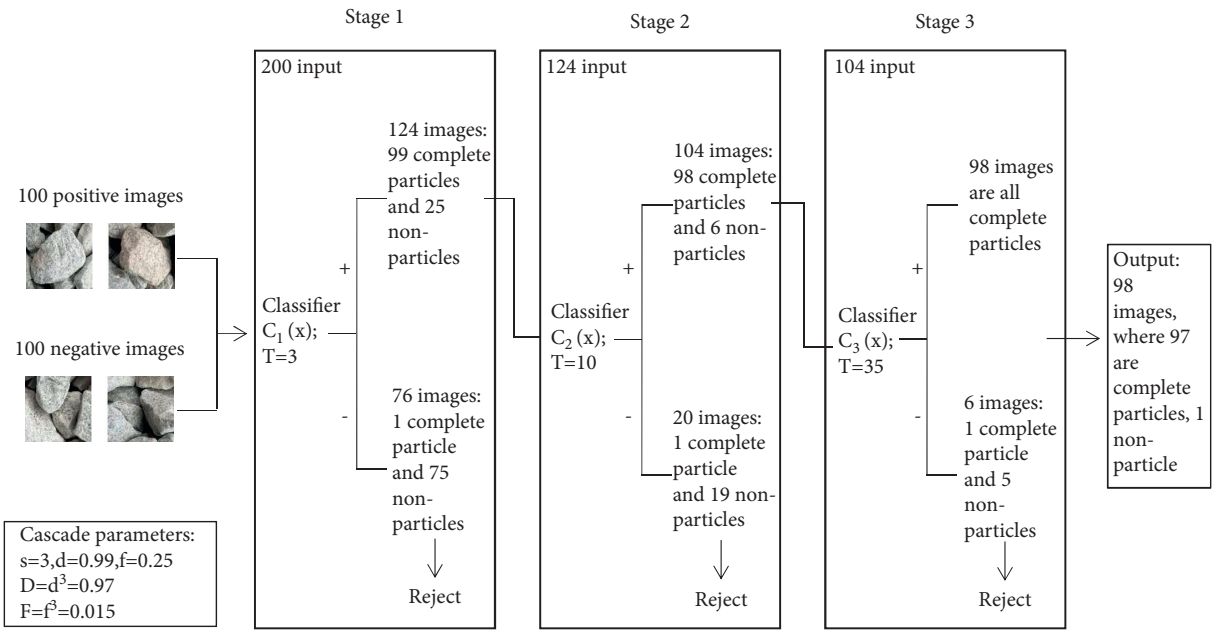

Figure 7: A hypothetical example of the Cascade algorithm.

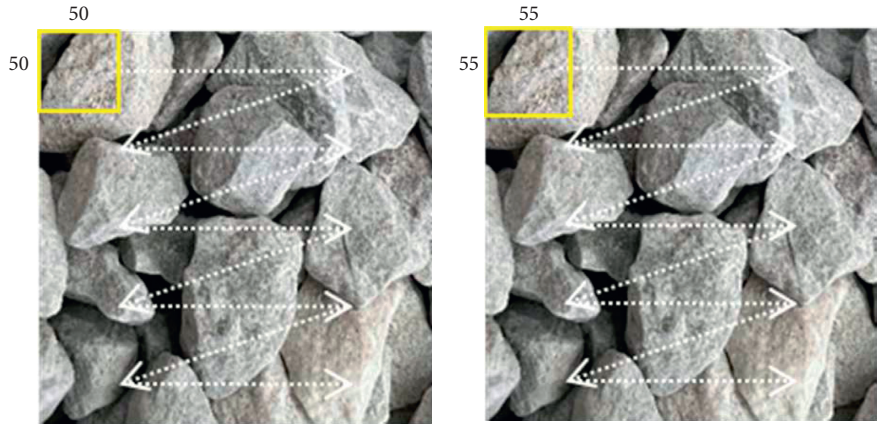

Figure 8: (a) The minimum sliding window; (b) the increment is 5 pixels.

same particle, resulting in multiple bounding boxes. In this case, we take the average value as a new single window, as shown in Figure 9.

3. Quantitative Shape Analysis

3.1. Calculation of Length Flatness of Particles. Common first-scale morphological indicators of particles include flatness, form factor, sphericity, and others. They are mostly used to measure the similarity between the overall contour of particles and the contour of the standard graph of the same diameter (round, square particles, etc.). Also, they are the indicators that have the greatest influence on the overall morphology and mechanical behavior of particles. Among them, the length flatness is widely used in engineering because of its simple measurement and simple concept. Although the existing definitions of length flatness indexes are very diversified, some basic geometric properties of particles are often adopted by most indexes and become common factors of the index system (as shown in Table 1). Therefore, the calculation of these basic indexes is the premise of the calculation of the length flatness index.

Feret's diameter $\mathrm{Fer}(a)$ of a particle describes the vernier caliper length of a particle at a certain direction angle, which is the basis of the index of particle length flatness. For the directional angle a_i of a particular particle O_{p1}, the Feret diameter $\mathrm{Fer}(a_i)$ corresponding to it can be given by the following equation:

$$O'_{p1} = \begin{pmatrix} i'_1 & j'_1 \\ i'_2 & j'_2 \\ i'_3 & j'_3 \\ \cdots & \cdots \\ i'_k & j'_k \end{pmatrix} = \begin{pmatrix} i_1 & j_1 \\ i_2 & j_2 \\ i_3 & j_3 \\ \cdots & \cdots \\ i_k & j_k \end{pmatrix} \begin{pmatrix} \cos(-a_i) & \sin(-a_i) \\ -\sin(-a_i) & \cos(-a_i) \end{pmatrix}, \tag{1}$$

$$\mathrm{Fer}(a_i) = \max(i'_1, i'_2 \ldots i'_k) - \min(i'_1, i'_2 \ldots i'_k), \tag{2}$$

where the function of equation (1) is to rotate the particle so that the direction corresponding to a_i is parallel to the X-axis.

The corresponding Feret diameter can be easily obtained with known direction angle a_i using equation (2). Therefore, when calculating the maximum (minimum) Feret diameter of particles, the most important problem is to find their corresponding direction angle a_i. The rotation method [18] is commonly used to solve this problem in existing research studies. The essence of the rotation method is to enumerate the direction angles between 0 and 180° with a certain angle step length and obtain the approximate maximum (minimum) Feret diameter through comparison by calculating the Feret diameter corresponding to each direction angle. This process is represented geometrically by rotating at angular intervals and measuring the particle profile. In general, the rotation method is simple and intuitive, with high calculation accuracy when the rotation step size is small. It is not affected by the concave part of particles. Therefore, the rotation method can well accomplish the calculation of the particle Feret diameter. Since the rotation method has a certain error when the rotation step is large, the calculation time is relatively great.

The calculation of the length flatness of particles can be divided into two basic ideas: the ratio of direct use of maximum (S_{major}) and minimum (S_{major}) Feret diameter and the aspect ratio of particle envelopment box. Among them, the definition of particle envelopment box is still controversial in academic circles. A more widely used definition is to take S_{major} as the length of the enclosing box and define length flatness $EI_1 = S^{90}_{\mathrm{minor}}/S_{\mathrm{major}}$. However, this method will give incorrect results when calculating the particles of the rectangle (or approximately rectangle). The other definition builds the bounding box indicator $EI_2 = S_{\mathrm{minor}}/S^{90}_{\mathrm{minor}}$ based on S_{major}. This method tends to get a smaller bounding box, and it cannot obtain the correct results when calculating rhombic particles. In fact, since EI_1 and EI_2 contain S_{major} and S_{major}, they are also statistically strongly related to another commonly used metric, $EI_3 = S_{\mathrm{minor}}/S_{\mathrm{minor}}$.

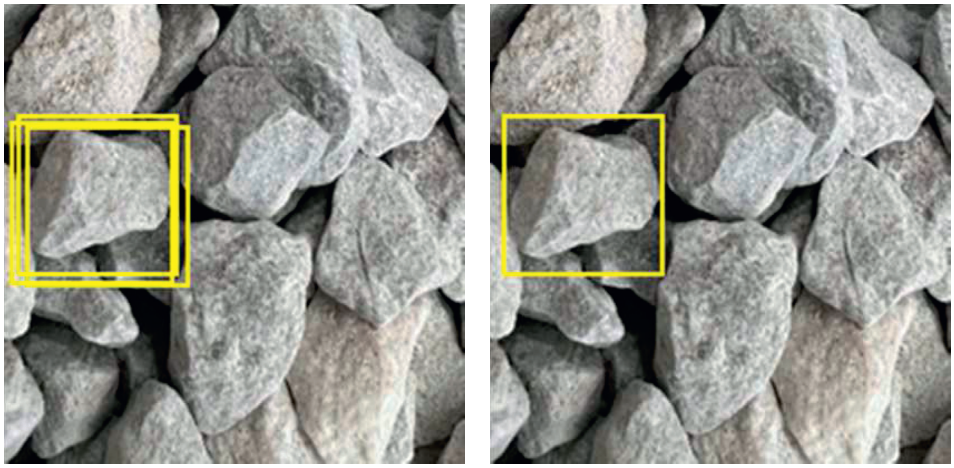

(a) (b)

Figure 9: (a) Several bounding box of a particle; (b) the average bounding box.

Table 1: Basic particle morphology indicators that are widely used.

Parameter	Symbol	Geometric meaning
Particle size	Ar	The area bounded by a particle contour
Particle circumference	Per	Particle contour perimeter
Feret's diameter	Fer(a)	"Ruler length" of corresponding direction angle a
Length scale	S_{major}	Maximum Feret's diameter
Vertical scale	S^{90}_{major} S^{90}_{major}	Feret's diameter orthogonal to the direction corresponding to the long scale (short scale)
Short scale	S_{minor}	Minimum Feret's diameter

In this study, referring to existing studies [19–21], EI_3 is selected as the index to evaluate the length and flatness of particles. A total of 991 real images of subgrade rockfill particles were extracted, and the calculation results of EI_3 can be obtained, as shown in Figure 10. From the figure, it can be seen that the results of EI_3 approximately follow a normal distribution, with a mean value of 0.73 and a width from 0.4 to 1.2.

3.2. Calculation of Edge Angles and Roundness of Particles. Barrett [22] expounded the advantages of the independence of grain morphology indexes among scales. However, in the existing research, the edge angle index is often difficult to maintain its independence from the first- and third-scale indexes. For example, *RI* calculation formula contains the basic indexes of the first scale, such as particle circumference and area, which are highly dependent on the morphological characteristics of the first scale. The *AT* index cannot guarantee its independence from the third-scale morphology because the grain angular and grain roughness effects are considered simultaneously. To solve this problem, Liu et al. [23] proposed an edge angle index *AI* based on a convex hull. The index is defined as the ratio of the equivalent elliptic perimeter of the particle to the circumference of the convex hull of the particle, where the equivalent ellipse of a particle is an ellipse with the same length flatness and area as the particle, and its semimajor axis (a) and semiminor axis (b) are given by the following equation:

$$a = \sqrt{\frac{\mathrm{Ar}}{\pi EI_3}}, \qquad b = aEI_3. \tag{3}$$

AI indicator has the following characteristics:

(1) For smooth particles, their circumference should be close to its equivalent ellipse circumference. The more trenchant the edges and corners particles are, the longer the perimeter will be, leading to *AI* value declining. Therefore, *AI* indicator can be used to reflect the degree of angular.

(2) By convex hull, the influence of particle contour roughness is excluded and the independence with the third-scale index is maintained.

(3) By comparing the equivalent ellipse with the same length flatness, the influence of length flatness is normalized and the dependence with the first-scale index is reduced.

The characteristics (2) and (3) guarantee the independence of this index, which is an advantage compared with other indexes. However, when the convex hull is used to exclude the roughness of the contour, the angular fluctuation of the particle will also be excluded, so that the concave part of the particle cannot be considered in this index. Therefore, this index has been modified in this study. Firstly, B-spline resampling technique was used to process the

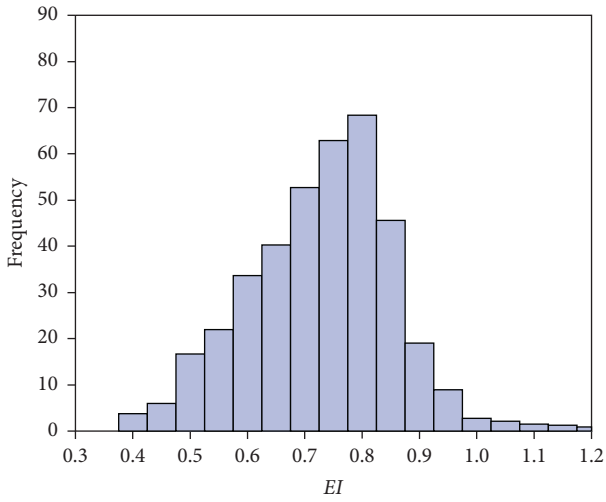

Figure 10: Statistical results of the length flatness index calculated by the rotation method.

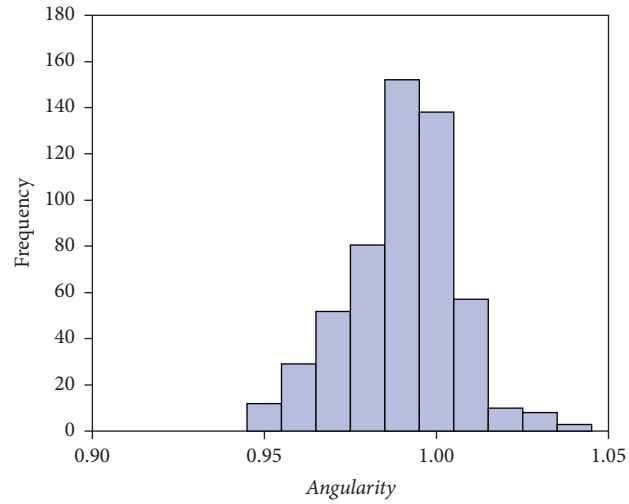

Figure 11: Statistical results of edge angles and improved posterior edge angles.

original particle outline, eliminating particle roughness and retaining edges and corners. Then, the improved edge angle $AI2$ is obtained by directly comparing the smoothed particle circumference per_s with the equivalent ellipse circumference Per_e:

$$AI_2 = \frac{\text{Per}_e}{\text{Per}_s}. \tag{4}$$

A total of 991 real subgrade rockfill particles is used to calculate the contour edge angle values, and the statistical curve is drawn in Figure 11. It can be seen that the edge angle approximately follows a negative skewness distribution.

3.3. Calculation of Particle Contour Roughness. Particle roughness describes the degree of fine fluctuation of the particle surface. In this section, the conventional particle roughness based on polar radius is improved. By using B-spline resampling to calculate the particle smooth and normal vector, an index for quantitative analysis of particle contour roughness was proposed. Based on the above three-segment intersection determination algorithm, a roughness index with scale invariance is proposed in this study. The calculation is as follows:

(1) B-spline resampling is carried out for the particle contour, and the normal vector of each sampling point is calculated

(2) A line segment is made at the sampling point along the normal vector, so that its length is equal to the radius R_{eq} of the equal-area circle (to ensure that the line segment has an intersection)

(3) The line segment is judged to be intersecting with the original particle contour, and the distance dist_i from the nearest intersection point to the sampling point is calculated

(4) Repeat steps (2) and (3) for all sampling points

Based on the above steps, roughness index R_g can be obtained as follows:

$$R_g = \sum_{i=1}^{n} \frac{\text{dist}_i}{nR_{\text{eq}}}, \tag{5}$$

where R_{eq} ensures the scale invariability of the index; that is, R_g remains unchanged when the particle contour is equilateral magnified.

The angle values of edges of 991 real subgrade rockfill particle contours are calculated, and the statistical curves are plotted in Figure 12, which is approximately a positive skewness distribution.

4. Application to DEM Simulation

4.1. Simulation of Earth Compaction of Rockfill Subgrade. Affected by the actual construction scale of the subgrade project, particle gradation and the irregular shape particles are adopted in the simulation, and the adoption of the 3D model will greatly increase the workload of the computer. Therefore, the two-dimensional model can also be used to simulate and analyze the particle motion characteristics of rockfill in the compaction process from a microscopic perspective.

In this study, discrete element software PFC2D was used to simulate the compaction process of rockfill in two dimensions. To ensure that the roller vibrator rolls rather than sliding during the movement, the relationship between the angular velocity w and the horizontal velocity v of the vibrator is shown in the following equation:

$$v = w \times R, \tag{6}$$

where, v, w, and R are the horizontal velocity, angular velocity, and radius of the vibration wheel, respectively.

The simulated material is rockfill for subgrade construction, and the linear elastic contact model is adopted in the discrete element model, which is widely used in similar studies [24]. The mesoscopic parameters used in the

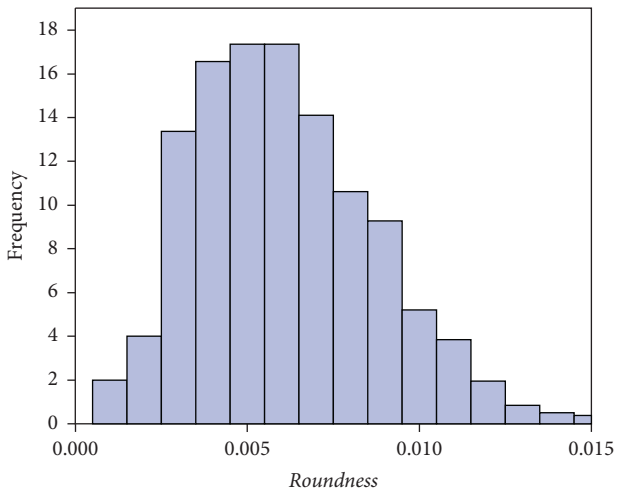

Figure 12: Statistical results of roughness index.

simulation refer to the research results of Liu et al. [24], and the specific parameters are shown in Table 2.

Referring to the research of Goldenberg and Goldhirsch [25], Ma et al. [11], Zhou et al. [9], Alaei and Mahboubi [26] and Nie et al. [12], in this study, 5 groups of two-dimensional particles with different edge angles were generated, with 8 samples in each group, as shown in Figure 13. To exclude the influence of elongation on the simulation results, the elongation of particles was controlled between 0.97 and 1.00. Note that particles of roundness 1 are standard circles and are not shown in Figure 13. In addition, the effect of particle roughness was not considered in this study, that is, $D_8 = 0.0$.

In PFC2D, the clump function can realize the fitting of complex particle contour, with the fitting accuracy control parameters distance (range 0–180) and ratio (range 0.0–1.0). The larger the distance, the smaller the ratio, and the fitted results are closer to the real model. However, more computational memory and running time are consumed. In this study, the distance was set as 162, and the ratio was set as 0.25. Figure 14 shows a clump model filled and generated under this setting. It can be seen that the set of two parameters is sufficient to reflect the external contour of the particle.

Coarse particle packing with a diameter greater than 10 mm was used in this simulation to improve the calculation efficiency, and the distribution of the size of the packing was calculated. The results show that the content percentage of diameter ranging from 10 to 20 mm, 20 to 30 mm, 30 to 40 mm, 40 to 50 mm, and 50 to 60 mm is 17%, 20%, 25%, 20%, and 18%, respectively.

The packing model was set in the range of height $(H) \times$ width $(W) = 0.8\,\text{m} \times 8\,\text{m}$. The initial model is generated by gravity sedimentation. The process is as follows:

(1) In the $2H \times W$ range, contactless particles slightly larger than the total volume of the target were randomly generated according to the particle size range and content, as shown in Figure 15(a).

(2) Under the action of gravity, particles fall freely, when the particle system reaches a quasi-static state and stops running, as shown in Figure 15(b).

(3) In order to ensure that fillers with different roundnesses are compacted at the same thickness, redundant particles above the thickness line are removed to simulate the leveling process. The final leveling filler is shown in Figure 15(c).

(4) A rigid body circular element is generated to simulate the roller. The movement parameters and attribute parameters of the roller are determined in Tables 2 and 3. The chord wave vibration load is applied to the filler during the movement of the roller, as shown in Figure 15(d). And the simulation is stopped after repeated rolling 12 times.

4.2. The Macroresult. Figure 16(a) shows the porosity of fillers with different roundnesses varying with the number of rolls. Obviously, with the increase in the number of rolling times, the pores first decreased sharply and then remained unchanged. But the correlation between roundness and vibratory compaction was not strong. The initial porosity was extracted (shown in Figure 16(b)), and it was found that with the increase of roundness, the initial porosity first decreased and then increased, which was consistent with the previous research results related to particle roundness [27]. Figure 16(c) shows the normalized porosity rate Δn obtained after conversion using equation (7). It is found that the small roundness of the particle indicates irregular shape and great drop in the particle porosity compared to the initial state. The normalized porosity rate is obtained as

$$\Delta n = \frac{n_0 - n_i}{n_0} \times 100\%, \tag{7}$$

where n_0 and n_i represent the porosity corresponding to the initial porosity and the porosity corresponding to the ith pass after rolling, respectively.

Figure 17 shows the cumulative settlement amount of the pavement corresponding to each roll pass of the filler, which shows a trend similar to the normalized pore change rate. It shows a trend of rapid settlement in the early stage and a trend of slow settlement in the later stage. This trend is consistent with the actual change in the monitored value in construction [24]. The indirect results showed that the particles sank under the vibratory compaction condition, which made the fillers squeeze and approach each other and rearrange the particles. This results in a smaller porosity, showing the changing trend as shown in Figure 16(a). In addition, a small value of roundness of the particles represents the great settlement of the fillers. Therefore, in

Table 2: Microscale parameters used in the DEM simulations.

Microscopic parameters	The normal stiffness, *kn* (N/m)	The tangential stiffness, *ks* (N/m)	The coefficient of friction, fric	Local damp	Normal/tangential damping dp_n, dp_t	Density (kg/m^3)
Value (particle)	1.5×10^7	2.9×10^7	0.5	0.9	0.5	2600
Value (wheel)	1.0×10^9	1.0×10^9	0.3	0.0	0.5	7800

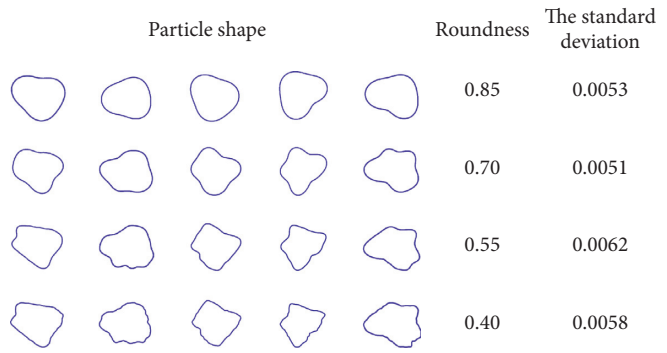

Figure 13: Two-dimensional particle models with different roundnesses.

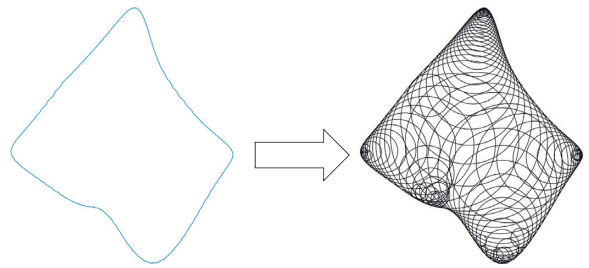

Figure 14: A DEM-simulated virtual particle from a Fourier-based particle contour.

practical engineering, the irregular shape of the packing requires more rolling times.

4.3. The Micromechanical Results

4.3.1. Coordination Number. Coordination number is an important index to characterize the internal structure of particle systems. For the irregular particle model composed of Clump, there are two different definitions of coordination number: one is the number of particles in contact with the specified particles, called the coordination number of particles; and the other is the number of contacts belonging to a given particle, called the contact coordination number.

Thornton [28] pointed out that there are particles in granular materials that do not contact with other particles or only contact with one particle, and such particles have no contribution to the overall stability of the material. Therefore, the mechanical average particle coordination number is defined as follows:

$$CN = \frac{2C - N_1}{N - N_0 - N_1}, \tag{8}$$

where C is the total number of particle contact, N is the total number of particles, and N_0 and N_1 are the numbers of particles in contact with zero or one particle in the particle system. Figure 18 shows the relationship between the mechanical particle coordination number and the rolling pass number of fillers with different roundnesses. For each roundness case, the particle coordination number showed a slight upward trend as the number of rolling passes increased; that is, the number of particles in contact with a certain particle increased. This was related to the overall looseness of the packing and reflected that the packing compactness increased as the number of rolling passes increased. For a certain roundness filler, the increase in the coordination number will lead to the enhancement of interlock between the particles, thus improving the anti-rotation ability of the particles. In addition, large roundness values of particles represent a large coordination number of the particles, indicating that the rounder particles are more likely to contact multiple particles.

Figure 19 shows the relationship between average contact coordination number and rolling pass number of fillers with different roundnesses. Similar to the variation trend of the particle coordination number, the contact coordination number of a certainly shaped particle increased only slightly on the whole. However, for the particles with different roundnesses, smaller roundness corresponds to a larger contact coordination number of the particles, indicating that the interlock phenomenon is more obvious.

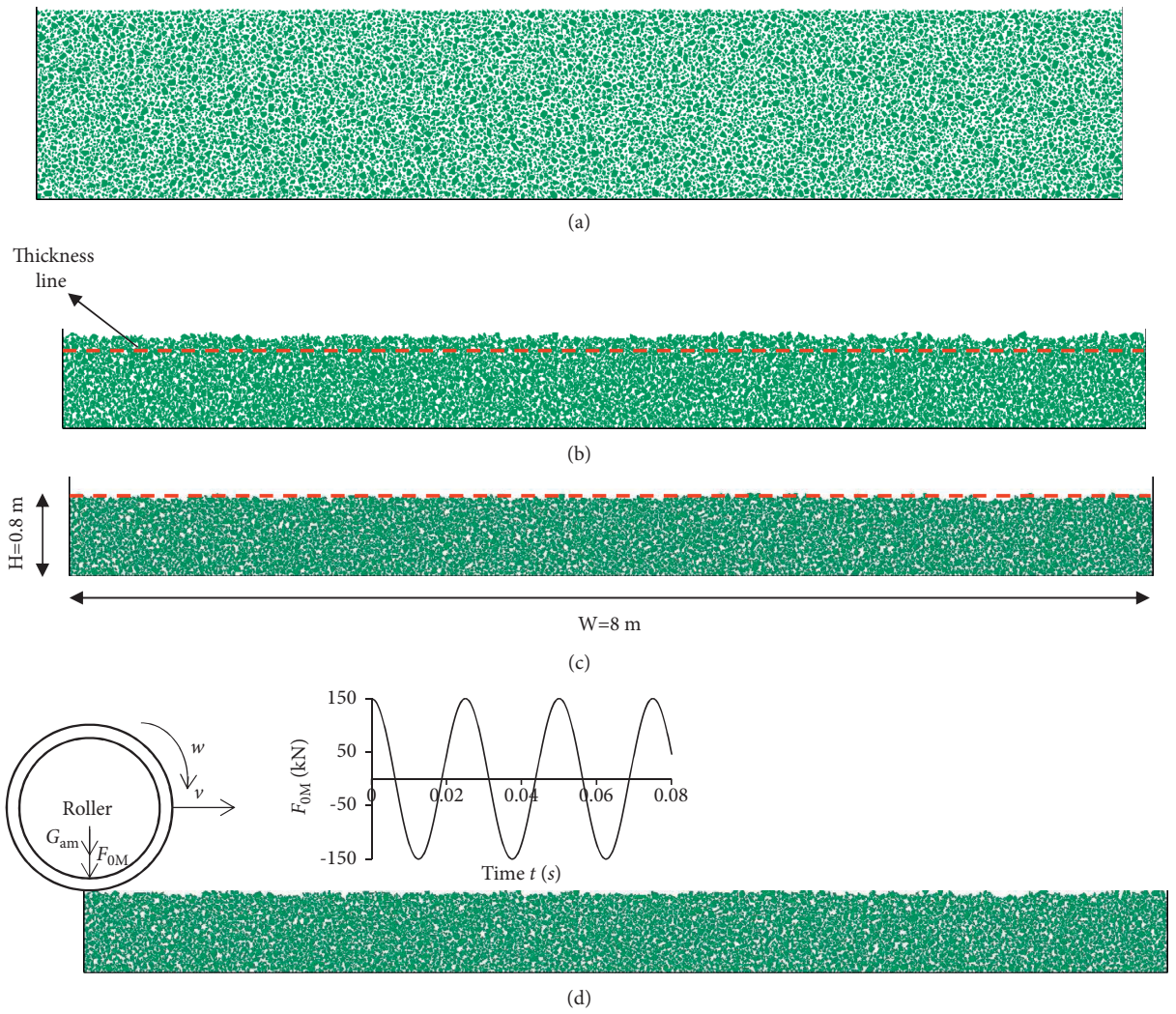

Figure 15: PFC simulation of vibratory compaction, including dumping, spreading, and compaction. (a) The contactless model; (b) sedimentation accumulation; (c) leveling; (d) vibratory compaction.

Table 3: External load parameters.

Rolling wheel parameters	Quality of grinding wheel, G (kg)	Grinding wheel diameter, D (mm)	Grinding wheel width, b (mm)	Vibration frequency, f (Hz)	Exciting force, F_0 (kN)	Speed, v (m/s)	Rolling pass
The actual parameter	1×10^4	1500	2000	40	300	1	12
Simulation parameters	5×10^3	1500	1000	40	150	1	12

4.3.2. Particle Rotation Momentum. Rotation is an important relative motion between particles in contact. The rotation between particles is related to the rotation behavior of individual particles along the reference axis. Figures 20(a) and 20(b) show the cumulative rotational momentum of fillers with different roundnesses along with clockwise and counterclockwise directions as a result of rolling. It can be seen from Figure 20 that the rotation momentum of the packing in the clockwise and counterclockwise directions is basically the same. Under a certain roundness, the rotation value of the particles increases with the increase in the number of rolling times, and the increase tends to slow down. This is because the increase in the particle coordination number and contact coordination number enhances the interlock between particles and hinders the rotation of particles. In addition, the smaller roundness of the particle represents the smaller rotational momentum of the particle, indicating that the more irregular the particle is, the stronger the antirotation ability is. The presumed reason is that the

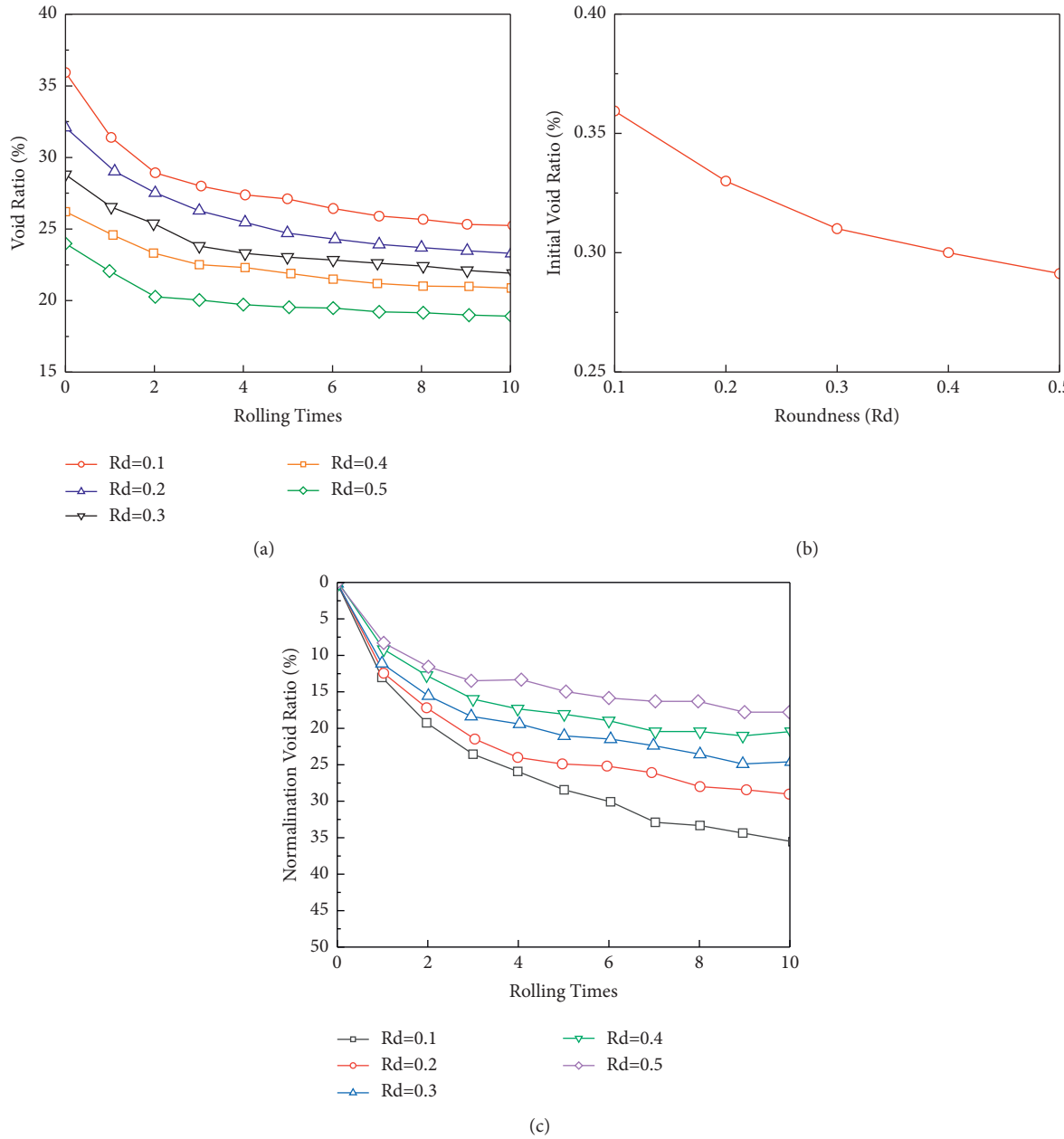

Figure 16: The relationship between the compactor pass and pore change of fillings with different roundnesses. (a) Porosity; (b) initial porosity; (c) normalized void change rate.

particles with lower roundness have a larger contact coordination number, which increases the interlock effect between the particles and thus hinders the rotation of the particles.

Figure 21(b) shows the vertical displacement of the packing. It showed a similar trend to the cumulative settlement; that is, with the increase in the number of rolling times, the particles gradually sank and the downward trend gradually slowed down. In addition, for fillers with different roundnesses, the smaller the particle roundness is, the greater the vertical displacement is. Estrada et al. [29] pointed out that when the particles in contact have relative movement, irregular particles with stronger antirotation ability will be forced to slide along the contact surface, so as to regulate the overall deformation of the particle system. Therefore, more irregular particles are more prone to relative sliding between particles, resulting in larger vertical displacement of particles.

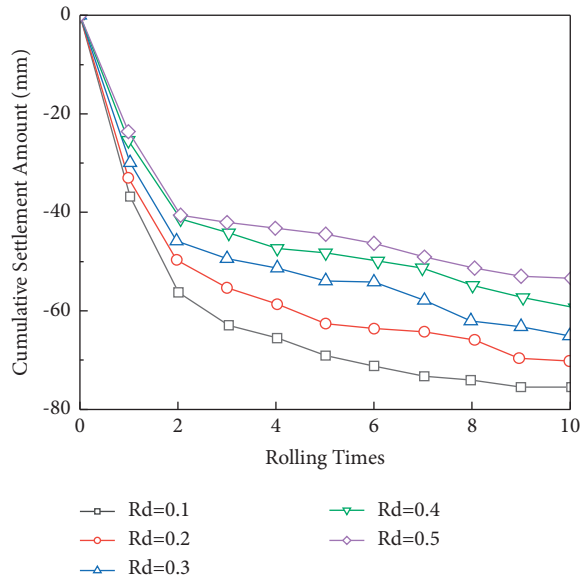

Figure 17: Cumulative settlement-compactor pass responses for fillings with different roundnesses.

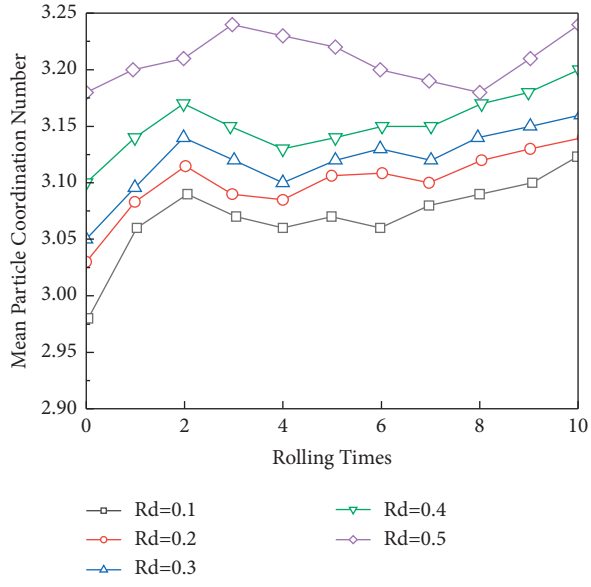

Figure 18: Mean particle coordination number-compactor pass responses for fillings with different roundnesses.

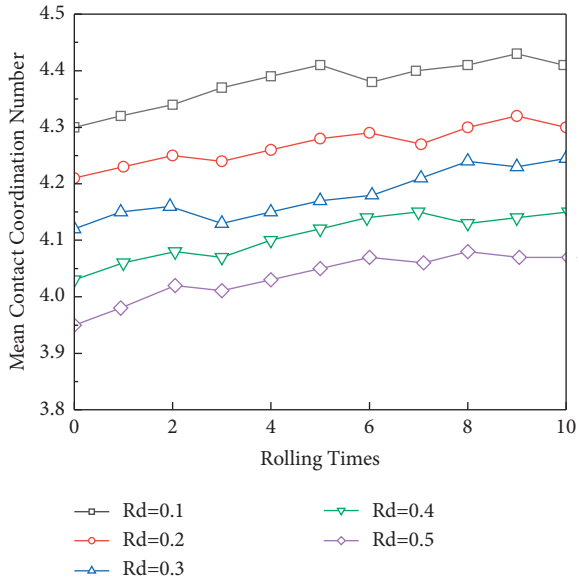

Figure 19: Mean contact coordination number-compactor pass responses for fillings with different roundnesses.

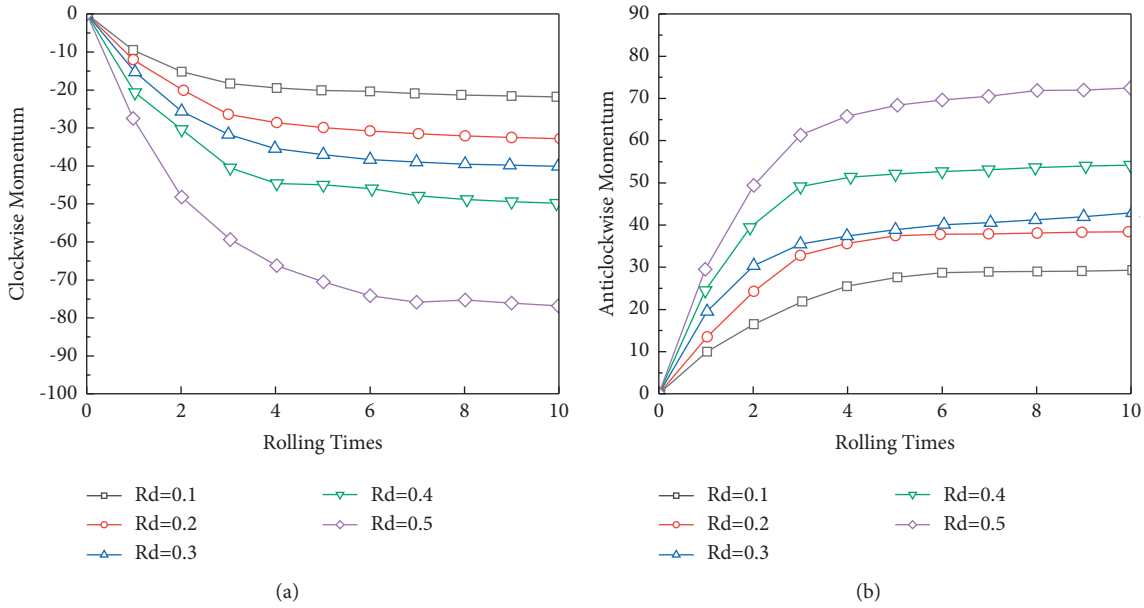

Figure 20: Particle rotation magnitude-compactor pass responses for fillings with different roundnesses. (a) Clockwise momentum; (b) rotational momentum in reverse time.

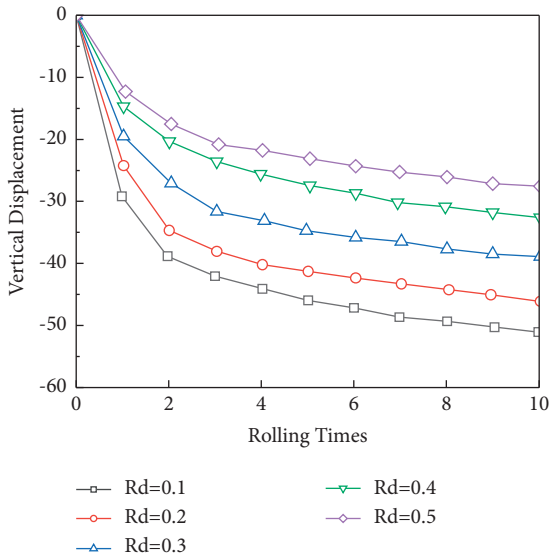

Figure 21: Displacement components of fillings in the vibration rolling process: vertical displacement.

5. Conclusion

Rockfill material is of great significance in the subgrade construction industry. The mechanical properties can be affected by the irregularity and variability of particle shape , which can be explored by discrete element simulation. In this study, the subgrade rockfill particle outlines are firstly extracted based on machine learning algorithms, including AdaBoost, Cascade, and sliding windows. Then, the shape evaluation indexes are quantified and the statistical analysis of each index is presented. In addition, the DEM simulation is implemented on the compaction of rockfill subgrade. Based on the simulation, the macroanalysis on the void ratio and cumulative settlement is given. Finally, the micro-analysis on the particle coordination number, rotation momentum, and displacement is studied. The specific results are as follows:

(1) 1206 pictures of the subgrade rockfill particles are taken as the training data. By training a strong classifier through AdaBoost in each stage of Cascade, only a small amount of pictures can pass all s stages in the Cascade algorithm. These pictures contain a complete outline of particles. Then, using sliding window and adding boundaries of particles, the final window of a particle can be obtained indicating that the particle is well extracted.

(2) The quantitative shape analysis is presented. For length flatness, 991 real particles show an approximately normal distribution, whereas the edge angle and roughness show a negative skewness distribution and positive skewness distribution, respectively.

(3) With the increase in the number of rolling passes, the porosity of the packing decreases gradually and the settlement increases gradually, and the change rate is fast at the beginning and slow in the end. In addition, smaller roundness of the particles represents a more obvious porosity drop and the greater settlement of the filler compared with the initial state.

(4) Under the rolling load, the particle coordination number and contact coordination number of the filler increased slightly. The smaller the roundness is, the larger the contact coordination number is, which increases the interlock effect and hinders the rotation of the particles. The horizontal displacement of particles shows a certain fluctuation, whereas the vertical displacement increases gradually. In addition, the smaller the roundness is, the larger the vertical displacement is and the smaller the horizontal displacement is.

Data Availability

The data used in the article are included in the article.

Conflicts of Interest

The authors declare that they have no conflicts of interest.

References

[1] A. Varadarajan, K. G. Sharma, K. Venkatachalam, and A. K. Gupta, "Testing and modeling two rockfill materials," *Journal of Geotechnical and Geoenvironmental Engineering*, vol. 129, no. 3, pp. 206–218, 2003.

[2] J. Zhang, J. Li, Y. Yao, J. Zheng, and F. Gu, "Geometric anisotropy modeling and shear behavior evaluation of graded crushed rocks," *Construction and Building Materials*, vol. 183, pp. 346–355, 2018.

[3] R. Pang, B. Xu, X. Kong, D. Zou, and Y. Zhou, "Seismic reliability assessment of earth-rockfill dam slopes considering strain-softening of rockfill based on generalized probability density evolution method," *Soil Dynamics and Earthquake*

Engineering, vol. 107, pp. 96–107, 2018.

[4] R. Deluzarche and B. Cambou, "Discrete numerical modelling of rockfill dams," *International Journal for Numerical and Analytical Methods in Geomechanics*, vol. 30, no. 11, pp. 1075–1096, 2006.

[5] J. Li, J. Zheng, Y. Yao, J. Zhang, and J. Peng, "Numerical method of flexible pavement considering moisture and stress sensitivity of subgrade soils," *Advances in Civil Engineering*, vol. 2019, Article ID 7091210, 10 pages, 2019.

[6] W. Hui, J. Li, F. Wang, J. Zheng, Y. Tao, and Y. Zhang, "Numerical investigation on fracture evolution of asphalt mixture compared with acoustic emission," *International Journal of Pavement Engineering*, vol. 2021, pp. 1–10, 2021.

[7] J. Raisianzadeh, S. Mohammadi, and A. A. Mirghasemi, "Micromechanical study of particle breakage in 2d angular rockfill media using combined dem and xfem," *Granular Matter*, vol. 21, no. 3, p. 48, 2019.

[8] W. Song, F. Xu, H. Wu, and Z. Xu, "Investigating the skeleton behaviors of open-graded friction course using discrete element method," *Powder Technology*, vol. 385, pp. 528–536, 2021.

[9] W. Zhou, G. Ma, X. Chang, and C. Zhou, "Influence of particle shape on behavior of rockfill using a three-dimensional deformable dem," *Journal of Engineering Mechanics*, vol. 139, no. 12, pp. 1868–1873, 2013.

[10] J. Li, J. Zhang, G. Qian, J. Zheng, and Y. Zhang, "Three-dimensional simulation of aggregate and asphalt mixture using parameterized shape and size gradation," *Journal of Materials in Civil Engineering*, vol. 31, no. 3, Article ID 04019004, 2019.

[11] G. Ma, W. Zhou, X.-L. Chang, and W. Yuan, "Combined fem/dem modeling of triaxial compression tests for rockfills with polyhedral particles," *International Journal of Geomechanics*, vol. 14, no. 4, Article ID 04014014, 2014.

[12] Z. Nie, Y. Zhu, X. Wang, and J. Gong, "Investigating the effects of Fourier-based particle shape on the shear behaviors of rockfill material via DEM," *Granular Matter*, vol. 21, no. 2, p. 22, 2019.

[13] M. Jones and P. Viola, "Fast multi-view face detection," *Mitsubishi Electric Research Lab TR-20003-96,*vol. 3, no. 14, p. 2, 2003.

[14] R. Lienhart and J. Maydt, "An extended set of haar-like features for rapid object detection," in *Proceedings of the International Conference on Image Processing*, vol. 1, September 2002.

[15] J. Zheng and R. D. Hryciw, "Identification and characterization of particle shapes from images of sand assemblies using pattern recognition," *Journal of Computing in Civil Engineering*, vol. 32, no. 3, Article ID 04018016, 2018.

[16] P. Viola and M. Jones, "Fast and robust classification using asymmetric adaboost and a detector cascade," *Advances in Neural Information Processing Systems*, vol. 14, pp. 1311–1318, 2001.

[17] A. Dosovitskiy, J. T. Springenberg, M. Riedmiller, and T. Brox, "Discriminative unsupervised feature learning with convolutional neural networks," *Advances in Neural Information Processing Systems*, vol. 1, pp. 766–774, 2014.

[18] J. Cardona, C. Ferreira, J. McGinty et al., "Image analysis framework with focus evaluation for in situ characterisation of particle size and shape attributes," *Chemical Engineering Science*, vol. 191, pp. 208–231, 2018.

[19] Z. Lianheng, H. Dongliang, D. Han-Cheng, Z. Shuaihao, and L. Dejian, "Reconstruction of granular railway ballast based on inverse discrete Fourier transform method," *Granular Matter*, vol. 19, no. 4, p. 74, 2017.

[20] W. Song, B. Huang, X. Shu, J. Stránský, and H. Wu, "Interaction between railroad ballast and sleeper: a DEM-FEM approach," *International Journal of Geomechanics*, vol. 19, no. 5, Article ID 04019030, 2019.

[21] H. Wu, L. Zhu, W. Song, Z. Xu, F. Xu, and H. Gong, "Impact performance of ballast by incorporating waste tire-derived aggregates," *Construction and Building Materials*, vol. 288, Article ID 122992, 2021.

[22] P. J. Barrett, "The shape of rock particles, a critical review," *Sedimentology*, vol. 27, no. 3, pp. 291–303, 1980.

[23] M. L. Hentschel and N. W. Page, "Selection of descriptors for particle shape characterization," *Particle & Particle Systems Characterization: Measurement and Description of Particle Properties and Behavior in Powders and Other Disperse Systems*, vol. 20, no. 1, pp. 25–38, 2003.

[24] D. Liu, L. Sun, H. Ma, and W. Cui, "Process simulation and mesoscopic analysis of rockfill dam compaction using discrete element method," *International Journal of Geomechanics*, vol. 20, no. 6, Article ID 04020047, 2020.

[25] C. Goldenberg and I. Goldhirsch, "Friction enhances elasticity in granular solids," *Nature*, vol. 435, no. 7039, pp. 188–191, 2005.

[26] E. Alaei and A. Mahboubi, "A discrete model for simulating shear strength and deformation behaviour of rockfill material, considering the particle breakage phenomenon," *Granular Matter*, vol. 14, no. 6, pp. 707–717, 2012.

[27] Z. Nie, C. Fang, J. Gong, and Z.-Y. Yin, "Exploring the effect of particle shape caused by erosion on the shear behaviour of granular materials via the DEM," *International Journal of Solids and Structures*, vol. 202, pp. 1–11, 2020.

[28] C. Thornton, "Numerical simulations of deviatoric shear deformation of granular media," *Géotechnique*, vol. 50, no. 1, pp. 43–53, 2000.

[29] N. Estrada, E. Azéma, F. Radjai, and A. Taboada, "Identification of rolling resistance as a shape parameter in sheared granular media," *Physical review. E, Statistical, nonlinear, and soft matter physics*, vol. 84, no. 1 Pt 1, Article ID 011306, 2011.

Hindawi
Advances in Materials Science and Engineering
Volume 2022, Article ID 9243361, 13 pages
https://doi.org/10.1155/2022/9243361

Research Article

Experimental Investigation Monitoring the Saturated Line of Slope Based on Distributed Optical Fiber Temperature System

Feng Li,[1] Weixing Qin ,[2] and Huiren Hu[3]

[1]*School of Civil Engineering and Architecture, East China Jiaotong University, Nanchang, China*
[2]*School of Hydraulic and Environmental Engineering, Key Laboratory of Water-Sediment Sciences and Water Disaster Prevention of Hunan Province, Changsha University of Science and Technology, Changsha, China*
[3]*National Engineering Laboratory of Highway Maintenance Technology, Changsha University of Science and Technology, Changsha, China*

Correspondence should be addressed to Weixing Qin; qinweixing@csust.edu.cn

Received 19 November 2021; Accepted 18 January 2022; Published 3 March 2022

Academic Editor: Yongsheng Yao

The position of the saturated line is an important basis for evaluating the stability of the slope, and the traditional sensors cannot be monitored for a long time because of poor durability and anti-interference. A method for measuring the saturated line with distributed optical fiber temperature measurement technology was proposed, and the one-dimensional and two-dimensional model experiments of measuring the saturated line at three kinds of electron flow (5 A, 10 A, and 15 A) were conducted, and their measuring data were carefully analyzed. The results showed the three stages of the optical fiber temperature difference with time: sudden-rising, fast-rising, and slow-rising. The temperature rising rate and stable temperature difference at the position of the saturated line are between saturated soil and unsaturated soil. The fiber optic temperature increases with the increment of heating electron flow, which also demonstrates stability and repeatability.

1. Introduction

With the rapid development of society and economy, infrastructures [1–3], including roads, railways, dams, bridges, waterways, etc., are the main investment directions to support the continued prosperity of the economy and the country. However, these facilities have been placed in complex and changeable environments [4, 5] for a long time, and the failure or collapse caused by the deterioration of their structure may cause casualties and major damage [6]. For example, various geological disasters occur every year around the world, such as landslides, earthquakes, floods, etc., of which landslides account for the highest proportion [7, 8]. The landslide because of the deterioration of built infrastructure [9] has been a challenging problem worldwide, with the rising cost of infrastructure maintenance and rehabilitation [10, 11]. Slope monitoring is a basic work that must be carried out, and the saturated line is assisted to evaluate the possibility of slope failure scientifically [12, 13]. Therefore, it is very meaningful to monitor the saturated line with an effective method.

At present, piezometers, pore water pressure gauges, volumetric water contents, and other instruments are being used in the monitoring of the saturated line [14, 15]. However, they cannot meet the long-term monitoring requirements in terms of sensor durability, electromagnetic interference, chemical, and corrosion resistance [16–18]. Masaoka et al. [19] installed 59 piezometers at the soil-bedrock interface to determine the permeability coefficient and obtained data from June 18 to July 18. Kim et al. [20] installed 4 vertical displacement sensors, 4 horizontal displacement sensors, and 3 wireless volumetric water content sensors to monitor the location and location of the fault. Liu et al. [21] installed 19 sensors in an array at 10 elevations on the right bank slope for long-term monitoring, and only the monitoring data from November 2014 to November 2016 was obtained. Shi et al. [22] studied the seepage lag time of dams and set up four seepage monitoring sections in the

dam body, and four piezometers and osmometers were embedded in each monitoring section to automatically and accurately monitor the seepage pressure of the dam. Liu and Wang [23] predicted the response of the pore water pressure (PWP) in the soil to the slope stability under heavy rain, and three sets of PWP sensors were used to measure.

Many researchers focused on fiber optic sensors [24, 25] that have unique advantages, such as antielectromagnetic interference and reliable durability, to withstand extreme temperatures and corrosion. However, the use of distributed optical fiber temperature system to determine the saturated line of the slope is rarely reported. Vogt et al. [24] proposed a high-resolution vertical temperature profile method for surface water sediments to quantify the depth and time of permeation flux in detail. By fitting the data to an analytical solution of convective conduction and heat transfer in a semi-infinite, uniform, one-dimensional area with a sinusoidal surface temperature, it is converted into an apparent seepage rate. Yan et al. [7] carried out an innovative distributed temperature system (DTS) for measuring seepage rate. The experiment results showed that in the same sandy soil, the characteristic temperature and seepage rate have a good linear relationship, however, it has nothing to do with the particle size distribution. Su et al. [26, 27] used a DTS, adopted an improved optical fiber layer layout scheme, applied it in an engineering case, and proposed a real-time seepage monitoring technology based on a combination method for the full section of the embankment. Chen et al. [12] established a mathematical model to describe the heat dissipation process of a linear heat source (LHS) in porous media based on seepage mechanics and heat transfer theory. The effects of seepage velocity and seepage direction on the heat dissipation law of LHS are studied. The results show that the heat dissipation process of LHS complies with Newton's law of cooling well, and the cooling rate is positively correlated with the seepage velocity and the infiltration angle. Zheng et al. [28] developed a "Fiber Bragg grating (FBG)-based leak detection device," and according to the temperature distribution along the diaphragm wall joints and the temperature curve, location, and time generated by the use of measuring points, leakage can be determined. Cao et al. [29] allowed the measurement of soil moisture in saturated and unsaturated zones with a deviation of 0.027 m^3/m^3 and used the active heating optical fiber method to monitor soil moisture profiles through model experiments. Wijaya et al. [30] studied the comparison of BOTDR strain measurement methods with pretensioned and nonpretensioned fiber optic cables by field applications. The prestretched fiber optic cable obtained to reduce the differences in observations from the point and distributed sensors may be a potential solution. Cheng et al. [31] used the distributed optical fiber temperature detection to obtain data from the dam seepage heat laboratory model and used optical frequency domain reflectance (OFDR) technology to monitor temperature, which has high time and space accuracy. The results show that OFDR has high temperature detection accuracy and high spatial resolution, which can reflect the characteristics of the temperature field in the seepage model of the dyke.

Thus, the objective of this paper was to propose a feasible method for measuring the saturated line of the slope with DTS sensors. This study was organized as follows: firstly, the composition of the distributed optical fiber temperature measurement system is introduced, and the one-dimensional and two-dimensional model experiments of measuring the saturated line are designed. Then, the model experiments under different electron flow heating effects are carried out. Finally, 170 sets of optical fiber temperature data are acquired and analyzed.

2. DTS Technology and Experiment Design

To accomplish the saturated line monitoring by DTS, an experimental platform is designed and assembled with DTS system, seepage generating system, heating system, and physical model. Various equipment, physical model, and composition system were shown in Figures 1–3.

2.1. DTS Technology and Composition Based on Raman Scattering Principle

2.1.1. DTS System. Using the pulse light injected into the fiber by the laser, in the transmission process, the thermal vibration of the molecules in the fiber is caused, resulting in light with a longer wavelength than the source, called Stokes light, and other light with a shorter wavelength than the light source, called anti-Stokes light [13]. The intensity of the anti-Stokes light produced varies with temperature, while Stokes light does not. Using the ratio of anti-Stokes-to-Stokes light intensity, the temperature T of this point can be obtained as equation (1).

$$T = \frac{hc_0 v}{\{k[\ln\alpha - \ln(l_{as}/l_s)]\}}, \quad (1)$$

where T is the absolute temperature value. h is Planck's coefficient. c_0 is the speed of light. v is the Raman shift. k is the Baltzmann constant. α is the temperature correlation coefficient. l_{as} is the intensity of the anti-Stokes light. l_s is the intensity of the Stokes light.

DTS system mainly consists of distributed optical fiber main unit for temperature measurement and linear multimode thermal optical cables. The former part accommodates some components, such as the optical device, laser device, data processing module, etc.

(1) Laser module: composed of a high-power pulsed semiconductor laser with tail fiber (output power >500 mW) and laser drive power supply.

(2) Optical fiber wavelength division multiplexer: it consists of a 1×3 bidirectional optical fiber coupler and wavelength division multiplexer system (multibeam interference optical filter with high isolation).

(3) Photoelectric receiving and amplifying components: composed of optical avalanche diode with tail fiber

(a)

(b)

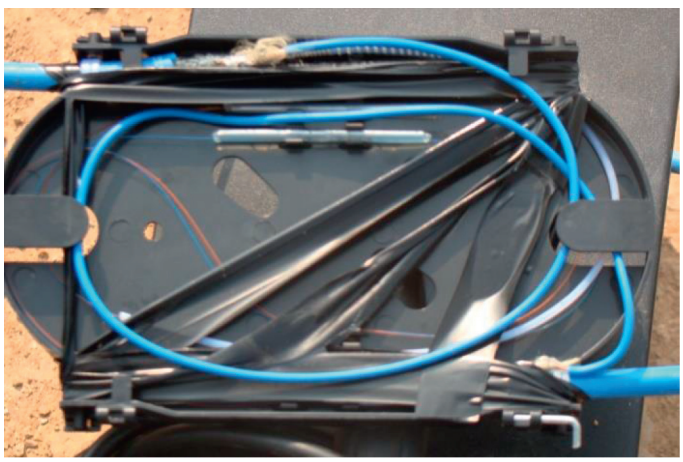

(c)

Figure 1: Continued.

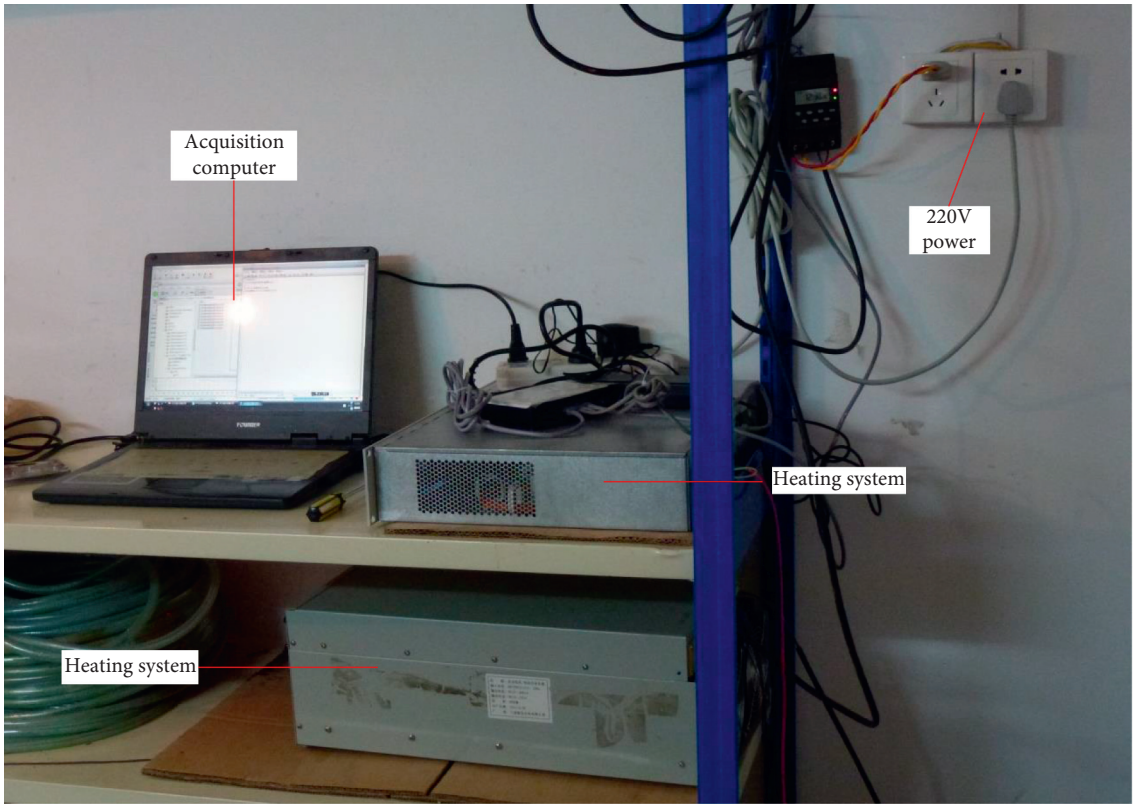

(d)

Figure 1: DTS equipment and system composition. (a) Optical fiber temperature acquisition instrument; (b) heating system; (c) distributed fiber optic sensor; (d) measuring system.

and main amplifier with high gain, wideband, and low noise.

(4) Signal processing system: it is composed of a double-channel, high-speed transient (50 MHz) signal acquisition, processing card, and signal processing software.

AP sensing distributed optical fiber temperature measuring host (shown in Figure 1(a)) was used. The single channel measurement was conducted with a maximum measurement length of 2 km, spatial resolution: 1m, positioning accuracy: 1m, sampling interval: 0.5 m, temperature accuracy: ±1°C, and temperature resolution: ±0.1°C.

2.1.2. Heating System. The heating system (Figure 1(b)) adopts an alternating straight heating equipment with a maximum output power of 6 kW and other auxiliary equipment, with a maximum output electron flow of 20 A and a maximum output voltage of 300 V. The system can automatically select the range according to the length, electron flow, or voltage of the optical cable, and the system can heat the copper network in the optical cable while ensuring the constant output of heating power.

2.1.3. Fiber Optic Sensor. Two-core, multimode (50/125), water-blocking, armored, heating fiber optic cable (Figure 1(c)) was used with a diameter of about 8 mm, outer sheath wall thickness >1.5 mm, and a resistance of about 20 Ω/km. The structure includes components, such as the outer sheath, heating copper mesh, stainless steel hose (easy to bend and loop), Kevlar fiber, oil-filled bundle tube, and two-core optical fiber.

2.2. Model Experiment Design of Measuring Saturated Line. To explore the cable temperature change with time under the condition of stability and variation of saturated line, one-dimensional cylinder experiment was selected for single point measurement and two-dimensional rectangular groove experiment for distributed measurement. The model design is as follows:

2.2.1. One-Dimensional Cylinder Experiment Model. The one-dimensional cylinder experiment model consists of a 35 cm diameter sealing steel tube, a 25 cm diameter sealing steel tube, and a 15 cm diameter dispersed spiral surround detection cable. The 35 cm diameter steel tube sidewall bottom hole welding fine steel tube is used for the inlet and outlet. The 25 cm diameter steel pipe is perforated at the bottom, and the inner and outer layers are wrapped with geotextile to protect the saturated soil from overflow and eliminate the influence of incoming and outgoing water directly hitting the cable on the experiment. The length of

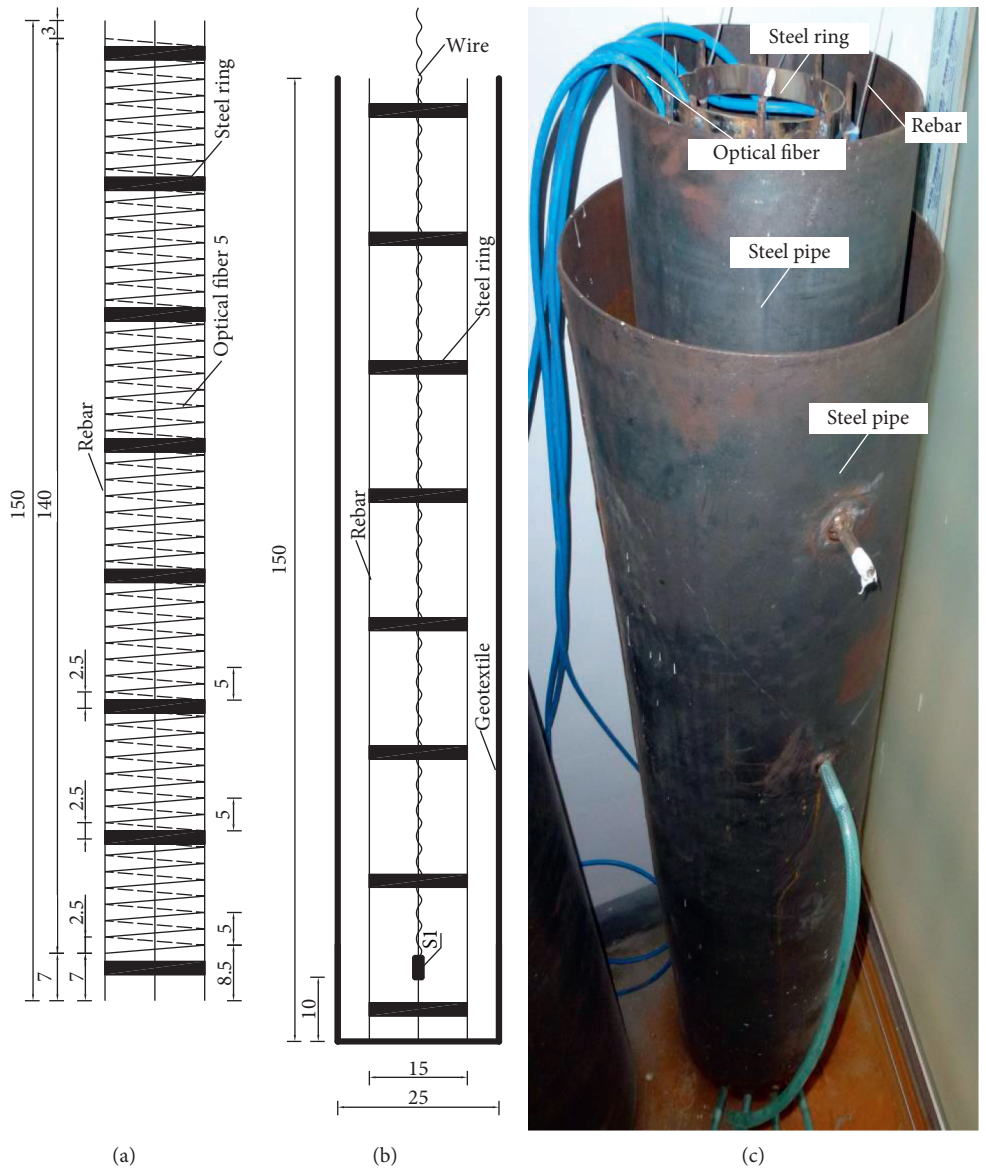

Figure 2: One-dimensional cylinder model and cable dispersion around design (unit: cm).

the scattered optical cable is 0.5 m/circle, and the height difference is 5 cm, as shown in Figure 2.

2.2.2. Two-Dimensional Rectangular Groove Experiment Model-Distributed Measurement. The two-dimensional experiment model was a rectangular steel trough of 300 cm × 50 cm × 100 cm (length × width × height), which was composed of the left inlet section, the middle experiment section, and the right outlet section. There were 7 groups of optical cable measuring points (J0 to J6) in the inlet section and outlet section, respectively. The experiment models are shown in Figure 3.

2.3. Experiment Conditions and Measurement Steps. Because of the difference in density and specific heat capacity of soil and water, when the heating system is heating the copper mesh, the temperature measured by the optical fiber of saturated soil and unsaturated soil is different. According to this situation, the experiment was designed to keep the saturated line stable, heat under different heating electron flow conditions, and understand the relationship between heating electron flow and fiber temperature difference value in saturated soil and unsaturated soil. One-dimensional cylinder experiment studied the relationship among fiber temperature difference, saturated line change, and heating electron flow from point measurement angle. The horizontal saturated line and normal stable seepage saturated line were formed in the two-dimensional rectangular groove experiment. The relationships among fiber temperature difference, saturated line stability, and heating electron flow were studied from the perspective of distributed measurement. There were 6 kinds of experimental conditions in total, as seen in Table 1.

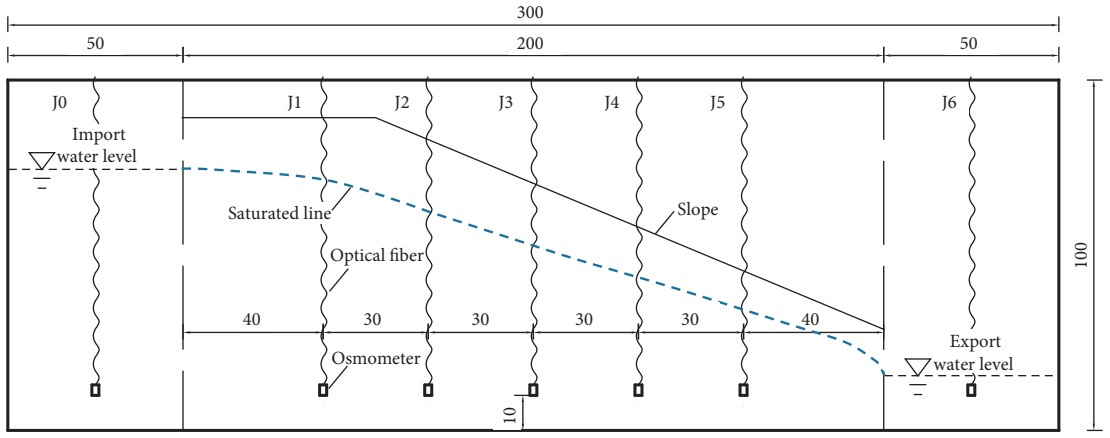

(a)

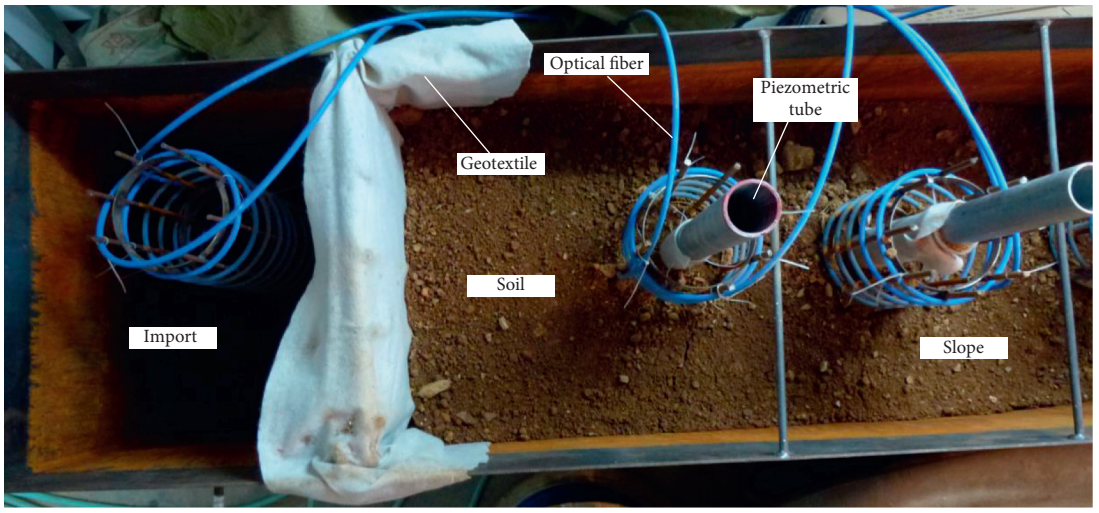

(b)

Figure 3: Two-dimensional rectangular model diagram and measurement process (unit: cm).

Table 1: Experimental conditions.

Experiment conditions	Heating electron flow			Note
	5 A	10 A	15 A	
Stabilization (130 cm)	1	2	3	One-dimensional cylinder (point)
Saturated line (35.00 cm)	4	5	6	Two-dimensional rectangular (distributed)

One-dimensional and two-dimensional experiment water level stability (working conditions 1~3, 4~6), measurement steps are as follows:

(1) Physical connection: the experiment cable tail fiber was inserted into the distributed optical fiber temperature measurement host optical fiber measurement port. The temperature measurement host is connected to the computer, and both ends of the cable and the heating system are connected to the positive and negative poles, and they are connected to the power supply (if connected, omit this step).

(2) Collection before heating: open the distributed optical fiber temperature measurement host and software, set parameters, and collect the unheated optical fiber temperature data for 30 minutes.

(3) Heating and collection: select the experiment heating electron flow, open the heating system, continue to heat the optical cable with the electron flow by the experiment for a long time (5 h). Then, collect optical fiber temperature data.

(4) Collection after heating: turn off the heating system and continue to collect optical fiber temperature data until the optical fiber temperature returns to normal temperature. Stop the collection and close the optical fiber temperature measurement software and the host.

(5) Physical disconnect: disconnect the power supply, remove all physical connections, and protect all important ports and connectors.

3. Results and Analysis

According to the experiment plan, a one-dimensional cylinder and two-dimensional rectangular groove saturated line experiment under the heating action of three electron flows were carried out, and a total of 24 sets of optical fiber temperature time history data at different positions were obtained. The following is a detailed analysis of the aspects of temperature and temperature difference.

3.1. Variation of Measured Temperature and Temperature Difference under Cylindrical Experiment. The temperature data at 30 locations in the one-dimensional cylinder over time were examined. Among them, the temperature measurement data of 11 points and the temperature difference data of 7 points (102 cm to 146 cm) near the set saturated line were displayed in Figure 4. It was specified that the abscissa takes the time just heated as 0. Then, it is a negative value without heating, and a positive value after heating.

After heating, the temperature of optical fiber presents three stages: sudden-rising, fast-rising, and slow-rising. After heating for 2 min, the temperature of all optical fibers suddenly rises to a certain value. After heating for 10 minutes, the temperature difference of the fiber begins to rise rapidly and gradually slows down, and the rising rate gradually decreases. Take figure 4(a) as an example, during the 0.5 hours before heating cable, the temperature of each point is 7.5°C to 11.5°C, the average temperature is 8.3°C to 11.0°C, and the fluctuation amplitude is 1.2°C to 1.6°C. When heated by 0.5 A electron flow, the temperature of each point rises slightly and then fluctuates up and down with a certain temperature as the center over time. After being heated by 0.5 A for 4~5 hours, the temperature of each point is 8.0°C to 12.5°C. The average temperature is 9.1°C to 12.4°C, and the fluctuation amplitude is 0.8°C to 2.2°C. Similarly, in figure 4(c), the temperature of the same point is 5.5°C to 8.5°C, the average temperature is 6.2°C to 8.0°C, and the fluctuation amplitude is 0.8°C to 1.2°C. When the optical cable is heated by the electron flow of 10A, the temperature rises rapidly from 0 to 0.2 h and then slowly rises, and it basically fluctuates with a certain temperature value after 0.5 h. After being heated for 4~5 hours, the temperature is 9.5°C to 21.5°C, the average temperature is 10.8°C to 17.0°C, and the fluctuation amplitude is 0.8°C to 1.4°C. If 15 A electron flow is used, the initial temperature is 9.3°C to 12.3°C, the initial average temperature is 10.1°C to 11.3°C, and the initial fluctuation amplitude is 1.1°C to 1.7°C. The temperature is 30.0°C to 36.1°C, the average temperature is 31.2°C to 34.9°C, and the fluctuation amplitude is 1.4°C to 2.6°C after heating for 4~5 hours.

It is comprehensively found that before heating, although there is a temperature difference at each measuring point near the 130 cm position of the infiltration point, it behaves differently because it is affected by the ambient temperature. However, the temperature difference between each point is basically equivalent to the fluctuation amplitude. As can be clearly seen from the figure after being heated by electron flow, the temperature of each point in the cylinder during the experiment changes dramatically, and they increase significantly with time at the beginning of heating and then reach a relatively stable value. Although the measured temperature value after heating has a large difference to a certain extent, it is still affected by the initial environment temperature. Therefore, the temperature difference with the initial temperature subtracted over time is shown in Figures 4(b), 4(d), and 4(f). It can be found from figure 4(b) that when heated by 5 A for 4~5 hours, the relatively stable temperature difference is 0.8°C to ~3.0°C, which is not much different from the fluctuation amplitude. When heated by 10 A or 15 A, the differentiation in temperature difference near the saturated point (130 cm) is very obvious. The temperature difference of each point is 5.3°C to 14.5°C (10 A), 20.1°C to 32.9°C (15 A), and the sable temperature difference is 6.5°C to 13.8°C (10 A), 20.8°C to 31.6°C (15 A), respectively.

To better distinguish and determine the saturated line, when the fiber is heated by 10 A and 15 A for 4 to 5 hours, the temperature difference of three key points of the point above the saturated line in the unsaturated soil (138 cm), the point on the saturated line (130 cm), and the point below the saturated line in the saturated soil (122 cm), is plotted in Figure 5. The differentiation in temperature difference near the saturated point (130 cm) is very obvious. In the 10 A working condition, the temperature difference, the stable temperature, and the fluctuation amplitude in the unsaturated soil are 14.1°C to 15.8°C, 15.0°C, and 1.7°C, and they are 11.0°C to 13.4°C, 12.1°C, and 2.4°C on the saturated line and 7.9°C to 9.7°C, 8.9°C, and 1.8°C in the saturated soil, respectively. Similarly, in another working condition, they are 30.8°C to 32.7°C, 31.6°C, and 2.1 °C in the unsaturated soil, 26.9°C to 28.7°C, 27.5°C, and 2.0°C in the saturated line, and 21.0°C to 23.7°C, 22.5°C, and 2.7°C in the saturated soil. The temperature rise range of the characteristic point above the saturated line (unsaturated soil) is slightly larger, and the temperature rise time is slightly longer than that of the characteristic point below the saturated line (saturated soil). After heating for 10 minutes, the temperature rise rate of the fiber temperature difference values at all characteristic points tends to be stable and small. The temperature difference of the characteristic point at the position of the saturated line is between the upper and lower positions of the saturated line. Basically, it shows that unsaturated soil >the saturated line >the saturated soil. It means that it is feasible to use a relatively stable temperature difference value to determine the infiltration point.

In addition, Figure 6 shows the temperature difference data of each measuring point in the cylinder along the height at 3 different times (initial (0 s), sudden rise (2 min), and relative stable (5 h)). From the data, it is impossible to distinguish the position of the saturated line in the initial time, howeverthe position of the saturated line can be easily

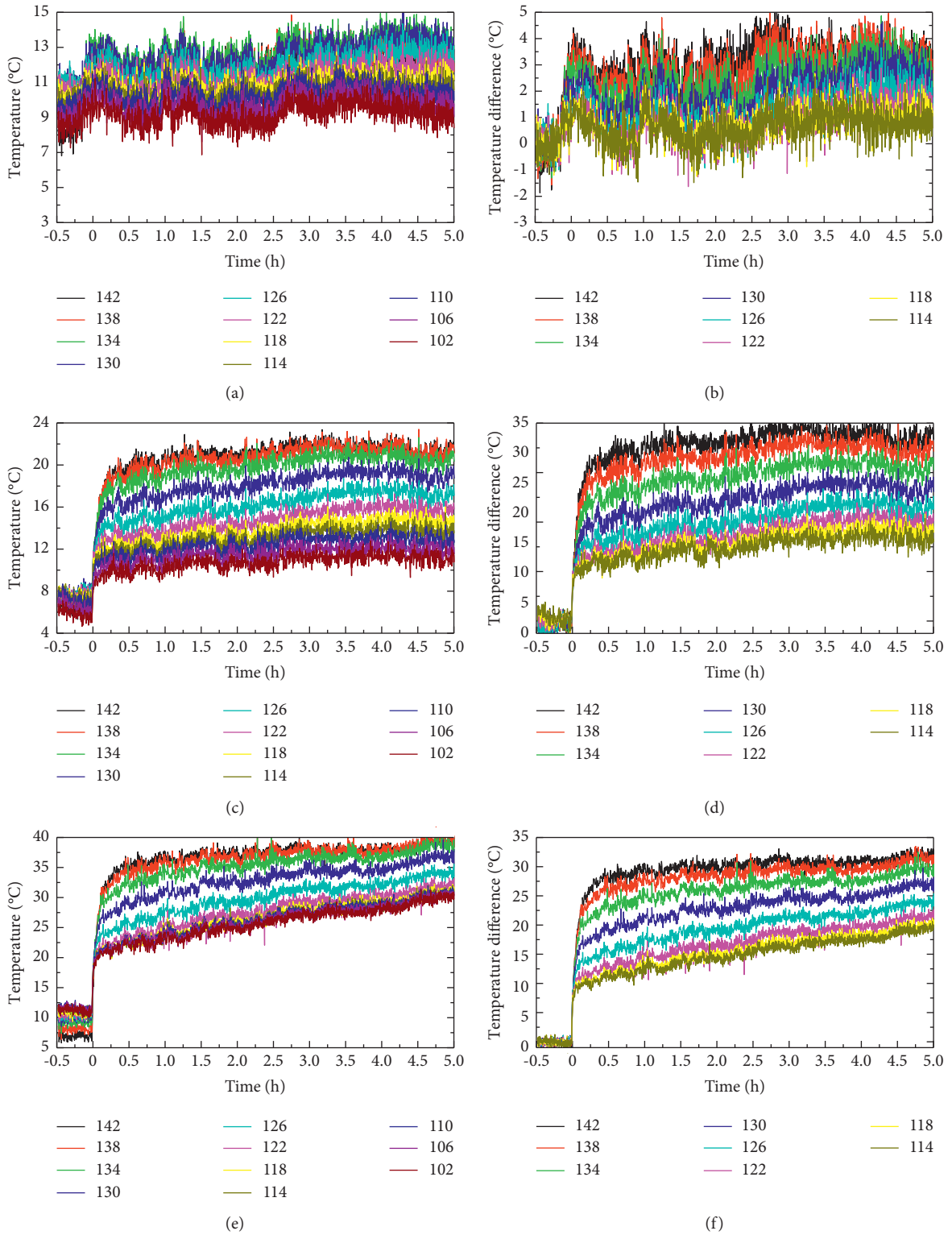

Figure 4: Variation of original temperature ((a) 5 A; (c) 10 A; (e) 15 A) and temperature difference ((b) 5 A; (d) 10 A; (f) 15 A) with time.

determined between the sudden-rise and the relatively stable phase. The temperature abrupt change is basically the same in all optical cables. With the temperature difference rising, the stable value of temperature difference at the position of unsaturated soil, saturated line, saturated soil decrease gradually, and the positions of the saturated line are almost the same with DTS system and the pore water pressure measurement seperately.

As shown in Table 2 and Figure 7 below, when the heating electron flow is 5 A, it is difficult to determine the position of

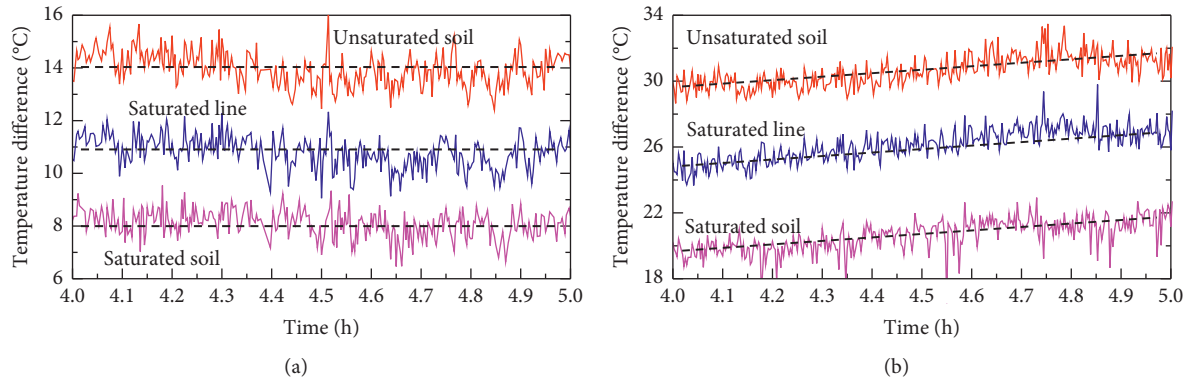

Figure 5: Variation of temperature difference under 4 to 5 hours after heating: (a) 10 A; (b) 15 A.

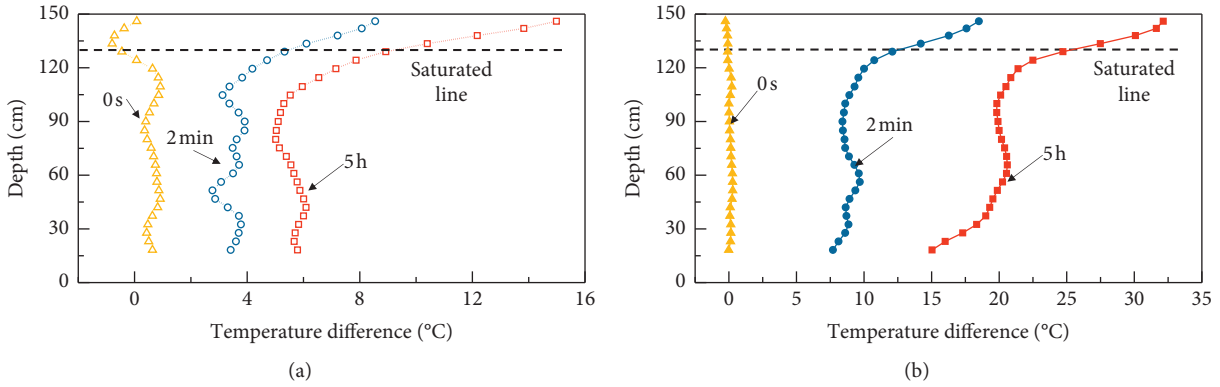

Figure 6: Distribution of temperature difference along height: (a) 10 A; (b) 15 A.

Table 2: Relationship between surge value, stable temperature difference, and heating electron flow.

Electron flow	sudden (°C)			Stable (°C)			Amplitude (°C)		
	5 A	10 A	15 A	5 A	10 A	15 A	5 A	10 A	15 A
unsaturated soil	1.87	8.07	17.58	2.98	13.83	31.63	0.51	0.62	2.10
saturated line	1.52	6.11	14.20	2.33	10.40	27.49	0.86	1.40	2.07
Saturated soil	1.32	4.71	10.76	1.25	7.87	22.49	1.81	1.41	2.77

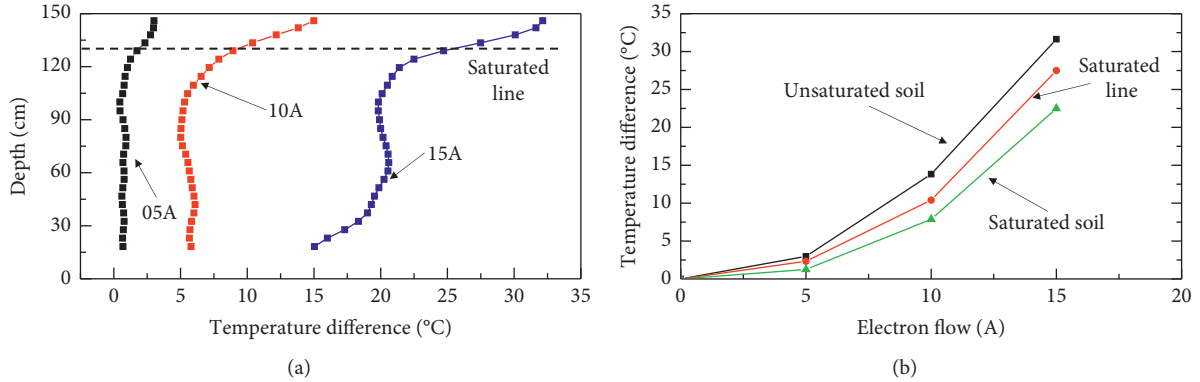

Figure 7: Distribution of temperature difference along (a) height and (b) electron flow.

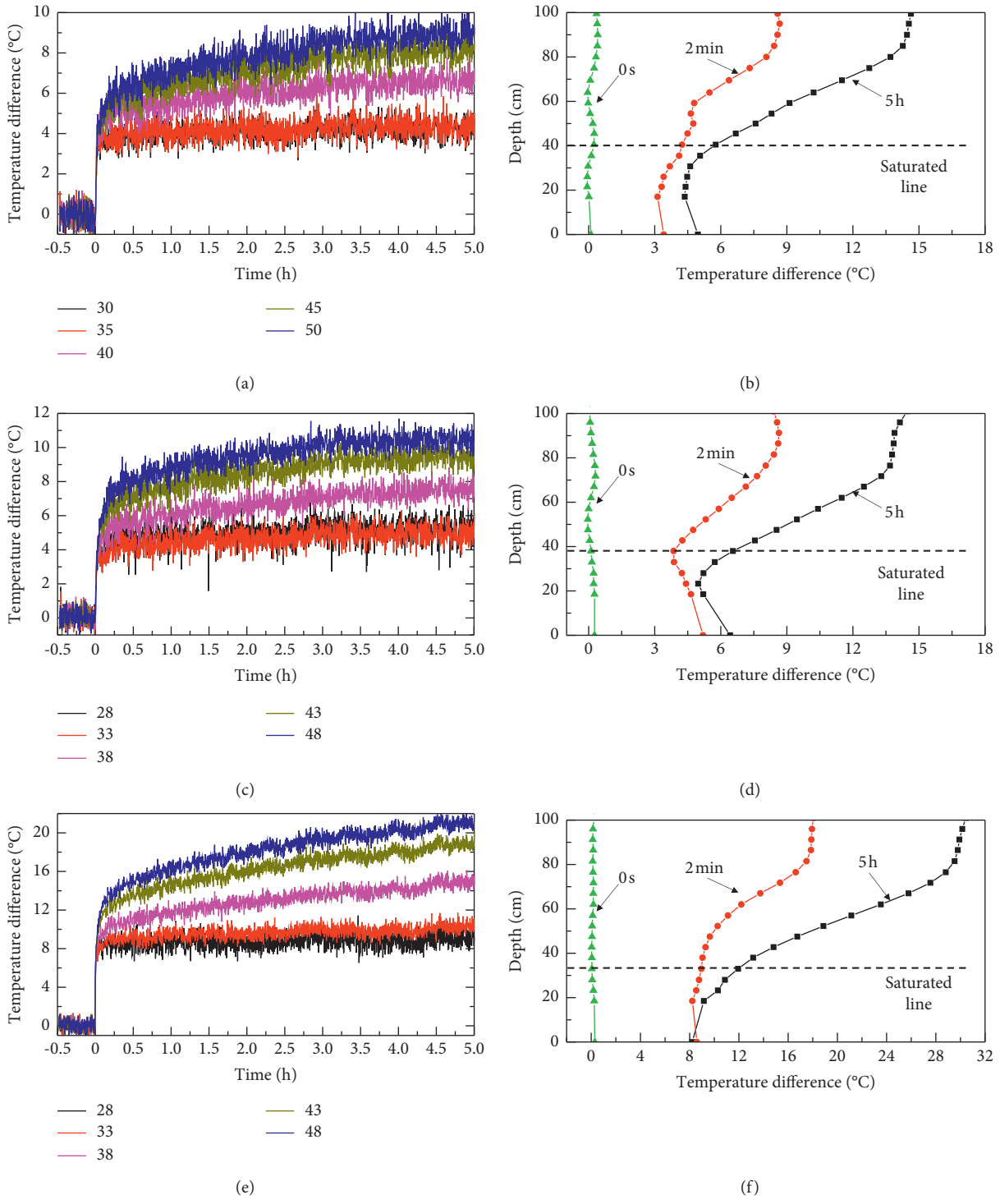

Figure 8: Variation with time ((a); (c); (e)) and along height ((b); (d); (f)) of temperature difference.

the saturated line because of the small difference in temperature difference between unsaturated soil and saturated soil after heating and the joint influence of optical fiber temperature measurement fluctuation. 10 A and 15 A are easier to determine. The greater the heating electron flow, the greater the difference in temperature, and the more obvious the

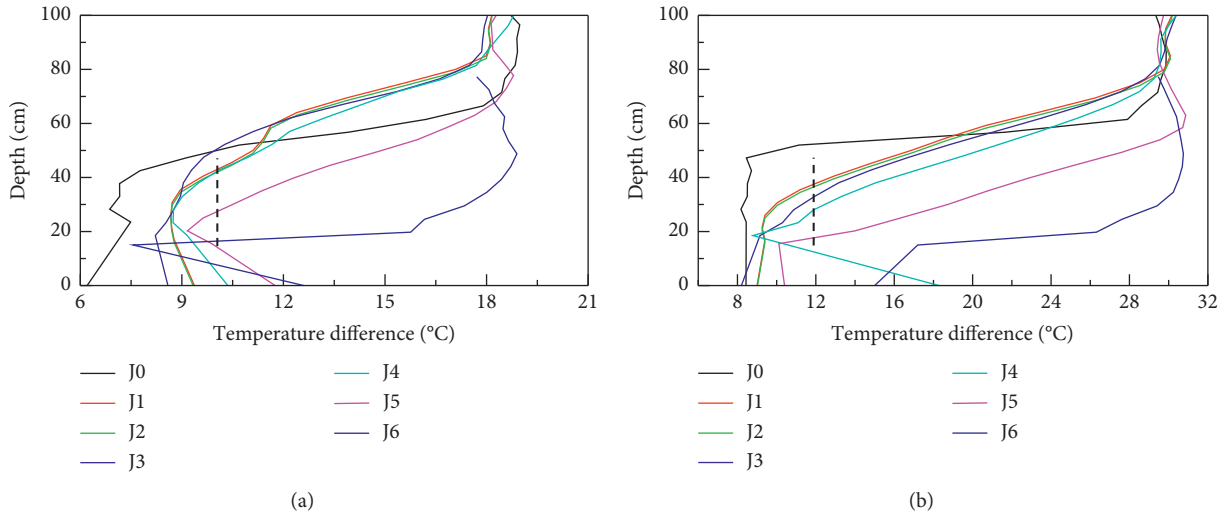

Figure 9: Distribution of temperature difference along height in different positions: (a) 10 A; (b) 15 A.

experiment effect. The variation of temperature difference at the wetted line is always between the upper and lower regions, which is consistent with the judgment at the water surface.

3.2. Variation of Measured Temperature and Temperature Difference under Rectangular Experiment. The temperature data at 140 cm locations in the two-dimensional rectangle over time were examined. Among them, the temperature difference of 5 points near the set saturated line with time and height were displayed in Figure 8.

Figure 8(a), 8(c), and 8(e) show that the temperature of optical fiber with time presents three stages: sudden rise, fast rise, and slow rise after heating, which is the same as the results of the one-dimensional cylinder test. After 2 min, the temperature of all optical fibers suddenly rises to a certain value. After heating for 10 minutes, the temperature difference of the fiber begins to rise rapidly and gradually slows down, and the rising rate gradually decreases. Take the second group of fibers (J1) in Figure 8(a) as an example. 0.5 hours before heating, the temperature difference of each point is −0.4°C to 0.9°C. The average temperature difference is −0.1°C to 0.2°C, and the fluctuation amplitude is 0.6°C to 1.3°C. When heated by 10 A electron flow, the temperature of each point rises slightly and then fluctuates up and down with a certain temperature as the center over time. After being heated for 4~5 hours, the temperature difference of each point is 3.5°C to 9.6°C, the average temperature difference is 4.4°C to 8.3°C, and the fluctuation amplitude is 1.3°C to 1.7°C. Similarly, the temperature difference of the fourth group of fibers (J3) in Figure 8(c) is -0.4°C to 1.8°C, the average temperature difference is -0.1°C to 0.2°C, and the fluctuation amplitude is 1.1°C to 2.4°C. After being heated for 4–5 hours, the temperature difference is 3.2°C to 9.7°C, the average temperature difference is 4.9°C to 9.4°C, and the fluctuation amplitude is 0.3°C to 1.1°C. If 15 A electron flow is used as shown in 8e, the temperature difference is -0.7°C to 1.2°C, the average temperature difference is 0.0°C to 0.3°C, and the fluctuation amplitude is 1.3°C to 2.0°C. The temperature difference is 9.1°C to 16.9°C, the average temperature difference is 10.3°C to 16.7°C, and the fluctuation amplitude is 0.1°C to 1.2°C after heating for 4–5 hours.

Figures 8(b), 8(d), 8(f) show the temperature difference data of measuring points in the two-dimensional rectangular model at 3 different times (initial (0 s), sudden rise (2 min), relative stable (5 h)). Similar to a one-dimensional cylinder test, it is impossible to distinguish the position of the saturated line in the initial time; however,the position of the saturated linecan be easily determined between the sudden-rise and the relatively-stable phase. The temperature abrupt change is basically the same in all optical cables. With the temperature difference rising, the stable value of temperature difference at the position of unsaturated soil, saturated line, saturated soil decrease gradually, and the position of the saturated linewith DTS sensors is consistent with the result of pore water pressure measurement. The relative stable temperature difference of the 7 groups of optical fibers in the two-dimensional rectangular test heated by two electric flows are plotted in Figure 9 along the height distribution diagram. By the above determination method, the position of the saturated line of each point can be easily determined so that it can be plotted as the saturated line of the entire slope.

According to the analysis of the heating experiment chart, the temperature difference of the optical fiber at the position of the saturated line is between saturated soil and unsaturated soil. Hence, it is convenient and quick to visually check the position of water level. When the heating electron flow is low, it is difficult to determine the position of the infiltrating line. As the heating electron flow increases, the difference becomes more obvious, and it is easier to determine the position of water surface. Therefore, it is recommended to use the electron flow of 10 A and above for experimenting. Through fitting analysis, it can be concluded that the sudden rise and stability of fiber temperature have a certain function relation with heating electron flow. By the above judgment method, optical fiber can be used in water conservancy, hydropower

engineering, environment, agriculture, and other fields for groundwater level measurement.

4. Conclusions

The position of the saturated line is an important basis for evaluating the stability of the slope. Traditional sensors cannot be monitored for a long time because of poor durability and anti-interference. In view of the above shortcomings, a method for measuring the saturated line with distributed optical fiber temperature measurement technology was proposed, and the two model tests were designed, and temperature with time at 170 locations was obtained. The main findings of this study were summarized as follows:

(1) Although in the same geotechnical material and water level, the temperatures of the cable are basically the same when the cable is not heated, which are not convenient to determine the position of saturated line .

(2) When the cable is heated at a stable water level, the temperature difference shows three stages of rising, namely sudden-rising, fast-rising, and slow-rising. The temperature rising rate and stable value of temperature difference above the water level are higher than those below the water level, and the value at water level is between unsaturated soil and saturated soil. The position of saturated line can be judged obviously.

(3) Under the same conditions, the temperature difference of the cable increases with the increase of heating electron flow. Heating cable with a higher current intensity is helpful for measurement and judgment of saturated line.

Data Availability

The data used to support the findings of this study are included within the article.

Conflicts of Interest

The authors declare that the research was conducted in the absence of any commercial or financial relationships.

Acknowledgments

The authors thank the support from the Hunan Provincial Transportation Science and Technology Plan Project (201140), the National Natural Science Foundation of China (51208062), the Hunan Provincial Innovation Foundation for Postgraduate (CX20190680, CX2018B527), the Research Funds for Safety Technical Specification for Slope Stability of Ultra Deep Foundation Pit (2022-WASLSL-STSSSUDFP), the Design Theory, Method and Demonstration of Durability Asphalt Pavement on Heavy-duty Traffic Conditions in Shanghai Area (CTKY-PTRC-2018-003), and the Science and Technology R&D Project of China Communications Construction Co., Ltd. (2021-ZJKJ-QNCX17).

References

[1] J. P. Galve, A. Cevasco, P. Brandolini et al., "Cost-based analysis of mitigation measures for shallow-landslide risk reduction strategies," *Engineering Geology*, vol. 213, pp. 142–157, 2016.

[2] J. Zhang, L. Ding, F. Li, and J. Peng, "Recycled aggregates from construction and demolition wastes as alternative filling materials for highway subgrades in China," *Journal of Cleaner Production*, vol. 255, Article ID 120223, 2020.

[3] J. Li, J. Zhang, G. Qian, J. Zheng, and Y. Zhang, "Three-dimensional simulation of aggregate and Asphalt mixture using parameterized shape and size gradation," *Journal of Materials in Civil Engineering*, vol. 31, no. 3, Article ID 04019004, 2019.

[4] T. CARLà, V. Tofani, L. Lombardi et al., "Combination of GNSS, satellite InSAR, and GBInSAR remote sensing monitoring to improve the understanding of a large landslide in high alpine environment," *Geomorphology*, vol. 335, pp. 62–75, 2019.

[5] Y. Yao, J. Ni, and J. Li, "Stress-dependent water retention of granite residual soil and its implications for ground settlement," *Computers and Geotechnics*, vol. 129, Article ID 103835, 2021.

[6] G. Amato, C. Eisank, D. Castro-Camilo, and L. Lombardo, "Accounting for covariate distributions in slope-unit-based landslide susceptibility models. A case study in the alpine environment," *Engineering Geology*, vol. 260, Article ID 105237, 2019.

[7] J.-F. Yan, B. Shi, H.-H. Zhu, B.-J. Wang, G.-Q. Wei, and D.-F. Cao, "A quantitative monitoring technology for seepage in slopes using DTS," *Engineering Geology*, vol. 186, pp. 100–104, 2015.

[8] K. Kreczmer, M. Dąbski, and A. Zmarz, "Terrestrial signature of a recently-tidewater glacier and adjacent periglaciation, windy glacier (south shetland islands, antarctic)," *Frontiers of Earth Science*, vol. 9, no. 299, Article ID 671985, 2021.

[9] J. Peng, J. Zhang, J. Li, Y. Yao, and A. Zhang, "Modeling humidity and stress-dependent subgrade soils in flexible pavements," *Computers and Geotechnics*, vol. 120, Article ID 103413, 2020.

[10] Y. Zheng, C. Chen, T. Liu, H. Zhang, K. Xia, and F. Liu, "Study on the mechanisms of flexural toppling failure in anti-inclined rock slopes using numerical and limit equilibrium models," *Engineering Geology*, vol. 237, pp. 116–128, 2018.

[11] J. Zhang, A. Zhang, C. Huang, H. Yu, and C. Zhou, "Characterising the resilient behaviour of pavement subgrade with construction and demolition waste under Freeze-Thaw cycles," *Journal of Cleaner Production*, vol. 300, p. 126702, 2021.

[12] J. Chen, F. Xiong, J. Zheng, Q. Ge, and F. Cheng, "The influence of infiltration angle on the identification effect of seepage with linear heat source method," *Measurement*, vol. 148, Article ID 106974, 2019.

[13] H. Su, S. Tian, Y. Kang, W. Xie, and J. Chen, "Monitoring water seepage velocity in dikes using distributed optical fiber temperature sensors," *Automation in Construction*, vol. 76, pp. 71–84, 2017.

[14] C. Duque, C. J. Russoniello, and D. O. Rosenberry, "History and evolution of seepage meters for quantifying flow between groundwater and surface water: Part 2 - marine settings and submarine groundwater discharge," *Earth-Science Reviews*, vol. 204, Article ID 103168, 2020.

[15] J. Shaikh, S. Bordoloi, A. K. Leung, S. K. Yamsani, S. Sekharan, and R. R. Rakesh, "Seepage characteristics of three-layered landfill cover system constituting fly-ash under extreme

ponding condition," *The Science of the Total Environment*, vol. 758, Article ID 143683, 2021.

[16] E. Deville, C. Scalabrin, G. Jouet et al., "Fluid seepage associated with slope destabilization along the Zambezi margin (Mozambique)," *Marine Geology*, vol. 428, Article ID 106275, 2020.

[17] Y. N. Lin, E. Park, Y. Wang et al., "The 2020 Hpakant Jade Mine Disaster, Myanmar: a multi-sensor investigation for slope failure," *ISPRS Journal of Photogrammetry and Remote Sensing*, vol. 177, pp. 291–305, 2021.

[18] J. Zhang, F. Li, L. Zeng, J. Peng, and J. Li, "Numerical simulation of the moisture migration of unsaturated clay embankments in southern China considering stress state," *Bulletin of Engineering Geology and the Environment*, vol. 80, no. 1, pp. 11–24, 2021.

[19] N. Masaoka, K. i. Kosugi, Y. Yamakawa, and D. Tsutsumi, "Processes of bedrock groundwater seepage and their effects on soil water fluxes in a foot slope area," *Journal of Hydrology*, vol. 535, pp. 160–172, 2016.

[20] M. S. Kim, Y. Onda, T. Uchida, J. K. Kim, and Y. S. Song, "Effect of seepage on shallow landslides in consideration of changes in topography: case study including an experimental sandy slope with artificial rainfall," *Catena*, vol. 161, pp. 50–62, 2018.

[21] X. Liu, C. a. Tang, L. Li, P. Lv, and R. Sun, "Microseismic monitoring and stability analysis of the right bank slope at Dagangshan hydropower station after the initial impoundment," *International Journal of Rock Mechanics and Mining Sciences*, vol. 108, pp. 128–141, 2018.

[22] Y. Shi, C. Zhao, Z. Peng, H. Yang, and J. He, "Analysis of the lag effect of embankment dam seepage based on delayed mutual information," *Engineering Geology*, vol. 234, pp. 132–137, 2018.

[23] X. Liu and Y. Wang, "Bayesian selection of slope hydraulic model and identification of model parameters using monitoring data and subset simulation," *Computers and Geotechnics*, vol. 139, Article ID 104428, 2021.

[24] T. Vogt, P. Schneider, L. Hahn-Woernle, and A. C. Olaf, "Estimation of seepage rates in a losing stream by means of fiber-optic high-resolution vertical temperature profiling," *Journal of Hydrology*, vol. 380, no. 1, pp. 154–164, 2010.

[25] Y. Zhang, C. Chen, Y. Zheng, Y. Shao, and C. Sun, "Application of fiber Bragg grating sensor technology to leak detection and monitoring in diaphragm wall joints: a field study," *Sensors*, vol. 21, no. 2, p. 441, 2021.

[26] H. Su, H. Li, Y. Kang, and Z. Wen, "Experimental study on distributed optical fiber-based approach monitoring saturation line in levee engineering," *Optics & Laser Technology*, vol. 99, pp. 19–29, 2018.

[27] H. Su, B. Ou, L. Yang, and Z. Wen, "Distributed optical fiber-based monitoring approach of spatial seepage behavior in dike engineering," *Optics & Laser Technology*, vol. 103, pp. 346–353, 2018.

[28] Y. Zheng, C. Chen, T. Liu, Y. Shao, and Y. Zhang, "Leakage detection and long-term monitoring in diaphragm wall joints using fiber Bragg grating sensing technology," *Tunnelling and Underground Space Technology*, vol. 98, Article ID 103331, 2020.

[29] D.-F. Cao, H.-H. Zhu, C.-C. Guo, J.-H. Wu, and B. Fatahi, "Investigating the hydro-mechanical properties of calcareous sand foundations using distributed fiber optic sensing," *Engineering Geology*, vol. 295, p. 106440, 2021.

[30] H. Wijaya, P. Rajeev, and E. Gad, "Distributed optical fibre sensor for infrastructure monitoring: field applications," *Optical Fiber Technology*, vol. 64, Article ID 102577, 2021.

[31] L. Cheng, A. Zhang, B. Cao, J. Yang, L. Hu, and Y. Li, "An experimental study on monitoring the phreatic line of an embankment dam based on temperature detection by OFDR," *Optical Fiber Technology*, vol. 63, Article ID 102510, 2021.

Hindawi
Advances in Materials Science and Engineering
Volume 2022, Article ID 9285623, 17 pages
https://doi.org/10.1155/2022/9285623

Research Article

Analysis of the Effect of the Friction Coefficient on a Pavement Structure

Lu Bai [1] **and Yong-sheng Zhang** [2]

[1]*School of Civil Engineering, Xuchang University, Xuchang 461000, China*
[2]*China Academy of Transportation Science, Beijing 100029, China*

Correspondence should be addressed to Lu Bai; lubai526@126.com

Received 20 September 2021; Revised 25 January 2022; Accepted 31 January 2022; Published 27 February 2022

Academic Editor: Yongsheng Yao

Insufficient skid resistance of pavement is one of the main causes of traffic accidents. In this study, the influence of the friction coefficient on the internal effect of the pavement structure is studied deeply by establishing the asymmetric finite element numerical model. The model analyzes the inner stress, strain, and displacement variations of the pavement, with friction coefficients under the conditions of 0.3, 0.5, 0.8, and 1.0 and the action of the nonlinear superposition between the single-point static vertical load and horizontal load. In addition, against the limitations of the scatter calculation results, this paper analyzes the distribution of the internal stress field and displacement field. The results show that, with the attenuation of the friction coefficient, the distribution law of stress, strain, and displacement on the road surface ($Z = 0$) remains unchanged, and the maximum principal strain and the third principal strain on the Z-axis decrease monotonically with increasing depth. With the attenuation of the friction coefficient, the horizontal displacement inside the pavement structure gradually decreases, the vertical displacement changes insignificantly, and the principal stress gradually decreases. The principal strain and maximum shear stress inside the pavement structure show different changing rules.

1. Introduction

The friction coefficient between a tire and a road surface is an important indicator for evaluating the antiskid performance of the road surface. This is the main factor affecting the friction performance of the tread and the road surface. It is also an important factor affecting the safety of road traffic [1–3]. With the cumulative action of loading and the continuous influence of temperature and humidity, the friction coefficient between the pavement and tire decreases gradually [4, 5], which will cause a change in the internal stress of the pavement structure. At present, the friction contact model between the tread and the road surface is established and numerically analyzed, and it is obtained that, in the full acceleration slip state, the greater the friction coefficient, the greater the contact stress [6, 7], but when the friction coefficient exceeds a certain critical value, with the increase of its value, the antiskid performance in the braking state is no longer improved, and the compressive stress of the road surface increases significantly [8]. Anupam et al. [9] studied the variation law of antiskid performance with ambient temperature and road surface temperature and proposed the relationship between slider resistance and different parameters. Li [10] used the simulation test to explore the relationship between tire-sand surface contact and antiskid performance and evaluated the durability of antiskid performance from the perspective of tire-tread contact occlusion. Guo [11]established a three-dimensional finite element model of the truck tire, asphalt pavement structure, and pavement changing temperature field for truck tires with longitudinal patterns and highly nonlinear characteristics and predicted the dynamic response law of the asphalt pavement structure under complex heavy loads. Hao [12] established a refined finite element model and found that the effect of pattern distribution on the stress distribution state is smaller. Yao et al. [13] used the developed DEM model to

accurately predict the mechanical properties and deformation behavior of SRM. Li et al. [14] carried out 2D finite element simulation of flexible pavement under half-sine load and established a numerical prediction method for flexible pavement dynamic characteristics considering the stress sensitivity and humidity change of subgrade soil.

Previous studies indicated that differences in the surface roughness may result in different results about internal force of the pavement structure [15–17]. However, relevant research on the influence of friction coefficient attenuation on the internal force of pavement structures under the action of nonlinear superposition between vertical and horizontal loads is lacking. By establishing a finite element model, this paper analyzes the inner stress, strain, and displacement variations of the pavement structure under different friction coefficients, explores the change in the internal force of pavement with the attenuation of the friction coefficient, and provides a reference for the design of the pavement structure and its antiskid performance.

2. Mechanical Analysis Model

In existing pavement structure analyses [18, 19], the linear superposition method is adopted for the analysis of the force state under the simultaneous action of vertical load and horizontal load. However, when the two act at the same time, it should be a coupled state, that is, a nonlinear superposition. Assuming that the contact surface between the wheel and the road is circular, the analysis is carried out according to the single-wheel load model. Under small deformation conditions, assuming that the pavement structure bears the vertical load, the load is evenly distributed in a circular area with a diameter of 2a ($a = 10.65$ cm). As shown in Figure 1, the corresponding friction load is P_0. The coordinate system is established, as shown in Figure 2.

The vehicle is moving at a constant speed v, and the formula for the vertical force is as follows:

$$F = F_0 H(a - r)\delta(x - vt)\delta(y) = F(a, r, x, y, t), \quad (1)$$

where $r = \sqrt{(x - vt)^2 + y^2}$, $\delta(\bullet)$ is Dirac Delta functions, and $H(\bullet)$ is load action density.

Therefore, the horizontally distributed load is assumed to be

$$P = P_0 H(a - r)\delta(x - vt)\delta(y), \quad (2)$$

where $P_0 = \mu F_0$ and μ is the dynamic friction coefficient.

3. Establish Governing Equations for Related Issues

Under the combined action of horizontal load and vertical load, the mechanical model of the pavement structure is an asymmetric semi-infinite body or an asymmetric layered semi-infinite body. Therefore, the governing equation of the problem in the cylindrical coordinate system can be established [20]. The equilibrium differential equation is shown in equation (3), which is the

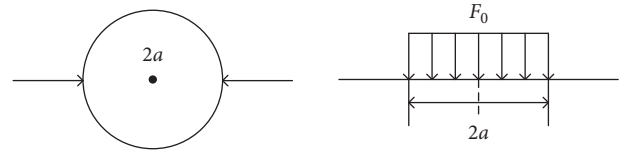

Figure 1: Schematic diagram of the vertical load borne by the pavement.

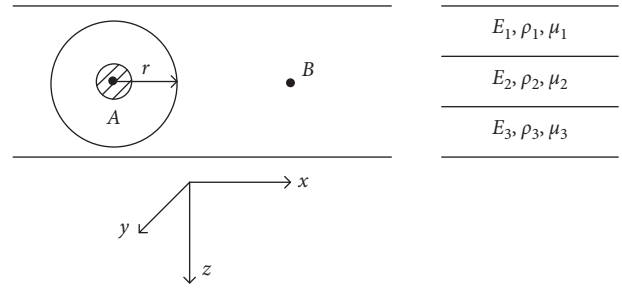

Figure 2: Coordinate system for analysis.

equilibrium differential equation of the pavement structure under nonaxisymmetric problems; the relationship between strain and displacement is shown in equation (4). The physical relationship of pavement materials obeys a generalized Hooke's law, and the Goodman model is used under the boundary conditions to characterize the state of interlayer bonding. The general formula of the boundary conditions for nonaxisymmetric subjects can be obtained as equation (5):

$$\begin{cases} \dfrac{\partial \sigma_r}{\partial r} + \dfrac{1}{r}\dfrac{\partial \tau_{r\theta}}{\partial \theta} + \dfrac{\partial \tau_{rz}}{\partial z} + \dfrac{\sigma_r - \sigma_\theta}{r} = \rho \dfrac{\partial^2 u}{\partial t^2} \\ \dfrac{\partial \tau_{r\theta}}{\partial r} + \dfrac{1}{r}\dfrac{\partial \sigma_\theta}{\partial \theta} + \dfrac{\partial \tau_{\theta z}}{\partial z} + \dfrac{2}{r}\tau_{r\theta} = \rho \dfrac{\partial^2 v}{\partial t^2} \\ \dfrac{\partial \tau_{rz}}{\partial r} + \dfrac{1}{r}\dfrac{\partial \tau_{\theta z}}{\partial \theta} + \dfrac{\partial \sigma_z}{\partial z} + \dfrac{\tau_{rz}}{r} = \rho \dfrac{\partial^2 w}{\partial t^2} \end{cases}, \quad (3)$$

$$\begin{cases} \xi_r = \dfrac{\partial u}{\partial r} \\ \xi_\theta = \dfrac{u}{r} + \dfrac{1}{r}\dfrac{\partial v}{\partial \theta} \\ \xi_z = \dfrac{\partial w}{\partial z} \\ \gamma_{r\theta} = \dfrac{1}{r}\dfrac{\partial u}{\partial \theta} + \dfrac{\partial v}{\partial r} - \dfrac{v}{r} \\ \gamma_{\theta z} = \dfrac{1}{r}\dfrac{\partial w}{\partial \theta} + \dfrac{\partial v}{\partial z} \\ \gamma_{rz} = \dfrac{\partial u}{\partial z} + \dfrac{\partial w}{\partial r} \end{cases}, \quad (4)$$

$$\begin{cases} \sigma_{z_i}\big|_{z=H_i} = \sigma_{z_{i+1}}|_{z=H_i}\big| \\ \tau_{\theta z_i}|_{z=H_i} = \tau_{\theta z_{i+1}}|_{z=H_i} \\ \tau_{rz_i}|_{z=H_i} = \tau_{rz_{i+1}}|_{z=H_i} \\ \tau_{\theta z_i}|_{z=H_i} = K_i(v_{i+1} - v_i)|_{z=H_i} \\ \tau_{rz_i}|_{z=H_i} = K_i(u_{i+1} - u_i)|_{z=H_i} \\ w_i|_{z=H_i} = w_{i+1}|_{z=H_i} \end{cases}, \tag{5}$$

where K is the interlayer adhesion coefficient, 0<K<∞.

The transfer matrix method is used to solve the governing equations under the action of static load and the nonlinear superposition of horizontal load and vertical load. The boundary conditions of vertical load μF and horizontal load F are

(1) At z = 0,

$$\begin{aligned} \tau_{\theta z}|_{z=0} &= \mu F \sin\theta\overline{\tau_{\theta z}}|_{z=0} = \frac{\mu F_0}{\pi\delta} \times \frac{J_1(\xi\delta)}{\xi}\sin\theta, \\ \tau_{rz}|_{z=0} &= -\mu F \cos\theta\overline{\tau_{rz}}|_{z=0} = \frac{\mu F_0}{\pi\delta} \times \frac{J_1(\xi\delta)}{\xi}\cos\theta, \\ \overline{F}(\xi) &= \frac{F_0}{\pi\delta} \times \frac{J_1(\xi\delta)}{\xi}\overline{\sigma_z}(\xi, 0) = \frac{F_0}{\pi\delta} \times \frac{J_1(\xi r)}{\xi}. \end{aligned} \tag{6}$$

(2) At $z = \infty$, for the Goodman model, when $\tau = \kappa\Delta u$ ($0 < \kappa < \infty$), $k \longrightarrow \infty$, the interface completely continuous boundary condition can be written as

$$\begin{aligned} &\left(\overline{\tau}_{\theta z_1} + \overline{\tau}_{rz_1}\right)|_{z=0} = 0, \\ &\left(\overline{\tau}_{\theta z_1} - \overline{\tau}_{rz_1}\right)|_{z=0} = \frac{2\mu F_0}{\pi\delta} \times \frac{J_1(\xi r)}{\xi}, \\ &\left(\overline{\tau}_{\theta z_i} + \overline{\tau}_{rz_i}\right)|_{z=H_i} = \left(\overline{\tau}_{\theta z_{i+1}} + \overline{\tau}_{rz_{i+1}}\right)|_{z=H_i}, \\ &\left(\overline{\tau}_{\theta z_i} - \overline{\tau}_{rz_i}\right)|_{z=H_i} = \left(\overline{\tau}_{\theta z_{i+1}} - \overline{\tau}_{rz_{i+1}}\right)|_{z=H_i}, \\ &\frac{1}{K}\left(\overline{\tau}_{\theta z_i} + \overline{\tau}_{rz_i} + \overline{v}_i - \overline{u}_i\right)|_{z=H_i} = \left(\overline{v}_{i+1} - \overline{u}_{i+1}\right)|_{z=H_i}, \\ &\overline{w}_i|_{z=H_i} = \overline{w}_{i+1}|_{z=H_i}. \end{aligned} \tag{7}$$

The stress field is

$$\begin{aligned} \sigma_r &= -\int_0^\infty \xi\left\{[A - (1 + 2\mu - \xi z)B]e^{-\xi z} - [C + (1 + 2\mu + \xi z)D]e^{\xi z}\right\}J_1(\xi r)\cos\theta\mathrm{d}\xi + \frac{1}{r}U_2\cos\theta, \\ \sigma_\theta &= 2\mu\int_0^\infty \xi\left\{Be^{-\xi z} + De^{\xi z}\right\}J_1(\xi r)\cos\theta\mathrm{d}\xi - \frac{1}{r}U_2\cos\theta, \\ \sigma_r &= \int_0^\infty \xi\left\{[A + (1 - 2\mu + \xi z)B]e^{-\xi z} - [C - (1 - 2\mu - \xi z)D]e^{\xi z}\right\}J_1(\xi r)\cos\theta\mathrm{d}\xi, \\ \tau_{r\theta} &= \int_0^\infty \xi\left\{Ee^{-\xi z} + Fe^{\xi z}\right\}J_1(\xi r)\sin\theta\mathrm{d}\xi + \frac{1}{r}U_2\sin\theta, \\ \tau_{\theta z} &= \frac{1}{2}(H_2 + H_0)\sin\theta, \\ \tau_{rz} &= \frac{1}{2}(H_2 - H_0)\cos\theta. \end{aligned} \tag{8}$$

Displacement field is

$$
\begin{aligned}
u &= -\frac{1+\mu}{2E}\left(U_2 - U_0\right)\cos\,\theta,\\
v &= -\frac{1+\mu}{2E}\left(U_2 + U_0\right)\sin\,\theta,\\
w &= -\frac{1+\mu}{2E}\int_0^{\infty}\left\{[A + (2-4\mu+\xi z)B]e^{-\xi z} + [C - (2-4\mu-\xi z)D]e^{\xi z}\right\}J_1(\xi r)\cos\,\theta\mathrm{d}\xi,\\
U_2 &= \int_0^{\infty}\left\{[A - (1-\xi z)B - 2E]e^{-\xi z} - [C + (1+\xi z)D + 2F]e^{\xi z}\right\}J_1(\xi r)\mathrm{d}\xi,\\
U_0 &= \int_0^{\infty}\left\{[A - (1-\xi z)B - 2E]e^{-\xi z} - [C + (1+\xi z)D - 2F]e^{\xi z}\right\}J_1(\xi r)\mathrm{d}\xi,\\
H_2 &= \int_0^{\infty}\xi\left\{[A - (2\mu-\xi z)B - E]e^{-\xi z} + [C + (2\mu+\xi z)D + F]e^{\xi z}\right\}J_2(\xi r)\mathrm{d}\xi,\\
H_0 &= \int_0^{\infty}\xi\left\{[A - (2\mu-\xi z)B + E]e^{-\xi z} + [C + (2\mu+\xi z)D - F]e^{\xi z}\right\}J_0(\xi r)\mathrm{d}\xi,\\
J_0(\xi r) &= \frac{2}{\xi r}J_1(\xi r) - J_0(\xi r)\mathrm{d}\xi.
\end{aligned}
\tag{9}
$$

A, B, C, D, E, and F are determined by boundary conditions.

4. Calculation Structure of Stress Field and Displacement Field

4.1. Displacement Field Distribution. Figure 3 is the horizontal displacement U under different friction coefficient conditions. The result shows that, with the attenuation of the friction coefficient, the horizontal displacement U inside the pavement structure gradually decreases, which is most obvious in the range affected by the load radius ($r = 0$~10.65 cm).

Figure 4 is the vertical displacement W under different friction coefficient conditions. The result shows that, as the friction coefficient decreases, the vertical displacement W inside the pavement structure shows an overall increasing trend.

4.2. Stress Field Distribution. In Figures 5 and 6, it is seen that, with the attenuation of the friction coefficient, the maximum principal stress inside the pavement structure gradually decreases. The area, depth, and tensile stress value of the tension zone decrease within 20 cm from the surface of the load circle. The maximum shear stress inside the pavement structure in the load circle gradually decreases, but the influence range becomes larger.

4.3. Strain Field Distribution. In Figure 7, it is seen that, as the attenuation of the friction coefficient, the maximum principal strain inside the pavement structure in the load circle gradually decreases, but the influence range becomes larger.

5. Analysis of Nonlinear Superposition of Static Vertical Load and Horizontal Load under Different Friction Coefficient Conditions

The following conditions are used to calculate the internal stress, strain, and displacement of the structure: a single circular load with a radius of 10.65 cm on the surface of the elastic half-space body, a load concentration of 0.7 MPa, a friction coefficient of 0.3, 0.5, 0.8, and 1.0, respectively, half-space body elastic modulus $E = 1500$ MPa, and Poisson's

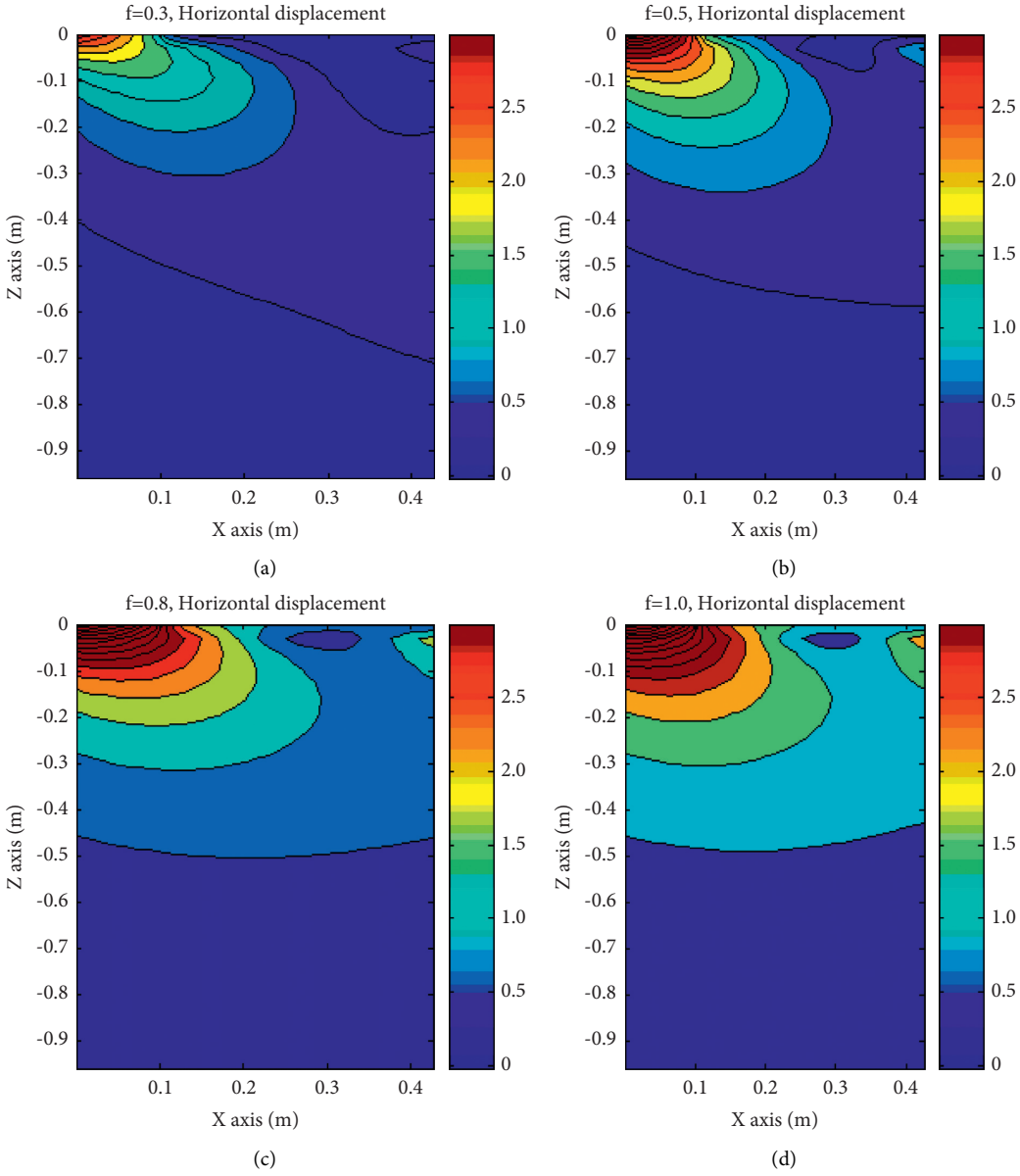

Figure 3: Horizontal displacement nephogram under different friction (f) coefficients. (a) $f = 0.3$. (b) $f = 0.5$. (c) $f = 0.8$. (d) $f = 1.0$.

ratio of 0.3. In the horizontal direction (x-axis), 10 points are calculated inside the load circle, 30 points are calculated outside the load circle, and 30 points are calculated in the vertical direction (z-axis).

5.1. The Calculated Value of Each Calculation Point on the Surface x-Axis ($z = 0$). Under different friction coefficient conditions, when the horizontal load (H) and the vertical load (V) are nonlinearly superimposed, the results of the stress, strain, and displacement of each calculation point on the x-axis ($z = 0$) of the calculated structure surface are shown in Figure 8.

Displacement changes: the horizontal displacement of each calculation point on the structure surface has the largest value at the center of the load circle, and this value decreases with the decrease of the friction coefficient, which is most obvious inside the load circle. This phenomenon shows that, along the direction of travel of the car (the positive direction of the x-axis), when the friction coefficient is attenuated, the horizontal displacement of the surface decreases, and the movement of the road surface weakens. As the friction

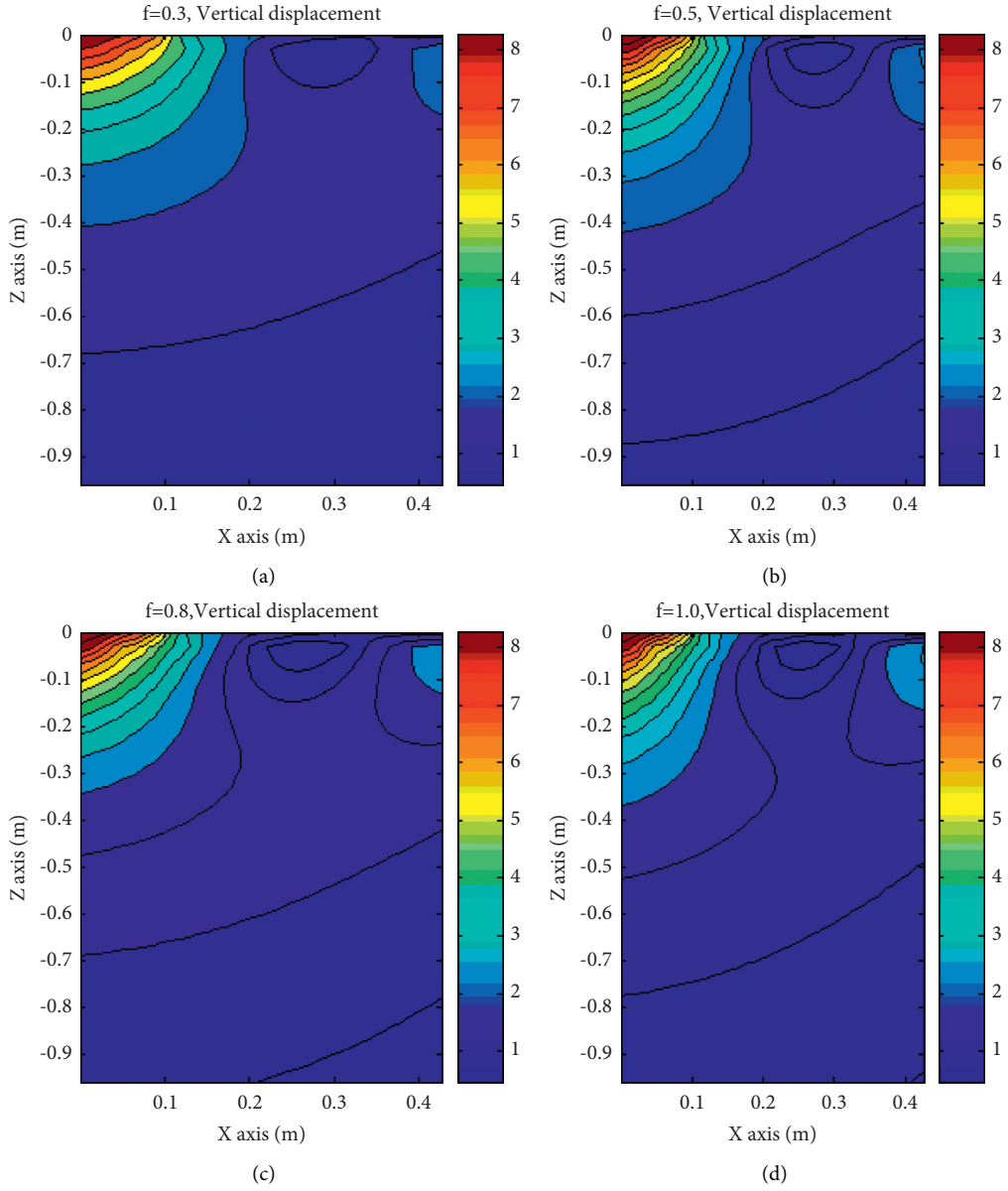

Figure 4: Vertical displacement nephogram under different friction coefficients. (a) $f = 0.3$. (b) $f = 0.5$. (c) $f = 0.8$. (d) $f = 1.0$.

coefficient decreases, the vertical displacement W of each calculation point on the surface does not change significantly.

The stress analysis results are shown in Figures 9 and 10(a) and 10(b). The normal stress curve in the x-direction shows that the normal stresses σ_x and σ_y on the x-axis have very similar trends to the principal stress curve. Inside the load circle, the maximum principal stress on the x-axis following the increase in x gradually changes from compressive stress to tensile stress. The tensile stress value reaches the maximum at the edge of the load circle, and the value gradually increases with increasing horizontal load, while the tensile stress value outside the load circle gradually decreases to 0. The third principal stress is mainly the compressive stress, and its value gradually decreases as the friction coefficient decreases; the value outside the load circle is close to 0. The z-direction stress σ_z of each calculation point on the x-axis does not change much in Figure 10(c), and the five curves under the condition of different friction coefficients completely overlap. This shows that the attenuation of the friction coefficient has no effect on the z-direction stress at each calculation point on the x-axis.

Inside the load circle, the shear stress τ_{zx} of each calculation point on the x-axis gradually decreases with the attenuation value of the friction coefficient and becomes 0 outside the load circle, as shown in Figure 10(d). Inside the load circle, the maximum shear stress gradually increases

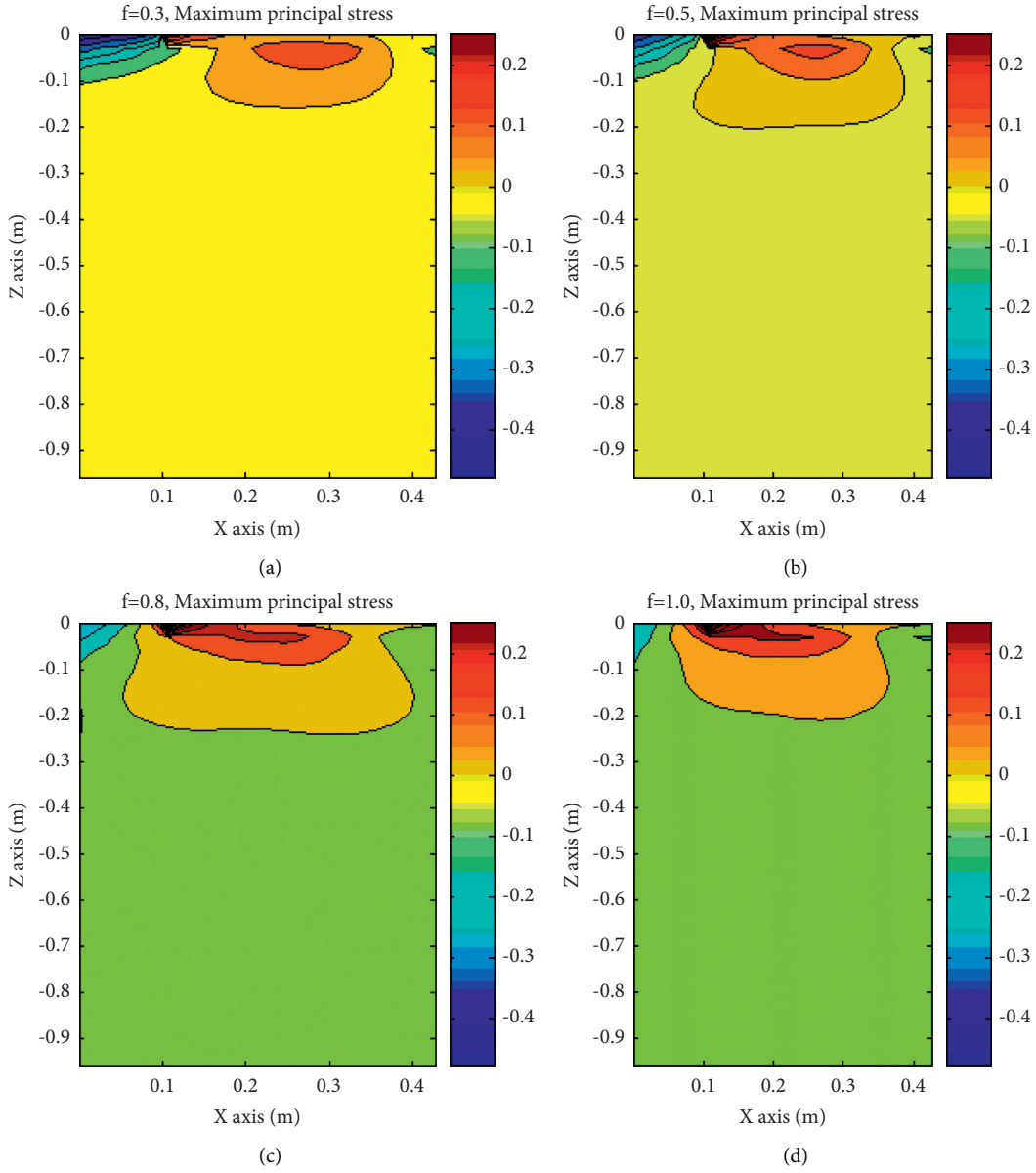

Figure 5: Maximum principal stress nephogram under different friction coefficients. (a) $f = 0.3$. (b) $f = 0.5$. (c) $f = 0.8$. (d) $f = 1.0$.

with increasing x, reaches the maximum value at the edge of the load circle, and gradually decreases as the friction coefficient attenuates, while the maximum shear stress value outside the load circle gradually decreases to 0.

The variation in strain with the friction coefficient is shown in Figure 11. Inside the load circle, the maximum principal strain on the x-axis gradually changes from compressive strain to tensile strain as x increases. The tensile strain value reaches the maximum at the edge of the load circle and gradually decreases as the friction coefficient decays, while the tensile strain value outside the load circle gradually decreases to zero. The third principal strain is all compressive strain. The value inside the load circle is very large, and its value gradually decreases with the attenuation of the friction coefficient; the value outside the load circle is close to zero. This is the same as the law of stress change.

5.2. The Calculated Value of Each Calculation Point on the z-Axis ($x = 0$) of the Load Center Axis of the Single Circle. Under different friction coefficient conditions, when the horizontal load and vertical load are nonlinearly superimposed, the calculation results of the stress, strain, and displacement at each calculation point on the central axis Z ($x = 0$) of the single circular load of the above calculation structure are shown in Figure 12. With the attenuation of the

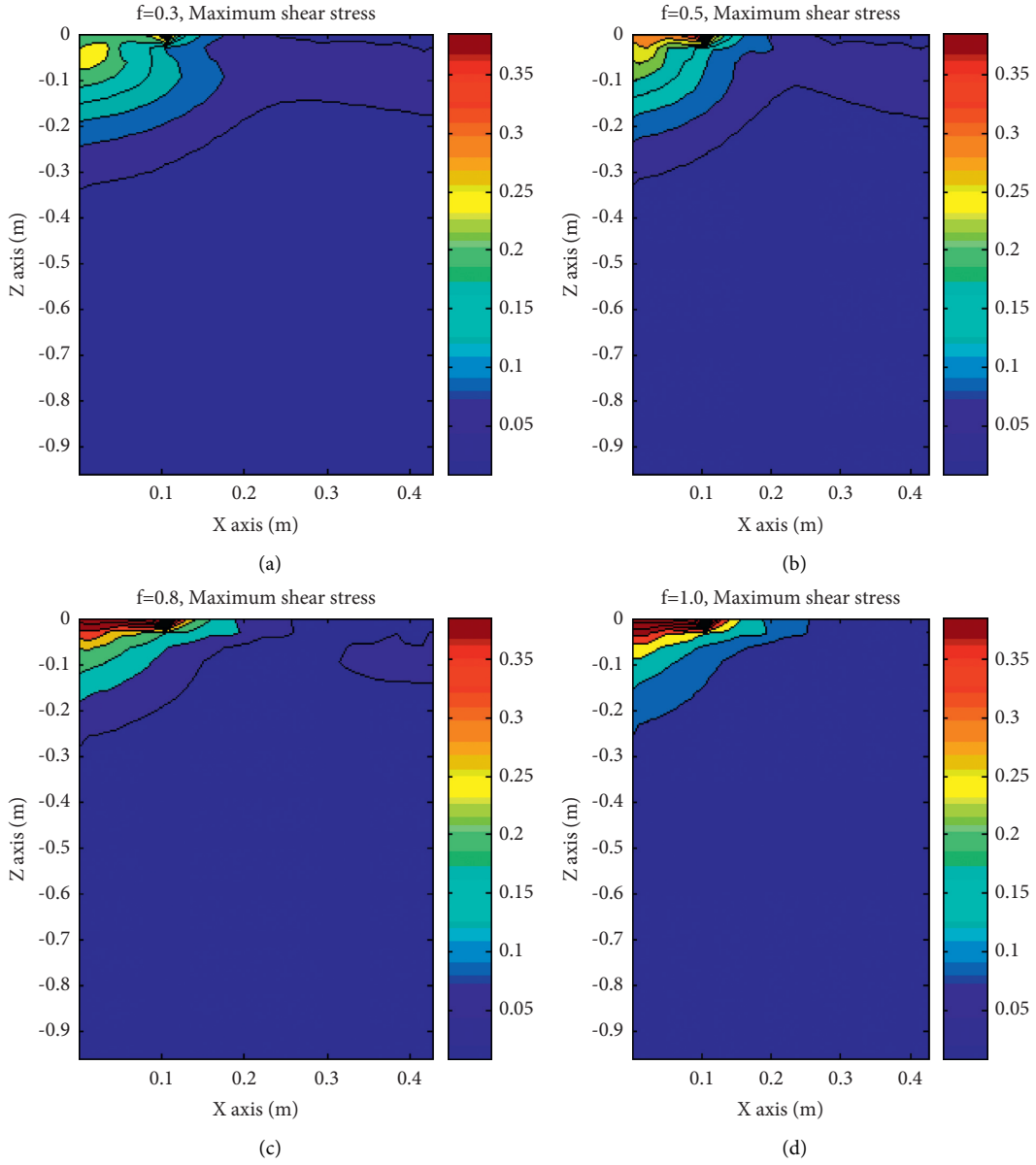

Figure 6: Maximum shear stress nephogram under different friction coefficients. (a) $f = 0.3$. (b) $f = 0.5$. (c) $f = 0.8$. (d) $f = 1.0$.

friction coefficient, the horizontal displacement on the z-axis gradually decreases, and the vertical displacement remains unchanged.

In Figures 13 and 14, it is seen that the normal stress curve in the x-direction shows that the stress σ_x on the z-axis is very similar to the principal stress. It appears as a compressive stress zone in the range of 0–115 cm and becomes tensile stress in the range of 15 cm–40 cm. The position of the maximum tensile stress appears at a depth of approximately 20 cm, and the maximum principal stress value below 40 cm is already very small, approximate to zero. In the compressive stress region, with the decay of the friction coefficient, the maximum principal stress on the z-axis gradually increases, while in the tensile stress region, it is the opposite; at the same time, with the decay of the friction coefficient, the normal stresses σy and σz are on the z-axis The value does not change much, while the shear stress τzx decreases gradually. When the friction coefficient $f = 0$ or 0.3, the maximum shear stress on the z-axis shows a trend of first increasing and then decreasing with increasing depth. The peak value of the maximum shear stress appears within a range of approximately 10 cm from the surface, and as the friction coefficient decreases, the maximum shear stress value decreases. When the friction coefficient $f = 0.5$, 0.8, or

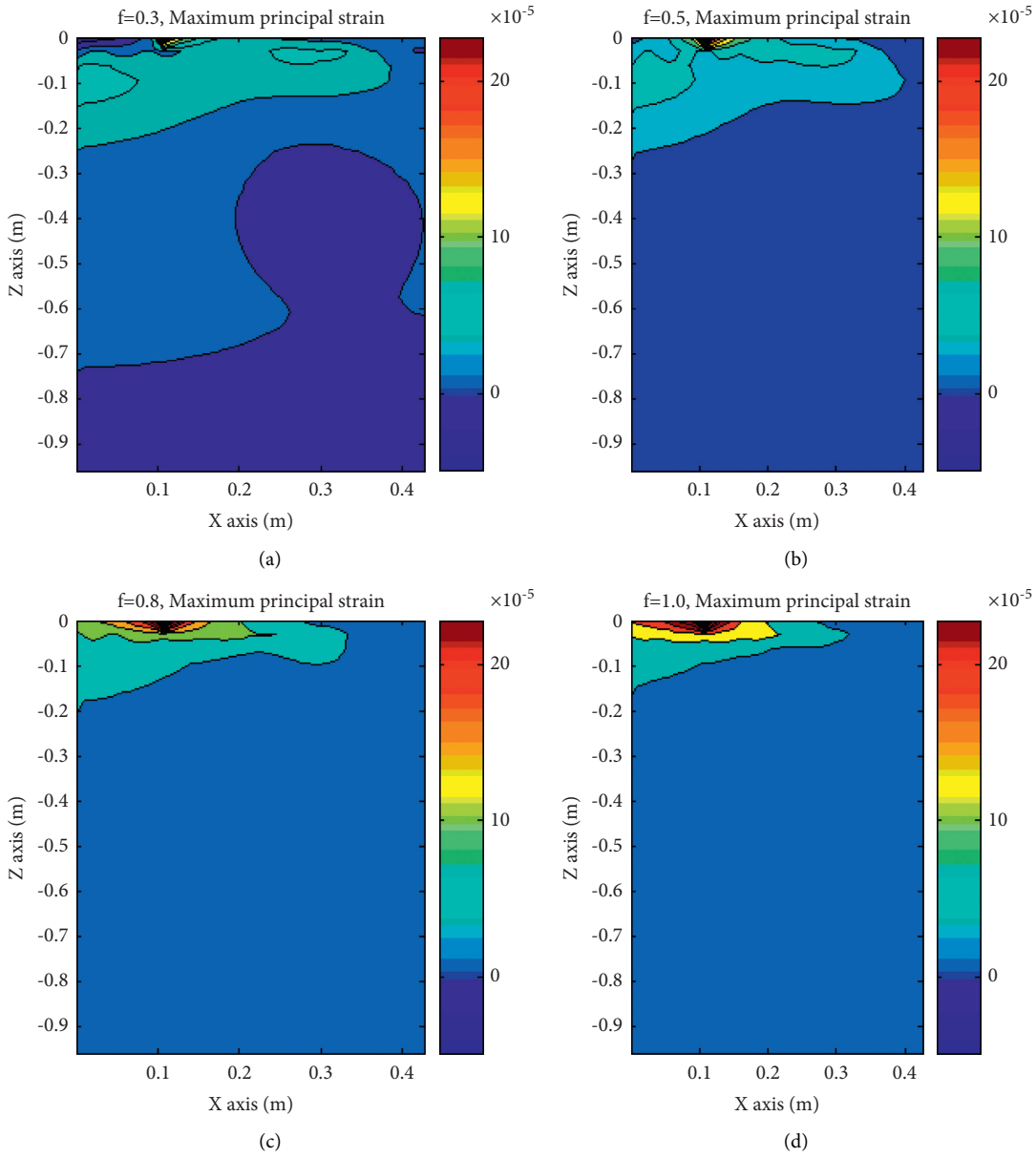

Figure 7: Maximum principal strain nephogram under different friction coefficients. (a) $f = 0.3$. (b) $f = 0.5$. (c) $f = 0.8$. (d) $f = 1.0$.

1.0, the maximum shear stress on the z-axis shows a monotonic decrease with increasing depth. The maximum shear stress peaks when the surface $z = 0$ and decreases with the attenuation of the friction coefficient.

The maximum principal strain curve in Figure 15(a) shows that when the friction coefficient $f = 0$ or 0.3, the maximum principal strain on the z-axis gradually changes from compressive strain to tensile strain as the depth increases. The range of 0 ~ 5 cm is the compressive strain zone, 5 cm below is the tensile strain zone, and the maximum tensile strain peaks at 10 cm from the surface. When the friction coefficient $f = 0.5$, the maximum principal strain on the z-axis is mainly tensile strain, and the value first increases and then decreases with increasing depth. The maximum tensile strain peak appears at a position approximately 10 cm from the surface. When the friction coefficient $f = 0.8$ or 1.0, the maximum principal strain on the z-axis decreases monotonically with increasing depth. The peak of the maximum tensile strain appears on the surface, and the value of the maximum principal strain increases with increasing horizontal load.

It can be seen in Figure 15(b) that the third principal strain is compressive strain, where when the friction coefficient $f = 0$ or 0.3, the third principal strain on the z-axis shows a trend of first increasing and then decreasing with the increase of depth, and the peaks are at 5 cm away from

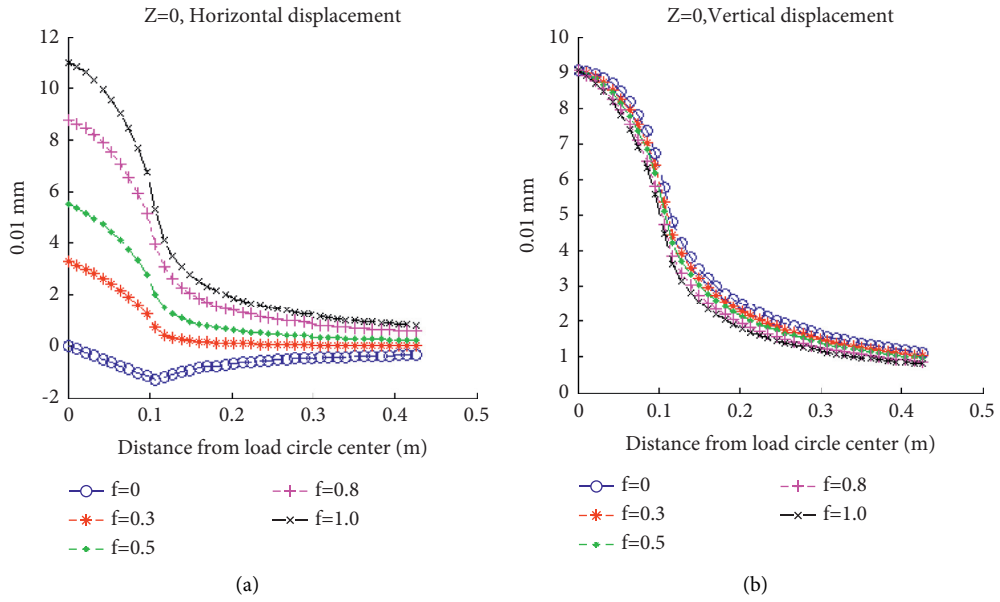

Figure 8: x-axis ($z = 0$) displacement calculation results of structure. (a) Calculation results of horizontal displacement of structure in x-axis ($z = 0$). (b) Calculation results of vertical displacement of structure in x-axis ($z = 0$).

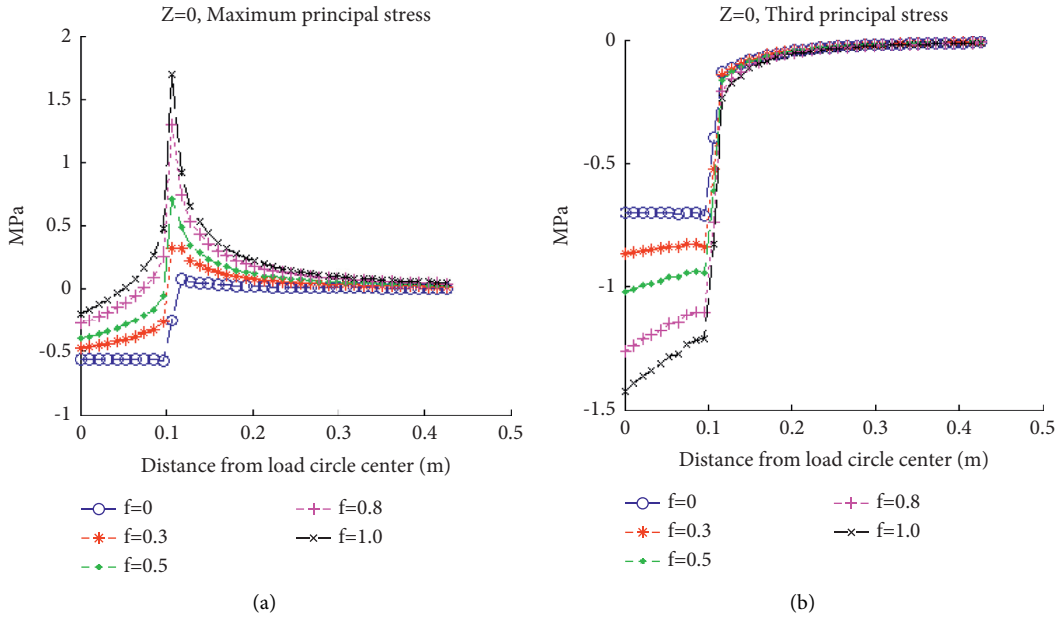

Figure 9: Continued.

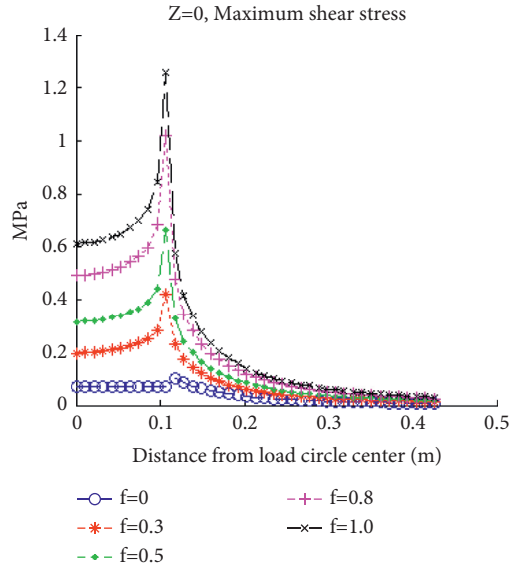

(c)

Figure 9: Calculation results of principal stress of structure in x-axis ($z = 0$). (a) Calculation results of maximum principal stress of structure in x-axis ($z = 0$). (b) Calculation results of third principal stress of structure in x-axis ($z = 0$). (c) Calculation results of maximum shear stress of structure in x-axis ($z = 0$).

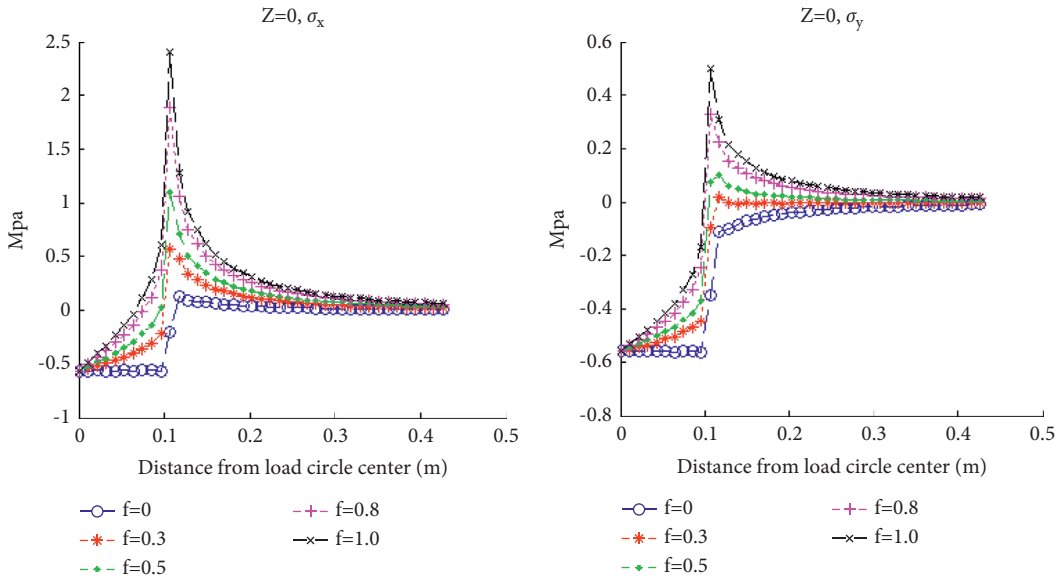

(a) (b)

Figure 10: Continued.

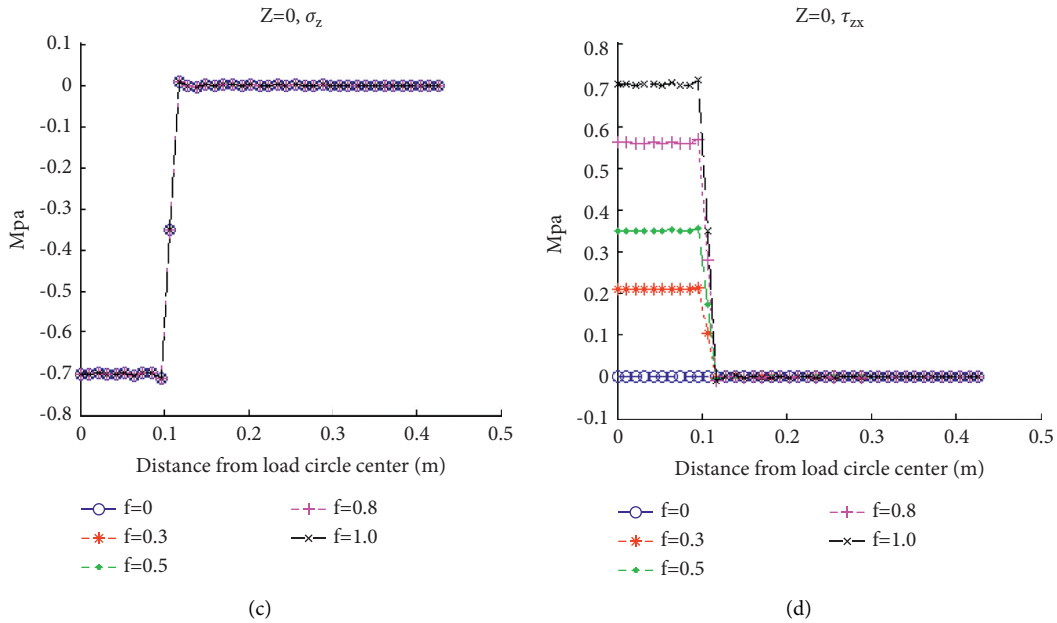

Figure 10: Calculation results of normal stress and shear stress of structure in x-axis ($z = 0$). (a) Calculation results of normal stress σ_x of structure in x-axis ($z = 0$). (b) Calculation results of normal stress σ_y of structure in x-axis ($z = 0$). (c) Calculation results of normal stress σ_Z of structure in x-axis ($z = 0$). (d) Calculation results of shear stress τ_{zx} of structure in x-axis ($z = 0$).

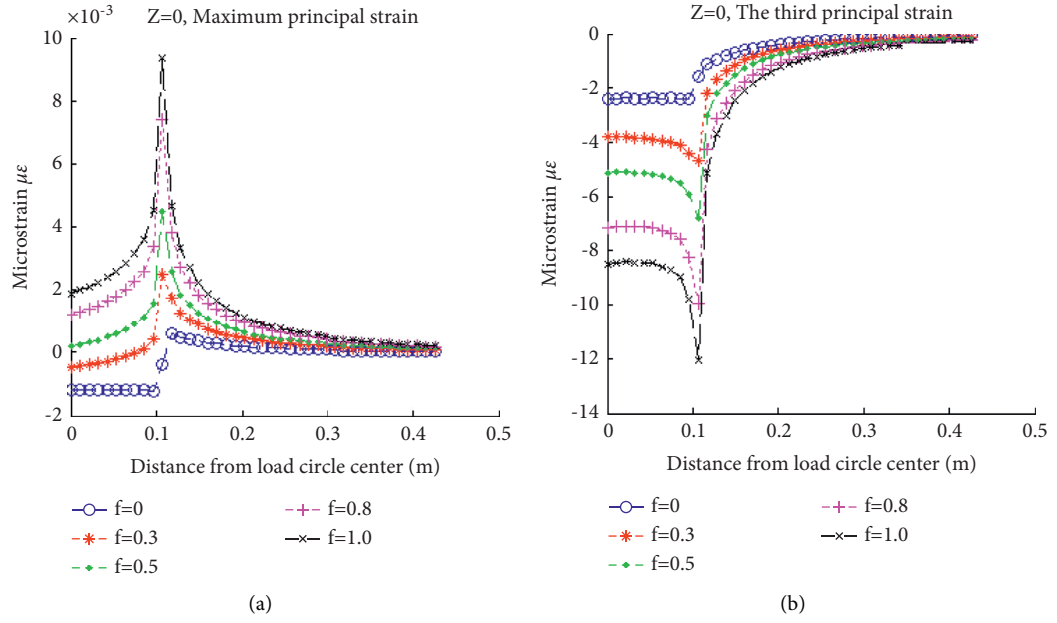

Figure 11: Calculation results of principal strain of structure in x-axis ($z = 0$). (a) Calculation results of maximum principal strain of structure in x-axis ($z = 0$). (b) Calculation results of third principal strain of structure in x-axis ($z = 0$).

the surface. When the friction coefficient $f = 0.5$, 0.8, or 1.0, the third principal strain on the z-axis decreases monotonically with increasing depth, the peak value of the third principal strain appears on the surface, and the value of the third principal strain increases with increasing friction coefficient.

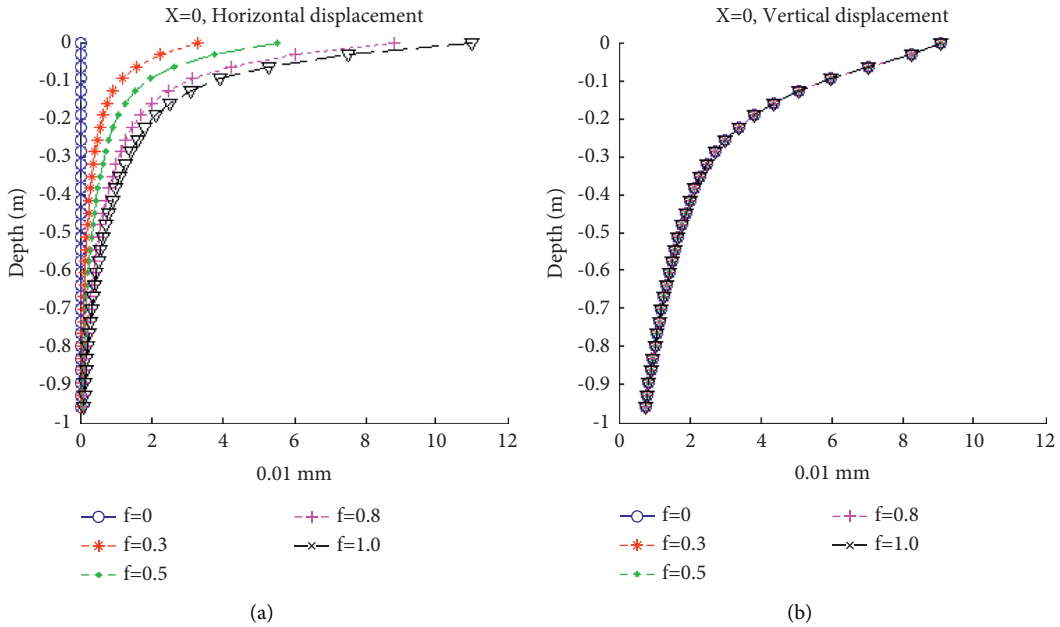

Figure 12: Calculation result of center point displacement of single circular load in z-axis ($x = 0$). (a) Calculation result of center point horizontal displacement of single circular load in z-axis ($x = 0$). (b) Calculation result of center point vertical displacement of single circular load in z-axis ($x = 0$).

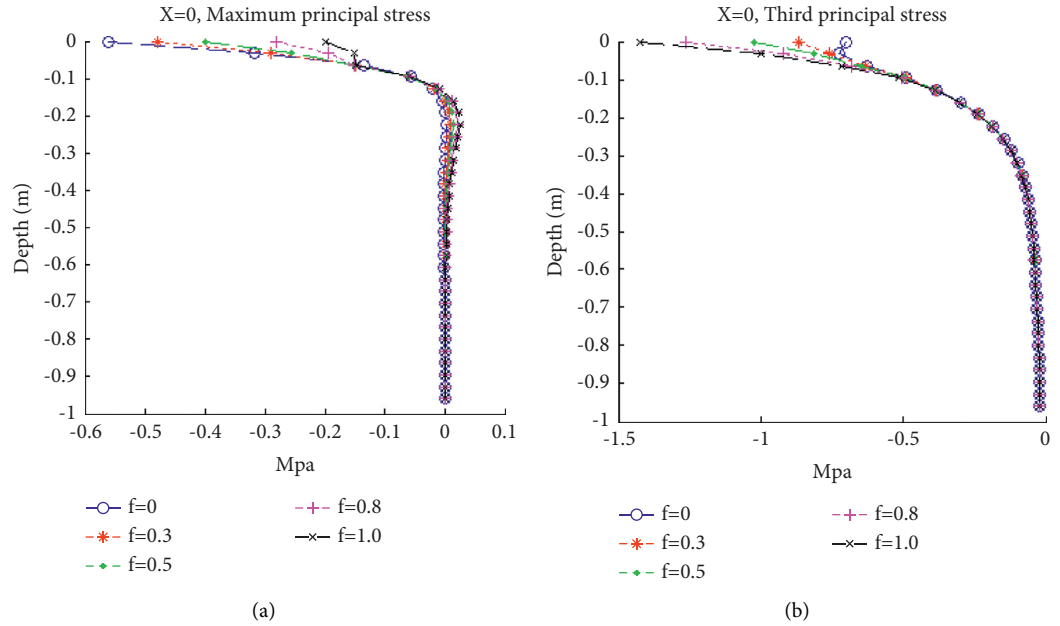

Figure 13: Continued.

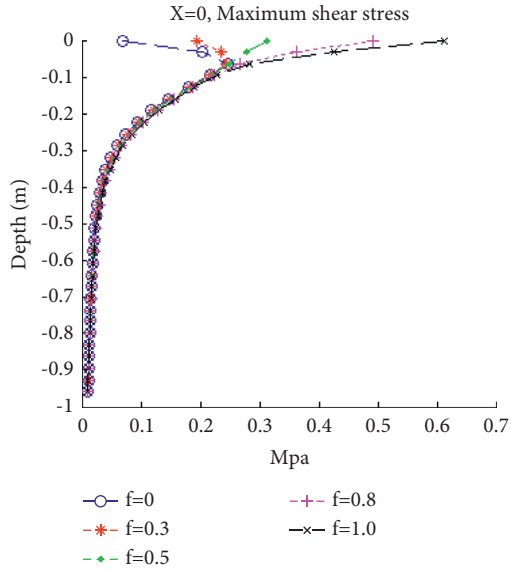

(c)

Figure 13: Calculation result of center point principal stress of single circular load in z-axis ($x = 0$). (a) Calculation result of center point maximum principal stress of single circular load in z-axis ($x = 0$). (b) Calculation result of center point third primary stress of single circular load in z-axis ($x = 0$). (c) Calculation result of center point maximum shear stress of single circular load in z-axis ($x = 0$).

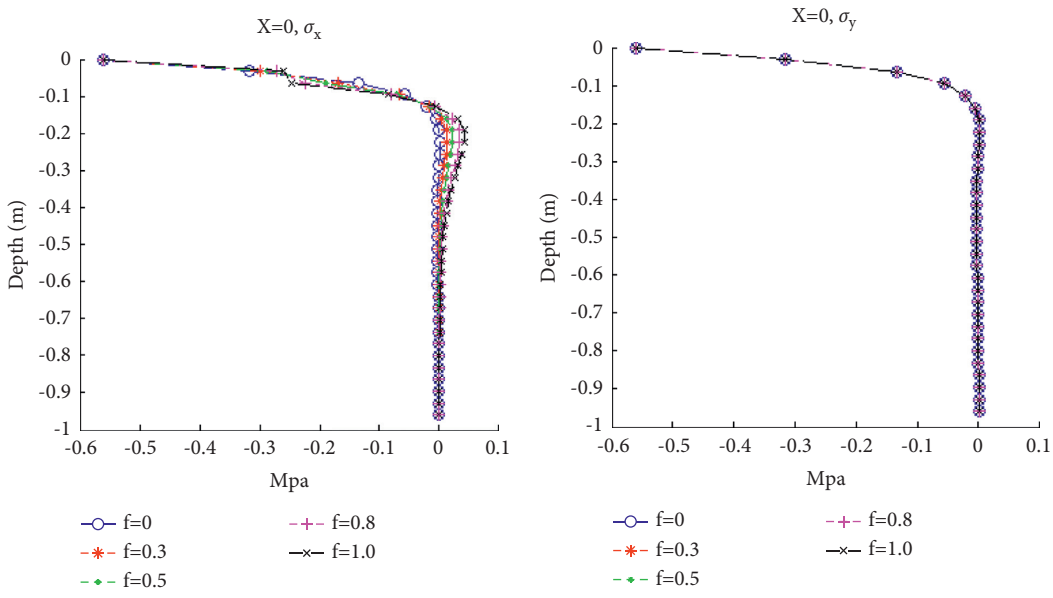

(a) (b)

Figure 14: Continued.

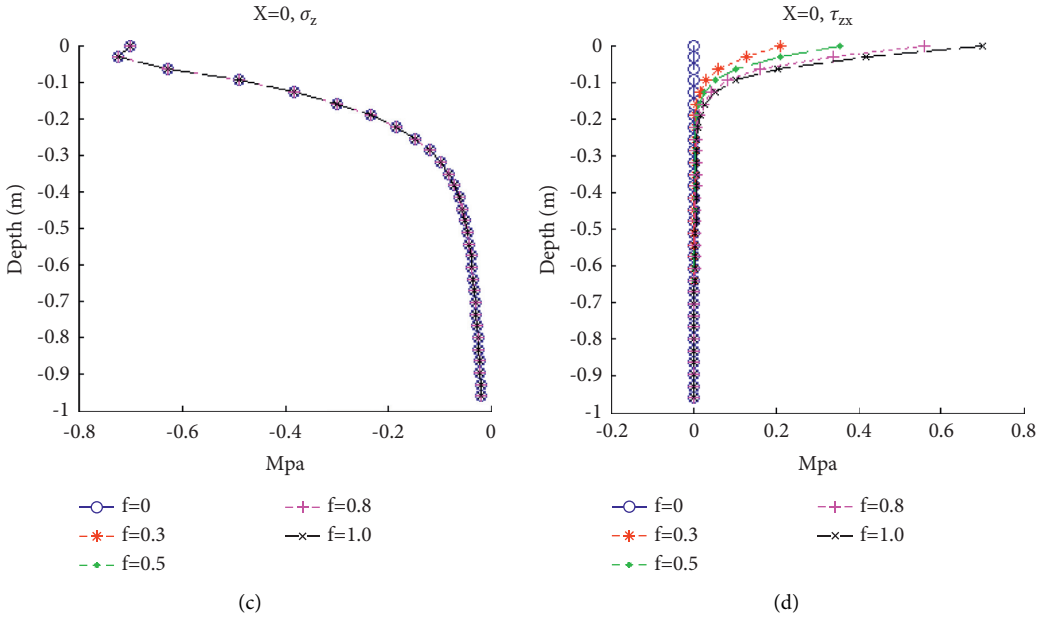

Figure 14: Calculation results of normal stress and shear stress in z-axis ($x = 0$) at center point of single circular load. (a) Calculation results of normal stress σ_x in z-axis ($x = 0$) at center point of single circular load. (b) Calculation results of normal stress σ_y in z-axis ($x = 0$) at center point of single circular load. (c) Calculation results of normal stress σ_z in z-axis ($x = 0$) at center point of single circular load. (d) Calculation results of shear stress τ_{zx} in z-axis ($x = 0$) at center point of single circular load.

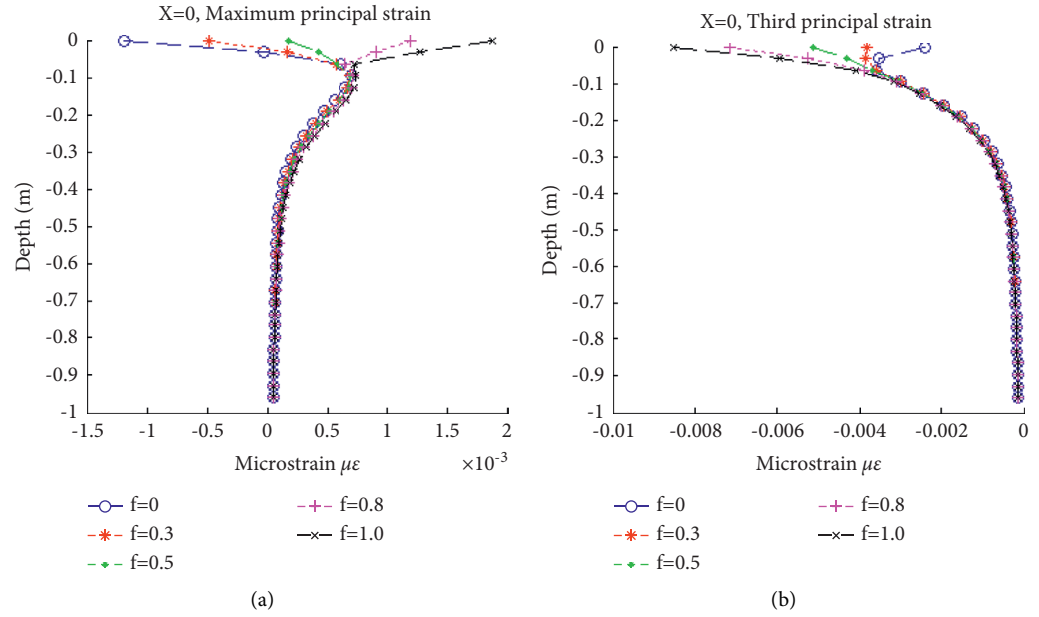

Figure 15: Calculation results of principal strain of z-axis ($x = 0$) at center point of single circular load. (a) Calculation results of maximum principal strain of z-axis ($x = 0$) at center point of single circular load. (b) Calculation results of third principal strain of z-axis ($x = 0$) at center point of single circular load.

6. Conclusions

This study proposed an asymmetric finite element numerical model approach to predict the internal stress, strain, and displacement of the elastic half-space structure under different friction coefficients, and the internal mechanics of the pavement structure is analyzed under the condition that the antiskid performance of the pavement is attenuated. The main contributions and conclusions are as follows:

(1) With the attenuation of the friction coefficient, when $Z = 0$, the distribution law of stress, strain, and

displacement of the pavement structure remains unchanged

(2) When the friction coefficient is 0 or 0.3, as the depth increases, the maximum principal strain on the z-axis gradually transitions from compressive strain to tensile strain, and the maximum shear stress and the third principal strain both increase first and then decrease

(3) When the friction coefficient is 0.5, with the increase of depth, the maximum principal strain value on the z-axis first increases and then decreases, and the maximum shear stress and the third principal strain decrease monotonically

(4) When the friction coefficient is 0.8 or 1.0, both the maximum principal strain and the third principal strain on the z-axis monotonically decrease with the increase of depth

(5) With the attenuation of the friction coefficient, the horizontal displacement inside the pavement structure gradually decreases, the vertical displacement inside the pavement structure generally increases, and the maximum principal stress inside the pavement structure gradually decreases

(6) The area, depth, and tensile stress of the tension zone decrease within 20 cm from the load circle surface, and the maximum shear stress and maximum principal strain inside the pavement structure within the load circle gradually decrease, but the influence range becomes larger

Due to the limitations of the epidemic and current conditions, the design thresholds of pavement skid resistance and the experimental verification of the model need to be further studied.

Data Availability

The data used to support the findings of this study are available from the corresponding author upon request.

Conflicts of Interest

The authors declare that there are no conflicts of interest regarding the publication of this paper.

Acknowledgments

The authors are thankful for the financial support received from the Science and Technology Project of Science and Technology Department of Henan Province (Grant no. 202102310582), Key scientific research project of Xuchang University (Grant no. 2021ZD005), and Horizontal project of Xuchang University in 2021 (Grant no. 2021HX146).

References

[1] X. Huang and B. Zheng, "Research status and progress for skid resistance performance of Asphalt pavements," *China Journal of Highway and Transport*, vol. 32, no. 4, pp. 32–49, 2019.

[2] M. Kane, L. Artamendi, and T. Scarpas, "Long-term skid resistance of asphalt surfacings:correlation between wehner-schulze friction values and the mineralogical composition of the aggregates," *Wear*, vol. 303, no. 1/2, pp. 235–243, 2013.

[3] A. Najaf and H. Saeid, "Statistical analysis of variables affecting tire - pavement friction," *International Journal of Pavement Research and Technology*, vol. 14, no. 3, pp. 378–384, 2020.

[4] Y. Han, Y. Zhao, J. Jiang, F. Ni, and X. Zhao, "Effects of design parameters and moisture conditions on interface bond strength between thin friction course (TFC) and underlying asphalt pavements," *Construction and Building Materials*, vol. 269, Article ID 121347, 2021.

[5] D. Yun, L. Hu, and C. Tang, "Tire-road contact area on asphalt concrete pavement and its relationship with the skid resistance," *Materials*, vol. 13, no. 3, p. 615, 2020.

[6] C. Dong, L. Zhou, and L. Chen, "Study on the stress response of tire pavement based on different driving conditions," *Highway Engineer*, vol. 43, no. 6, pp. 146–150, 2018.

[7] X. Huang, Q. Dai, and K. Ping, "Numeric analysis of friction contact between tread and flexible pavement," *Journal of Highway and Transportation Research and Development*, vol. 25, no. 1, pp. 16–20, 2008.

[8] J. R. Cho, H. W. Lee, J. S. Sohn, G. J. Kim, and J. S. Woo, "Numerical investigation of hydroplaning characteristics of three-dimensional patterned tire," *European Journal of Mechanics - A: Solids*, vol. 25, no. 6, pp. 914–926, 2006.

[9] K. Anupam, T. Tang, C. Kasbergen, A. Scarpas, and S. Erkens, "3-D thermomechanical tire-pavement interaction model for evaluation of pavement skid resistance," *Transportation Research Record: Journal of the Transportation Research Board*, vol. 2675, no. 3, pp. 65–80, 2021.

[10] D. Li, *Simulation Research on Anti-sliding Performance Based on Tire-Surface Contact Characteristics*, South China University of Technology, Guang zhou, China, 2020.

[11] M. Guo, *Research on Mechanical Behavior of Asphalt Pavement Structure under Complex Heavy Loads*, Wuhan University of Technology, Wuhan, China, 2021.

[12] L. Hao, *Finite Element Simulation and Measurement of Tire-Pavement Contact State Based on Pavement Texture*, Chang'an University, Xi'an, China, 2021.

[13] Y. Yao, J. Li, J. Ni, C. Liang, and A. Zhang, "Effects of gravel content and shape on shear behaviour of soil-rock mixture: experiment and DEM modelling," *Computers and Geotechnics*, vol. 141, no. 1, Article ID 104476, 2022.

[14] J. Li, J. Zheng, Y. Yao, J. Zhang, and J. Peng, "Numerical method of flexible pavement considering moisture and stress sensitivity of subgrade soils," *Advances in Civil Engineering*, vol. 2019, Article ID 7091210, 10 pages, 2019.

[15] B. N. J. Persson, O. Albohr, U. Tartaglino, A. I. Volokitin, and E. Tosatti, "On the nature of surface roughness with application to contact mechanics, sealing, rubber friction and adhesion," *Journal of Physics: Condensed Matter*, vol. 17, no. 1, pp. R1–R62, 2005.

[16] K. Matsuda, D. Hashimoto, and K. Nakamura, "Real contact area and friction property of rubber with two-dimensional regular wavy surface," *Tribology International*, vol. 93, pp. 523–529, 2016.

[17] B. Song and S. Yan, "Relationship between the real contact area and contact force in pre-sliding regime," *Chinese Physics B*, vol. 26, no. 7, Article ID 74601, 2017.

[18] S. Wu, H. Chen, J. Zhang, and Z. Zhang, "Effects of interlayer bonding conditions between semi-rigid base layer and asphalt layer on mechanical responses of asphalt pavement structure," *International Journal of Pavement Research and Technology*, vol. 10, no. 3, 2017.

[19] People's Communications Press, *Industry Standard of the People's Republic of China. JTG D50-2017 Design Code for Highway Asphalt Pavement*, People's Communications Press, Beijing, China, 2017.

[20] K. Wang, *Mechanical Analysis and Calculation of Layered Elastic System*, pp. 33–35, Science Press, Beijing, China, 2009.

Hindawi
Advances in Materials Science and Engineering
Volume 2022, Article ID 4901879, 13 pages
https://doi.org/10.1155/2022/4901879

Research Article

High-Temperature Rheology Characteristics of Hard Petroleum Asphalt Used in China

Bo Li,[1] **Binghui Wang**,[1] **Xijun Zhang**,[1] **Xixiong Lin**,[2] **and Yan Zhang**[1]

[1]*Key Laboratory of Road & Bridge and Underground Engineering of Gansu Province, Lanzhou Jiaotong University, Lanzhou 730070, China*
[2]*PetroChina Karamay Petrochemical Co. Ltd., Karamay, Xinjiang 834003, China*

Correspondence should be addressed to Bo Li; libolzjtu@hotmail.com

Received 24 November 2021; Accepted 13 January 2022; Published 15 February 2022

Academic Editor: Carlo Santulli

Hard petroleum asphalt, which is a high modulus asphalt binder material, is used for improving asphalt pavement rutting distress. This property is attributed to the good high-temperature rheological characteristics of hard petroleum asphalt. The study investigates the performance of hard petroleum asphalt and Styrene-Butadiene-Styrene polymer modified asphalt (SBSPMA) based on three aspects: asphalt oil source, asphalt grade, and aging degree. The short-term and long-term aging of four hard petroleum asphalts and SBSPMA of comparative samples were measured using the rolling thin film oven test (RTFOT) and the pressure aging test (PAV). Firstly, the viscosity-temperature curve of hard petroleum asphalt was obtained using the Brookfield viscosity test at different temperatures combined with the improved REFUTAS formula. The complex shear modulus (G^*), phase angle (δ), and rutting factor ($|G^*|/\sin\delta$) of each asphalt sample were then measured by the dynamic shear rheometer test (DSR). Furthermore, the temperature sensitivity of each asphalt sample was calculated using the complex modulus index method (GTS). The compaction and paving temperature ranges of each asphalt were then confirmed. The results showed that the high-temperature rheological characteristics of hard petroleum asphalt were similar to those of SBSPMA. The temperature sensitivity of hard petroleum asphalt was basically the same as that of SBSPMA, while the influence of aging on the G^* of hard petroleum asphalt was greater than that of SBSPMA. In addition, the hard petroleum asphalt construction temperature was lower than that of SBSPMA.

1. Introduction

With the continuous and rapid development of China's economy, the total mileage of existing highways has steadily increased [1]. However, during the maintenance of the pavement, more and more rutting distress has appeared at the entrance of highways and urban road intersections in China [2, 3]. Asphalt pavement rutting is caused by the shear resistance of asphalt pavement decreases in hot weather, and the reason for this condition is the low thickness and low load bearing capacity in the early design of asphalt pavement. As the total traffic volume and proportion of heavy vehicles increases, the pavement produces increasingly more rutting distress [4, 5]. The asphalt surface layer is also prone to rutting caused by the small permanent deformation capacity of the semirigid base [6, 7].

In response to the previously mentioned factors, academics have suggested many possible solutions through continuous research, which has shown that asphalt binder materials can contribute approximately 40% and aggregates can contribute 60% in the rutting resistance performance of the mixture from the perspective of raw materials [8]. High viscosity asphalt and high modulus asphalt can significantly improve the high-temperature performance of asphalt mixtures [9–12]. Also, the asphalt mixture can reduce the rutting distress of asphalt pavements by adding antirutting agents, which have primarily achieved the prevention of asphalt pavement rutting distress by improving the shearing strength of the asphalt mixture [13, 14]. Thirdly, rutting distress can be solved by improving the actual structure of the asphalt pavement [15]. However, these methods require a greater economic investment and higher technical level to

be supported. Therefore, a cheaper material with excellent rutting resistance is sought in order to improve the overall asphalt pavement rutting resistance.

In recent years, studies have shown that the use of hard petroleum asphalt obtained directly through petroleum refining is the least expensive and most effective measure to be taken. This method can improve the rutting resistance and increase the service life of asphalt pavement [16], and it has both relatively low penetration grade and excellent high-temperature performance. Compared with SBS modified asphalt, it also has good application prospects without adding special additives and having to undergo a complicated manufacturing process. Over the past several decades, the utilization of asphalt with high modulus in pavement has become an acceptable practice in many countries. In their research of hard petroleum asphalt mixtures, Brown et al. [17–19] used the linear elasticity theory in order to study fatigue cracking and the permanent deformation of hard petroleum asphalt mixtures by combining the effects of temperature and load. Hafeez et al. [20] compared six mixtures prepared by three kinds of the hard petroleum asphalt with the modified asphalt mixture. The high-temperature permanent deformation and permanent deformation coefficient of hard petroleum asphalt mixture was the same as those of modified asphalt. Garba [21–23] investigated the influence of load, temperature, and mixture type on the permanent transformation of hard petroleum asphalt mixture, and through a triaxial test and a creep recovery test, the prediction model and method for determining the permanent deformation of the hard petroleum asphalt mixture were obtained. Ouyang et al. [24] proposed the improvement of asphalt pavement rutting by enhancing the modulus of the asphalt mixture, and the results showed that the application of hard petroleum asphalt to intermediate layers could maximize the reduction of pavement rutting. Wu et al. [25] tested the dynamic modulus and fatigue parameters of asphalt mixture with high modulus (AC20, Sup20, and EME20) prepared hard petroleum asphalt, based on LPC asphalt mixture design guidelines.

In the area of hard petroleum asphalt research, Dong et al. [26] investigated the effects of SBS/CR on the high-temperature damage temperature and temperature sensitivity of hard-graded asphalt and found that the addition of SBS/CR to hard-graded asphalt could reduce the compaction temperature, enhance the temperature sensitivity, and strengthen the high-temperature fatigue resistance of the mixture. Xin et al. [27] selected SBSPMA, TLA, and NES-1 in order to modify the hard petroleum asphalt and obtained the regression equation between each component and the high-temperature performance of hard petroleum asphalt through a viscosity test and a softening point test. Sha et al. [28, 29] evaluated the high-temperature performance of two kinds of 50# hard petroleum asphalt through a DSR test, and the results showed that the shear and deformation resistance of hard petroleum asphalt mixture were excellent, while the penetration index was difficult to correctly assess for high-temperature performance. In summary, a relatively large number of studies have been carried out regarding the high-temperature properties of hard petroleum asphalt. The high-temperature performance of hard petroleum asphalt and hard petroleum asphalt mixes from various angles and methods has also been studied. However, there has been no comparative analysis of the rheological parameters of hard petroleum asphalt before and after aging, and the temperature sensitivity of hard petroleum asphalt at high temperatures remains unclear.

In this study, frequency sweep and temperature sweep were employed in order to interpret the high-temperature rheology characteristics of hard petroleum asphalt and SBSPMA at different aging levels. The index of GTS was carried out to evaluate the temperature sensitivity of hard petroleum asphalt, and the viscosity-temperature curves were obtained by a Brookfield viscosity test at different temperatures. The purpose of this study was to evaluate the high-temperature performance and to provide the applicable range of hard petroleum asphalt in order to guide the promotion of hard petroleum asphalt application.

2. Materials and Methods

2.1. Test Materials. The source of Kelian (KL) hard petroleum asphalt was Karamay, while the Gaofu (GF) hard petroleum asphalt was from Venezuela, and SBSPMA was provided by Gansu Road and the Bridge Research and Development Center. The asphalt includes Kelian, with a penetration grade of 20/40 and 40/60, and Gaofu, with penetration grades of 20/40 and 40/60, as well as SBSPMA. In order to facilitate the description, the asphalts were named K1, K2, G1, G2, and S1, respectively. The indexes of asphalt samples meet the requirements of standard demands (JTG E20-2011) [30, 31], and the basic performance is shown in Table 1.

2.2. Aging Test. When asphalt pavement is exposed to the air for long periods of time, it is subjected to the coupling effects of oxygen, ultraviolet light, and ozone. This causes the lighter components of the asphalt to volatilize and the adhesion properties of the asphalt to decay, and then the asphalt pavement subsequently produces cracks, looseness, spalling, and other types of distress. Therefore, the aging of asphalt is one of the key factors to determining the durability of asphalt pavement. Asphalt mixture in the mixing, transportation, and paving processes of aging is called short-term aging, while asphalt in the asphalt pavement service process of aging is called long-term aging.

2.2.1. Short-Term Aging. The SHRP plan proposes to use the RTFOT in order to carry out the short-term aging of asphalt. In this study, the temperature of RTFOT was 163°C ± 0.5°C, and the aging time was 85 minutes, according to ASTM D 2872.

2.2.2. Long-Term Aging. A PAV test is widely used to simulate the aging of asphalt in service. In this work, the test temperature was 100 ± 0.5°C, the aging time was 20h, and the test pressure was 2.10 ± 0.10 MPa, according to ASTM D 6521.

Table 1: Properties of asphalt.

Asphalt type	Penetration (25°C)/0.1 mm	Softening point/°C	Flash point/°C	Ductility (15°C)/cm	Density (25°C)/g/cm^3
K1	33.5	56.2	325	7.0	1.020
K2	51.7	52.7	315	21.3	1.035
G1	30.5	58.6	306	3.7	1.034
G2	44.7	52.5	290	28.6	1.081
S1	69.3	65.5	232	116.4	1.139

2.3. Brookfield Viscosity. The viscosity of asphalt can reflect the rheological properties and shear resistance of asphalt at the corresponding temperature. The greater the viscosity, the greater the shear resistance, and shear failure at high temperature will also be less likely. In order to facilitate mixing and construction, asphalt viscosity should not be too great. In our work, the Brookfield viscosity of each asphalt was determined using the NDJ-1C Brookfield viscometer with an operating temperature range of 0°C~300°C, according to ASTM D 4402. The rotor type was selected as no. 27, and 12.5 g of asphalt was taken for each test. The test temperature ranged from 60°C to 165°C, with 15°C as a temperature interval. The torque range in the test was 10%~98%, and the rotational speed was adjusted according to the test temperature and torque.

2.4. DSR Test. In the late 1980s, the SHRP project introduced the Dynamic Shear Rheometer (DSR) from the material field into civil engineering, thus solving the formlessness issue during asphalt fatigue experiments. Until now, the primary study on asphalt fatigue properties was implemented by the DSR parallel plate. In this study, the HR-1 Dynamic Shear Rheometer (DSR) produced by the TA Company of the United States was used for the temperature and frequency scanning of each asphalt (ASTM D7175). The spacing between the two parallel plates was adjusted to 1 mm, and the trimming gap was 50 μm. The temperature scanning test temperature ranged from 52°C to 76°C, with 6°C as a temperature interval, and the loading angular frequency was 10 rad/s. The frequency scanning test temperature ranged from 58°C to 70°C, with 6°C as a temperature interval, and the loading strain was 5%, while the frequency range was 0.1~100 rad/s.

The G^* and δ are the most important evaluation indexes in temperature scanning and frequency scanning, and the other rheological parameters can be calculated by the following two indexes. Equations (1)~(3) show the relationship between the viscoelastic parameters and G^* and δ.

$$G^* = G' + iG'', \tag{1}$$

$$G' = \left|G^*\right| * \cos\delta, \tag{2}$$

$$G'' = \left|G^*\right| * \sin\delta. \tag{3}$$

3. Results and Discussion

3.1. Viscosity-Temperature Performance. The viscosity of asphalt as a viscoelastic material is closely related to temperature. However, the demand for viscosity of asphalt pavement during construction and service is contradictory. Asphalt mixtures need low viscosity during construction, which allows the mixture to keep flowing and makes it easy to construct. However, in the summer high-temperature season, the temperature of asphalt pavement can reach more than 50°C. Under these conditions, the asphalt mixture needs to maintain a high viscosity in order to reduce high-temperature distress. The viscosity temperature curve can effectively mirror the trend of asphalt viscosity with temperature change, and therefore it was very important to establish a reasonable viscosity-temperature relationship for the construction and normal use of hard petroleum asphalt. The viscosity of each asphalt was measured with a Brookfield rotational viscometer, as shown in Table 2. Based on this, the temperature-viscosity curve and equation were obtained.

Table 2 compares the Brookfield viscosity at eight different temperatures. The viscosity decreased with the increase of temperature, and with the same oil source, it was determined that the higher the asphalt grade, the lower the viscosity. With a different oil source, GF viscosity was greater than KL. However, at the test temperature of 135°C, the viscosity of K2 was greater than G2, a result that may have been caused by human error. Compared with SBSPMA, the hard petroleum asphalt viscosity was lower. In order to reflect the content of the table more intuitively, it was necessary to use the viscosity-temperature relationship equation to further process the data in the diagram and to complete it through the REFUTAS curve.

The REFUTAS curve has been widely used in the area of petroleum asphalt and can be linear in a wide temperature range. The REFUTAS curve equation describes the relationship between viscosity and temperature, as shown in

$$\log\ \log(\eta + 0.8) = m \log K, \tag{4}$$

where η is viscosity, m is a constant, and K is the absolute temperature.

After the constant 0.8 is omitted, the above equation is standardized, and the viscosity-temperature curve expression shown in equation (5) can thus be obtained.

$$\log\ \log\left(\eta \times 10^3\right) = n - m \log(T + 273.13), \tag{5}$$

where η is viscosity, T is Celsius temperature, and m and n are regression coefficients.

As shown in Figure 1, the overall viscosity of hard petroleum asphalt is less than that of S1. The viscosity of S1 had obvious differences from other types of asphalt. Under the same grade, the viscosity of GF was greater than KL, indicating that the road performance of KL was better than that of GF. The higher the asphalt grade, the lower the viscosity at the same oil source.

Table 2: Viscosity of asphalt with different temperature.

Temperature/°C	60	75	90	105	120	135	150	165
K1/Pa s	1085.00	120.00	22.41	6.21	2.02	0.82	0.37	0.21
K2/Pa s	785.00	99.14	21.45	5.64	1.84	0.80	0.32	0.18
G1/Pa s	1095.00	124.21	24.25	6.54	2.24	0.84	0.40	0.23
G2/Pa s	920.00	116.25	21.84	6.01	1.96	0.65	0.35	0.20
S1/Pa s	2960.00	299.50	46.50	12.10	3.80	1.85	0.57	0.31

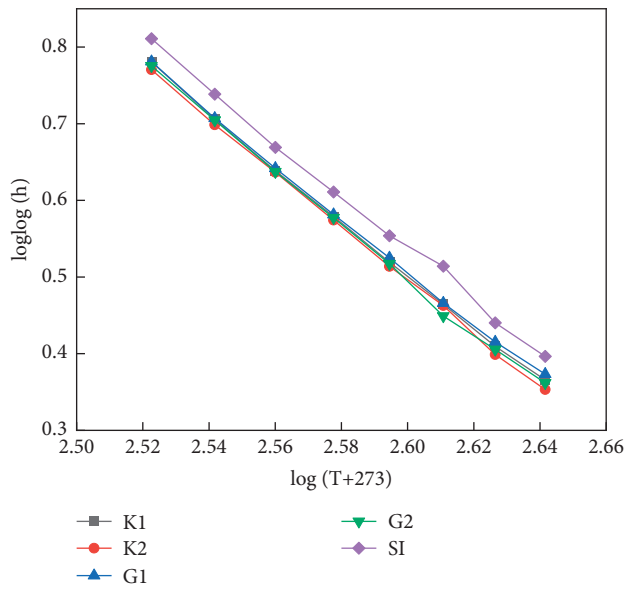

Figure 1: Viscosity-temperature curve.

Table 3 demonstrates the regression results and regression coefficients of the viscosity-temperature curves of each type of asphalt. The regression coefficients of different asphalts were greater than 0.997, indicating that the improved REFUTAS formula was reliable in terms of characterizing the viscosity-temperature relationship of hard petroleum asphalt. The variation trend of the viscosity of each hard petroleum asphalt with temperature was basically the same as S1.

The viscosity-temperature curve allows us to obtain the mixing and compaction temperatures of the hard petroleum asphalt mix. The viscosity levels of $(0.17 \pm 0.02$ Pa-s) and $(0.28 \pm 0.03$ Pa-s) were used as the mixing temperature range and compaction temperature range, respectively, in the viscosity-temperature curve [32–34]. According to the fitting parameters in Table 4, the mixing and compaction temperature ranges of asphalt could be calculated.

Table 4 reports that the construction temperature of asphalt is K2 < G2 < K1 < G1 < S1 and that the construction temperature of hard petroleum asphalt is slightly lower than that of S1. With the same oil source of hard petroleum asphalt, the higher the grade of asphalt, the lower the construction temperature, and for different oil sources of hard petroleum asphalt, KL construction temperature was lower than GF. Also, compared with S1, hard petroleum asphalt was reduced by approximately 10 °C during construction, thus reducing energy consumption and facilitating construction.

Table 3: Viscosity-temperature curve regression results.

Regression coefficient	K1	K2	G1	G2	S1
m	3.488	3.509	3.439	3.521	3.450
n	9.571	9.620	9.450	9.655	9.506
R^2	0.999	0.999	0.999	0.998	0.997

3.2. Temperature Dependence. The temperature dependence of each type of asphalt was studied by using the temperature scanning mode of DSR. The δ and G^* at the same frequency were tested at different temperatures in order to study the effect of temperature and aging degree on the dynamic viscoelastic parameters of hard petroleum asphalt. $|G^*|/\sin\delta$ was calculated by the previously mentioned two parameters in order to characterize the high-temperature resistance to the permanent deformation of asphalt.

3.2.1. Complex Shear Modulus. The G^* represents the resistance of asphalt under dynamic shear deformation and also reflects the deformation resistance of the material. The smaller the G^* value, the worse the ability to resist the deformation of asphalt. Figure 2 shows the G^* changes with the temperatures of five asphalts under different aging conditions.

All of the asphalts in Figure 2 experience similar changes at different test temperatures, and they are different from each other in values. The G^* of K2, G2, and S1 decreased first and then tended to be stable with increased temperature. The ability to resist the deformation of GF and KL reaches the level of S1. Due to the influence of the oil source, G^* of the hard petroleum asphalt with the same grade varies greatly, and the result of the comparison was K2 > G2, but G1 > K1. And with different asphalt from the same oil source, the smaller the grade, the greater the G^* of asphalt. The G^* of hard petroleum asphalt was greater than that of other asphalt, and the total resistance was the highest under repeated shear deformation.

The G^* decreased continuously with increasing temperature, whether the asphalt was described before or after the aging process. This indicated that the rutting resistance of asphalt deteriorated with increasing temperature. At the same test temperature, the G^* increased just as the degree of aging increased, indicating that aging causes the asphalt to change from soft to hard. The reason for this was the volatilization of light components and the generation of strong polar substances during the aging process. The change of G^* of G1 before and after aging was the greatest, and taking the initial temperature of 52 °C as an example, the G^* of asphalt increased by approximately 140% after RTFOT aging and 340% after PAV aging. At the same time, the slope of the G^*

Table 4: Construction temperature.

Temperature/°C	K1	K2	G1	G2	S1
Mixing temperature	165~171	163~169	167~173	164~170	175~181
Compaction temperature	154~158	152~157	156~161	153~158	164~169

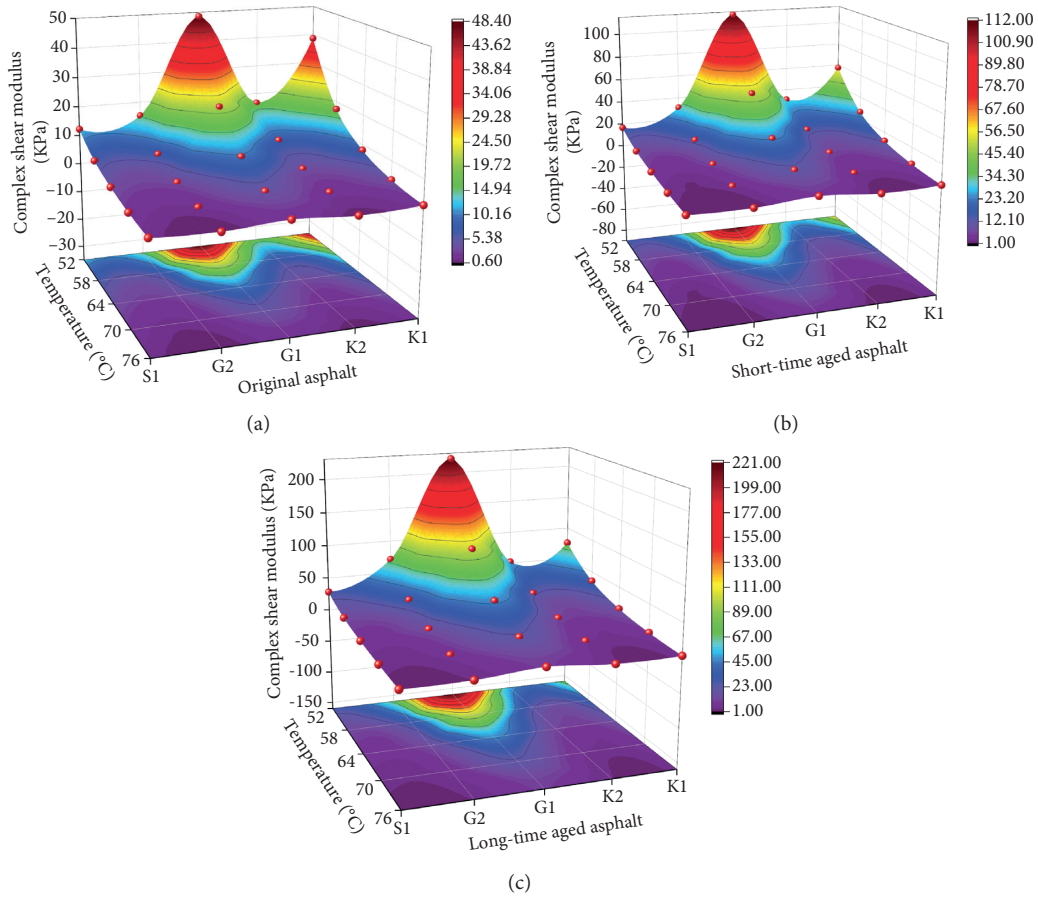

Figure 2: G^* at different aging states. (a) Original asphalt. (b) Short-time aged asphalt. (c) Long-time aged asphalt.

curve gradually increased with increased aging, and the temperature sensitivity of hard petroleum asphalt increased, where G1 had the greatest temperature sensitivity. Moreover, by comparing the maximum and minimum values of G^* before and after aging, it was found that long-term aging had the greatest impact on the G^* of hard petroleum asphalt.

3.2.2. Phase Angle. In dynamic rheological mechanics, the δ characterizes the ratio of viscosity to elasticity in materials. For a complete elastic material with no phase lag of stress and strain, $\delta = 0^\circ$. Correspondingly, for a complete viscous material with a constant phase lag of stress and strain response, $\delta = 90^\circ$. Thus, the phase lag of stress and strain response for viscoelastic material was between 0° and 90°[34]. The δ of KL, GF, and SBSPMA with different aging degrees are shown in Figure 3.

Figure 3 shows that the δ of asphalt in different states are greater than 45°C, thus indicating that each asphalt showed a viscous state in the test temperature range. δ of the five asphalts before and after aging gradually increased as the temperature increased, which indicates that the viscous components of asphalt increased and the elastic components decreased with the increase of temperature. For hard petroleum asphalt with different oil sources, the viscosity of G1 was smaller than that of K1, while the viscosity of G2 was larger than that of K2. This indicates that asphalt from different oil sources exhibited different changes in viscoelastic properties with changes in the hard petroleum asphalt grade. And for asphalt from the same oil source, the greater the grade, the higher the viscosity ratio. The δ of KL and GF under different aging conditions was greater than that of S1 due to the fact that the viscoelastic properties of S1 were stable under different test temperatures. Additionally, the δ of each hard petroleum asphalt decreased the test temperature as aging increased. This indicates that aging increases the elasticity of the hard petroleum asphalt, decreases the viscosity, increases the stability of the colloidal structure, decreases the temperature sensitive properties, and strengthens the deformation resistance.

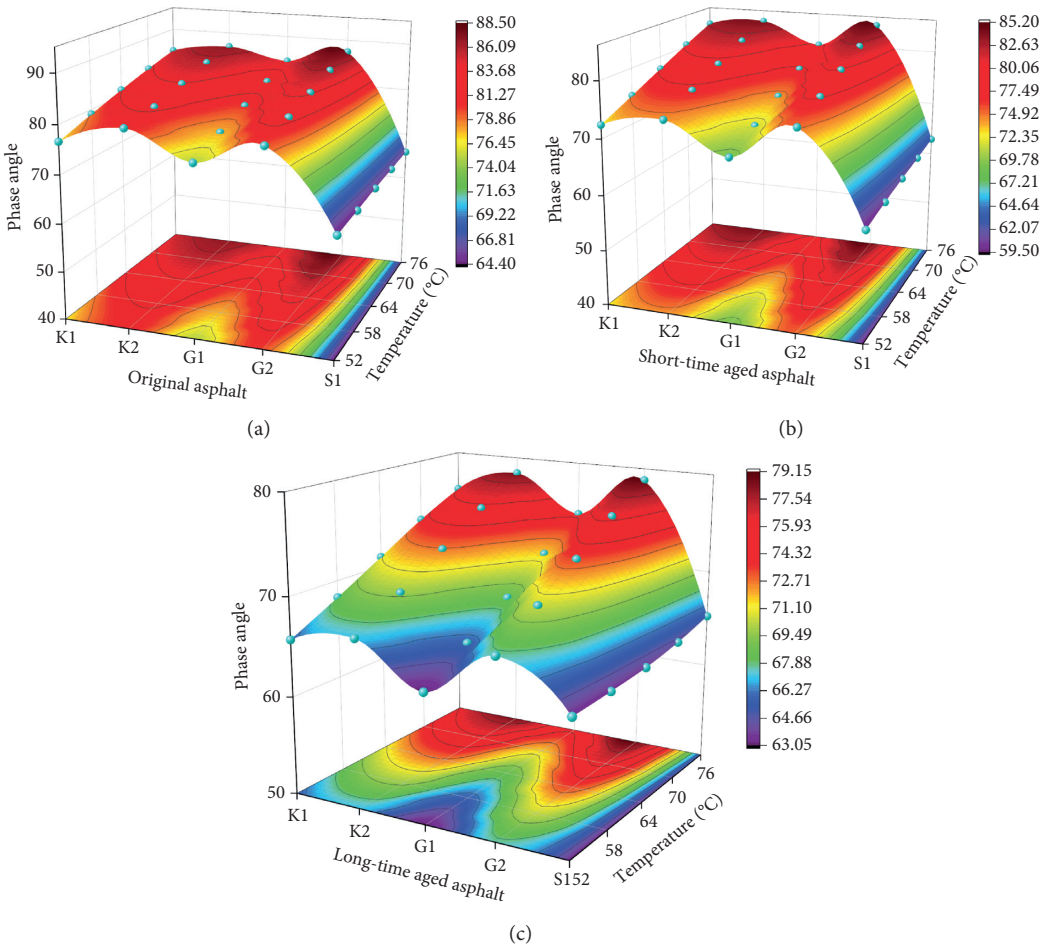

Figure 3: Phase angle at different aging states. (a) Original asphalt. (b) Short-time aged asphalt. (c) Long-time aged asphalt.

3.2.3. Rutting Factor. $|G^*|/\sin\delta$ can be obtained by G^* and δ. $|G^*|/\sin\delta$ reflects the high-temperature deformation resistance of asphalt. The higher its value, the stronger deformation resistance. The $|G^*|/\sin\delta$ of five asphalts under different aging degrees are listed in Figure 4.

Figure 4 lists $|G^*|/\sin\delta$ of five kinds of asphalt before and after aging decrease with the increase of temperature, indicating that the increase of temperature caused the rutting resistance of each asphalt to decrease. Compared with the hard petroleum asphalt from different oil sources, the rutting factor of K1 was smaller than that of G1 in each state, while the rutting factor of G2 at each temperature was gradually greater than that of K2 with the deepening of aging, indicating that GF has a strong antiaging ability. The rutting factor of G1 decreased most obviously as the temperature increased, indicating that the rutting stability of G1 was poorer than that of other asphalts. With the increase of aging degree, the change trend of the rutting factor of K1 was gradually flat, and its high-temperature performance was stable. The decreasing trend of the rutting factor of K2 and G2 was basically the same as that of S1.

Combined with the information from Table 1, it could be concluded that the rutting factor was negatively correlated with the penetration by comparing the rutting factor and the penetration of asphalt in various states. Due to the low penetration of G1, it was shown to have greater advantages in terms of its antirutting ability. As aging made the components of asphalt more stable, $|G^*|/\sin\delta$ of each asphalt was relatively close. This fully reflects the relationship between the deformation resistance of asphalt and temperature. Under different temperatures and different aging degrees, hard petroleum asphalt had a higher rutting resistance than S1, and this also proved that hard petroleum asphalt had better deformation resistance than S1.

3.2.4. Temperature Sensitivity. Because asphalt is a viscous temperature characteristic material, its sensitivity to temperature is particularly important to note. The temperature sensitivity of asphalt can be realized by the complex modulus index (GTS) method. The greater the GTS value, the higher the temperature sensitivity of asphalt [35]. The calculation formula of GTS is shown in

$$\lg\lg G^* = \mathrm{GTS} \times \lg T + c. \tag{6}$$

The temperature sensitivity of asphalt with different aging degrees was measured in the temperature range of 52~76°C. Figure 5 shows the double logarithmic curve of G^*

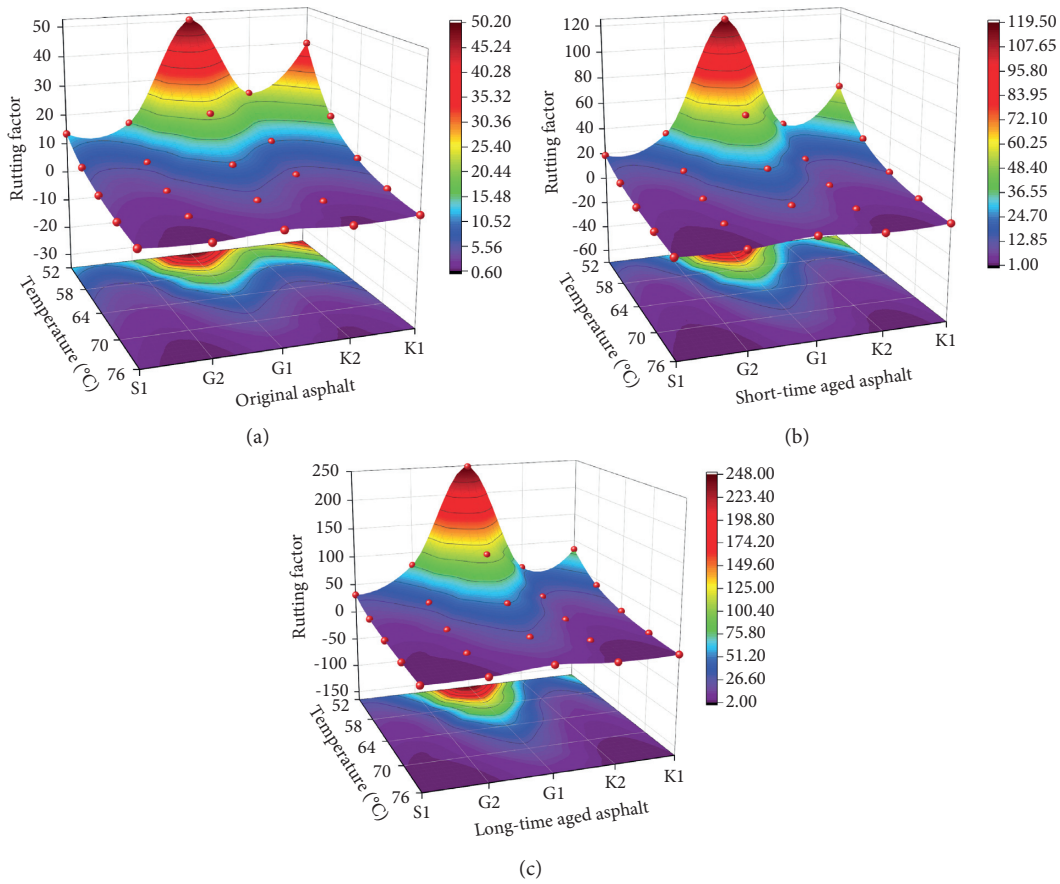

Figure 4: Rutting factor at different aging states. (a) Original asphalt. (b) Short-time aged asphalt. (c) Long-time aged asphalt.

of each asphalt changing with temperature. Table 5 shows the GTS value of each asphalt and the corresponding regression formula.

Table 5 lists the GTS values and regression coefficients of different aged asphalts. The regression coefficients of different asphalts were greater than 0.985, indicating that the G^* data of hard petroleum asphalt tested by the DSR test were relatively stable. The GTS method was reliable in terms of characterizing the temperature sensitivity of hard petroleum asphalt. Compared with asphalt samples of different aging states, the GTS value of hard petroleum asphalt decreased gradually with the deepening of aging. In addition, the GTS value of asphalt from the same oil source increased as the grade increased. There was no obvious pattern of GTS variation for asphalts of different oil sources due to the influence of the oil source. Comparing the hard asphalt with different oil sources, the GTS value of K2 was less than that of G2 in all states. While the GTS value of K1 was greater than that of G1 before aging, the GTS value of K1 was less than that of G1 after aging, which indicated that the overall temperature sensitivity of KL hard asphalt was lower than that of GF hard asphalt. Due to the role of the modifier GTS value, S1 was small, and with the increase of aging degree, there was no obvious rule. The GTS values of GF and KL were greater than those of S1 under different aging conditions, indicating a higher temperature sensitivity.

In terms of an analysis of its causes, the presence of wax made the asphalt reduce at high-temperature viscosity. Low temperature due to the formation of wax crystalline skeleton asphalt rheology characteristics became poor. Thus, it has been shown that the presence of wax would improve the temperature sensitivity of asphalt at high temperatures. In addition, for different varieties of asphalt, the molecular weight also affects its temperature sensitivity. If the intermolecular force is strong, and the relative displacement of molecular chain segments or the possibility of molecular movement is small, then the asphalt temperature sensitivity is also small [36]. In general, the deepening of aging can improve the temperature sensitivity of hard petroleum asphalt in high-temperature regions.

3.3. Time Dependence. G^* and δ values were obtained through the use of frequency scan DSR tests. Furthermore, the time dependence of each asphalt at different temperatures and frequencies was also investigated. The influence of aging on the time dependence of hard petroleum asphalt was determined by comparing asphalt samples with different degrees of aging.

3.3.1. Complex Shear Modulus. The curves of G^* of asphalt with different aging degrees at different temperatures with the change of loading frequency are shown in Figure 6.

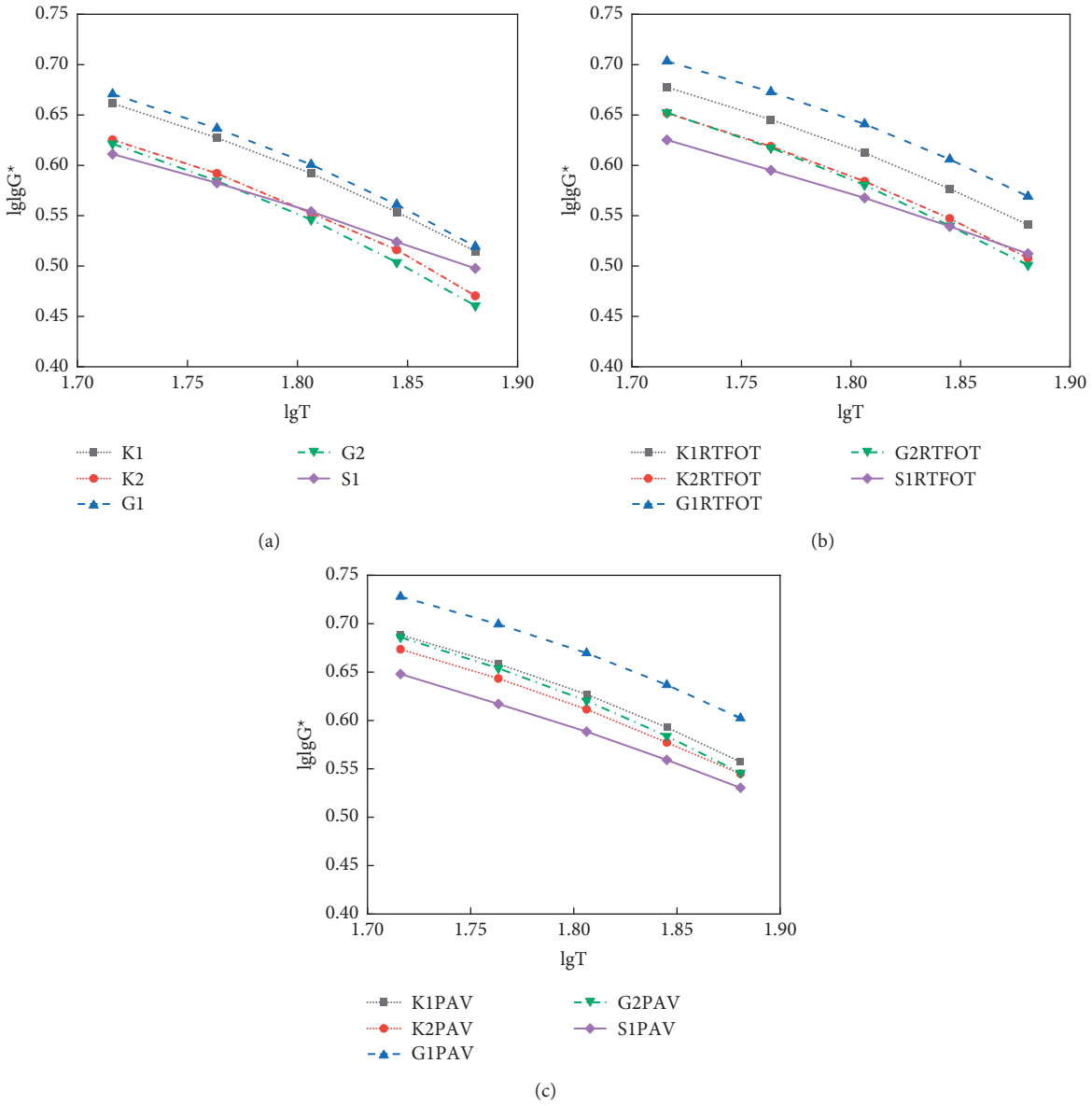

Figure 5: The relationship between the double logarithm of G^* and temperature. (a) Original asphalt. (b) Short-time aged asphalt. (c) Long-time aged asphalt.

It is apparent from Figure 6 that with the increase of scanning frequency, G^* of each asphalt increases gradually, and the total resistance generated by repeated shear deformation increases. The higher the temperature, the lower the G^* of the sample, and the smaller the total resistance produced by repeated shear deformation. At the same temperature, with the increase of aging degree, G^* of each asphalt sample decreased. In addition, due to the influence of the oil source, the influence of aging on low-temperature high-frequency and high-temperature low-frequency of GF was greater than that of KL. The G^* of S1 was less than that of KL and GF. As the angular frequency increased, the smaller the asphalt grade of the same oil source became and the greater the G^*. At the same time, with the gradual increase of scanning frequency, the difference of G^* under different temperature conditions gradually increased. This indicated that the total resistance to repeated shear deformation of hard graded asphalt varied more with increasing loading frequency under different ambient temperature conditions. We compared the variation pattern of G^* of each asphalt under the most unfavorable conditions of load action (i.e., angular frequency of 100 rad/s). Comparing hard petroleum asphalt with different oil sources, it was found that G^* of KL hard asphalt was less than that of GF hard asphalt at the same temperature and aging state. When the oil source was the same, there was no obvious pattern in the variation of G^* of each asphalt with the grade.

Under the same temperature conditions, G^* of asphalt increased with the increase in load frequency, indicating that the viscoelastic properties of asphalt tended towards elastic behavior at higher load frequencies. The asphalt

Table 5: Asphalt GTS value and regression equation.

Asphalt type	GTS	Regression formula	R^2
K1	0.889	$y = -0.889x + 2.192$	0.990
K2	0.932	$y = -0.932x + 2.232$	0.985
G1	0.915	$y = -0.915x + 2.246$	0.987
G2	0.973	$y = -0.973x + 2.298$	0.989
S1	0.693	$y = -0.693x + 1.803$	0.997
K1RTFOT	0.827	$y = -0.827x + 2.102$	0.991
K2RTFOT	0.871	$y = -0.871x + 2.151$	0.989
G1RTFOT	0.811	$y = -0.811x + 2.100$	0.988
G2RTFOT	0.920	$y = -0.920x + 2.237$	0.991
S1RTFOT	0.683	$y = -0.683x + 1.799$	0.998
K1PAV	0.794	$y = -0.794x + 2.056$	0.989
K2PAV	0.783	$y = -0.783x + 2.022$	0.992
G1PAV	0.759	$y = -0.759x + 2.035$	0.988
G2PAV	0.847	$y = -0.847x + 2.145$	0.989
S1PAV	0.711	$y = -0.711x + 1.840$	0.997

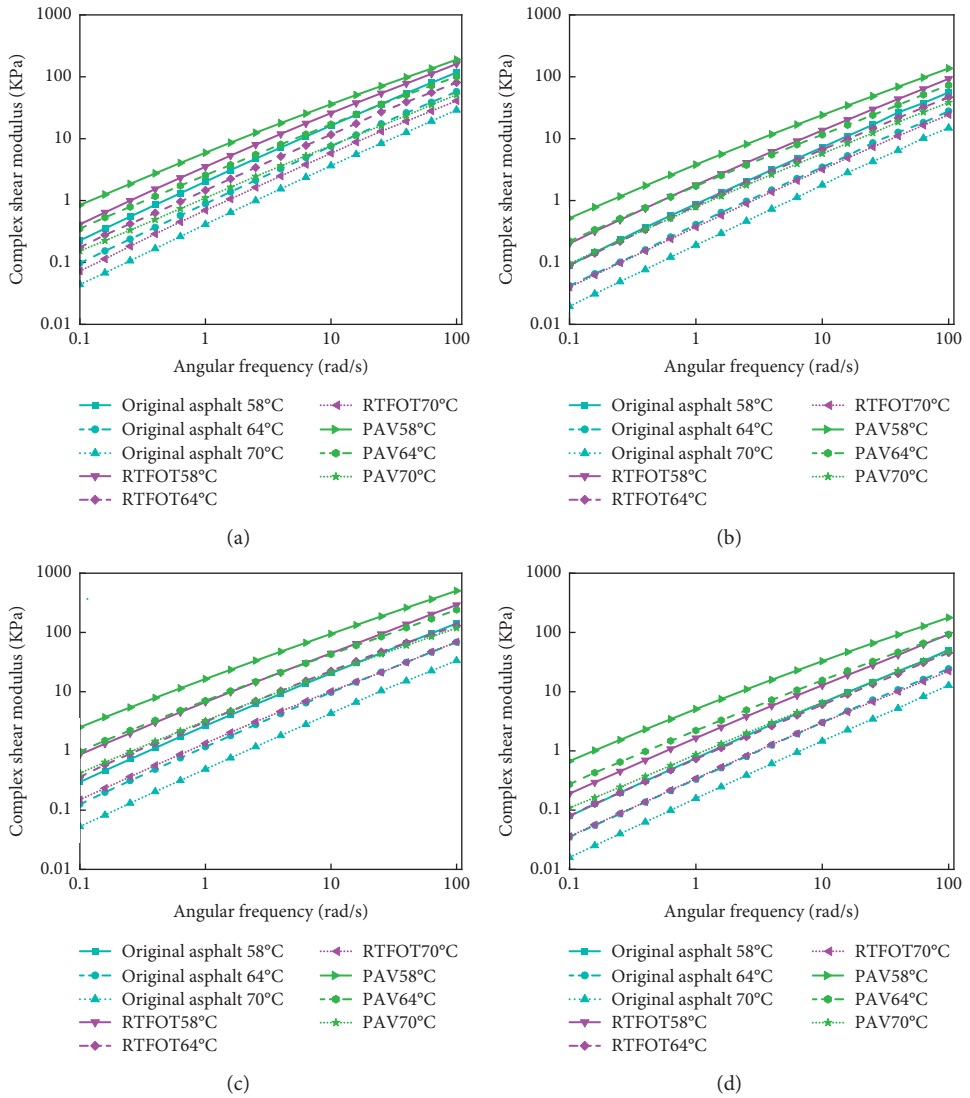

Figure 6: Continued.

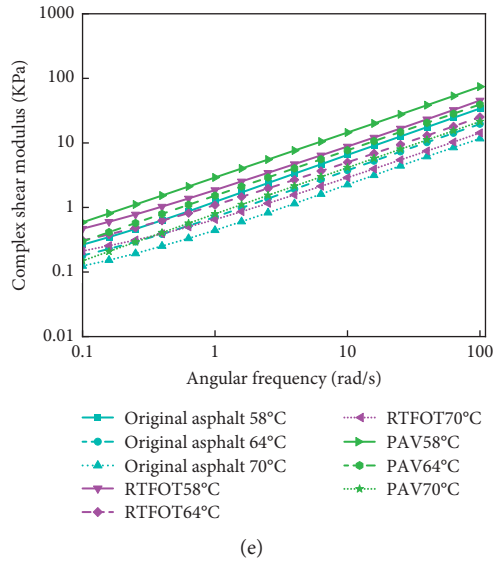

(e)

Figure 6: Frequency sweep G^* curve of each asphalt. (a) K1. (b) K2. (c) G1. (d) G2. (e) S1.

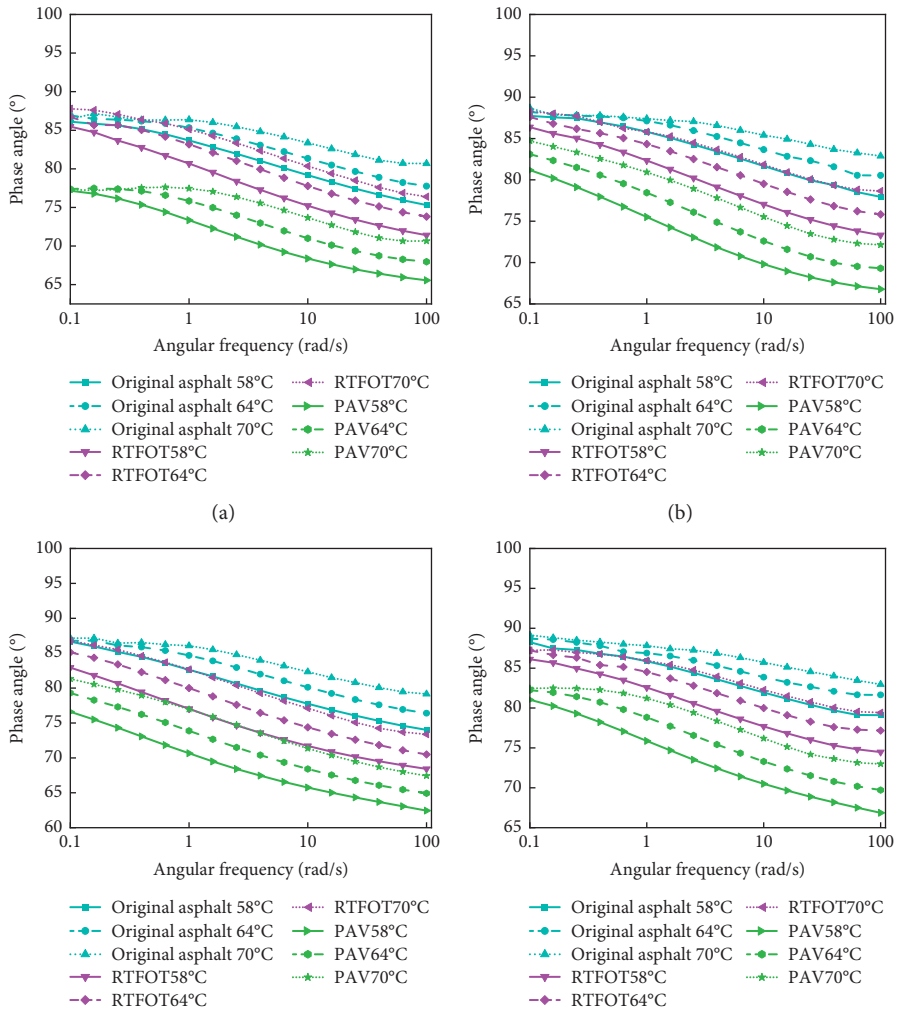

(a) (b) (c) (d)

Figure 7: Continued.

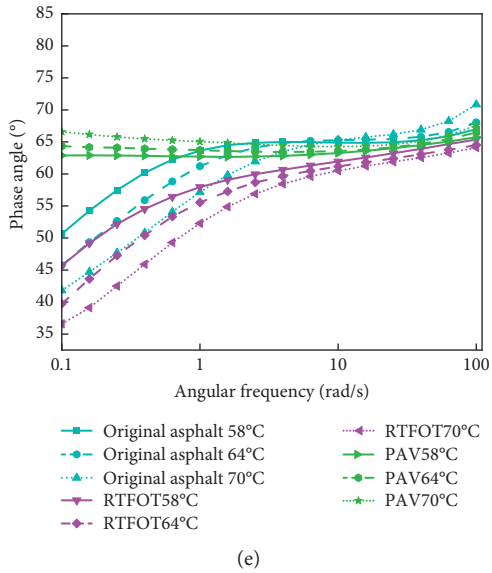

(e)

Figure 7: Frequency sweep phase angle of each asphalt. (a) K1. (b) K2. (c) G1. (d) G2. (e) S1.

material had a better recovery from deformation and could better resist deformation at high temperatures. Comparing KL, GF, and S1 under the same temperature conditions, G^* of KL and GF were greater than that of S1, which meant that the elastic properties of hard petroleum asphalt under the same conditions were better than S1 elastic properties. Thus, hard petroleum asphalt had better deformation recovery ability, and it had stronger resistance to rutting deformation as well.

3.3.2. Phase Angle. Figure 7 presents the δ of asphalt with different aging degree changes with the load frequency at different temperatures.

Figure 7 demonstrates that with the increase of temperature and the decrease of frequency, δ of hard petroleum asphalt increased. Under the same test temperature and scanning frequency, δ of hard petroleum asphalt was decreased as the aging degree increases. δ of hard petroleum asphalt under each aging state had no change with the attenuation trend of scanning frequency. Following an analysis of asphalt from different oil sources, δ of G1 was found to be less than that of other hard petroleum asphalt at the same frequency and temperature, indicating that there were more elastic components in G1. For asphalt from the same oil source, δ increased with the increase of hard petroleum asphalt label. δ of S1 increased as the scanning frequency increased, and δ of S1 increased as the temperature increased in the original sample and PAV aging state, but the overall change was small. This indicated that the elastic component of S1 was relatively stable. In general, when the frequency was in the range of 0.1–100 rad/s, δ of hard petroleum asphalt and S1 presented different rules with regards to frequency. At a lower frequency, the elastic component of S1 was better than that of hard petroleum asphalt, but at a higher frequency, the elastic component of hard petroleum asphalt was equivalent to S1.

4. Conclusion

The high-temperature viscoelastic properties of hard petroleum asphalt and S1 in their original state, as well as in different aging states, were investigated by Brookfield viscosity tests, temperature scan tests, and frequency scan tests. The main conclusions were as follows:

(1) The improved REFUTAS equation can better characterize the hard petroleum asphalt viscosity-temperature relationship with a correlation coefficient greater than 0.997. KL also exhibits better workability compared to S1 and can reduce the construction temperature by approximately 10°C.

(2) Compared to S1, hard petroleum asphalt had a higher G^*. At the same time, aging has a greater impact on G^* of GF at low-temperature high-frequency and high-temperature low-frequency conditions.

(3) The hard petroleum asphalt has higher rutting resistance compared to S1 at different temperatures and aging conditions. Among the four hard petroleum asphalts, the antirutting ability of G1 decreases most with temperature, but still has good antirutting ability.

(4) The correlation coefficients of each asphalt's G^* and temperature change curve obtained by the GTS method were greater than 0.985. This can better describe the sensitivity of hard petroleum asphalt to temperature. Also, the temperature sensitivity of hard petroleum asphalt decreased with increased aging.

Data Availability

The data used to support the findings of this study are included within the article.

Conflicts of Interest

All authors confirm that there are no conflicts of interest in this research article.

Acknowledgments

The authors gratefully acknowledge the financial supports by the National Natural Science Foundation of China (51408287, 51668038, and 51868042), the Distinguished Young Scholars Fund of Gansu Province (1606RJDA318), the Natural Science Foundation of Gansu Province (1506RJZA064 and 20JR10RA227), Industry Support and Guidance Project by University and College in Gansu Province (2020C-13), and Foundation of A Hundred Youth Talents Training Program of Lanzhou Jiaotong University and Research Institute of PetroChina Fuel Oil Co.

References

[1] X. Wang, *Research on Preventive Maintenance Decision of Expressway Asphalt Pavement*, Dalian University of Technology, Dalian, China, 2020.

[2] Q. Cao, *Rutting Analysis of Influencing Factors of Asphalt Pavement based on Temperature Field*, Shijiazhuang Tiedao University, Shijiazhuang, China, 2020.

[3] Y. Yi, *Research and Application of High Temperature Stability of Asphalt Mixture under High Temperature and Heavy Load*, Southeast University, Nanjing, China, 2019.

[4] L. Jia, *Rutting Predication of Asphalt Pavement Based on Total-Thickness Rutting Test*, Huazhong University of Science and Technology, Wuhan, China, 2015.

[5] A. K. KumarSingh and J. P. Sahoo, "Rutting prediction models for flexible pavement structures: a review of historical and recent developments," *Journal of Traffic and Transportation Engineering*, vol. 8, no. 3, pp. 315–338, 2021.

[6] B. Yi, *Evaluation Method of High Temperature Stability of Asphalt Mixture*, Suzhou University of Science and Technology, Suzhou, China, 2019.

[7] Q. Song, *Study on the Hard Paving Grade Asphalt Binder and Mixtures*, Chang'an University, Xi'an, China, 2015.

[8] E. Behzadfar and S. G. Hatzikiriakos, "Viscoelastic properties and constitutive modelling of bitumen," *Fuel*, vol. 108, pp. 391–399, 2013.

[9] M. Espersson, "Effect in the high modulus asphalt concrete with the temperature," *Construction and Building Materials*, vol. 71, pp. 638–643, 2014.

[10] H. Geng, C. S. Clopotel, and H. U. Bahia, "Effects of high modulus asphalt binders on performance of typical asphalt pavement structures," *Construction and Building Materials*, vol. 44, pp. 207–213, 2013.

[11] Q. He, "research on damage characteristics and preventive maintenance measures of expressway asphalt pavement," *Construction & Design for Engineering*, vol. 19, pp. 94–96, 2019.

[12] Y. Chen, C. Ji, and H. Wang, "Evaluation of crumb rubber modification and short-term aging on the rutting performance of bioasphalt," *Construction and Building Materials*, vol. 193, pp. 467–473, 2018.

[13] R. Zhang and Y. Huang, "Review on influence of rigid asphalt and asphalt temperature index," *International Journal of Civil Engineering and Machinery Manufacture*, vol. 5, no. 1, pp. 115–123, 2020.

[14] Z. Dong, G. Xiao, and X. Gong, "Analysis on impact of gradation and anti-rutting additive on rutting resistance of asphalt mixture," *Journal of Highway and Transportation Research and Development*, vol. 31, no. 2, pp. 27–31, 2014.

[15] X. Zou, A. Sha, and W. Jiang, "Modification mechanism of high modulus asphalt binders and mixtures performance evaluation," *Construction and Building Materials*, vol. 90, pp. 53–58, 2015.

[16] C. Han, *Application Research on Durable High Modulus Asphalt Mixture Design Using Hard Paving Bitumen*, Southeast University, Nanjing, China, 2018.

[17] S. F. Brown, J. M. Brunton, and A. F. Stock, "The analytical design of bituminous pavements," *Proceedings - Institution of Civil Engineers*, vol. 79, no. No. 1, pp. 1–31, 1985.

[18] M. E. Nunn, A. Brown, and D. Weston, *Design of Long-Life Flexible Pavements for Heavy Traffic*, Transport Research Laboratory, Berkshire, USA, 1997.

[19] D. E. Newcomb, M. Buncher, and I. J. Huddleston, *Concepts of Perpetual Pavements*, TRB, National Research Council, Washington (DC), 2001.

[20] I. Hafeez, M. A. Kamal, and W. Mirza, "Domains of permanent deformation coefficient alpha and mu for hard grade asphalt concrete mixtures," *Proceedings of Pakistan Academic Science*, vol. 47, pp. 65–74, 2010.

[21] B. Garba, *Permanent Deformation Properties of Asphalt concrete Mixtures*, Norwegian University of Science and Technology, Oslo, Norway, 2002.

[22] M. P. Mwangi, *Permanent Deformation of Asphalt Mixtures," Section of Road and Railway Engineering*, pp. 35–56, Faculty of Civil Engineering and Geosciences, Delft University of Technology, Netherlands, 2007.

[23] H. Zhu and J. Yang, "Comparative analysis of rutting resistance of hard-grade Asphalt," *Journal of China & Foreign Highway*, vol. 6, pp. 214–216, 2006.

[24] W. Ouyang, G. Yu, and F. Zhu, "Research on anti-rutting performance of high modulus asphalt concrete pavement," *Advanced Materials Research*, vol. 1067, pp. 4474–4477, 2010.

[25] C. Wu, B. Jing, and X. Li, "Performance evaluation of highmodulus asphalt mixture," *Advanced Materials Research*, vol. 311–313, pp. 2138–2141, 2011.

[26] F. Dong, X. Yu, and S. Liu, "Rheological behaviors and microstructure of SBS/CR composite modified hard grade asphalt," *Construction and Building Materials*, vol. 115, pp. 285–293, 2016.

[27] C. Xin, Q. Lu, and C. Ai, "Optimization of hard modified asphalt formula for gussasphalt based on uniform experimental design," *Construction and Building Materials*, vol. 136, pp. 556–564, 2017.

[28] A. Sha, J. Cao, and Q. Zhou, "High temperature performance of domestic hard grade asphalt and asphalt mix," *Journal of Wuhan University of Technology*, vol. 31, no. 1, pp. 41–44, 2009.

[29] W. Wang, D. Ma, and C. Fan, "Rheological property and comparison of high-temperature performance of hard-grade Asphalt before and after aging," *Journal of Chongqing Jianzhu University*, vol. 36, no. 6, pp. 48–52, 2017.

[30] JTG E20-2011, *Standard Test Methods of Bitumen and Bituminous Mixtures for Highway Engineering*, China Communications Press, Beijing, China, 2011.

[31] X. Jia, *Study on Performance of Rubber Powder/sbs Composite Modified Asphalt and Mixture*, Lanzhou Jiaotong University, Lanzhou, China, 2020.

[32] Z. Liu, Q. Sha, and Z. Li, "Experimental investigation on property of hard grade asphalt A-30 and asphalt mixture," *Petroleum Asphalt*, vol. 22, no. 2, pp. 7–13, 2008.
[33] Z. Hu, *Research on Technical Index of Grade Hard Grade Asphalt and Pavement Performance of its Mixture*, South China University of Technology, Changsha, China, 2011.
[34] Y. Dong and Y. Tan, "Research on high temperature performance of hard grade Asphalt based on repeated shear creep test," *Highways*, vol. 60, no. 2, pp. 160–164, 2015.
[35] Z. Zhang, B. Li, and X. Ren, "research on thermal aging properties of microwave crumb rubber modified asphalt," *Journal of Materials Science and Engineering*, vol. 37, no. 6, pp. 1001–1007, 2019.
[36] L. Wang, J. Hu, G. Chen, Y.-J. Jia, and Y. Wang, "Temperature susceptibility of different kings of modified asphalt," *Journal of Functional Materials*, vol. 46, no. 4, pp. 4086–4090, 2015.

Hindawi
Advances in Materials Science and Engineering
Volume 2021, Article ID 1532994, 10 pages
https://doi.org/10.1155/2021/1532994

Research Article

Evaluation of Susceptibility of Asphalt Binders to Rutting through MSCR Test

Rong Chang,[1,2] **Aimin Sha**,[1] **Pinxue Zhao**,[1] **Songchang Huang**,[2] **and Cong Qi**[3]

[1]*Key Laboratory for Special Area Highway Engineering of Ministry of Education, Chang'an University, Xi'an 710064, China*
[2]*Resrarch Institute of Highway Ministry of Transport, Beijing 100088, China*
[3]*Shandong Chambroad Petrochemicals Co. Ltd., Binzhou, Shandong 256500, China*

Correspondence should be addressed to Aimin Sha; ams@chd.edu.cn

Received 17 November 2021; Accepted 13 December 2021; Published 30 December 2021

Academic Editor: Meng Guo

Using modified asphalt binder is one of the most effective methods to solve the rutting problem of asphalt pavement, but the traditional $G^*/\sin\delta$ parameter is not enough to characterize the rutting resistance of modified asphalt in field use. In order to accurately evaluate the high temperature performance of asphalt and establish the relationship between the rutting resistance of binder and mixture, two kinds of matrix asphalt and three kinds of modified asphalt were selected for DSR and MSCR tests. $G^*/\sin\delta$, nonrecoverable creep compliance J_{nr}, recovery rate R, and other parameters were used to characterize the permanent deformation resistance of the binder, and the correlation between these parameters and the results of rutting test was analyzed. The results show that $J_{nr3.2}$ can accurately characterize the permanent deformation resistance of asphalt, while the stress sensitivity index J_{nrdiff} is not applicable to all types of modified asphalt. In contrast, $J_{nrslope}$ can better reflect the stress sensitivity of asphalt, and $J_{nrslope}$ is significantly correlated with the results of rutting test.

1. Introduction

Rutting is one of the main forms of pavement damage. For semirigid base pavement, the cumulative plastic deformation under repeated load is the main reason for rutting of asphalt mixture [1, 2]. The cohesive force of asphalt and the extrusion force between aggregate constitute the rutting resistance of asphalt mixture, of which the contribution of cohesive force of asphalt accounts for about 40% [3–5]. Compared with the rutting test of asphalt mixture, it is much easier to predict the rutting performance of asphalt mixture by testing the permanent deformation resistance of asphalt binder. However, the difficulty lies in finding the most representative asphalt parameters to characterize the rutting resistance of asphalt mixture.

Penetration, softening point, and viscosity are commonly used to evaluate the rutting resistance of asphalt binders. However, relevant research shows that these indicators have no good correlation with the field performance of asphalt pavement [6]. The asphalt performance grading system of SUPERPAVE measures the rheological properties of asphalt binders at specific temperature and loading frequency through dynamic shear rheometer (DSR) test, and the rutting factor $G^*/\sin\delta$ derived based on dissipative energy theory is used as the high temperature performance evaluation index for original asphalt and residual asphalt aged by rolling thin film oven (RTFO) test [7]. However, relevant studies show that compared with evaluating modified asphalt performance, $G^*/\sin\delta$ is more accurate in evaluating the performance of matrix asphalt with linear viscoelasticity. Moreover, the dynamic sinusoidal alternating load applied continuously in DSR test does not reflect the better delayed elastic recovery ability of modified asphalt, and the study of NCHRP9-10 also proves this point. The correlation between the permanent deformation rate measured by repeated shear test (constant height) (RSCH) and $G^*/\sin\delta$ is not significant [8–10].

With the increase of traffic load and environmental temperature, more and more modified asphalts are used to solve the problem of pavement rutting. In order to

characterize the rutting resistance of asphalt more accurately, new parameters such as Sheony parameter, zero shear viscosity (ZSV), and unrecoverable creep compliance are proposed. Among them, the unrecoverable creep compliance obtained by multiple stress creep recovery (MSCR) test is considered to be able to evaluate the rutting resistance potential of asphalt [11–14].

MSCR test is developed from repeated creep and recovery (RCR) test. It evaluates the high temperature rutting resistance of asphalt binder with unrecoverable creep compliance J_{nr} and recovery rate R and takes J_{nrdiff} as the stress sensitivity index of asphalt binder. AASHTO MP 19-10 proposed an asphalt classification method based on MSCR test [15]. The unrecoverable creep compliance $J_{nr3.2}$ was used to classify the performance grade of asphalt at service temperature and then judge which of the four traffic grades (S (standard), H (heavy), V (very heavy), E (extreme)) can the asphalt serve for. At the same time, the stress sensitivity index J_{nrdiff} is required to be no more than 75%. MSCR test leaves a recovery time for the viscoelastic strain generated by the creep part of asphalt after unloading, thus providing a method to separate the permanent strain from the total strain, which is better correlated with the field rutting [16]. Compared with DSR test, the parameters obtained by MSCR test can better evaluate the rutting resistance of modified asphalt [17, 18]. The unrecoverable creep compliance measured at 0.1 kPa and 3.2 kPa shows excellent repeatability and reproducibility [19].

This study aims to evaluate the high temperature permanent deformation resistance of asphalt binder and study the relationship between asphalt binder and rutting resistance of asphalt mixture. In this study, MSCR and DSR were used to evaluate the high temperature performance of two kinds of matrix asphalt and three kinds of modified asphalt before and after aging. At the same time, the asphalt mixture with the same mineral gradation was prepared for rutting test, and the test results of asphalt binder and mixture were compared.

2. Materials and Asphalt Mixture Design

2.1. Binders. In this study, five kinds of asphalt were selected, including Shandong Jingbo AH-70, Jiangxi Sinopec AH-90, Jiangsu Sinopec SBS I-C, Jiangsu Sinopec SBS I-D, and Gansu high viscosity asphalt HVG. Among them, AH-70 and AH-90 were matrix asphalt, and SBS I-C, SBS I-D, and HVG were modified asphalt. According to Standard Test Methods of Asphalt and Asphalt Mixtures for Highway Engineering (JTG E20-2011) T0610 method, five kinds of asphalt were heated by rotating thin film oven for 75 min at $163 \pm 1^{\circ}C$ to simulate the short-term aging state of asphalt [20]. The conventional properties of unaged and aged asphalt are, respectively, given in Tables 1 and 2.

2.2. Aggregates. Both coarse aggregate and fine aggregate are limestone, and the filler is limestone powder. Aggregate and filler are from the same origin, and their properties (shown in Table 3) meet the requirements of Technical Specifications for Construction of Highway Asphalt Pavements (JTG F40-2004) [21].

2.3. Asphalt Mixture Design. In this paper, the gradation types of asphalt mixtures prepared with five different asphalts are all continuous gradation AC-13, and the gradation curves are shown in Figure 1.

The asphalt mixture in this study is designed by Marshall test. The optimum amount of asphalt mixture prepared by five different asphalts is determined by Marshall test to control the porosity of rutting test made by each asphalt. The Marshall test results are shown in Table 4.

3. Experimental Program

3.1. Dynamic Shear Rheometer (DSR) Test. The dynamic shear rheometer (DSR) test was performed in accordance with the AASHTO T315 standard test method [7]. Malvern dynamic shear rheometer (Figure 2) was used as the test instrument. The strain control mode is adopted in the test. The control strain value of the unaged asphalt is 12%, and the control strain value of the aged asphalt is 10%. The shear rate of the test is 10 rad/s (1.592 Hz), and the test temperature is 64°C~88°C. The binder sample was placed between two parallel plates (25.0 mm diameter, 1.0 mm plate spacing) of the dynamic shear rheometer, and the test can start after 15 minutes of constant temperature.

3.2. Multiple Stress Creep Recovery (MSCR) Test. The MSCR test in this paper is carried out according to the AASHTO T350 standard test method [22]. The test instrument is still Kinexus Ultra + intelligent rotary rheometer from Malvern Company, and the test temperature is also 64°C ~ 88°C. After 20 cycles of loading and recovery at a stress level of 0.1 kPa, the aged asphalt sample was immediately subjected to 10 cycles of loading and recovery at a stress level of 3.2 kPa, without any interval between the two stages. Loading and looping is usually done after 1 s of loading, and the sample is removed to allow it to resume for 9 s.

The nonrecoverable creep compliance J_{nr} (equation (1)) and recovery rate R (equation (2)) reflecting the rutting resistance potential of asphalt can be obtained through MSCR test. Considering the variability of measured values, $J_{nr0.1}$ and $R_{0.1}$ of asphalt samples under 0.1 kPa stress cycle and $J_{nr3.2}$ and $R_{3.2}$ of asphalt samples under 3.2 kPa stress cycle are calculated according to equation (3)~(6).

$$R = \frac{\varepsilon_p - \varepsilon_u}{\varepsilon_p} \times 100\%, \quad (1)$$

$$J_{nr} = \frac{\varepsilon_u}{\sigma}, \quad (2)$$

where ε_p is the peak strain, ε_u is the residual strain that cannot be restored at the end of the recovery stage, and σ is the corresponding stress level imposed by the two stages.

Table 1: Properties of unaged binders.

Items	Unit	AH-70	AH-90	SBS I-C	SBS I-D	HVG	Experiment method
Penetration (15°C)	dmm	33	28	29	22	29	T0604
Penetration (25°C)	dmm	77	85	78	60	72	T0604
Penetration (30°C)	dmm	123	139	114	87	97	T0604
Penetration index	n/a	0	−1	0	0	1	T0604
Softening point	°C	54	53	92	95	87	T0606
Viscosity (60°C)	Pa · s	287	208	28728	52243	58061	T0620

Table 2: Properties of aged binders.

Items	Unit	AH-70	AH-90	SBS I-C	SBS I-D	HVG	Experiment method
Penetration (15°C)	dmm	18	19	21	21	29	T0604
Penetration (25°C)	dmm	41	48	49	43	53	T0604
Penetration (30°C)	dmm	60	75	79	61	75	T0604
Penetration index	n/a	1	0	0	2	3	T0604
Softening point	°C	60	58	69	70	85	T0606
Viscosity (60°C)	Pa · s	809	593	36543	58061	96442	T0620

Table 3: Properties of aggregates.

Items	Unit	Experimental value	Normative value
Apparent density	—	2.689	≥2.5
Water absorption	%	0.64	—
Angularity	*s*	41.7	≥30
Sediment concentration	%	64	≥60

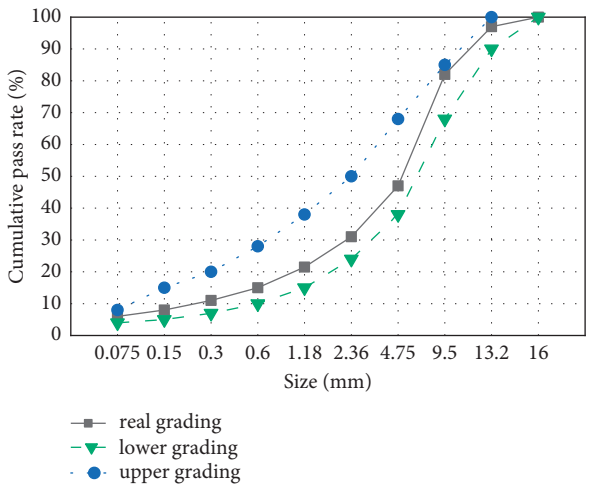

Figure 1: Grading curve.

Table 4: Result of Marshall test.

Type of binders	Optimum asphalt content (%)	Apparent density (g/cm^3)	VV (%)	VMA (%)	VFA (%)
AH-70	4.6	2.507	4.60	14.64	70.56
AH-90	4.6	2.510	4.69	14.53	69.83
SBS I-C	4.9	2.486	4.43	15.27	73.13
SBS I-D	4.9	2.492	4.46	15.10	72.62
HVG	5.1	2.481	4.38	15.42	73.44

Figure 2: Kinexus ultra + rotational rheometer.

$$J_{nr0.1} = \frac{\mathrm{SUM}\left[J_{nr}(0.1, N)\right]}{10}, \quad (N = 11 \sim 20), \tag{3}$$

$$J_{nr3.2} = \frac{\mathrm{SUM}\left[J_{nr}(3.2, N)\right]}{10}, \quad (N = 1 \sim 10), \tag{4}$$

$$R_{0.1} = \frac{\mathrm{SUM}\left[\varepsilon_r(0.1, N)\right]}{10}, \quad (N = 11 \sim 20), \tag{5}$$

$$R_{3.2} = \frac{\mathrm{SUM}\left[\varepsilon_r(0.1, N)\right]}{10}, \quad (N = 1 \sim 10). \tag{6}$$

$J_{\mathrm{nr}0.1}$ and $R_{0.1}$ are the mean values of J_{nr} and R% measured in the ten 0.1 kPa stress cycles after preshearing of the first ten 0.1 kPa stress cycles, while $J_{\mathrm{nr}3.2}$ and $R_{3.2}$ are the mean values of J_{nr} and R% measured in the ten 3.2 kPa stress cycles of the asphalt samples.

J_{nrdiff} (equation (7)) is used as an evaluation index of stress sensitivity of asphalt binder to ensure that asphalt performance will not be degraded due to excessive temperature or excessive load in actual use, and its maximum limit is 75%[23]. However, some researchers have found that the J_{nrdiff} of some modified asphalts with strong resilience is usually greater than 75% due to too small $J_{\mathrm{nr}0.1}$ or too large $J_{\mathrm{nr}3.2}$, and there is no significant correlation between J_{nrdiff} and rutting test results [24, 25]. Therefore, Stempihar proposed a new parameter J_{nrslope} (equation (8)) as a new stress sensitivity evaluation index. J_{nrslope} is the slope (percentage) of the J_{nr}-stress relationship between 0.1 and 3.2 kPa stress levels, which can better describe the relationship between the nonrecoverable creep compliance variable and the rut variable [26].

$$J_{nr\,\mathrm{diff}} = \frac{J_{nr3.2} - J_{nr0.1}}{J_{nr0.1}} \times 100\%, \tag{7}$$

$$J_{\mathrm{nr\,slope}} = \frac{J_{nr3.2} - J_{nr0.1}}{3.1} \times 100\%. \tag{8}$$

3.3. Wheel Rut Test. The rutting test method adopted in this paper is carried out in accordance with the method specified in the Standard Test Methods of Asphalt and Asphalt Mixtures for Highway Engineering (JTG E20-2011) [20]. The plate specimen of asphalt mixture was formed by rolling molding method (T0703-2011) with the size of 300 mm × 300 mm × 50 mm. The test temperature was 60°C, and the wheel pressure was 0.7 MPa. The test wheel walked along the same track on the specimen surface repeatedly at the frequency of 42 ± 1 time/min, and the depth of the rut formed on the specimen surface under the repeated action of the test wheel was tested to calculate the number of walks required for each 1 mm of rutting deformation, namely, the dynamic stability (DS). The rutting resistance of asphalt mixture is evaluated by the dynamic stability. The calculation formula of dynamic stability is

$$DS = \frac{(t_2 - t_1) \times N}{d_2 - d_1} \times c_1 \times c_2, \tag{9}$$

where DS is the dynamic stability; t_1, t_2 are the test time of 45 min and 60 min; and d_1, d_2 are the vertical deformation depth corresponding to t_1, t_2; c_1, c_2 are the type of testing machine and the correction coefficient of specimen, both of which are 1.0.

4. Results and Discussion

4.1. Temperature Sweep Test. The complex modulus G* and phase angle δ were obtained by DSR test, and then the rutting factor $G^*/\sin\delta$ was calculated to evaluate the rutting potential of asphalt. The calculated results are shown in Figure 3. The rutting factor $G^*/\sin\delta$ decreases with the increase of temperature, indicating that the higher the temperature, the worse the antirutting ability of asphalt. According to Superpave, the original asphalt $G^*/\sin\delta \geq 1.0$ kPa and aged asphalt $G^*/\sin\delta \geq 2.2$ kPa can be considered to have good resistance to permanent deformation. In this study, $G^*/\sin\delta$ of the unaged base asphalt decreases to less than 1 kPa before 70°C. That is to say, the base asphalt at 70°C high temperature resistance to permanent deformation ability can no longer meet the requirements of pavement, while the modified asphalt still has good resistance to permanent deformation at 76°C ~ 82°C. After short-term aging, the resistance to permanent deformation of both modified and unmodified asphalt decreases. However, in general, $G^*/\sin\delta$ of modified asphalt is greater than that of matrix asphalt, indicating that the rutting resistance of modified asphalt is better than that of matrix asphalt.

4.2. MSCR Test. Figure 4 shows that the J_{nr} value of asphalt increases exponentially with the increase of temperature T, which indicates that, under high temperature conditions, the high temperature stability of asphalt will weaken with the increase of temperature. The overall trend of R value of asphalt decreases with the increase of temperature T, indicating that, with the increase of temperature, the elastic recovery of asphalt decreases and the property of asphalt is

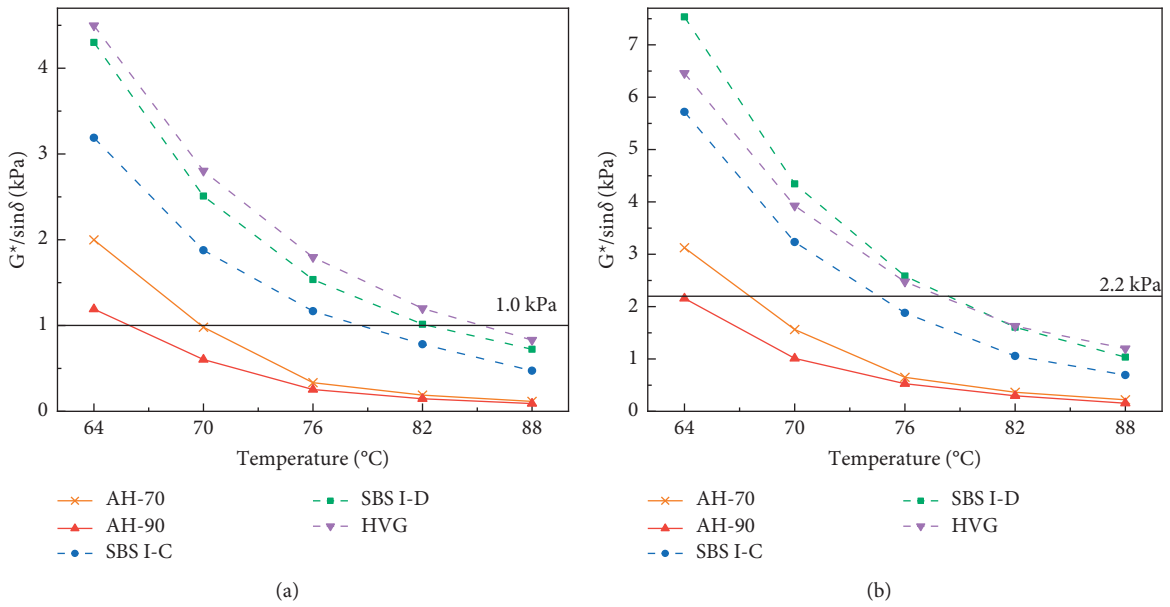

Figure 3: $G^*/\sin\delta$ at five different testing temperatures: (a) unaged and (b) aged.

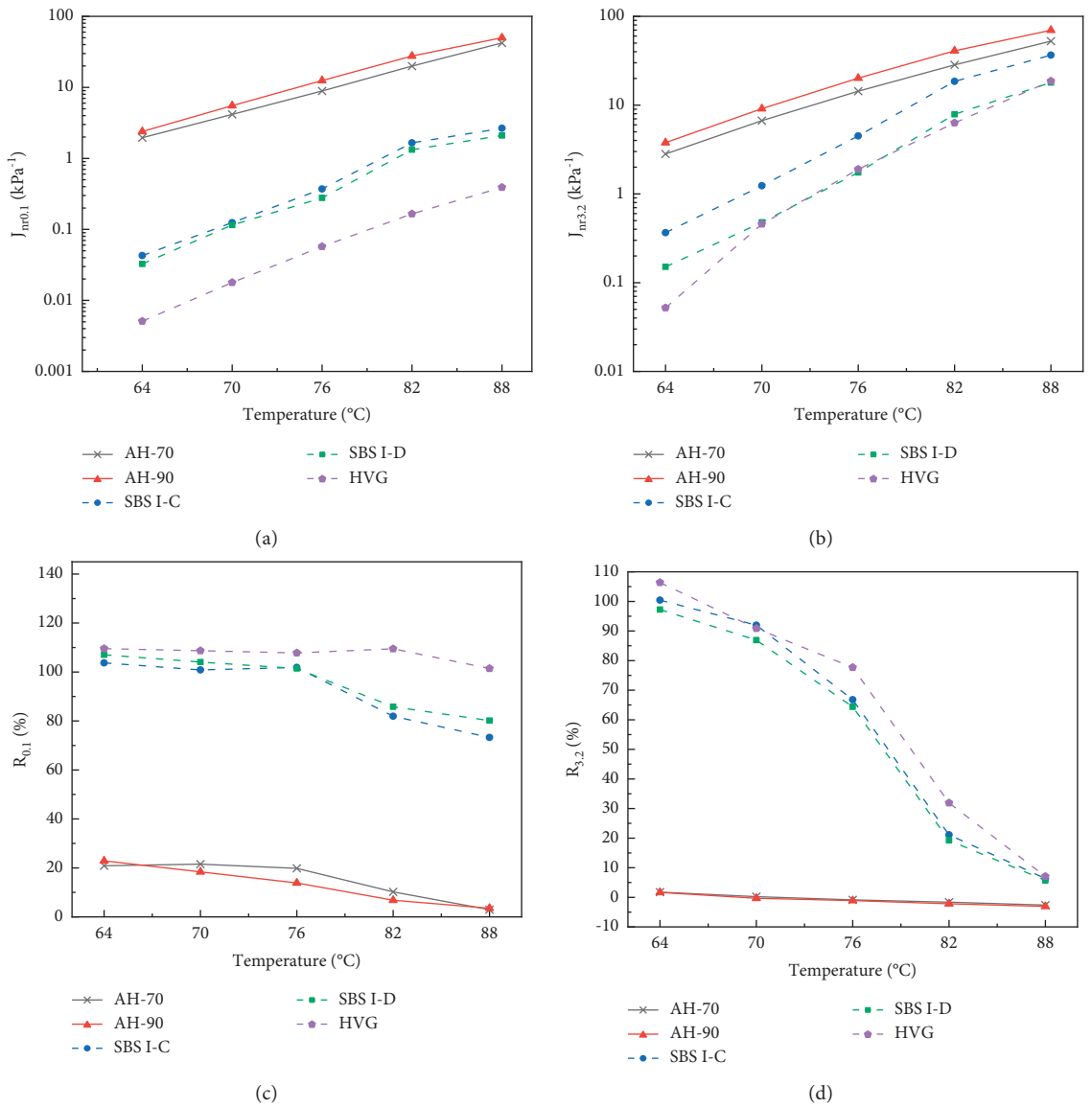

Figure 4: Continued.

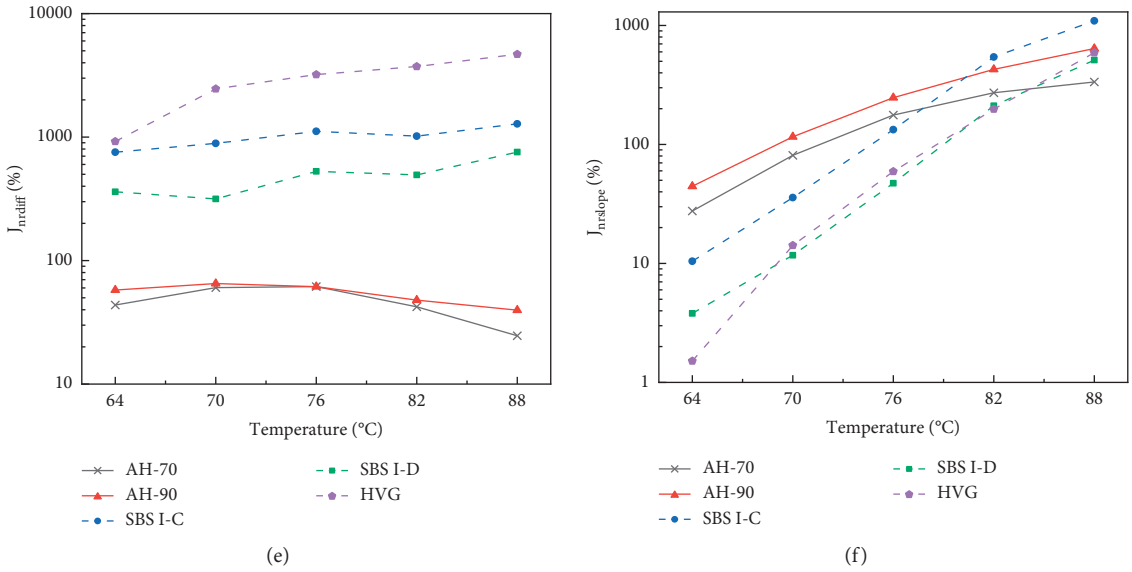

Figure 4: MSCR results at five different temperatures: (a) $J_{nr0.1}$. (b) $J_{nr3.2}$. (c) $R_{0.1}$ (d) $R_{3.2}$. (e) J_{nrdiff} (f) $J_{nrslope}$.

closer to the viscous materials. In addition, $R_{0.1}$ of all asphalts is greater than $R_{3.2}$, indicating that the deformation of asphalt under high stress horizontal shear is more difficult to recover than that under low stress horizontal shear, which is also illustrated by the J_{nr} results.

The $R_{0.1}$ of base and modified asphalt hardly changes in a certain temperature range and begins to decline rapidly after exceeding a certain temperature threshold. It shows that the structure of asphalt can be kept stable and the viscoelastic properties do not change in a certain temperature range at a lower temperature and stress level. However, when the temperature exceeds a certain critical temperature, the elasticity ratio decreases and the asphalt structure is damaged. It can be observed from Figure 4 that $R_{3.2}$ of AH-70 and AH-90 asphalt is less than 0 after 76°C and 70°C, respectively. Similar reports have been reported in other studies [27, 28]. The reason for this may be that the matrix asphalt has a weak ability to resist high temperature deformation and generates third-order creep under the action of high temperature and high stress, which can still flow when the stress is 0. Another possible reason is that there is a delay in unloading the DSR, and part of the minor stress still acts on the asphalt after unloading, resulting in the deformation of the substrate asphalt which is too soft at high temperature. $R_{3.2}$ of modified asphalt decreased rapidly in the temperature range of 76°C–82°C, and the corresponding $J_{nr3.2}$ also began to rise rapidly, indicating that the modified asphalt could still maintain structural stability to a certain extent at low temperature, while maintaining good rutting resistance. However, once the temperature exceeded the critical value, the viscoelastic properties of modified asphalt changed, the elastic ratio decreased rapidly, and the rutting resistance also decreased rapidly.

If J_{nrdiff} is used as an indicator of asphalt stress sensitivity, HVG is considered to have the highest stress sensitivity, while AH-70 is considered to have the lowest stress sensitivity, which contradicts the results of J_{nr}. Meanwhile, the J_{nrdiff} of SBS I-C at 70°C was 1.18 times that at 64°C, but the $J_{nr3.2}$ increased by 3.37 times, which was obviously unreasonable. It indicates that, for some modified asphalts, too small $J_{nr0.1}$ or too large $J_{nr3.2}$ will lead to the J_{nrdiff} cannot be less than 75% of the specification, which cannot accurately reflect the stress sensitivity of asphalt. Meanwhile, it is noted that results of $J_{nrslope}$ and $J_{nr3.2}$ are consistent. The $J_{nrslope}$ of SBS I-D at 82°C is 4.47 times that at 76°C, and the corresponding $V_{nr3.2}$ is also expanded by 4.52 times. Similar rules are reflected in different temperatures and different asphalts, which indicates that J_{nrslop} can well describe the stress sensitivity of modified asphalt. As can be seen from Figure 4(f), the stress sensitivity of modified asphalt becomes more significant with the increase of temperature. At 88°C, the stress sensitivity of modified asphalt approaches or exceeds that of matrix asphalt.

Table 5: Rutting test results of asphalt mixtures.

Mixture types	AH-70	AH-90	SBS I-C	SBS I-D	HVG
DS/times·mm^{-1}	868	597	4741	8395	10263

4.3. Comparison of the Test Results. Rutting test results of five asphalt mixtures selected in this paper are shown in Table 5. According to the rutting test results of asphalt mixture at 60°C and MSCR and DSR test results at 64°C, the rutting performance of the five types asphalts were ranked. It can be seen from Table 6 that the ranking results of $J_{nr0.1}$, $J_{nr3.2}$, and $J_{nrslope}$ were consistent with the rutting test results, but J_{nrdiff}, $G^*/\sin\delta$, is different from them. The latter two indexes can not characterize the rutting resistance of modified asphalt. Figure 5 shows that $J_{nr0.1}$, $J_{nr3.2}$, and $J_{nrslope}$ are significantly correlated with rutting test results of asphalt mixture at the 5% level, and their correlation coefficients R are all greater than the critical value of 0.8783 at the 5% level. As predicted above, J_{nrdiff} is not correlated with rutting test results. It is worth noting that $G^*/\sin\delta$ has a good linear relationship with rutting test results

Table 6: Ranking of rutting resistance based on rutting test results at 60°C; MSCR and DSR results at 64°C.

Type of binders	DS	$J_{nr0.1}$	$J_{nr3.2}$	$J_{nrslope}$	J_{nrdiff}	$G^*/\sin\delta$ after RTFOT
HVG	1	1	1	1	1	2
SBS I-D	2	2	s	2	4	1
SBS I-C	3	3	3	3	5	3
AH-70	4	4	4	4	2	4
AH-90	5	5	5	5	3	5

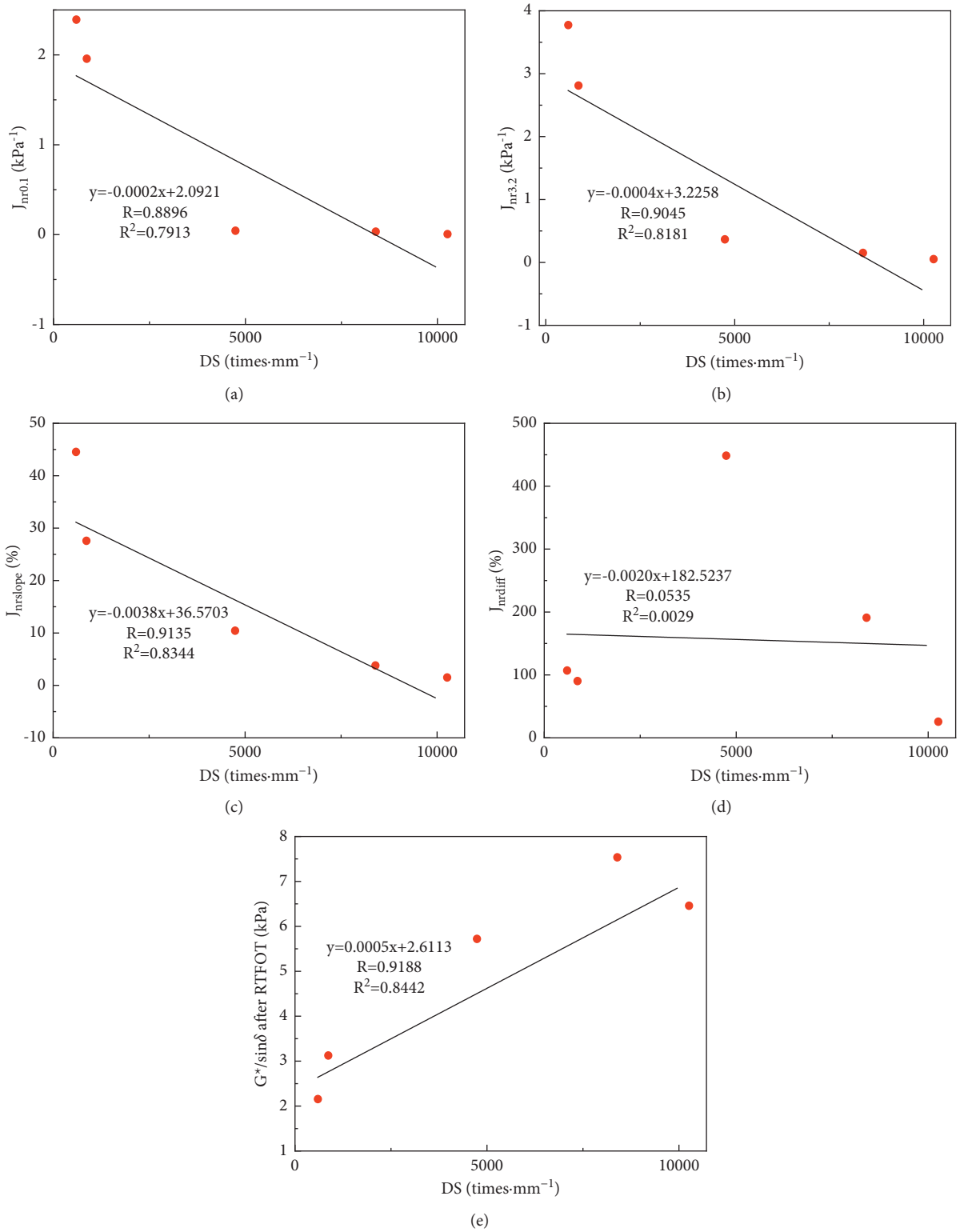

Figure 5: Correlations of DS and (a) $J_{nr0.1}$. (b) $J_{nr3.2}$. (c) $J_{nrslope}$. (d) J_{nrdiff}. (e)$G^*/\sin\delta$ after RTFOT at 64°C.

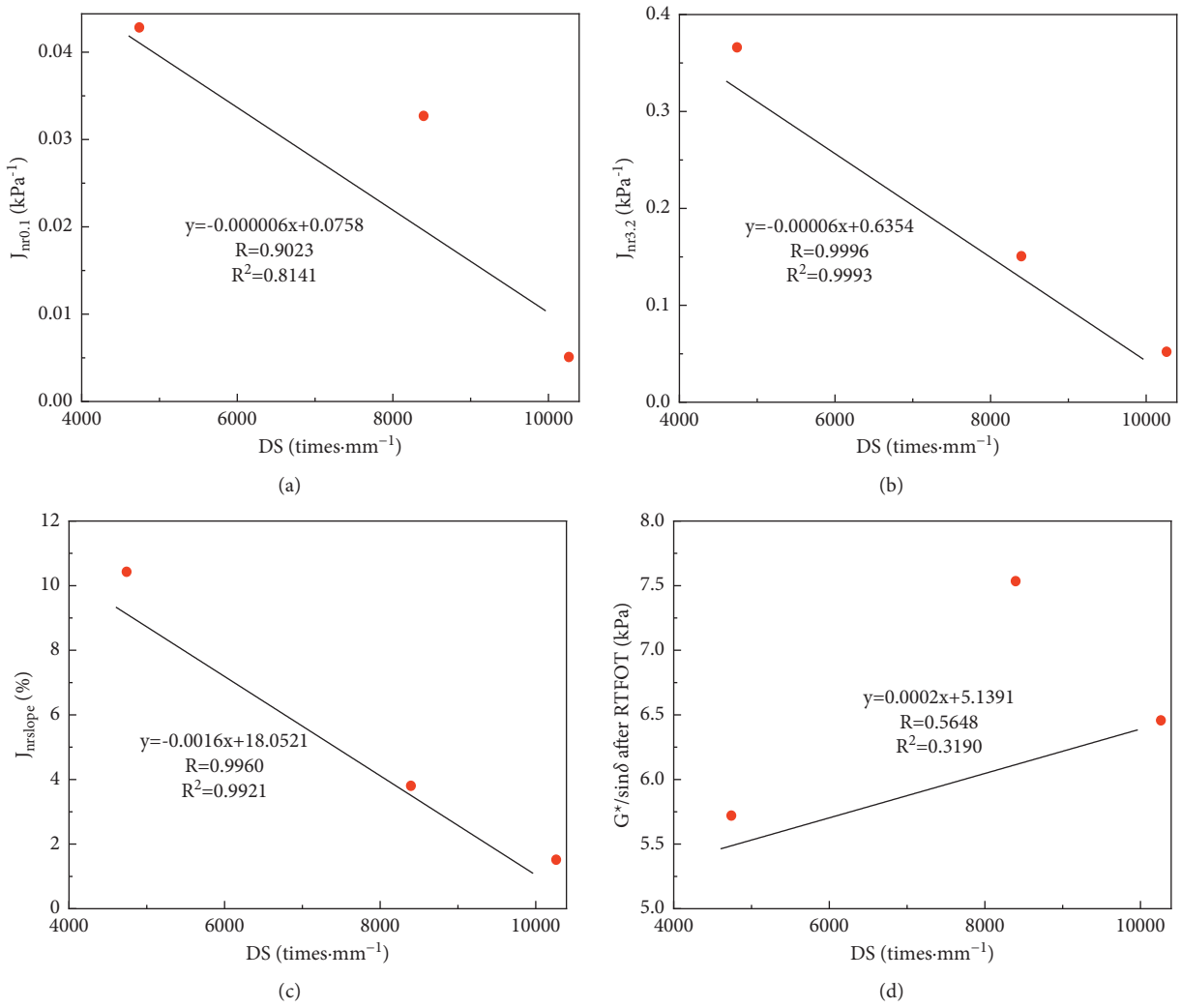

FIGURE 6: Correlations of DS and (a) $J_{nr0.1}$ of modified asphalt. (b) $J_{nr3.2}$ of modified asphalt. (c) $J_{nrslope}$ of modified asphalt. (d) $G^*/\sin\delta$ after RTFOT of modified asphalt.

after RTFO aging, which is contradictory to the conclusion of other researchers that DSR is not applicable to modified asphalt [8–10]. Therefore, the experimental results of modified asphalt need further correlation analysis.

Figure 6 shows the linear correlation between test results of modified asphalt binder and rutting results of mixture at 64°C. It can be seen that, at 5% level, $J_{nr3.2}$ still has significant correlation with rutting test results, and its correlation coefficient R is greater than the critical correlation coefficient 0.9969. At the 10% level, $J_{nrslope}$ is significantly correlated with rutting test results, while $J_{nr0.1}$ and $G^*/\sin\delta$ are not significantly correlated with rutting test results. This indicates that $J_{nr3.2}$ and $J_{nrslope}$ can well characterize the rutting resistance of asphalt, while $J_{nr0.1}$ and $G^*/\sin\delta$ are not suitable for characterizing the rutting resistance of modified asphalt.

5. Conclusion

In this study, the permanent deformation resistance of five different asphalts was evaluated. DSR and MSCR tests were carried out to obtain the irreversible creep compliance and strain recovery rate of the material. The rutting test of dense-graded asphalt mixture with the same binder composition was carried out to determine its antirutting ability. The key findings are summarized as follows:

(1) Modified asphalt has better rutting resistance than matrix asphalt and can maintain good permanent deformation resistance at higher temperature, but the stress sensitivity of modified asphalt increases with the temperature.

(2) The $J_{nr3.2}$ obtained by MSCR test is significantly correlated with the rutting test result DS of asphalt mixture, indicating that $J_{nr3.2}$ can well correlate the permanent deformation resistance of binder with the rutting resistance of asphalt mixture and is an important index to evaluate the rutting resistance effect of binder in asphalt mixture.

(3) J_{nrdiff} is no longer suitable as an evaluation index of asphalt stress sensitivity due to too small $J_{nr0.1}$ or too large $J_{nr3.2}$ in some modified asphalt; $J_{nrslope}$ can better characterize the stress sensitivity of asphalt,

and linear correlation analysis results show that it has significant correlation with the results of rutting test.

(4) The negative recovery rate R is usually found in the matrix asphalt with weak rutting resistance, and this phenomenon is more obvious under the test conditions of high temperature and high stress. It is suggested that lower temperature and lower stress level should be used to evaluate the deformation recovery performance of matrix asphalt.

6. Prospect

This study only compared the rutting performance of five asphalt binder and dense-graded asphalt mixture prepared from the same binder. It is necessary to study the relationship between discontinuous gradation and open gradation asphalt mixture and asphalt binder performance in the future. Additionally, it is necessary to study the relationship between rutting and high temperature rutting resistance of asphalt in future.

Data Availability

The data used to support the findings of this study are included within the article.

Conflicts of Interest

The author declares no conflicts of interest.

Acknowledgments

This research was supported by the Basic Scientific Research of Central Institute (2020-9049).

References

[1] M. D. I. Domingos and A. L. Faxina, "Susceptibility of asphalt binders to rutting: literature review," *Journal of Materials in Civil Engineering*, vol. 28, no. 2, Article ID 04015134, 2016.

[2] J. Zhang, C. Zhu, X. Li, J. Pei, and J. Chen, "Characterizing the three-stage rutting behavior of asphalt pavement with semi-rigid base by using UMAT in ABAQUS," *Construction and Building Materials*, vol. 140, pp. 496–507, 2017.

[3] Y. Du, J. Chen, Z. Han, and W. Liu, "A review on solutions for improving rutting resistance of asphalt pavement and test methods," *Construction and Building Materials*, vol. 168, pp. 893–905, 2018.

[4] M. N. Partl, H. U. Bahia, F. Canestrari et al., *Advances in Interlaboratory Testing and Evaluation of Bituminous Materials: State-Of-The-Art Report of the RILEM Technical Committee 206-ATB*, pp. 18–83, Springer Science & Business Media, Heidelberg, Germany, 2012.

[5] L. F. Walubita, E. Mahmoud, L. Fuentes et al., "Correlating the asphalt-binder high-temperature properties (DSR) to HMA permanent deformation (RLPD) and field rutting: a laboratory-field study," *Construction and Building Materials*, vol. 262, p. 120761, 2020.

[6] J. Petersen, R. Robertson, J. Branthaver et al., *Binder Characterization and Evaluation: Volume 1. Rep. No. SHRP-A-367, Strategic Highway Research Program*, National Research Council, Washington, DC, USA, 1994.

[7] AASHTO, *Standard Test Method for Determining the Rheological Properties of Asphalt Binder Using a Dynamic Shear Rheometer (DSR)*, AASHTO T, Washington, DC, USA, 2012.

[8] H. Bahia, D. Hanson, M. Zeng, H. Zhai, M. Khatri, and R. Anderson, *NCHRP Report 459: Characterization of Modified Asphalt Binders in Superpave Mix Design*, Transportation Research Board of the National Academies, Washington, DC, USA, 2001.

[9] H. U. Bahia, H. Zhai, M. Zeng, Y. Hu, and P. Turner, "Development of binder specification parameters based on characterization of damage behavior (with discussion)," *Journal of the Association of Asphalt Paving Technologists*, vol. 70, 2001.

[10] R. Dongré and J. D'Angelo, "Refinement of Superpave high-temperature binder specification based on pavement performance in the accelerated loading facility," *Transportation Research Record*, vol. 1829, no. 1, pp. 39–46, 2003.

[11] J. A. D'Angelo, "The relationship of the MSCR test to rutting," *Road Materials and Pavement Design*, vol. 10, no. sup1, pp. 61–80, 2009.

[12] Z. I. Qasim, A. H. Abed, and K. A. Almomen, "Evaluation of mixing and compaction Temperatures (MCT) for modified asphalt binders using zero shear viscosity and Cross-Williamson model," *Case Studies in Construction Materials*, vol. 11, Article ID e00302, 2019.

[13] A. Shenoy, "Refinement of the Superpave specification parameter for performance grading of asphalt," *Journal of Transportation Engineering*, vol. 127, no. 5, pp. 357–362, 2001.

[14] K. Yan, L. You, and D. Wang, "High-temperature performance of polymer-modified asphalt mixes: preliminary evaluation of the usefulness of standard technical index in polymer-modified asphalt," *Polymers*, vol. 11, no. 9, p. 1404, 2019.

[15] AASHTO, *MP19-10*, American Association of State Highway and Transportation Officials, Washington, DC, USA, 2014.

[16] H. Liu, W. Zeiada, G. G. Al-Khateeb, A. Shanableh, and M. Samarai, "Use of the multiple stress creep recovery (MSCR) test to characterize the rutting potential of asphalt binders: a literature review," *Construction and Building Materials*, vol. 269, p. 121320, 2021.

[17] K. Al-Adham, M. A. Dalhat, and H. I. Al-Abdul Wahhab, "Strain recovery rate and absolute per cent recovery of polymer-modified asphalt binders," *International Journal of Pavement Engineering*, vol. 21, no. 7, pp. 919–929, 2020.

[18] N. Saboo and P. Kumar, "Analysis of different test methods for quantifying rutting susceptibility of asphalt binders," *Journal of Materials in Civil Engineering*, vol. 28, no. 7, Article ID 04016024, 2016.

[19] F. Zhou, H. Li, P. Chen, and T. Scullion, *Laboratory Evaluation of Asphalt Binder Rutting, Fracture, and Adhesion Tests*, Texas A&M Transportation Institute, Austin, TX, US, 2014.

[20] China, *Standard Test Methods of Asphalt and Asphalt Mixtures for Highway Engineering*, China Communication Press, Beijing, China, 2011.

[21] China, *Technical Specifications for Construction of Highway Asphalt Pavements JTG F40-2004*, Ministry of Transport of the People's Republic of China, Beijing, China, 2004.

[22] AASHTO, *Standard Method of Test for Multiple Stress Creep Recovery (MSCR) Test of Asphalt Binder Using a Dynamic Shear Rheometer (DSR)*, AASHTO T, Washington, DC, USA, 2014.

[23] J. B. S. Bastos, L. F. A. L. Babadopulos, and J. B. Soares, "Relationship between multiple stress creep recovery (MSCR) binder test results and asphalt concrete rutting resistance in

Brazilian roadways," *Construction and Building Materials*, vol. 145, pp. 20–27, 2017.

[24] M. Gaspar, B. Nogueira, K. Vasconcelos, L. Leite, and L. Bernucci, "Effect of different creep and recovery times on the MSCR test for highly modified asphalt binder," *Journal of Testing and Evaluation*, vol. 49, 2019.

[25] O.-V. Laukkanen, H. Soenen, T. Pellinen, S. Heyrman, and G. Lemoine, "Creep-recovery behavior of bituminous binders and its relation to asphalt mixture rutting," *Materials and Structures*, vol. 48, no. 12, pp. 4039–4053, 2015.

[26] J. Stempihar, A. Gundla, and B. S. Underwood, "Interpreting stress sensitivity in the multiple stress creep and recovery test," *Journal of Materials in Civil Engineering*, vol. 30, no. 2, Article ID 04017283, 2018.

[27] M. Jafari, A. Babazadeh, and S. Aflaki, "Effects of stress levels on creep and recovery behavior of modified asphalt binders with the same continuous performance grades," *Transportation Research Record: Journal of the Transportation Research Board*, vol. 2505, no. 1, pp. 15–23, 2015.

[28] B. Singh, N. Saboo, and P. Kumar, "Effect of short-term aging on creep and recovery response of asphalt binders," *Journal of Transportation Engineering, Part B: Pavements*, vol. 143, no. 4, Article ID 04017017, 2017.

Hindawi
Advances in Materials Science and Engineering
Volume 2021, Article ID 4445185, 11 pages
https://doi.org/10.1155/2021/4445185

Research Article

Research on Mechanical Response of Pavement Structure to Differential Settlement of Subgrade on Highway Widening

Quanjun Shen,[1] Yu Lu ,[2] Yaohui Yang,[1] and Guanxu Long[1]

[1]*Shandong Hi-Speed Group Co., Jinan, Shandong 250000, China*
[2]*School of Civil Engineering, Shandong University, Jinan, Shandong 250000, China*

Correspondence should be addressed to Yu Lu; luyu_99925@163.com

Received 18 August 2021; Accepted 29 November 2021; Published 29 December 2021

Academic Editor: Yongsheng Yao

Based on the widening project of Ri-Lan highway in China, the finite element model is established by PLAXIS. By applying differential settlement at the bottom of the pavement, the mechanical response of the pavement structure is analysed. Finally, the differential settlement control standard indicated by crack strength is proposed. The results show that, under the effect of differential settlement, within about 4 cm of old pavement surface and upper base bear tensile stress, the base first reaches the failure strength. Under 4 cm of the old pavement surface, the subbase first reaches the failure strength. The differential settlement control standard of the pavement structure is determined by the splitting strength of the material, and we, respectively, control the differential settlement of less than 23.4 mm, where the corresponding cross-slope rate is 0.33%, and below 75.2 mm, where the corresponding cross-slope rate is 0.54%. It could support practical engineering applications.

1. Introduction

In order to deal with the problem between the highway capacity and service level, the highway has entered an era of parallel construction and reconstruction and expansion. At present, the experience of highway expansion project shows that if the new subgrade construction method is unreasonable, the differential settlement control standards are not perfect, it will cause the top settlement of the subgrade, and then it will cause the longitudinal cracking of the pavement. Then it affects the use performance of the pavement, serious subgrade collapse, and other road disasters. The force deformation characteristics of highway construction and expansion are different, mainly manifested in the different consolidation degree of the foundation under the new and old subgrade of the highway reconstruction and expansion project, which will cause the differential settlement of the foundation, and then reflected in the top surface of the subgrade, and eventually cause the longitudinal cracking of the road surface. The highway widening project is more difficult with higher quality requirements than the new highway and lacks a more in-depth understanding of the formation mechanism and treatment technology of all kinds of diseases.

At present, the differential settlement control standard of highway widening engineering is mainly considered from structural and functional requirements and by numerical simulation. By establishing elastic-plastic finite element model of pavement, subgrade, and foundation interaction, Yang et al. [1] analysed the mechanical response of pavement structure under postengineering differential settlement and put forward the differential settlement control standard of bilateral widening projects. The results show that different settlement curves of different forms have saddle-shaped distribution, and the postengineering slope rate shall not exceed 0.3% and 0.45% during inverted bell distribution. By establishing finite element model to calculate the internal force of pavement structure, Ye et al. [2] proposed that the variation of lateral slope change rate of 0.55% should be taken as the differential settlement control standard for the single-side widening project of Fo-Kai Expressway. Relying on the Shanghai-Nanjing Expressway reconstruction project, Zhang [3] established the finite element model of new and old road surface through ABAQUS and determined the

differential settlement control standard from the functional and structural aspects. The result is that the horizontal slope rate is below 0.5%. The structural index required the old horizontal slope rate of the construction road below 0.25%, and below 0.2%. Zhao et al. [4–6] relied on the highway widening project, the road structure layer calculation model under the action of vehicle load is established, and the differential settlement control index is proposed to broaden the change rate of some horizontal slope. Relying on the Anxin highway widening project, Zhen et al. [7] studied the differential settlement control standard and graded it by considering the pavement structural requirements and functional requirements. The results show that the maximum slope rate of 0.19% is the low limit, and the maximum slope rate of 0.43% is the high limit. Liu et al. [8], combined with the reconstruction and expansion project of Ankang and Pingli secondary highway, used the finite element calculation method to solve the maximum differential settlement value, and the results showed that when the transverse slope rate was less than 0.3%. Then, the pavement structure would not be damaged. Based on the reconstruction and expansion project of Ji-Qing Expressway, Wang [9] proposed the differential settlement control standard by means of numerical simulation and, combined with the typical pavement structure in Shandong Province, drew the conclusion that the maximum allowable slope change rate was 0.11% ~ 0.13%. Through the finite element numerical analysis model, Wang [10] adopted the maximum difference settlement and slope change rate as the index. The results showed that the ultimate tensile strength was taken as the damage index. The differential settlement limit of the old pavement is 9.07 cm and the corresponding horizontal slope rate is 0.66%. The differential settlement limit of new pavement is 0.98 cm. The corresponding horizontal slope rate is 0.07%. Lu [11], combined with the widening project example of Changyu Expressway, used COMSOL finite element software and proposed that the maximum allowable after-working difference settlement value of the pavement structure shall be determined by the maximum tensile strength at the joint.

To sum up, most of the existing studies put forward the corresponding specific different settlement control indicators based on the actual project. Due to the large difference in different foundation and subgrade properties of different projects, the change range of different settlement control indicators is large, which varies between 0.11% and 0.5%. Therefore, it is difficult to guide the application of the project, and it also needs to be carried out in combination with the actual situation of the Ri-Lan highway reconstruction and expansion project. The old pavement and split width pavement are discussed, respectively, in this paper, based on the calculation results of subgrade top settlement. PLAXIS finite element software is used to analyse the mechanical response of old and new pavement structural layers to differential settlement. Then, the additional stress of each structural layer under different difference settlement is calculated, and furthermore, the differential settlement control standard is proposed taking the split strength as the index.

2. Analysis of Subgrade Widening Stress and Deformation Characteristics

2.1. PLAXIS Introduction. PLAXIS is a powerful geotechnical finite element computing software that has been widely used in the finite element analysis of various complex geotechnical projects, including four subroutines of input, calculation, output, and curve, which used together for geotechnical deformation, stability analysis, and coupling analysis. Preprocessing of PLAXIS is completed by an input subroutine, mainly including establishing geometric models, defining load and boundary conditions, dividing grids, defining soil layers and structural units, and setting initial conditions. Postprocessing of PLAXIS is realized by output and curve subroutine. The output of various kinds of stress, strain, and deformation can be set, as well as the stress strain state of the point and the relationship with time.

2.2. Calculation Model and Mechanical Parameters

2.2.1. Basic Assumption. Considering the complexity of the actual situation of the project, make the following assumption with little impact on the calculation results:

① Embankment is long enough to be strain.

② Mohr–Coulomb model is used for Coulomb and foundation soil.

③ Materials of each layer are homogeneous, continuous, and isotropic.

④ Pavement load equivalent of 1 m high filling acts on the subgrade. As a static simulation, the driving load equivalent of 10 kPa uniform load acts on the subgrade.

In order to simulate the early consolidation of the old subgrade, the process of the calculation starts from the filling of the old subgrade. The construction period and operation period of the old road are considered. After the operation, the displacement field of the old subgrade and the stress field are retained as the initial stress state of the widening subgrade calculation to ensure that the settlement value is generated by the widened subgrade. According to the specification, the working life of the new subgrade is 15 years. Subgrade filling rate is one meter per month and the consolidation rate is one meter per month.

2.2.2. Geometric Model. Combined with the actual situation of the widening project, the original subgrade width is 28 m and the cross section is 42 m. The cross section with subgrade height of 4 m is selected for finite element calculation and analysis. The slope rate of the new and old subgrade is 1 : 1.5, and the foundation drainage consolidation is considered. Semisymmetric structure is selected to consider the influence of boundary effect. The foundation calculation width is 60 m and the depth is 40 m. The boundary constraints of the model are that horizontal displacement is restrained from the left and the right and the bottom of the model is a fixed constraint. The groundwater level line is

located 3 m below the foundation surface with permeable boundary and the rest with impermeable boundary. The finite element model and the grid division model are shown in Figures 1 and 2.

2.2.3. Mechanical Parameters of the Foundation and the Subgrade. For average foundation, the compaction degree of subgrade layer in the project is shown in Table 1. γ is the natural weight. γ_{sat} is the saturated capacity weight. e_0 is the initial pore ratio. E_s is the modulus of compression. ν is Poisson's ratio. c is the cohesive force. φ is the internal friction angle. k is the osmotic coefficient (Table 2). Horizontal permeability coefficient and vertical permeability coefficient are the same.

2.3. Analysis of the Calculation Results

2.3.1. Transfer Distribution. As shown in Figure 3 (the 15 years after the settlement), the equivalent area of the vertical displacement is roughly inverted bell distribution, and the vertical shift shows a trend from the left to the right of the model. As shown in Figure 4 (the 15 years after the horizontal shift), the filling makes the horizontal displacement to the inside of the highway and the maximum horizontal displacement to the outside of the highway. The maximum displacement of the subgrade slope position to the inside of the inside of the highway is constantly increasing, and the maximum value range also increases.

The vertical displacement of the foundation surface and the top of the subgrade is drawn in Figures 5 and 6. It can be seen that under the action of the new subgrade, the foundation surface is a deep spoon; that is, the vertical displacement from the middle line of the old subgrade to the new subgrade slope toe is increased first. Then, the displacement reaches the maximum value below the new subgrade core. The vertical displacement of the subgrade top surface is a shallow spoon shape. The maximum value appears on the shoulder of the new subgrade, and the curve is the steeper near the splicing point of the new and old subgrade, where the subgrade cross-slope ratio is the maximum. The contrast diagram shows that the difference between the two vertical displacement is not obvious. This is because the old subgrade has been completely compacted after years of operation and the new subgrade was also filled and compacted. According to the stress diffusion principle of the subgrade, the widening subgrade bears significant wheel pressure, and the compression deformation of the new and old subgrade itself is small.

The data drawing in the horizontal displacement cloud map is extracted to Figures 7 and 8. It is seen that the foundation surface is taken at the excavation steps (x is 18.5 m) as the boundary point. The horizontal displacement movement on both sides is the opposite, and the old subgrade area moves to the centre of the old road and the toe of the new subgrade. Here, corresponding measures can be taken to avoid damage of the soil body. As can be seen from Figure 8, the overall top surface of the subgrade moves to the outside of the highway, and the horizontal displacement from the centre of the old subgrade to the outside of the highway gradually increases. At the first inflection point of the curve of the new and old subgrade splicing, after the horizontal displacement has reached the maximum value, the displacement is gradually reduced.

It shows the change curve of horizontal displacement below the old subgrade slope along with the foundation depth (Figure 9). It can be seen that the horizontal displacement direction below the old subgrade slope is different. Within the foundation depth is 5 m, the inside of the road is horizontal, and the outside of the road is within more than 5 m depth. and the maximum value is near 20 m below the foundation. It shows the change curve of the horizontal displacement below the new subgrade toe with the foundation depth (Figure 10). It can be seen that the soil body below the new subgrade toe is presented as the whole moves to the outside of the highway, and the maximum horizontal displacement appears at a certain depth below the surface.

2.3.2. Safety Analysis. The safety calculation module in PLAXIS 2D software is calculated in the limit state for 15 years after the subgrade widening. Under the limit state, the plastic area of the subgrade and foundation in the foundation is shown in Figure 11. The red part in the figure is the plastic area, which can intuitively show that the soil reaches the range of shear strength of Mohr–Coulomb. It shows the displacement cloud map of the subgrade under the filling limit. Figure 12 shows that the potential sliding surface is roughly circular arc and close to the area of the plastic area from the shallow foundation, which shows that the treatment of the new and old subgrade joints should be paid attention to closely connect and improve the overall stability of the subgrade.

3. Mechanical Response of the Pavement Structure to the Differential Settlement

3.1. Settlement Distribution Form of the Top Surface of the Subgrade. The pavement structure produces additional stress under the action of widening the size of the subgrade differential settlement, and the size of the additional stress is closely related to the settlement curve of the subgrade top surface [12]. Therefore, the mechanical response of the pavement structure to the differential settlement needs to determine the distribution form of the subgrade top surface. The calculation time of the top settlement of the old subgrade is the construction period and 15 years after the work. The previous calculation results show that, under the reconstruction and expansion load, the differential settlement distribution of the old subgrade is a curved basin. The farther the middle line of the old road, the greater the settlement value. The settlement curve of the top surface of the old subgrade is moved below, so that the centre of the old road coincides with the coordinate origin, and is fitted with the quadratic parabolic function (1) [13]. For the subgrade settlement, the calculation time of the width part is 15 years after work, the distribution of the settlement curve on the top surface of the subgrade is basically parabolic, and the

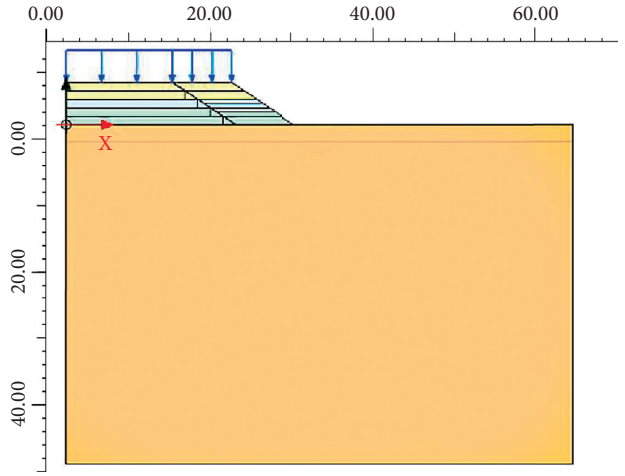

Figure 1: Finite element model schematic diagram.

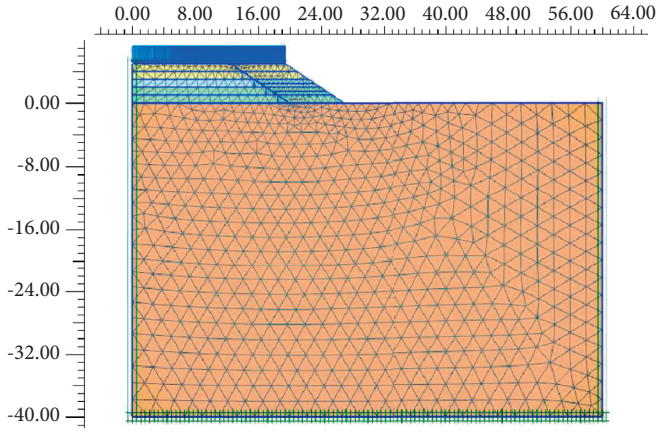

Figure 2: Mesh division model schematic diagram.

Table 1: Subgrade compaction degree.

Fill dig type		Depth below pavement surface (cm)	Compactness (%)
Fill with the subgrade	Road bed	0~30	≥97
	Lower bed	30~120	≥97
	Upper embankment	120~190	≥95
	Lower embankment	Below 190	≥94

Table 2: Calculation parameters of foundation and subgrade.

Solum	γ (kN/m^3)	γ_{sat} (kN/m^3)	e_0	E_s (kN/m^3)	ν	c (kN/m^3)	φ (°)	k (m/day)
Foundation	17.30	19.90	0.707	7500	0.25	11.0	22.5	0.02
District 94	1.83	20.00	0.689	13990	0.25	27.3	35.1	—
District 95	1.88	20.16	0.664	15000	0.25	23.6	39.0	—
District 97	1.97	20.43	0.621	16000	0.25	30.6	35.0	—

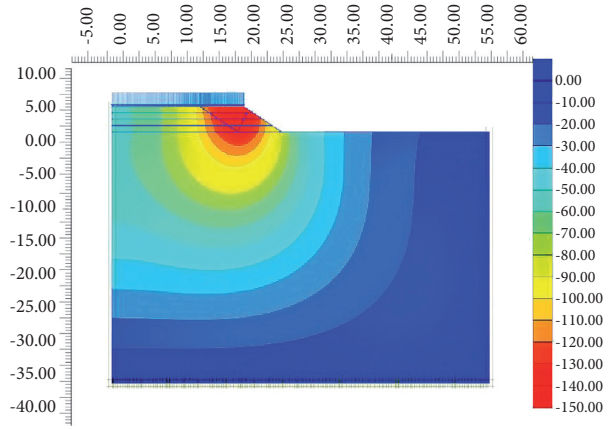

Figure 3: Vertical settlement cloud map.

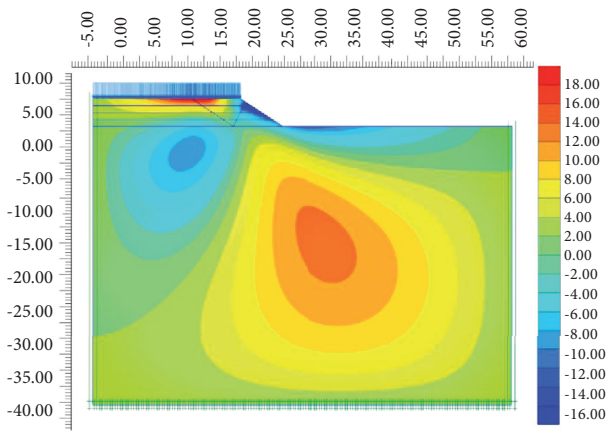

Figure 4: Horizontal displacement cloud map.

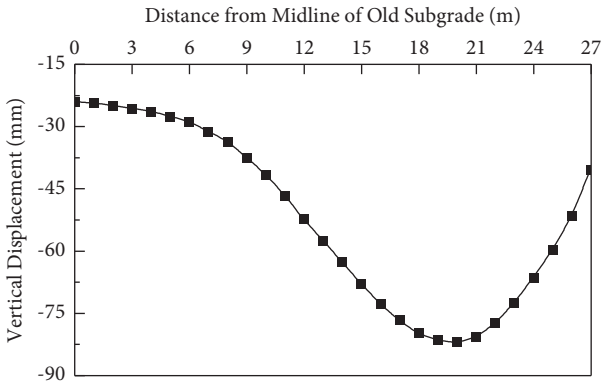

Figure 5: Vertical displacement of ground surface.

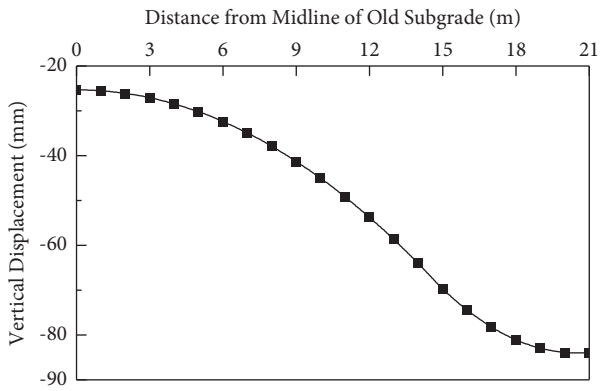

Figure 6: Vertical displacement of subgrade top surface.

coordinate origin is also located in the middle point of the old road. The quadratic function (2) is adopted for fitting. The settlement curve of old and new subgrade is shown in Figure 13:

$$y = -u_1\left(\frac{x}{l_1}\right)^2, \tag{1}$$

where u_1 is the maximum differential settlement of top surface of old subgrade, and l_1 is the distance of the old road shoulder to the center of the old road.

$$y = -u_1 + u_2\left(\frac{1}{l_2}x - \frac{l_1}{l_2}\right)\left(\frac{1}{l_2}x - \frac{l_1}{l_2} - 2\right), \tag{2}$$

where u_2 is the maximum differential settlement value of the top surface of the widened subgrade, and l_2 is the maximum differential settlement to the old and new subgrade splicing.

3.2. Calculation Model and Calculation Parameters. ABAQUS finite element software is used to calculate the impact of differential settlement of old and new roadbed on the pavement in this chapter [14] (Figure 14). According to the actual situation of Ri-Lan Expressway Reconstruction and Widening Project, the thickness of the pavement is 0.84 m. For the finite element model, the model length is 21 m and the width is 0.84 m. The CPE4 unit is selected for the unit type. The following assumptions are used in the numerical simulation calculations.

① The pavement structure is calculated and analysed according to the plane strain problem.

② Each layer of the pavement structure is of continuous homogeneous and isotropic linear elastic materials.

③ The boundary conditions are the vertical displacement applied at the bottom of the model as the settlement fitting function of the subgrade top surface and the left and right boundary horizontal constraints, and the upper boundary is free [15].

The material calculation parameters are calculated according to the pavement structure design documents of Ri-Lan Expressway Reconstruction and Widening Project.

In Table 3 SMA-13 means 3 cm Stone Mastic Asphalt mixture, AK-16 means 4 cm medium grain asphalt concrete, AC-20 means 5 cm medium grain asphalt concrete, and AC-30 means coarse graded bituminous concrete. The parameters of the new pavement structure layer are calculated in Table 4.

3.3. Analysis of the Calculation Results. The pavement material has a high compressive strength and low tensile strength. However, the differential settlement caused by the

Figure 7: Horizontal displacement of ground surface.

Figure 8: Horizontal displacement of subgrade top surface.

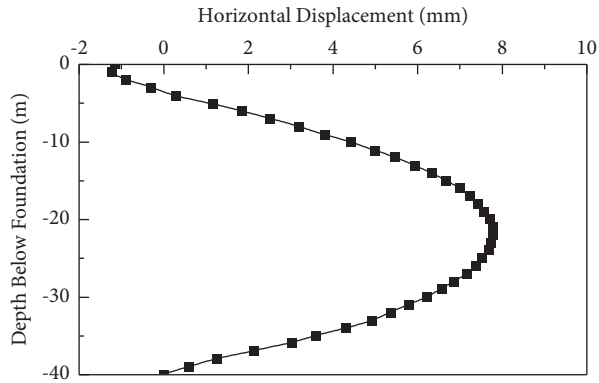

Figure 9: Horizontal displacement at the foot of old roadbed slope.

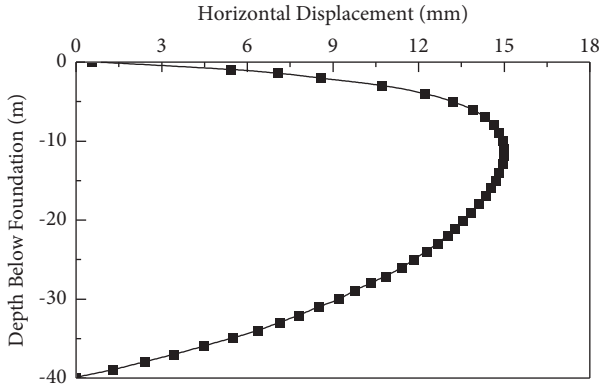

Figure 10: Horizontal displacement at foot of new subgrade slope.

highway reconstruction and expansion causes the pavement structure layer to bear the additional bending tensile stress, and the higher tensile stress will make the pavement crack. In this paper, the formula of subgrade top surface settlement curve fitting is incorporated into the subprogram DISP of ABAQUS to specify the displacement of the boundary nodes under the pavement model and then to calculate the additional stress of each pavement structural layer caused by the difference settlement of subgrade top surface.

The additional stress cloud map of the road surface structure is shown in Figure 15. In the direction of the cross section along the road, the differential settlement is gradually increased. Under the action of differential settlement, the old road surface layer and the new road subbase are in the pulled state, the base part is in the pulled state, and the part is in the pressure state. Drawing the horizontal stress data at the top and the bottom of the surface layer and the curve as shown in Figures 16 and 17, we can find that the tensile stress at the top of the surface layer remains basically unchanged within 12 m from the centre of the old road, then increases slowly, and drops sharply after the peak of the new and old subgrade junction near 13 m, and the compressive stress is within 15 m to 20 m, which is approximately uniform distribution. The stress curve trend at the bottom of the pavement subbase is contrary to the top of the surface layer, and the tensile stress is reached the maximum at the old and new pavement splices.

The maximum tension stress position at the top and the bottom of the bottom base is drawn along the thickness direction as shown in Figures 18 and 19, and the bottom of the bottom of the bottom is required to consider the old pavement surface layer and the base top and the bottom base layer and the new pavement.

4. Proposal of the Subgrade Difference Settlement Control Standard

If the bending tensile capacity of the pavement structure layer shortly after the widening highway is insufficient to resist the additional stress caused by excessive differential settlement, the longitudinal cracks along the highway because the cracks occur in the early operation period called early damage. In this stage, the asphalt pavement periodic traffic load cycle is less and the asphalt is not aging. The bending resistance of the pavement structure layer does not experience fatigue decay. The early damage should be as the control index of the splitting strength of each pavement structural layer [16]. The splitting strength of each layer is shown in Table 5.

The maximum tensile stress of the old pavement surface layer and base structure layer under the action of different differential settlement are shown in Figure 20. It is found that the maximum additional tensile stress of each layer of the pavement structure is basically linear with the differential

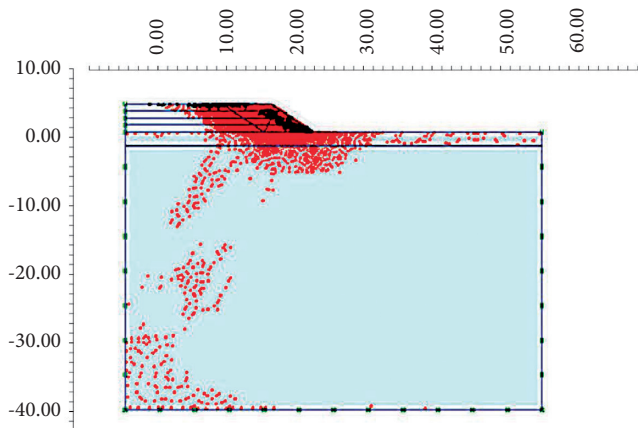

Figure 11: Plastic zone in the limit state.

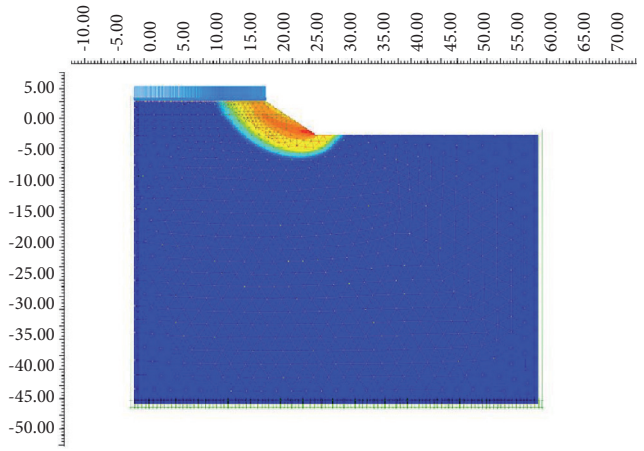

Figure 12: Displacement cloud map in the limit state.

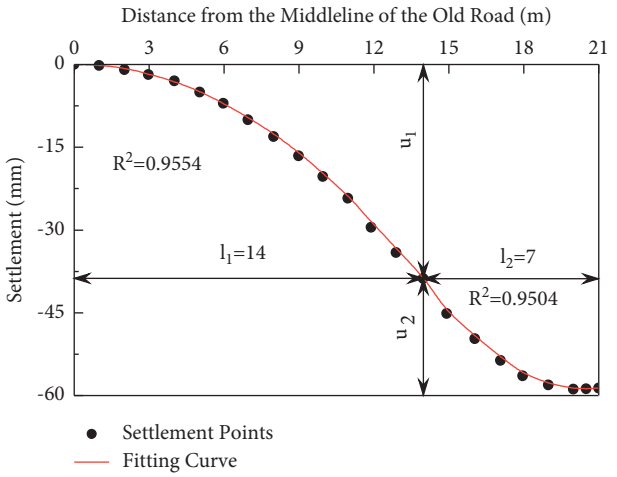

Figure 13: Settlement and fitting curve of the top surface of the subgrade.

settlement, and they show positive correlation. The maximum differential settlement increased from 20 mm to 80 mm, the maximum additional tensile stress along the old road reinforcement to the secondary gravel layer (base) and the old road reinforcement layer from 0.198 MPa to 0.932 MPa, and the maximum tensile stress of the base from 0.102 MPa to 0.532 MPa. The maximum tensile stress of the old base at 80 mm exceeds 0.532 MPa, and the splitting strength is 0.5 MPa. The interpolation method can find that when the differential settlement is 75.2 mm, the splitting strength and the surface layer do not reach the splitting strength of the material. Under the same difference settlement, the old base takes the lead in reaching the splitting strength of the material. To sum up, in order to prevent the early cracking and damage of the old pavement, the differential settlement of the old pavement during the widening construction period and the early operation period should be controlled at 0.54% of the old pavement, which is less than 75.2 mm.

The maximum tensile stress of the new pavement structural layer under different differential settlement is shown in Figure 21, and the new pavement cement-stabilized aggregate layer (base) and low-dose cement-stabilized gravel layer (subbase) are basically positively related to the differential settlement. Under the same differential settlement, the new pavement subbase bears greater tensile stress than the base level, and with the increase of differential settlement, the maximum additional tensile stress change of the subbase is greater. As shown in Table 7, the maximum

Table 3: Calculation parameters of the old pavement structure layer.

Pavement structural layer	Thickness (mm)	Modulus of elasticity (MPa)	Poisson's ratio
Reinforcing layer of road	130	1600	0.25
SMA-13	30	1200	0.25
AK-16	40	1000	0.25
AC-20	50	1100	0.25
AC-30	60	900	0.25
Lime-flyash-stabilized base	350	1400	0.25
Lime flyash soil	180	900	0.35

Table 4: Calculation parameters of the new pavement structure layer.

Pavement structural layer	Thickness (mm)	Modulus of elasticity (MPa)	Poisson's ratio
SMA-13	40	1400	0.25
AC-20	60	1200	0.25
AC-25	80	1000	0.25
ATB-25	100	1000	0.25
Cement-stabilized aggregate	360	1500	0.25
Low dose cement	200	1100	0.25

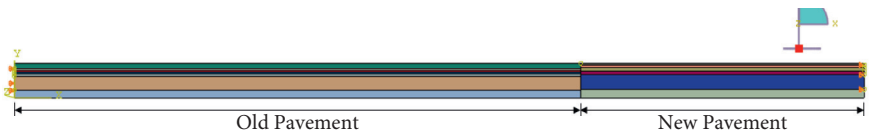

Figure 14: Finite element model of pavement structure.

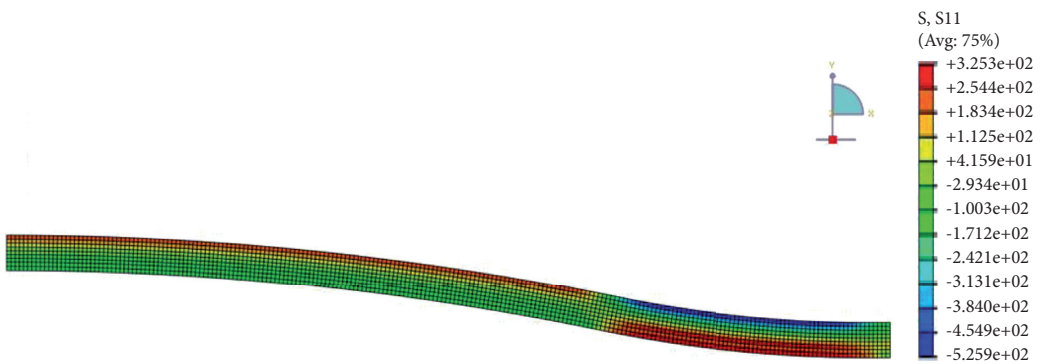

Figure 15: Nephogram of additional stress of pavement structure.

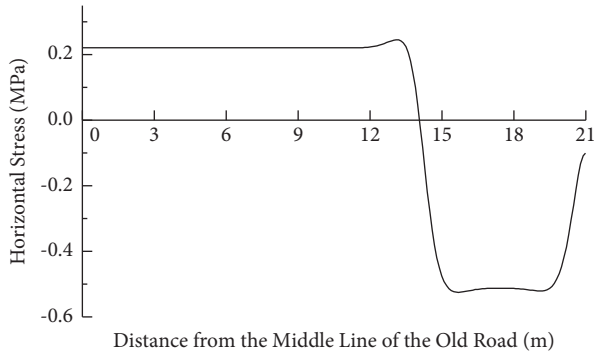

Figure 16: Settlement and fitting curve of the top surface of the subgrade.

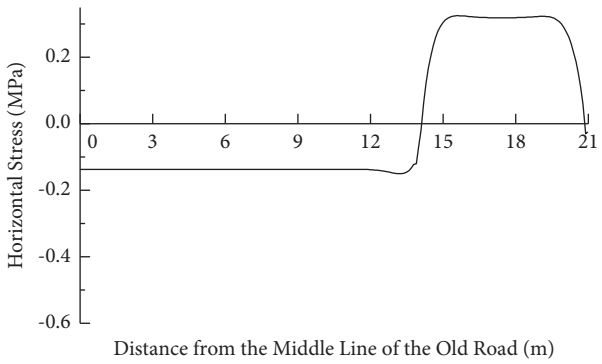

Figure 17: Horizontal stress at the bottom of the subbase.

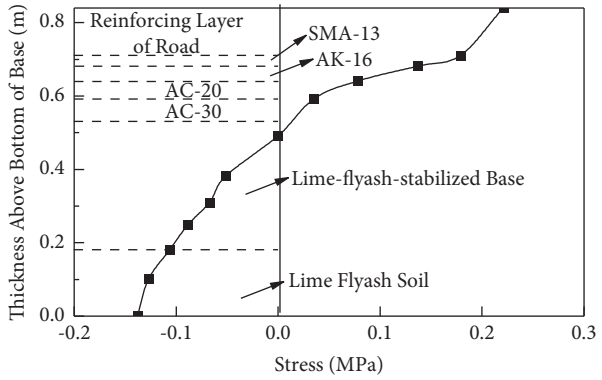

Figure 18: Maximum tensile stress position of surface.

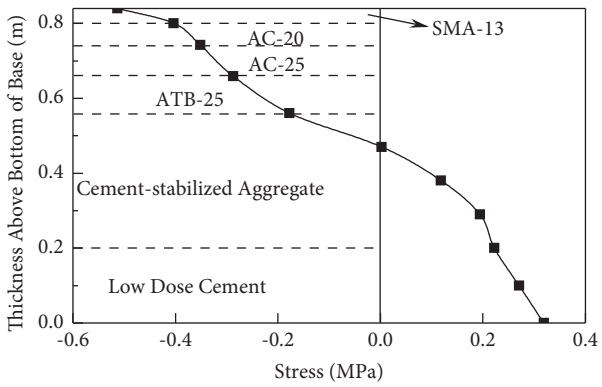

Figure 19: Maximum tensile stress at the bottom of the subbase.

Table 5: Splitting strength of the pavement material.

Old pavement	Splitting strength (MPa)	New pavement	Splitting strength (MPa)
Reinforcing layer of road	1.4	Cement-stabilized aggregate	0.5
SMA-13	1.2	Low dose cement	0.3
AK-16	1.1		
AC-20	1.0		
AC-30	0.7		
Lime-flyash-stabilized base	0.5		

differential settlement increases from 5 mm to 25 mm. The maximum tensile stress of the base layer increases from 0.042 MPa to 0.225 MPa which is up to the splitting strength of the material. The maximum tensile stress of the subbase is increased from 0.068 MPa to 0.321 MPa, and the maximum tensile stress is 0.3 MPa, which is up to the splitting strength

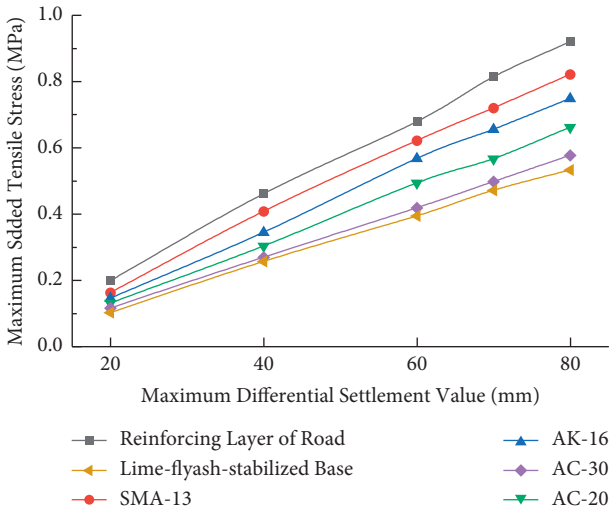

Figure 20: Maximum tensile stress of the old pavement structure layer under different difference settlement.

Table 6: Calculation results of maximum tensile stress of structural layer of the old pavement under different differential settlements (MPa).

Pavement structural layer	Maximum differential settlement (mm)				
	20	40	60	70	80
Reinforcing layer of road	0.198	0.461	0.678	0.814	0.932
SMA-13	0.162	0.407	0.622	0.720	0.821
AK-16	0.145	0.344	0.567	0.655	0.748
AC-20	0.130	0.302	0.493	0.566	0.661
AC-30	0.115	0.269	0.418	0.497	0.577
Lime-flyash-stabilized base	0.102	0.256	0.394	0.471	0.532

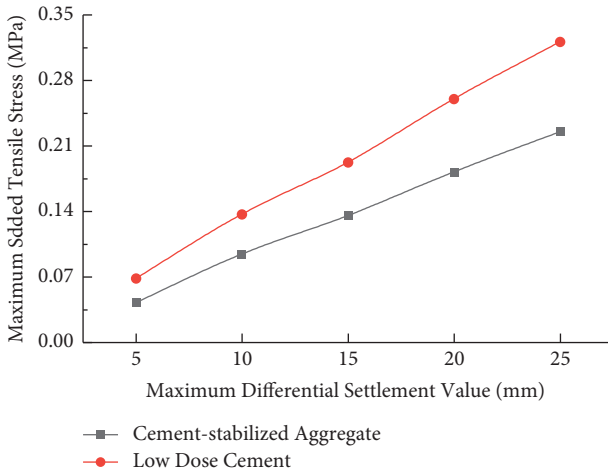

Figure 21: Maximum tensile stress of the new pavement structure layer under different differential settlements.

Table 7: Calculation results of maximum tensile stress of the new pavement structure layer under different differential settlements (MPa).

Pavement structural layer	Maximum differential settlement (mm)				
	5	10	15	20	25
Cement-stabilized aggregate	0.042	0.094	0.135	0.182	0.225
Low dose cement	0.068	0.137	0.192	0.260	0.321

when the differential settlement is 23.4 mm by interpolation. Therefore, to prevent early damage of the new road surface, the differential settlement is less than 23.4 mm, and the horizontal slope rate of the new road surface is 0.33%.

5. Conclusions

This paper discusses the new and old pavement separately. Based on the calculation results of subgrade top settlement, the mechanical response of pavement structure under different differential settlement is analysed through the finite element software, and we determined the differential settlement control standard of pavement structure by considering the splitting strength of materials. The specific conclusions are as follows.

(1) Top settlement curve of the new and old subgrade is fitted by quadratic function by applying the fitting results to the bottom of the pavement for calculation. The results showed that the whole surface of the old pavement is about 4 cm of the upper layer, and the whole bottom layer is about 27 cm of the lower layer.

(2) Under the action of differential settlement, the old pavement base first reached the damage strength, and the new pavement subbase first reached the damage strength. When the material splitting strength is taken as the control index of the new and old pavement, the differential settlement should be less than 23.4 mm (cross-slope rate is 0.33%), and the horizontal slope rate should be less than 75.2 mm (cross-slope rate is 0.54%).

Data Availability

The data used to support the findings of this study are included within the article.

Conflicts of Interest

There are no conflicts of interest regarding the publication of this paper.

Acknowledgments

This work was supported by the National Key Research and Development Project of China (no. 2018YFB1600100), the Natural Science Foundations of China (nos. 51778346 and 52027813), and the Key Research and Development Project of Shandong Province of China (no. 2019GSF111007).

References

[1] T. Yang, L. Li, and G. W. Li, "Research on differential settlement control standard for road bilateral widening project," *Journal of Highway and Transportation Research and Development*, vol. 31, no. 5, pp. 15–20, 2014.

[2] Y. C. Ye, S. Q. Li, and P. Z. Ma, "Study on differential settlement control standard of one-side widening project of Fokai Expressway," *Journal of China and Foreign Highway*, vol. 33, no. 5, pp. 1–4, 2013.

[3] J. H. Zhang, *Research on Deformation Behaviour and Differential Settlement Limitation of Expressway Widening on Soft Soil Foundation*, Southeast University, Nanjing, China, 2006.

[4] Q. S. Zhao, G. S. Zhao, and C. H. Zhang, "Threshold of settlement control for widened Jing-Shi embankments," *Journal of Liaoning Technical University*, vol. 31, no. 1, pp. 69–72, 2012.

[5] J. F. Hua, L. Guo, and H. J. Yu, "Study on subgrade differential Settlement and treatment measures of Changyu Expressway," *Highways*, vol. 66, no. 1, pp. 370–374, 2021.

[6] S. Zhang, *Study on Differential Settlement Characteristic and Control Standards of Subgrade Widening of Yan'an north Transit Line*, Chang'an University, Xi'an, China, 2019.

[7] F. Zhen, X. C. Wang, X. G. Chen, and H. Z. Li, "Controlling criterion of differential settlements after widening expressway," *Journal of Chang'an University (Natural Science Edition)*, vol. 28, no. 5, pp. 10–13, 2008.

[8] H. Q. Liu, G. D. Zeng, and R. H. Ying, "Study on non-uniform settlement index of old road widening after construction," *Highways*, vol. 3, no. 3, pp. 37–39, 2004.

[9] K. Wang, *Research on Deformation Behavior and Control Criterion of Deferential Settlement in Express Highway Widening Project*, Shandong University, Jinan, China, 2018.

[10] J. H. Wang, *Study on Differential Settlement Characteristics and Control Technology of Subgrade in G320 (Quzhou Section) Reconstruction and Expansion Project*, Chang'an University, Xi'an, China, 2017.

[11] X. F. Lu, *Study on Differential Settlement Mechanism and Control Standard of Widening Subgrade of Changyu Expressway*, Harbin Institute of Technology, Harbin, China, 2016.

[12] Y. Yao, J. Ni, and J. Li, "Stress-dependent water retention of granite residual soil and its implications for ground settlement," *Computers and Geotechnics*, vol. 129, Article ID 103835, 2021.

[13] Y. Yao, J. Li, J. Ni, C. Liang, and A. Zhang, "Effects of gravel content and shape on shear behaviour of soil-rock mixture: experiment and DEM modelling," *Computers and Geotechnics*, vol. 141, 2022.

[14] J. H. Zhang, A. S. Zhang, C. Huang, and H. Yu, "Characterising the resilient behaviour of pavement subgrade with construction and demolition waste under Freeze-Thaw cycles," *Journal of Cleaner Production*, vol. 300, 2021.

[15] J. Han and M. A. Gabr, "Numerical analysis of geosynthetic-reinforced and pile-supported earth platforms over soft soil," *Journal of Geotechnical and Geoenvironmental Engineering*, vol. 128, no. 5, pp. 44–53, 2002.

[16] Z. Fu, *Study on the Differential Settlement and Controlling Technology of Expressway Widening Subgrade*, Chang'an University, Xi'an, China, 2007.

Hindawi
Advances in Materials Science and Engineering
Volume 2021, Article ID 9995926, 10 pages
https://doi.org/10.1155/2021/9995926

Research Article

Contribution Modeling on Condition Evaluation of Asphalt Pavement Using Uncertainty Measurement and Entropy Theory

Jue Li,[1] **Hui Wei**,[2] **Yongsheng Yao**,[1] **Xin Hu**,[3] **and Lei Wang**[1]

[1]*College of Traffic & Transportation, Chongqing Jiaotong University, Chongqing 400074, China*
[2]*School of Traffic & Transportation Engineering, Changsha University of Science & Technology, Changsha 410114, China*
[3]*School of Civil Engineering, Central South University of Forestry and Technology, Changsha 410004, China*

Correspondence should be addressed to Hui Wei; wh@csust.edu.cn

Received 18 November 2021; Accepted 8 December 2021; Published 24 December 2021

Academic Editor: Robert Černý

In view of the deficiency that traditional pavement performance evaluation index did not consider the influence of their difference on weight, the grade of the evaluation index also did not take into account intermediate state and the impact of uncertainty on the evaluation results, a determination method of pavement performance evaluation index weight based on entropy theory was developed. The unascertained measurement function of evaluation index was performed by left-half ladder distribution, and unascertained measurement matrix was obtained. The index weight was calculated by minimum entropy theory, and the practicability of this method was verified through a concrete example finally. The results show that there were different weights in different samples, which depended on index measurement function and were the overall characterization of comprehensive measurement of every index. The method which is based on the given weighting factor did not conform to the engineering facts. It was difficult to identify the importance of the pavement performance evaluation index in different samples. The balance of the various indexes is better to be considered in the proposed method, and the comprehensive situation of pavement performance is really reflected, which improves the evaluation of the reliability.

1. Introduction

It is of great sense, value to evaluate the pavement condition in a science and reasoned way for getting more out of the service living of highway structure [1]. In the service process, different diseases come into view as on the asphalt pavement under the heavy loading and changeable environment [2, 3]. For effects of these diseases on pavement performance, different evaluation models and classification methods were adopted in countries all over the world [4]. For instance, the Federal Highway Administration (FHWA) systematically discussed asphalt pavement diseases based on the mechanism of damage generation and severity and classified them into several forms, including crack, settlement, and rut [5]. In China, the pavement maintenance department suggested that there are four main diseases, such as crack, surface loosening, distortion, and so on [6]. Moreover, the relegation of pavement condition decreases the service quality of highway and increases the risk of traffic accidents [7]. Consequently, effective detection and treatment of pavement diseases are essential to sustain the operation of the whole transportation system.

In general, it is very important and meaningful for the sustainability of pavement system to evaluate the health of highway network in vast regions with different terrain and climate [8]. Federal Aviation Administration (FAA) has confirmed that in-time maintenance guided by accurate evaluation model can save up to 75–80% of the cost than that with the relatively poor management [9]. Therefore, pavement condition evaluation is a fundamental part of maintenance decision activity as well as a challenge in pavement engineering [10]. The evaluation of highway condition first appeared with the Present Service Index (PSI) in USA [11]. Mejias and Rushing [12] provided a set of evaluation criteria based on pavement conditions, traffic, and environmental factors through research and calculation, which helped to

reasonably select the optimal cost-benefit ratio of conservation measures. Pantuso et al. [13] introduced an approach to analyze the time sequence of maintenance treatments using the survey data of the falling weight deflectometer (FWD). The purpose of pavement management is to provide a reliable pavement condition evaluation model to realize the optimization process of pavement life and resource allocation [14]. At present, many researches have adopted a simple method to predict the damage condition of pavement performance through the preset classification and weight of each evaluation index [15, 16]. However, this way cannot be applied to characterize the influence of the difference of each evaluation index on the contribution of decision-making results [17]. Moreover, influence factors on pavement condition are many and complicated, and its process involves design, construction, and operation. For example, asphalt pavement is subjected to the repeated action of vehicle load and the alternation of climate and environment [18]. In addition to these external factors, material properties, pavement type, construction quality, and maintenance time sequence also affect the service life of pavement [19, 20]. Therefore, the evaluation of these influencing factors usually requires long-term pavement condition data, and the credibility of the proposed evaluation model is difficult to determine due to the uncertainty of the results.

In recent years, researchers began to employ a variety of mathematical methods in performance evaluation and maintenance decision of asphalt pavement. Fakhri and Shahni Dezfoulian [21] pointed out that the limitations of uncertain factors and human effects were inevitable in the evaluation process, and the Artificial Neural Networks (ANNs) were applied to establish the relation between testing data and pavement surface distresses. Despite this attempt, these models did not present the determination of subjective influences and their weight on pavement evaluation. In another effort, Bianchini et al. [22], based on the principal-component analysis (PCA), tried to determine the variance contributions of each distresses on the condition assessment of asphalt pavement. This method could capture the representative variance as the comprehensive evaluation value to avoid possible misevaluation of subjective factors and redundant information. In the pavement management, the reliability and weight of testing data represent a concern because of the difficulty of directly evaluating the pavement condition. Elhadidy et al. [23] established a simply decision-making model to associate international roughness index (IRI) and pavement condition index (PCI). The multi-objective decision-making evaluation to classify the contributions of PCI, running quality index (RQI), rutting depth index RDI, and antislide performance index (SRI), exploiting the radar map of entropy weight, was also investigated by Yao et al. [24]. Their algorithm was tested to be simple and have strong practicability. Nevertheless, the further study needs to be carried out since the selection of evaluation function lacks relevant theoretical basis only using simple geometric average. Sun and Gu [25] provided a new idea for the selection of maintenance countermeasures that the method of multiphase fuzzy statistics was applied to identify the pavement damage and the pavement smoothness, which was related to the project prioritization. However, its applicability was still limited since this evaluation method was derived from the experience of engineering experts in Beijing. Therefore, due to different climates and pavement surface types in each region, contribution models for pavement surface evaluation need to be recalibrated using local data, including weights for each factor.

The weight of evaluation parameters is viewed as the relative importance in assessing the pavement performance and identifying the prioritize projects for the overall pavement maintenance [26]. Meanwhile, its weighted average operation can describe the quantitative distribution of contributions of different aspects of the tested object through mathematical tools [27]. The application of analytic hierarchy process [28], fuzzy mathematics [29], genetic algorithm [30], and grey system [31] has been proved to improve the evaluation results of pavement condition. However, the determination of the weight has not been fully solved that the essential attribute of the index weight cannot be reflected, resulting in the deviation between the evaluation grade and subjective feeling. Attention should be paid to the differences in the application of rating results considering different regions and climates.

In view of the above issues, the objective of this paper is to propose a calculable method to determine the contributions of condition evaluation parameters based on the unascertained measure and minimum entropy theory. This approach takes into account the difference of each index, the intermediate state of evaluation index classification, and the uncertainty of influencing factors. One case study of a highway in Hunan province is used to illustrate the method through the collected data including PCI, RQI, RDI, and SRI.

2. Methodology

Figure 1 illustrates the methodology of the research, which determines the reasonable weight of evaluation factors of pavement condition through steps, based on unascertained measure and minimum entropy theory.

2.1. Evaluation Indicators. The research and application of engineering structure reliability theory is one of the effective ways to solve the problems of uncertain structure analysis and design. Pavement structure is a huge and complex system engineering. There are many factors that affect pavement condition, and these factors have a lot of uncertain information, which have a great influence on pavement condition evaluation.

In China, the deterministic evaluation method of given weight is adopted by traffic management departments. Two evaluation parameters are proposed, including maintenance quality indicator (MQI) and pavement quality index (PQI). These indexes can be calculated, respectively, by

$$\mathrm{MQI} = w_P \mathrm{PQI} + w_S \mathrm{SCI} + w_B \mathrm{BCI} + w_T \mathrm{TCI}, \quad (1)$$

$$\mathrm{PQI} = w'_P\ \mathrm{PCI} + w'_R\ \mathrm{RQI} + w'_R\ \mathrm{RDI} + w'_S\ \mathrm{SRI}, \quad (2)$$

where w_p, w_s, w_B, and w_T are, respectively the weights of the PQI, the subgrade condition index (SCI), the bridge (tunnel,

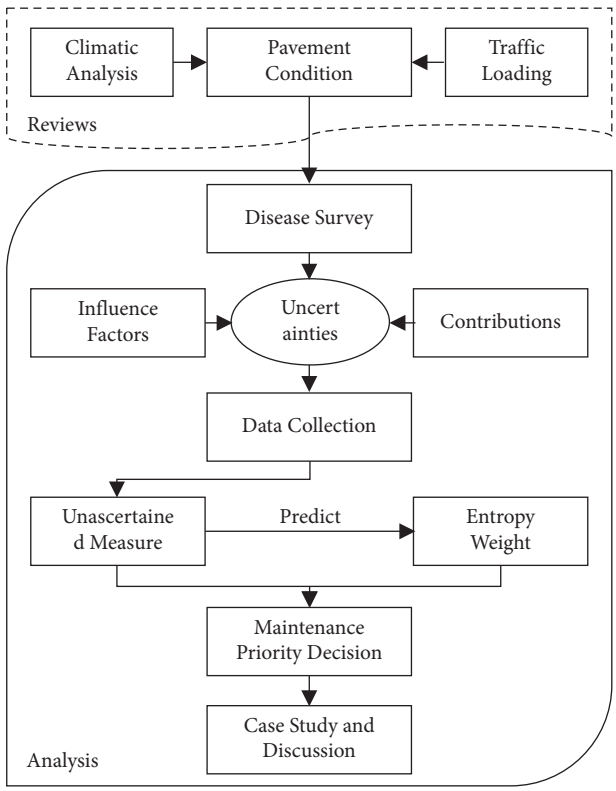

Figure 1: Flow diagram of study methodology.

culvert) condition index (BCI), and the traffic-facility condition index (TCI) in the MQI evaluation, respectively; w_p', w_s', w_B', and w_T' are, respectively, the weights of PCI, RQI, RDI, and SRI in the PQI evaluation.

The above method assumes that the calculated weight of the pavement condition evaluation index is constant. For the calculation of MQI, w_p is 0.7, w_s is 0.08, w_B is 0.12, and w_T is 0.10. Although it is simple and easy to operate, the evaluation process does not consider the impact of the difference of evaluation indexes on the weight, nor does the classification of evaluation indexes consider the intermediate state, and there is ambiguity in the characteristics and categories of pavement conditions. Therefore, the credibility of the evaluation cannot be known because a large number of uncertain factors may be ignored to cause completely wrong evaluation results. These issues will severely mislead the maintenance management system to guide the timely and reasonable pavement maintenance process.

2.2. Data Collection. Pavement condition refers to the damage degree and service level of pavement under the long-term combined action of load and environment. Under different pavement structure composition, material ratio, climatic conditions, and traffic load, the main characteristics and severity of the disease are different, resulting in a great difference in the attenuation of pavement condition, which will also determine the probability distribution characteristics of the pavement condition evaluation index parameters.

In this study, the pavement diseases of several expressways in operation in Hunan province were investigated and analyzed by means of laser 3D intelligent pavement inspection vehicle and manual investigation. These road segments are from plain microknoll area, mountain heavy hilly area, or typical mountain area, respectively. Due to the wide area involved and the long opening time, the cases studied are representative in terms of engineering geological conditions, traffic load, pavement structure, pavement material properties, and so on. Therefore, the data acquisition results can reflect the influence of different conditions on the probability distribution of pavement condition evaluation indexes.

2.3. Uncertainty Measurement Theory. In recent years, unascertained measure theory has been widely used in slope stability evaluation, tailings dam, and tunnel safety evaluation. As a mathematical method to study unascertained information, unascertained measure theory can quantitatively analyze the unascertained size or unascertained state of the evaluation object, which can avoid the subjectivity of evaluators and the limitations caused by other mathematical methods and improve the scientificity and practicability of evaluation.

It supposes n groups of objects to be evaluated, such as $x_1, x_2, x_3, \ldots, x_n$, which constitute the domain U, also known as the evaluation object space. For a single evaluation object x_n, suppose there are m test indicators $D_1, D_2, D_3, \ldots, D_m$. The evaluation index space can be represented by $D = \{D_1, D_2, D_3, \ldots, D_m\}$. X_{ij} represents the measured value of evaluation object x_i on evaluation index D_j. F is the property space in the U, representing the degree to which x has a certain property (or state) to be evaluated.

If the measured value x_{ij} belongs to the kth evaluation grade C_k, $\mu_{ijk} = \mu(x_{ij} \in C_k)$ can be expressed. μ satisfies $0 \le \mu(x_{ij} \in C_k) \le 1$. Meanwhile, μ is defined as unascertained measure according to additivity and normalization criteria. Measure evaluation matrix of single index $[\mu_{ijk}]_{m\times p}$, as follows:

$$\left(\mu_{ijk}\right)_{m\times p} = \begin{bmatrix} \mu_{i11} & \mu_{i12} & \cdots & \mu_{i1p} \\ \mu_{i21} & \mu_{i22} & \cdots & \mu_{i2p} \\ \cdots & \cdots & \cdots & \cdots \\ \mu_{im1} & \mu_{im2} & \cdots & \mu_{imp} \end{bmatrix}. \quad (3)$$

If there are k kinds of specific properties in the property space F, k-1 equal or nonequal points (a) can be inserted into the distribution interval of measured values. It is assumed that the measured value x_{ij} is at the evaluation level C_i, and its position is to the left of the equinox point a_i. When the measured value x_{ij} changes from left to right (i.e., from a_i to a_{i+1}), the degree of the measured value in the evaluation level C_i gradually weakens. When the measured value changes to a_{i+1}, the degree of the measured value in the evaluation grade C_i decreases to 0. At this point, when the measured value changes from a_i to a_{i+1}, the degree of the measured value x_{ij} in the evaluation grade C_i increases from

0 to 1. Therefore, the degree to which the measured value is in a certain evaluation level is within the interval of [0, 1].

In this study, unascertained measure function was used to characterize the unascertained state of pavement condition evaluation indexes in different evaluation grades. There are four commonly used unconfirmed measure functions, including sinusoidal distribution, quadratic parabolic distribution, left-half trapezoidal distribution, and S-type distribution, as shown in Figure 2. In pavement engineering, the condition evaluation index adopts the evaluation method of point grade, as shown in Table 1. In order to facilitate management and data analysis, this paper adopts the left-half trapezoidal distribution for research, as shown in (4). Figure 3 shows the functional relationship between pavement condition evaluation indexes and unascertained measures.

$$\mu(x) = \begin{cases} 0, & x \le a, \\ \dfrac{x-a}{b-a}, & a < x \le b, \\ 1, & x > b. \end{cases} \tag{4}$$

2.4. Determination of Index Weight. According to the principle of minimum entropy, it is assumed that a regression model $P(x(—))$ contains N variables obtained through measurement; that is, $x(—) = \{x_1, x_2, \ldots, x_N\}$. These variables may be the main variables reflecting the characteristics of the system, and there may be some internal correlation. Then, the variables in the study set can be combined to form 2^N-2 subsets. Each subset S_i constitutes a submodel of probability density distribution function; namely, $P_S(\mathrm{x}(—)_{Si}) = P(\mathrm{x}(—)_{Si})$. Therefore, the contribution rate of each variable to the system can be calculated by studying the explanatory degree of each submodel to the system. Furthermore, this study can determine the main variables and their weight values in the prediction system.

The Logit model is used to associate the responses between variables in each submodel, as shown in (5). The binary result "1" means that the variable is associated with the goal decision result, and "0" means that the variable is not associated with the goal decision result. The coefficient β_i is obtained by fitting the measured variable data through maximum likelihood estimation.

$$\frac{R(\overline{x}) = \left[\exp\left(\sum_{i=1}^{N} \beta_i x_i\right)\right]}{\left[1 + \exp\left(\sum_{i=1}^{N} \beta_i x_i\right)\right]}. \tag{5}$$

Normalization of (5) can obtain the response probability distribution function containing a given subset of all variables, as shown in (6) and (7). The parameter Z is a normalized constant and can be obtained by fitting functions. Therefore, the minimum entropy of the corresponding submodel is shown in (8).

$$\frac{P(\overline{x}) = 1/Z\left[\exp\left(\sum_{i=1}^{N} \beta_i x_i\right)\right]}{\left[1 + \exp\left(\sum_{i=1}^{N} \beta_i x_i\right)\right]}, \tag{6}$$

$$Z = \sum_{\overline{x}} \left\{ \frac{\left[\exp\left(\sum_{i=1}^{N} \beta_i x_i\right)\right]}{\left[1 + \exp\left(\sum_{i=1}^{N} \beta_i x_i\right)\right]} \right\}, \tag{7}$$

$$S(P_S) = -\sum_{i=1}^{N} P\left(\overline{x}_{s_i}\right) \ln P\left(\overline{x}_{s_i}\right). \tag{8}$$

All submodels are sorted according to the entropy value, and the effective submodel is determined according to some decision rules, namely, the first-m submodels with the lowest entropy value. At the same time, based on these models, the probability of the occurrence of each variable is calculated to determine its contribution rate to the system. According to model analysis, the higher the probability, the greater the contribution of this variable to the system. Therefore, this study can determine the main variables and relative weights of the system through the minimum entropy theory.

2.5. Calculation Procedure

(1) Determine the unascertained measure function according to the classification standard of each index.

(2) According to the unascertained measure function, the unascertained measure value of each index in the evaluation object is solved to form a single-index measure matrix.

(3) The distribution of index weight represents the importance of the index in the whole system. According to the above calculation theory, a simplified method was adopted in this study; that is, parameter w_j was used to characterize the relative importance of measurement index D_j compared with other indexes. w_j is called the weight of index D_j, which is in the range of 0–1, and the sum is 1. The weight vector of this indicator is represented as $\{w_1, w_2, \ldots w_n\}$. Therefore, the information entropy determined by the unascertained measure μ_{jik} can be expressed as follows:

$$\begin{aligned} H_j &= \sum_{i=1}^{k} \mu_{jik} \lg \mu_{jik}, \\ v_j &= 1 + \frac{1}{\lg k} \sum_{i=1}^{k} \mu_{jik} \lg \mu_{jik}, \\ w_j &= \frac{v_j}{\sum_{i=1}^{n} v_i}. \end{aligned} \tag{9}$$

3. Case Study

The detection data of asphalt pavement came from a highway in Hunan province, taking it as an example. The highway was built in 2000, and its maximum design load

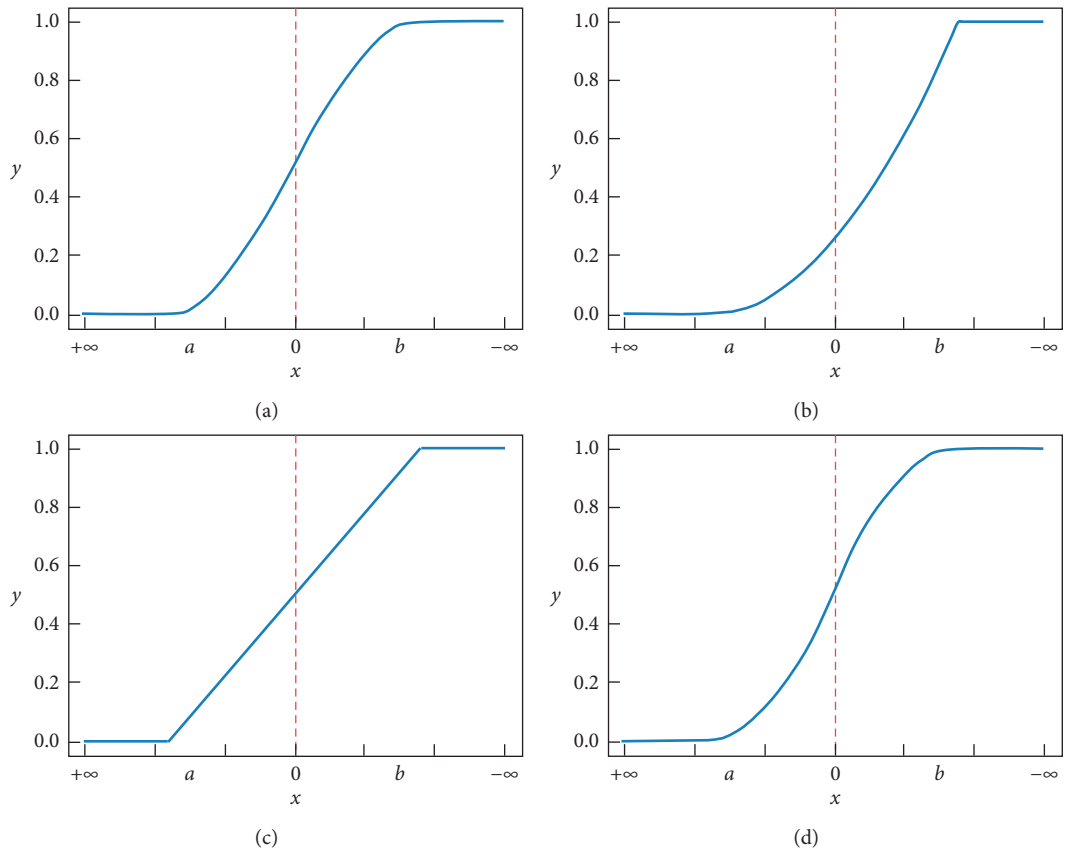

Figure 2: Distribution of unconfirmed measure functions. (a) Sinusoidal curve; (b) quadratic parabolic curve; (c) left-half trapezoidal curve; and (d) S-type curve.

Table 1: Evaluation standard of highway technical condition.

Evaluation level	Excellent	Good	Medium	Inferior	Poor
Range of index	≥90	80–90	70–80	60–70	< 60

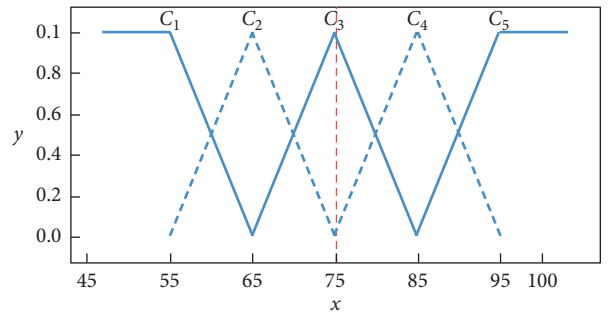

Figure 3: Unascertained measurement function of evaluation index in PQI and MQI.

times is 6.581×10^7. The climate is humid and hot in southern China. Table 2 presents the design pavement structure.

Using the above method, the weight of different evaluation indexes in PQI evaluation of pavement condition was investigated. Each sample represents the 1000 m section as the basic assessment unit. The pavement condition evaluation results are shown in Figure 4. The subindexes of pavement condition were collected according to China's highway technical condition assessment standard.

4. Results and Discussion

4.1. Analysis of Uncertainty Measurement. According to the steps in Section 2.5, the unascertained measure values of the four conditions' rating indicators are solved. Using the

Table 2: Main parts of pavement structure.

Layer	Thickness (cm)	Material
Upper surface course	5	SBS modified AK-16I asphalt mixture
Middle surface course	6	SBS modified AK-20I asphalt mixture
Lower surface course	7	AC-25I asphalt mixture
Base course	40	6% cement stabilized macadam
Subbase course	20	4% cement stabilized macadam

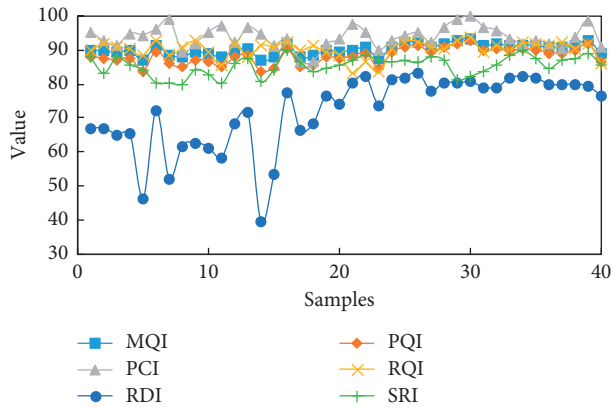

Figure 4: Collected data of pavement condition evaluation.

function relation in (4), the unascertained measure matrices of PCI, RQI, RDI, and SRI with single index were established as follows. According to (9) and (10), the weights of each index are 0.3253, 0.1856, 0.2316, and 0.2575, respectively. Complete calculation results are shown in Table 3.

$$\begin{aligned} \text{PCI} &= [\,0 \;\; 0 \;\; 0 \;\; 0 \;\; 1\,], \\ \text{RQI} &= [\,0 \;\; 0 \;\; 0 \;\; 0.529 \;\; 0.471\,], \\ \text{RDI} &= [\,0 \;\; 0.825 \;\; 0.175 \;\; 0 \;\; 0\,], \\ \text{SRI} &= [\,0 \;\; 0 \;\; 0 \;\; 0.715 \;\; 0.285\,]. \end{aligned} \tag{10}$$

Figure 5 shows the proportion radar diagram of PCI, RQI, RDI, and SRI. The results show that for different samples, the importance of evaluation indexes in the evaluation system is different. The single indicator measure covers C_1, C_2, C_3, C_4, and C_5, namely, all levels. In the single indicator measure of PCI, C_4 and C_5 play a leading role, and the proportion of C_5 is about 0.8. In the single indicator measure of RQI, C_3, C_4, and C_5 play a leading role, with C_4 and C_5 in the majority, accounting for about 0.4 and 0.55 on average. The single index measures C_1, C_2, C_3, and C_4 of RDI play a leading role, and the proportion of C_3 is much higher than that of C_1, C_2, and C_4, indicating that the status of subindex RDI in this sample group is poor, and most of the RDI evaluation grade is medium. Therefore, attention should be paid when determining the index weight. The single index measures C_3 and C_4 of SRI play a leading role, accounting for about 0.3 and 0.6 on average. The subindex SRI in this sample group is not in good condition, and most of SRI is rated as medium or good, so its importance in the whole evaluation system should also be reflected.

4.2. Comparison with Standard Method. Figure 6 shows the weight representation of different subindexes in PQI evaluation. The results show that it is particularly important to determine the weight of indicators to accurately evaluate the pavement condition. Each index in different samples has different weight, which depends on the measure function of each index and is the overall representation of the comprehensive measure of each index.

For the current assessment standard in China, the evaluation model is suggested by fixed weights of each index, which is 0.35, 0.4, 0.15, and 0.1, respectively. Taking sample 5 as an example, the on-site investigation of this section is shown in Figure 7. Rut is a typical disease of this section. However, the weight of rut depth index in the current standard is only 0.15, so the importance of rut typical disease is not reflected, and there is a deviation from subjective feeling, which is obviously not in line with reality.

The weight information entropy weight method of pavement condition index proposed in this study can overcome the disadvantages of the traditional pavement condition evaluation method based on given weight without considering the influence of the differences of each index on the weight. It also solves the problems of

Table 3: Results of weights of each evaluation index.

Sample	v_{PCI}	v_{RQI}	v_{RDI}	v_{SRI}	w_{PCI}	w_{RQI}	w_{RDI}	w_{SRI}
1	1.0000	0.5704	0.7119	0.7916	0.3253	0.1856	0.2316	0.2575
2	0.6612	0.6226	0.6917	0.7100	0.2462	0.2318	0.2576	0.2644
3	0.5973	0.5853	0.9681	0.7854	0.2034	0.1993	0.3297	0.2675
4	0.9710	0.5700	0.9367	0.9522	0.2831	0.1662	0.2731	0.2776
5	0.8767	0.6001	1.0000	0.8440	0.2640	0.1807	0.3011	0.2542
6	1.0000	0.6823	0.6316	0.5714	0.3466	0.2365	0.2189	0.1980
7	1.0000	0.5893	1.0000	0.5704	0.3165	0.1865	0.3165	0.1805
8	0.5711	0.5751	0.6082	0.5693	0.2458	0.2475	0.2617	0.2450
9	0.6226	0.6687	0.6612	0.8456	0.2225	0.2390	0.2363	0.3022
10	1.0000	0.5732	0.5883	0.6857	0.3512	0.2013	0.2066	0.2408
11	1.0000	0.8573	0.6105	0.5697	0.3292	0.2822	0.2010	0.1876
12	0.6316	0.6231	0.6096	0.9414	0.2251	0.2221	0.2173	0.3355
13	1.0000	0.6220	0.6096	0.8221	0.3275	0.2037	0.1996	0.2692
14	0.8937	0.5955	1.0000	0.5740	0.2918	0.1944	0.3265	0.1874
15	0.5966	0.5823	1.0000	0.8456	0.1972	0.1925	0.3306	0.2796
16	0.7320	0.6562	0.6627	0.5504	0.2814	0.2522	0.2548	0.2116
17	0.7177	0.5693	0.7576	0.9041	0.2434	0.1931	0.2569	0.3066
18	0.7128	0.5874	0.6087	0.7623	0.2669	0.2199	0.2279	0.2854
19	0.6134	0.5744	0.7299	0.9343	0.2151	0.2014	0.2559	0.3276
20	0.6988	0.5902	0.8253	0.9629	0.2271	0.1918	0.2682	0.3129
21	1.0000	0.7207	0.5694	0.8551	0.3179	0.2291	0.1810	0.2719
22	1.0000	0.7299	0.6382	0.7188	0.3239	0.2365	0.2067	0.2329
23	0.5696	0.7417	0.7696	0.8660	0.1933	0.2517	0.2611	0.2939
24	0.6758	0.5700	0.5842	0.8865	0.2488	0.2098	0.2151	0.3263
25	0.8314	0.6562	0.6163	0.8683	0.2797	0.2208	0.2074	0.2921
26	1.0000	0.6520	0.7217	0.9106	0.3045	0.1985	0.2197	0.2773
27	0.6420	0.5826	0.6270	0.7685	0.2450	0.2224	0.2393	0.2933
28	1.0000	0.5712	0.5721	0.8520	0.3339	0.1907	0.1910	0.2844
29	1.0000	0.6790	0.5697	0.5973	0.3514	0.2386	0.2002	0.2099
30	1.0000	0.8035	0.5737	0.6401	0.3314	0.2663	0.1901	0.2121
31	1.0000	0.5758	0.5831	0.7796	0.3403	0.1959	0.1984	0.2653
32	1.0000	0.5947	0.5829	0.9455	0.3202	0.1904	0.1866	0.3027
33	0.7341	0.5696	0.6042	0.7465	0.2766	0.2146	0.2276	0.2812
34	0.6158	0.6328	0.6407	0.5913	0.2483	0.2551	0.2583	0.2384
35	0.6695	0.6051	0.6068	0.8053	0.2492	0.2252	0.2259	0.2997
36	0.6184	0.5947	0.5694	0.9016	0.2304	0.2216	0.2121	0.3359
37	0.5713	0.6382	0.5710	0.8488	0.2173	0.2427	0.2172	0.3228
38	0.7671	0.5749	0.5693	0.8246	0.2804	0.2101	0.2081	0.3014
39	1.0000	0.6042	0.5783	0.6669	0.3509	0.2121	0.2030	0.2340
40	0.5773	0.7576	0.7374	0.9516	0.1909	0.2505	0.2439	0.3147

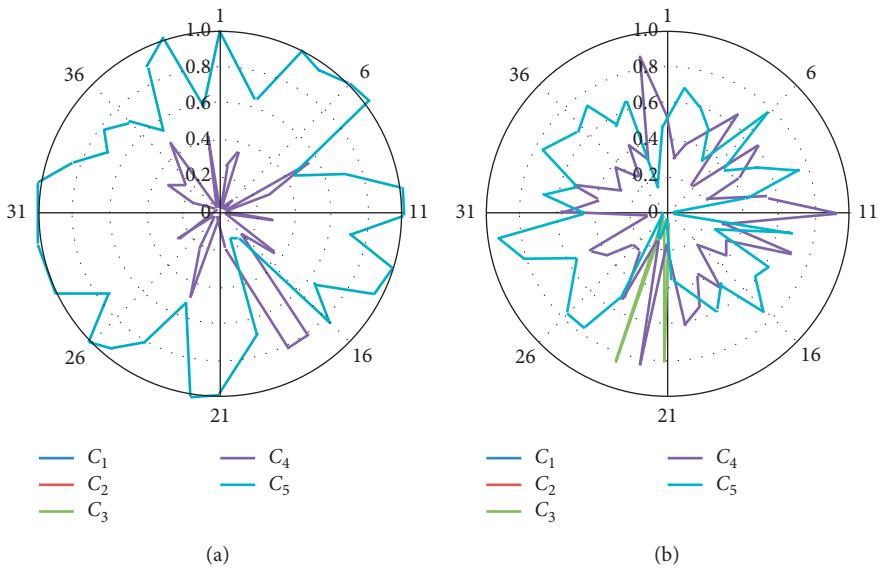

Figure 5: Continued.

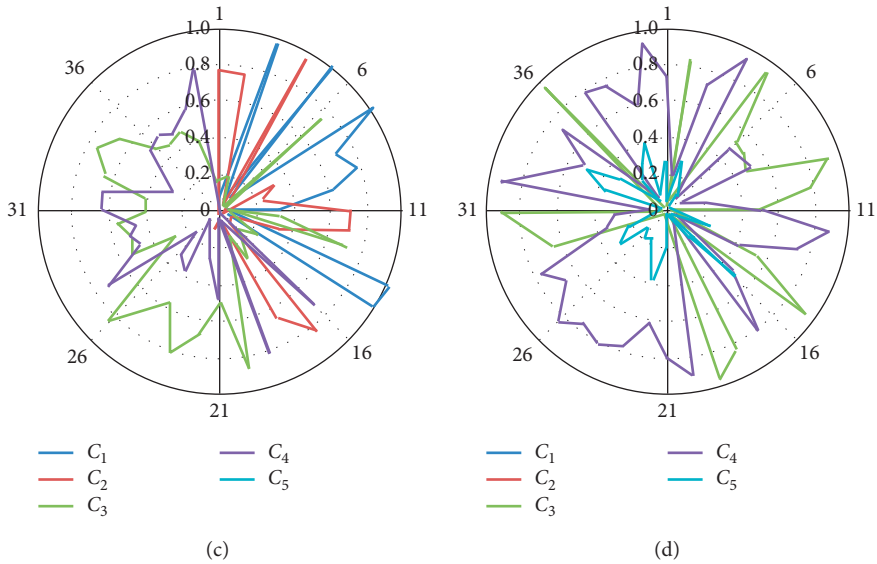

Figure 5: Measure characterization of single index. (a) PCI. (b) RQI. (c) RDI. and (d) SRI.

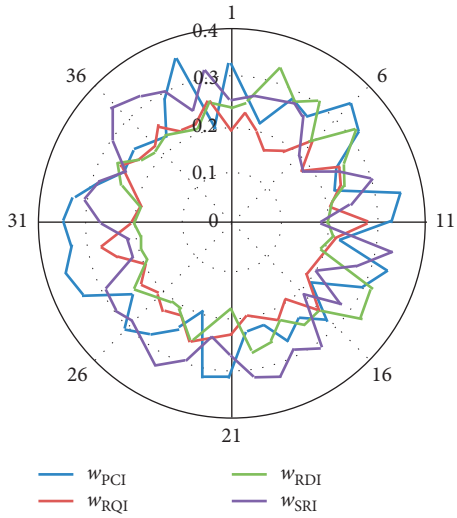

Figure 6: Weight characterization of pavement condition evaluation index.

Figure 7: Result of the rutting survey at sample 5.

not considering the intermediate state in the evaluation index grading and the influence of the uncertainty of the influencing factors on the evaluation results, which improves the credibility of the evaluation.

5. Conclusions

Unascertained measure and minimum entropy theory were introduced to study the determination method of weight information entropy of pavement condition evaluation index. The main findings of this study are as follows.

(1) There are many uncertainties and fuzziness in the process of pavement condition evaluation. The unascertained measure function is used to represent the unascertained state of each index in the grades of excellent, good, medium, secondary and poor condition evaluation, and the segmentation "order" of evaluation space is realized.

(2) For the weight of each evaluation indicator, the principle of minimum entropy analysis was applied to reduce the influence of subjective factors. The calculated result could objectively and comprehensively describe the importance of evaluation indicators and the actual situation of pavement condition.

(3) The application of fixed weight in the Chinese standard is unsuitable and difficult to identify the grade differences of pavement condition in different highway. Based on the case study, it was proved that the proposed method improved the comparability and reliability of condition evaluation for multiple pavement network, considering the unascertained measure and alterable weight of these contributions.

Data Availability

The testing data used to support the findings of this study are included within the article.

Conflicts of Interest

The authors declare that they have no conflicts of interest regarding the publication of this paper.

Acknowledgments

This research was funded by the National Natural Science Foundation of China (Grant no. 51908562); the Standardization Project of Hunan Province; the Youth Scientific Research Foundation, Central South University of Forestry and Technology (Grant no. QJ2018008B); the Research Foundation of Education Bureau of Hunan Province, China (Grant no. 19B581); the Natural Science Foundation of Hunan Province, China (Grant no. 2020JJ5987); the Natural Science Foundation of Chongqing, China (Grant no. cstc2018jcyjAX0640); and the Scientific Research Foundation for the Talent Introduction of the Central South University of Forestry Science and Technology (Grant no. 2019YJ033).

References

[1] M. M. Rahman, M. M. Uddin, and S. L. Gassman, "Pavement performance evaluation models for South Carolina," *KSCE Journal of Civil Engineering*, vol. 21, no. 7, pp. 2695–2706, 2017.

[2] B. S. Underwood, "A method to select general circulation models for pavement performance evaluation," *International Journal of Pavement Engineering*, vol. 22, no. 2, pp. 134–146, 2021.

[3] Y. Yao, J. Ni, and J. Li, "Stress-dependent water retention of granite residual soil and its implications for ground settlement," *Computers and Geotechnics*, vol. 129, Article ID 103835, 2021.

[4] G. Loprencipe and P. Zoccali, "Comparison of methods for evaluating airport pavement roughness," *International Journal of Pavement Engineering*, vol. 20, no. 7, pp. 782–791, 2019.

[5] A. Ali, H. Dhasmana, K. Hossain, and A. Hussein, "Modeling pavement performance indices in harsh climate regions," *Journal of Transportation Engineering, Part B: Pavements*, vol. 147, no. 4, Article ID 04021049, 2021.

[6] M. Huang, Q. Dong, F. Ni, and L. Wang, "LCA and LCCA based multi-objective optimization of pavement maintenance," *Journal of Cleaner Production*, vol. 283, Article ID 124583, 2021.

[7] D. Deme, "A review on effect of pavement surface failure on road traffic accident," *American international journal of sciences and engineering research*, vol. 3, no. 1, pp. 14–19, 2020.

[8] Y. U. Shah, S. S. Jain, and M. Parida, "Evaluation of prioritization methods for effective pavement maintenance of urban roads," *International Journal of Pavement Engineering*, vol. 15, no. 3, pp. 238–250, 2014.

[9] V. Vyas, A. P. Singh, and A. Srivastava, "Entropy-based fuzzy SWOT decision-making for condition assessment of airfield pavements," *International Journal of Pavement Engineering*, vol. 22, no. 10, pp. 1226–1237, 2021.

[10] C. Torres-Machi, A. Osorio-Lird, A. Chamorro, C. Videla, S. L. Tighe, and C. Mourgues, "Impact of environmental assessment and budgetary restrictions in pavement maintenance decisions: application to an urban network," *Transportation Research Part D: Transport and Environment*, vol. 59, pp. 192–204, 2018.

[11] American Association of State Highway and Transportation Officials, *AASHTO guide for design of pavement structures*, Vol. 1, American Association of State Highway and Transportation Officials, , Washington, DC, USA, 1986.

[12] M. Mejias and J. F. Rushing, "Performance evaluation of military airfield pavement drainage layers," *International Journal of Pavement Research and Technology*, vol. 4, p. 365, 2011.

[13] A. Pantuso, G. Loprencipe, G. Bonin, and B. B. Teltayev, "Analysis of pavement condition survey data for effective implementation of a network level pavement management program for Kazakhstan," *Sustainability*, vol. 11, no. 3, p. 901, 2019.

[14] S. Yoon, K. Kang, Y. Yoon, M. Hastak, and R. Ji, "Systematic decision-making process for composite pavement maintenance," *Journal of Construction Engineering and Management*, vol. 144, no. 6, Article ID 04018044, 2018.

[15] C. Torres-Machi, F. Nasir, J. Achebe, R. Saari, and S. L. Tighe, "Sustainability evaluation of pavement technologies through multicriteria decision techniques," *Journal of Infrastructure Systems*, vol. 25, no. 3, Article ID 04019023, 2019.

[16] S. Ahmed, P. Vedagiri, and K. V. Krishna Rao, "Prioritization of pavement maintenance sections using objective based Analytic Hierarchy Process," *International Journal of Pavement Research and Technology*, vol. 10, no. 2, pp. 158–170, 2017.

[17] Y. Zhang and J. P. Mohsen, "A project-based sustainability rating tool for pavement maintenance," *Engineering*, vol. 4, no. 2, pp. 200–208, 2018.

[18] J. Peng, J. Zhang, J. Li, Y. Yao, and A. Zhang, "Modeling humidity and stress-dependent subgrade soils in flexible pavements," *Computers and Geotechnics*, vol. 120, Article ID 103413, 2020.

[19] J. Li, J. Zhang, G. Qian, J. Zheng, and Y. Zhang, "Three-dimensional simulation of aggregate and asphalt mixture using parameterized shape and size gradation," *Journal of Materials in Civil Engineering*, vol. 31, no. 3, Article ID 04019004, 2019.

[20] Y. Yao, J. Li, J. Ni, C. Liang, and A. Zhang, "Effects of gravel content and shape on shear behaviour of soil-rock mixture: experiment and DEM modelling," *Computers and Geotechnics*, vol. 141, Article ID 104476, 2022.

[21] M. Fakhri and R. Shahni Dezfoulian, "Pavement structural evaluation based on roughness and surface distress survey using neural network model," *Construction and Building Materials*, vol. 204, pp. 768–780, 2019.

[22] A. Bianchini, "Pavement maintenance planning at the network level with principal component analysis," *Journal of Infrastructure Systems*, vol. 20, no. 2, Article ID 04013013, 2014.

[23] A. A. Elhadidy, S. M. El-Badawy, and E. E. Elbeltagi, "A simplified pavement condition index regression model for pavement evaluation," *International Journal of Pavement Engineering*, vol. 22, no. 5, pp. 643–652, 2021.

[24] H. Yao, R. Xing, and P. Xu, "Pavement performance evaluation based on entropy weight radar chart theory," in *Proceedings of the 2010 IEEE International Conference on Industrial Engineering and Engineering Management*, pp. 1791–1795, Macao, China, December 2010.

[25] L. Sun and W. Gu, "Pavement condition assessment using fuzzy logic theory and analytic hierarchy process," *Journal of Transportation Engineering*, vol. 137, no. 9, pp. 648–655, 2011.

[26] J. Kim, D. Park, Y. Suh, and D. Jung, "Development of sidewalk block pavement condition index (SBPCI) using analytical hierarchy process," *Sustainability*, vol. 11, no. 24, p. 7086, 2019.

[27] S. Abu-Samra, T. Zayed, and W. Tabra, "Pavement condition rating using multiattribute utility theory," *Journal of Transportation Engineering, Part B: Pavements*, vol. 143, no. 3, Article ID 04017011, 2017.

[28] C. Xu, T. Tang, H. Jia et al., "Benefits of coupled green and grey infrastructure systems: evidence based on analytic hierarchy process and life cycle costing," *Resources, Conservation and Recycling*, vol. 151, Article ID 104478, 2019.

[29] S. Yang, M. Guo, X. Liu, P. Wang, Q. Li, and H. Liu, "Highway performance evaluation index in semiarid climate region based on fuzzy mathematics," *Advances in Materials Science and Engineering*, vol. 2019, Article ID 6708102, 2019.

[30] J. Santos, A. Ferreira, and G. Flintsch, "An adaptive hybrid genetic algorithm for pavement management," *International Journal of Pavement Engineering*, vol. 20, no. 3, pp. 266–286, 2019.

[31] J. Yu, X. Zhang, and C. Xiong, "A methodology for evaluating micro-surfacing treatment on asphalt pavement based on grey system models and grey rational degree theory," *Construction and Building Materials*, vol. 150, pp. 214–226, 2017.

Hindawi
Advances in Materials Science and Engineering
Volume 2021, Article ID 3532935, 11 pages
https://doi.org/10.1155/2021/3532935

Research Article

Influence of Humidity State on Dynamic Resilient Modulus of Subgrade Soils: Considering Repeated Wetting-Drying Cycles

Gongfeng Xin,[1] Anshun Zhang ,[2] Zijian Wang,[1] Quanjun Shen,[1] and Minghao Mu[1]

[1]*Shandong Hi-Speed Group Innovation Research Institute, Jinan 250098, China*
[2]*National Engineering Laboratory of Highway Maintenance Technology, Changsha University of Science & Technology, Changsha 410114, China*

Correspondence should be addressed to Anshun Zhang; zas@stu.csust.edu.cn

Received 20 August 2021; Accepted 25 November 2021; Published 14 December 2021

Academic Editor: Abílio De Jesus

The service performance of subgrade depends on the dynamic resilient modulus (M_R) of subgrade soils. Meanwhile, due to complicated conditions such as rainfall infiltration, high temperature evaporation, and groundwater level fluctuations, it can be safely said that the humidity state and repeated wetting-drying (WD) cycles affect the M_R of subgrade soils. The object of this study is to conduct a series of dynamic triaxial tests after WD cycles to investigate the characteristics of the M_R under various factors. The main results are as follows: (i) the M_R decreased with the increase of deviator stress and rose with the growth of confining pressure; (ii) the humidification effect caused by the increase in moisture content attenuated the M_R; (iii) the accumulation of WD cycles damaged the M_R; however the decline rate was gradually retarded until it was stable with WD cycles 5 times; (iv) the satisfactory prediction model for the M_R of subgrade soils considering WD cycles was proposed and verified. It is expected that the findings can provide valuable contributions for road engineering.

1. Introduction

The dynamic resilient modulus (M_R) is a key parameter to characterize the stiffness characteristics of subgrade soils [1, 2], and it is employed as a basic input for determining the pavement structure thickness and combination method, for example, in the design standard of asphalt pavement in China (JTG D50-2017) and the guide of the American Association of State Highway and Transportation Officials (AASHTO 2002). Moreover, considering the stability and durability during the operation period, in addition to meeting stiffness requirements, the influence due to complex working environments on the service performance of road materials such as asphalt mixtures [3, 4], graded crushed rocks [5], and subgrade soils [6] is also a crucial issue that cannot be ignored. One of the universal occurrences is the change in the humidity of subgrade soils caused by a serious of reasons such as rainfall infiltration. According to long-term field tests data, the humidity of subgrade soils is not constant but gradually exceeds to the optimal moisture content (OMC) and eventually stabilized [7, 8]. The harmful wetting effect attenuates the M_R of subgrade soils with varying degrees, as many pavement diseases are attributed to this phenomenon, e.g., rutting [9], cracking [10], and bulge [11]. Therefore, it is of great significance to research the influence of humidity state on M_R of subgrade soils.

At present, researchers have carried out numerous studies on the influence of humidity changes on M_R of subgrade soils. Through two-year on-site monitoring, Elliott et al. [12] found that the actual moisture content of the subgrade soils progressively increased to 1.1 OMC. Subsequently, Zhang et al. [13] conducted soils humidity surveys on several expressways in southern China and reported that the moisture content of the subgrade soils continued to increase and finally stabilized at around 116% OMC. On this basis, they prepared high plasticity clays specimens under the moisture content conditions of 0.9 OMC, OMC, 1.1 OMC, 1.2 OMC, and 1.3 OMC, respectively, and performed corresponding repeated loading triaxial (RLT) tests [14]. The results showed that, under the given stress and compaction

state, the increase in the moisture content of the specimen reduced the M_R. This rule was observed in the test results of Yao et al. [15] and Han et al. [16] for low liquid limit clays and seven different Canadian clays, respectively. For low liquid limit clays specimens with various moisture contents (OMC – 2%, OMC, and OMC + 2%) subjected to freeze-thaw cycles, Zhao et al. [17] claimed that whether it is a closed or open freezing method, the higher the moisture content, the lower the M_R, but the degree of attenuation is different. Zhang et al. [18] also used this level of moisture content to compact coarse grained fillers and organized RLT tests. The results captured the weakening effect of humidity growth on the M_R, in agreement with the findings on unbonded granular materials reported by Gu et al. [19] and recycled construction wastes reported by Azam et al. [20].

In addition to the experimental studies, the prediction model contributes to a better understanding of the M_R of subgrade soils. According to previous study, some representative models are available for M_R prediction. Hicks et al. [21] indicated that the stress level is the main factor affecting the M_R of materials and developed the k-θ model containing only the bulk stress, as shown in the following equation:

$$M_R = k_1 \theta^{k_2}, \tag{1}$$

where θ is the bulk stress, $\theta = \sigma_1 + \sigma_2 + \sigma_3$, σ_1, σ_2, and σ_3 are the major principal stress, the intermediate principal stress, and the confining pressure, respectively, and k_1 and k_2 are regression coefficients.

Lytton et al. [22] adopted the octahedral shear stress to characterize the shear effect, and the model was finally embodied in AASHTO 2002, as shown in the following equation:

$$M_R = k_1 P_a \left(\frac{\theta}{P_a}\right)^{k_2} \left(\frac{\tau_{\text{oct}}}{P_a} + 1\right)^{k_3}, \tag{2}$$

where $P_a = 101.3$ kPa, which is the atmospheric pressure; τ_{oct} is the octahedral shear stress, $\tau_{\text{oct}} = (\sqrt{2}/3)\sigma_d$, $\sigma_d = \sigma_1 - \sigma_3$ is the deviator stress; k_3 is the regression coefficient.

Several scholars proposed that the influence of humidity state on the M_R should be directly reflected in the prediction model. Hence, the humidity parameter commonly employed in unsaturated soils mechanics, that is, the matric suction, was widely included in the prediction models. Liang et al. [23] believed the matric suction has the confinement impact, such as the bulk stress, so the matric suction and the bulk stress were combined into the same term, as shown in the following equation:

$$M_R = k_1 P_a \left(\frac{\theta + \chi\psi}{P_a}\right)^{k_2} \left(\frac{\tau_{\text{oct}}}{P_a} + 1\right)^{k_3}, \tag{3}$$

where χ is the effective stress parameter ($\chi \in [0,1]$, determined by the properties of different materials); ψ is the matric suction, $\psi = u_a - u_w$, u_a is the pore-air pressure, and u_w is the pore-water pressure.

Given that the bulk stress could not separate the constraint effect and shear effect because the bulk stress contains the confining stress and maximum cyclic stress, Yao et al. [15] defined the minimum bulk stress θ_m and built

$$M_R = k_1 P_a \left(\frac{\psi}{P_a} + 1\right)^{k_2} \left(\frac{\theta_m}{P_a}\right)^{k_3} \left(\frac{\tau_{\text{oct}}}{P_a} + 1\right)^{k_4}, \tag{4}$$

where $\theta_m = \sigma_1 + \sigma_2 + \sigma_3 - \sigma_d = 3\sigma_3$ is the minimum bulk stress; k_4 is the regression coefficient.

Zhang et al. [18], based on the laws obtained from the RLT tests of construction and demolition wastes, established the model that can consider the number of freeze-thaw cycles, compactness, humidity state, and stress state as shown in the following equation:

$$M_R = k_1 P_a [\ln(N + e)]^{k_2} C^{k_3} \left(\frac{\psi}{P_a} + 1\right)^{k_4} \left(\frac{\theta_m}{P_a}\right)^{k_5} \left(\frac{\tau_{\text{oct}}}{P_a} + 1\right)^{k_6}, \tag{5}$$

where N is the number of freeze-thaw cycles; C is the compactness; and k_5 and k_6 are regression coefficients.

In general, the related studies provided insightful and constructive comments into the influence of humidity state on M_R of subgrade soils. However, to the best of the authors' knowledge, due to rainwater infiltration and lateral migration, and transpiration during high temperature periods, the humidity of subgrade soils is not increasing continuously but undergoes intricate wetting and drying processes and finally reaches an equilibrium state. Therefore, the specimens were directly prepared with the final equilibrium moisture content and the tests conducted failed to accurately fit the actual humidity change process of the subgrade soils. Also, limited by the cumbersome and time-consuming test process [24, 25], it is inconvenient to use the matric suction as the humidity parameter. Furthermore, there are few reports on the prediction model of M_R considering the repeated wetting-drying (WD) cycles.

To address the above problems, the subgrade soils were investigated through a series of WD cycles tests and RLT tests. From the experimental results, the influences of stress state, humidity state, and WD cycles on the M_R were analyzed. On this basis, the prediction model of the M_R that can consider repeated WD cycles was established and verified. The main findings of this study were summarized in the last section, which can supply novel contributions and technical supports to the theory for pavement design.

2. Experiments Approach

2.1. Materials and Specimens. The studied soils in this study were from Changsha City, Hunan Province, China. The particle size analysis is listed in Figure 1. The standard heavy compaction tests were conducted to acquire the OMC and maximum dry density of the soils. In accordance with the Chinese Guidance for Test Methods of Soils on Highway Engineering, other main basic physical properties had also been determined in Table 1. Based on these parameters, the soils were named as high liquid limit silts (MH) according to the Unified Soils Classification System.

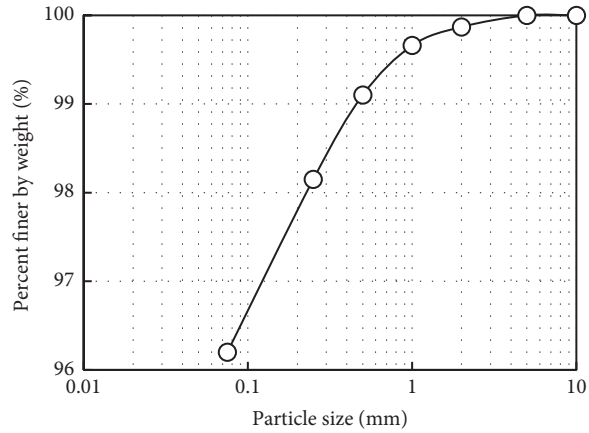

Figure 1: Distribution curves of particle size.

Table 1: Basic physical properties of the used soils.

Liquid limit (%)	Plastic limit (%)	Plastic index	Maximum dry density	Optimum moisture content (%)	Specific gravity
51.7	37.1	14.6	1.62 g/cm^3	22.6	2.71

To ensure consistent compactness and humidity levels between specimens, all the soils were prepared in the laboratory. Firstly, the soils were crushed and collected after filtering by the 5 mm sieve and then dried at 105°C for 12 h. Subsequently, the dry soils were mixed with distilled water under the OMC in order to simulate the initial humidity state of soils during subgrades filling [26] and then stored in a sealed plastic bag for 24 h so that the moisture was uniform. Meanwhile, the compactness of the specimens was set to 96% based on China's current requirements for road beds. Afterwards, the wet soils with the calculated mass were compacted by five layers into a cylinder that was 100 mm in diameter and 200 mm in height. Finally, the specimens were wrapped to avoid water evaporation.

2.2. Wetting-Drying Cycles. At present, the common practice to achieve WD cycles is to soak the specimens in water to the target wet side moisture content and then place them in the oven to dry at high temperature to the target dry side moisture content [27, 28]. Although this pattern speeds up the test process, the water absorption and dehydration of the specimens are obviously much faster than the actual water exchange rate of subgrade soils. To this end, this study applied a novel method as shown in Figure 2; that is, the specimens were set in the diffuse misty air generated by the atomizer to absorb water and add humidity by capillary action. After the moisture content of the specimens reached the target value, they were transferred to an oven with an internal temperature of 50°C for drying. Such a way is more suitable for depicting the wetting and drying condition of soils on site.

Given the possible variation range of the equilibrium humidity state of the subgrade soils, the final actual moisture contents of specimens were set to 0.9 OMC, OMC, 1.1 OMC, 1.2 OMC, and 1.3 OMC, respectively. The specimens prepared under OMC were first humidified to 1.3 OMC and then dehumidified to 0.9 OMC. The two parts were regarded as one WD cycle, and then so on. The numbers of WD cycles in this study were designed as 0, 1, 3, and 5. After the specimens have experienced the preset WD cycles, they changed from 0.9 OMC to the anticipant target moisture content. Taking the WD cycles 3 times and the final actual moisture content of 1.2 OMC as an example, the humidity change path is as follows: OMC $\longrightarrow$ 1.3 OMC $\longrightarrow$ 0.9 OMC $\longrightarrow$ 1.3 OMC $\longrightarrow$ 0.9 OMC $\longrightarrow$ 1.3 OMC $\longrightarrow$ 0.9 OMC $\longrightarrow$ 1.2 OMC $\longrightarrow$ wrapped and allowed to stand for 1–2 days $\longrightarrow$ RLT tests. In order to determine the key nodes when the humidification moisture content (w_w) and the dehumidification moisture content (w_D) of the specimens reached the target level, it is necessary to grasp the humidity change rate. In this study, the specimens were weighed every about 10 h, and the results are summarized in Figure 3. Based on this finding, the moment when the humidity of the specimen reached the target value can be estimated, namely, the weighing frequency can be increased for some time before this moment to control the required moisture content of the specimen.

2.3. Repeated Loading Triaxial Tests. DYNATRIAX-100/14, the dynamic triaxial test equipment, was used to measure the M_R of specimens in this study. The load form adopted half-sine wave, the frequency was 1 Hz, the action time was 0.2 s, and the intermittent time was 0.8 s. The stress conditions referred to the RLT sequence for subgrade fine-grained soils proposed by Luo [29], as shown in Table 2, benefiting from its comprehensive coverage of the stress range of the subgrade work area in China. In this sequence, the deviator stresses were designed as four groups from low to high, and the confining pressures in each group were divided into four levels from great to small so as to reduce the possibility of premature failure of the specimens during the loading process. The test data of the last five cycles in each stress combination are to acquire the corresponding M_R value.

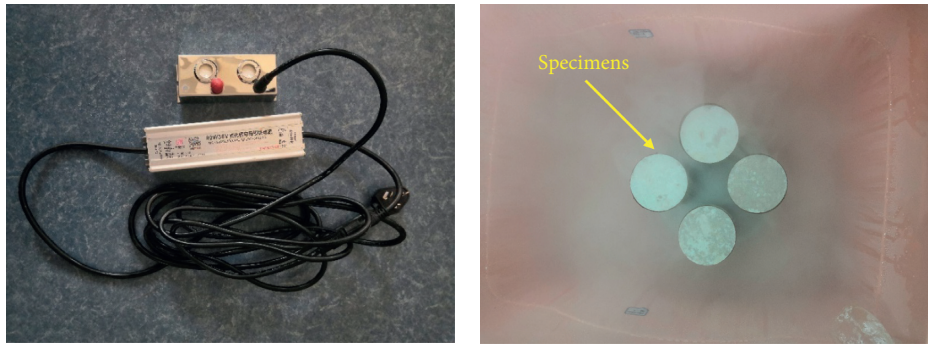

(a) (b)

Figure 2: The atomization and humidification process of the specimens. (a) Atomizer. (b) Humidification.

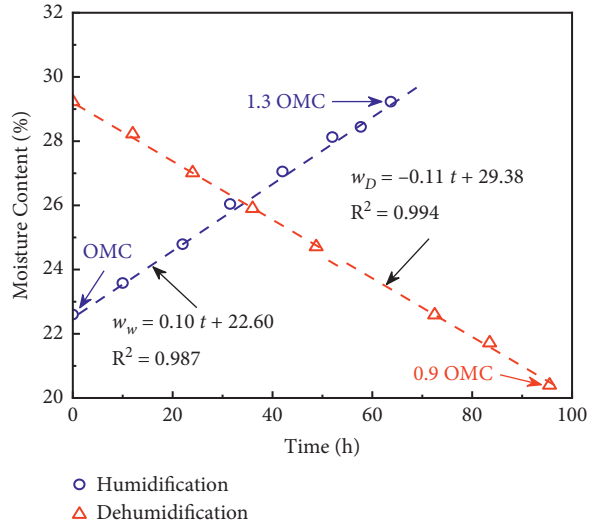

Figure 3: The relationship between w_w and w_D and time (t), respectively.

Table 2: The stress-loading sequence in this study.

No.	Confining pressure σ_3 (kPa)	Contact pressure 0.2 σ_3 (kPa)	Deviator stress σ_d (kPa)	Principal stress ratio σ_1/σ_3	Number of cycles
0 (preloading)	30	6	55	2.8	2000
1	60	12	30	1.5	100
2	40	9	30	1.8	100
3	30	6	30	2.0	100
4	15	3	30	3.0	100
5	60	12	55	1.9	100
6	40	9	55	2.4	100
7	30	6	55	2.8	100
8	15	3	55	4.7	100
9	60	12	75	2.3	100
10	40	9	75	2.9	100
11	30	6	75	3.5	100
12	15	3	75	6.0	100
13	60	12	105	2.8	100
14	40	9	105	3.6	100
15	30	6	105	4.5	100
16	15	3	105	8.0	100

3. Analysis of Influence Factors of the Dynamic Resilient Modulus

3.1. Influence of Deviator Stress on the Dynamic Resilient Modulus. Figure 4 shows the variation of M_R with deviator stress under different confining pressures and moisture content before WD cycles. It can be observed that M_R decreases with the enhancement of deviator stress. The possible principle behind this phenomenon is that the growth of the deviator stress leads to an increase in the vertical strain, and the increase of the vertical strain is greater than the increase of the deviator stress, which ultimately leads to a decrease in M_R. Taking the event of confining pressure of 30 kPa and moisture content of 1.1 OMC as an example, when the deviator stress rises from 30 kPa to 55 kPa, 75 kPa, and 105 kPa, M_R attenuates by 12.03%, 14.18%, and 30.55%, respectively. Obviously, the soils specimens presented softening behavior, which is consistent with the previous findings of many researchers [14, 15]. It is worth pointing out that because $\tau_{oct} = (\sqrt{2}/3)\sigma_d$, the octahedral shear stress and deviator stress have the same influence rule on the M_R.

3.2. Influence of Confining Pressure on the Dynamic Resilient Modulus. Figure 5 reveals the nonlinear positive correlation between M_R and the confining pressure with various moisture content and deviator stress at WD cycle 1 time. For instance, under the deviator stress of 75 kPa and the moisture content of 0.9 OMC, as the confining pressure gradually increases from 15 kPa to 30 kPa, 40 kPa, and 60 kPa, M_R value expands 19.74%, 28.95%, and 43.42% respectively. It can be seen that the confining pressure has a considerable lateral restraint effect on the specimens, so that it has a better stiffness holding capacity to resist vertical deformation under a higher deviator stress, in agreement with the results obtained in the past few decades [14, 16, 30]. Similarly, according to the equivalence relationship $\theta_m = 3\sigma_3$, the minimum bulk stress and confining pressure also have the coincident influence on the M_R.

3.3. Influence of Moisture Content on the Dynamic Resilient Modulus. Figure 6 illustrates that, under the given stress states, the humidification effect significantly reduces the M_R of the specimens. For example, for the case of WD cycles 5 times and the confining pressure of 40 kPa, as the moisture content increases from 0.9 OMC to 1.3 OMC, the attenuation range of M_R with various deviator stresses is 43.02%–67.35%. It shows that the increased humidity causes the specimens to soften. The possible explanation is that water has a certain lubricating effect among soils particles. When the moisture content decreases, the water film on the surface of the soils particles is thinner, and the relative movement between the soils particles is more difficult, so the specimens have a stronger ability to resist deformation. Conversely, the increase in moisture content makes the relative movement between soils particles simpler, and the specimens are less resistant to deformation; namely, the stiffness is reduced.

3.4. Influence of Wetting-Drying Cycles on the Dynamic Resilient Modulus. In order to intuitively reflect the impact of repeated WD cycles on the M_R, referring to the way that Zhang et al. [18] defined the freeze-thaw damage factor, this study employed the WD damage factor as the evaluation indicator, as shown in the following equation:

$$D = \frac{M_{R(0)} - M_{R(i)}}{M_{R(0)}}, \tag{6}$$

where D is the WD damage factor; $M_{R(0)}$ is M_R before WD cycles; $M_{R(i)}$ is M_R after the i times WD cycles, and $i = 0, 1, 3, 5$ here.

Figure 7 indicates that, under the given moisture content and stress state, the damage factor increases with the accumulation of WD cycles. In particular, the attenuation of M_R is the most obvious by the first WD effect, and the damage factor ranges from 0.27 to 0.54. With the increase of the numbers of WD cycles, the growth rate of the damage factor gradually slows down and finally basically stabilizes. At the same time, the damage factor of M_R after WD cycles 5 times is 0.63 to 0.95. Compared with the 3th cycle of WD cycles, the increase of the damage factor is less than 10%. It can be considered that the stiffness of the specimen is stable after 5 WD cycles.

Annotation: (60 kPa, 30 kPa) denotes that the confining pressure is 60 kPa, and the deviator stress is 30 kPa. For clarity, only partial test results under various stress states are given.

4. Prediction Model for the Dynamic Resilient Modulus with Wetting-Drying Cycles

This section aims to establish a phenomenological model of the M_R that can consider the WD cycles. A satisfactory prediction model should comprehensively include influencing factors and reasonably reflect the influence law of each factor on M_R [31]. Based on the analysis in the previous section, the numbers of WD cycles, actual moisture content, minimum bulk stress, and octahedral shear stress are selected as independent variables. In particular, the actual moisture content is used instead of matric suction to characterize the humidity state, and the rewritten exponential form is applied to reflect the WD cycles impact, the established model as shown in (7). A total of $4 \times 5 \times 16$ (the numbers of WD cycles × the actual moisture content levels × the stress states) = 320 sets of tests data in this study were used to fit the model, and the results were summarized in Table 3.

$$M_R = k_1 P_a e^{k_2 N} \left(\frac{w}{\text{OMC}}\right)^{k_3} \left(\frac{\theta_m}{P_a}\right)^{k_4} \left(\frac{\tau_{oct}}{P_a} + 1\right)^{k_5}, \tag{7}$$

where N is the numbers of WD cycles; w is the actual moisture content; k_1~k_5 are the model parameters, and other symbols have the same meaning as above.

For the fit result, k_1 is the coefficient which must be a positive number because M_R cannot be negative. k_2 as an exponent must be a negative number, because with the growth of the number of WD cycles, M_R reduces. k_3 should

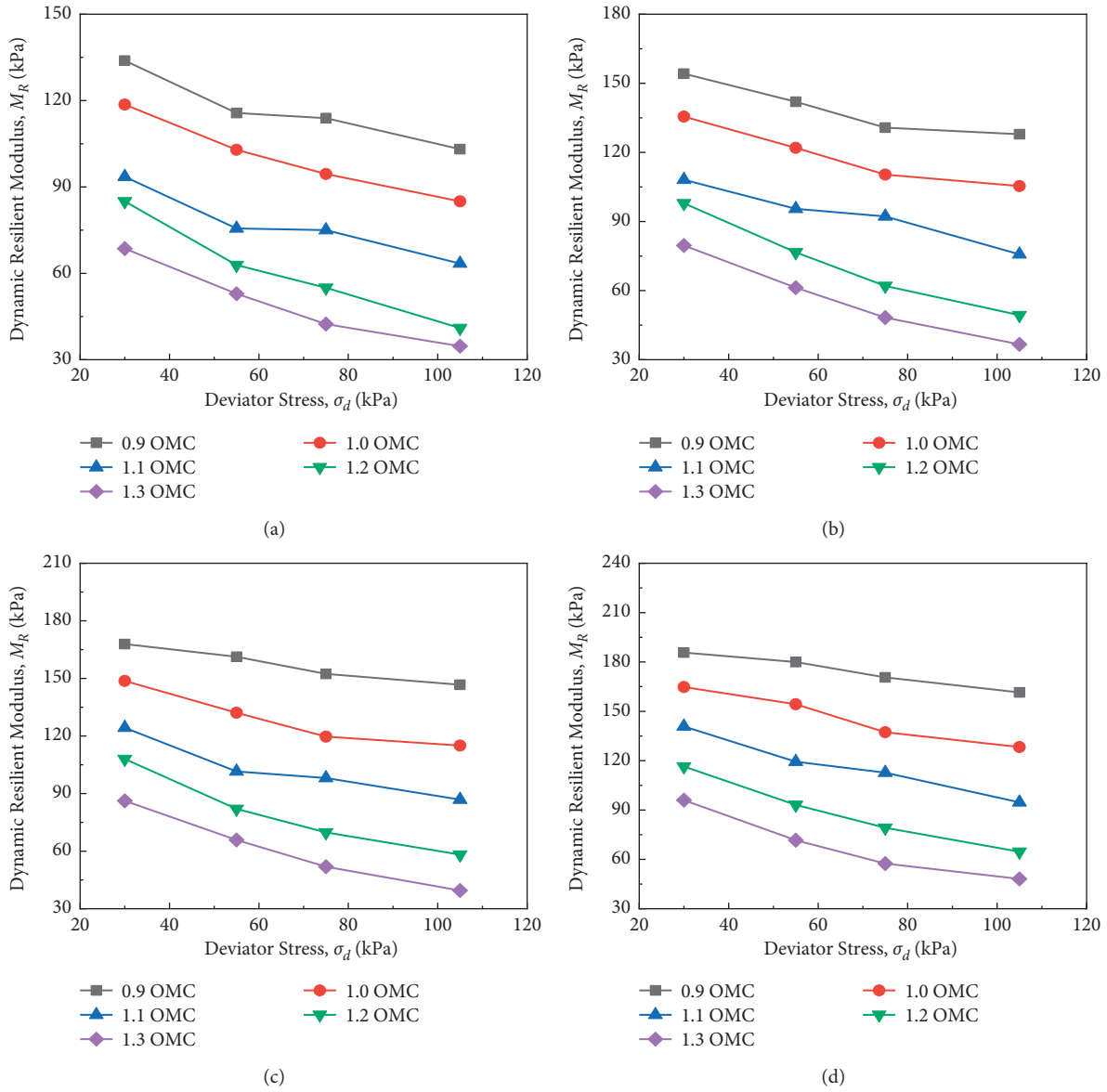

Figure 4: The relationship between σ_d, moisture content, and M_R at WD cycles = 0. (a) $\sigma 3 = 15$ kPa. (b) $\sigma 3 = 30$ kPa. (c) $\sigma 3 = 40$ kPa. (d) $\sigma 3 = 60$ kPa.

be a negative number, on account of the higher the actual moisture content, the smaller the M_R. According to the restraint effect caused by the minimum bulk stress and the softening effect produced by the octahedral shear stress on the soils specimens, it can be inferred that $k_4 > 0$ and $k_5 < 0$. Obviously, the results shown in Table 3 are consistent with the analysis of the experimental rules in this study. In addition, the value of the determination coefficient R^2 exceeds 0.9, indicating that the prediction model exhibited in (7) is excellent. In order to have confidence in this model, this study is done in conjunction with relevant experimental data from other researchers to verify (7) [32], and the results are shown in Figure 8. It can be seen that the measured M_R is close to the predicted value. Although R^2 is slightly lowered, this may be due to the difference in the actual process of the specimens being subjected to WD cycles, which leads to a decrease in the accuracy of (7), but the prediction effect is still excellent based on the recommended criteria for evaluating R^2 in road engineering [33–35]. Therefore, it can be speculated that this model is applicable to other soils although it is only proposed based on the high liquid limit silts taken from Changsha City, China, in this study.

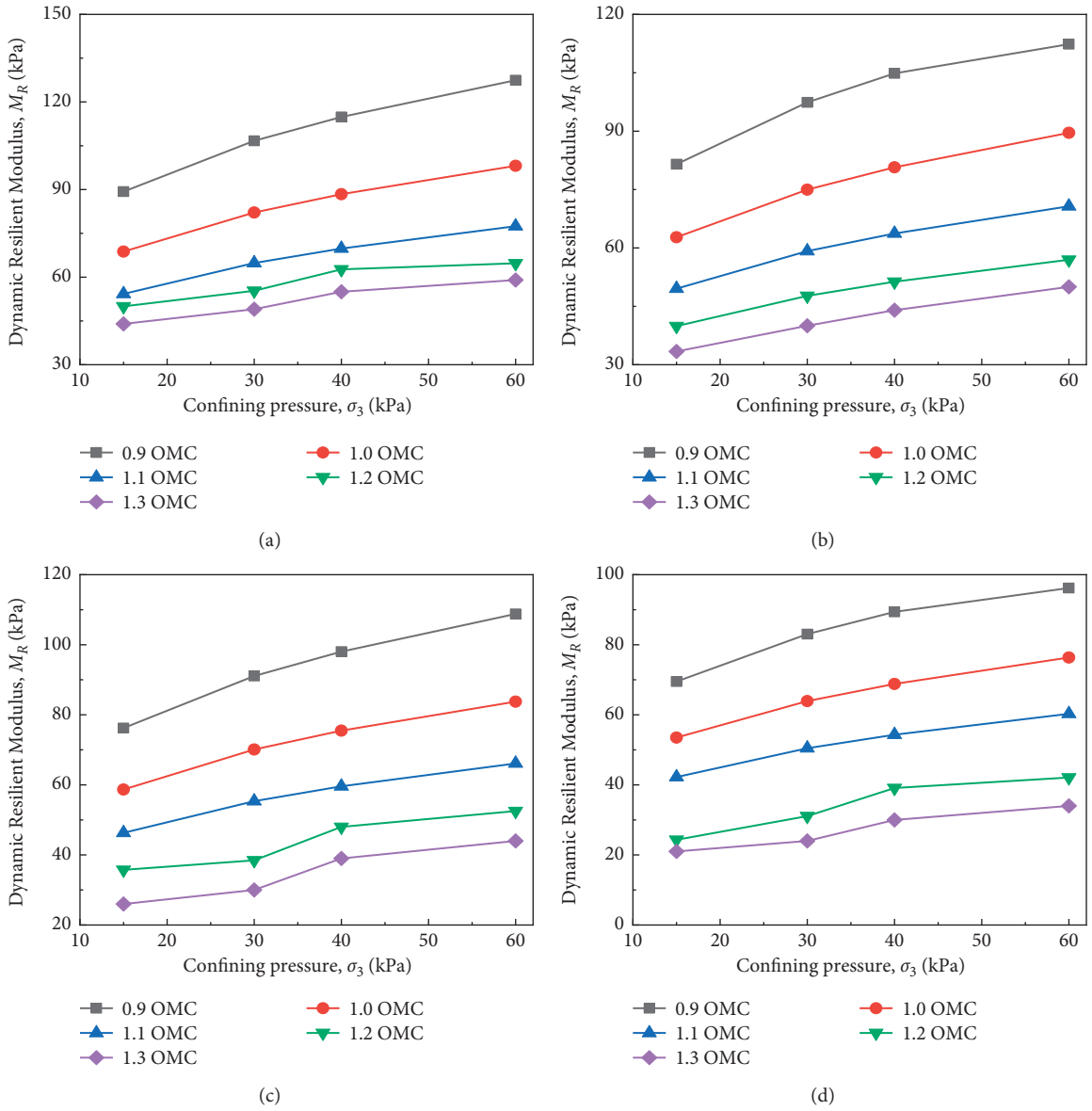

Figure 5: The relationship between σ_3, moisture content, and M_R at WD cycles = 1. (a) $\sigma_d = 30$ kPa. (b) $\sigma_d = 55$ kPa. (c) $\sigma_d = 75$ kPa. (d) $\sigma_d = 105$ kPa.

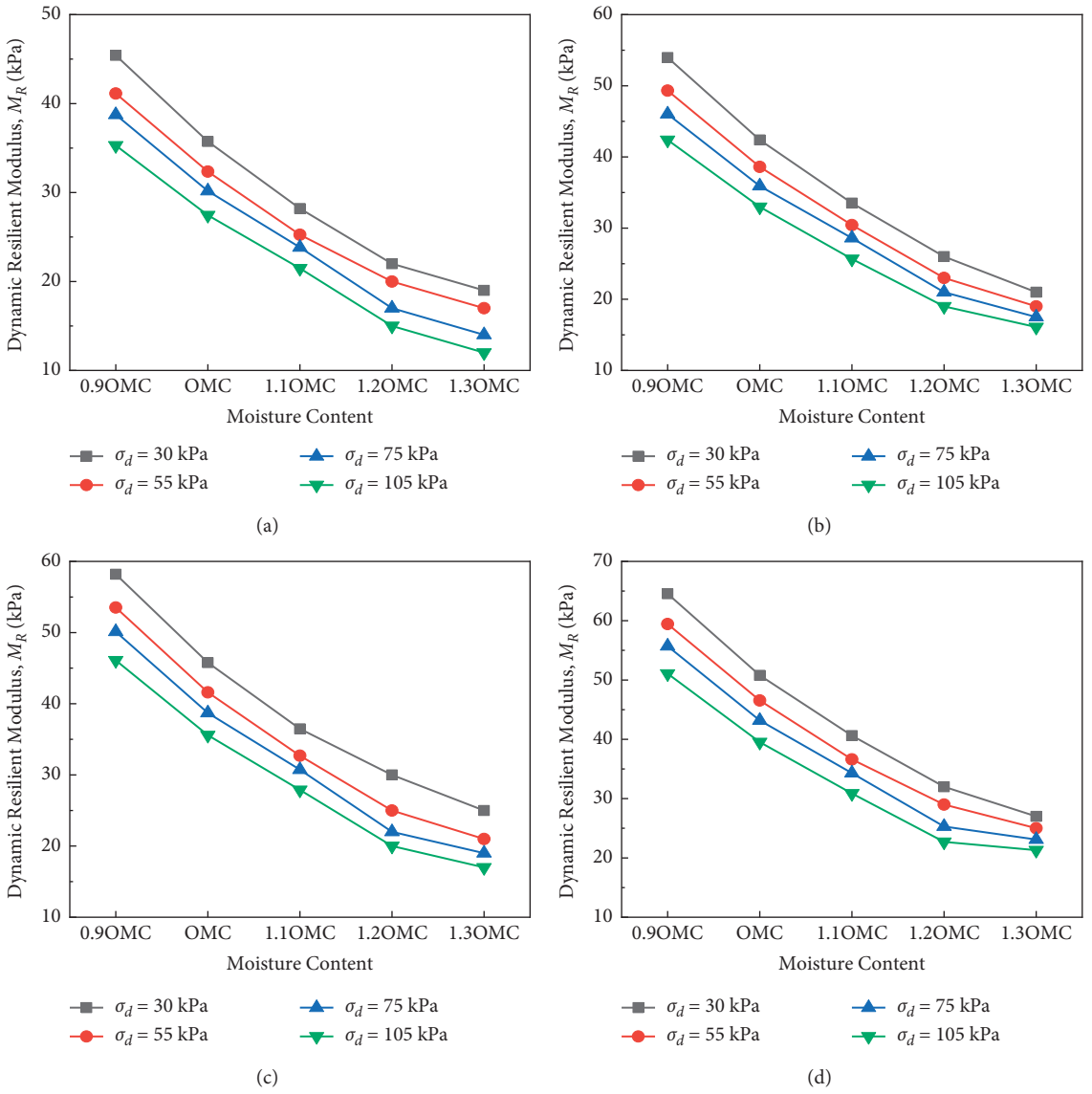

Figure 6: The relationship between σ_d, moisture content, and M_R at WD cycles = 5. (a) $\sigma_3 = 15$ kPa. (b) $\sigma_3 = 30$ kPa. (c) $\sigma_3 = 40$ kPa. (d) $\sigma_3 = 60$ kPa.

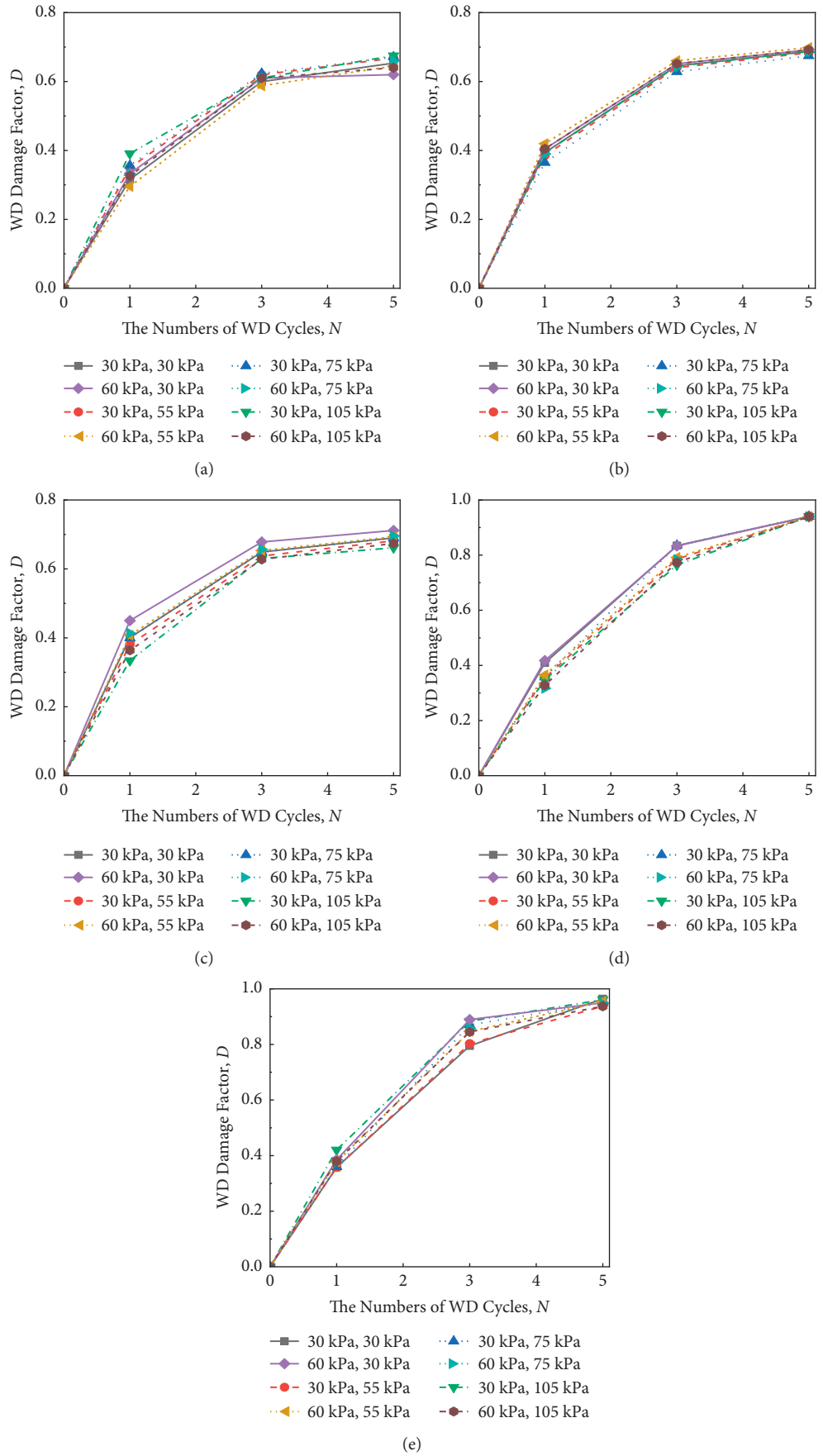

Figure 7: Damage factors of M_R after WD cycles under different conditions. (a) 0.9 OMC. (b) OMC. (c) 1.1 OMC. (d) 1.2 OMC. (e) 1.3 OMC.

Table 3: The fitting results of equation (7) in this study.

k_1	k_2	k_3	k_4	k_5	R^2
1.49	−0.29	−2.35	0.28	−1.13	0.94

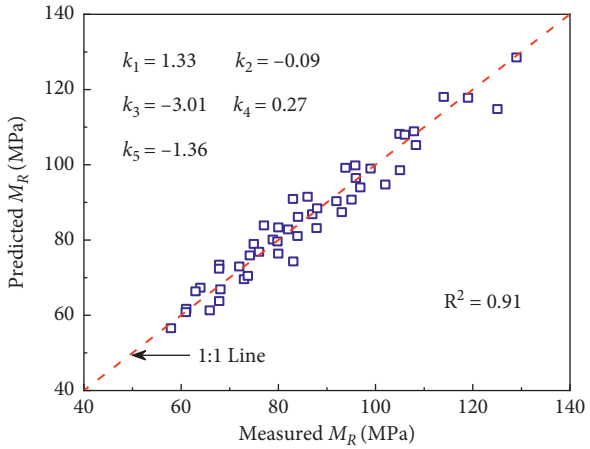

Figure 8: The predicted by equation (7) and measured M_R in another studies.

5. Conclusions

This study aimed at revealing the influence of humidity state on M_R of subgrade soils considering WD cycles. For this purpose, this study carried out a series of WD cycles and RLT tests. Based on the analysis of experimental results, the main findings of this research can be summarized as follows:

(1) The innovative humidification method was realized by using atomizer, which was more consistent with the actual WD cycles condition of subgrade soils. According to the exploratory tests, the change relationship between moisture content and time in the process of humidification and dehumidification of the specimens was mastered, so as to provide technical support for accurately controlling the key nodes of WD cycles.

(2) The stress state has a significant effect on the stiffness of subgrade soils; that is, M_R decreased with the increase of deviator stress and increased with the rise of confining pressure. Meanwhile, the humidification due to the growth in moisture content led to a decrease in M_R. In addition, the accumulation of repeated WD cycles attenuated M_R, but the decay rate gradually slowed down until it stabilized after 5 WD cycles.

(3) This study employed the ratio of actual moisture content to OMC to characterize the humidity state, the improved exponential form reflected the influence of WD cycles, and the minimum bulk stress and octahedral shear stress embodied the constraint and shear effect, respectively. On this basis, a novel and excellent prediction model for M_R of subgrade soils was established.

It is worth emphasizing that although the applicability of the proposed model to the data of other researchers is successful, the focus in the future should continue to search for more soils tests data for verification to ensure the robustness of the model.

Data Availability

Some or all data and models that support the findings of this study are available from the corresponding author upon reasonable request.

Conflicts of Interest

The authors declare that they have no conflicts of interest.

Acknowledgments

The authors gratefully acknowledge the program offered by the Shandong Hi-Speed Group Innovation Research Institute: Key technologies for green and intelligent construction of durable expressways (CYZX-JT-2020-05), and the financial support by the Science and Technology R&D Project (2021-ZJKJ-QNCX17) from China Communications Construction Co., Ltd.

References

[1] J. Qian, Y. Yao, J. Li, H. Xiao, and S. Luo, "Resilient properties of soil-rock mixture materials: preliminary investigation of the effect of composition and structure," *Materials*, vol. 13, no. 7, Article ID 1658, 2020.

[2] J. Zhang, H. Fan, S. Zhang, J. Liu, and J. Peng, "Back-calculation of elastic modulus of high liquid limit clay subgrades based on viscoelastic theory and multipopulation Genetic algorithm," *International Journal of Geomechanics*, vol. 20, no. 10, Article ID 04020194, 2020.

[3] K. Zhang, W. Li, and F. Han, "Performance deterioration mechanism and improvement techniques of asphalt mixture in salty and humid environment," *Construction and Building Materials*, vol. 208, pp. 749–757, 2019.

[4] J. Li, J. Zhang, G. Qian, J. Zheng, and Y. Zhang, "Three-dimensional simulation of aggregate and asphalt mixture using parameterized shape and size gradation," *Journal of Materials in Civil Engineering*, vol. 31, no. 3, Article ID 04019004, 2019.

[5] Y. Yao, J. Li, C. Liang, J. Zheng, and F. Gu, "Effects of gravel content and shape on shear behaviour of soil-rock mixture: experiment and DEM modelling," *Computers and Geotechnics*, vol. 141, Article ID 104476, 2022.

[6] H. b Liu, S. Sun, H. b Wei, and W. j Li, "Effect of freeze-thaw cycles on static properties of cement stabilised subgrade silty soil," *International Journal of Pavement Engineering*, pp. 1–13, 2021.

[7] Y. Yao, J. Zheng, Z. Chen, J. Zhang, and Y. Li, "Field measurements and numerical simulations of temperature and moisture in highway engineering using a frequency domain reflectometry sensor," *Sensors*, vol. 16, no. 6, Article ID 857, 2016.

[8] J. Zhang, J. Peng, A. Zhang, and J. Li, "Prediction of permanent deformation for subgrade soils under traffic loading in Southern China," *International Journal of Pavement Engineering*, pp. 1–10, 2020.

[9] S. Zhao and J. Liu, "Rutting evaluation of alaskan asphalt pavement containing sustainable materials," *Journal of Testing and Evaluation*, vol. 46, no. 4, pp. 1366–1375, 2018.

[10] H. Wei, J. Li, F. Wang, J. Zheng, Y. Tao, and Y. Zhang, "Numerical investigation on fracture evolution of asphalt mixture compared with acoustic emission," *International Journal of Pavement Engineering*, 2021.

[11] W. Liu, H. Lin, H. Guo et al., "An approach to investigate coarse aggregates movement of asphalt mixture based on wheel tracking test," *Construction and Building Materials*, vol. 309, no. 22, Article ID 125161, 2021.

[12] R. Elliott, "Selection of subgrade modulus for AASHTO flexible pavement design," *Transportation Research Record*, vol. 1354, pp. 39–44, 1992.

[13] J. Zhang, F. Li, L. Zeng, J. Peng, and J. Li, "Numerical simulation of the moisture migration of unsaturated clay embankments in southern China considering stress state," *Bulletin of Engineering Geology and the Environment*, vol. 80, no. 1, pp. 11–24, 2020.

[14] J. Zhang, J. Peng, J. Zheng, and Y. Yao, "Characterisation of stress and moisture-dependent resilient behaviour for compacted clays in South China," *Road Materials and Pavement Design*, vol. 21, no. 1, pp. 262–275, 2018.

[15] Y. Yao, J. Zheng, J. Zhang, J. Peng, and J. Li, "Model for predicting resilient modulus of unsaturated subgrade soils in south China," *KSCE Journal of Civil Engineering*, vol. 22, no. 6, pp. 2089–2098, 2018.

[16] Z. Han, S. K. Vanapalli, J. P. Ren, and W. L. Zou, "Characterizing cyclic and static moduli and strength of compacted pavement subgrade soils considering moisture variation," *Soils and Foundations*, vol. 58, no. 5, pp. 1187–1199, 2018.

[17] Y. Zhao, Z. Lu, H.-L. Yao, F. Gu, and Y.-H. Duan, "Experimental study of dynamic resilient modulus of subgrade soils under coupling of freeze-thaw cycles and dynamic load," *Journal of Central South University*, vol. 27, no. 7, pp. 2043–2053, 2020.

[18] J. Zhang, A. Zhang, C. Huang, H. Yu, and C. Zhou, "Characterising the resilient behaviour of pavement subgrade with construction and demolition waste under freeze–thaw cycles," *Journal of Cleaner Production*, vol. 300, Article ID 126702, 2021.

[19] F. Gu, H. Sahin, X. Luo, R. Luo, and R. L. Lytton, "Estimation of resilient modulus of unbound aggregates using performance-related base course properties," *Journal of Materials in Civil Engineering*, vol. 27, Article ID 04014188, 2015.

[20] A. M. Azam, D. A. Cameron, and M. M. Rahman, "Model for prediction of resilient modulus incorporating matric suction for recycled unbound granular materials," *Canadian Geotechnical Journal*, vol. 50, no. 11, pp. 1143–1158, 2013.

[21] R. G. Hicks and C. L. Monismith, "Factors influencing the resilient response of granular materials," *Transportation Research Record*, vol. 345, pp. 14–31, 1971.

[22] R. L. Lytton, J. Uzan, and E. G. Fernando, *Development and Validation of Performance Prediction Models and Specifications for Asphalt Binders and Paving Mixes*, Strategic Highway Research Program, 1993.

[23] R. Y. Liang, S. Rabab'ah, and M. Khasawneh, "Predicting moisture-dependent resilient modulus of cohesive soils using soil suction concept," *Journal of Transportation Engineering*, vol. 134, no. 1, pp. 34–40, 2008.

[24] Y. Yao, S. Luo, J. Qian, J. Li, H. Xiao, and X. Luo, "Soil-water characteristics of the low liquid limit silt considering compaction and freeze-thaw action," *Advances in Civil Engineering*, vol. 2020, Article ID 8823666, 3 pages, 2020.

[25] Y. Yao, J. Ni, and J. Li, "Stress-dependent water retention of granite residual soil and its implications for ground settlement," *Computers and Geotechnics*, vol. 129, Article ID 103835, 2021.

[26] J. Zhang, L. Ding, F. Li, and J. Peng, "Recycled aggregates from construction and demolition wastes as alternative filling materials for highway subgrades in China," *Journal of Cleaner Production*, vol. 255, Article ID 120223, 2020.

[27] X. Zhou, J. Hu, Y. Wei, and C. Cai, "Estimation of soil detachment capacity on steep slopes in permanent gullies under wetting-drying cycles," *Catena*, vol. 206, Article ID 105450, 2021.

[28] W. Liu, X. Tang, Q. Yang, and W. Li, "Influence of drying/wetting cycles on the mechanical cyclic behaviours of silty clay," *European Journal of Environmental and Civil Engineering*, vol. 19, no. 7, pp. 867–883, 2014.

[29] Z. Luo, *Study on dynamic resilient modulus of subgrade and granular layer*, Ph.D. Thesis, Tongji University, Shanghai, China, 2007.

[30] J. Li, J. Zheng, Y. Yao, J. Zhang, and J. Peng, "Numerical method of flexible pavement considering moisture and stress sensitivity of subgrade soils," *Advances in Civil Engineering*, vol. 2019, Article ID 7091210, 10 pages, 2019.

[31] J. Zhang, J. Peng, L. Zeng, J. Li, and F. Li, "Rapid estimation of resilient modulus of subgrade soils using performance-related soil properties," *International Journal of Pavement Engineering*, vol. 22, no. 6, pp. 732–739, 2019.

[32] J. Ceratti, W. Gehling, and W. Núñez, "Seasonal variations of a subgrade soil resilient modulus in southern Brazil," *Transportation Research Record*, vol. 1874, pp. 165–173, 2004.

[33] J. Zhang, A. Zhang, J. Li, F. Li, and J. Peng, "Gray correlation analysis and prediction on permanent deformation of subgrade filled with construction and demolition materials," *Materials*, vol. 12, no. 18, Article ID 3035, 2019.

[34] Z. Han and S. Vanapalli, "State-of-the-art: prediction of resilient modulus of unsaturated subgrade soils," *International Journal of Geomechanics*, vol. 16, no. 4, Article ID 04015104, 2016.

[35] J. Zhang, J. Peng, J. Zheng, L. Dai, and Y. Yao, "Prediction of resilient modulus of compacted cohesive soils in south China," *International Journal of Geomechanics*, vol. 19, no. 17, Article ID 04019068, 2019.

Hindawi
Advances in Materials Science and Engineering
Volume 2021, Article ID 3313460, 9 pages
https://doi.org/10.1155/2021/3313460

Research Article

Influence of Different Types of Emulsifiers on Properties of Emulsified Asphalt Binder and Its Evaporation Residue by Molecular Dynamics Simulation

Ying-feng Wu[1] **and Xin Qu**[2]

[1]*Zhejiang Institute of Communications, Hangzhou, China*
[2]*Key Laboratory of Road Structure and Material, Ministry of Communication, Chang'an University, Xi'an, China*

Correspondence should be addressed to Ying-feng Wu; wuyingf_hz@hotmail.com

Received 2 September 2021; Accepted 29 November 2021; Published 9 December 2021

Academic Editor: Antonio Caggiano

There is an important role in the properties of emulsified asphalt binder and its evaporation residue about emulsifier, which has been confirmed by experiment and chemical tests. However, there is little research about the emulsifier at microperspective. Therefore, the influence of two kinds of emulsifiers, a typical cationic emulsifier (dodecyl benzene sulfonate) and a typical anionic emulsifier (dodecyl primary amine), on technical properties of emulsified asphalt binder and its evaporation residues such as store stability, workability, breaking behavior, and mechanical properties are investigated using a microapproach. Results show that there is an effective role in the storage stability, workability, and demulsification of emulsified asphalt binder about cationic emulsifier compared with anionic emulsifier. The anionic emulsifier makes the density of evaporation residue larger. However, the mechanical properties of anionic emulsified asphalt evaporation residue are conversely smaller compared with the cationic emulsified asphalt evaporation residue. The adhesion behavior results have confirmed that the anionic emulsified asphalt evaporation residue has a negative adhesion with aggregate due to its anion. The mechanism of the different emulsifiers on asphalt binders and their evaporation residue is explored at a microscale to help us to understand emulsified asphalt binder and its evaporation residue more in depth.

1. Introduction

Emulsified asphalt refers to an oil-in-water (O/W) emulsion formed by heating and melting asphalt and dispersing fine particles in a solution containing an emulsifier and water under mechanical agitation [1]. In other words, emulsified asphalt is a mixture of asphalt material with compositions of chemical composition, such as emulsifier and water. It is liquid state at room temperature, so it can be mixed with aggregate at room temperature to prepare the asphalt mixture, mixing paving; the real process does not need to consume energy and will not emit gas such as asphalt smoke. Emulsified asphalt saves energy by 40%~50%, improves construction conditions, reduces construction cost by 20%~30%, and can effectively reduce the excessive aging of asphalt caused by high-temperature heating and a large amount of volatilization of carcinogen benzoyl [2]. In addition, the application of emulsified asphalt in metal anticorrosion, desert sand fixation, slope stability, etc., has also been reported [3–5]. Therefore, in recent years, with the deterioration of environmental problems [6–8], emulsified asphalt has once again become the focus of research.

Emulsified asphalt is developed along with the development and application of surfactants for asphalt. In addition to the processing technology, the type, structure, and composition of the emulsifier determine the basic properties and application range of the emulsified asphalt for the determined matrix asphalt. According to the electrical properties of the emulsifier used, it is classified into three types, including cationic emulsified asphalt, anionic emulsified asphalt, and nonionic emulsified

asphalt [9, 10]. In the emulsified asphalt, the asphalt binder and water are mature and their natures are stable. Some previous research has confirmed that the properties of emulsifiers are crucial to the properties of emulsified asphalt. So, the emulsifier has been studied in this paper.

From the clay emulsified asphalt of the United States in 1914, a variety of anionic emulsified asphalt products were developed. There are many varieties of anionic emulsifiers, and the price is relatively low, but the anionic emulsified asphalt has poor adhesion to mineral materials, especially moist mineral materials and alkaline mineral materials. With the deepening of the understanding of surfactants and the development of colloidal chemistry and interfacial chemistry, the cationic emulsified asphalt that appeared in the 1960s effectively compensated for the shortage of anionic emulsified asphalt and improved the early strength of film formation. The performance is better under the conditions. In the 1960s, France and the United States realized the commercialization of cationic asphalt emulsions. At the end of the 1970s, China began to study cationic asphalt emulsion and achieved a series of achievements in the processing technology of emulsion, emulsification equipment, and emulsion-testing standards and methods, which laid a good foundation for the promotion and application of emulsified asphalt.

From the structural point of view, the emulsifier is an amphiphilic molecule, which consists of a nonpolar hydrophobic group and a polar hydrophilic group. This structure causes the emulsifier to form a tightly aligned orientation on the surface of the solution, which changes the surface chemistry of the system. When the concentration of the emulsifier exceeds its critical micelle concentration (CMC), the surface tension is minimized, thereby having functions of emulsification, defoaming, dispersion, and so on. According to the hydrophilic and lipophilic balance value (HLB) of the emulsifier, the range of application can be preliminarily determined [11]. The asphalt emulsifier is between 10 and 18. Since the specific surface area of asphalt is large in the emulsion, the emulsifier concentration is much larger than that of the CMC to achieve the purpose of sufficient emulsification, and the amount of the emulsifier is generally controlled in the range of 0.13% to 3% (mass fraction) of the emulsion.

The influence of emulsifiers on the properties of emulsified asphalt binder and its evaporation residue has been researched comprehensively [1]. However, there are still some microissues that have not yet been clarified. So, the microscopic parameters of the emulsified asphalt binder are studied with molecular dynamics (MD) simulation, to understand the microscopic mechanism affecting the properties of the emulsified asphalt binder.

The influence of a typical cationic emulsifier (dodecyl benzene sulfonate) and a typical anionic emulsifier (dodecyl primary amine) are studied on the properties of the emulsified asphalt binder such as store stability, workability, and breaking behavior, as well as the mechanical properties and adhesion behavior of their evaporation residue.

2. Model and Methodology

2.1. The Molecular Dynamics Simulation. The influence of asphalt emulsifiers is studied with molecular dynamics simulation, which is a powerful tool to study asphalt binder [4, 5, 12–14]. Some applications of this technology in our previous studies were researched. The self-healing behavior of the asphalt binder is affected by different parameters [15], and the microproperties are affected by asphalt aging [16].

The structural characteristics of ionic liquids consisting of anions or cations often make them uniquely different from traditional asphalt binders. Well comprehending of the physicochemical properties of ionic liquids and the relationship between structure and physicochemical properties are the basis for the correct application of them to actual production. Many parameters of emulsified asphalt are directly related to their chemical stability and mechanical properties; therefore, the MD simulation research of the emulsified asphalt binder is necessary based on a microscopic viewpoint.

2.2. Establishment of the Molecular Structure Model

2.2.1. Asphalt Binder. Asphalt binders consist of millions of different components [17]. For the purpose of convenience of asphalt binder research, which was divided into three, four, or six fractions with similar properties, and then, the molecular structure has been created for each fraction [18, 19]. Later, the 12-component asphalt model was first put forward by Li and Greenfield [3] to describe SHRP core asphalt binder AAA-1, and it has been popularized and applied in the research field [14, 16]. So, the structure of 12 molecules for the asphalt binder is created in this paper; the number of each structure and the verification process can be found in the work of Li and Greenfield [3].

2.2.2. Typical Emulsifier. A cationic emulsifier, like other types of emulsifiers, consists of a long-chain oleophilic group and a hydrophilic group, except that its hydrophilic group is a positively charged group, and its long-chain lipophilic group is usually composed of fatty acids or petroleum chemicals are derived. Theoretical studies and experiments have shown that the emulsifier oleophilic group is a linear alkane with a strong emulsification performance, and the emulsion tends to be stable with the increase of the emulsifier ketone-based carbon chain length grade saturation, so we initially designed the emulsification.

In this study, a typical cationic emulsifier (dodecyl benzene sulfonate) and a typical anionic emulsifier (dodecyl primary amine) are studied, which are shown in Figure 1. These two molecules were chosen because of their typical structure and have been studied in depth by scholars [20–22], so they can effectively characterize the characteristics of typical cationic and anionic emulsifiers.

2.2.3. Emulsified Asphalt Binder. According to the molecular structure models of the asphalt binder and the emulsifier, models of the emulsified asphalt binder should be created to investigate the influence of the emulsifier on the

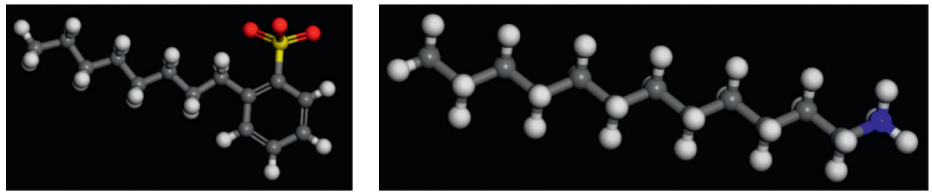

(a) (b)

Figure 1: (a) Dodecyl benzene sulfonate. (b) Dodecyl primary amine.

emulsified asphalt binder. So, we put some molecular models of emulsifier and water into the asphalt binder model to create models of the emulsified asphalt binder; then, two kinds of the emulsified asphalt binder are created. In this paper, the solid content of the emulsified asphalt is assumed to be 60%, and we put 1207 water molecules into the asphalt binder model, therefore, to create mixture of asphalt binder and water. Then, we put 3 dodecyl benzene sulfonate and 5 dodecyl primary amine into this mixture to create cationic and anionic emulsified asphalt binder, respectively.

2.2.4. Emulsified Asphalt Evaporation Residue. The forms of the emulsified asphalt binder are different because, after the pavement construction, the water is extruded out and volatilized from the emulsified asphalt binder; then, the emulsified asphalt evaporation residue works in the pavement. However, the emulsifier is still in the asphalt binder, so we take out the water molecules from the emulsified asphalt binder created above to build models of emulsified asphalt evaporation residue.

3. Results and Discussion

Currently, the emulsified asphalt binder is widely used in road engineering due to its construction convenience and environmental friendliness. However, its form changes during the usage: a lot of water are in the emulsified asphalt binder, so it is liquid before construction; while it will be semisolid after construction because the emulsified asphalt binder will be demulsified during the mixing with aggregate, and the evaporation residue of emulsion is similar as the asphalt binder. So, these different forms should be considered to investigate the influence of emulsifiers on the emulsified asphalt binder and its evaporation residue.

Therefore, the microproperties of emulsifiers, emulsified asphalt binder, and emulsified asphalt evaporation residue will be investigated in this paper. After the different models were created, molecular dynamics simulation was calculated with 100 ps ($1\,\text{ps} = 10^{-12}\text{s}$). In the particular (NPT) state, which means the environment of the molecule is isothermal and isobaric, then the microproperties of models were obtained after the calculation.

3.1. Surface Tension of Emulsifier. The surface tension is a kind of basic property of the emulsifier, which can be obtained by the simulation directly. In the emulsified asphalt binder, the lower the surface tension of the cationic emulsifier, the easier the emulsification [23]. So, the surface tension of the two kinds of emulsifiers is calculated firstly. The results are shown in Figure 2.

It is seen that the surface tension of the cationic emulsifier is lower comparing with the anionic emulsifier. Hence, it is concluded that the cationic emulsifier is easier to mix with asphalt and water, i.e., it has a better effect to produce the emulsified asphalt binder.

3.2. Stability of the Emulsified Asphalt Binder. The emulsified asphalt binder is a kind of thermodynamic instability system, so the stability of the emulsified asphalt binder is analyzed with the classical Derjguin–Landau–Verwey–Overbeek (DLVO) theory. The theory concludes that the structural stability of emulsion depends on the interaction between particles in the emulsified asphalt binder [24]. The system is stable if the repulsive force is greater than the attractive force, otherwise, it is unstable [25, 26]. The force between the colloidal particles is Van der Waals forces. The colloidal particles are aggregates of many molecules, so the interaction between them is the sum of the interaction between molecules.

The Van der Waals forces of the cationic emulsified asphalt, anionic emulsified asphalt, and asphalt binder are shown in Figure 3(a).

Figure 3(a) shows that the asphalt binder has the lowest Van der Waals force, indicating that the asphalt binder has the most stable colloidal structure. Meanwhile, the stability of the both emulsified asphalt binders is worse, which is in line with objective facts, i.e., the emulsified asphalt binder has the possibility of breaking. Compared with the two kinds of the emulsified asphalt binder, the cationic emulsified asphalt binder has a low Van der Waals force, indicating that repulsive force in the cationic emulsified asphalt binder is smaller; therefore, the stability of which is slightly superior to that of the anionic binder; it is consistent with the result of surface tension mentioned in the last section. It can be inferred that the cationic binder is also superior to anionic one in storage stability; this is the same as Tian's conclusion [27]. The storage stability is studied by the storage test; the results indicate the difference of softening point values between the bottom and top of the experimental sample. So, the larger the result value is, the more unstable the emulsified asphalt binder is.

3.3. Workability of the Emulsified Asphalt Binder. The workability of the emulsified binder is important for road construction because, when starting to mix with the

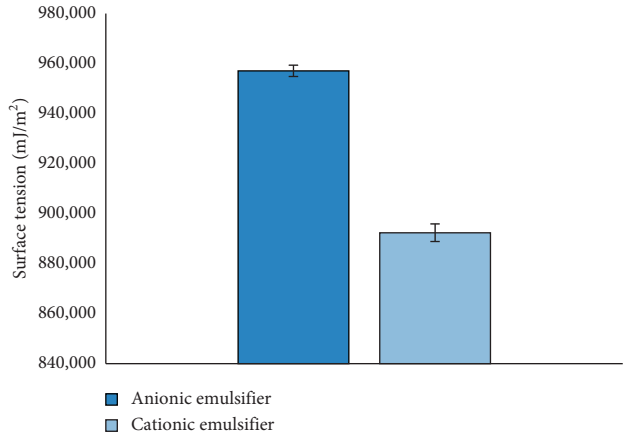

Figure 2: The surface tension results of the two kinds of the emulsifier.

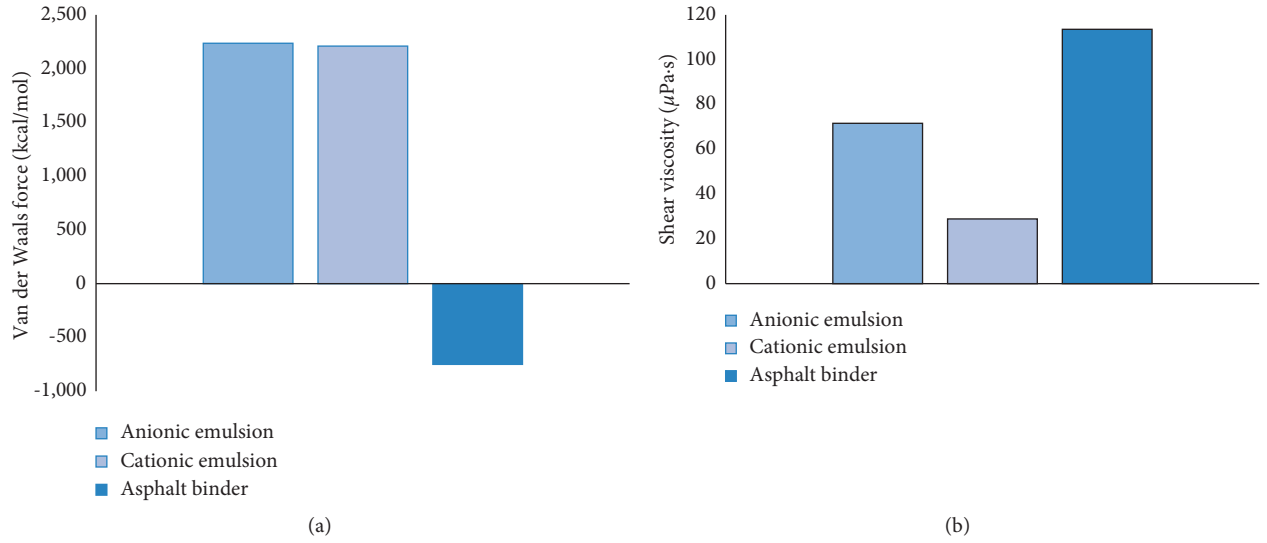

Figure 3: (a) The Van der Waals force of different kinds of samples. (b) The shear viscosity of different kinds of samples.

aggregate, it will have breaking behavior [27, 28]. Therefore, its viscosity should be as small as possible to make the mixing more uniform [29].

The viscosity of the emulsified asphalt binder is calculated using the MD simulation. Here, the shear viscosity is employed to investigate the workability because the shear viscosity is the main force characteristics during mixing; the shear viscosity is the main force characteristics during mixing if the shear viscosity is smaller, indicating the workability is better. The shear viscosity at 25°C of different samples is shown in Figure 3(b).

It shows that the shear viscosity of the binder is larger than the two kinds of the emulsified binder, while the cationic emulsified asphalt binder has the lowest shear viscosity. It means the cationic emulsified asphalt binder provides a lower mixing resistance, leading to better workability and road construction quality.

3.4. Breaking of the Emulsified Asphalt Binder. In the emulsified asphalt, the emulsifier lies between the asphalt binder and water and keeps stable due to chemical response. The chemical response will be broken during the emulsified asphalt breaking. Furthermore, the breaking process is curial for the emulsified asphalt mixture; it determines the wrap effect of the binder on aggregate, and it influences the mechanical properties of asphalt mixture significantly [30]. So, it should be understood more in depth.

To research the interaction response between emulsifier and asphalt binder/water, four interface models are created to investigate the interface energy; they are shown in Figure 4.

To evaluate the interface response, the interaction energy between the bituminous binder and the emulsifier is calculated based on equation (1), and the interaction energy between water and emulsifier is calculated by equation (2).

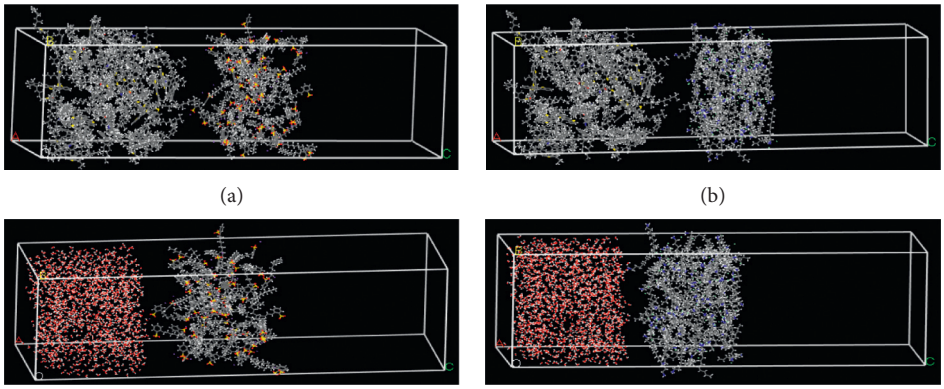

(a) (b) (c) (d)

Figure 4: The interface between emulsifier and asphalt binder/water: (a) asphalt binder vs. cationic emulsifier; (b) asphalt binder vs. anionic emulsifier; (c) water vs. cationic emulsifier; (d) water vs. anionic emulsifier.

This method draws on some research on the adhesion between aggregate and bituminous binder. This approach was successfully used to calculate the adhesion work between aggregate and bituminous binder [31]:

$$\Delta E_{\text{interface}} = E_{\text{total}} - \left(E_{\text{asphalt binder}} + E_{\text{emulsifier}}\right), \quad (1)$$

$$\Delta E_{\text{interface}} = E_{\text{total}} - \left(E_{\text{water}} + E_{\text{emulsifier}}\right). \quad (2)$$

The interaction of emulsifiers in the asphalt binder is shown in Figure 5. The results show that the anionic emulsifier has larger energy with either asphalt binder or water than the cationic emulsifier. The interaction between the asphalt binder and the anionic emulsifier is 3.9% larger than that of the asphalt binder and the cationic emulsifier; while the interaction between water and anionic emulsifier is 39.7% larger than the cationic emulsifier. Based on some research, the larger the energy is, the less the stability is [31]. So, the cationic emulsifier is more stable with asphalt binder and water, confirming the conclusion mentioned above: the cationic emulsified asphalt binder is more stable than the anionic emulsified asphalt binder.

In addition, these interactions have relationship with breaking; therefore, it is inferred that the two emulsifiers on the interaction with water are significantly different; the stability between anionic emulsifier and water is poorer than the cationic emulsifier obviously, so it means that the anionic emulsifier would lose water easier during breaking, resulting in a larger viscosity shortly, which cause the mixable time too short, and workability is poor. This conclusion is consistent with the workability results.

3.5. Properties of Emulsified Asphalt Evaporation Residue. To investigate the emulsifier on properties of asphalt binder quantitatively, the emulsifier in 0.6%, 1.7%, and 3.0% contents was added into the asphalt binder model in this section. For convenience, ID for different models was created: A0.6, A1.7, and A3.0 mean the emulsified asphalt evaporation residue with anionic emulsifier in dosage 0.6%, 1.7%, and 3.0%, respectively. Similarly, C0.6, C1.7, and C3.0

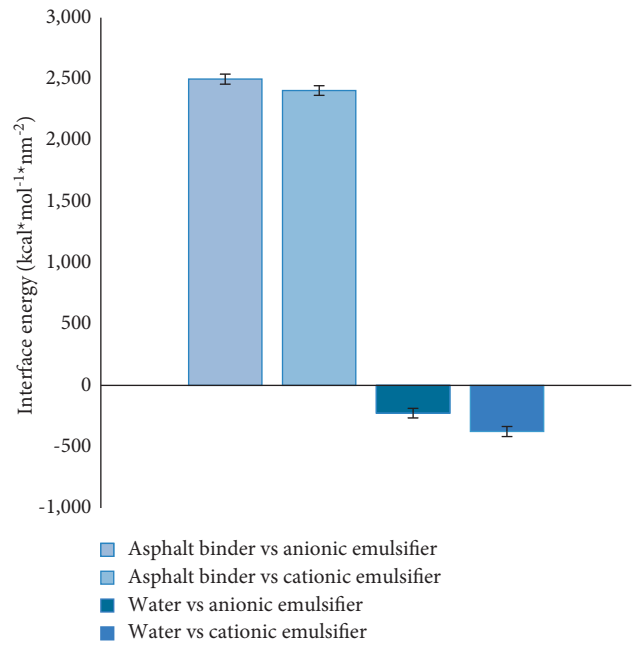

Figure 5: The interface energy results of the emulsifier.

mean the emulsified asphalt evaporation residue with the cationic emulsifier in dosage 0.6%, 1.7%, and 3.0%, respectively.

3.5.1. Density. For these three kinds of samples, the density of emulsified asphalt evaporation residue is simulated and calculated in this section. The specific results are shown in Figures 6(a) and 6(b).

Figure 6(a) shows the overall distribution of the density values of three samples: asphalt binder, A3.0, and C3.0 in the stable state; the ordering of these density values can be clearly seen; from large to small, it is A3.0, asphalt binder, and C3.0. Figure 6(b) shows the calculated average density value in the stable state of all samples. It is seen that the density of anionic emulsified asphalt evaporation residue decreases with the anionic emulsifier contents, while the

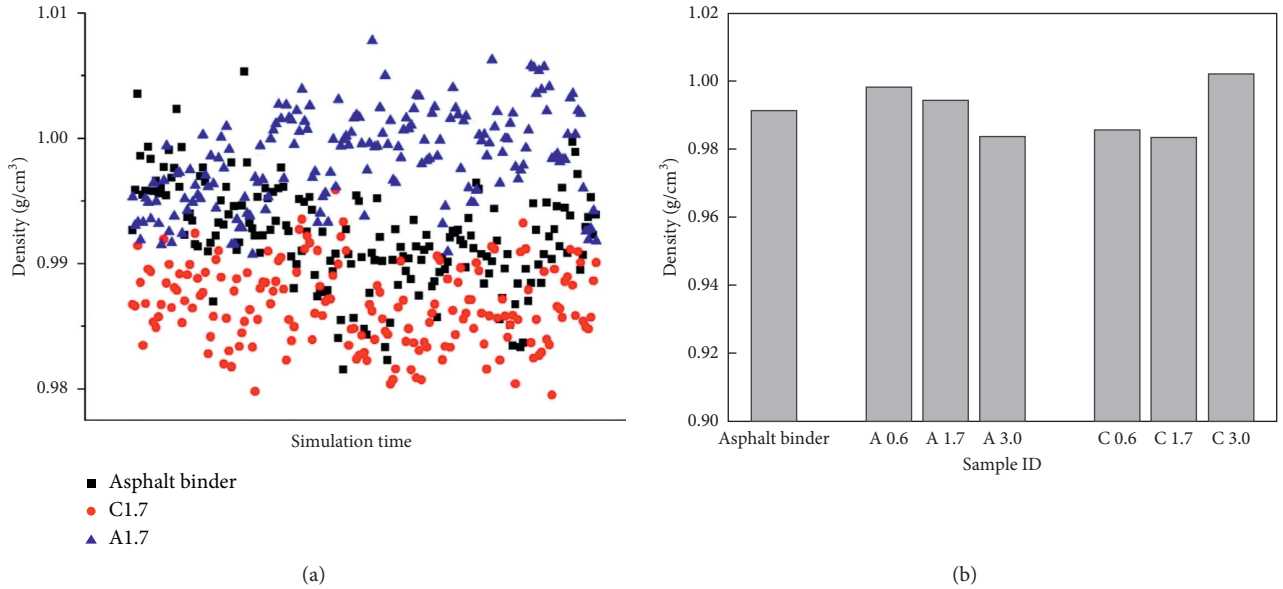

Figure 6: (a) The simulated density values of three kinds of samples; (b) the average density results.

trend between cationic emulsified asphalt evaporation residue and cationic emulsifier is not obvious, but the density of C3.0 is obviously larger than C0.6 and C1.7. In addition, the density of A0.6, A1.7, and C3.0 is greater than that of the asphalt binder based on the previous research [32]; there is a certain positive correlation between density and compressive strength of the asphalt binder; hence, the different types of emulsifiers should add into the asphalt binder in different contents. This point of view will be investigated more in depth in the subsequent section.

However, the compressive strength of emulsified asphalt mixture is generally worse comparing with the hot asphalt mixture due to its large void ratio. Therefore, the compressive strength of the emulsified asphalt mixture can be improved if its mixing process would be optimized.

3.5.2. Mechanical Properties. The mechanical properties of the asphalt binder have an important influence on road performance. So, the mechanical properties about two kinds of emulsified asphalt evaporation residue should be analyzed. Based on some previous research [15, 33], there is an obvious correlation between cohesive energy density (CED) and mechanical properties. The CED results are simulated and shown in Figure 7.

It is seen that both the anionic and cationic emulsified asphalt evaporation residue have a larger CED value comparing with the asphalt binder, indicating the anionic and cationic emulsified asphalt evaporation residue have better mechanical properties. There is an interesting pheromone; the density of emulsified asphalt evaporation residue A3, C0.6, and C1.7 is smaller, while their cohesive energy density is larger than the asphalt binder, concluding that the emulsifier plays a certain role in improving the mechanical properties of the asphalt binder.

However, as mentioned above, the mechanical properties of emulsified asphalt mixture are generally worse

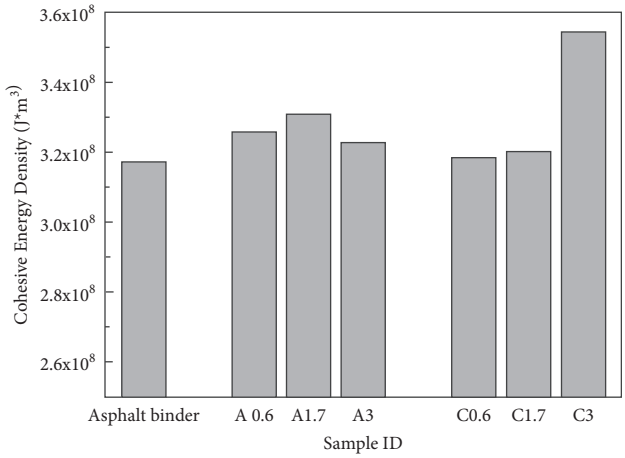

Figure 7: The CED results of different samples.

comparing with the hot asphalt mixture due to its large void ratio. So, it is theoretically inferred that the mechanical properties of the emulsified asphalt mixture would be better if its mixing process would be optimized to control the void ratio.

3.5.3. Adhesion Behavior. Some previous research has proven that the adhesion capability of the anionic emulsified asphalt binder is relatively poor due to its anion, which creates a repulsive force with the charge on the aggregate surface [34]. So, the adhesion behavior is investigated in this section.

The adhesion is a complex behavior, which contains micro- and macroscale behavior. However, a preliminary research of adhesion behavior is carried out on the micro; therefore, physical adhesion and roughness of the aggregate is ignored macroscopically.

In order to research the adhesion behavior of the various kinds of bituminous binders, interface systems of silica and bituminous binders are established by putting a 30A vacuum pad in them [27]. This interface model of aggregate and emulsified asphalt is almost the same with the interface model of aggregate and asphalt binder [33]. Based on the previous calculation method, their interface energy for adhesion results is shown in Figure 8.

The simulation result shows that the adhesion of each anionic bituminous binder is worse compared with the asphalt binder; meanwhile, the emulsified bituminous binder C0.6 has better adhesion, while C1.7 and C3.0 have worse adhesion than the bituminous binder. The adhesion properties of emulsified asphalt binders decrease with increasing emulsifier content. In general, cationic asphalt binders have good adhesion due to their positive charge [34], but as the cationic emulsifier content increases, their adhesion gradually decreases. This is mainly due to the limitations of the test method, i.e., the use of a macroscopic device to test the adhesion between the aggregate and the bituminous binder. The roughness of aggregate and macroscopic physical adhesion affects the results of the microadhesion properties. In this study, only the adhesion behavior at the microscopic scale was investigated.

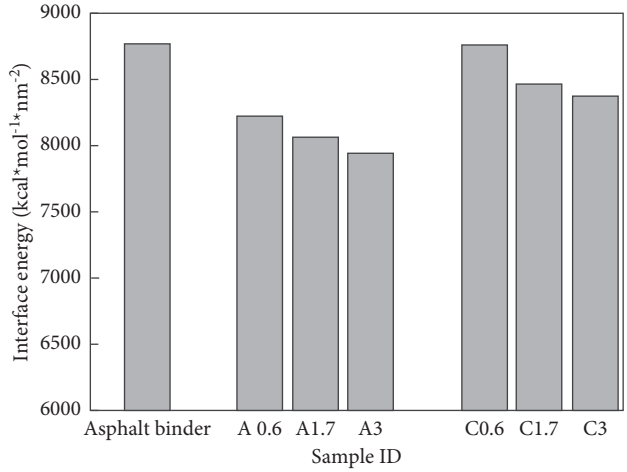

Figure 8: The interface energy results of three kinds of samples.

Table 1: ANOVA of density, CED, and interaction energy.

Source	Significance of variable		
	Density	CED	Interaction energy
Emulsifier	0.883	0.771	0.008
Content	0.948	0.649	0.040

3.6. Relationship between Emulsifier and Properties of Emulsified Asphalt Evaporation Residue. According to the results of properties of emulsified asphalt evaporation residue mentioned in Section 3.5, the different aging states about the same kind of the asphalt binder are analyzed; then, the effects of emulsifier type and content on the properties of emulsified asphalt evaporation residue are studied by variance (ANOVA) in SPSS. The analysis of ANOVA is shown in Table 1.

It is seen that the significance of the emulsifier type and content on density and CED are larger than 0.05, indicating that the emulsifier type and content have little influence on the density and CED of the residue; while the significance of the emulsifier type and content on interaction energy is smaller than 0.05, meaning that the emulsifier type and content have an obvious impact on the adhesion behavior of the residue. According to this finding, the type and content of the emulsifier have a significant influence on the storage stability, workability, etc., of the emulsified asphalt binder, although they have limited effect on the density and CED of the residue, so it is favorable for emulsified asphalt that the emulsifier only works on emulsifying the asphalt binder into water and has no significant impact on the properties of residue. However, according to the analysis of ANOVA for interaction energy, it is suggested that the adhesion property should be considered in the production process of the emulsified asphalt binder.

4. Conclusion and Outlook

A typical cationic emulsifier (dodecyl benzene sulfonate) and a typical anionic emulsifier (dodecyl primary amine) are studied from a microperspective in this study. Six models for two emulsifiers, two emulsified asphalt binders, and emulsified asphalt evaporation residue with different contents of the emulsifier are designed to research the influence of emulsifiers on the stability and workability of emulsified asphalt binder, and the properties of emulsified asphalt evaporation residue are also explored. Some conclusions are as follows:

(i) According to the microproperties of the emulsifier, it is found that the workability of cationic emulsified asphalt mixture is better, and the stability of the cationic emulsified asphalt binder is better.

(ii) The technical performance of the emulsified asphalt binder indicates that the cationic emulsified asphalt binder has better workability and road construction quality.

(iii) Based on the interaction between the emulsifier and asphalt binder/water, it is known that the stability of cationic emulsified asphalt is better than that of the anionic emulsified asphalt binder; on the contrary, the anionic emulsifier would lose water easier in the breaking, resulting in a larger viscosity shortly,

which causes the mixable time to be too short, and workability is poor.

(iv) The properties of two kinds of emulsified asphalt evaporation residue show that the density of anionic emulsified asphalt evaporation residue is larger, while the mechanical properties of cationic emulsified asphalt evaporation residue are larger, indicating that the cationic emulsifier has some effect to improve the mechanical property of the asphalt binder theoretically.

Finally, according to the simulation analysis, some properties of the emulsified asphalt binder are better than those of the asphalt binder because the simulation is an ideal method to investigate these bituminous materials; if the construction process of emulsified asphalt mixture would be ideal, the porosity would be in the desired range, and the performance of the emulsified asphalt mixture would be better. So, the optimization of the construction process of the emulsified asphalt mixture will be the next focus in the future.

Data Availability

The data used to support the findings of this study are available from the corresponding author upon request.

Conflicts of Interest

The authors declare that there are no known conflicts of interest associated with this publication.

Acknowledgments

This study was supported by the National Natural Science Foundation of China, under Grant nos. 52078048 and 52008029. The researchers gratefully acknowledge financial support of the foundation, and they are in charge of the authenticity of the test data.

References

[1] Y. Tan, J. Ouyang, J. Lv, and Y. Li, "Effect of emulsifier on cement hydration in cement asphalt mortar," *Construction and Building Materials*, vol. 47, pp. 159–164, 2013.

[2] Z. Wang, Q. Wang, T. Ai, J. Conbuildmat, C. E. A. Mixture, and C. Ages, "Comparative study on effects of binders and curing ages on properties of cement emulsified asphalt mixture using gray correlation entropy analysis," *Construction and Building Materials*, vol. 54, pp. 615–622, 2014.

[3] D. D. Li and M. L. Greenfield, "Chemical compositions of improved model asphalt systems for molecular simulations," *Fuel*, vol. 115, pp. 347–356, 2014.

[4] L. Zhang and M. L. Greenfield, "Relaxation time, diffusion, and viscosity analysis of model asphalt systems using molecular simulation," *The Journal of Chemical Physics*, vol. 127, no. 19, Article ID 194502, 2007.

[5] L. Zhang and M. L. Greenfield, "Effects of polymer modification on properties and microstructure of model asphalt systems," *Energy & Fuels*, vol. 22, no. 5, pp. 3363–3375, 2008.

[6] M. Guo, M. Liang, A. Anand, A. Amit, and D. Luo, "Characterisation of rejuvenation of various modified asphalt binders based on simplified chromatographic techniques," *International Journal of Pavement Engineering*, vol. 2, pp. 1–11, 2021.

[7] M. Guo, X. Liu, Y. Jiao, Y. Tan, and D. Luo, "Rheological characterization of reversibility between aging and rejuvenation of common modified asphalt binders," *Construction and Building Materials*, vol. 301, Article ID 124077, 2021.

[8] M. Guo, H. Liu, Y. Jiao et al., "Effect of WMA-RAP technology on pavement performance of asphalt mixture: a state-of-the-art review," *Journal of Cleaner Production*, vol. 266, Article ID 121704, 2020.

[9] H. T. Osborn and C. C. Akoh, "Effect of emulsifier type, droplet size, and oil concentration on lipid oxidation in structured lipid-based oil-in-water emulsions," *Food Chemistry*, vol. 84, no. 3, pp. 451–456, 2004.

[10] P. D. Ribotta, G. T. Pérez, A. E. León, and M. C. Añón, "Effect of emulsifier and guar gum on micro structural, rheological and baking performance of frozen bread dough," *Food Hydrocolloids*, vol. 18, no. 2, pp. 305–313, 2004.

[11] W. G. Waggoner and J. H. Fincher, "Influence of hlb values of surfactants on ephedrine release from emulsified liquid systems," *Journal of Pharmaceutical Sciences*, vol. 60, no. 12, pp. 1830–1835, 2010.

[12] L. Zhang and M. L. Greenfield, "Analyzing properties of model asphalts using molecular simulation," *Energy & Fuels*, vol. 21, no. 3, pp. 1712–1716, 2007.

[13] L. Zhang and M. L. Greenfield, "Rotational relaxation times of individual compounds within simulations of molecular asphalt models," *The Journal of Chemical Physics*, vol. 132, no. 18, 2010.

[14] Y. Hou, L. Wang, D. Wang, M. Guo, P. Liu, and J. Yu, "Characterization of bitumen micro-mechanical behaviors using AFM, phase dynamics theory and MD simulation," *Materials*, vol. 10, no. 2, 2017.

[15] X. Qu, D. Wang, Y. Hou, Q. Liu, M. Oeser, and L. Wang, "Investigation on self-healing behavior of asphalt binder using a six-fraction molecular model," *Journal of Materials in Civil Engineering*, vol. 31, no. 5, Article ID 04019046, 2019.

[16] X. Qu, Q. Liu, M. Guo, D. Wang, and M. Oeser, "Study on the effect of aging on physical properties of asphalt binder from a microscale perspective," *Construction and Building Materials*, vol. 187, pp. 718–729, 2018.

[17] I. A. Wiehe and K. S. Liang, "Asphaltenes, resins, and other petroleum macromolecules," *Fluid Phase Equilibria*, vol. 117, no. 1–2, pp. 201–210, 1996.

[18] L. W. Corbett, "Composition of asphalt based on generic fractionation, using solvent deasphaltening, elution-adsorption chromatography, and densimetric characterization," *Analytical Chemistry*, vol. 41, no. 4, pp. 576–579, 1969.

[19] G. Šebor, J. Blažek, and M. F. Nemer, "Optimization of the preparative separation of petroleum maltenes by liquid adsorption chromatography," *Journal of Chromatography A*, vol. 847, no. 1–2, pp. 323–330, 1999.

[20] X. Quan, L. Kong, H. Wang, Y. Zhang, W. Luo, and B. Yang, "Molecular dynamics and experimental study on the influence of hydrophilic group on the adsorption of dodecyl anionic emulsifier on SiO2 surface," *Acta Materiae Compositae Sinica*, pp. 1–15, 2021.

[21] L. Shi, L. Cao, M. Wang, Y. Chen, and T. Ji, "Synthesis of octadecyl-bis(2-hydroxypropyl)-sodium acetate-based ammonium chloride asphalt emulsifier," *Journal of Pingdingshan University*, vol. 035, no. 2, pp. 30–35, 2020.

[22] L. Shi, Z. Yang, R. Zhao, Z. Ren, T. Wang, and Y. Chen, "Synthesis and performance of quaternary ammonium

asphalt emulsifier based on octadecylamine," *Journal of Pingdingshan University*, vol. 34, no. 2, pp. 50–57, 2019.

[23] D. W. V. Krevelen and K. T. Nijenhuis, *Properties of Polymers: Their Correlation with Chemical Structure; Their Numerical Estimation and Prediction from Additive Group Contributions*, Elsevier, Amsterdam, Netherland, 2009.

[24] H. Wang, C. Wang, and Z. Wang, "The Influence of Emulsifier System on the storage stability of emulsified asphalt," *Petroleum asphalt*, vol. 22, no. 4, pp. 10–13, 2008.

[25] B. Derjaguin and L. Landau, "Theory of the stability of strongly charged lyophobic sols and of the adhesion of strongly charged particles in solutions of electrolytes," *Progress in Surface Science*, vol. 43, pp. 30–59, 1941.

[26] E. J. W. Verwey, "Theory of the stability of lyophobic colloids," *The Journal of Physical and Colloid Chemistry*, vol. 51, no. 3, 636 pages, 1947.

[27] D. Tian, Q. Yuan, R. Zhu, C. Wang, and D. Deng, "Effect of water on static mechanical properties of cement emulsified asphalt mortar," *Journal of the Chinese Ceramic Society*, vol. 40, no. 11, pp. 1544–1552, 2012.

[28] D. Wang, P. Hao, N. Liu, H. Zhang, and Z. Li, "Workability Indicator For Emulsified Asphalt Recycled Mixture And Influence Factors," *Journal of Beijing University Technology*, 2016.

[29] M. F. Kuo, C. T. Lu, J. C. Du, and Y. K. Chen, "Workability of fresh cement-asphalt mastic," *Applied Mechanics and Materials*, vol. 368-370, pp. 1027–1030, 2013.

[30] J. Ouyang, Y. Tan, Y. Li, and J. Zhao, "Demulsification process of asphalt emulsion in fresh cement-asphalt emulsion paste," *Materials and Structures*, vol. 48, no. 12, pp. 3875–3883, 2015.

[31] G. Xu and H. Wang, "Study of cohesion and adhesion properties of asphalt concrete with molecular dynamics simulation," *Computational Materials Science*, vol. 112, pp. 161–169, 2016.

[32] X. Qu, D. Wang, Y. Hou, M. Oeser, and L. Wang, "Influence of paraffin on the microproperties of asphalt binder using MD simulation," *Journal of Materials in Civil Engineering*, vol. 30, no. 8, Article ID 04018191, 2018.

[33] X. Qu, Q. Liu, C. Wang, D. Wang, and M. Oeser, "Effect of Co-production of renewable biomaterials on the performance of asphalt binder in macro and micro perspectives," *Materials*, vol. 11, no. 2, 2018.

[34] S. Han and D. Zhang, "Study on factors affecting the adhesion of mineral materials and emulsified asphalt," *Petroleum asphalt*, vol. 9, no. 1, pp. 23–25, 1995.

Hindawi
Advances in Materials Science and Engineering
Volume 2021, Article ID 8181688, 11 pages
https://doi.org/10.1155/2021/8181688

Research Article

Research on the Ecological Protection of Coal Gangue Slope Based on a Polymer Curing Agent

Jian Zhang, Wen Yi, Weijia Yuan, Yifang Liu, and Zifan Sui

School of Civil Engineering, Central South University of Forestry and Technology, Changsha 410004, China

Correspondence should be addressed to Wen Yi; yiwengangbiao@163.com

Received 19 August 2021; Accepted 6 November 2021; Published 18 November 2021

Academic Editor: Baskaran Rangasamy

To improve the ecological protection of coal gangue slopes, this work developed a polymer curing agent using a pure acrylic emulsion and cement as the main raw materials. By testing the workability, waterproofing, durability, and adhesion of the curing agent with different polymer-to-cement ratios, the optimum mixing ratio of the polymer curing agent was obtained, and the protection mechanism was analysed based on the test results and by scanning electron microscopy (SEM). Then, simulated slope and practical engineering applications were carried out. The results show that pure acrylic emulsion curing agent with a polymer-to-cement ratio of 6 : 5 is most suitable for the ecological protection of coal gangue slopes. The polymer curing agent can form a network structure film layer with a good waterproofing effect on the coal gangue surface. Simultaneously, the network structure film layer can reduce the influence of weathering and leaching on the coal gangue, prevent the heavy metal elements in coal gangue from entering the surrounding soil, improve the growth environment of plants, and improve the effect of ecological restoration. This research can be applied to the ecological protection of coal gangue slopes.

1. Introduction

Coal gangue is solid waste discharged in the process of coal mining and washing. It is a black, grey rock with a lower carbon content and harder structure than coal and is associated with the coal seam in the process of coal formation. Under weathering, the physical and chemical properties of coal gangue accumulating on the ground continuously change; with the increase in degree of weathering, the conductivity and pH of coal gangue decrease, and its tendency to disintegrate gradually increases [1]. Coal gangue piled in open air is prone to spontaneous combustion, generates harmful gases and heavy metals, and results in severe geological disasters and environmental pollution [2, 3]. Under the action of weathering and leaching, heavy metal elements in coal gangue enter the surrounding soil and water, degrade the ecological environment, and hinder plant growth and ecological restoration [4–6]. Gangue slopes are special rock slopes formed by gangue accumulation that are more complex and difficult to protect. Gangue slopes are often unstable due to the weathering and disintegration of gangue. Due to the influence of the unfavourable properties of gangue, plants cannot grow normally on these slopes, and it is difficult to achieve the desired ideal slope protection effects using conventional ecological protection methods [7–10].

Currently, mortar plaster, concrete, wall protection, and other methods are commonly used to protect coal gangue slopes. Although these methods have good protection effects, materials such as mortar and concrete hinder the growth of plants, and it is difficult to achieve the goals of both slope protection and ecological restoration [11–14]. Ecological protection mainly relies on the reinforcing effect of plant roots on soil to achieve the slope protection effect. The commonly used methods include soil spraying, plant fibre blankets, and planting belts. The key to the effect of slope protection by these methods is the normal growth of plants on the slope [15–20]. Coal gangue after spontaneous combustion shows weak acid and high heavy metal contents that are not conducive to plant growth. Many researchers have studied the reclamation of coal mining areas. For example, Sydnor et al. [21] found that the addition of organic

matter to surface soil could increase the biomass and required nutrient elements for plant growth in mining areas and promote the restoration of vegetation in mining areas. Liu et al. [22] improved the growth environment of plants in mining areas by covering coal gangue with loess and achieved good ecological restoration results. Du et al. [23] used coal gangue as the component of planting substrate, configured a planting substrate suitable for ecological restoration in coal mine areas, and proved that the new substrate configuration was effective through experiments. Although these studies have made some progress in the reclamation of coal mine areas, their application is limited due to different properties of coal gangue in different areas, and the existing vegetation restoration methods cannot solve the problem that coal gangue is prone to weathering and disintegration.

Polymer curing agents are chemical reinforcement materials mainly composed of polymer materials and supplemented by other materials. There are many polymer curing agents, and they have been widely used in the field of soil reinforcement and slope protection in recent years [24–30]. Liu et al. [31–33] developed a polyurethane polymer curing agent, conducted a thorough study on its properties of strengthening sand and clay, and found that the polyurethane polymer curing agent mainly increased the cohesion between the soil particles and the erosion resistance of slope soil through the physical and chemical action between the polymer functional groups and the surface ions of soil particles. Yang et al. [34] developed a new polymer soil stability additive (M-CMC) composed of methyl cellulose (CMC) and polyacrylamide (PAM) and experimentally showed that it could improve the soil strength, water stability, and erosion resistance. Yao et al. [35] developed a polymer curing agent suitable to protect soft rock slopes, and practical engineering applications showed that its protection effect was good and conducive to the ecological restoration of soft rock slopes. Qin et al. [36] adopted W-OH hydrophilic polyurethane material to solidify and protect red clay slopes, and based on experiments, they concluded that W-OH could significantly improve the antierosion ability of red clay slope soil, increase the water retention performance of the soil, and promote the germination and growth of plants on the slope. Therefore, the study of the application of polymer curing agents in the ecological protection of gangue slopes is highly important.

To solve the problems posed by coal gangue, such as easy weathering, easy disintegration in water, low pH value, high heavy metal content, and difficulties in the ecological protection of slopes, this work uses a pure acrylic emulsion and ordinary Portland cement as the main raw materials and polymer curing agents with different polymer-to-cement ratios. The optimal mixing ratio of polymer curing agent suitable for coal gangue slope protection was determined through workability, waterproofing, durability, and adhesion tests. Simultaneously, the protection mechanism was analysed by matching the test results and scanning electron microscopy (SEM) images. Finally, a new method for the ecological protection of gangue slopes with polymer curing agents was proposed and applied to simulated slopes and in actual engineering practice. Then, the application effect of polymer curing agents in the ecological protection of gangue slopes was analysed according to the application results.

2. Materials and Methods

2.1. Materials

2.1.1. Polymer Emulsion. Polymer emulsions are formed by dispersing polymer particles in micron aqueous solutions that show good water resistance, durability, and bond strength and are important raw materials for the configuration of polymer curing agents. Considering the difficulty of obtaining raw materials and suitability for ecological slope protection, a pure acrylic emulsion produced by Luyuan Chemical Company was selected as the configuration of the polymer curing agent. As a widely used waterproof building material, pure acrylic emulsions are easy to obtain, environmentally friendly, and conducive to ecological restoration. Pure acrylic emulsion is shown in Figure 1. The performance index of the pure acrylic emulsion indicated by the manufacturing company is shown in Table 1.

2.1.2. Cement. Cement is also one of the main components of polymer curing agents, and its type and dosage directly affect the strength of polymer curing agents. In consideration of economy and durability, common silicate P.O42.5 cement produced by Yangchun Cement Limited Company was selected to configure the polymer curing agent. The performance indices of the P.O42.5 cement indicated by the manufacturing company are shown in Table 2.

2.1.3. Coalescing Agents. A coalescence agent is a material that can promote the plastic flow and elastic deformation of polymer emulsions, improve their coalescence performance, and form films over a wide range of construction temperatures. It can clearly reduce the minimum film forming temperature of polymer emulsions and improve their coalescence, durability, and storage stability. In this experiment, the alcohol ester coalescing agents produced by Luyuan Chemical Company were used in the polymer emulsion material configuration. The performance indices of the film forming additives indicated by the manufacturing company are shown in Table 3.

2.1.4. Defoaming Agent. When mixing a polymer emulsion and cement, many bubbles will be generated. Bubbles will cause many pores to solidify the curing agent, which affects the curing effect. Therefore, an appropriate amount of defoamer should be added in the preparation process to reduce the number of bubbles and enhance the curing effect of the polymer curing agent. In this work, an emulsion-type silicone defoamer produced by Luyuan Chemical Company was used to configure the polymer curing agent. The performance indices of the silicone defoamer agent indicated by the manufacturing company are shown in Table 4.

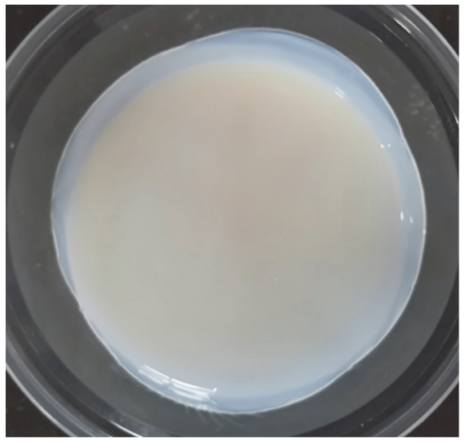

Figure 1: Pure acrylic emulsion.

Table 1: Performance indices of pure acrylic emulsion.

Order number	Technical indicators	Test results
1	Appearance	Milky white uniform liquid, no impurities, no precipitation, and no stratification
2	Solid content (%)	50
3	pH	7.4
4	Viscosity (mPa·s)	800
5	Residual stability (%)	0.03

Table 2: Performance indices of P.O42.5 cement.

Order number	Technical indicators	Test conditions	Test results
1	Fineness	—	14.0%
2	Standard consistency	—	25.2%
3	Curing time	Initial curing	105 min
		Final curing	229 min
4	Rupture strength (MPa)	3d	6.2 MPa
		28d	8.3 MPa
5	Compressive strength (MPa)	3d	26.8 MPa
		28d	59.1 MPa

Table 3: Performance indices of coalescing agents.

Order number	Technical indicators	Test results
1	Appearance	Colourless transparent liquid, without soluble matter
2	Freezing point (°C)	−50.0
3	Flash point (°C)	120

Table 4: Performance indices of the silicone defoamer agent.

Order number	Technical indicators	Test results
1	Appearance	Milky white uniform emulsion liquid, no precipitate, no visible mechanical impurities
2	pH	7.2
3	Solid content (%)	15
4	Stability (mL)	0.02
5	Defoaming time (s)	11 (10 times)
		25 (100 times)

2.2. Configuration Method. The pure acrylic emulsion curing agent consists of a pure acrylic emulsion with waterproof performance, cement, small amounts of coalescing agents, and defoaming agent. It is a polymer cement-based composite material with the main properties of pure acrylic emulsion and cement. The pure acrylic emulsion curing agent can be prepared by simple stirring and mixing. Under normal temperature and pressure, the raw materials were

weighed according to the weight percentage of each raw material, and the pure acrylic emulsion was artificially stirred at low speed for 60 s. Then, the corresponding amount of cement was added to the pure acrylic emulsion. Finally, the mixture was stirred by a cement mixer at high speed for 120 s and left standing for 300 s. To reduce the bubbles generated during mixing, 1% of the total weight of the mixture defoaming agent was added during mechanical mixing. Simultaneously, 3% of the total weight of the mixture coalescing agents was added to ensure the final film-forming effect.

2.3. Test Methods. The weight ratio between the content of the polymer solid particles in the polymer curing agent and the mass of cement is called the polymer-to-cement ratio and expressed by P/C. In this work, five pure acrylic emulsion curing agents with different polymer-to-cement ratios (P/C = 0.6, 0.8, 1, 1.2, 1.4) were set up; then, mixing proportion tests were performed, including workability tests, waterproof property tests, durability tests, and adhesion tests. Based on the test results, the mixing ratio of the pure acrylic emulsion curing agent that was most suitable for coal gangue slope protection was obtained, and the protective mechanism was analysed by scanning microscopy.

2.3.1. Workability Test. The workability of the polymer curing agent refers to its setting time and viscosity, which represent the difficulty of its construction. If the initial setting time is too short, the construction is difficult; if the final setting time is too long, the construction progress will be affected. In this test, according to the test method of cement setting time in the China standard (GB/T 1346–2011) [37], a Vicat instrument was used to test the curing time of pure acrylic emulsion curing agents with different polymer-to-cement ratios. The viscosity of the polymer curing agent represents the friction force of its internal molecules. Greater viscosity corresponds to smaller fluidity and leads to greater difficulty of construction. Meanwhile, a smaller viscosity corresponds to greater fluidity, delamination, and segregation. According to the Chinese standard (JJG 1002–2005) [38], a rotary viscometer was used to determine the viscosity of the pure acrylic emulsion curing agent.

2.3.2. Waterproof Test. The waterproofing ability of the polymer curing agent is an important index to evaluate its performance and the basis to solve the problem of the easy disintegration of coal gangue when encountering water. The water resistance can be expressed by the natural water absorption rate of the material, that is, under the condition of standard atmospheric pressure, the ratio of the mass of water in the experimental specimen that was soaked in water for 48 h to the mass of the dried experimental specimen. In this work, coal gangue with basically identical size was selected as the test specimen, and polymer curing agents with different polymer-cement ratios were evenly applied to the sample with a coating thickness of 5–6 mm for the 48 h waterproof test. The experiment was performed according to the steps of the rock water absorption test in the Chinese standard (JTG E41–2005) [39]. The coal gangue sample coated with pure acrylic emulsion curing agent is shown in Figure 2.

2.3.3. Durability Test. The durability of the polymer curing agent represents its long-term protection performance and is an important parameter to evaluate whether the agent is suitable for coal gangue slope protection. In this work, the durability of the curing agent of a pure acrylic emulsion was evaluated by the number of cracks produced by gangue samples with different polymer-to-cement ratios. The test is based on the frost resistance test method specified in the China Standard (JC/T 984–2011) [40], and the number of cracks on the surface of the specimens after 25 cycles of drying and wetting was observed.

2.3.4. Adhesion Test. The bonding strength of the polymer curing agent usually refers to the cohesion of the polymer curing agent and the bonding force between the specimen coating and the bonding surface, which indicates the strength of its bonding. A greater bonding strength makes it more difficult for the agent to fall off on the slope surface and leads to an improved protection effect. In this work, referring to the test method of mortar tensile bond strength in the Chinese code (JGJ/T70–2009) [41], a tensile testing machine was used to test the bond strength of the pure acrylic emulsion curing agent.

2.3.5. Microscanning Test. In this paper, a HITACHI SU8100 scanning electron microscope (SEM, Hitachi, Japan) was used to conduct the scanning microscopy test. Under the condition of 1000-fold magnification, the microscopic surface morphology characteristics of coal gangue specimens sprayed with different polymer-to-cement ratios of pure acrylic emulsion curing agent and coal gangue specimens not sprayed with curing agent were observed.

3. Results and Discussion

3.1. Mixing Ratio Test. The test results for the workability, waterproofing ability, durability, and adhesion of the curing agent of pure acrylic emulsions with different polymer-to-cement ratios are shown in Table 5.

Table 5 shows that a greater P/C leads to a longer setting time of the pure acrylic emulsion curing agent, smaller viscosity, and greater fluidity. With the increase in P/C, the water absorption rate of the test specimen gradually decreases and tends to be stable. The number of cracks on the surface of the test specimen and bonding strength of the curing agent first decrease and subsequently increase. When P/C is 1.2, the number of cracks on the surface of the test specimen is lowest, and the curing agent has the maximal bonding strength. The workability of the pure acrylic emulsion curing agent mainly depends on the cement content, so with the increase in P/C, the cement content shows a relative decrease, the setting time of the curing agent

Figure 2: Coal gangue specimens coated with pure acrylic emulsion curing agent.

Table 5: Performance test results for pure acrylic emulsion curing agents with different polymer-to-cement ratios.

P/C	Initial setting time (min)	Final setting time (min)	Viscosity (MPa·s)	Bibulous rate (%)	Number of cracks	Bonding strength (MPa)
0.6	104	341	64	5.71	6	1.54
0.8	113	382	56	3.15	4	1.73
1.0	126	429	48	1.42	2	1.96
1.2	134	447	46	0.39	1	2.05
1.4	151	524	44	0.33	3	1.86

becomes longer, and the viscosity decreases. The workability of pure acrylic emulsion curing agents with different polymer-to-cement ratios can satisfy the construction requirements, and the workability is the best when P/C is 1.2.

When P/C is small, the cement content in the curing agent is relatively high, and the polymer emulsion content is low. The hydration product of cement is mainly the network structure, and a small amount of polymer particles cannot completely fill the network structure. Therefore, the polymer network structure film formed is relatively small, which results in a relatively large water absorption of gangue sample block. With the increase in P/C, the polymer emulsion plays a dominant role in the curing agent, and the formed network film almost completely covers the surface of gangue, which decreases the water penetration rate and water absorption rate of the test block. The lowest value is obtained when P/C is 1.2. The bonding strength of the polymer curing agent is mainly determined by the solid content of the polymer emulsion and hydration product of cement. When P/C is less than 1.2, the content of pure acrylic emulsion increases with increasing P/C, and so, the bonding strength increases. When P/C is greater than 1.2, the bonding strength of the pure acrylic emulsion reaches its peak, the cement content in the polymer curing agent is relatively reduced, and the content of cement hydration products is relatively reduced, and so, the bonding strength begins to decrease. According to the mixing ratio test, the pure acrylic emulsion curing agent with a P/C of 1.2 is most suitable for the protection of coal gangue slopes.

3.2. Microscopy Results. The scanning electron microscopy (SEM) results of coal gangue specimens are shown in Figure 3.

As shown in Figure 3(a), the surface of coal gangue is loose and porous. Under infiltration and erosion by rain, it is easily weathered and disintegrated. As shown in Figures 3(b)–3(f) the polymer particles of the pure propylene emulsion and hydration products of cement connect with each other, which form a reticular membrane structure. When P/C is less than 1.2, the content of pure acrylic emulsion is small, polymer particles are not sufficient to completely wrap the cement hydration product, and the network film formed has more pores, which makes the curing agent waterproof and endows it with poor durability. With the increase in P/C, the pores of the curing agent of the pure acrylic emulsion gradually decrease. When P/C is 1.2, the polymer particles almost completely wrap around the hydration product of cement, which leads to a lower porosity of the curing agent film and good waterproofing performance. When P/C is greater than 1.2, the content of cement hydration products in the curing agent film decreases, and the strength of the curing agent film also decreases. Therefore, the durability and bond strength gradually decrease.

In summary, after pure acrylic emulsion has been mixed with cement, the pure acrylic emulsion loses water due to cement hydration, and its polymer particles and cement hydration products interweave and intertwine to form a mesh film with good waterproof ability. By spraying pure acrylic emulsion curing agent on the surface of coal gangue, we can bond and solidify the loose and porous surface of coal gangue. The network film that covers the surface of coal gangue can increase its waterproof ability, prevent its weathering and disintegration, and improve the long-term stability of coal gangue slopes.

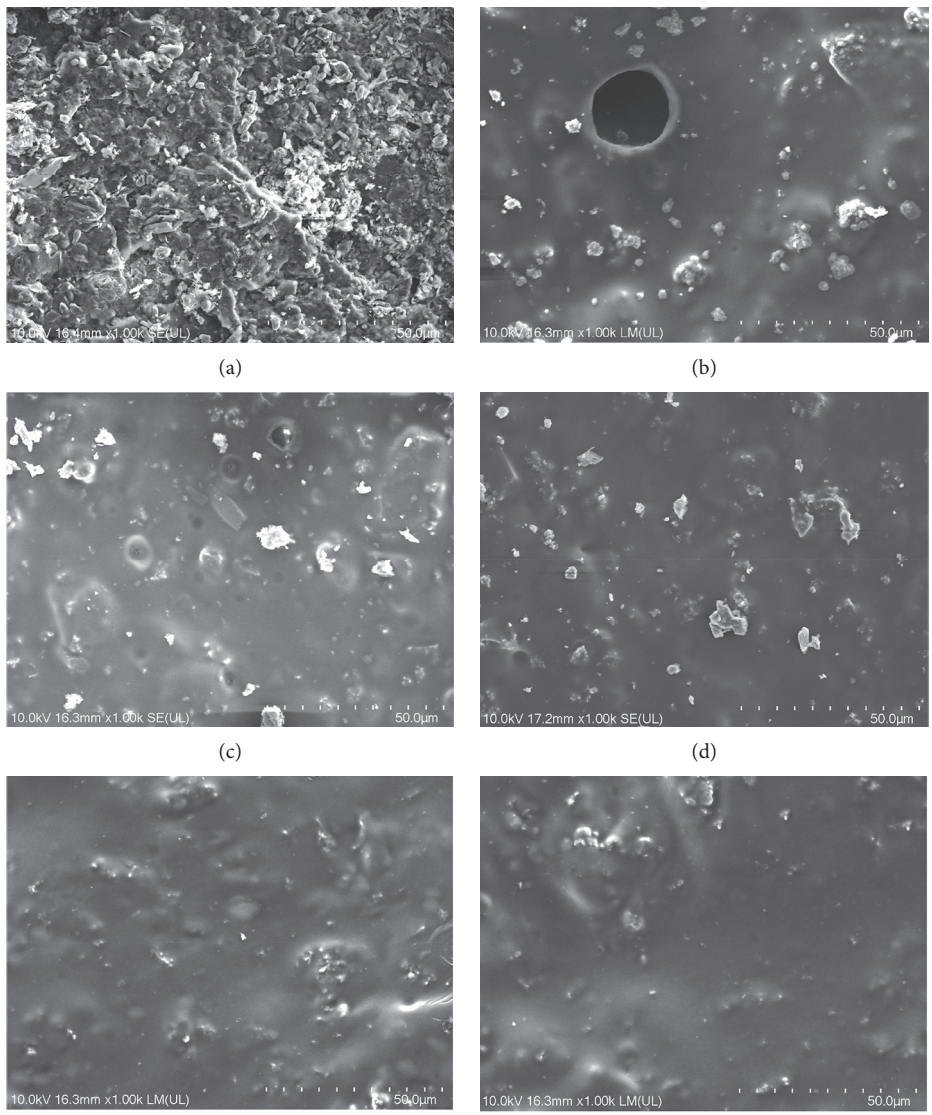

Figure 3: SEM images: (a) no curing agent was sprayed; (b) spray curing agent (P/C = 0.6); (c) spray curing agent (P/C = 0.8); (d) spray curing agent (P/C = 1.0); (e) spray curing agent (P/C = 1.2); (f) spray curing agent (P/C = 1.4).

4. Simulated Slope and Practical Engineering Application

In this work, a new ecological protection technology for coal gangue slopes is proposed, which involves first spraying with a pure acrylic emulsion curing agent and subsequently spraying into the guest soil. Polymer curing agents are mainly used for the surface protection and reinforcement of coal gangue, and the soil spraying technique is a green technology that benefits ecological protection. The combination of these two technologies results in a new ecological protection-enhancing technology for coal gangue slopes. To analyse the feasibility of the new ecological protection technology, this work studies the effect of the application of the new ecological protection technology on coal gangue slopes through simulated slope tests and practical engineering applications.

4.1. Simulated Slope Test

4.1.1. Test Method. The slope simulation test was performed using an outdoor model box. To accurately simulate the gangue slope, a 10–15-cm-thick layer of field sampled coal gangue was placed on the surface of each model box. Two slope model boxes with heights and widths of 1.2 m were designed and are referred to as model boxes A and B, respectively. Then, each model box was divided into three zones with different heights. In model box A, the surface of the laid coal gangue was directly sprayed with guest soil; in model box B, the surface of the laid gangue was first sprayed with pure acrylic emulsion curing agent with a P/C of 1.2 and subsequently sprayed with guest soil after solidification. Other construction methods and conditions are consistent. The proportion of plant seeds sprayed in foreign soil was 50 wt% herb seeds (30 wt% *Cynodon dactylon* (L.) Pers and 20

wt% *Festuca elata* Keng ex E. Alexeev) and 50 wt% shrub seeds (15 wt% *Sophora xanthoantha* C. Y. Ma, 15 wt% *Amorpha fruticosa L*, and 20 wt% *Magnolia multiflora* M. C. Wang et C. L. Min).

All simulated slopes were placed in the open area, and the management measures of seedlings were identical. Observations were made once every two weeks for six months, including the germination rate, coverage rate, height, soil erosion rate, and soil pH value. A collection tank is placed at the bottom of each simulated slope to collect the soil lost on the slope. The soil in the collection tank was collected and dried every two weeks, and the mass ratio between the collected soil mass and the initial substrate was calculated to evaluate the soil erosion. Model box A after laid coal gangue is shown in Figure 4(a), and model box B after spraying the pure acrylic emulsion curing agent is shown in Figure 4(b).

4.1.2. Results and Analysis. Figure 5 shows the plant growth on the simulated slope. The test results of the simulated slope are shown in Table 6.

As shown in Table 6, the plant germination rate of model box B was much higher than that of A, and the soil of model box A was acidic. The soil of model box B is neutral, which indicates that spraying pure acrylic emulsion curing agent on gangue slopes reduces the influence of weakly acidic coal gangue and heavy metal substances on the plant growth and improves the environment for plant growth. Model box B had a much higher vegetation coverage rate and a much lower soil erosion rate than model box A. With increasing time, the difference increased. These results show that spraying pure acrylic emulsion curing agent can improve the water retention ability of soil, increase the antierosion ability of foreign soil, and improve the growth environment of plants. In model box B, plant germination is high, vegetation coverage is high, and the soil and water loss is low. Three months after construction, vegetation basically covered the slope, and soil erosion was further reduced in the later stage, which benefited the slope protection.

As shown in Figure 5, due to the spraying of pure acrylic emulsion curing agent, the slope of model box B is complete, the vegetation development is much better than that of A, and an elastic consolidation layer with certain strength and toughness is formed on the surface of the slope. Three months after construction, the plants in model box B were mainly herbaceous plants, and the shrubs were mainly in the form of seedlings. Herbaceous and shrubbery grow well six months after construction. Due to the influences of weak acidity and heavy metals in coal gangue, the vegetation of model box A was not well developed. Three months after construction, the growth height of herbaceous plants and germination rate of shrubs were low, and the overall vegetation coverage was low. Six months after construction, most of the herbaceous plants withered, and only a few shrubs grew normally. At the top of the slope of model box A, few plants grew, and the slope scour was serious. With the increase in slope, the scour became increasingly severe and even exposed the laid coal gangue. Thus, the plant seeds sprayed at the slope top of model box A were washed away by rain, the coal gangue disintegrated under the infiltration of rain, and the surface guest soil slid with the disintegrating coal gangue, which resulted in a low plant germination rate and poor slope protection effect. As shown in Figure 6, the roots of slope protection plants do not have difficulty growing into the slope because there is a polymer curing agent layer, and their roots can pass through the sprayed pure acrylic emulsion curing agent layer to achieve ecological slope protection.

The simulated slope test shows that the newly proposed ecological protection method of coal gangue slopes in this paper is feasible. On one hand, the reticulated film of pure acrylic emulsion curing agent can greatly reduce the influence of weathering and leaching on coal gangue and prevent heavy metal elements in coal gangue from entering the surrounding soil. On the other hand, the pure acrylic emulsion curing agent can reduce the loss of water in the slope soil by preventing water from penetrating the rock formation, which improves the growth environment of plants and makes the plants luxuriantly grow, so the roots are developed and play a role of reinforcement for the soil.

4.2. Practical Engineering Application. Taking the coal gangue slope at K68 + 720 of the Longlang Expressway in Loudi City, Hunan Province, as the application object of the new protection scheme and taking the K72 + 630 coal gangue slope with the ordinary ecological slope protection method as the control, we studied the feasibility of the new protection scheme by evaluating the ecological protection status for both slopes after construction.

4.2.1. Project Overview. The Longlang Expressway starts from Longtang Town, Lianyuan City, Hunan Province, and ends at Langtang Town, Xinhua County, Hunan Province. The route strike zone is located in Xinhua County, Loudi City, Hunan Province, and the mountain trend is basically consistent with the geological structure line, that is, northeast trend. The corridor belt is composed of eroded middle and low mountains and hills. The terrain is generally high in the middle and low on the east and west sides. The tectonic denudation and dissolution in the area are strong with high mountains and steep slopes, developed gullies, mostly northeast trending gullies, and "V"-shaped gullies and valley sections. The surface water system is relatively developed, the bedrock is mostly exposed, and the vegetation is less developed. Some areas are abandoned mining areas. Many coal gangue slopes are formed by subgrade excavation with poor construction conditions and difficult ecological restoration.

4.2.2. Construction Method. First, the slope surface was levelled, depressions and cracks were filled, dangerous stones and pumice on the slope surface were removed, and the slope surface was wetted with water. Then, the wet jet machine was segmented, the pure acrylic emulsion curing agent was sprayed from top to bottom, and the spraying

(a) (b)

Figure 4: (a) Model box A after the laid coal gangue; (b) model box B after spraying the pure acrylic emulsion curing agent.

(a) (b)

(c) (d)

Figure 5: Plant growth on the simulated slope: (a) model box A after three months of construction; (b) model box B after three months of construction; (c) model box A after six months of construction; (d) model box B after six months of construction.

Table 6: Test results of the simulated slope.

	Ratio of germination (%)	Vegetation coverage (%)			Cumulative soil erosion (%)			*p*H
Time (d)	30	30	90	180	30	90	180	180
Model box A	52.3	21.2	31.5	36.7	13.6	23.1	33.4	5.6
Model box B	86.4	36.6	87.4	92.4	4.7	6.7	8.2	7.1

thickness was 6–8 mm. After the curing agent was completely solidified, the guest soil was sprayed. The method of external-soil spray seeding is as follows: first, the guest soil was sprayed without seeds, and the spraying thickness was approximately 7/10 of the actual spraying and sowing thickness of guest soil. Second, after the subbase was stable, the guest soil containing seeds was sprayed, and the spraying thickness was approximately 1/10 of the actual spraying

Figure 6: Plant roots passing through the curing agent layer.

Figure 7: External-soil spray seeding.

(a) (b)

Figure 8: Test coal gangue slope one year after construction: (a) with added polymer curing agent; (b) without polymer curing agent.

thickness of the substrate. Finally, guest soil without seeds was sprayed, the spraying thickness was approximately 1/5 of the actual spraying thickness, and the total spraying thickness was 18–22 cm. External-soil spray seeding is shown in Figure 7.

4.2.3. Results and Analysis. The test coal gangue slope one year after construction is shown in Figure 8. Figure 8 shows that the coal gangue slope constructed by the traditional ecological slope protection method has poor plant development, low vegetation coverage, and obvious rainwater scouring traces on the slope. The coal gangue slope constructed by the new protection method with a polymer curing agent shows good results. Its slope greening is essentially covered, the vegetation is well developed, the environmental quality is clearly optimized, and the effect of slope protection and ecological restoration is preliminarily manifested. Thus, the new ecological protection technology of coal gangue slopes combined with external-soil spray seeding and polymer curing agents can achieve slope protection and ecological restoration and can be popularized and applied in similar projects.

5. Conclusions

In this paper, pure acrylic emulsion and ordinary Portland cement were used as the main raw materials to prepare an organic polymer curing agent, and the best mixing ratio was experimentally determined. Then, its protection mechanism was analysed. Finally, a new ecological protection technology for coal gangue slopes with pure acrylic emulsion curing agents was proposed, and its protection effect was analysed through slope simulation and practical engineering applications. The main conclusions are as follows.

(1) The pure acrylic emulsion curing agent with a P/C of 1.2 satisfies the requirements of workability, water resistance, durability, and bond strength and is most suitable to protect coal gangue slopes.

(2) Polymer particles of pure acrylic emulsion and hydration products of cement were interwoven to form a network film with good waterproof ability; the film covered the coal gangue surface to prevent the weathering and disintegration of coal gangue and improve the stability of coal gangue slopes.

(3) The net film layer of the pure acrylic emulsion curing agent greatly reduces the influence of weathering and leaching on the coal gangue, prevents the heavy metal elements in the coal gangue from entering the surrounding soil, increases the water storage capacity of slope soil, and improves the growth environment of plants. Moreover, plant roots can pass through the pure acrylic emulsion curing agent layer, and the presence of a curing agent does not affect the growth of plant roots.

(4) Simulated slope tests and practical engineering applications prove that stabilizing the surface of the slope by first using a pure acrylic emulsion curing agent and subsequently spraying guest soil is a new method to ecologically protect coal gangue slope. This new method can achieve slope protection and ecological restoration, and it has high popularization and application value.

Data Availability

The data used to support the findings of this study are included within the article.

Conflicts of Interest

The authors declare that they have no conflicts of interest.

Acknowledgments

This research was supported by the Introduction of Key Technologies for Landscape Restoration of Deep Cut Slopes (State Forestry Administration, China; no. 2015-4-38) and Research on Key Technology of Ecological Landscape Restoration of Highway Slope Road in Ecological Fragile Area (Hunan Provincial Department of Communications, China; no. 201803). The authors thank all who contributed to the imaging technique and experimental part of this study.

References

[1] J. Yan, X. Chen, Y. Cai, and H. Huang, "Physicochemical property change regularities of coal gangue with different weathering ages in Huainan minging area," *Transactions of the Chinese Society of Agricultural Engineering*, vol. 33, no. 3, pp. 168–174, 2017.

[2] W. Fan, H. Li, Z. Bai, and J. Qiao, "Effect of gangue spontaneous combustion on reclaimed soil quality of large-scaled opencast mine in loess area," *Transactions of the Chinese Society of Agricultural Engineering*, vol. 26, no. 2, pp. 319–324, 2010.

[3] X. Querol, M. Izquierdo, E. Monfort et al., "Environmental characterization of burnt coal gangue banks at Yangquan, Shanxi Province, China," *International Journal of Coal Geology*, vol. 75, no. 2, pp. 93–104, 2008.

[4] S. Chen, Z. Hu, and S. Chen, "Construction of isolation layers for preventing spontaneous combustion of coal gangue dump and its effects," *Transactions of the Chinese Society of Agricultural Engineering*, vol. 30, no. 2, pp. 235–243, 2014.

[5] H. He, F. F. Hong, X. X. Tao, and G. Huang, "A study on soil basic characteristics, main microbial flora and typical metal fraction surrounding coal gangue dump in Xiangtan Hunan Province, south of China," *Environmental Earth Sciences*, vol. 75, no. 6, Article ID 488, 2016.

[6] A. Khalil, L. Hanich, A. Bannari, L. Zouhri, O. Pourret, and R. Hakkou, "Assessment of soil contamination around an abandoned mine in a semi-arid environment using geochemistry and geostatistics: pre-work of geochemical process modeling with numerical models," *Journal of Geochemical Exploration*, vol. 125, pp. 117–129, 2013.

[7] N. Tripathi, R. S. Singh, and C. D. Hills, "Soil carbon development in rejuvenated Indian coal mine spoil," *Ecological Engineering*, vol. 90, pp. 482–490, 2016.

[8] M. Gomo and D. Vermeulen, "Hydrogeochemical characteristics of a flooded underground coal mine groundwater system," *Journal of African Earth Sciences*, vol. 92, pp. 68–75, 2014.

[9] Y. Yao, J. Ni, and J. Li, "Stress-dependent water retention of granite residual soil and its implications for ground settlement," *Computers and Geotechnics*, vol. 129, Article ID 103835, 2021.

[10] M. J. Chadwick, "Methods of assessment of acid colliery spoil as a medium for plant growth," *Ecology and Reclamation of Devastated Land International Symp on Ecol and Reveg of Drastically Disturbed Areas*, vol. 1, pp. 81–91, 1973.

[11] J. C. Fan, C. L. Huang, C. H. Yang, and K. Liao, "Effect evaluation of shotcrete vegetation mulching technique applied to steep concrete-face slopes on a highway of Taiwan," *Paddy and Water Environment*, vol. 11, no. 1, pp. 145–159, 2013.

[12] D. H. Lee, Y. E. Yang, and H. M. Lin, "Assessing slope protection methods for weak rock slopes in Southwestern Taiwan," *Engineering Geology*, vol. 91, no. 2-4, pp. 100–116, 2007.

[13] J. Zhang, A. Zhang, C. Huang, and H. Yu, "Characterising the resilient behaviour of pavement subgrade with construction and demolition waste under Freeze-Thaw cycles," *Journal of Cleaner Production*, vol. 300, Article ID 126702, 2021.

[14] J. Y. Wu, K. Huang, and M. Sungkar, "Remediation of slope failure by compacted soil-cement fill," *Journal of Performance of Constructed Facilities*, vol. 31, no. 4, Article ID 04017022, 2017.

[15] E. Blanco-Fernandez, D. Castro-Fresno, J. J. del Coz Diaz, A. Navarro-Manso, and M. Alonso-Martinez, "Flexible membranes anchored to the ground for slope stabilisation: numerical modelling of soil slopes using SPH," *Computers and Geotechnics*, vol. 78, pp. 1–10, 2016.

[16] L.-j. Su, B.-l. Hu, Q.-j. Xie, F.-w. Yu, and C.-l. Zhang, "Experimental and theoretical study of mechanical properties of root-soil interface for slope protection," *Journal of Mountain Science*, vol. 17, no. 11, pp. 2784–2795, 2020.

[17] A. Medl, R. Stangl, and F. Florineth, "Vertical greening systems - a review on recent technologies and research advancement," *Building and Environment*, vol. 125, pp. 227–239, 2017.

[18] Q. Ma, C. Huang, H. Xiao, and Q. Chen, "Thermal properties of carbon fiber-reinforced lightweight substrate for ecological slope protection," *Energies*, vol. 12, no. 15, Article ID 2927, 2019.

[19] P. Jiang, J. Li, S. Zuo, and X. Cui, "Ecological retaining wall for high-steep slopes: a case study in the ji-lai expressway, eastern China," *Advances in Civil Engineering*, vol. 2020, Article ID 5106397, 2020.

[20] H. Fu, H. Zha, L. Zeng, C. Chen, C. Jia, and H. Bian, "Research progress on ecological protection technology of highway slope: status and challenges," *Transportation Safety and Environment*, vol. 2, no. 1, pp. 3–17, 2020.

[21] M. E. W. Sydnor and E. F. Redente, "Reclamation of high-elevation, acidic mine waste with organic amendments and topsoil," *Journal of Environmental Quality*, vol. 31, no. 5, pp. 1528–1537, 2002.

[22] B. Liu, Z. Tang, S. Dong, L. Wang, and D. Liu, "Vegetation recovery and groundwater pollution control of coal gangue field in a semi-arid area for a field application," *International Biodeterioration & Biodegradation*, vol. 128, pp. 134–140, 2018.

[23] T. Du, D. Wang, Y. Bai, and Z. Zhang, "Optimizing the formulation of coal gangue planting substrate using wastes: the sustainability of coal mine ecological restoration," *Ecological Engineering*, vol. 143, Article ID 105669, 2020.

[24] P. V. Barry, R. F. Turco, D. E. Stott, and J. M. Bradford, "Organic polymers' effect on soil shear strength and detachment by single raindrops," *Soil Science Society of America Journal*, vol. 55, no. 3, pp. 799–804, 1991.

[25] W. Huang, Z. Liu, C. Zhou, and X. Yang, "Enhancement of soil ecological self-repair using a polymer composite material," *Catena*, vol. 188, Article ID 104443, 2020.

[26] M. A. Mohsin and N. F. Attia, "Inverse emulsion polymerization for the synthesis of high molecular weight polyacrylamide and its application as sand stabilizer," *International Journal of Polymer Science*, vol. 2015, Article ID 436583, 2015.

[27] B. Zhang, W. Jiang, Q. Xu, D. Yuan, J. Shan, and R. Lu, "Experimental feasibility study of ethylene-vinyl acetate copolymer (EVA) as cement stabilized soil curing agent," *Road Materials and Pavement Design*, vol. 2020, pp. 1–22, 2020.

[28] J. Li, J. Zheng, Y. Yao, J. Zhang, and J. Peng, "Numerical method of flexible pavement considering moisture and stress sensitivity of subgrade soils," *Advances in Civil Engineering*, vol. 2019, Article ID 7091210, 2019.

[29] Q. Y. Mu, C. Zhou, and C. W. W. Ng, "Compression and wetting induced volumetric behavior of loess: macro-and micro-investigations," *Transportation Geotechnics*, vol. 23, Article ID 100345, 2020.

[30] J. Yuan, C. Ye, L. Luo et al., "Sand fixation property and erosion control through new cellulose-based curing agent on sandy slopes under rainfall," *Bulletin of Engineering Geology and the Environment*, vol. 79, no. 8, pp. 4051–4061, 2020.

[31] J. Liu, B. Shi, H. T. Jiang, and H. Huang, "Experimental study on the water-stability property of clay aggregates stabilized by STW polymer soil stabilizer," *Hydrogeology & Engineering Geology*, vol. 36, no. 2, pp. 77–80, 2009.

[32] J. Liu, B. Shi, H. Jiang, and H. Huang, "Research on the stabilization treatment of clay slope topsoil by organic polymer soil stabilizer," *Engineering Geology*, vol. 117, no. 1-2, pp. 114–120, 2011.

[33] J. Liu, B. Shi, and K. Gu, "Laboratory study on soil modified by polyurethane sand-fixing agents," *Journal of Disaster Prevention and Mitigation Engineering*, vol. 33, no. 1, pp. 29–34, 2013.

[34] Q.-w. Yang, X.-j. Pei, and R.-q. Huang, "Impact of polymer mixtures on the stabilization and erosion control of silty sand slope," *Journal of Mountain Science*, vol. 16, no. 2, pp. 470–485, 2019.

[35] D. Yao, G. Qian, J. Liu, and J. Yao, "Application of polymer curing agent in ecological protection engineering of weak rock slopes," *Applied Sciences*, vol. 9, no. 8, Article ID 1585, 2019.

[36] X. Qin, A. Ni, N. Zhang, and Z. Chen, "Erosion control and growth promotion of w-oh material on red clay highway slopes: a case study in South China," *Sustainability*, vol. 13, no. 3, Article ID 1144, 2021.

[37] Chinese Standard, *Test Methods for Water Requirement of normal Consistency, Setting Time, and Soundness of the portland Cement*, China Standards Press, GBT1346, Beijing, China, 2011.

[38] Chinese Standard, *Verification Regulation of Rotational Viscometers*, China Measurement Press, JJG 1002, Beijing, China, 2005.

[39] Chinese Standard, *Test Methods of Rock for Highway Engineering*, China Communications Press, JTG E41, Beijing, China, 2005.

[40] Chinese Standard, *Polymer Modified Cement Mortar for waterproof*, China Standards Press, JC/T 984–2011, Beijing, China, 2011.

[41] Chinese Standard, *Standard for Test Method of Basic Properties of Construction Mortar*, China Standards Press, JGJ T70, Beijing, China, 2009.

Hindawi
Advances in Materials Science and Engineering
Volume 2021, Article ID 3785943, 11 pages
https://doi.org/10.1155/2021/3785943

Research Article

Stability Analysis of Ecological Slopes Based on a 3D Finite Element Model

ZiFan Sui,[1] Weijia Yuan,[1] Wen Yi,[1] and Weihuan Yang[2]

[1]*Central South University of Forestry & Technology, Changsha, Hunan 410004, China*
[2]*Zhejiang Runcheng Environmental Protection Group Co.,Ltd., Hangzhou, Zhejiang 311500, China*

Correspondence should be addressed to Wen Yi; yiwengangbiao@163.com

Received 19 August 2021; Revised 7 October 2021; Accepted 13 October 2021; Published 5 November 2021

Academic Editor: Qiao Dong

To explore the effect of grass and shrub plant roots on the stability of soil slopes in rainy areas in the south, this article relies on the Longlang Expressway construction project. *Cynodon dactylon* and *Magnolia multiflora* were selected as research subjects. The plant distribution characteristics and mechanical properties are analyzed. This paper uses ABAQUS finite element software to construct a 3D model of the planted slope in the test section. The stress and strain on the root system and the soil were observed, and the variation law of slope stability before and after plant protection under different rainfall events was compared and analyzed. The test and simulation results show that the root content of *Cynodon dactylon* gradually decreases with increasing depth. *Cynodon dactylon* was mainly distributed in the 0–30 cm soil body, and its effect on improving the cohesion of the soil body reached 75%. *Magnolia multiflora* belongs to vertical roots and has a strong and longer main root with relatively developed lateral roots. Its root system passes through the sliding surface of the slope bottom, which reduces the maximum equivalent plastic stress generated inside the slope by 61%. When the total rainfall duration is unchanged, under the three rainfall intensities of small, medium, and large, herbaceous plants increase the safety factor of the soil by 1.33%, 2.08%, and 6.1%, respectively, and the roots of shrubs increase the safety factor of the soil by 3.29%, 4.08%, and 4.32%, respectively. When the rainfall intensity does not change, as the rainfall time increases, the effect of plants on the slope safety factor first gradually increases and eventually stabilizes. The research results provide a reliable theoretical basis for analyzing the effect of plant roots on soil consolidation and slope protection, and they also lay a technical foundation for the promotion and application of ecological slope protection technology.

1. Introduction

Soil erosion is one of the world's major environmental disasters, and China is also the country with the most serious soil erosion and the most threatened level in the world [1, 2]. During road construction, especially when excavating the soil in mountainous areas, a large amount of secondary bare land will be produced, and the original vegetation cover will be disturbed and changed, often causing serious water and soil erosion problems [3–5]. The proposal of ecological slope protection technology has made a great contribution to the improvement of this problem [6]. Plants rely on the hydrological effects of their stems and leaves and the mechanical effects of the root system to ensure a stable slope while also achieving the purpose of preventing soil erosion, saving project costs, and beautifying road landscapes [7, 8]. It is an environmentally friendly slope protection method that has been widely used in highway slope protection projects [9].

The role of plants on slopes has advantages and disadvantages. Some scholars have pointed out that the weight of plants will cause the slope to bear greater vertical pressure. Under the action of wind load, the root system has a tendency to be pulled out, and the slope is more prone to instability and damage [10, 11]. However, more scholars believe that plants can have a reinforcing effect on slopes. Plant stems and leaves reduce the erosion and splash erosion of the soil on the slope surface by rain and effectively inhibit the generation of runoff; at the same time, the dense root system in the soil is interwoven into a network, which

significantly improves the strength of the soil [12, 13]. To further explore the influence of roots on slopes, scholars have carried out direct shear, triaxial, and unconfined compressive tests by observing changes in the shear strength of root–soil complexes and quantitatively analyzed the strengthening effects of plant roots on the soil [14–17]. There are also some studies that estimate the influence of roots on the soil by constructing theoretical models between roots and soils, such as the Wu model, Waldron model, and FBM model [18–20].

However, the relationship between plant roots and soil is more complicated, there are many factors that affect the process of experimental and theoretical analysis, and the results cannot intuitively reflect the changing laws of slope stability before and after planting [21, 22]. With the improvement of computer performance, many scholars have begun to use finite element software to analyze actual engineering problems. By constructing a 1D, 2D, or 3D model of the slope and observing the plastic zone and the stress and strain, the safety factor of the slope can be easily solved and the stability of the slope can be analyzed [23–25]. In recent years, many studies have also begun to use numerical simulation methods to analyze root–soil coupling problems. In the modeling process, the construction of plant root units and the choice of root–soil contact types will determine the calculation accuracy of the model [26]. There are mainly four modeling methods that are widely used at present: (1) regardless of the morphology of the plant root system, the plant and soil are regarded as composite materials, and attributes are given as a whole; (2) the interaction between the plant and the soil is converted into a load, which is directly applied to the soil element; (3) the soil and root models are built separately, assuming that the deformation between the two can be automatically coordinated; (4) while separating the root system of the plant and the soil, the relative movement of the two is restricted by setting the contact method between the two [27–30].

Plants are biological materials, and their mechanical properties are closely related to factors such as root morphology and soil moisture content. In previous studies, this was often simplified, resulting in large errors in the simulation results [17, 31]. In this paper, based on the geological and hydrological conditions of the test area and the distribution characteristics of plants on the slope, ABAQUS finite element software is used to construct 3D models of shallow grass, deep shrub roots, and soil slopes, and the strength reduction method is used to analyze the influence of plant roots on slope stability during rainfall. This research has important theoretical guiding significance for preventing and controlling the occurrence of slope geological disasters in rainy areas in the south and has laid a technical foundation for the promotion and application of ecological slope protection technology.

2. Materials and Methods

2.1. Introduction of the Study Area. The study area is located in Section K72 + 123-K72 + 321 of the Longlang Expressway, Xinhua County, Loudi City, Hunan Province, with a length of 198 m and a maximum slope height of 30.6 m. This area is located between 111°15′10″ and 112°9′6″ east longitude and between 27°25′33″ and 28°48′27″ north latitude. It has a midsubtropical monsoon humid climate. The measured average monthly rainfall over the years is shown in Figure 1. The rainfall is mainly concentrated in April to July. The annual average temperature is 16.5°C–17.5°C, the extreme maximum temperature is 40.1°C, the extreme minimum temperature is −12.1°C, the annual average wind speed is 1.5–2.2 m/s, and the maximum wind speed is 40 m/s. The previously mentioned climatic conditions will play a decisive role in the formulation of ecological slope protection schemes, such as plant species, planting density, and construction season.

Combining the survey results and construction design, it can be seen that the main stratum of the slope of the test section is limestone and marl, which are basically soft rock. There are a small number of weak interlayers in the bedding slope rock layer, and the overall stability is good. However, surface water and groundwater are developed in the rainy season, and the stability of the shallow overburden and joint fissures is poor. If the construction stage is not handled properly, shallow slope instability and block loss are likely to occur locally. To stabilize the slope, relevant measures have been taken at the construction site, comprehensively considering the effects of the local landscape and using ecological slope protection technology to reinforce the soil. The engineering effects before and after protection are shown in Figure 2.

2.2. Material Parameters. The soil on the slope was selected as the soil for this test, the soil sample was dried, 3000 g was weighed for the particle screening test, and the particle grading curve and uneven coefficient were obtained. The particle composition of the soil is shown in Table 1. In the test, 15–30 g of soil samples was taken from representative locations. The soil was weighed and dried in an oven at 105–110°C to a constant weight. The samples were removed and cooled and weighed again to determine the natural moisture content of the soil. The dry density of the soil was measured by sampling on the soil slope with a ring knife. The liquid limit and plastic limit of the soil were measured by a photoelectric liquid limit and plastic limit combined tester (the cone mass was 100 g). The basic parameters of soil samples measured through the previously mentioned tests are shown in Table 2.

Taking into account the effect of slope protection and local geological and hydrological conditions, the four-year-growing herb *Cynodon dactylon* and the shrub *Magnolia multiflora* roots were selected as the research objects.

There are many kinds of herbaceous plants, the shallow soil has a large root-containing rate, and the root system mainly has a reinforcing effect [32]. The root–soil composite sample was obtained by ring knife sampling, and its root content and shear strength were determined. When sampling on-site, one can first take a large piece of soil, bring it back to the laboratory, and use a sharp knife to remove the excess part. When cutting the excess root system and

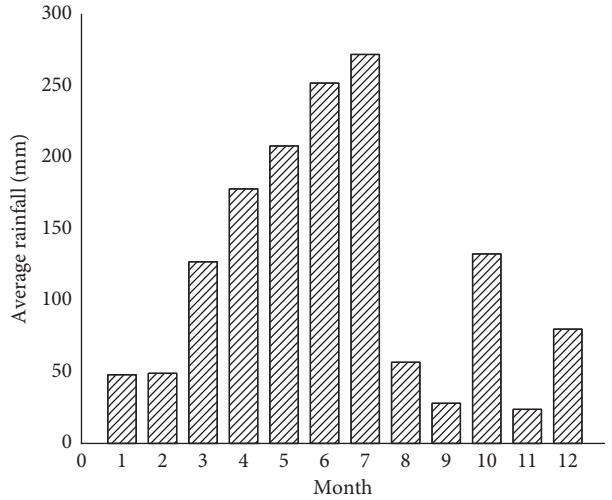

Figure 1: The average rainfall of the Longlang Expressway from 2015 to 2019.

(a) (b)

Figure 2: Landscape of the studied slope: (a) before slope protection; (b) after planting plants.

Table 1: Results of the sieving analysis test [26].

Sieve diameter (mm)	Percentage (%)	Sieve diameter (mm)	Percentage (%)
40	0	1	11.8
20	5.0	0.5	15.3
10	14.2	0.25	5.7
5	17.8	0.075	1.5
2	28.3	<0.075	0.3

Table 2: Basic parameters of the soil sample.

Optimal moisture content (%)	Maximum dry density (g/cm^3)	Liquid limit (%)	Plastic limit (%)	Plasticity index
18.62	1.82	48.5	25.6	22.9

surrounding soil, care should be taken not to disturb the soil sample in the ring knife. The prepared test block should be wrapped in plastic wrap and left for 5–7 days to reduce the loss of water content between the soil samples. The sample after shearing was retrieved on-site, as shown in Figure 3. The analysis shows that the herbaceous plants are mainly distributed in the 0–30 cm soil, and the root content decreases with increasing depth. The content of *Cynodon dactylon* roots in soil is shown in Figure 4. Twelve samples are taken for indoor direct shear test at three depths of 0–10 cm, 10–20 cm and 20–30 cm. Coulomb formula can be used to solve parameters such as cohesion and friction angle. The soil and root composite material parameters measured through indoor tests are shown in Table 3. The root system improves the shear strength and permeability of the soil.

The root system of shrubs in the soil is not large, but the root system is deep in the soil and mainly serves as an anchor [33]. The whole plant excavation method was

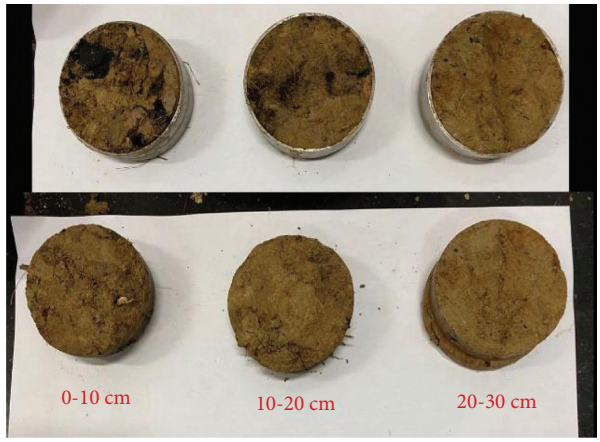

Figure 3: Root–soil composite sample after the direct shear test.

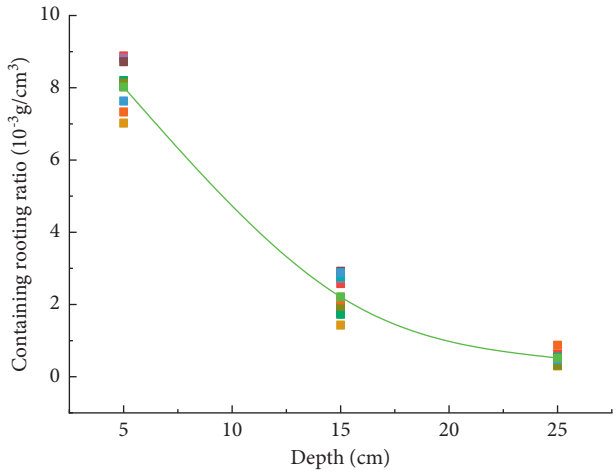

Figure 4: Root content change curve with depth (each point in the figure is test data, and the curve is an average value).

Table 3: Physical and mechanical parameters of soil materials.

Category	Unit weight (kN/m^3)	Elastic modulus (MPa)	Cohesion (kPa)	Internal friction angle (°)	Poisson's ratio	Saturated permeability coefficient (10^{-4} cm/s)
Soil	18.75	10	29.78	10.31	0.35	1.02
Root–soil composite	18.75	3.9	52.02	10.68	0.30	5.32

adopted to collect all the multiple magnolias on the test slope, and the remaining 50 plants after removing the incomplete roots were classified according to the morphological characteristics of primary and lateral roots, and the root morphology was scanned and analyzed. Care should be taken to ensure the integrity of the root system during collection; the excavated root system should be covered with wet soil, and water should be regularly added to maintain it until the end of the test. Typical root morphology is shown in Figure 5. *Magnolia multiflora* belongs to vertical roots, with obviously thicker and longer tap roots, and some lateral roots are also more developed. The mechanical parameters determined by laboratory tests are shown in Table 4.

2.3. Model Construction. By taking the slope of the Longlang Expressway in Loudi City, Hunan Province, as the supporting project, the 3D model of the soil slope and plant root system is constructed by ABAQUS finite element software. The slope model has a height of 6 m, a length of 9 m, a width of 6 m, a subgrade height of 4 m, and a slope of 1 : 1.5. Taking into account the range of influence of the numerical simulation calculation, the top and toe of the slope are extended 6 m in each direction.

The main distribution depth of the herbaceous bermudagrass is 0–30 cm, the root system is finer, and the root content is larger. When modeling, the plant and soil are regarded as root–soil composite materials. The unit type is the same as that of the soil, and C3D8 units are used.

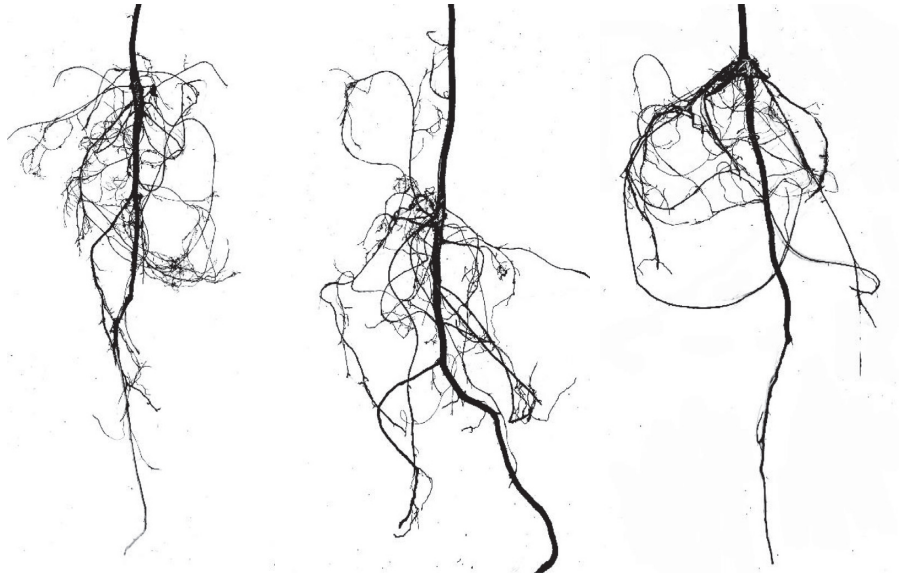

Figure 5: Schematic diagram of characteristic root scanning of *Magnolia multiflora*.

Table 4: Physical and mechanical parameters of the root of *Magnolia multiflora*.

Material	Elastic modulus (GPa)	Poisson's ratio	Density (kN/m^3)
Root of *Magnolia multiflora*	0.5	0.35	13

Compared with herbs, there are far fewer shrubs on the slope. According to statistics, there is a root system of 2-3 m per 2 m^2, which is mainly used for anchoring; therefore, it is not suitable to use composite material models. According to the scan results of the characteristic roots of shrubs, after the main roots are retained and the finer lateral roots are removed, we use the T3D2 unit to construct a properly simplified root model of *Magnolia multiflora*. The main roots are distributed vertically downwards, with a length of 3 m and a diameter of 0.1 m, there are 5 lateral roots on each side, the inclination of the root system is 60°, the length of the root system from top to bottom is 0.6, 0.8, 0.6, 0.5, and 0.4 m, and the diameter is 0.02 m. The roots of *Magnolia multiflora* are in close contact with soil, and there are two main ways of interaction between them: the first is the adhesion between the soil and the organic colloid, and the other is the friction caused by the root system being squeezed by the soil. The adhesion effect is relatively weak. To simplify the simulation, it will not be considered for the time being. The friction effect is similar to that of reinforced soil, which can be embodied by the embedded model in ABAQUS.

The plant-grown slope model is shown in Figure 6. Combined with the results of the indoor test, the soil, the *Cynodon dactylon* soil composite, and the *Magnolia multiflora* root system are given the corresponding material properties.

2.4. Boundary Conditions. The boundary conditions of the model are set according to the actual force on the slope. The displacement degrees of freedom in the X, Y, and Z directions of the slope bottom are constrained in the initial analysis step. To ensure that the soil can move up and down under gravity or vertical load, the displacements in the X and Y directions of the front, rear, left, and right ends of the slope are constrained.

In addition to displacement constraints, according to the distribution of the groundwater level, one should also set pore pressure boundary conditions. The distribution function is used to set the pore pressure boundary that linearly increases with depth below the water level on both sides of the slope, namely, $10 \times 4 - y$. At the same time, the pore pressure of the top surface of the soil layer outside the slope toe is set to 0, and the remaining boundaries are set as impervious boundaries.

The load boundary condition is mainly composed of two parts: the weight of the material and the rainfall. The self-weight can be defined by setting the density of the soil, root-soil composite, and deep root system and then adding the vertical downward acceleration of gravity.

The simulation of rainfall is mainly realized by applying vertical loads on the slope. The average rainfall in the test area is used as the rainfall intensity in the previous steady-state analysis, and the calculation result of the subsequent steady-state analysis is used as the initial state of the subsequent transient analysis. The transient analysis is divided into three working conditions: light rain, moderate rain, and heavy rain according to the amount of rainfall. Under the three working conditions, the stability analysis of slopes with and without plants is carried out. The total rainfall duration is 72 hours, the rainfall is shown in Table 5, and the intensity amplitude variation curve is shown in Figure 7.

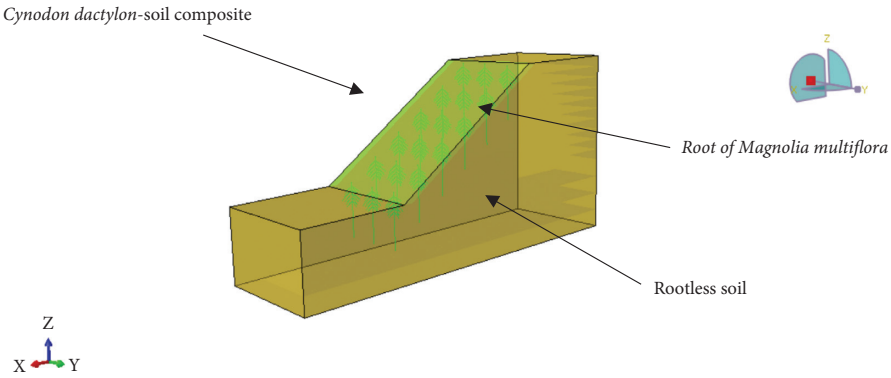

Figure 6: Schematic diagram of the model.

Table 5: Daily rainfall grade.

Working condition	Light rain	Moderate rain	Heavy rain
Daily precipitation/mm	0.8–1.6	1.8–4.4	5.9–10

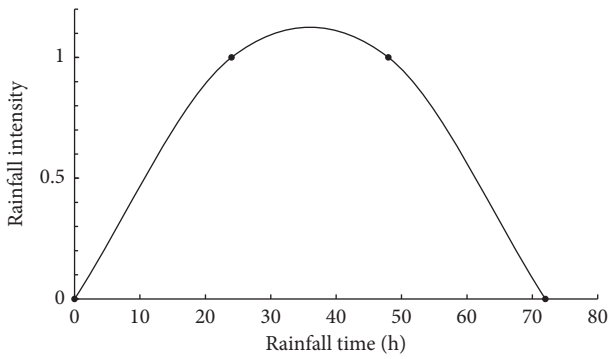

Figure 7: Curve of rainfall intensity amplitude.

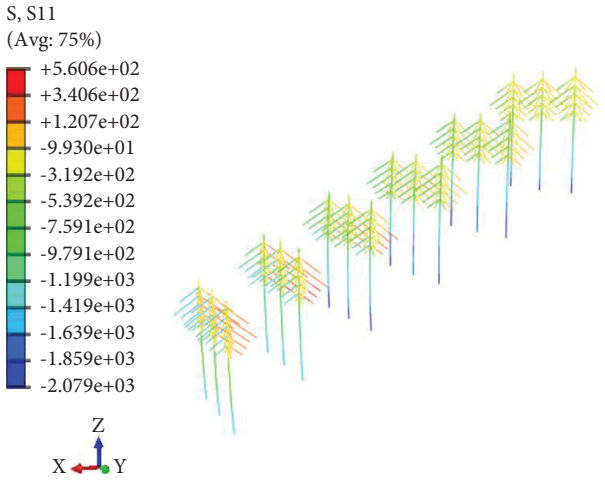

Figure 8: Stress distribution cloud diagram of the root of *Magnolia multiflora*.

3. Results

3.1. Stress Distribution Characteristics. Taking the slope model after grass and shrub protection under moderate rain conditions as an example, the force of plant roots in the soil is analyzed. Figure 8 is a cloud diagram of the stress distribution of plant roots. Through analysis, it is found that the stress on the root system is mainly concentrated on the main root in the vertical direction, and the magnitude of the stress increases downward along the root system. In addition, the lateral roots distributed around also bear part of the stress, which is mainly manifested as a positive X root system > a negative X root system > a Y direction distributed root system. Figure 9 is a cloud diagram of the plastic strain of the slope after grass and shrub protection. It describes the change in plastic strain in the process of soil deformation and reflects the process of slope instability. It can be seen from the figure that the root system at the toe of the slope passes through the sliding surface, and the root system anchors the shallow soil and the deep soil, which makes a significant contribution to the improvement of the slope stability.

3.2. Displacement and Plastic Zone Distribution Characteristics. Sudden changes in displacement are one of the indicators for judging slope failure. In engineering, slope displacement is often used to observe the working status of the slope [34]. When a landslide occurs, a circular arc-shaped sliding surface is usually formed between the landslide body and the parent body [35]. Feature points are uniformly selected along the slope from the center of the slope toe to the center of the top of the slope, and the horizontal and vertical displacements of each point at each time under moderate rain conditions are recorded, as shown in Figures 10 and 11.

The analysis found that $t = 0$ h to $t = 10$ h is the initial stage, and the soil is stable under its own weight and pore water pressure. At this time, both the horizontal displacement (U1) and the vertical displacement (U3) of the slope surface are small. After rain begins, rainwater infiltrates, and the soil swells slightly. With the increase in rainfall, the

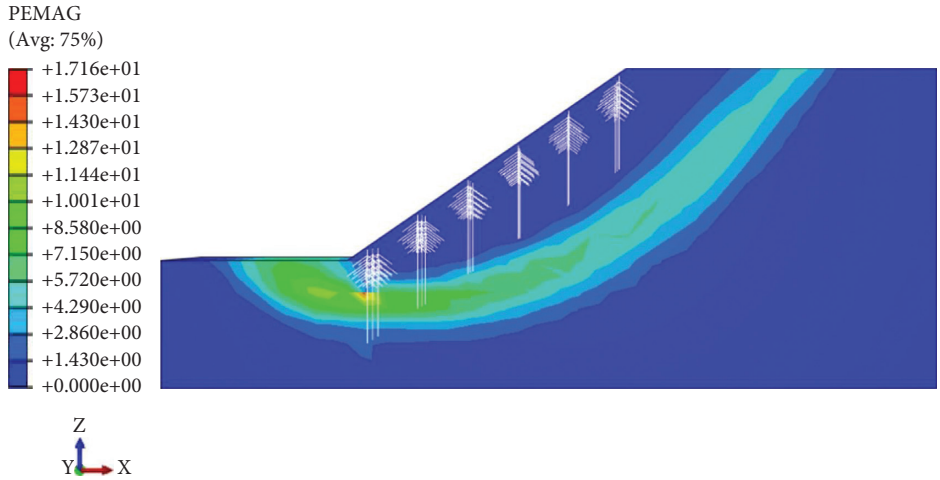

Figure 9: Cloud map of the distribution of the plastic strain area of the slope.

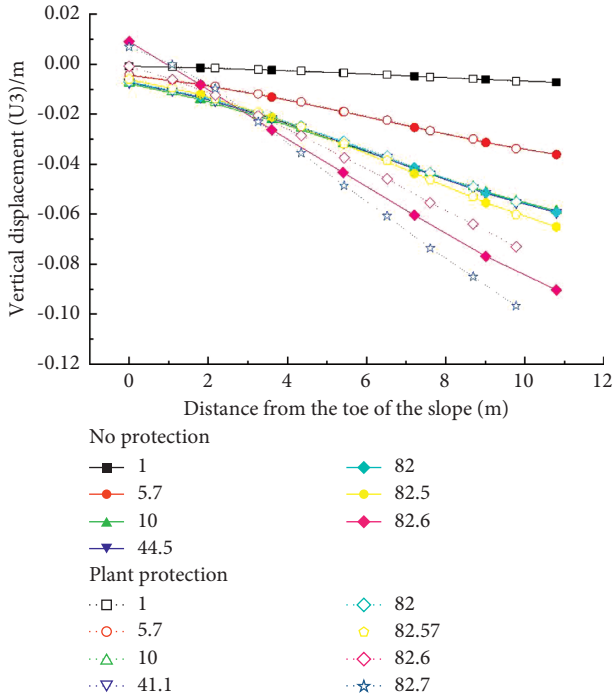

Figure 10: Vertical displacement of each characteristic point of the downhill foot at each time.

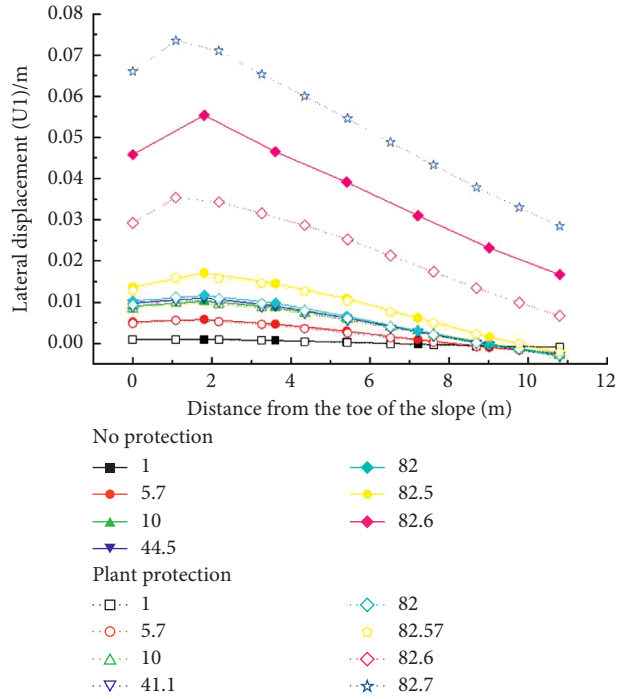

Figure 11: Lateral displacement of each characteristic point of the downslope foot at each time.

lateral displacement at the bottom of the slope and the vertical displacement at the top of the slope gradually develop. At $t = 82$ h, the rainfall ends, and the slope settles slightly under the action of rain and appears to slide forward. The cohesive force and internal friction angle of the soil are reduced, and the stability of the slope after infiltration is analyzed by the strength reduction method. From $t = 82.5$ h to $t = 82.6$ h, the vertical displacement (U3) gradually reaches the extreme value at the toe and top of the slope, and the horizontal displacement (U1) reaches the extreme value at a distance of 1 to 2 m from the toe. Subsequently, the displacement occurs abruptly, and the slope becomes unstable.

In Figures 10 and 11, the solid line is the displacement change curve without protection, and the dashed line is the displacement change curve after grass and shrub protection. Obviously, it can be observed that the root system of the plant has a better protective effect on the soil. When $t = 82.6$ h, compared with no protection, the maximum horizontal displacement of the soil body after protection is reduced by 35.4%, and the maximum vertical displacement and maximum negative displacement are reduced by 100% and 11%, respectively. At the same time, the protected slope is still in a relatively stable state at $t = 82.7$ h, and at this time, the unprotected slope has already suffered instability damage.

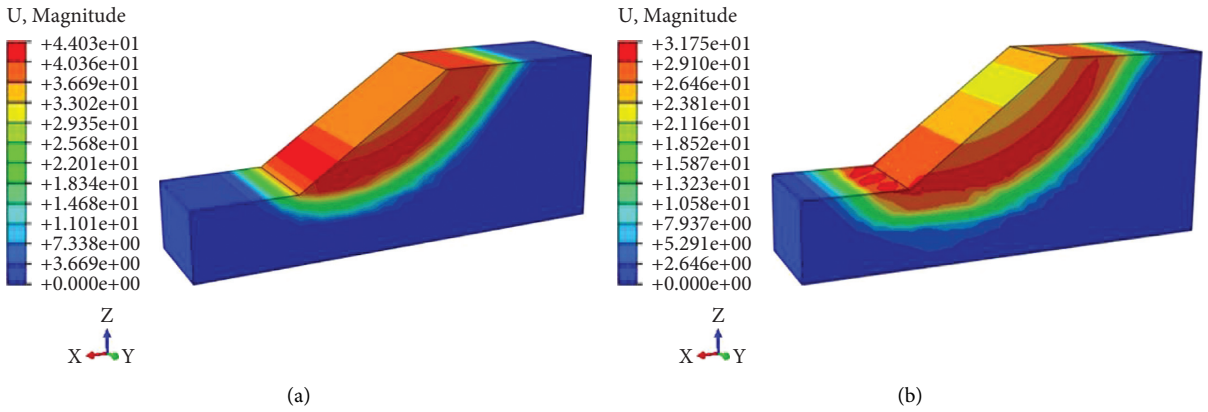

Figure 12: Slope displacement cloud map. (a) Before slope protection; (b) after planting plants.

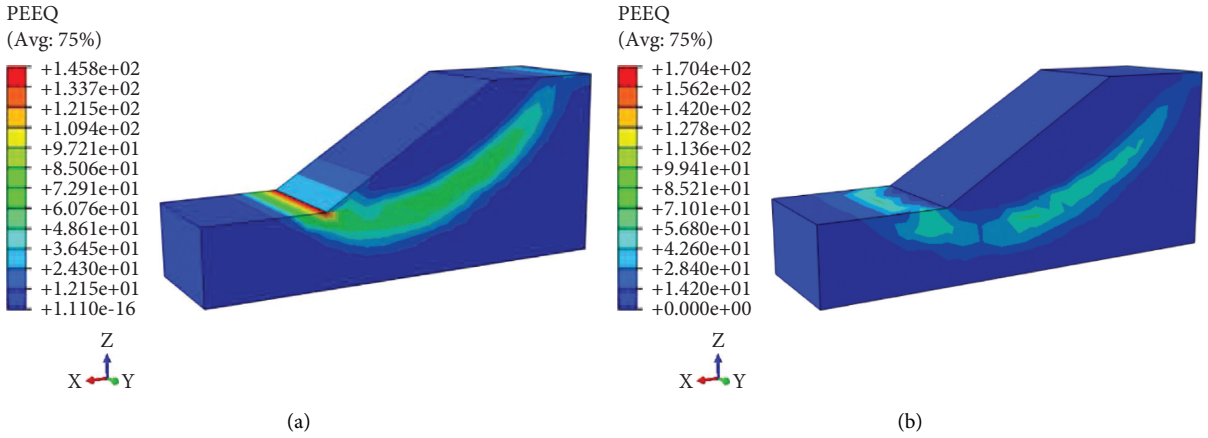

Figure 13: Equivalent plastic stress cloud diagram when an unprotected slope fails. (a) Before slope protection; (b) after planting plants.

Figure 12 is a cloud diagram of the slope displacement. Comparative analysis shows that the overall displacement of the slope has been effectively reduced after the plant root system is used for protection. Soil protection by plant roots on the slope is mainly reflected in two aspects: (1) after grass and shrub protection, the maximum displacement of shallow soil is reduced by 30%; (2) the plant root system connects and anchors the soil as a whole, and its displacement mutation position expands to the rear.

Figure 13 is the equivalent stress cloud diagram after the plastic zone of the slope is completely penetrated. The analysis found that the maximum equivalent plastic stress of an unprotected slope appeared at the foot of the slope, reaching 145 kPa. After grass and shrub protection, the slope was connected by the reinforcement effect of shallow roots and the anchoring effect of deep roots, the plastic stress distribution in the slope was more uniform, and the maximum plastic stress value was reduced to 56 kPa. While the plant root system delays the plastic strain area through the slope, it also reduces the maximum equivalent plastic stress generated inside the slope.

3.3. Stability Analysis. The center of the slope bottom is selected as a feature point, ABAQUS finite element software is used to draw the relationship curve between the reduction factor (F_s) and the lateral displacement (U1), the size of the safety factor under each working condition of the slope is obtained by observing the inflection point of the curve, and the result is shown in Figure 14. The analysis found that when there is no protection, the safety factor of light rain to moderate rain is reduced by 4%, and the safety factor of heavy rain to moderate rain is reduced by 9.03%. As the rainfall intensity increases, the safety factor of the slope decreases and the stability decreases, and its downward trend gradually increases. After the protection of herbaceous plants, the permeability coefficient of the root–soil composite is greater than that of the soil, the rainwater penetrates into the deep soil faster, and the slope reaches saturation faster. At this time, the reinforcement effect of the shallow root system is reflected, and the safety factor of the slope is improved to a certain extent. The increase in the safety factor of herbaceous plants to the soil under the three rainfall intensities of small, medium and large is 1.33%, 2.08% and 6.1%,

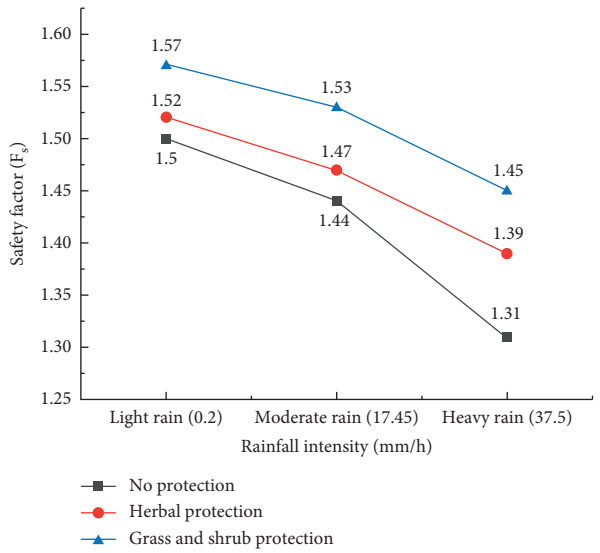

Figure 14: Curve of the relationship between rainfall intensity and safety factor.

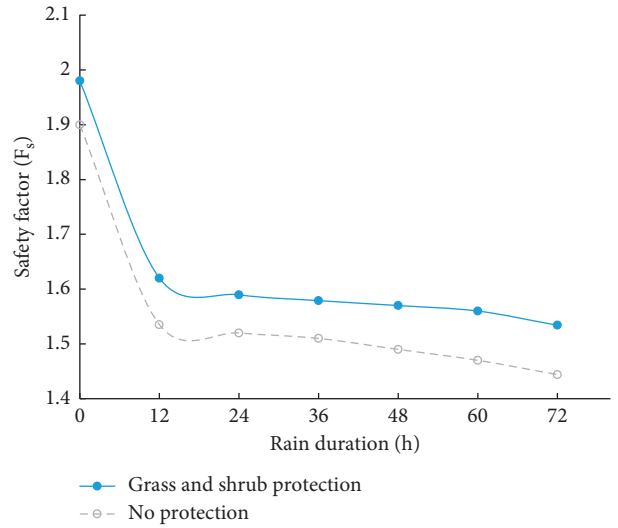

Figure 15: Curve of the relationship between rainfall time and safety factor.

respectively, and the reinforcement effect is on the rise. After shrub root protection, compared with herb protection, the safety factor of the soil is increased by 3.29%, 4.08%, and 4.32% under the three rainfall intensities of small, medium, and large, respectively. The slope stability is further improved, and since deep roots are mainly anchored, the enhancement effect is relatively stable. Based on the previously mentioned analysis, after mixing grass and shrubs, as the rainfall intensity increases, the effect of plant roots on soil stability is expected to remain stable after reaching the peak.

Under normal circumstances, as the rainfall time increases, rainwater infiltrates gradually, the pore water pressure of the soil increases, the water content increases, and the safety factor of the slope decreases. Taking moderate rain conditions as an example, the stability analysis of slopes after 0 h, 12 h, 24 h, 36 h, 48 h, 60 h, and 72 h of rainfall is carried out, and the relationship between the strength reduction coefficient and the lateral displacement is drawn, respectively. The relationship curve between the strength reduction factor and the lateral displacement is drawn separately, and the corresponding safety factor is determined by observing the sudden change of displacement. The collated data are drawn in Figure 15. The analysis shows that, with increasing rainfall time, the stability of the slope first decreases sharply, then decreases slowly, and finally stabilizes. Compared with the bare slope, the safety factor of the vegetation slope is larger, and the root system has a better reinforcement effect on the soil. The analysis shows that because the permeability coefficient of the root–soil composite is greater than that of the rootless soil, rainwater on the planted slope will seep more quickly, which has a certain negative impact on the stability of the slope. But as the soil gradually becomes saturated, this effect gradually decreases, and the reinforcement effect of herb roots and the anchoring effect of shrub roots begin to dominate. Therefore, as the rainfall time increases, the protection effect of plant roots on slopes is better.

4. Conclusions

This study conducted a finite element simulation of the direct shear test of the root–soil composite. This paper uses ABAQUS finite element software to carry out a numerical simulation study on the soil, herb roots, and shrub roots on ecological slopes. According to the actual project, the material properties are assigned, and the boundary conditions are defined. Later, the strength reduction method is used to analyze the stability of the planted slope. By observing the changes in the stress, plastic strain area on the slope, and the safety factor of the characteristic points at the slope toe under different rainfall conditions, the protective effect of the plant root system is explored. The main conclusions are as follows.

(1) The root system of herbaceous plants has a high root content and is mainly distributed in shallow soil, and it has a reinforcing effect on the soil. According to the theory of composite materials, the combination of the soil and root system can be regarded as a composite material. Parameters such as cohesion, internal friction angle, and permeability coefficient are measured through experiments, and the model is constructed with the same type of elements as the soil. Shrubs have a low root content, but the root system is deeply rooted below the sliding surface to anchor the slope. It can be regarded as an anchor material. The model is constructed by using rod elements embedded in the slope soil.

(2) With the increase in rainfall time and rainfall intensity, the water content of the soil increases, the pore water pressure increases, the matrix suction decreases, the safety factor of the slope will gradually decrease, and the slope will lose stability. As a reinforcing material, plant roots can effectively improve the stability of slopes. When the total rainfall duration is constant, the effect of plant roots on the

slope safety factor increases with the increase in rainfall. When the rainfall intensity is constant, as the rainfall time increases, the safety factor of the slope after plant root protection gradually increases first and finally stabilizes.

(3) The stress borne by plant roots is mainly concentrated on the main root in the vertical direction, and the stress increases downward along the root system. The lateral roots distributed around will also bear part of the stress, and the lateral roots bear greater stress along the slope. It is precisely because the root system shares part of the soil stress that the time for the appearance, development, and penetration of the slope plastic zone is delayed, and the maximum lateral and vertical displacements when the slope soil is damaged are reduced. Plant roots anchor the soil as a whole, and the slope soil can withstand greater stress.

Data Availability

The data used to support the findings of this study are included within the article.

Conflicts of Interest

The authors declare that there are no conflicts of interest regarding the publication of this paper.

Acknowledgments

This research was funded by the Introduction of Key Technologies for Landscape Restoration of Deep Cut Slopes (grant no. 2015-4-38) and Research on Key Technology of Ecological Landscape Restoration of Highway Slope Road in Ecological Fragile Area (grant no. 201803).

References

[1] H. Zhu and L. M. Zhang, "Field investigation of erosion resistance of common grass species for soil bioengineering in Hong Kong," *Acta Geotechnica*, vol. 11, no. 5, pp. 1047–1059, 2016.

[2] D. Pimentel, "Soil erosion: a food and environmental threat," *Environment, Development and Sustainability*, vol. 8, no. 1, pp. 119–137, 2006.

[3] D. R. Montgomery, "Soil erosion and agricultural sustainability," *Proceedings of the National Academy of Sciences*, vol. 104, no. 33, pp. 13268–13272, 2007.

[4] H. Zhu, L. M. Zhang, T. Xiao, and X. Y. Li, "Enhancement of slope stability by vegetation considering uncertainties in root distribution," *Computers and Geotechnics*, vol. 85, pp. 84–89, 2017.

[5] P. Reichenbach, C. Busca, A. C. Mondini, and M. Rossi, "The influence of land use change on landslide susceptibility zonation: the Briga catchment test site (Messina, Italy)," *Environmental Management*, vol. 54, no. 6, pp. 1372–1384, 2014.

[6] J. J. Roering, K. M. Schmidt, J. D. Stock, W. E. Dietrich, and D. R. Montgomery, "Shallow landsliding, root reinforcement, and the spatial distribution of trees in the Oregon Coast Range," *Canadian Geotechnical Journal*, vol. 40, no. 2, pp. 237–253, 2003.

[7] B. Indraratna, B. Fatahi, and H. Khabbaz, "Numerical analysis of matric suction effects of tree roots," *Proceedings of the Institution of Civil Engineers - Geotechnical Engineering*, vol. 159, no. 2, pp. 77–90, 2006.

[8] G. B. Crosta and P. Frattini, "Rainfall-induced landslides and debris flows," *Hydrological Processes*, vol. 22, no. 4, pp. 473–477, 2008.

[9] F. Tan, W.-H. Zhou, and K. V. Yuen, "Modeling the soil water retention properties of same-textured soils with different initial void ratios," *Journal of Hydrology*, vol. 542, pp. 731–743, 2016.

[10] W. Wu, B. M. Switala, M. S. Acharya et al., "Effect of vegetation on stability of soil slopes: numerical aspect," *Springer Series in Geomechanics and Geoengineering*, Springer, Berlin, Germany, pp. 163–177, 2015.

[11] C. O'Loughlin, "The effect of timber removal on the stability of forest soils," *Journal of Hydrology (New Zealand)*, vol. 13, no. 2, pp. 121–134, 1974.

[12] N. P. Bankhead and A. Simon, "Hydrologic and hydraulic effects of riparian root networks on streambank stability: is mechanical root-reinforcement the whole story?" *Geomorphology*, vol. 116, no. 3-4, pp. 353–362, 2010.

[13] E. B. Masi, S. Segoni, and V. Tofani, "Root reinforcement in slope stability models: a review," *Geosciences*, vol. 11, no. 5, p. 212, 2021.

[14] M. Schwarz, A. Rist, D. Cohen et al., "Root reinforcement of soils under compression," *Journal of Geophysical Research: Earth Surface*, vol. 120, no. 10, pp. 2103–2120, 2015.

[15] W. H. Zhou and X.-H. Qi, "Root cohesion estimation of riparian trees based on model uncertainty characterization," *Journal of Materials in Civil Engineering*, vol. 31, no. 2, Article ID 04018389, 2019.

[16] M. Pallewattha, B. Indraratna, A. Heitor, and C. Rujikiatkamjorn, "Shear strength of a vegetated soil incorporating both root reinforcement and suction," *Transportation Geotechnics*, vol. 18, pp. 72–82, 2019.

[17] T. C. Hales and C. F. Miniat, "Soil moisture causes dynamic adjustments to root reinforcement that reduce slope stability," *Earth Surface Processes and Landforms*, vol. 42, no. 5, pp. 803–813, 2017.

[18] T. H. Wu, *Investigation of Landslides on Prince of Wales Island Alaska*, Ohio State University, Columbus OH U S A, 1976.

[19] L. J. Waldron, "The shear resistance of root-permeated homogeneous and stratified soil," *Soil Science Society of America Journal*, vol. 41, no. 5, pp. 843–849, 1977.

[20] N. Pollen and A. Simon, "Estimating the mechanical effects of riparian vegetation on stream bank stability using a fiber bundle model," *Water Resources Research*, vol. 41, no. 7, 2005.

[21] D. Cohen, M. Schwarz, and D. Or, "An analytical fiber bundle model for pullout mechanics of root bundles," *Journal of Geophysical Research: Earth Surface*, vol. 116, no. F3, 2011.

[22] J. C. Bathurst, C. I. Bovolo, and F. Cisneros, "Modelling the effect of forest cover on shallow landslides at the river basin scale," *Ecological Engineering*, vol. 36, no. 3, pp. 317–327, 2010.

[23] M. Xie, T. Esaki, G. Zhou, and Y. Mitani, "Geographic information systems-based three-dimensional critical slope stability analysis and landslide hazard assessment," *Journal of Geotechnical and Geoenvironmental Engineering*, vol. 129, no. 12, pp. 1109–1118, 2003.

[24] D. V. Griffiths and P. A. Lane, "Slope stability analysis by finite elements," *Géotechnique*, vol. 49, no. 3, pp. 387–403, 1999.

[25] V. J. Terwilliger and L. J. Waldron, "Effects of root reinforcement on soil-slip patterns in the Transverse Ranges of southern California," *The Geological Society of America Bulletin*, vol. 103, no. 6, pp. 775–785, 1991.

[26] Z. F. Sui, W. Yi, Y. G. Lu, and L. Deng, "Experimental and numerical simulation study on the shear strength characteristics of magnolia multiflora root-soil composites," *Advances in Civil Engineering*, vol. 2021, Article ID 6642594, 12 pages, 2021.

[27] A. G. T. Temgoua, N. K. Kokutse, and Z. Kavazović, "Influence of forest stands and root morphologies on hillslope stability," *Ecological Engineering*, vol. 95, pp. 622–634, 2016.

[28] N. K. Kokutse, A. G. T. Temgoua, and Z. Kavazović, "Slope stability and vegetation: conceptual and numerical investigation of mechanical effects," *Ecological Engineering*, vol. 86, pp. 146–153, 2016.

[29] Y. H. Chok, M. B. Jaksa, W. S. Kaggwa, and D. V. Griffiths, "Assessing the influence of root reinforcement on slope stability by finite elements," *International Journal of Geo-Engineering*, vol. 6, no. 1, pp. 1–13, 2015.

[30] E. M. Schmaltz and M. Mergili, "Integration of root systems into a GIS-based slip surface model: computational experiments in a generic hillslope environment," *Landslides*, vol. 15, no. 8, pp. 1561–1575, 2018.

[31] F. Giadrossich, M. Schwarz, D. Cohen et al., "Methods to measure the mechanical behaviour of tree roots: a review," *Ecological Engineering*, vol. 109, pp. 256–271, 2017.

[32] P. P. Capilleri, M. Cuomo, E. Motta, and M. Todaro, "Experimental investigation of root tensile strength for slope stabilization," *Indian Geotechnical Journal*, vol. 49, no. 6, pp. 687–697, 2019.

[33] E. M. Schmaltz, L. P. H. Van Beek, T. A. Bogaard, S. Kraushaar, S. Steger, and T. Glade, "Strategies to improve the explanatory power of a dynamic slope stability model by enhancing land cover parameterisation and model complexity," *Earth Surface Processes and Landforms*, vol. 44, no. 6, pp. 1259–1273, 2019.

[34] H. Wang, Y. He, Z. Shang, C. Han, and Y. Wang, "Model test of the reinforcement of surface soil by plant roots under the influence of precipitation," *Advances in Materials Science and Engineering*, vol. 2018, Article ID 3625053, 2018.

[35] X. Wang, M. M. Hong, Z. Huang et al., "Biomechanical properties of plant root systems and their ability to stabilize slopes in geohazard-prone regions," *Soil and Tillage Research*, vol. 189, pp. 148–157, 2019.

Hindawi
Advances in Materials Science and Engineering
Volume 2021, Article ID 7658444, 11 pages
https://doi.org/10.1155/2021/7658444

Research Article

Study on Mechanical Properties of Recycled Mixture with High Content of Iron Tailings Sand

Yuanshuai Dong,[1,2,3] Hong Zhang,[1] Yun Hou,[2,3] Zhenyu Qian,[2,3] and Jialei Tian[2,3]

[1]*Department of Civil Engineering, Chongqing Jiaotong University, Chongqing 400047, China*
[2]*China Highway Engineering Consulting Corporation, Beijing 100089, China*
[3]*Highway Construction and Maintenance Technology, Materials and Equipment Transportation Industry Research and Development Center, Beijing 100089, China*

Correspondence should be addressed to Hong Zhang; zh1223021307@163.com and Jialei Tian; tianjialei99@126.com

Received 18 August 2021; Revised 15 October 2021; Accepted 18 October 2021; Published 31 October 2021

Academic Editor: Meng Guo

This paper focuses on the disposal of iron tailings sand (ITS) and reclaimed inorganic binder stabilized aggregate (RAI), and a new "ITS plus RAI" solid waste treatment method is innovatively proposed, which uses ITS and RAI as a new base course material to replace of new aggregates by 100%. It is found that the new ITS and RAI mixture has excellent compressive performance by designing the material composition of the mixture, which can meet the design strength of different levels of pavement under various load conditions. A series of laboratory tests are used to study the effect of the content of special cementitious material and iron tailings on the uniaxial compressive strength, flexural-tensile strength, compressive resilience modulus, and flexural-tensile resilience modulus of recycled mixture. And, the scanning electron microscope test (SEM) and X-ray diffraction test (XRD) are used to compare the surface morphology characteristics and hydration products of the recycled mixture under different ratios and to discuss the formation mechanism of the strength of the mixture. The test results show that the macroscopic change pattern in laboratory tests is basically consistent with the results in microanalysis. The relationship between compressive strength and compressive resilience modulus and flexural resilience modulus is also established by linear regression. This solid waste treatment method is applied to the pavement renovation project of national and provincial roads in Shanxi Province (within Linfen), to replace the existing base material by using recycled mixture, and the results show that it can save not only the carbon emission from stone mining and processing but also the construction cost, while producing good social and economic benefits and promoting the process of carbon neutralization in the world.

1. Introduction

In recent years, the concept of sustainable development is deeply rooted among the people. The recycling of solid industrial waste as engineering materials can not only effectively dispose the solid waste but also save social resources and protect the ecological environment, which is currently one of the research hotspots that engineers and technicians all over the world are committed to promoting. ITS is the grain size less than 4.75 mm produced by iron ore after grinding and sorting. Iron tailings sand is the main component of industrial solid waste; for example, in China, there are nearly 2 billion tons of iron tailings sands in existence and the annual discharge is over 75 million tons; the large quantity iron tailings sand not only occupies land and pollutes the environment but also has great safety risks [1].

Many scholars are devoted to the application of ITS in engineering materials and have achieved a large number of results, among which the proportion of studies on the use of ITS in cement concrete is larger. In contrast, there is less research on ITS in pavement base or subgrade filler. Although some existing studies [2–10] have a comprehensive research on the strength formation mechanism, mechanical properties, and road performance of cement-stabilized ITS, however, most studies only focus on the feasibility of the mixture from pavement performance, while ignoring the

study of micromechanism. Coupled with the grading limits of current design codes, the ITS has a low substitution rate for fine aggregate in the base course, which restricts the utilization rate of ITS.

Meanwhile, a large amount of RAI are generated from maintenance and reconstruction works of the pavement every year, and the raw RAI is generally used as subgrade filler or the base course and subbase of low-grade pavement, or even directly discarded; thus, all of these treatments brought a low addition value to RAI [11]. There are a lot of micron-sized cement hydrate particles on the surface of RAI, which will affect the strength, cracking resistance, and durability of the recycled mixture [12, 13]. Physical and chemical measures can effectively improve its properties, while the engineering application is complex and difficult [11].

In summary, it is feasible to, respectively, use ITS and RAI as the pavement base course, while the content is generally low, and there is no precedent to use both two materials simultaneously. This paper aimed at "ITS plus RAI" solid waste treatment technology, which replaces 100% of natural aggregates with ITS and RAI as pavement base course material. It can reduce carbon emission and promote the green, high efficiency, high quality, high value, and scale utilization of ITS, can improve the utilization level of ITS, and help the ecological civilization. This paper investigated the strength formation mechanism of recycled mixtures, the hydration products of the mixture in microscale are analyzed by using SEM and XRD test, and the mechanical properties of the mixtures in macroscale are analyzed by using unconfined compressive strength and flexural strength test.

2. Materials and Material Composition Design

This study intends to maximize the utilization rate of ITS on the premise of meeting the strength design requirements of semirigid base material, and relevant studies have already designed the mixture for stabilized ITS with natural aggregates [14]. Therefore, the test selected ITS and RAI blending ratio of 50%:50%, 60%: 40%, and 70%: 30%, respectively, cementitious material (external) blending 4%, 6%, 8%, and 10% of the ratio. Considering that the recycled mixture belongs to the inorganic bonding material, the compaction test and unconfined compressive strength test in this section refer to the relevant test requirements of the Test Methods of Materials Stabilized with Inorganic Binders for Highway Engineering (JTG E51-2009).

2.1. Materials

2.1.1. ITS. ITS is retrieved from Xianfen County, Linfen City, Shanxi Province. The selected ITS is extra fine sand with good cleanliness and negligible content of harmful metal elements below 0.01%, which will not cause pollution to the environment or water bodies. The screening result and basic physical properties are shown in Tables 1 and 2.

2.1.2. RAI. The RAI used in this study are selected from the recycled material of the base course of Linxia section of the provincial pavement in Linfen City, Shanxi Province. 56.2% of the coarse aggregate and the measured crushing value of 10–15 mm reach 25.8%, and the sand equivalent of the fine aggregate of the RAI reaches 75%, with a great degree of cleanliness, which is conducive to the bonding of the cementitious material with the aggregate. The screening result of the RAI is shown in Table 3.

2.1.3. Cementitious Material. The cementitious material, from Nanjing Runcheng Engineering Consulting Co., Ltd., is mainly composed of calcium oxide (CaO) and silicon dioxide (SiO_2), whose basic physical properties and main components are shown in Tables 4 and 5.

2.2. Material Composition Design

2.2.1. Heavy Compaction Test. In this study, a heavy compaction test is used to determine the optimum water content and maximum dry density of the recycled mixture; according to the Test Methods of Materials Stabilized with Inorganic Binders for Highway Engineering *T* 0804–1994 (JTG E51 -2009), the compaction test apparatus is shown in Figure 1, the hammer weight is 4.5 kg, the drop distance is 45 cm, and the compaction is done in three layers and the number of times each layer is 98. The compaction test results for different designs of recycled mixtures are shown in Table 6.

The test results show that the maximum dry density of the recycled mixture tends to rise with the increase of cementitious material admixture under the same amount of ITS and the optimum water content is stable between 8.5% and 9.5%. And, the optimum water content and maximum dry density decrease, with the increase of ITS admixture under the same amount of cementitious material, is mainly caused by the water absorption rate and density of ITS and RAI.

2.2.2. Unconfined Compressive Strength Test. Based on the results of the compaction test, 150 mm∗150 mm cylindrical specimens are formed under the optimum water content by 2000 kN Press Machine (Figure 2) at a loading speed of 10 mm/min, raising in a standard room at a temperature of $20 \pm 2^{\circ}$C and relative humidity of 95% or more for 6 days; after immersing in water for 24 hours, wipe the water on the surface with a damp cloth to determine its unconfined compressive strength by pavement material strength tester (Figure 3) at a loading speed of 1 mm/min. The results of the 7 d unconfined compressive strength test of the recycled mixture are shown in Figure 4.

The test results show that the recycled mixture has good compressive strength. In the same ITS content, the compressive strength increases with the increase of the cementitious material content; in the same cementitious material content, the compressive strength decreases with the increase of the ITS content. Mainly because when the

Table 1: ITS gradation.

Sieve size (mm)	4.75	2.36	1.18	0.6	0.3	0.15	0.075
Pass-rate (%)	100	99.8	98	90.4	60.2	35.8	13.2

Table 2: Technical indexes of ITS.

Fineness modulus	Water content (%)	Apparent density (g/cm^3)	Water absorption (%)	Sand equivalent (%)	SiO_2 (%)	CaO (%)	Cr (%)	Pb (%)
1.1	8.2	2.99	3.7	82	41.01	24.35	0.004	0.001

Table 3: RAI gradation.

Sieve size (mm)	26.5	19	16	13.2	9.5	4.75
Pass rate (%)	100	97.0	92.2	86.9	63.7	43.8
Sieve size (mm)	2.36	1.18	0.6	0.3	0.15	0.075
Pass rate (%)	23.2	14.5	7.7	3.3	1.4	0.5

Table 4: Technical indexes of special cementitious material.

Apparent density (g/cm^3)	Specific surface area (m^2/kg)	Setting time (min)		Strength of 7 d (MPa)		Strength of 28 d (MPa)	
		Initial set	Final set	Compressive strength	Rupture strength	Compressive strength	Rupture strength
2.85	350	246	531	31.9	6.7	61.2	8.8

Table 5: Main compositions of special cementitious material.

Items	CaO	Si_2O	Al_2O_3	MgO	SO_3	Fe_2O_3	K_2O	TiO_2	Na_2O
Rate/%	39.98	27.67	13	7.656	2.55	0.69	0.525	0.517	0.422

Figure 1: Compaction test apparatus.

Table 6: Compaction test results.

Mixture proportion	Optimum water content (%)				Maximum dry density (g/cm^3)			
	4	6	8	10	4	6	8	10
50%:50%	9.0	9.3	9.4	9.4	2.109	2.117	2.128	2.132
60%:40%	8.9	9.2	9.1	9.1	2.083	2.089	2.100	2.114
70%:30%	8.8	8.9	8.8	9.0	2.072	2.073	2.085	2.112

Figure 2: 2000 kN press machine.

Figure 3: Pavement material strength tester.

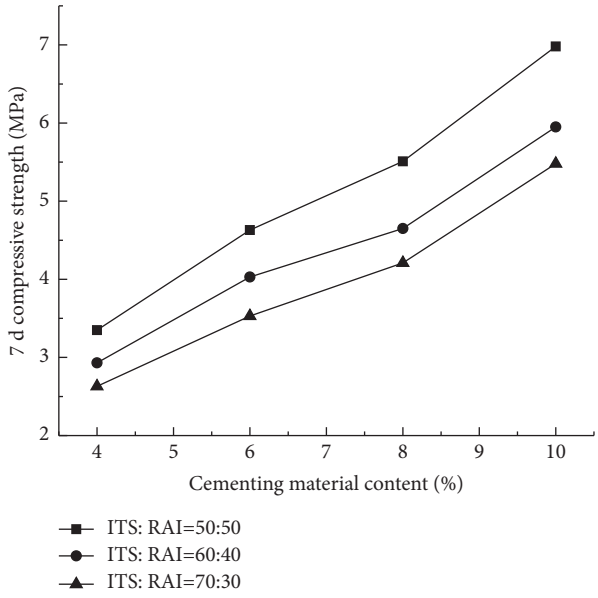

Figure 4: 7 d compressive strength test results.

hydration product is certain, the higher the amount of ITS is, the finer the particles are and the more difficult to form a stable whole. At the same time, the reduction of RAI reduces the skeletal support, which is also one of the reasons for the reduction in strength. The compressive strength of the recycled mixture can be up to 7 MPa, which can meet the design strength requirements of different levels of pavements under various load conditions. However, the higher the strength, the more likely to produce the cracking problem, so the design should be a reasonable choice of the content of cementitious materials.

3. Mechanical Properties Test and Results Analysis

According to material design composition, the mechanical properties of the recycled mixture of different ratios are tested and compared with commonly used materials stabilized with inorganic binders to evaluate the mechanical properties of the recycled mixture. And, through linear fitting analysis, the relationship between strength and rebound modulus is established.

3.1. Compressive Strength. Figure 5 shows the unconfined compressive strength test results for the recycled mixture at the age of 3, 7, 14, 28, and 90 d at 8% cementitious material dosage. The following conclusions can be drawn from the analysis of the test results.

(1) From Figure 5, the test results show that the compressive strength of the recycled mixture grows fastest from 3 d to 7 d. After 28 d, the trend of strength growth slows down gradually, and the compressive strength of the three ratios of the recycled mixture at 7 d all reaches about 80% at 90 d. It indicates that the cementitious material can promote the rapid formation of the early strength of the recycled mixture.

(2) Combined with Figures 4 and 5, we can see that the compressive strength of the recycled mixture can reach 7 MPa which has good compressive properties, through the adjustment of material composition, which can meet the design strength requirements of different levels of pavements under various load conditions and has good compressive properties.

3.2. Flexural-Tensile Strength. At present, with the increasing traffic volume, the base course materials not only need high compressive strength but also need good tensile strength. And, the real force state of the pavement is closer to the flexural-tensile state, so this paper uses flexural-tensile strength to analyze the tensile performance of the recycled mixture. Combined with Section 2.2.2, the flexural-tensile strength of five different blending ratios (which can meet the 7 d unconfined compressive strength requirements of high-grade pavements) is analyzed to explore the influences of the number of cementitious materials and ITS on the flexural-tensile strength of the recycled mixture.

According to the Test Methods of Materials Stabilized with Inorganic Binders for Highway Engineering (JTG E51-2009), 100∗100∗400 mm medium beam specimens (Figure 6) are formed by the hydrostatic method under the OWC, with the pressure rate of 5 mm/min. The flexural-tensile strength of the recycled mixture is tested (Figure 7) after different ages (28 d, 90 d, and 180 d) of regeneration under standard conditions, and the test rate is 50 mm/min. The test results are shown in Figure 8, and the analysis of the test results can be concluded as follows.

(1) In the same ITS content, the flexural-tensile strength increases with the increase of the cementitious material content; in the same cementitious material content, the strength decreases with the increase of the ITS content, which is the same as the regular pattern of compressive strength.

(2) It is calculated that the 28 d flexural-tensile strength of recycled mixture at studied ratios is 70%–80% of the 180 d strength. And, the later strength growth trend is larger when the ITS is lower, which may be due to the low amount of ITS. The specific surface area of the recycled mixture is small, and the surplus of cementitious material consumed in the early formation of strength is relatively more. Thus, the hydration reaction can occur continuously in the later stage to promote the formation of strength. The flexural-tensile strength increases about 20% for every 2% increase in the amount of cementitious material under 50% ITS content. When the amount of cementitious material is 8%, the flexural-tensile strength decreases about 10% for every 10% increase in the amount of ITS. So, the influence of cementitious material on the recycled mixture is greater.

(3) Compared with the 90 d flexural-tensile strength (0.9–2.0 MPa) of cement-stabilized aggregates in the

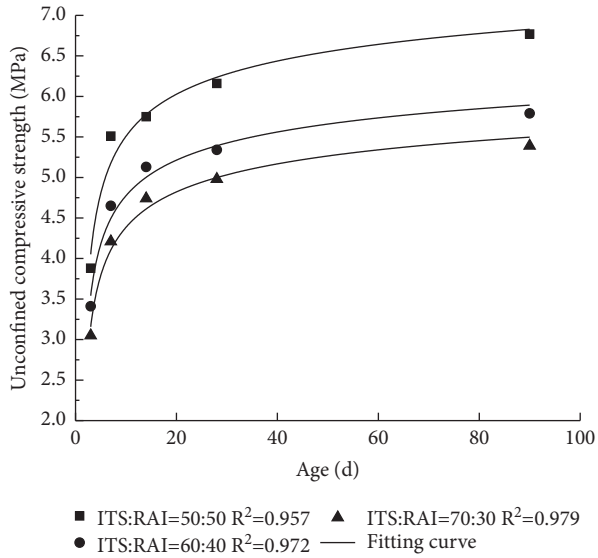

Figure 5: Change rule of compressive strength with ages.

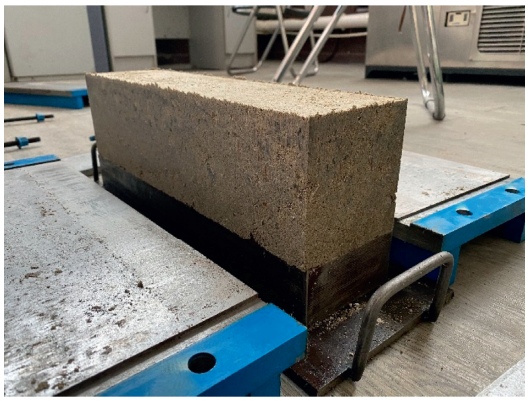

Figure 6: Medium beam specimen.

Specification for Design of Highway Asphalt Pavements (D50-2017), the recycled mixture has good tensile properties.

3.3. Resilient Modulus. Considering the nonlinear elastoplastic properties of soils and granular material [15] and their differences with the traditional elasticity theory, we usually define the ratio of the repetitive stress to the refundable strain after stabilization of deformation under repeated loading as the rebound modulus, which is an important indicator of pavement materials, and an in-depth understanding of the rebound modulus of materials is of great significance to understand the mechanical properties of materials. Guo [16], from Southeast University, conducted an experimental evaluation of compressive strength and compressive rebound modulus (CRM) and concluded the process of unconfined compressive strength test experienced in the process of rebound modulus test. So, they emphasized the importance of compressive rebound modulus to the construction quality control. On the contrary, the real force state of pavement is closer to the flexural-tensile state, so the flexural-tensile rebound modulus (FTRM) also needs to analyze. Concerning the existing approved modulus determination age, the five preferred ratios measured for compressive resilient modulus and flexural-tensile resilient modulus at 90 d. The test results are shown in Table 7.

From the test results, it can be seen that the compressive and flexural-tensile modulus of the recycled mixture increases with the increase of the amount of cementitious material under the same amount of ITS, while it decreases with the increase of ITS under the same amount of cementitious material. Through calculation, the compressive resilient modulus is 2–3 times of the flexural-tensile resilient modulus, which is similar to cement-stabilized aggregates. According to studies [17, 18], the compressive resilient modulus of cement-stabilized aggregates is close to 10,000 MPa at the same strength level, while the flexural-tensile resilient modulus of the recycled mixture is less than 1/3 of it. Through analysis [19, 20], on the one hand, there is relatively high water content in the recycled mixture. The existence of water will "lubricate" the particles and increase elastic deformation. On the other hand, the increase of the fines content leads to the decrease of the rebound modulus of the recycled mixture. However, the lower modulus of the material is beneficial to the crack resistance of the material under the premise of good strength.

3.4. Compressive Strength and Rebound Modulus Relationship Establishment. Considering that the unconfined compressive strength is used as the proportional design index during construction, there may not be conditions to determine the rebound modulus of the material, and the modulus is a key factor in the design of the pavement structural layer thickness. So, it is necessary to establish the relationship between compressive strength and rebound modulus for construction reference or as an index for construction quality control. The relationship between 7 d compressive strength and 90 d rebound modulus of the recycled mixture

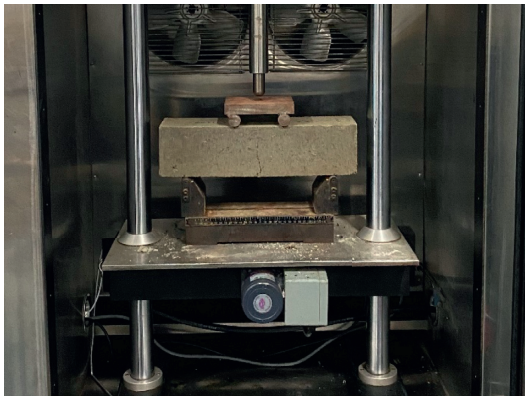

Figure 7: Flexural-tensile strength testing.

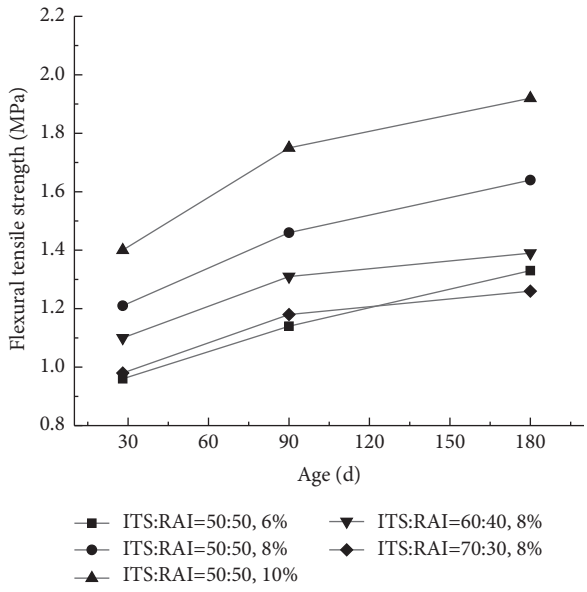

Figure 8: Change rule of flexural-tensile strength with ages.

in this study is shown in Figure 9, where FTRM refers to flexural-tensile resilient modulus and CRM refers to compressive resilient modulus.

Regression of the data in Figure 4 and Table 7 yields the equation for the relationship between 7 d compressive strength and 90 d rebound modulus; for compressive rebound modulus, $E_c = 913R_c\text{-}68$ ($R^2 = 0.976$); for flexural-tensile rebound modulus, $E_s = 510R_s\text{-}517$ ($R^2 = 0.909$).

4. Strength Formation Mechanism

The micromorphology can reflect the surface structure and crystallization of the material; it can also intuitively and qualitatively evaluate the aggregation characteristic of hydration products such as the morphology or the degree. The hydration product is an important factor affecting the strength characteristic of the material, and the amount is the main measure of the product amount [5]. In this study, SEM and XRD tests are used to compare the surface morphological characteristics and the differences in the dosage of hydration products of the recycled mixtures with different ratios that meet the strength design requirements of high-grade pavement, and the strength formation mechanism of the recycled mixture is explored. And finally, the macro-strength changes rules of the recycled mixture which are compared with the microconclusion.

4.1. Surface Morphology. Taking samples from the specimens with different ratios and different ages after testing and the agglomerated ITS and RAI with the volume of 1 cm^3~2 cm^3 which are immersed in alcohol to terminate the hydration, then the obtained samples and the RAI obtained from pavement milling are dried in an oven at 60°C and then SEM tests are conducted. The surface morphology of RAI on recycled mixture and RAI obtained from pavement milling are compared, as shown in Figures 10 and 11, and the agglomerated iron tailing sand results are shown in Figures 12~15. The name of the figures corresponds to the amount of ITS admixture, the amount of cementitious material admixture, the age of the specimen, and the magnification of the test observation and figure, respectively.

From Figure 10, it can be seen that there is a large amount of floating slurry on the surface of RAI obtained from pavement milling. And, compared with Figure 11, the hydration products are in the shape of a net, and this net structure intertwines and bonds the floating slurry on the surface of RAI and then bonds with ITS to form the strength. Combined with Figures 12–15 and based on the existing studies on the mechanism of materials stabilized with inorganic binders [5, 21] and the shape of hydration products in microscopic morphology, it is found that the formation of high strength is through the mutual cross-linking of the gel generated by the volcanic ash effect (shown by arrows in the figure) and the pin-rod crystals and block crystals generated by the crystallization effect (shown by rectangular boxes in the figure).

Compared with Figures 12 and 13, it can be seen that the recycled mixture with 50% ITS admixture already has a large number of needle-rod crystals at the age of 7 days. And, they are considered to be the main reason for the early strength formation through its intersection with the gel. At the age of 28 days, the number of needle-stick crystals increased, but it can be seen from the tops of the needle-stick crystals (elliptical box in Figure 8), and they developed radially but more slowly. So, it is believed that the strength of the recycled mixture from 7 d to 28 d in the continued growth, but the trend is relatively slow, and it also verifies the conclusion of the macroscopic test that strength formation is slower after 7 d. Compared with Figures 13 and 14, it can be seen that when the amount of cementitious material increased to 8%, the number of needle-rod crystals increases significantly, and a large number of block crystals generated, and they are intertwined together to form a network skeleton, which is conducive to promoting the formation of the strength of the recycled mixture, so it is believed that the higher the amount of cementitious material under the same iron tailings sand admixture is, the better the mechanical properties of the recycled mixture are.

Table 7: Resilient modulus results.

ITS content (%)	RAI content (%)	Cementitious material content (%)	Ages (d)	Compressive resilient modulus (MPa)	Flexural-tensile resilient modulus (MPa)
50	50	6		4177	1758
50	50	8		5057	2325
50	50	10	90	6300	3010
60	40	8		3960	2105
70	30	8		3904	1488

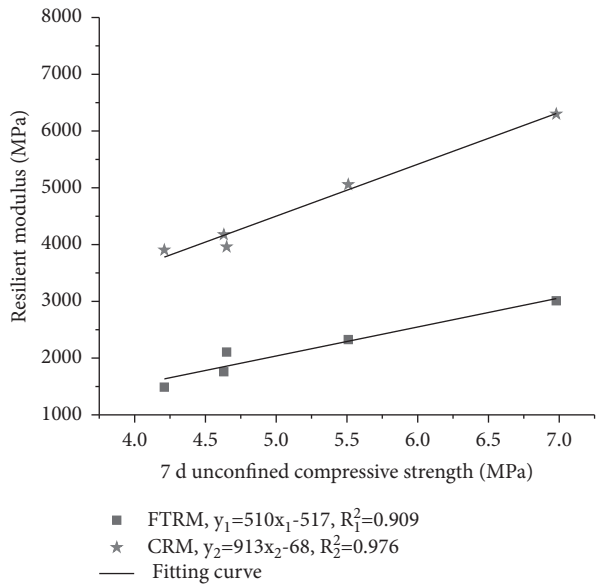

Figure 9: Relationship between compressive strength and resilient modulus.

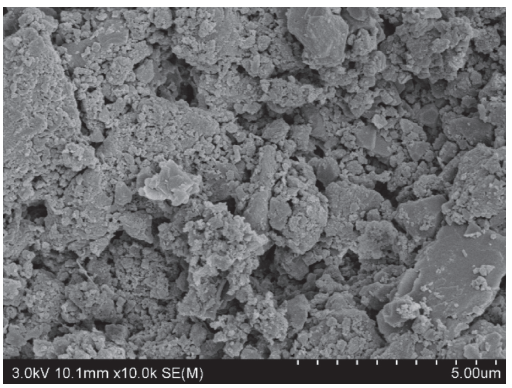

Figure 10: RAI from pavement milling.

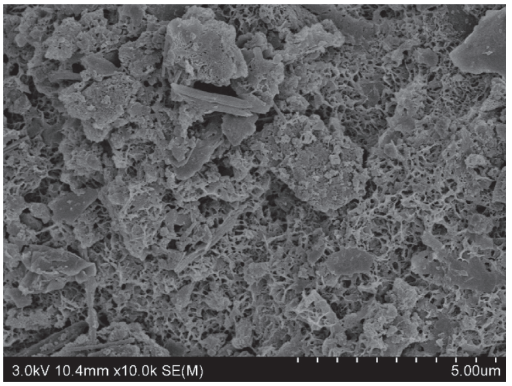

Figure 11: RAI from recycled mixture.

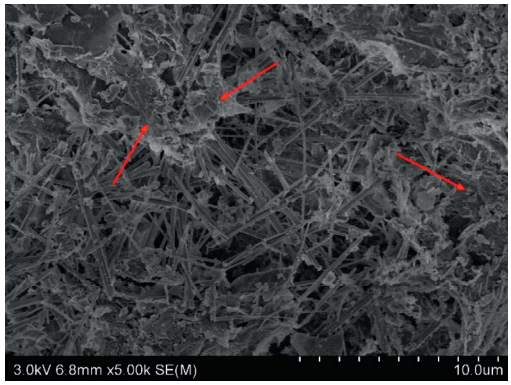

Figure 12: 50%, 6%, 7 d, and 5000.

Figure 15 shows the apparent morphology at the age of 7 days with 70% of ITS and 8% of cementitious material, which is magnified 10,000 times. It is found that the degree of crystallization is low at this time, compared with the formation of embedded cross-linking in Figure 14; a few crystals are connecting a large number of gels to form strength. So, it is believed that the higher the content of ITS with the same cementitious material, the worse the mechanical properties of the recycled mixture, and it also verifies the macroconclusions.

4.2. Analysis of Hydration Products. Taking samples from the specimens with different ratios and different ages after testing, the samples are dried after terminating hydration, ground into powder, and passed through 0.075 mm sieve. And, the lower part of the sieve is taken for compositional analysis, and the test incidence angle is selected from 5 to 75° wide range for detection, and the scanning rate is 5°/min. The Origin software is used to process the characteristic peaks (hydration products), and the processing results are shown in Figures 16 and 17.

Figure 16 compares the characteristic peaks of the age of 7 days with 6% and 8% of cementitious material at 50% of ITS content and finds that the characteristic peaks basically overlap, and only the peaks differ significantly, which means that the difference in hydration product types is not significant while the degree of hydration is different. Figure 17 compared the characteristic peaks of the age of 7 days with 50% and 70% of ITS content at 8% of cementitious material. In comparison with Figure 16, it is found that the overlap of the characteristic peaks of the two recycled mixtures in Figure 17 is lower and the peak difference is larger, so it is believed that there is a large difference between the hydration products and the degree of hydration at this stage, which is consistent with the SEM test results. And, except for the characteristic peak maximum, the other peak strength differences are low, so the characteristic peak maximum strength is considered to be the main factor affecting the performance of the recycled mixture.

At the same curing age, the maximum characteristic peak strength of 6% of cementitious material with 50% of ITS is 2694 pcs, 345 pcs smaller than 3048 pcs with 8% of cementitious material. It means the cementitious material content increased by 2%, and the character peak strength of recycled mixture increases about 13%. The character peak strength of ITS content at 70% with 8% of cementitious material is 2365 pcs, which is 683 pcs smaller than 3048 pcs at 50%, which means the ITS content increases by 20%, the character peak strength of recycled mixture reduced about 22%, which corresponds with flexural-tensile strength data from macrotests. Through analysis, the performance of the recycled mixture becomes stronger with the increase of cementitious materials content and becomes weaker with the increase of ITS content, and the degree of influence of cementitious materials is greater, which further verifies the macroconclusions.

5. Environmental and Economic Benefits

At present, China is the world's largest greenhouse gas emissions while green low-carbon is an important part of the new development concept; if the recycled mixture 100% replacement of cement-stabilized aggregates is applied to the pavement, it not only helps to solve the problem of iron tailings sand stockpile and reduce construction costs but also reduces carbon emissions.

5.1. Environmental Benefits. According to the PBL (Planetary Boundary Layer) Norwegian EIA (Ecological Impact Assessment), global greenhouse gas emissions in 2018 were about 55.6 billion tons of carbon dioxide equivalent, of which China accounted for 26%. The carbon emissions will reduce in the gravel mining and processing process if the recycled mixture replaces the traditional cement-stabilized aggregates base course materials, which can promote the decarbonization process of the world. Consider the large variability of transportation distance, and this study does not consider the carbon emission difference generated in the transportation process.

According to the field research, the energy consumption of stone in mining process p_{11} is about 1.1 kg/t, and the energy consumption of processing process p_{12} is about 0.12 kg/t, where the energy consumption is all in diesel. According to the General Principles for Calculation of Total Production Energy Consumption GB/T2589-2008, the formula for calculating comprehensive energy consumption is shown as

$$E = \sum_{1}^{n} (e_i \times p_i), \tag{1}$$

where E denotes comprehensive energy consumption, n denotes the number of energy species consumed, e_i denotes the ith energy substance consumed in production, and p_i denotes the conversion factor of the ith energy.

In this study, e_i only calculates aggregates, so the energy saving is $\Delta E = e_{11} \times p_{11} + e_{12} \times p_{12}$. If the average width of the base course is 15 m and thickness is 0.2 m, it is expected that the recycled mixture can be consumed about 7000 tons per kilometer, so the energy saving of diesel per kilometer is 8540 kg. According to the General Principles for Calculation of Total Production Energy Consumption, the coal

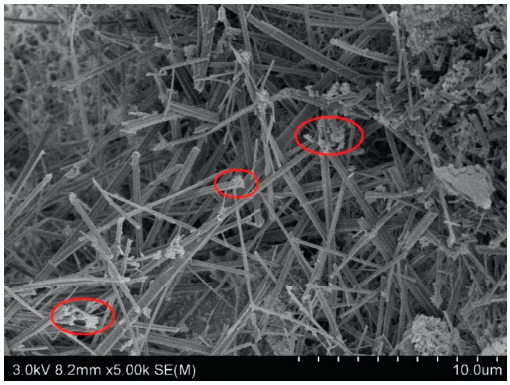

Figure 13: 50%, 6%, 28 d, and 5000.

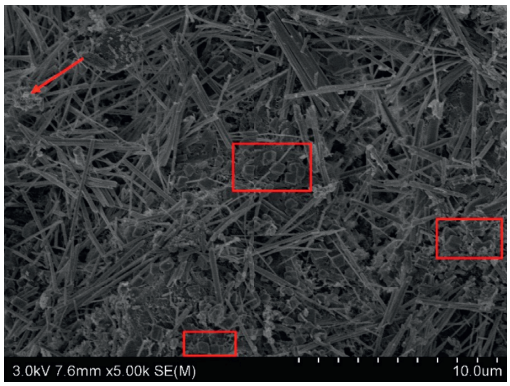

Figure 14: 50%, 8%, 7 d, and 5000.

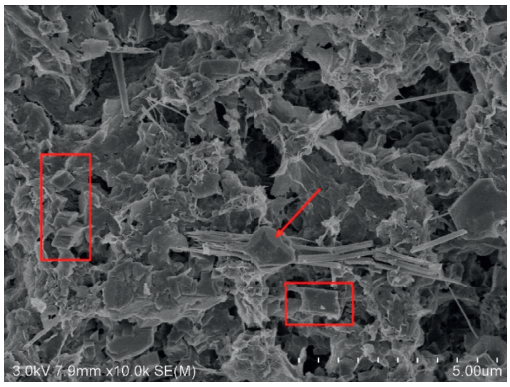

Figure 15: 70%, 8%, 7 d, and 10000.

conversion factor of diesel fuel is 1.4571 kgce/kg, and the CO_2 emission factor is 3.0959 kg-co_2/kg. The calculated energy saving of recycled mixture per kilometer is 12.45 tce, and the carbon reduction is 26.44 tCO_2.

5.2. Economic Benefits. If the average width of the base course is 15 m and thickness is 0.2 m, it is expected that each kilometer can consume about 7000 tons of recycled mixture. If the mixing ratio of the recycled mixture is considered as ITS: RAI = 70%:30%, each kilometer will consume nearly 5000 tons of ITS and 2000 tons of RAI. In terms of social

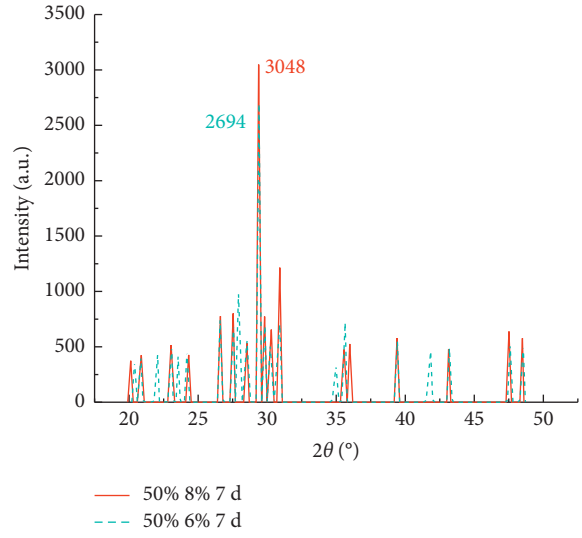

Figure 16: Peak comparison 1.

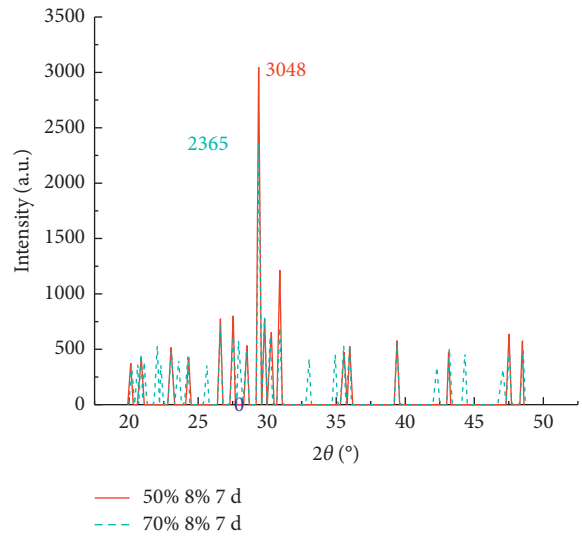

Figure 17: Peak comparison 2.

costs, according to the price of treatment in the backing project (Shanxi Province), it is assumed that the disposal fee of ITS is 30 yuan per ton and the disposal fee of RAI is 20 yuan per ton, and each kilometer will save nearly 200,000 RMB. In terms of construction costs, according to the aggregates price in the backing project (Shanxi Province), it is assumed that the cement-stabilized aggregates are 100–150 RMB per ton and the recycled mixture is 50–100 RMB per ton, which will save at least 350,000 RMB per kilometer of construction capital.

6. Conclusions

(1) Results of laboratory tests show that the recycled mixture has excellent mechanical properties; the material strength is more affected by the content of cementitious materials. In addition, the recycled

mixture also can meet the strength requirements of the base course on the various grades of pavement by adjusting the material composition.

(2) Results of SEM and XRD test show that the strength of recycled mixtures are mainly formed by filling the internal space of the mixture with gels and crystals of hydration products and cross-linking each other to stabilize the surrounding scattered particles.

(3) The relationship between 7 d compressive strength and rebound modulus is established by linear regression analysis; for compressive rebound modulus, $E_c = 913R_c\text{-}68$ ($R^2 = 0.976$); for flexural-tensile rebound modulus, $E_s = 510R_s\text{-}517$ ($R^2 = 0.909$).

(4) The "ITS plus RAI" solid waste treatment method proposed in this paper can effectively reduce carbon emissions from stone mining and processing and save construction costs. The engineering application in Shanxi province shows that the average energy saving per kilometer is about 12.45 tce and carbon reduction is about 26.44 t of CO_2. In terms of social costs, it will save nearly 200,000 RMB per kilometer, and in terms of construction costs, it will save at least 350,000 RMB per kilometer, which has great social and economic benefits.

This paper only studied the mechanical properties of the recycled mixture, and further research is needed on the pavement performance such as shrinkage and fatigue characteristics.

Data Availability

The data used to support the findings of this study are included within the article.

Conflicts of Interest

The authors declare that they have no conflicts of interest.

Acknowledgments

The authors thank China Highway Engineering Consulting Corporation for their support.

References

[1] A Liu, M Cao, and X Zhang, "The research status of large-scale utilization of iron tailings and its utilization methods," *Chinese Metal Bulletin*, vol. 11, pp. 279-280, 2019.

[2] H. Li, "Research on the influence of iron tailings on the performance of cement stabilized crushed stone base course," *Highway*, vol. 12, 2014.

[3] B. F. Pan, H. Yu Shi, and C. H. Zhou, "Experimental research on shrinkage properties of cement stabilized iron tailings sand mixture," *Applied Mechanics and Materials*, vol. 423, 2013.

[4] H. Song, H. Feng, and Z. Pan, "Analysis of design parameters of curing agent stabilized iron tailing base structure," *Shanghai Highway*, vol. 3, pp. 69–72+101, 2020.

[5] W. Jiang, *Research on the Strength Mechanism of Inorganic Binder Iron Tailings and the Optimization Design Application to the Base Layer*, Harbin Institute of Technology, Heilongjiang, China, 2018.

[6] Q. Bai, H. Zhang, and W. Bao, "Experimental study on stabilization of iron tailings sand gravel by inorganic binding material," *Urban Roads and Bridges and Hong*, vol. 4, pp. 159–161+171+22, 2020.

[7] D. Xue, "The application of iron tailings sand in the water-stable gravel base of national and provincial trunk roads," *Shandong Communications Science and Technology*, vol. 6, pp. 46–48+64, 2020.

[8] S. Lu, P. Jiang, B. Qian, W. Wang, and N. Li, "Research progress on mechanical properties and recycling of iron tailings sand," *Bulletin of the Chinese Ceramic Society*, vol. 39, no. 2, pp. 466–470+512, 2020.

[9] X. Niu and Y. Sun, "Numerical analysis on settlement and stability of iron ore tailings subgrade," *Journal of Chang'an University (Natural Science Edition)*, vol. 38, no. 1, pp. 9–16, 2018.

[10] R. Hou, S. Chen, and M Xiao, "Study on the mechanical properties of iron tailing sand cement composite soil," *China & Foreign Highway*, vol. 39, no. 1, pp. 206–209, 2019.

[11] L. Fu, *Study on Strengthening Treatment and Application of Cement Stabilized Aggregate Milling Material*, Shandong University of Technology, Shandong, China, 2019.

[12] Z. Ma, H. Li, and Y. Lu, "Study on the properties and grading influencing factors of cement in-situ cold recycled base milling material," *China & Foreign Highway*, vol. 38, no. 2, pp. 263–268, 2018.

[13] W. Gu, P. Xiao, and Y. Yang, "Experimental study on shrinkage and fatigue properties of recycled cement stabilized crushed stone base materials," *Concrete and Cement Products*, vol. 12, pp. 95–100, 2018.

[14] Q. Bai, H. Zhang, and W. Bao, "Study on the road performance of solidified iron tailings," *Hunan Transportation Science and Technology*, vol. 46, no. 3, pp. 40–43+47, 2020.

[15] X. Yan, C. Liang, J. Xu, Y. Q. long, and A. Li, "Elastoplastic of characteristics cement-stabilized aggregate bases," *China Journal of Highway and Transport*, vol. 32, no. 1, pp. 29–36, 2019.

[16] G. Guo, J. Wang, and C. Fei, "A study on relationship between unconfined compressive strength and compression rebound modulus of cement stabilized aggregate," *Highway*, vol. 1, pp. 171–174, 2007.

[17] P. Zhang, *Research on Anti-cracking Performance of Semi-rigid Base Course in High-Grad Highway*, Dalian University of Technology, China, Liaoning, 2007.

[18] A. Sha and L. Hu, "Structural characteristics of semi-rigid base course material," *China Journal of Highway and Transport*, vol. 4, pp. 1–5+42, 2008.

[19] N. H. Thom and S. F. Brown, *Effect of Moisture on the Structural Performance of a Crushed-Limestone Road Base*, Transportation Research Record, Nottingham, England, 1987.

[20] R. Hicks and C. Monismith, "Factors influencing the resilient response of granular materials," *Highway Research Record*, vol. 345, pp. 15–31, 1971.

[21] M. Dong, T. Ling, and J. Xu, "Mechanism on the phospho-gypsum-improved semi-rigid basecourse," *China Journal of Highway and Transport*, vol. 2, pp. 14–18, 2002.

Hindawi
Advances in Materials Science and Engineering
Volume 2021, Article ID 3463363, 14 pages
https://doi.org/10.1155/2021/3463363

Research Article

Automated Shape Analysis and DEM Study on Graded Crushed Stone

Hao Bai,[1,2] **Ruidong Li**,[3] **Xiangyu Hu**,[3] **Fei Chen**,[2,4] **and Zhiyong Liao**[1,2]

[1]*Sichuan Expressway Construction & Development Group Co., Ltd., Chengdu 610041, China*
[2]*Shudao Investment Group Co., Ltd., Chengdu 610041, China*
[3]*School of Civil Engineering, Central South University, Changsha 410075, China*
[4]*Sichuan Intelligent High-Speed Technology Co., Ltd., Chengdu 610000, China*

Correspondence should be addressed to Ruidong Li; kylelee0731@outlook.com

Received 19 May 2021; Revised 25 July 2021; Accepted 14 August 2021; Published 7 October 2021

Academic Editor: Yongsheng Yao

Graded crushed stone (GCS), as a cheap and essential component, is of great importance in road construction. The irregularity and variability of particle shape is known to affect the packing characteristics of GCS, such as compactness and void ratio. In this study, the realistic particle outline is first automatically extracted based on digital image processing and deep learning algorithms. Then, the elongation (*EI*), roundness (*Rd*), and roughness (*Rg*) of GCS are quantified by shape evaluation algorithms. Moreover, based on the establishment of the GCS shape library, the gravity deposition with various elongations is simulated using the discrete element method to study the packing features of GCS. The elongation effects on the macroscopic and microscopic quantities are explored. Finally, the shear behavior of GCS is studied. The results illustrate that elongation has a significant effect on the packing of GCS.

1. Introduction

With the development of the highway industry and the deepening of engineering practice, the asphalt pavement structure used in China has been diversified from the single semirigid asphalt base, and the graded crushed stone flexible base asphalt pavement has become one of the main pavement structure forms in China. As a mixture composed of aggregates of different sizes, the graded crushed stone (GCS) is widely applied between the asphalt surface and semirigid base and can effectively weaken the cracks in the top of the semirigid base and the stress concentration effect. Additionally, GCS can also reduce the temperature shrinkage and dry shrinkage stress caused by the change of temperature and humidity of the semirigid base [1, 2].

Due to the great significance of GCS to highway construction, it is particularly essential to study its mechanical properties, deformation, and failure mechanism. However, it is difficult to analyze its mechanical properties quantitatively and qualitatively by conventional methods because of its granular structural characteristics and nonlinear mechanical properties [3]. On the one hand, the conventional laboratory test for GCS is complex and costly, which makes it difficult to reveal the macro-meso mechanical characteristics of GCS under load. On the other hand, the granular material such as GCS has great variability and the data results of different specimens in the same group are relatively low in correlation, which makes experimental data unreliable [4]. Hence, it is very necessary to use the numerical test method to study the mechanical properties of GCS from the microscopic point of view, to make up for the lack of laboratory tests and provide a powerful means for the in-depth understanding of GCS [5, 6].

As a basic road material, the shape of crushed stone particles has a significant effect on its mechanical properties. Scholars have done much research on the mechanical properties of GCS influenced by GCS shape. An [7] carried out a quantitative analysis on the particle shape of GCS to explore the relationship between the real particle shape and particle accumulation porosity. Le Pen et al. [8] set out

methods for evaluating form and roundness (aspects of shape) and proposed a new measure for evaluating roundness, termed ellipses for crushed stone. Zhang et al. [9] simulated the geometric anisotropy of the GCS using randomly generated models. The results showed that the changes of both friction and anisotropy had a similar trend with the particle size enlarging in the dense assembly, which maintains stability when the size is less than 3.0 mm.

Numerical simulation methods are often used in exploring the properties of GCS. Jiang et al. [10] used PFC^{2D} to establish a numerical test method for California bearing ratio (CBR) and found that CBR values increase with the friction coefficient at the contact and shear modulus of the rocks, while the influence of Poisson's ratio on the CBR values is insignificant. Ren et al. [11] proposed a random calculation model for GCS and studied the Direct Shear Tests (DST) of GCS by PFC^{2D}. Xu et al. [12] proposed Plastic Deformation Index (PDI) as the evaluation indicator and founded that the PDI should be less than or equal to 1900 mm number for expressway and first-grade highway. Jiang et al. [13] established a numerical model of dynamic triaxial test of GCS based on PFC^{2D} and founded that the size of the specimen has a slight influence on the simulated value of axial strain when specimen height is greater than 40 cm and diameter is greater than 20 cm.

In this study, the particle outlines are firstly extracted based on deep learning algorithms. The U-NET model is trained for contour extraction. Then, the shape evaluation indexes including elongation, roundness, and roughness are quantified. In addition, the gravity deposition with a distinct *EI* value is simulated by the discrete element method to explore the elongation effects on the macroscopic and microscopic quantities. Finally, the shear behavior of GCS is studied. Overall, this study lays a foundation for future research about GCS.

2. Materials and Equipment

In construction projects, GCS are transported by large-scale transport equipment. To simulate the real conveyance cases, a conveyor belt is used to carry GCS obtained from the laboratory of civil engineering materials in Shenzhen University. The GCS is first screened and the stone with a particle size of 4.75 mm~25 mm is selected for preparation. Then, in order to obtain the data set with images of GCS in batches, the equipment shown in Figure 1(a) is used. The specific components are illustrated as follows:

Component (1): A Fujinon X-T20 camera as shown in Figure 1(b) with a resolution of 24 million pixels (6000×4000 pixels) and two lenses: Fujinon XF60 mm F2.4 R Macro and Fujinon XF35 mm F2 R WR. At least 90 pixels are used to represent the smallest diameter of the particle.

Component (2): A conveyor belt as shown in Figure 1(c) used to carry GCS to simulate the real transport of GCS.

Component (3): Two lamps composed of 256 LEDs as shown in Figure 1(d) provide controllable lighting conditions. The light is scattered uniformly so the lamps have good color rendering. The LED lamp arm is installed on the copy stand and is perpendicular to the plane of each LED lamp. In addition, the lamp is placed 45 cm above the transparent plastic plate. Besides, the side of the lamp is parallel to the side of the base of the copy stand. The color temperature is 5600 K at the maximum brightness value.

3. Automated Extraction of GCS Contours

3.1. Implementation of Algorithms. For image processing, convolutional neural network (CNN) and full convolutional network (FCN) are the main frames for image segmentation. However, CNN has two obvious drawbacks: (1) slow training process because of too much redundancy and (2) asynchronism between obtaining sensing field and positioning accuracy. Mostly, CNN is used for image classification at the image level. By contrast, FCN can classify images at pixel level with good training results. In order to avoid these defects as much as possible, in this study, according to Liang et al. [14] a lightweight U-NET [15] method of a fully convolutional neural network is adopted for image segmentation.

3.1.1. Lightweight U-NET and Operation. In this study, a U-NET deep neural network is introduced. Firstly, the lightweight U-NET particle image is converted into a 3D matrix $W \times C \times h$ as the input data, where W and h are the width and height of the input image, respectively; C is the number of color channels of input images, where $C = 3$ represents RGB image and $C = 1$ represents gray/binary image. The gray images are input data, and binary images are output data. Then, the network generates a mask by a matrix with a size of $W \times h \times 1$ to record the pixels on the projection of GCS. For clarity, three parts of the operation of lightweight U-NET are briefly explained: convolution, Maxpool, and deconvolution.

The kernel of convolution used in this study is defined as a square matrix. And the overwritten elements in the input matrix are transformed into feature mapping elements (y_{ij}) by multiplying elements:

$$y_{ij} = AF\left(\sum_{m=i-s}^{i+s}\sum_{n=j-s}^{j+s}\left(X_{mn}W_{mn} + b\right)\right), \quad s = \left(\frac{k_n}{2}\right), \tag{1}$$

where k_n is the size of the kernel matrix; x_{mn} is the element at position (m, n) of the input matrix; w_{mn} is the element of the nuclear matrix overlapping with x_{mn}; b is the bias term of the output feature graph, and $AF(\cdot)$ is the activation function. During the training process, both parameters w_{mn} and b are the targets of training. According to the recommended values [16], the default value of k_n is 3 and the default activation function is ReLu ($AF(x) = \mathrm{Max}(0, x)$) in this study. The principle of convolution is shown in Figure 2.

The Maxpool and Upconv operations use different kernels and computations to downsample and upsample the input matrix, respectively. But they are both executed by

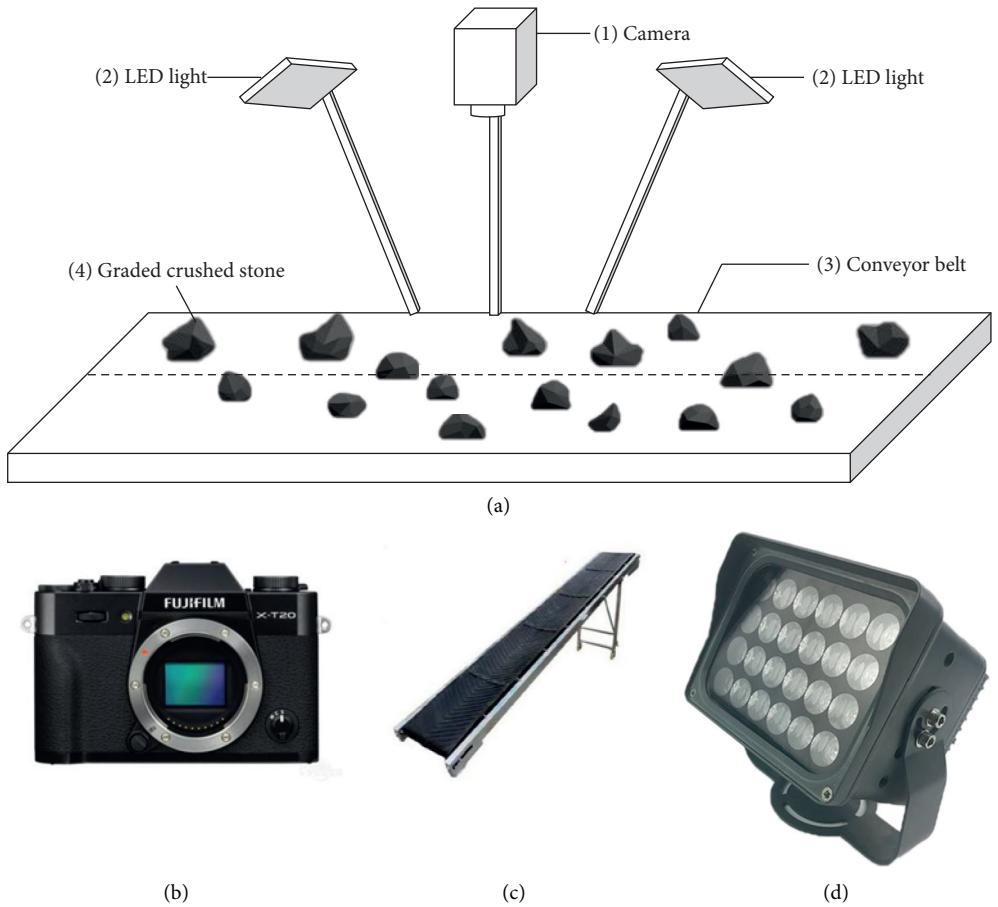

Figure 1: Materials and equipment for GCS images capture. (a) The equipment to photograph GCS. (b) Fujinon camera. (c) Conveyor belt. (d) LED light.

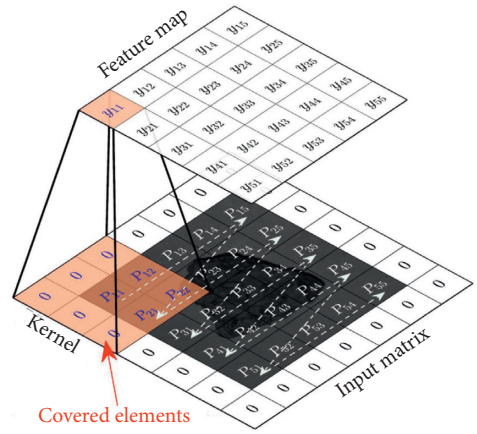

Figure 2: Convolution operation [14].

sliding Windows, just like convolution operations. The Maxpool operation can be regarded as a special convolution operation, with $k_n = 2$ and $S = 2$, and the function of formula y_{ij} which outputs the maximum element covered by the kernel. Deconvolution, as opposed to convolution, has different interpretations like upsampling or transposed convolution. In this study, we used a UpSampling2D built-in Keras to implement the upsampling operation.

3.1.2. Model Optimization. Considering the limited size and computing power of the model, the size of the network was reduced by half; thus, the number of channels (c) of all operations was reduced to half of the original number except for the number of channels at the end and the beginning. At the same time, in order to prevent overfitting, part of neural network units are temporarily dropped from the network according to a certain probability, which is equivalent to

finding a thinner network from the original network. Dropout [17] should be performed after the fourth Maxpool operation with the parameter keep_prob_(the probability of which part of the network would not be dropped) set to 0.6. It is a parameter of the dropout method. The overall structure of U-NET is shown in Figure 3.

The commonly used optimization method Adam of deep learning is used to dynamically adjust the learning rate of each parameter by using the first-order moment estimation and second-order moment estimation of the gradient. For the loss function, cross-entropy was used in this study.

3.2. Training of the Model

3.2.1. Data Set Preparation. For the collected pictures, the "labelme" image marking tool was used to manually mark the GCS. A total of 400 pictures is collected as the training set. Meanwhile, 50 pictures are collected as the validation set.

3.2.2. Data Enhancement. Image enhancement is a widely used training sample expansion method. In order to improve the diversity of training samples and enhance the antinoise performance of the model, image enhancement technology was used to expand the obtained samples. A total of 4 categories and 8 image enhancement technologies were used, including (1) image rotation; (2) image flipping; (3) random brightness transformation; and (4) random pepper and salt noise, as shown in Figures 4.

3.2.3. Recognition Effect. Parameters are adjusted manually. Through multiple experiments of different parameter setting, the best parameter is chosen. By adjusting the parameters, the learning rate was set to 1×10^{-4}, the scale of the U-NET network was reduced, and the effect of the data set was enhanced. The performance of U-NET model is validated by the validation data set. After each iteration of 30 times and 300 rounds of epochs training, the accuracy of the validation set reached a value of 96%, which shows a strong generalization ability of this U-NET model. The loss function reached a value of about 0.01. The curves of accuracy and loss value of the trained model are shown in Figures 5 and 6, respectively.

The particle identification effect is shown in Figure 7.

3.3. Segmentation of GCS. Generally, images obtained through the trained network still have some defects. The red marked area in Figure 8 shows the adhesion between particles, which affects further morphological analysis and calculation.

The binary image output by the neural network often contains some defects, and postprocessing technology is needed to improve the accuracy. Among all the defects, the two most obvious problems are as follows: (1) there are holes in the particles. (2) There are interconnected particles. To solve the problem of holes, a relatively mature pore filling algorithm can be used [18]. For the segmentation of connected particles, algorithms based on image morphology, such as the watershed method [19] and the corrosion-flooding method [20] are mostly adopted. Among them, the classic corrosion-flooding method used by Liu et al. [20] has a simple concept and has a good effect on the segmentation of objects with small contact sizes. The main steps are shown in Figure 9.

(1) The corrosion algorithm is used to separate the connected particles into several independent parts, and each part is labeled as the expanded seed of the flooding method.

(2) The seed is taken as the base point and expanded outward in the way of coloring. When the pixel meets the boundary of other seeds or particles, freeze the pixel and stop the expansion of this part.

(3) When the expansion of all seed pixels stops, the segmented particles are obtained.

The radius r_{ero} of the corrosion mask is a decisive parameter in the corrosion operation, and a fixed value is often used in the existing research. Liu et al. [20] suggested the value of r_{ero} as follows:

$$r_{ero} = 0.3\sqrt{S_0}. \tag{2}$$

4. Quantitatively Analysis of GCS Shapes

4.1. Methods for Quantifying the Particle Shape Indexes

4.1.1. Quantification of Elongation. To reflect the particle contour, elongation (*EI*) is often used:

$$EI = \frac{D_{\text{minor}}}{D_{\text{major}}}, \tag{3}$$

where D_{minor} is the width along the minor principal axis and D_{major} is the length along the major principal axis. Apparently, a smaller *EI* value represents the greater slenderness of the particle. Through a second-order tensor matrix based on the normal vector of particle contour, the two principal axes can be determined by

$$\left.\begin{aligned} \Omega_{ij} &= \frac{1}{L_p}\sum_{k=1}^{n} l^k T_i^k T_j^k, \\ C &= \begin{bmatrix} \Omega_{11} & \Omega_{12} \\ \Omega_{21} & \Omega_{22} \end{bmatrix} = \begin{bmatrix} \cos\theta & -\sin\theta \\ \sin\theta & \cos\theta \end{bmatrix} \begin{bmatrix} \lambda_a & 0 \\ 0 & \lambda_b \end{bmatrix} \begin{bmatrix} \cos\theta & \sin\theta \\ -\sin\theta & \cos\theta \end{bmatrix}, \end{aligned}\right\} \tag{4}$$

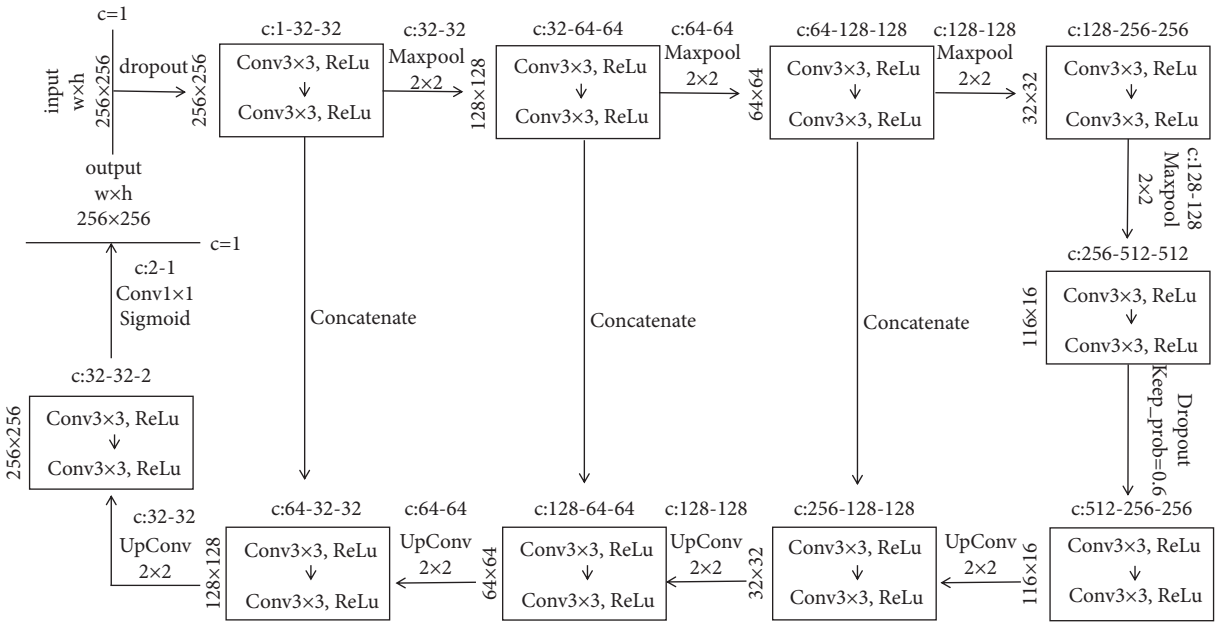

Figure 3: Improved overall U-NET architecture.

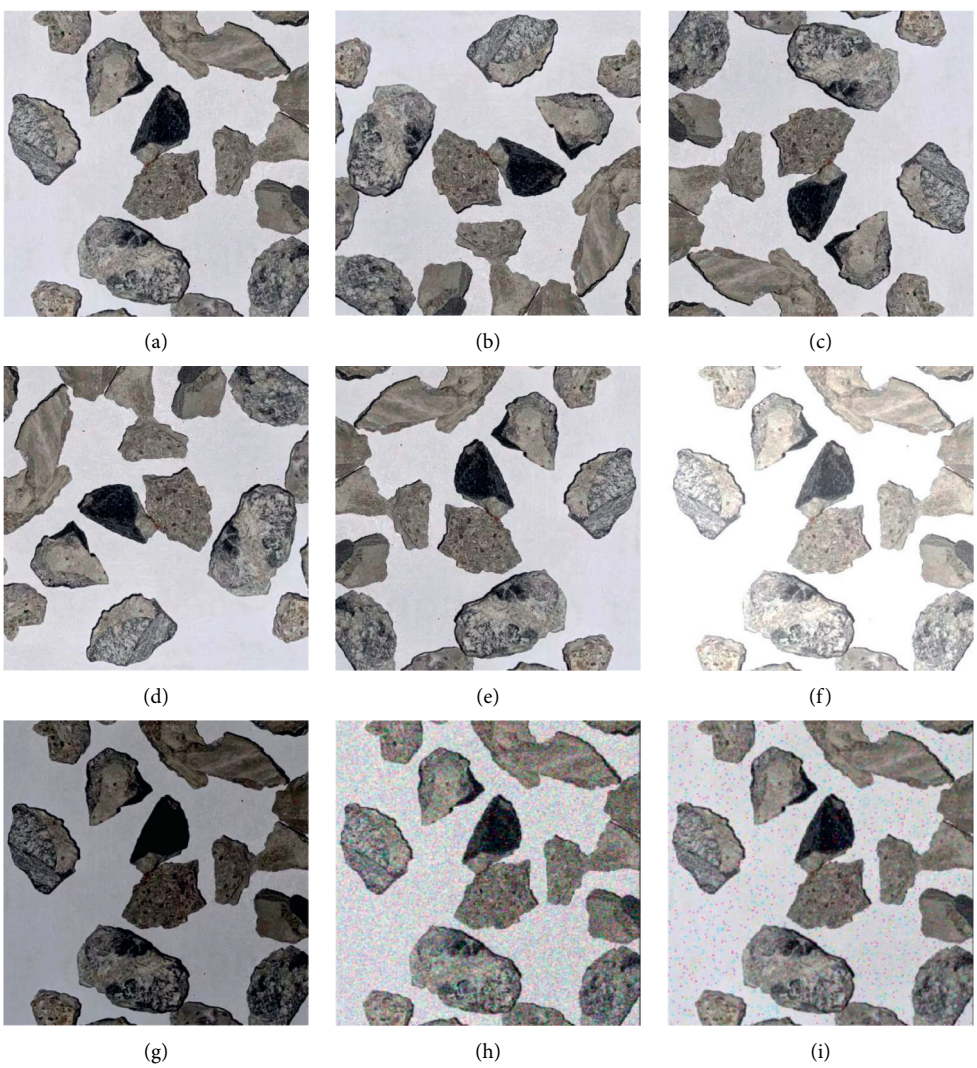

Figure 4: Data enhancement techniques: (a) initial image; (b–d) rotated image; (e) flipped image; (f-g) brightness transformed image; (h-i) image with salt and pepper noise.

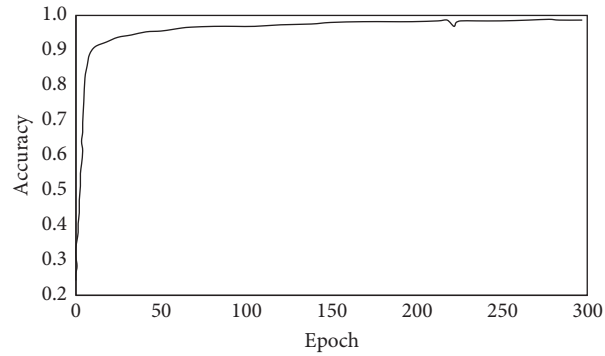

Figure 5: Accuracy of the validation set.

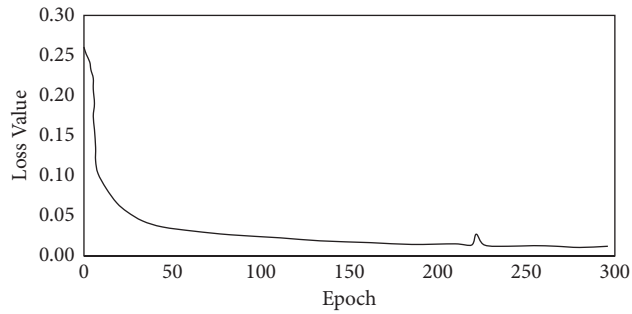

Figure 6: Loss value of loss function.

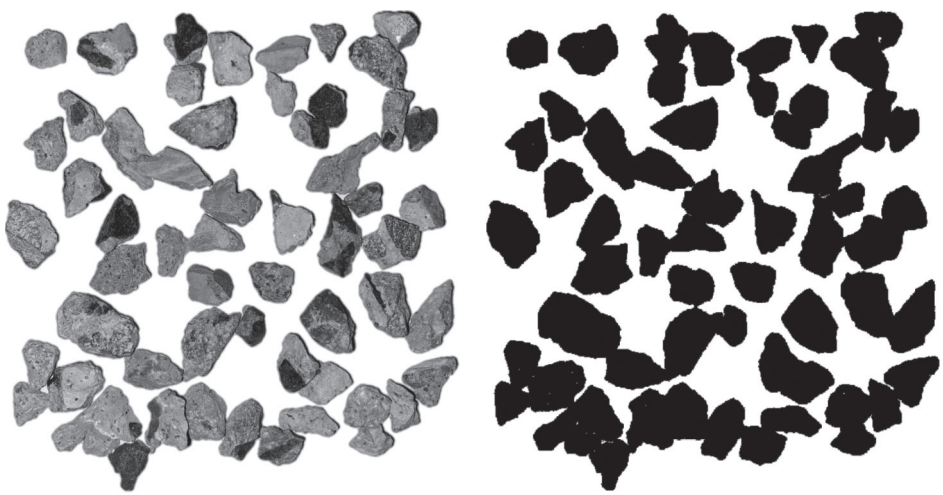

Figure 7: (a) Grayscale. (b) Recognition effect.

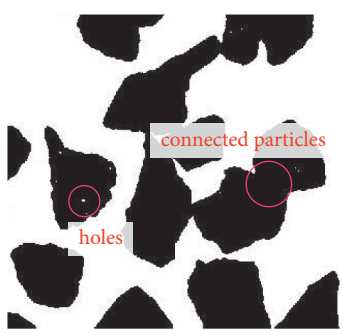

Figure 8: Problems existing in neural network output images.

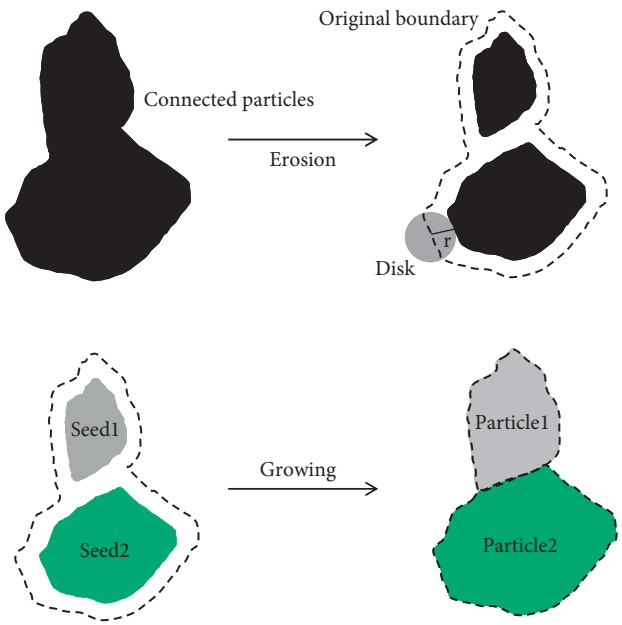

Figure 9: Main steps of the corrosion-flooding process [14].

where T_i^k is the component of the unit normal vector T^k and the k_{th} micro arc in i direction and T_j^k is the counterpart in j direction; L^k is the length of the kth micro arc; L_P is the circumference of the particle contour, which is the sum of lengths of n micro arcs; and λ_a and λ_b are eigenvalues of matrix C, $\lambda_a \geq \lambda_b$. The value of λ_b is the minimum percentage of the arc length in particle contour circumference along the major principal axis direction of Ω_{ij}. The value of λ_a is the maximum percentage along the minor principal axis direction of Ω_{ij}. After having two principle axis directions, D_{minor} and D_{major} can be calculated in a rectangular boundary containing the particle contour (Figure 10).

4.1.2. Quantification of Roundness. Roundness (Rd) reflects the sharpness and smoothness of the particle corners. Rd can be calculated by the ratio between the mean curvature of particle corner and the radius of the maximum inscribed circle of particle contour, as shown below:

$$R_d = \frac{1}{N}\sum_{i=1}^{N}\frac{r_i}{R_{insc}}, \tag{5}$$

where N is the number of corners; r_i is the curvature radius of the ith corner, and R_{insc} is the radius of the maximum inscribed circle of the particle contour.

Wadell [21] presented that a point belongs to the corner region when the curvature radius of the point is less than R_{insc}. Thus, the curvature radius of all contour points should be calculated to classify the corner region. For Fourier-presented contour curve, the curvature radius of the contour point can be calculated as

$$r(\theta) = \frac{\left(r(\theta)^2 + (\mathrm{d}r(\theta)/\mathrm{d}\theta)^2\right)^{3/2}}{r(\theta)^2 + 2(\mathrm{d}r(\theta)/\mathrm{d}\theta)^2 - r(\theta)\left(\mathrm{d}^2 r(\theta)/\mathrm{d}\theta^2\right)}, \tag{6}$$

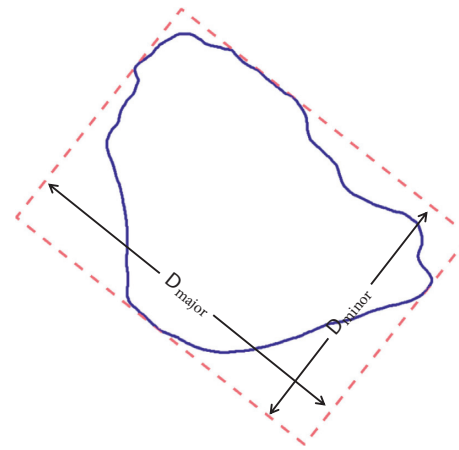

Figure 10: Rectangular box surrounding the particle contour.

where $r(\theta)$ is the curvature radius.

The contour point $P(\theta, r(\theta))$ can be seen as a corner point when $r(\theta) < R_{\text{insc}}$. Thus, the corner region is the contour of all corner points (Figure 11(a)). The ODEC algorithm [22] can be used to calculate the radius of the inscribed circle of corner points, as shown in Figure 11(b). To be specific, the inner normal vector $\overrightarrow{N_i}$ of the ith corner point is first calculated. Then, the inscribed circle along the direction of $\overrightarrow{N_i}$ is determined, by starting from the ith corner point with a radius of Δr. After that, whether the inscribed circle is tangent to any other contour point is determined. If not, the radius Δr is increased and the last two steps are repeated; otherwise, terminate the process and take Δr as the radius of the inscribed circle of the ith corner point.

The optimal inscribed circle of the corner can be determined by having the inscribed circles of all corner points. To value the fit performance of the inscribed circle of a corner point relative to other corner points, e_{fit} is defined:

$$e_{\text{fit}} = \sum_{i=1}^{n_{cp}} \frac{\left|\sqrt{(x_i - x_c)^2 + (y_i - y_c)^2} - r_c\right|}{n_{cp}}, \tag{7}$$

where n_{cp} is the number of corner points; (x_i, y_i) are the coordinates of the ith corner point; (x_c, y_c) are the center coordinates of the inscribed circle; and r_c is the radius of inscribed circle radius. Particularly, the minimum value of e_{fit} represents the optimal inscribed circle of the corner. Through the optimal inscribed circles of all corners shown in Figure 11(c), the curvature radius of each corner and Rd can be calculated.

4.1.3. Quantification of Roughness. Roughness is a shape index that evaluates the concavity of the particle contour and it can show the shape difference between the real contour and the smoothed contour of particles. Fourier transform can be used to calculate the smoothed contour of a particle. The larger Fourier series (N) corresponds to a higher similarity between the real contour and the smoothed contour [23]. In this study, the Fourier series N is set to 16 to calculate the smoothed contour. The deviation between the smoothed contour and the real contour is shown in Figure 12.

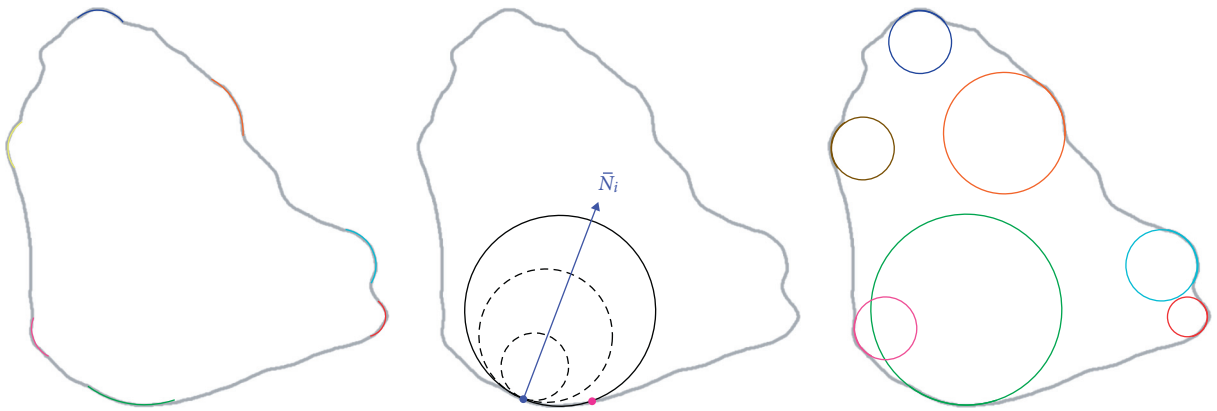

Figure 11: (a) Corner region of the particle contour, (b) determining the inscribed circle of a corner point, and (c) optimal inscribed circles of all corners.

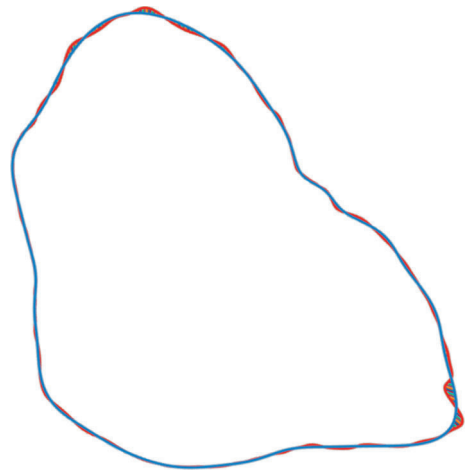

Figure 12: Smoothed contour and real contour of a particle.

Next, the deviation regions and the geometric types are extracted and determined. For nonintersecting parts between smoothed contour and real contour, the deviation region can be calculated as a quadrilateral area. For intersecting parts, the deviation region is simplified to two triangles. At the ith microunit, the deviation distance ($\triangle d_i$) is the ratio of the deviation area to the corresponding length. Based on the average deviation distance of all microunits, Rg can be expressed as

$$\left.\begin{aligned} \triangle d_i &= \frac{A_i}{l_i}, \\ Rg &= \frac{\triangle \overline{d}}{\overline{r}} = \sqrt{\frac{\pi}{A_p}} \cdot \frac{1}{L_p} \sum_{i=1}^{N_d} \triangle d_i \times l_i, \end{aligned}\right\} \tag{8}$$

where $\triangle \overline{d}$ is the average deviation distance, N_d is the number of all microunits, A_p is the area of the particle contour, A_i is the deviation area, l_i is the corresponding arc length, and L_p is the perimeter of the particle contour.

4.2. Statistics of Shape Indexes. Through the quantification algorithms introduced above, the elongation (*EI*), roundness (*Ed*), and roughness (*Rg*) of 1200 GCS were calculated. The fitting results are shown in Table 1.

Normal distribution tests were implemented on the probability density of the three shape indexes. The results showed that all three indexes satisfied normal distribution appropriately. Within the results, the width of the distribution of elongation is the maximum and the width of the distribution of roundness is the minimum, with ranges from 0.4 to 1 and from 0.2 to 0.5, respectively. Furthermore, the mean values of the three shape indexes *EI*, *Rd*, and *Rg* are 0.68, 0.33, and 0.0039, respectively.

4.3. Establish Shape Library. To facilitate retrieval and sample preparation, the shape indicators of the GCS are stored together with the coordinates, with the storage format [number, outline, slender length, elongation, roundness, roughness].

The steps for sample preparation from the particle library are as follows:

Table 1: Fitting function and related parameters.

Shape index	Fitting function	Mean value	Goodness of fit R^2	Range
EI	Normal distribution	0.68	0.98	From 0.25 to 1
Rd	Normal distribution	0.33	0.98	From 0.2 to 0.6
Rg	Normal distribution	0.0039	0.97	From 0.002 to 0.006

(1) The required shape parameter range is input

(2) According to the range of these values, the two-dimensional contour that meets the requirements can be searched automatically

(3) The visualized two-dimensional contour is selected and is output to the "d*xf*" file

After establishing the particle library, it will be very convenient to select the two-dimensional contours of GCS that meet specific requirements, so as to facilitate the discrete element modeling of GCS. Moreover, it lays the foundation for further study on the relationship between the geometric information and mechanical properties of GCS.

5. Application to DEM Simulation of GCS Packing

5.1. Simulation of Gravity Deposition. The mechanical parameters of GCS like shear strength and deformation modulus can be affected by the packing characteristics. The shape index *EI* is set as the DEM [24] simulation variable to explore the influence of particle shape on packing properties, as shown in Figure 13(a). Considering the elongation variable, the GCS were selected and divided into 7 groups where *EI* is set from 0.4 to 1.0. In this study, the particles in DEM are not generated randomly; on the contrary, real GCS were used as samples to enhance the reliability of the simulations.

Stratified gravity deposition simulation of the natural packing process of particles is the common way to generate particle models. In the model, DEM particles fall naturally with gravity. After completing the previous layer deposition, a new layer of particles is generated and the deposition process is repeated until the whole simulation is completed, as shown in Figure 13(b) [25]. The gravity deposition process is simulated by PFC^{2D}, and the interparticle contact and the wall-particle contact are both linear contacts. The parameters of the model are shown in Table 2.

5.2. Analysis of Macro-Meso Parameter. Macro-meso parameters reflect the particle packing properties, such as void ratio, compactness, and coordination number. In this section, the effect on *EI* is considered.

5.2.1. Macro Parameter. The degree of density of particles can be described by a macro parameter, void ratio (e), which is affected by particle shape.

The change curves of the void ratio with respect to *EI* are shown in Figure 14. Void ratio e decreases with the growth of *EI*, indicating that the particle packing gets closer with *EI* increasing. Then, the void ratio reaches a bottom value of 0.187 and starts to soar at the point where *EI* is 0.9.

5.2.2. Micro Parameter. The degree of particle contact can be measured by a micro parameter, the mean coordination number (C_{mean}), which can reflect the internal structure of particle packing [26]:

$$C_{\text{mean}} = \frac{1}{N_p}\sum_{i=1}^{N_p} C_i, \tag{9}$$

where N_p is the number of particles and C_i is the contact particle number of the ith particle.

In the change curve of the mean coordination number with respect to *EI* shown in Figure 15, a reflection point also appears at the point where *EI* is 0.9. Similar to the curve of void ratio, C_{mean} exhibits a decreasing trend with *EI* increasing. After reaching the bottom of the curve, C_{mean} stays stable and has a slight increase.

5.2.3. Fabric Anisotropy. The fabric anisotropy is the anisotropy between the spatial distribution of particle contacts and the length of branch vectors. The branch vector is the vector connecting the mass centers of two particles. Fabric anisotropy coefficients can be used to quantify the fabric anisotropy properties, including coefficient of contact (a_c), coefficient of normal contact forces (a_n), coefficient of tangential contact forces (a_t), and coefficient of branch vectors (a_d). The anisotropy coefficients can be calculated as

$$a_* = \sqrt{\frac{3}{2}a_{ij}^* a_{ij}^*}, \tag{10}$$

where $a*$ is the anisotropy coefficients (a_c, a_n, a_t, and a_d) and a_{ij}^* is the tensors (a_{ij}^c, a_{ij}^n, a_{ij}^t, and a_{ij}^d) indicating the directional distribution of a_c, a_n, a_t, and a_d. The tensors can be calculated as

$$\left.\begin{aligned} a_{ij}^c &= \frac{15}{2}\Phi_{ij}^{c'}, \quad a_{ij}^n = \frac{15F_{ij}^{n'}}{2\overline{f_n}}, \\ a_{ij}^t &= \frac{15F_{ij}^{t'}}{3\overline{f_n}}, \quad a_{ij}^d = \frac{15D_{ij}^{n'}}{3\overline{d_0}}, \end{aligned}\right\} \tag{11}$$

where $\overline{f_n}$ is the average normal contact force, $\overline{d_0}$ is the average length of the branch vector, $\Phi_{ij}^{c'}$ is the partial tensor of Φ_{ij}^c, $F_{ij}^{n'}$ is the partial tensor of F_{ij}^n, $F_{ij}^{t'}$ is the partial tensor of F_{ij}^t, and $D_{ij}^{n'}$ is the partial tensor of D_{ij}^n. Φ_{ij}^c, F_{ij}^n, F_{ij}^t, and D_{ij}^n can be calculated as

$$\left.\begin{aligned} \Phi_{ij}^c &= \frac{1}{N_c}\sum_{c\in N_c} n_i^c n_j^c, & F_{ij}^n &= \frac{1}{N_c}\sum_{c\in N_c}\frac{f_c^n n_i^c n_j^c}{1+a_{kl}^c n_k^c n_l^c}, \\ F_{ij}^t &= \frac{1}{N_c}\sum_{c\in N_c}\frac{f_c^t n_i^c n_j^c}{1+a_{kl}^c n_k^c n_l^c}, & D_{ij}^n &= \frac{1}{N_c}\sum_{c\in N_c}\frac{d_c^n n_i^c n_j^c}{1+a_{kl}^c n_k^c n_l^c}, \end{aligned}\right\} \tag{12}$$

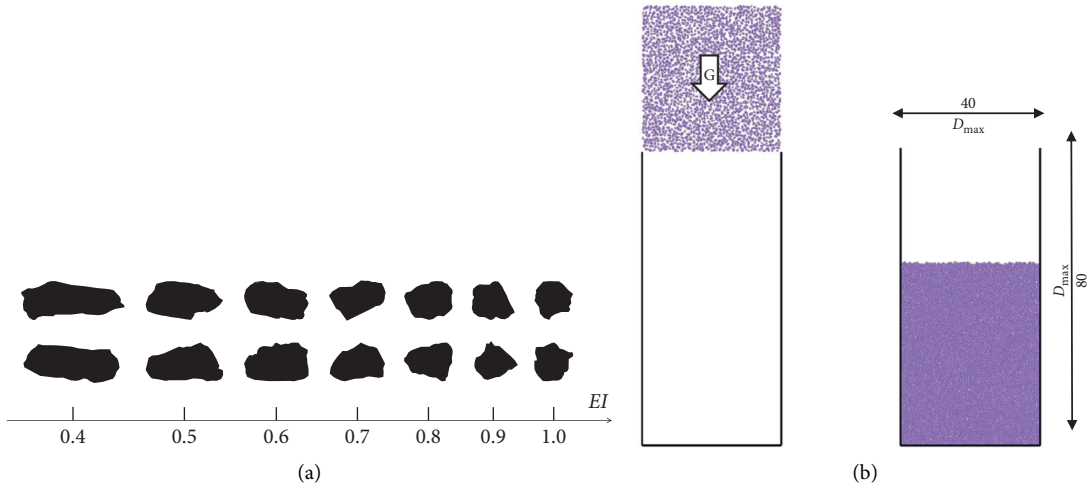

Figure 13: (a) GCS particles with different elongation; (b) stratified gravity deposition model.

Table 2: Particle number and model parameters.

Parameter	Value
Particle number	1000×3
Particle density (kg/m^3)	2650
Interparticle frictional coefficient	0.5
Wall-particle frictional coefficient	0
Effective modulus (Pa)	1×10^8
Stiffness ratio	4/3
Damping factor	0.7

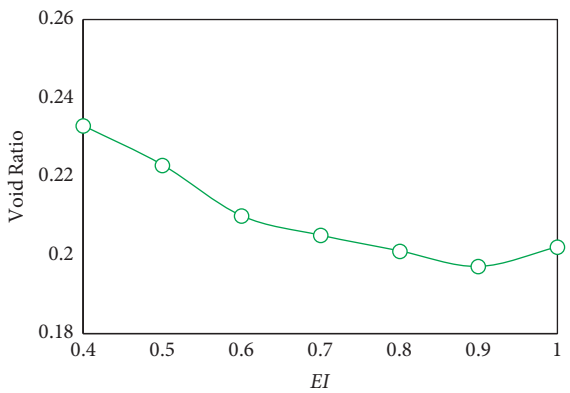

Figure 14: Change curves of the void ratio with respect to elongation.

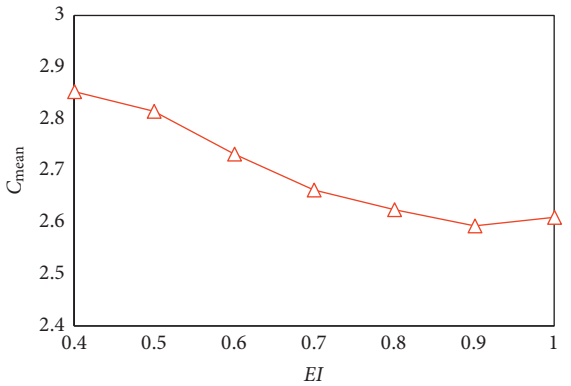

Figure 15: Change curve of the mean coordination number with respect to elongation.

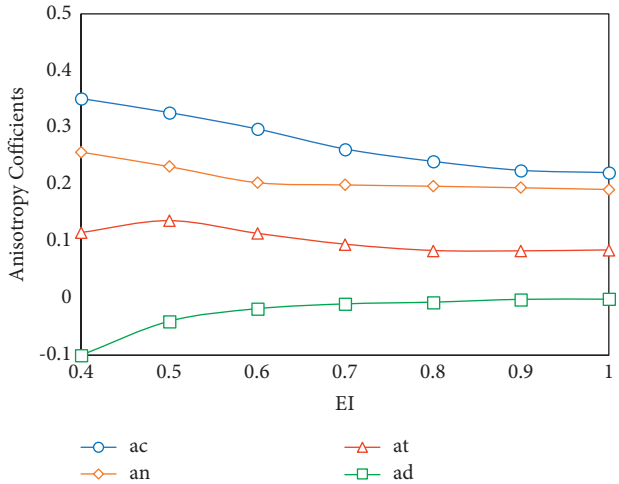

Figure 16: Change curves of the fabric anisotropy coefficients with respect to *EI*.

where n_i^c and n_j^c are the ith and jth components of the unit normal vector of contact c, respectively, and f_c^n, f_c^t, and d_c^n are the normal contact force, tangential contact force and normal branch vector of contact c, respectively.

Figure 16 shows the change curves of the fabric anisotropy coefficients with respect to *EI*. Among all coefficients, a_c, a_n, and a_t slightly decrease with the increase of *EI*, that is, the anisotropy degree of the normal contact force and tangential contact force decreases with *EI* collapsing. On the contrary, a_d shows a positive correlation with *EI*, indicating that the anisotropy degree of branch vector declines with *EI* increasing. Furthermore, a_d slightly stabilizes to 0 with *EI* increasing from 0.4 to 1.0, showing that the anisotropy of branch vector almost disappears. Thus, the degree of fabric anisotropy decreases with *EI* decreasing. Note that when

$EI \geq 0.8$, the fabric anisotropy coefficients stay relatively stable; thus, the degree of fabric anisotropy is not affected by EI.

6. Application to DEM Simulation of GCS Shear Behavior

6.1. Simulation of Biaxial Compression Test. First, five samples with different elongation ($EI = 0.4$, 0.5, 0.6, 0.7, 0.9) were constructed. Each sample has an initial size of 9 m $*$ 18 m and contains approximately 5000 GCS particles. The linear elastic model is used as the contact law between particles. The samples are compressed by shifting the four rigid boundaries, and the boundary has a force at 100 kPa (stress boundary condition controlled by numerical servo). During the shearing process, in order to make the state of samples quasistatic (to make the loading process of the sample quasistatic loading), the rate of shear strain is supposed to be relatively small. Thus, the inertial parameters are introduced as follows:

$$I_{\text{intertia}} = \dot{\varepsilon}_1 \frac{d}{\sqrt{\sigma_0/\rho}} < 10^{-3}, \tag{13}$$

where $\dot{\varepsilon}_1$ is the loading strain rate, d is mean particle size, ρ is material density, σ_0 is the consolidation stress. Previous studies have shown that the value of the Inertia parameter should be less than 2.5×10^{-3}. Thus, the shifting speed of the rigid wall is fixed to 0.05 m/s. The inertia parameter is less than 10^{-4} throughout the tests' negative correlation.

6.2. Analysis of Macro-Meso Parameter

6.2.1. Analysis of Stress Ratio. The mean stress p and deviator stress q are calculated to explore the sample shear strength. In the two-dimensional biaxial shear test, the valid average stress p' and deviator stress q are shown as follows:

$$p' = \frac{(\sigma_1 + \sigma_2)}{2}, \tag{14}$$

$$q = \sigma_1 - \sigma_2. \tag{15}$$

For different EI values of samples, Figure 17 shows the variation of the stress ratio q/p' with the axial strain ε_1. In the initial stage, as the axial strain increases, the stress ratio of all samples rises significantly. After increasing to a peak value, the stress ratio slightly descends and tends to stabilize.

6.2.2. Analysis of Volumetric Deformation. In this section, the evolution of volumetric deformation is analyzed. Regarding the boundaries of the simulation being rigid walls, the axial strain and volume strain can be calculated as

$$\varepsilon_1 = \frac{(h_0 - h)}{h_0}, \qquad \varepsilon_v = \frac{(v_0 - v)}{v_0}, \tag{16}$$

where h_0 and h are the original height and the current height of the sample, respectively; v_0 and v are the original volume and the current volume of the sample, respectively; negative volume strain indicates volume expansion. In order to study the critical state characteristics of the stabilized sample, all samples were sheared to the axial strain $\varepsilon_1 = 30\%$. Under this deformation, the typical conditions of the critical state are basically satisfied (i.e., the stress and volume remain constant with strain).

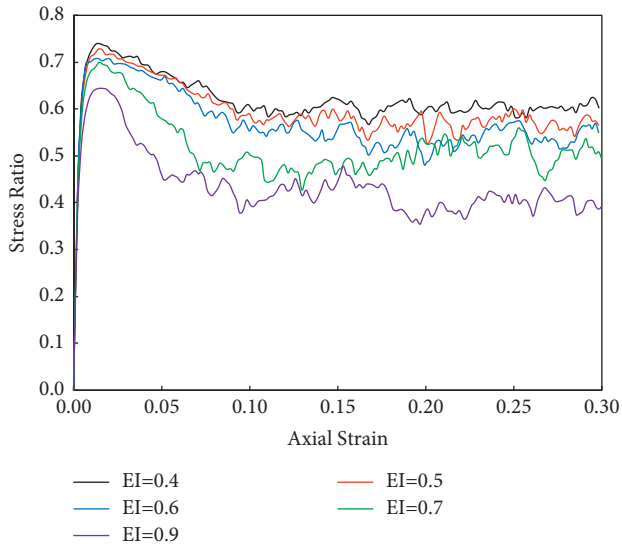

Figure 17: The evolution of stress ratio versus axial strain.

As shown in Figure 18, in the initial stage, the volume strain descends with the ascent of the axial strain. After the axial strain reaches about 1%, the volume strain reverses. As the axial strain increases to a range of 20% to 30% which is a critical state, the volume deformation of the sample remains constant, which indicates that all samples show shear-induced dilatancy deformation with strain softening. Moreover, as the sample gets a steady state, the volume strain shows a negative correlation with the EI value. Therefore, a sample with a smaller EI value has stronger dilatancy.

6.2.3. Analysis of Mean Coordination Number. In this section, we focus on the mean coordination number (MCN), which can reflect the microscopic packing structure of the simulated GCS. The evolution of MCN versus axial strain is illustrated in Figure 19 for samples with various values. In the beginning stage of shear, the MCN of samples decreases significantly with axial strain. Then, MCN declines with a lower speed when the axial strain is greater than 2%. When the axial strain is greater than 10%, the MCN is roughly steady. Then, as the EI value rises from 0.4 to 0.9, the MCN collapses from 5.0 to 4.0; thus, a negative correlation with the EI value can be found.

6.2.4. Analysis of Sliding Contact Percentage. The Mohr–Coulomb law conducts the percentage of sliding contact. The sliding coefficient is shown as follows:

$$S_C = \frac{\left|f_t^c\right|}{(\mu f_n^c)}, \tag{17}$$

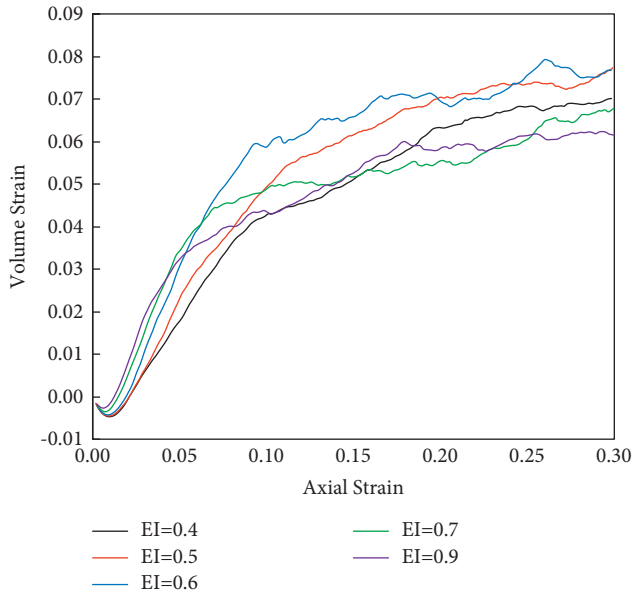

Figure 18: The evolution of volume strain versus axial strain.

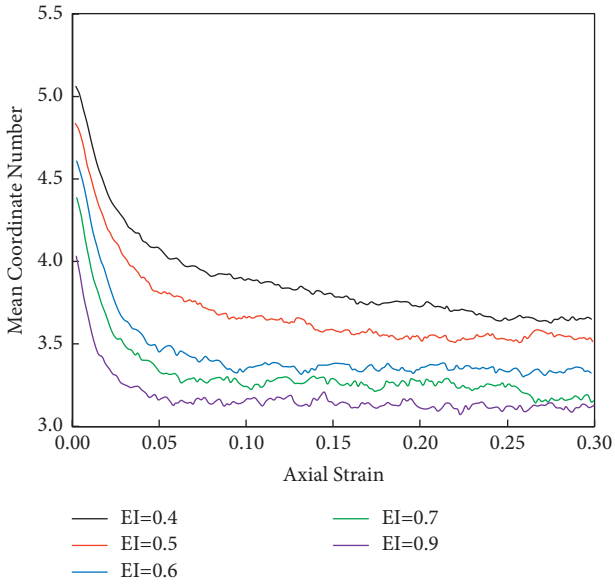

Figure 19: The evolution of mean coordination number versus axial strain.

where f_t^c is the tangential contact force of contact c, f_n^c is the normal contact force of contact c, and μ is the friction factor. When $S_C > 0.9999$, it is considered that a contact slip has occurred. The percentage of sliding contact in the particle system is as follows:

$$S_P = \frac{N_{SC}}{N_C} \times 100\%, \tag{18}$$

where N_{SC} indicates the number of sliding contacts in the particle system and N_C is the total number of contacts. Figure 20 shows the variation of S_P of each sample with axial strain. The variation of S_P with an axial strain of all samples is basically the same. As ε_1 increases, S_P rapidly increases to a peak value and then gradually decreases to a stable value. Figure 20 also indicates that the contact slip rate descends with *EI* climbing. As the *EI* value rises from 0.4 to 0.9, the maximum value and the stability value of S_P descends from 0.36 to about 0.16, and from 11% to approximately 5%, respectively.

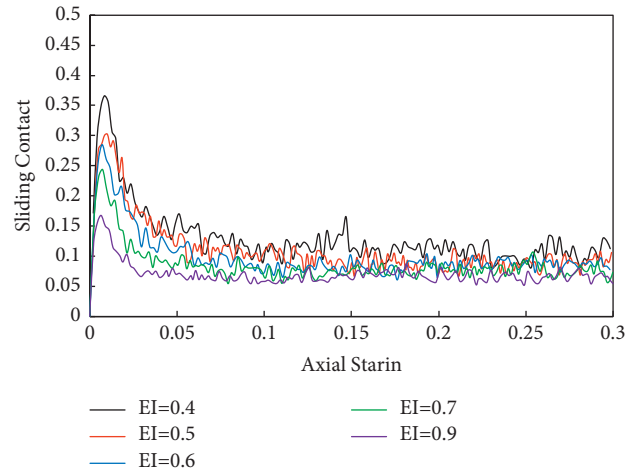

Figure 20: The evolution of the percentage of sliding contact versus axial strain.

7. Conclusion

Graded crushed stone (GCS) is of great significance in road construction as an essential material used in the base or transition layer. The packing properties like compactness and void ratio can be affected by the irregularity and variability of particle shape. In this study, the particle outlines are firstly extracted based on deep learning algorithms. Then, the shape evaluation indexes are quantified. In addition, the gravity deposition with distinct *EI* value is simulated by the discrete element method. Finally, the shear behavior of GCS is studied. The specific results are as follows:

(1) The realistic particle contour is first automatically extracted based on digital image processing and deep learning algorithms. The lightweight U-NET model is trained and the results show the accuracy of the training set reached a value of 97% and the loss value is about 0.01.

(2) The elongation (*EI*), roundness (*Rd*), and roughness (*Rg*) of GCS are quantified by shape evaluation algorithms.

(3) Based on the establishment of the GCS shape library, the gravity deposition with various elongation is simulated using the discrete element method to study the packing properties of GCS. The elongation effects on the macroscopic and microscopic quantities are explored. The results illustrate that the void ratio decreases with increasing elongation before a reflection point where *EI* value is 0.9. Similar to the void ratio, the mean coordinate number C_{mean} exhibits a decreasing trend with *EI* increasing. After

reaching the bottom of the curve, C_{mean} stays stable and has a slight increase.

(4) The shear behavior of GCS is studied by simulation of the biaxial compression test. The stress ratio of all samples increases rapidly, and then reaches the peak stage, after which the stress ratio gradually decreases and tends to stabilize. The volume strain decreases with the increase of the axial strain, and when the axial strain reaches about 1%, the volume strain reverses. Then, in the range of 20% to 30%, the volume strain stays constant, indicating a shear-induced dilatancy deformation accompanied by strain softening. The mean coordinate number of all samples increases with axial strain at the beginning; then, after the value of axial strain reaching 2%, the MCN reaches its peak and decreases to be stable when the axial strain is greater than 10%. The variation of the percentage of sliding contact S_P with the axial strain of all samples is basically the same. As ε_1 increases, S_P rapidly increases to a peak value and then gradually decreases to a stable value.

Data Availability

The data used in the paper are including in the article.

Conflicts of Interest

The authors declare that they have no conflicts of interest.

Acknowledgments

This research was funded by the Ministry of Transport of China (Grant no. 2020-MS5-145) and the State Archives Bureau of China (Grant no. 2021-X-45).

References

[1] W. Long, X. Xiaoguang, and L. Hai, "Influence of laboratory compaction methods on shear performance of graded crushed stone," *Journal of Materials in Civil Engineering*, vol. 23, no. 10, pp. 1483–1487, 2011.

[2] J. Li, J. Zheng, Y. Yao et al., "Numerical method of flexible pavement considering moisture and stress sensitivity of subgrade soils," *Advances in Civil Engineering*, vol. 2019, Article ID 7091210, 10 pages, 2019.

[3] J. Yi, C. Liang, J. Qian et al., "Laboratory evaluation and design of construction and demolition wastes for granular base," *Advances in Civil Engineering*, vol. 2020, pp. 1–10, 2020.

[4] J. Li, J. Zhang, G. Qian, J. Zheng, and Y. Zhang, "Three-dimensional simulation of aggregate and asphalt mixture using parameterized shape and size gradation," *Journal of Materials in Civil Engineering*, vol. 31, no. 3, Article ID 04019004, 2019.

[5] W. Hui, J. Li, F. Wang, J. Zheng, Y. Tao, and Y. Zhang, "Numerical investigation on fracture evolution of asphalt mixture compared with acoustic emission," *International Journal of Pavement Engineering*, pp. 1–11, 2021.

[6] G. Qian, K. Hu, J. Li, X. Bai, and N. Li, "Compaction process tracking for asphalt mixture using discrete element method," *Construction and Building Materials*, vol. 235, Article ID 117478, 2020.

[7] Y. Wang, S. Shao, and Z. Wang, "Effect of particle breakage and shape on the mechanical behaviors of granular materials," *Advances in Civil Engineering*, vol. 2019, no. S2, pp. 1–15, 2019.

[8] L. M. Le Pen, W. Powrie, A. Zervos, S. Ahmed, and S. Aingaran, "Dependence of shape on particle size for a crushed rock railway ballast," *Granular Matter*, vol. 15, no. 6, pp. 849–861, 2013.

[9] J. Zhang, J. Li, Y. Yao, J. Zheng, and F. Gu, "Geometric anisotropy modeling and shear behavior evaluation of graded crushed rocks," *Construction and Building Materials*, vol. 183, pp. 346–355, 2018.

[10] Y. Jiang, L. N. Y. Wong, and J. Ren, "A numerical test method of California bearing ratio on graded crushed rocks using particle flow modeling," *Journal of Traffic and Transportation Engineering*, vol. 2, no. 2, pp. 107–115, 2015.

[11] L. Ren, Z. Xiao, and X. Hu, "Micromechanical analysis for direct shear tests of grade crushed stones," *Highways*, vol. 5, pp. 152–156, 2008.

[12] G. Xu, Z. Chen, X. Li, G. Lu, D. Dong, and Z. Liu, "Establishment of control standard for plastic deformation performance of graded crushed stone," *Construction and Building Materials*, vol. 211, pp. 383–394, 2019.

[13] Y. Jiang, S. Li, and T. Wang, "Numerical method of dynamic triaxial test on graded crushed rock," *Journal of Southeast University (Natural Science Edition)*, vol. 43, no. 3, pp. 604–609, 2013.

[14] Z. Liang, Z. Nie, A. An, J. Gong, and X. Wang, "A particle shape extraction and evaluation method using a deep convolutional neural network and digital image processing," *Powder Technology*, vol. 353, pp. 156–170, 2019.

[15] O. Ronneberger, P. Fischer, and T. Brox, "U-net: convolutional networks for biomedical image segmentation," in *Proceedings of International Conference on Medical Image Computing and Computer-Assisted Intervention*, pp. 234–241, Springer, Munich, Germany, 2015.

[16] J. Yang, Y. U. Runyang, and F. Lianghui, *Early Smoke Segmentation Method Based on U-Net Convolutional Network*, Fire Safety ence, 2019.

[17] N. Srivastava, G. Hinton, A. Krizhevsky et al., "Dropout: a simple way to prevent neural networks from overfitting," *Journal of Machine Learning Research*, vol. 15, no. 1, pp. 1929–1958, 2014.

[18] P. Soille, *Morphological Image Analysis: Principles and Applications*, Springer Science & Business Media, Berlin, Germany, 2013.

[19] J. Zheng and R. D. Hryciw, "Segmentation of contacting soil particles in images by modified watershed analysis," *Computers and Geotechnics*, vol. 73, pp. 142–152, 2016.

[20] C. Liu, B. Shi, J. Zhou, and C. Tang, "Quantification and characterization of microporosity by image processing, geometric measurement and statistical methods: application on SEM images of clay materials," *Applied Clay Science*, vol. 54, no. 1, pp. 97–106, 2011.

[21] H. Wadell, "Sphericity and roundness of rock particles," *The Journal of Geology*, vol. 41, no. 3, pp. 310–331, 1933.

[22] X. Garcia, J.-P. Latham, J. Xiang, and J. P. Harrison, "A clustered overlapping sphere algorithm to represent real particles in discrete element modelling," *Géotechnique*, vol. 59, no. 9, pp. 779–784, 2009.

[23] Z.-H. Nie, X. Wang, D.-L. Huang, and L.-H. Zhao, "Fourier-shape-based reconstruction of rock joint profile with realistic unevenness and waviness features," *Journal of Central South University*, vol. 26, no. 11, pp. 3103–3113, 2019.

[24] H. Zhao and J. Chen, "A numerical study of railway ballast subjected to direct shearing using the discrete element method," *Advances in Materials Science and Engineering*, vol. 2020, pp. 1–13, 2020.

[25] Y. Zhu, Z. Nie, and J. Gong, "Influence of the rolling-resistance-based shape of coarse particles on the shear responses of granular mixtures," *Particuology*, vol. 52, pp. 67–82, 2020.

[26] X. Jia and R. A. Williams, "A packing algorithm for particles of arbitrary shapes," *Powder Technology*, vol. 120, no. 3, pp. 175–186, 2001.

Hindawi
Advances in Materials Science and Engineering
Volume 2021, Article ID 6035564, 11 pages
https://doi.org/10.1155/2021/6035564

Research Article

Earth Pressure of Three-Dimensional Stress States under Different Strength Criteria and Its Application

Yu Zhang,[1,2] **Jin Liu**,[1] **Te-Jia Fan**,[1] **Chen-Yang Xu**,[1] **Tian-Yi Meng**,[1] **Yang Zhao**,[1] **and An Su**[3]

[1]*Civil and Architecture Engineering, Xi'an Technological University, Xi'an, Shaanxi 710021, China*
[2]*Shaanxi Key Laboratory of Loess Mechanics and Engineering, Xi'an University of Technology, Xi'an, Shaanxi 710048, China*
[3]*Northwest Electric Power Design Institute Co. Ltd. of China Power Engineering Consulting Group, Xi'an, Shaanxi 710075, China*

Correspondence should be addressed to Yu Zhang; zhangyu0331@xatu.edu.cn

Received 17 May 2021; Revised 13 August 2021; Accepted 2 September 2021; Published 15 September 2021

Academic Editor: Yongsheng Yao

To solve the Earth pressure problems in practical engineering, such as retaining walls and foundation pits, we derive active and passive Earth pressure formulas in accordance with the relationship between intermediate principal stress and excavation under three-dimensional stress states. The formulas are derived on the basis of the Mohr–Coulomb, spatially mobilized plane (SMP), $\sqrt[3]{\sigma}$ SMP, Lade–Duncan, axisymmetric compression- (AC-) SMP strength, and generalized Mises (Gen-Mises) criteria and then extended to clay. We also compare the calculated Earth pressure with the measured data. Results indicate that the Earth pressure considering medium principal stress contribution under a three-dimensional stress state is consistent with the actual engineering. The calculated active Earth pressure in the Mohr–Coulomb strength criterion is larger, and the passive Earth pressure is smaller than the practical one because the intermediate principal stress effect is not considered. The calculated results of the SMP, $\sqrt[3]{\sigma}$ SMP, Lade–Duncan, AC-SMP strength, and Gen-Mises criteria are close to the measured data, among which the result of the Gen-Mises criterion is closer. The Earth pressure calculated using the Lade–Duncan criterion is no longer appropriate to describe the Earth pressure under medium principal stress condition in this study. The results of this study have theoretical significance for retaining structure design under a three-dimensional stress state.

1. Introduction

In practical engineering, the Earth pressure problems of retaining walls and vertical excavation of foundation pits are usually in a three-dimensional stress state. The classical Rankine Earth pressure theory is based on the Mohr–Coulomb strength criterion, only considering the influence of large and small principal stresses on strength and ignoring the contribution of intermediate principal stress. This limitation leads to underrating Earth pressure, which has been confirmed by many experimental results [1]. To obtain the real Earth pressure, numerous studies, such as on the passive Earth pressure under seismic load, have been conducted [2–5]. However, most research focuses on the Earth pressure under static load, which can be divided into two categories. The first one regards the retaining structure as a plane strain problem, the intermediate principal stress condition is obtained on the basis of a specific strength criterion in accordance with the deformation conditions and elastic-plastic theory [6–9], and the general stress state strength theory is introduced into the Earth pressure calculation. Otherwise, the formula of the intermediate principal stress, obtained in accordance with the generalized Hooke's law and the strain conditions in the plane strain direction [10], is substituted into the strength criterion to determine the Earth pressure. The second one obtains the Earth pressure under a specific strength criterion in accordance with the empirical or assumed intermediate principal stress conditions under three-dimensional stress states [11–15]. Overall, the study of the Earth pressure is still based on certain strength criterion and the corresponding intermediate principal stress condition. A systematic study of Earth pressure theory under different strength criteria and its comparative analysis should be conducted.

Therefore, a calculation method for Earth pressure in a three-dimensional stress state, considering the contribution of intermediate principal stress and revealing the differences of the results based on various strength criteria, should be established, and its applicability should be studied. In this paper, we propose the design formulas of active and passive Earth pressures for cohesionless and cohesive soils under three-dimensional stress states. The calculated results are compared with the measured data of sand and clay soil to verify the precision and applicability of the formulas.

2. Several Common Strength Criteria for Soils

The soil strength criterion reflects the relationship among the shear stress, normal stress, and characteristic parameters of soil on a specific shear plane when destroyed. The state of principal stress can be expressed as $F(\sigma_{ij}, k_f) = 0$. The strength criteria for soils are Mohr–Coulomb, spatially mobilized plane (SMP), Lade–Duncan, generalized Mises (Gen-Mises), axisymmetric compression- (AC-) SMP [16], and $\sqrt[3]{\sigma}$ SMP [17], which can be expressed as follows.

2.1. Mohr–Coulomb Strength Criterion

$$\sigma_1 = K_p \sigma_3, \tag{1}$$

where $K_p = \tan^2(45^\circ + \varphi/2)$.

The Mohr–Coulomb criterion does not consider the effect of intermediate principal stress; thus, the mobilized plane is $45^\circ + \varphi/2$, as shown in Figure 1.

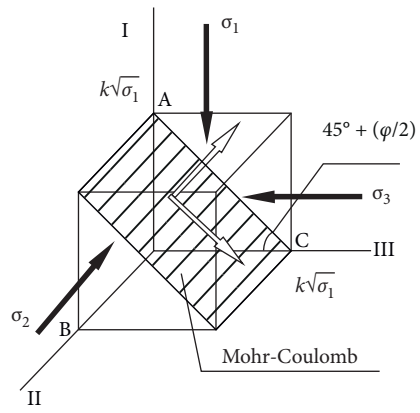

Figure 1: Mohr–Coulomb criterion.

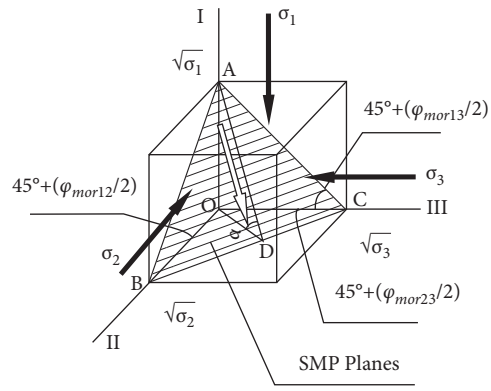

Figure 2: SMP.

2.2. SMP Strength Criterion.

On the basis of the Mohr–Coulomb criterion, the $45^\circ + \varphi_{ij}/2$ plane is regarded as the three edges of a three-dimensional space plane, and SMP can be obtained, as shown in Figure 2. The SMP criterion describes the condition that the shear and normal stresses obey on SMP when soil is destroyed, as indicated in the following equation:

$$\begin{aligned} &\frac{(\sigma_1 + \sigma_2 + \sigma_3)(\sigma_1\sigma_2 + \sigma_2\sigma_3 + \sigma_3\sigma_1)}{\sigma_1\sigma_2\sigma_3} \\ &= \frac{(2K_p + 1)(K_p + 2)}{K_p} = K_{\mathrm{SMP}}. \end{aligned} \tag{2}$$

2.3. Lade–Duncan Strength Criterion.

The Lade–Duncan strength criterion is fitted on the basis of the true triaxial test results of sand, and no clear failure surface exists. The principal stress state is as follows:

$$\frac{(\sigma_1 + \sigma_2 + \sigma_3)^3}{\sigma_1\sigma_2\sigma_3} = \frac{(K_p + 2)^3}{K_p} = K_{\mathrm{LD}}. \tag{3}$$

2.4. Gen-Mises Strength Criterion.

The spatial slip surface of the Gen-Mises strength criterion is octahedral, as depicted in Figure 3, and the principal stress state is shown as follows:

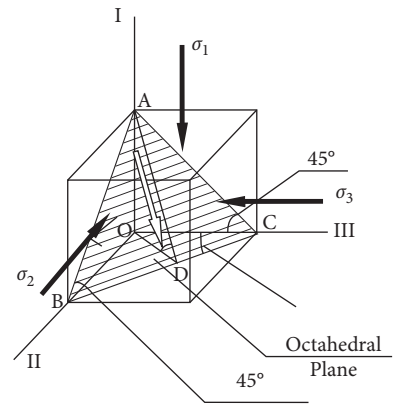

Figure 3: Octahedral SMP.

$$\frac{(\sigma_1 - \sigma_2)^2 + (\sigma_2 - \sigma_3)^2 + (\sigma_1 - \sigma_3)^2}{(\sigma_1 + \sigma_2 + \sigma_3)^2} = \frac{2(K_p - 1)^2}{(K_p + 2)^2} = K_{\mathrm{MIS}}. \tag{4}$$

2.5. AC-SMP Strength Criterion.

The AC space sliding surface of the AC-SMP strength criterion is shown in Figure 4, and the principal stress state is presented as follows:

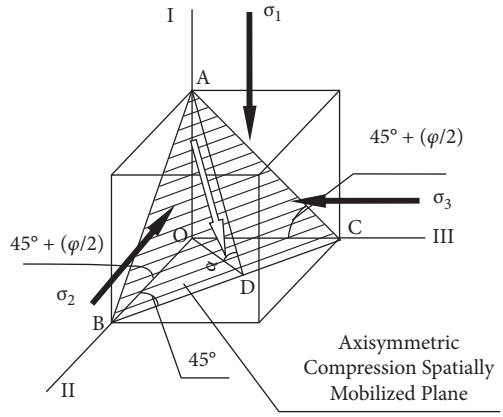

Figure 4: AC-SMP.

$$\frac{(\sigma_1-\sigma_2)^2+(\sigma_1-\sigma_3)^2+K_p(\sigma_2-\sigma_3)^2}{(\sigma_1+\sigma_2K_p+\sigma_3K_p)^2}=\frac{2(K_p-1)^2}{9K_p^2}=K_{AC}. \tag{5}$$

2.6. $\sqrt[3]{\sigma}$ SMP Criterion. A new SMP is proposed on the basis of the concept of SMP when soil has shear failure. This plane (Figure 5) has three intersections with coordinate axes in three dimensions, which are $k\sqrt[3]{\sigma_1}$, $k\sqrt[3]{\sigma_2}$, and $k\sqrt[3]{\sigma_3}$. The principal stress state is shown as follows:

$$\sqrt{\frac{\left((\sigma_1\sigma_2)^{2/3}+(\sigma_2\sigma_3)^{2/3}+(\sigma_3\sigma_1)^{2/3}\right)\left(\sigma_1^{4/3}+\sigma_2^{4/3}+\sigma_3^{4/3}\right)}{\left(\sigma_1^{1/3}+\sigma_2^{1/3}+\sigma_3^{1/3}\right)^2(\sigma_1\sigma_2\sigma_3)^{2/3}}}$$

$$-1*\frac{\sqrt[3]{K_p}\left(\sqrt[3]{K_p}+2\right)}{\sqrt{2}(K_p-1)}=1. \tag{6}$$

The failure shear planes of each criterion are different, and the shear and normal stresses are irrelevant to the intermediate principal stress in the Mohr–Coulomb criterion. For the other criteria, the shear and normal stresses include the intermediate principal stress. Thus, the soil strength described by different criteria differs. To describe the soil strength defined by each strength criterion clearly, we plot the failure lines of each strength criterion when the internal friction angle is 35° on the π plane in the principal stress space (Figure 6).

From Figure 6, the criteria are arranged in descending order on the basis of described soil strength: Gen-Mises, AC-SMP, Lade–Duncan and $\sqrt[3]{\sigma}$ SMP, SMP, and Mohr–Coulomb. The strength of Lade–Duncan and $\sqrt[3]{\sigma}$ SMP are the same. Previous studies have also indicated the SMP of the Lade–Duncan strength criterion and $\sqrt[3]{\sigma}$ SMP criterion [17]. The soil strength differs greatly based on different strength criteria because of the different intermediate principal stresses in each strength criterion. When the soil is damaged, the higher the degree of the intermediate principal stress, the greater the soil strength will be. Previous

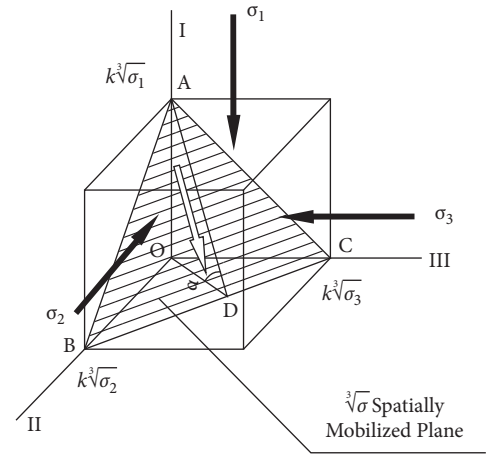

Figure 5: $\sqrt[3]{\sigma}$ SMP.

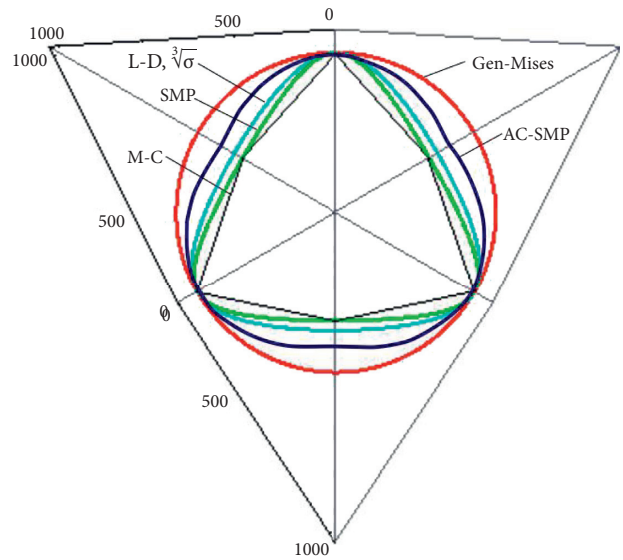

Figure 6: Critical failure lines of each strength criterion on the π plane.

research results [18–21] indicate that the strength criterion considering the effect of intermediate principal stress can better exert the strength characteristics of the rock and soil. For the practical project, proper strength criterion will exert the maximum resistance of soil and therefore be more economical.

3. Active and Passive Soil Pressures of Cohesive Soils with Various Strength Criteria under a Three-Dimensional Stress State

The classical Rankine Earth pressure theory is based on the Mohr–Coulomb strength criterion, disregarding the contribution of intermediate principal stress. In practice, soil is generally in a three-dimensional stress state $\sigma_1 > \sigma_2 > \sigma_3$, and the soil pressure calculated using the Mohr–Coulomb strength criterion is inconsistent with the real one. Therefore, the analysis of the calculation method for Earth

pressure with the consideration of intermediate principal stress is of great importance. From equations (2)–(6), the development of intermediate principal stress directly determines the soil strength described by the strength criteria and then affects the calculated value. The intermediate principal stress of soil should be determined to acquire the Earth pressure under a three-dimensional stress state. Then, the result should be integrated into the strength criteria of each three-dimensional stress state, and the relationship between large and small principal stresses of the failure soil can be obtained.

For excavation and unloading projects, such as foundation pits and retaining walls, the soil is in the initial stress state before excavation and the horizontal and vertical planes of any soil element are principal stress planes. The vertical principal stress is $\sigma_1 = \gamma z$ and horizontal principal stress is $\sigma_2 = \sigma_3 = K_0 \gamma z$, where z is the depth and K_0 is the coefficient of static Earth pressure, i.e., $K_0 = 1 - \sin\varphi$ [22, 23]. After the excavation, the minor principal stress σ_3 of the Earth decreases, forming a frontage and an active Earth pressure and causing the retaining structure to move. At the same time, the principal stress of σ_2 is transferred to σ_3 and $\sigma_2 < K_0 \gamma z$. With the increase in excavation depth, the principal stress of σ_2 is transferred considerably and σ_2 decreases. From the discussion above, in three-dimensional stress states, the principal stress of σ_2 is no longer a fixed value; it decreases as the excavation depth increases and can be expressed as $\sigma_2 = k_2 \gamma z$, where k_2 is the lateral pressure coefficient of σ_2. In accordance with previous studies and measured data, the relationship of k_2, K_0 (lateral pressure coefficient of σ_2 before and after the excavation), and excavation depth can be expressed as [24]

$$k_2 = K_0 \left[1 - \left(0.2 \sim 0.5 \frac{z}{H}\right)\right], \tag{7}$$

where z is the current excavation depth and H is the final excavation depth.

When calculating the active Earth pressure, $\sigma_1 = \gamma z$ and $\sigma_2 = k_2 \gamma z$ (γ is the soil unit weight, and z is the depth) are integrated into each strength criterion and $P_a = \sigma_3$ and $P_p = \sigma_1$ can be obtained. Then, we can derive the active and passive Earth pressure expressions based on each strength criterion.

3.1. Earth Pressure Based on the Mohr–Coulomb Strength Criterion. The active Earth pressure is

$$P_a = \sigma_3 = K_a \sigma_1 = K_a \gamma z, \tag{8}$$

where $K_a = \tan^2(45^\circ - \varphi/2)$.

The passive Earth pressure is

$$P_p = \sigma_1 = \frac{\sigma_3}{K_a} = \frac{\gamma z}{K_a}. \tag{9}$$

3.2. Earth Pressure Based on the SMP Strength Criterion. On the basis of the SMP strength criterion, we place $\sigma_2 = k_2 \gamma z$ into equation (2) and obtain the following:

$$\frac{\sigma_3}{\sigma_1} = \frac{-1 - 3k_2 - k_2^2 + k_2 K_{\mathrm{SMP}} - C}{2(1 + k_2)}, \tag{10}$$

where $C = \sqrt{-4(1 + k_2)(k_2 + k_2^2) + (1 + 3k_2 + k_2^2 - k_2 K_{\mathrm{SMP}})^2}$.

The active Earth pressure based on the SMP strength criterion is

$$P_a = \sigma_3 = K_{a\text{–SMP}} \sigma_1 = K_{a\text{–SMP}} \gamma z, \tag{11}$$

where $K_{a\text{–SMP}} = (-1 - 3k_2 - k_2^2 + k_2 K_{\mathrm{SMP}} - C)/2 + 2k_2$.

The passive Earth pressure is

$$P_p = \sigma_1 = \frac{\sigma_3}{K_{a\text{–SMP}}} = \frac{\gamma z}{K_{a\text{–SMP}}}. \tag{12}$$

3.3. Earth Pressure Based on the Lade–Duncan Strength Criterion. In accordance with the Lade–Duncan strength criterion, the medium principal stress $\sigma_2 = k_2 \gamma z$ is aligned with equation (3), and we can obtain

$$\frac{\sigma_3}{\sigma_1} = -1 - k_2 + \frac{2^{1/3} k_2 K_{\mathrm{LD}}}{A} + \frac{A}{3 \times 2^{1/3}}, \tag{13}$$

where $A = [-27k_2 K_{\mathrm{LD}} - 27k_2^2 K_{\mathrm{LD}} + \sqrt{-108k_2^3 K_{\mathrm{LD}}^3 + (-27k_2 K_{\mathrm{LD}} - 27k_2^2 K_{\mathrm{LD}})^2}\,]^{1/3}$.

The active Earth pressure is

$$P_a = \sigma_3 = K_{a\text{–LD}} \sigma_1 = K_{a\text{–LD}} \gamma z, \tag{14}$$

where $K_{a\text{–LD}} = -1 - k_2 + 2^{1/3} k_2 K_{\mathrm{LD}}/A + A/3 \times 2^{1/3}$.

The passive Earth pressure is

$$K_{a\text{–LD}} = -1 - k_2 + \frac{2^{1/3} k_2 K_{\mathrm{LD}}}{A} + \frac{A}{3 \times 2^{1/3}}. \tag{15}$$

3.4. Earth Pressure Based on the Gen-Mises Strength Criterion. In accordance with the Gen-Mises strength criterion, the medium principal stress $\sigma_2 = k_2 \gamma z$ is aligned with equation (4), and we can obtain

$$\frac{\sigma_3}{\sigma_1} = \frac{-1 - k_2 - K_{\mathrm{MIS}} - k_2 K_{\mathrm{MIS}} + \sqrt{3}B}{K_{\mathrm{MIS}} - 2}, \tag{16}$$

where $B = \sqrt{-1 + 2k_2 - k_2^2 + 2K_{\mathrm{MIS}} + 2k_2 K_{\mathrm{MIS}} + 2k_2^2 K_{\mathrm{MIS}}}$.

The active Earth pressure is

$$P_a = \sigma_3 = K_{a\text{–MIS}} \sigma_1 = K_{a\text{–MIS}} \gamma z, \tag{17}$$

where $K_{a\text{–MIS}} = -1 - k_2 - K_{\mathrm{MIS}} - k_2 K_{\mathrm{MIS}} + \sqrt{3}B/K_{\mathrm{MIS}} - 2$.

The passive Earth pressure is

$$P_p = \sigma_1 = \frac{\sigma_3}{K_{a\text{–MIS}}} = \frac{\gamma z}{K_{a\text{–MIS}}}. \tag{18}$$

3.5. Earth Pressure Based on the AC-SMP Strength Criterion. In accordance with the AC-SMP strength criterion, the medium principal stress $\sigma_2 = k_2 \gamma z$ is combined with equation (5), and we can obtain

$$\frac{\sigma_3}{\sigma_1} = \frac{D - F}{2\left(1 + K_P - K_{\text{AC–SMP}} K_P^2\right)}, \tag{19}$$

where $D = 2 + 2k_2 K_P + 2K_{\text{AC–SMP}} K_P + 2k_2 K_{\text{AC–SMP}}\ K_P^2$,$E = (2 - 2k_2 + k_2^2 - K_{\text{AC–SMP}} + k_2^2 K_P - 2k_2 K_{\text{AC–SMP}} K_P - k_2^2 K_{\text{AC–SMP}} K_P^2)$, and $F = \sqrt{D^2 - 4E(1 + K_P - K_{\text{AC–SMP}} K_P^2)}$.

The active Earth pressure is

$$P_a = \sigma_3 = K_{a\text{–AC}} \sigma_1 = K_{a\text{–AC}} \gamma z, \tag{20}$$

where $K_{a\text{–AC}} = D - F/2\,(1 + K_P - K_{\text{AC–SMP}} K_P^2)$.

The passive Earth pressure is

$$P_p = \sigma_1 = \frac{\sigma_3}{K_{a\text{–AC}}} = \frac{\gamma z}{K_{a\text{–AC}}}. \tag{21}$$

3.6. Earth Pressure Based on the $\sqrt[3]{\sigma}$ SMP Criterion. In accordance with $\sqrt[3]{\sigma}$ SMP strength criterion, the medium principal stress $\sigma_2 = k_2 \gamma z$ is combined with equation (6), and we can obtain

$$\frac{\sigma_3}{\sigma_1} = 1.219 K_{\sqrt[3]{\sigma}}^2 - 3.964 K_{\sqrt[3]{\sigma}} + 3.4, \tag{22}$$

where $K_{\sqrt[3]{\sigma}} = (2\sqrt[3]{K_p^2} + 1)\,(\sqrt[3]{K_p^4} + 2)/\sqrt[3]{K_p^2}\,(\sqrt[3]{K_p} + 2)^2$.

The active Earth pressure is

$$P_a = \sigma_3 = K_{a\text{–}\sqrt[3]{\sigma}} \sigma_1 = K_{a\text{–}\sqrt[3]{\sigma}} \gamma z, \tag{23}$$

where $K_{a\text{–}\sqrt[3]{\sigma}} = 1.219 K_{\sqrt[3]{\sigma}}^2 - 3.964 K_{\sqrt[3]{\sigma}} + 3.4$.

The passive Earth pressure is

$$P_p = \sigma_1 = \frac{\sigma_3}{K_{a\text{–}\sqrt[3]{\sigma}}} = \frac{\gamma z}{K_{a\text{–}\sqrt[3]{\sigma}}}. \tag{24}$$

4. Analysis of the Active and Passive Earth Pressure Coefficients of Cohesionless Soil Based on Each Strength Criterion

The core of Earth pressure theory is the determination of Earth pressure coefficient, and the key of Earth pressure problem in three-dimensional stress state is the influence of intermediate principal stress on the Earth pressure coefficient. The relative difference value of the Earth pressure coefficient calculated based on each strength criterion essentially reflects the contribution of intermediate principal stress to strength and also clearly reflects the influence of each strength criterion on Earth pressure. For test parameters fitting, R^2 (the correlation coefficient) is usually applied to describe the correlation of parameters [25–27]. For the theoretical analysis in this paper, we assumed the same soil parameters and the calculation results of each strength criterion and the Mohr–Coulomb strength criterion could reflect the difference clearly. Equations (25) and (26) are used to conduct the coefficient of Earth pressure based on each strength criterion.

In accordance with the expression of active Earth pressure coefficient K_a obtained using different strength criteria, the active Earth pressure coefficient under different strength criteria can be obtained by putting in the internal friction angle φ. In accordance with Earth pressure theory, the active Earth pressure coefficient K_a should be less than 1. From the failure line on the π plane (Figure 6), the more the Earth strength described by the criterion is, the less the active Earth pressure when soil breaks will be. The active Earth pressure coefficient in the order of small to large is obtained using the Gen-Mises, AC-SMP, Lade–Duncan, $\sqrt[3]{\sigma}$ SMP, SMP, and Mohr–Coulomb strength criteria. The active Earth pressure coefficient based on each criterion should satisfy two conditions. The active Earth pressure coefficient is calculated when φ is in the range of $0^\circ < \varphi \le 50^\circ$. The results show that when $15^\circ \le \varphi$, the Gen-Mises, AC-SMP, $\sqrt[3]{\sigma}$ SMP, SMP, and Mohr–Coulomb strength criteria meet the above two conditions, which could reflect the Earth pressure on the retaining structure well. The Lade–Duncan strength criterion could not meet the condition with any range of friction angle and is no longer applicable to describe the Earth pressure under the condition of medium principal stress. Therefore, the Lade–Duncan criterion will not be involved in the subsequent discussion.

4.1. Analysis of the Active Earth Pressure Coefficient. The variation in the active Earth pressure coefficient K_a with internal friction angle φ based on each strength criterion is shown in Figure 7.

From Figure 7, the active Earth pressure coefficients decrease nonlinearly with the increase in internal friction angle. The larger the internal friction angle is, the greater the difference will be. The value of the active Earth pressure coefficients is less than that calculated using the Mohr–Coulomb strength criterion. The active Earth pressure coefficient in the order of large to small is obtained using the Mohr–Coulomb, SMP, $\sqrt[3]{\sigma}$, AC-SMP, and Gen-Mises strength criteria, consistent with the Earth strength described by the strength criteria. When the contribution of intermediate principal stress to strength is considered, the soil strength can be further developed and the soil can bear increased deformation and maintain stability with active unloading.

The active Earth pressure coefficient K_a^{M-C} obtained using the Mohr–Coulomb strength criterion is regarded as the reference, and the variation in the relative difference R_a (equation 25) of the active Earth pressure coefficient K_a with internal friction angle φ based on each strength criterion in this paper is illustrated in Figure 8.

$$R_a = \frac{\left(K_a^{M-C} - K_a\right)}{K_a^{M-C}}. \tag{25}$$

From Figure 8, the relative difference between the active Earth pressure coefficient and the Mohr–Coulomb strength criterion increases rapidly with the increase in the internal friction angle. When $\varphi < 50^\circ$, the maximum value of relative difference of active Earth pressure coefficients is less than 40%, indicating that active Earth pressure can be well calculated using each strength criterion.

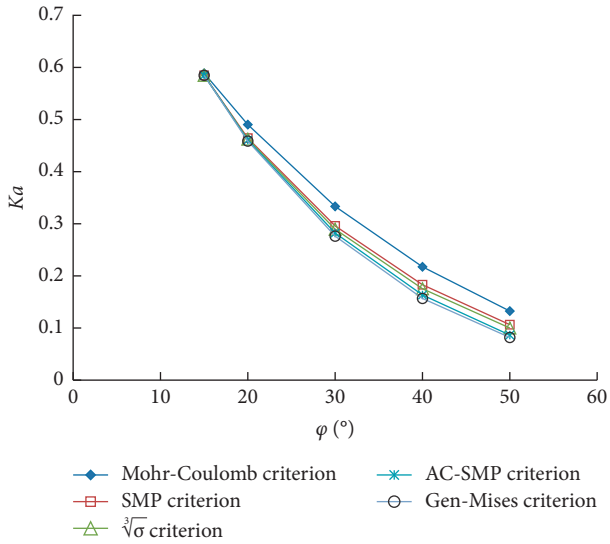

Figure 7: Relationship between active Earth pressure coefficients and internal friction angle.

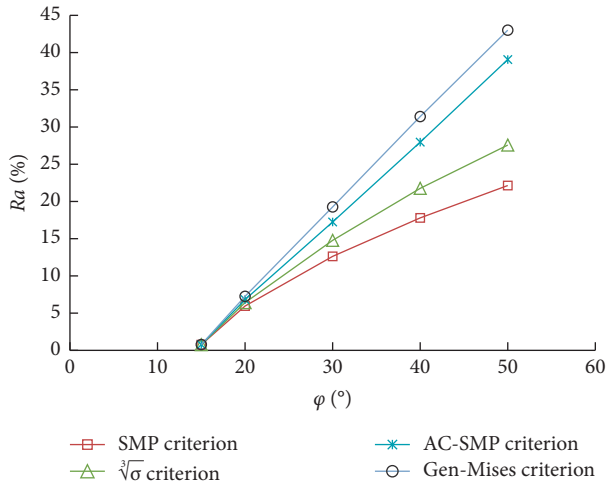

Figure 8: Relative error of active Earth pressure coefficients.

4.2. Analysis of the Passive Earth Pressure Coefficient. Similarly, the variation in the passive Earth pressure coefficient with internal friction angle calculated based on each strength criterion can be calculated, as shown in Figure 9. The active Earth pressure coefficient K_p^{M-C} obtained using the Mohr–Coulomb strength criterion is regarded as the reference, and the variation in the relative difference R_p (equation (26)) of passive Earth pressure coefficient K_p with internal friction angle φ based on each strength criterion in this paper is illustrated in Figure 10.

$$R_p = \frac{\left(K_p - K_p^{M-C}\right)}{K_p^{M-C}}. \tag{26}$$

From Figure 9, the passive Earth pressure coefficient increases nonlinearly with the increase in the internal friction angle. The larger the internal friction angle is, the greater the difference in the passive Earth pressure

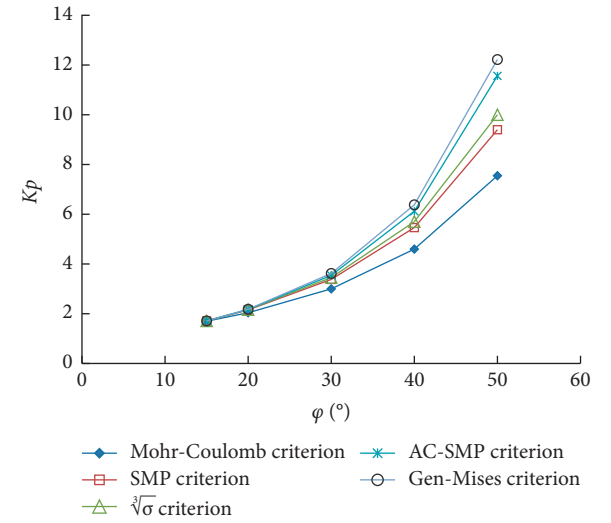

Figure 9: Relationship between passive Earth pressure coefficients and internal friction angle.

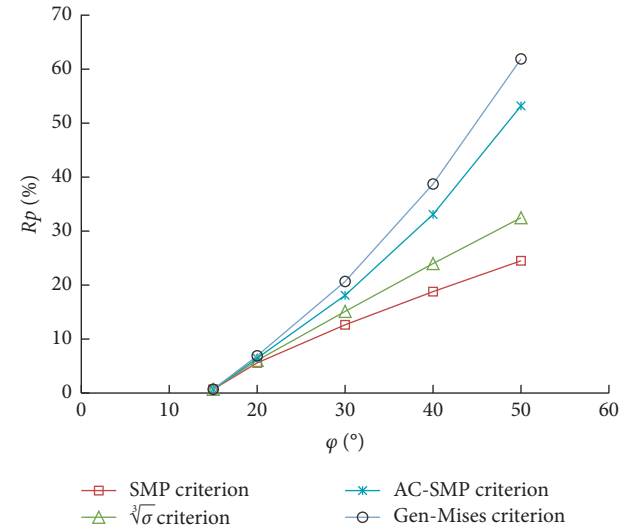

Figure 10: Relative error of passive Earth pressure coefficients.

coefficient will be. When $\varphi > 40^\circ$, the difference in passive Earth pressure coefficient increases rapidly but can reflect the passive Earth pressure well.

As shown in Figure 10, the relative difference in passive Earth pressure coefficient also increases nonlinearly with the increase in internal friction angle. The larger the internal friction angle is, the larger the relative difference in passive Earth pressure coefficient will be. When $\varphi > 50^\circ$, the relative differences of the Gen-Mises and AC-SMP strength criteria exceed 40% and the rationality of the calculation results should be verified.

From the active and passive Earth pressure coefficients in Figures 7–10, the active Earth pressure coefficient based on the Mohr–Coulomb strength criterion is large, whereas the passive Earth pressure coefficient is small because the contribution of intermediate principal stress is disregarded and the results are conservative. Different from the

axisymmetrical state, the intermediate principal stress is always greater than the small principal stress under the three-dimensional stress state. This strengthens the constraint in the direction of the intermediate principal stress, which plays a positive role in improving the soil strength. Therefore, the active Earth pressure coefficient is smaller and the passive Earth pressure coefficient is larger. The three-dimensional stress-state strength criteria can exert the Earth strength entirely. Under a three-dimensional stress state, when $\varphi > 15^{\circ}$, the calculation results of each strength criterion can describe the Earth pressure of the retaining structure well. When $\varphi > 50^{\circ}$, the calculation errors of the Gen-Mises and AC-SMP strength criteria are relatively large. The soil internal friction angle is generally less than 50°; hence, the calculation results based on the strength criteria can be used to describe the value of Earth pressure in a three-dimensional stress state. The selection of reasonable strength criterion calculation results for different soil properties and engineering problems could enhance the Earth strength, reduce the support strength, and make projects considerably economical.

5. Active and Passive Soil Pressures of Cohesive Soil Based on Various Strength Criteria under a Three-Dimensional Stress State

On the basis of the above strength criteria, the active and passive Earth pressure formulas of cohesionless soil are obtained. When the principal stress state is transformed using equation (27), we can obtain the Earth pressure of cohesive soil:

$$\widehat{\sigma}_i = \sigma_i + c\cot\varphi \quad i = 1, 2, 3. \tag{27}$$

Here, σ_i in the expression of the Earth pressure of cohesionless soil is replaced with $\widehat{\sigma}_i$, and the Earth pressure considering cohesive force can be obtained. C and φ are the strength parameters of cohesion and friction angle, respectively.

5.1. Earth Pressure of Cohesive Soil Based on the Mohr–Coulomb Strength Criterion. The large and small principal stresses of cohesionless soil based on the Mohr–Coulomb strength criterion are replaced with $\widehat{\sigma}_i$, and the expression of Earth pressure for cohesive soil can be obtained as follows.

The active Earth pressure is

$$\begin{aligned} P_a &= \sigma_3 = K_a\sigma_1 - c\cot\varphi\left(1 - K_a\right) \\ &= K_a\gamma z - c\cot\varphi\left(1 - K_a\right). \end{aligned} \tag{28}$$

The passive Earth pressure is

$$\begin{aligned} P_p &= \sigma_1 = \frac{\left[\sigma_3 + c\cot\varphi\left(1 - K_a\right)\right]}{K_a} \\ &= \frac{\left[\gamma z + c\cot\varphi\left(1 - K_a\right)\right]}{K_a}. \end{aligned} \tag{29}$$

5.2. Earth Pressure of Cohesive Soil Based on the SMP Strength Criterion. In accordance with equation (27), the expression of Earth pressure based on the SMP strength criterion can be obtained as follows.

The active Earth pressure is

$$\begin{aligned} P_a &= \sigma_3 = K_{a\text{–SMP}}\sigma_1 - c\cot\varphi\left(1 - K_{a\text{–SMP}}\right) \\ &= K_{a\text{–SMP}}\gamma z - c\cot\varphi\left(1 - K_{a\text{–SMP}}\right). \end{aligned} \tag{30}$$

The passive Earth pressure is

$$\begin{aligned} P_p &= \sigma_1 = \frac{\left[\sigma_3 + c\cot\varphi\left(1 - K_{a\text{–SMP}}\right)\right]}{K_{a\text{–SMP}}} \\ &= \frac{\left[\gamma z + c\cot\varphi\left(1 - K_{a\text{–SMP}}\right)\right]}{K_{a\text{–SMP}}}. \end{aligned} \tag{31}$$

5.3. Earth Pressure of Cohesive Soil Based on the Lade–Duncan Strength Criterion. In accordance with equation (27), the expression of Earth pressure based on the Lade–Duncan strength criterion can be obtained as follows.

The active Earth pressure is

$$\begin{aligned} P_a &= \sigma_3 = K_{a\text{–LD}}\sigma_1 - c\cot\varphi\left(1 - K_{a\text{–LD}}\right) \\ &= K_{a\text{–LD}}\gamma z - c\cot\varphi\left(1 - K_{a\text{–LD}}\right). \end{aligned} \tag{32}$$

The passive Earth pressure is

$$\begin{aligned} P_p &= \sigma_1 = \frac{\left[\sigma_3 + c\cot\varphi\left(1 - K_{a\text{–LD}}\right)\right]}{K_{a\text{–LD}}} \\ &= \frac{\left[\gamma z + c\cot\varphi\left(1 - K_{a\text{–LD}}\right)\right]}{K_{a\text{–}LD}}. \end{aligned} \tag{33}$$

5.4. Earth Pressure of Cohesive Soil Based on the Gen-Mises Strength Criterion. In accordance with equation (27), the expression of Earth pressure based on the Gen-Mises strength criterion can be obtained as follows.

The active Earth pressure is

$$\begin{aligned} P_a &= \sigma_3 = K_{a\text{–MIS}}\sigma_1 - c\cot\varphi\left(1 - K_{a\text{–MIS}}\right) \\ &= K_{a\text{–MIS}}\gamma z - c\cot\varphi\left(1 - K_{a\text{–MIS}}\right). \end{aligned} \tag{34}$$

The passive Earth pressure is

$$\begin{aligned} P_p &= \sigma_1 = \frac{\left[\sigma_3 + c\cot\varphi\left(1 - K_{a\text{–MIS}}\right)\right]}{K_{a\text{–MIS}}} \\ &= \frac{\left[\gamma z + c\cot\varphi\left(1 - K_{a\text{–MIS}}\right)\right]}{K_{a\text{–MIS}}}. \end{aligned} \tag{35}$$

5.5. Earth Pressure of Cohesive Soil Based on the AC-SMP Strength Criterion. In accordance with equation (27), the expression of Earth pressure based on the AC-SMP strength criterion can be obtained as follows.

The active Earth pressure is

$$P_a = \sigma_3 = K_{a-\mathrm{AC}}\sigma_1 - c\cot\varphi\left(1 - K_{a-\mathrm{AC}}\right) = K_{a-\mathrm{AC}}\gamma z - c\cot\varphi\left(1 - K_{a-\mathrm{AC}}\right). \quad (36)$$

The passive Earth pressure is

$$P_p = \sigma_1 = \frac{\left[\sigma_3 + c\cot\varphi\left(1 - K_{a-\mathrm{AC}}\right)\right]}{K_{a-\mathrm{AC}}} = \frac{\left[\gamma z + c\cot\varphi\left(1 - K_{a-\mathrm{AC}}\right)\right]}{K_{a-\mathrm{AC}}}. \quad (37)$$

5.6. Earth Pressure of Cohesive Soil Based on $\sqrt[3]{\sigma}$ Strength Criterion. In accordance with equation (27), the expression of Earth pressure based on $\sqrt[3]{\sigma}$ strength criterion can be obtained as follows.

The active Earth pressure is

$$P_a = \sigma_3 = K_{a-\sqrt[3]{\sigma}}\sigma_1 - c\cot\varphi\left(1 - K_{a-\sqrt[3]{\sigma}}\right) = K_{a-\sqrt[3]{\sigma}}\gamma z - c\cot\varphi\left(1 - K_{a-\sqrt[3]{\sigma}}\right). \quad (38)$$

The passive Earth pressure is

$$P_p = \sigma_1 = \frac{\left[\sigma_3 + c\cot\varphi\left(1 - K_{a-\sqrt[3]{\sigma}}\right)\right]}{K_{a-\sqrt[3]{\sigma}}} = \frac{\left[\gamma z + c\cot\varphi\left(1 - K_{a-\sqrt[3]{\sigma}}\right)\right]}{K_{a-\sqrt[3]{\sigma}}}. \quad (39)$$

6. Theoretical Calculation and Analysis of Earth Pressure

6.1. Verification of Earth Pressure in Cohesionless Soil. The cohesionless sand used in the test [28] has an internal friction angle φ of 34° and a volume weight γ of 19.56 kN/m3. The retaining wall is made of mixed wooden planks and is 5 cm thick, 1 m high, and 1 m wide. It is reinforced to meet the stiffness requirements. The active Earth pressure measured during the test is shown in Figure 11, where H is the height of the wall and Pa is the active Earth pressure. The sand property parameters are substituted into the active Earth pressure expression based on each strength criterion, and the active Earth pressure values in a three-dimensional stress state at different depths of the retaining wall can be calculated. A comparison between the calculated and measured results is shown in Figure 11.

From Figure 11, the active Earth pressure in a three-dimensional stress state calculated in accordance with the strength criteria increases approximately linearly with the increase in depth. The active Earth pressures in the order of large to small are obtained using the Mohr–Coulomb, SMP, $\sqrt[3]{\sigma}$ SMP, AC-SMP, and Gen-Mises strength criteria. The measured active Earth pressure is remarkably less than the calculated value based on the Mohr–Coulomb strength criterion, implying that the calculation result of the Mohr–Coulomb strength criterion is excessively conservative. In engineering construction, the support strength can be appropriately reduced to improve the economy.

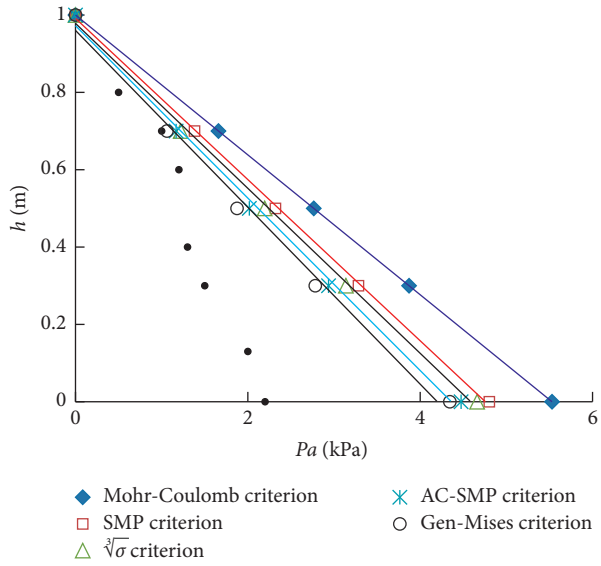

Figure 11: Active Earth pressure of sand.

The difference in active Earth pressure based on the strength criteria is increased with increasing excavation depth. The active Earth pressures based on the SMP, $\sqrt[3]{\sigma}$ SMP, AC-SMP, and Gen-Mises strength criteria reflect the contribution of intermediate principal stress to Earth strength, which could reveal the Earth pressure on the retaining wall well. The calculation result based on the Gen-Mises strength criterion is closer to the measured Earth pressure value than others.

6.2. Verification of Earth Pressure in Cohesive Soil

6.2.1. Analysis of Homogeneous Cohesive Soil. In a deep foundation pit project, the excavation depth is 14 m, the continuous retaining wall is 5 m into the bottom, and the soil is homogeneous clay. The parameters are as follows: c = 20 kPa, $\varphi = 20^o$, and γ = 19kN/m^3. The calculation diagram is shown in Figure 12. When the soil in the pit is excavated, the soil behind the pit will shift to the free face because of the horizontal discharge and the active Earth pressure will be generated at the continuous retaining wall. At the same time, the soil at the bottom of the pit, compressed by the wall embedded in the pit bottom, exerts passive Earth pressure.

In accordance with equations (28)–(39), the active and passive Earth pressure values of the continuous retaining wall at different depths under the condition of three-dimensional stress state can be calculated on the basis of different strength criteria. The values are shown in Table 1.

Table 1 presents that the active and passive Earth pressures at various depths calculated in accordance with the strength criteria are different. The maximum active Earth pressure on the retaining wall is calculated using the Mohr–Coulomb strength criterion, and the minimum is obtained using the Gen-Mises strength criterion. The

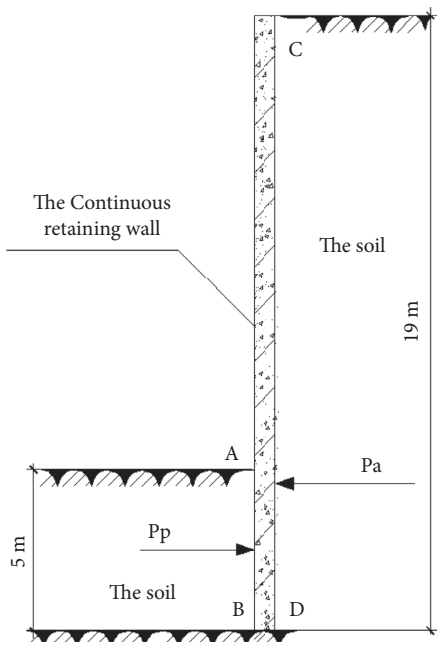

Figure 12: Calculation diagram.

Table 1: Earth pressure under different strength criteria.

Strength criterion	P_pA (kPa)	P_pB (kPa)	P_aC (kPa)	P_aD (kPa)
Mohr–Coulomb criterion	57.13	250.89	−28.01	148.99
SMP criterion	58.7	263.29	−27.26	140.37
$\sqrt[3]{\sigma}$ criterion	58.83	264.3	−27.19	139.71
AC-SMP criterion	58.94	265.2	−27.15	139.12
Gen-Mises criterion	59.06	266.19	−27.09	138.49

calculation results of passive Earth pressure are opposite. The three-dimensional stress-state Earth pressure calculation results of each strength criterion can well describe the Earth pressure on the homogeneous clay-retaining structure. This result indicates that the intermediate principal stress has an evident contribution to the improvement of soil strength by helping the excavated soil withstand great passive Earth pressure and small active Earth pressure, which could develop the strength of soil to resist the external load and reduce the support strength.

6.2.2. Analysis of Layered Cohesive Soil. A deep foundation pit with a depth of 7.1 m is supported by 800 mm cantilever piles with a length of 12.70 m. The distribution of soil layers in the pit depth and the soil properties of each soil layer are shown in Figure 13 [12].

In accordance with the formula of the active Earth pressure of cohesive soil and the soil parameters of each layer, the active Earth pressure at different depths based on each strength criterion can be calculated, as shown in Table 2. A comparison of calculated and measured Earth pressure values at the upper and lower interfaces is shown in Figure 14.

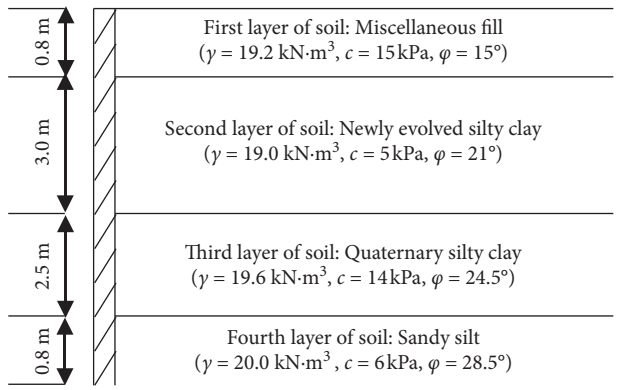

Figure 13: Layers of soils.

Table 2 and Figure 14 demonstrate that the variation in active Earth pressure of layered cohesive soil is consistent with that of cohesionless soil and homogeneous cohesive soil calculated on the basis of each strength criterion. The calculation results of each strength criterion show that positive active Earth pressure begins to be generated when the foundation pit is excavated to approximately 0.8 m. This result means that the depth of the foundation pit that can be excavated without support is 0.8 m theoretically. The measured results show that positive active Earth pressure develops until the foundation pit is excavated to 3 m, indicating the complexity of Earth pressure in actual engineering. When the excavation depth is less than 3.8 m, the calculated results of Earth pressure in accordance with the strength criteria differ greatly from the measured values. However, the failure of the foundation pit is generally at the middle and bottom, and the difference in calculation results of soil pressure on the top of the foundation pit will not affect the safety. When the excavation depth is greater than 3.8 m, the

Table 2: Active Earth pressure under different strength criteria.

Strength criterion	Pa (kPa) 0 m	Pa (kPa) above 0.8 m	Pa (kPa) below 0.8 m	Pa (kPa) above 3.8 m	Pa (kPa) below 3.8 m	Pa (kPa) above 6.3 m	Pa (kPa) below 6.3 m	Pa (kPa) 7.1 m
Mohr–Coulomb criterion	−23.02	−13.98	0.38	27.31	11.69	31.73	35.82	41.48
SMP criterion	−22.94	−13.95	0.16	25.46	9.97	28.32	31.71	36.78
$\sqrt[3]{\sigma}$ criterion	−22.94	−13.96	0.14	25.29	9.59	27.56	31	35.97
AC-SMP criterion	−22.94	−13.96	0.12	25.15	9.53	27.46	30.3	35.2
Gen-Mises criterion	−22.94	−13.96	0.1	25	9.33	27	29.7	34.5

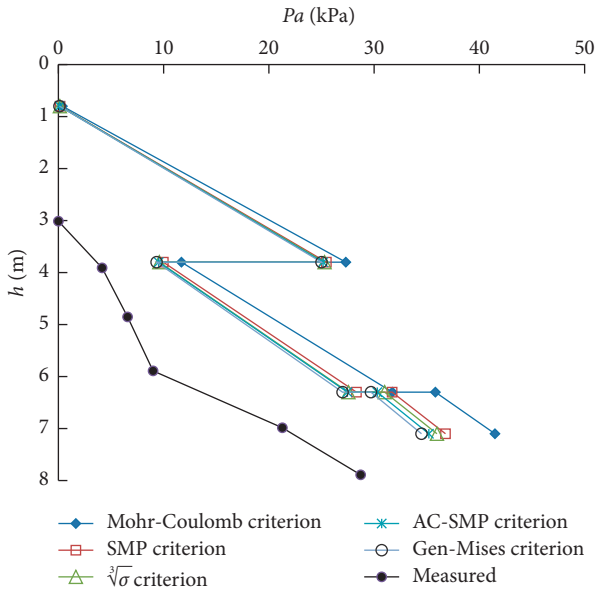

Figure 14: Active Earth pressure distribution diagram under different strength criteria.

Earth pressure calculation results of each strength criterion basically reflect the variation law of Earth pressure, but all of them are conservative. The preceding analysis indicates that for layered soil sites under a three-dimensional stress state, the Earth pressure calculation results based on each strength criterion can describe the value of Earth pressure well on the retaining structure. The calculated results presented in this paper are closer to the measured values than those of the Mohr–Coulomb strength criterion, and the result of the Gen-Mises strength criterion is the most accurate. On the premise of safety, when calculating Earth pressure under the condition of three-dimensional stress state, the theory in this paper can fully consider the contribution of intermediate principal stress to Earth strength, which is consistent with actual engineering.

7. Conclusions

(1) Under the condition of three-dimensional stress state, large and small principal stresses based on different strength criteria are obtained in accordance with the equation of the Earth pressure coefficient in the direction of intermediate principal stress and excavation depth. The active and passive Earth pressures in a three-dimensional stress state are deduced on the basis of each strength criterion and extended to cohesive soil.

(2) Under the condition of three-dimensional stress state, when $15^{\circ} \leq \varphi$, the Earth pressure coefficient based on each strength criterion can be used to calculate the active and passive Earth pressures. When $\varphi > 50^{\circ}$, the errors of the Earth pressure calculation based on AC-SMP and Gen-Mises criteria are larger than those of the Mohr–Coulomb criterion.

(3) Under the condition of three-dimensional stress state, the calculation results of active and passive Earth pressures of cohesionless and cohesive soils based on each strength criterion show that the calculated active Earth pressure is small and the passive Earth pressure is large after considering the effect of intermediate principal stress. This finding is closer to actual engineering.

(4) Under the condition of three-dimensional stress state, the comparison analysis between the measured Earth pressure data and the calculation results of cohesionless and cohesive soils shows that the Mohr–Coulomb strength criterion tends to be conservative in retaining the structure design because it does not consider the contribution of intermediate principal stress. The Lade–Duncan strength criterion is unsuitable for calculating the Earth pressure on the retaining wall under the condition of principal stress in this paper. The calculated results of the SMP, $\sqrt[3]{\sigma}$ SMP, AC-SMP, and Gen-Mises strength criteria can be used to show the Earth pressure on the retaining structure in actual engineering. The calculation result of the Gen-Mises strength criterion is the most accurate.

Data Availability

The data used to support the findings of this study are available from the corresponding author upon request.

Conflicts of Interest

The authors declare no conflicts of interest.

Acknowledgments

This work was supported by the National Natural Science Foundation of China (nos. 11802218 and 42007257), Science

and Technology Plan Project of Shaanxi Province (no. 2019JQ-349), Shaanxi Key Laboratory of Loess Mechanics and Engineering (no. LME201801), and Natural Science Foundation of Shaanxi Provincial Department of Education (no. 20JK0670).

References

[1] W. C. Gu, *Calculation of Earth Pressure on Retaining wall*, China Building Material Industry Publishing House, Beijing, China, 2002.

[2] S. J. Shao, F. Chen, and G. H. Deng, "Seismic passive earth pressure against the retaining wall of structural loess based on plane strain unified strength formula," *Rock and Soil Mechanics*, vol. 40, no. 4, pp. 1255–1262, 2019.

[3] J. Koseki, F. Tatsuoka, Y. Munaf, M. Tateyama, and K. Kojima, "A modified procedure to evaluate active earth pressure at high seismic loads," *Soils and Foundations*, vol. 38, pp. 209–216, 1998.

[4] J. M. Zhang, F. Song, and D. J. Li, "Effects of strain localization on seismic active earth pressures," *Journal of Geotechnical and Geoenvironmental Engineering*, vol. 136, no. 7, pp. 999–1003, 2010.

[5] G.-X. Zhang and M. Wang, "Derivation and improvement of formula for calculating seismic active earth pressure in new 'Technical code for building slope engineering'," *Rock and Soil Mechanics*, vol. 38, no. 4, pp. 1097–1102, 2017.

[6] D. C. Lu, Z. M. Zhang, X. L. du, and Y. P. Yao, "Limit earth pressure under plane Strain condition," *Chinese Journal of Rock Mechanics and Engineering*, vol. 27, no. 2, pp. 3354–3359, 2008.

[7] R. G. Yang, Z. Y. Liu, and H. Li, "Calculation of active earth pressure considering the effect of the intermediate principal stress," *Journal of Zhengzhou University*, vol. 27, no. 1, pp. 27–30, 2006.

[8] H. Matsuoka and T. Nakai, "Stress-deformation and strength characteristics of soil under three different principal stresses," *Proceedings of Japan Society of Civil Engineers*, vol. 1974, no. 232, pp. 59–70, 1974.

[9] Y. Zhang, S.-J. Shao, M. Zhao, X. Ding, J. Liu, and F. T. She, "An application research of soil strength criterion in loess engineering problems under plain strain condition," *China Civil Engineering Journal*, vol. 51, no. 8, pp. 71–80, 2018.

[10] X. S. Zhuagn, D. X. Li, and Y. He, "Calculation of earth pressure based on the lade-duncan yield criterion," *Soil Engineering and Foundation*, vol. 21, no. 5, pp. 40–42, 2007.

[11] Q. Jiang, J. M. Zhu, and Y. P. Yao, "Earth pressures of three-dimensional soil stress states based on SMP failure criterion," *Chinese Journal of Geotechnical Engineering*, vol. 28, no. s1, pp. 1415–1417, 2006.

[12] Q.-D. Xie, J. He, J. Liu, and J. X. Ouyang, "The application of the double-shear unified strength theory," *Chinese Journal of Geotechnical Engineering*, vol. 25, no. 3, pp. 343–345, 2003.

[13] Q.-N. Chen, Y.-X. Zhang, and X.-P. Zhou, "Formula of Rankine Passive earth pressure under triaxial compressive loading," *Chinese Journal of Rock Mechanics and Engineering*, vol. 24, no. 5, pp. 880–882, 2005.

[14] J. Zhang, R. L. Hu, H. B. Liu, and S. S. Wang, "Calculation study of Rankine e earth pressure based on unified strength theory," *Chinese Journal of Rock Mechanics and Engineering*, vol. 29, no. s1, pp. 3169–3176, 2010.

[15] X. Q. Yang, Z. C. Wu, and Z. K. Yang, "Research on active soil pressure on retaining wall under general stress states," *China Journal of Highway and Transport*, vol. 23, no. 2, pp. 25–29, 2010.

[16] S. J. Shao, P. Xu, and C. L. Chen, "Several shear spatially mobilized planes and anisotropic strength criteria of soils," *Chinese Journal of Geotechnical Engineering*, vol. 35, no. 3, pp. 422–435, 2013.

[17] S.-J. Shao, Y. Zhang, and C.-L. Chen, "A strength criterion based on spatially mobilized plane of soil and its comparing with conventional criteria," *Chinese Journal of Geotechnical Engineering*, vol. 37, no. 4, pp. 577–585, 2015.

[18] X. G. Zhao, J. Wang, M. Cai, and G. S. Su, "Influence of intermediate principal stress on the strainburst characteristics of beishan granite with consideration of end effect," *Rock Mechanics and Rock Engineering*, vol. 54, pp. 1–21, 2021.

[19] Z. X. Li, C. G. Zhang, J. Y. Zhao, Q. Yan, and D. Rossana, "Safety factor of unsaturated soil slopes considering the intermediate principal stress effect and different profiles of matric suction," *Mathematical Problems in Engineering*, vol. 2021, Article ID 6622522, 10 pages, 2021.

[20] J. P. Gao, J. Q. Yang, and X. Sun, "Research on D-P series yield criteria considering the influence coefficient of double shear intermediate principal stress," *Chinese Journal of Rock Mechanics and Engineering*, vol. 40, no. 6, pp. 1081–1091, 2021.

[21] T. Y. Meng, Y. Zhang, J. Liu, Y. Zhao, X. Ding, and T. J. Fan, "Earth pressure problem and applicability under the plane strain condition based on the principal stress condition in Lade-Duncan strength criterion," *Journal of Civil and Environmental Engineering*, vol. 2, pp. 1–9, 2021.

[22] Y.-C. Liu, *Soil mechanics*, China Railway Press, Beijing, China, 2000.

[23] C. P. Wroth and G. T. Houbly, "Soil mechanics-property characterization and analysis problem procedures," in *Proceedings of the 11th International Conference Soil Mechcanic and Found Engrg, ISSMFE*, pp. 1–55, Calif, San Francisco, May 1985.

[24] G. B. Liu, Y. X. Huang, and X. Y. Hou, "Discussion on water and earth pressure of supporting structure in soft area," *Chinese Journal of Rock Mechanics and Engineering*, vol. 19, no. 2, pp. 205–210, 2000.

[25] J. H. Peng, J. H. Zhang, J. Liu, Y. S. Yao, and A. S. Zhang, "Modeling humidity and stress-dependent subgrade soils in flexible pavements," *Computers and Geotechnics*, vol. 120, pp. 1–9, 2020.

[26] J. H. Zhang, A. S. Zhang, C. Huang, H. Y. Yu, and C. Zhou, "Characterising the resilient behaviour of pavement subgrade with construction and demolition waste under FreezeeThaw cycles," *Journal of Cleaner Production*, vol. 300, pp. 1–13, 2021.

[27] Y. S. Yao, J. J. Ni, and J. Li, "Stress-dependent water retention of granite residual soil and its implications for ground settlement," *Computers and Geotechnics*, vol. 129, pp. 1–11, 2020.

[28] Y.-Y. Zhou and M.-L. Ren, "An experimental study on active earth pressure behind rigid retaining wall," *Chinese Journal of Geotechnical Engineering*, vol. 12, no. 2, pp. 19–26, 1990.

Hindawi
Advances in Materials Science and Engineering
Volume 2021, Article ID 9934250, 10 pages
https://doi.org/10.1155/2021/9934250

Research Article

Crack Identification Method of Steel Fiber Reinforced Concrete Based on Deep Learning: A Comparative Study and Shared Crack Database

Yang Ding,[1,2,3] **Shuang-Xi Zhou**,[4] **Hai-Qiang Yuan**,[4] **Yuan Pan**,[4] **Jing-Liang Dong**,[4] **Zhong-Ping Wang**,[1,2] **Tong-Lin Yang**,[5] **and An-Ming She**[1,2]

[1]*Key Laboratory of Advanced Civil Engineering Materials of Ministry of Education, Tongji University, Shanghai 201804, China*
[2]*School of Materials Science and Engineering, Tongji University, Shanghai 201804, China*
[3]*Department of Civil Engineering, Zhejiang University, Hangzhou 310058, China*
[4]*School of Civil Engineering and Architecture, East China Jiao Tong University, Nanchang 330013, China*
[5]*College of Chemistry and Chemical Engineering, Hunan University, Changsha 410082, China*

Correspondence should be addressed to An-Ming She; sheanming@tongji.edu.cn

Received 23 June 2021; Revised 8 August 2021; Accepted 23 August 2021; Published 11 September 2021

Academic Editor: Chundi Si

As a common disease of concrete structure in engineering, cracks mainly lead to durability problems such as steel corrosion, rain erosion, and protection layer peeling, and then the building gets destroyed. In order to detect the cracks of concrete structure in time, the bending test of steel fiber reinforced concrete is carried out, and the pictures of concrete cracks are obtained. Furthermore, the crack database is expanded by the migration learning method and the crack database is shared on the Baidu online disk. Finally, a concrete crack identification model based on YOLOv4 and Mask R-CNN is established. In addition, the improved Mask R-CNN method is proposed in order to improve the prediction accuracy based on the Mask R-CNN. The results show that the average prediction accuracy of concrete crack identification is 82.60% based on the YOLO v4 method. The average prediction accuracy of concrete crack identification is 90.44% based on the Mask R-CNN method. The average prediction accuracy of concrete crack identification is 96.09% based on the improved Mask R-CNN method.

1. Introduction

Nowadays, the concrete crack detection is mainly through manual identification [1, 2]. The manual detection method is not only time consuming but also requires a lot of energy from the relevant detection personnel [3, 4]. There are some problems such as low detection accuracy and subjectivity of operators [5, 6]. In addition, cracks in some special areas cannot be detected manually, such as bridge piers, mountainous areas, and high-risk urban areas [7, 8]. These cracks, which are difficult to detect, may cause structural weakness, leading to ductile failure and brittle failure, leading to serious safety accidents [9, 10].

In recent years, the deep learning method has been widely used in the field of civil engineering and has attracted the attention of many researchers [11]. Hinton et al. [12] proposed the deep learning model for the first time. The result showed that the artificial neural network with multiple hidden layers optimizes the network through layer by layer initialization, realizes feature learning, and opens a new era of deep learning. Krizhevsky et al. [13] designed the AlexNet algorithm, which is the first deep neural network model established by convolutional neural network. Girshick [14] proposed a new algorithm based on R-CNN and SPPNet: fast R-CNN. The result showed that the speed and accuracy have been improved, but there is still a long way to go from real end-to-end processing. Ren et al. [15] proposed fast R-CNN algorithm based on fast R-CNN network model and regional recommendation network, which achieved 78.8% detection accuracy on VOC2007 dataset. Lin et al. [16]

designed the feature pyramid network according to the different semantic and target location of different feature maps, which has certain advantages in small target detection. Redmon et al. [17] proposed a regression problem that unifies the classification regression problem into a coordinate frame, that is, Yolo algorithm. The results show that Yolo algorithm has very fast detection speed, but its accuracy is lower than that of the existing R-CNN series algorithm model, and the detection effect is poor when the object is small. Du et al. [18] proposed a new method to detect severe vehicle occlusion, which can be applied to aerial images of weak infrared camera with complex field background. Yu et al. [19] proposed the Mask R-CNN fruit detection model. The results show that the average detection accuracy is 95.78%, the recall rate is 95.41%, and the average intersection rate of instance segmentation is 89.85%. Pang et al. [20] proposed a segmented crack defect segmentation method, which solved the problems of uneven brightness and high noise of dam concrete surface image. Yu et al. [21] proposed a deep learning model YOLOv4-FPM based on the YOLOv4 model. The results show that the average accuracy of YOLOv4-FPM is 0.064 higher than that of original YOLOv4.

This paper takes steel fiber reinforced concrete as the research object, obtains concrete crack pictures through bending test, and expands the crack database based on the transfer learning method. Based on the deep learning algorithm, an automatic crack detection model is established, that is, YOLOv4 and Mask R-CNN. Furthermore, an improved Mask R-CNN concrete crack identification model is proposed based on the Mask R-CNN model.

2. Image Acquisition and Processing

2.1. Materials. Portland cement (42.5) was produced by China United Cement Group Co., Ltd., and its main components are shown in Table 1. Xiamen ISO standard sand is adopted. Steel fiber is a flat copper plated steel fiber with diameter of 0.2 mm and length of 13 mm. Distilled water was used.

Steel fiber concrete with fixed water binder ratio and limestone ratio of 0.4 and 1 : 2 was prepared. In this experiment, 10 batches of steel fiber mortar specimens were prepared, which were 0.1%, 0.3%, 0.5%, 1%, 1.5%, 2%, and 3%, respectively. Each batch was divided into five groups according to the vibration time of 0.5 min, 1 min, 1.5 min, 2 min, and 2.5 min. Firstly, sand and cement are added to dry mix for 1-2 minutes. After mixing evenly, 90% and 10% water are added in turn. When the cementitious material is gradually formed, steel fibers are evenly sprinkled and fully stirred to avoid fiber polymerization at one place of the test block. After the specimen is vibrated, it is placed in the room for 24 hours before demoulding and soaking in water for curing. At the same time, ensure that the water level overflows the specimen. The curing time of the specimens was 90 days. The specimens were dried at room temperature for 12 hours in advance. The concrete bending test is carried out with the size of 100 mm × 100 mm × 400 mm prism specimen. Specifically, the effective span of the beam is 300 mm, the beam height is 100 mm, and the beam width is 100 mm. Based on the CECS 13-2009 standard, the bending test of fiber-reinforced concrete is carried out, and then the pictures of concrete cracks are obtained. Figure 1 shows the initial and final crack pictures of different steel fiber reinforced concrete.

Table 1: Main components of cement.

Materials	Chemical composition (mass ratio (%))							
	CaO	SiO_2	Al_2O_3	Fe_2O_3	MgO	K_2O	SO_3	CaO
Cement	65.87	21.62	5.49	4.08	0.81	0.85	1.28	65.87

2.2. Image Preprocessing. Because the resolution of the original image is too large, the calculation cost will be too high if the original image is directly input [22]. Therefore, the original image will be cropped to include only the concrete test block image, which is also conducive to better learning the defect features of the model, as shown in Figure 2.

The image input model is transformed into a vector matrix to enter the network, and the latitude of the vector is fixed, so the resolution should be adjusted [23]. In this paper, the image is adjusted to 512 × 512 size, as shown in Figure 3.

Due to the experimental limitations, it is impossible to make enough sample data, so the crack data are enhanced to improve the robustness and generalization ability of the training model [24]. Rotating, blurring, flipping, and noise adding can be seen in Figure 4. Specifically, rotation refers to rotating the image randomly by an angle of 45, 90, and 180 degrees; flipping refers to rotating the image along the horizontal X axis or vertical Y axis; blurring refers to blurring the image; and adding noise refers to adding salt and pepper noise or Gaussian noise into the crack image. Finally, there are 1200 crack images as the training dataset, 400 crack images as the validation dataset, and 400 crack images as the test dataset.

3. Deep Learning Method

3.1. Model of Object Detection Algorithm for YOLOv4. The YOLOv4 algorithm model not only improves the speed but also improves the detection accuracy [25]. The YOLOv4 network structure includes four parts [26]. (1) The algorithm provides data-enhanced mosaic, cmBN, and SAT self-confrontation training at the input end, which enriches the detection dataset and reduces GPU calculation. (2) In feature extraction network, the activation function uses the Mish activation function to enhance the learning ability of the feature extraction network, ensure the lightweight of the network, reduce the calculation cost, and maintain the accuracy. (3) Neck network consists of SPP module and FPN + PAN structure. (4) In head detection network and loss function, CIoU_Loss is the loss function, which can be expressed by [27]

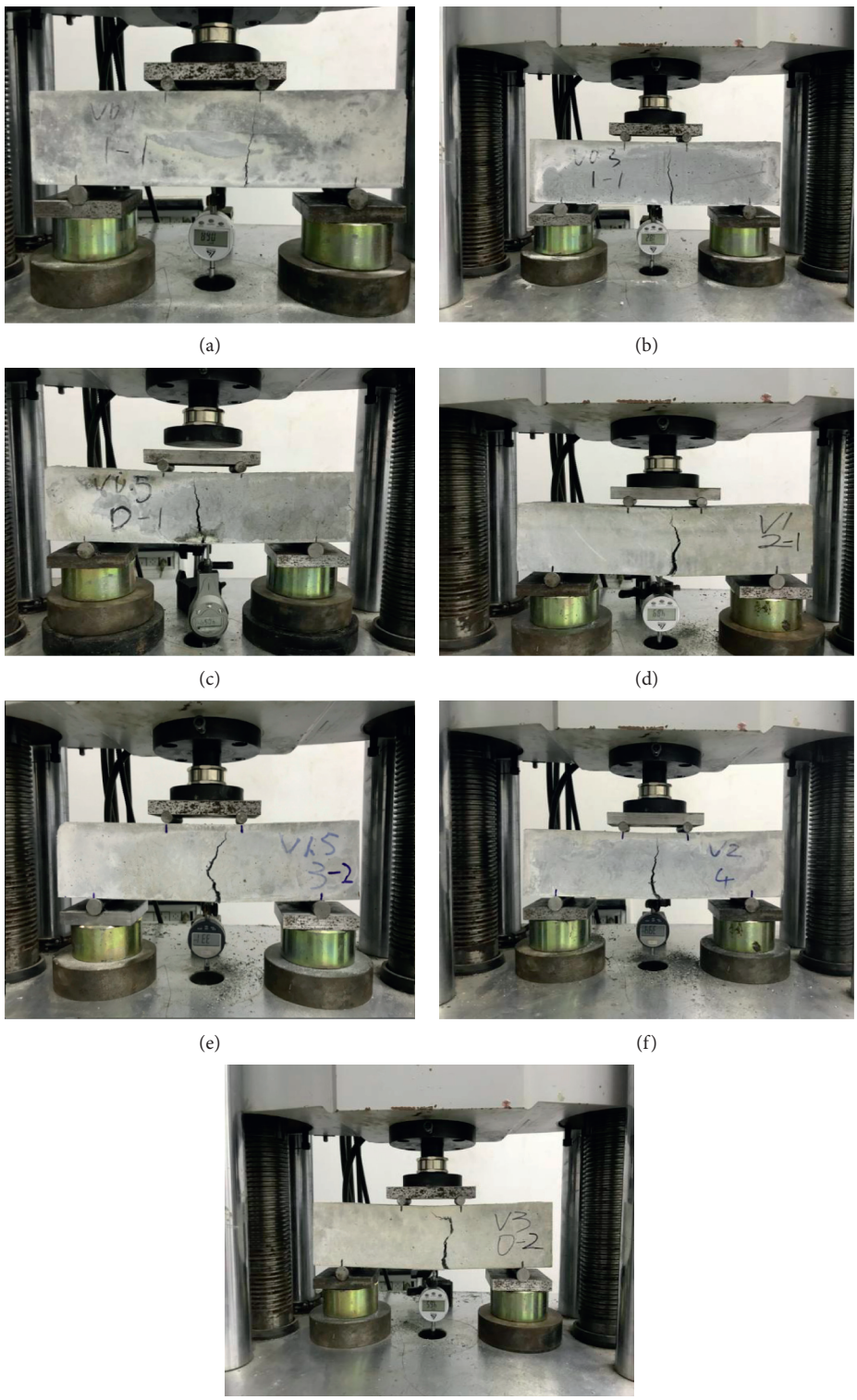

(a) (b) (c) (d) (e) (f) (g)

Figure 1: Crack image acquisition (final crack picture). (a) 0.1% steel fiber. (b) 0.3% steel fiber. (c) 0.5% steel fiber. (d) 1.0% steel fiber. (e) 1.5% steel fiber. (f) 2.0% steel fiber. (g) 3.0% steel fiber.

(a) (b)

Figure 2: Before and after cropping. (a) Before cropping. (b) After cropping.

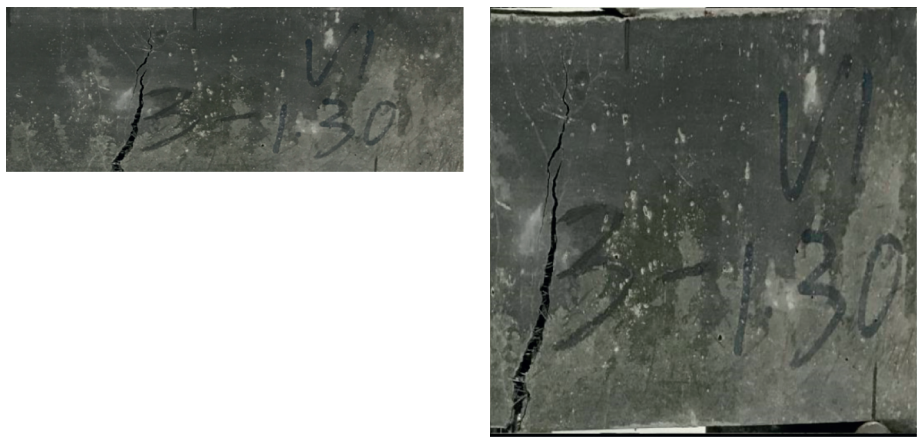

(a) (b)

Figure 3: Resizing to 512×512. (a) Original picture. (b) Reconstructed images.

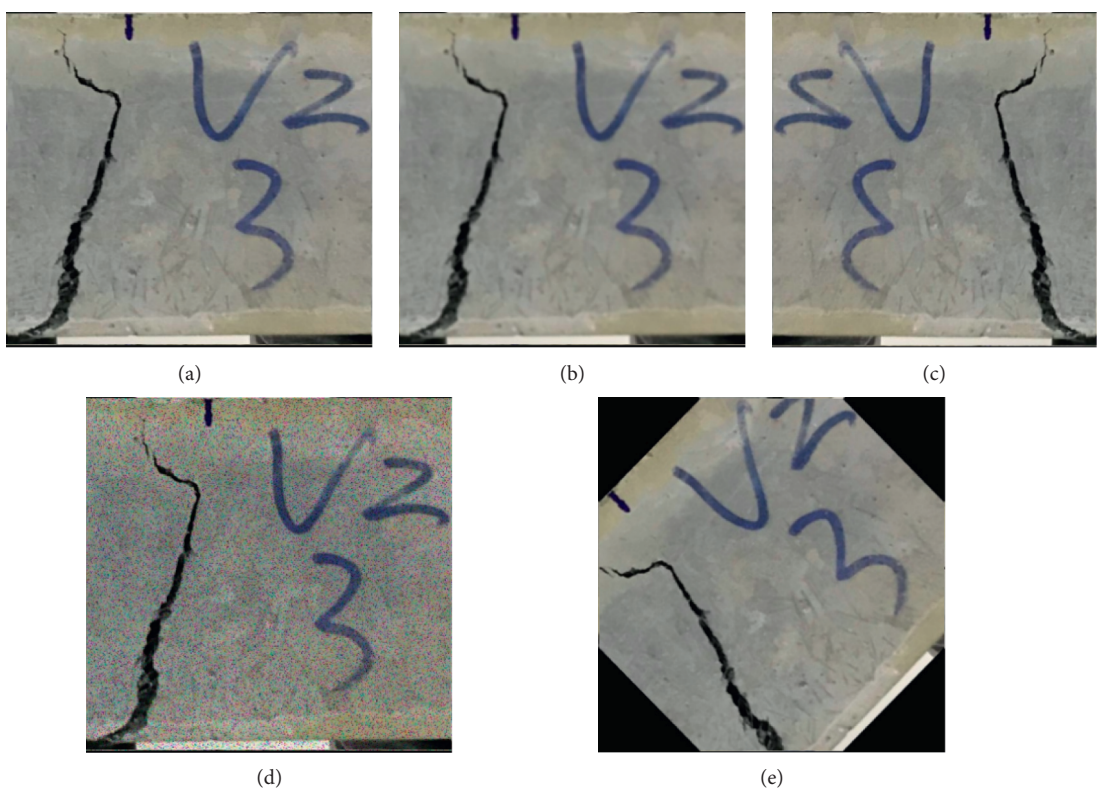

(a) (b) (c)

(d) (e)

Figure 4: Crack image data augmentation. (a) Original picture. (b) Blurring. (c) Flipping. (d) Noise adding. (e) Rotating.

$$\begin{aligned} \text{Loss}_{\text{CIOU}} &= 1 - \text{IOU} + \frac{\rho^2\left(b, b^{\text{gt}}\right)}{c^2} + \text{av}, \\ a &= \frac{v}{1 - \text{IOU} + v}, \\ v &= \frac{4}{\Pi^2}\left(\arctan\frac{\omega^{\text{gt}}}{h^{\text{gt}}} - \arctan\frac{\omega}{h}\right)^2, \end{aligned} \tag{1}$$

where $\rho^2(b, b^{gt})$ represents the Euclidean distance of the center point of the prediction box and the real box, respectively, and C represents the diagonal distance of the smallest closure region that can contain both prediction box and real box.

YOLOv4 model's parameters are as follows: (1) epoch = 100, that is, 1200 crack image data are trained for 100 times; (2) batch size = 16, that is, one round of 16 image data samples is used for model training; (3) iterations = 75, that is, 1200 pictures, 16 pictures are extracted each time, and there are 75 groups in total, i.e., one epoch is completed; (4) learning rate = 10^{-5}; and (5) momentum = 0.9.

3.2. Model of Object Detection Algorithm for Mask R-CNN. He et al. [28] proposed the Mask R-CNN algorithm model to complete the task of target detection combined with instance segmentation, and at the same time, the target was segmented at the pixel level, which can be seen in Figure 5.

The Mask R-CNN network structure includes three parts [29, 30]: (1) feature extraction network—the fusion feature map generated by feature extraction network residual network combined with feature pyramid network will cause aliasing effect, and the target detection feature map is obtained by a 3×3 convolution; (2) RPN network—$3 \times 3 \times 256$ convolution kernel is used to convolute it into $1 \times 1 \times 256$ dimensional feature results, and 2n classification and 4n coordinate regression are obtained through classification layer and regression layer; (3) head detection network and loss function—detection network includes mask branch, prediction category, and frame regression after full connection. The Mask R-CNN model is used to complete classification and location and mask generation, and its loss function is composed of the sum of three loss functions, which can be expressed by [31]

$$\begin{aligned} L &= L_{\text{cls}} + L_{\text{box}} + L_{\text{mask}}, \\ L_{\text{cls}} &= \frac{1}{N_{\text{cls}}}\sum_i L_{\text{cls}}\left(p_i, p_i*\right), \\ L_{\text{box}} &= \lambda\frac{1}{N_{\text{reg}}}\sum_i p_i * L_{\text{CIoU}}, \\ L_{\text{mask}} &= -\frac{1}{s}\sum_i \left[s_i * \lg p\left(s_i\right) - \left(1 - s_i^*\right)\lg\left(1 - p\left(s_i\right)\right)\right], \end{aligned} \tag{2}$$

where L_{cls} is the classification loss function; L_{box} is the regression loss function; L_{mask} is the average binary cross entropy; p_i is the probability of predicting the target; p_i^* indicates whether it is a real target; N_{cls} is the number of classification layers; N_{reg} is the number of regression layers; s is the sum of the total number of a category for each pixel; s_i^* is the label of the pixel category; and $p(s_i)$ is the probability of prediction category.

Mask R-CNN model's parameters are as follows: (1) epoch = 100; (2) batch size = 4; (3) iterations = 300; (4) learning rate = 10^{-5}; and (5) momentum = 0.9.

3.3. Model of Object Detection Algorithm for Improved Mask R-CNN. In order to improve the accuracy of classification and location, the Mask R-CNN algorithm in the crack detection model is improved, which mainly improves the backbone network and enhances its feature expression ability. The main network of Mask R-CNN algorithm in the crack detection model is composed of residual network and feature pyramid network [32]. Based on the repeat layer strategy network of residual network, k–1 cardinal numbers are added to each module. After splitting, the cardinal numbers are decentralized. Each cardinal number is summed and fused by multiple segmentation elements to get the output of feature graph: h, w, and c. In the Cardinal layer, the (1×1) network is convoluted into (3×3). (3×3) The input of the base array is divided into r scattered blocks, and each scattered block is transformed into the distraction module [33]. The elements are added one by one, and the feature graph is fused into the output dimension: $h \times w \times c$. Then, the fusion feature map is pooled globally, and the image spatial dimension is compressed to output dimension c. The dense c in the weight graph of each scattered block is calculated based on Softmax. The module input characteristic graph and its weight are multiplied to get the cardinality group, and then the output dimension $h \times w \times c$ is weighted and fused [34]. Distractor fuses the corresponding weights calculated from the scatter block feature graph to form ResNeSt unit module, which can be seen in Figure 6.

3.4. Evaluating Indicator. Average precision can reflect the fracture identification accuracy of the network model, which can be expressed by [35]

$$\begin{aligned} F1 &= \frac{2PR}{P + R}, \\ P &= \frac{T_P}{T_P + F_P} \times 100\%, \\ R &= \frac{T_P}{T_P + F_N} \times 100\%, \end{aligned} \tag{3}$$

where $F1$ is the average mean precision; P is the accuracy rate, that is, the proportion of correctly predicted positive case data to predicted positive case data; R is the recall rate, that is, the proportion of the predicted positive case data to the actual positive case data; T_P is the number of positive samples correctly predicted; F_P is the number of negative

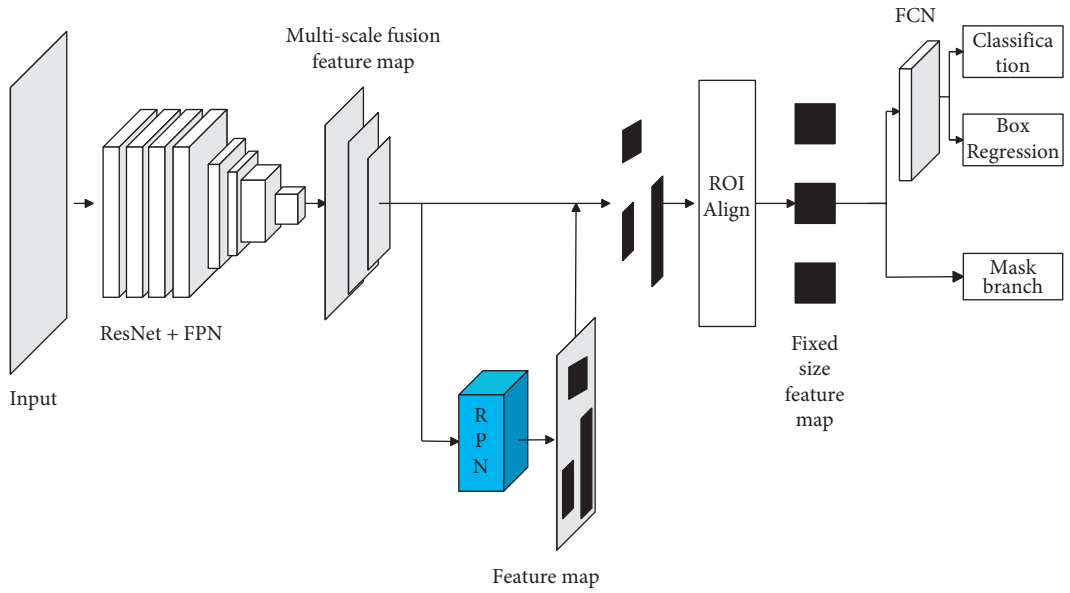

Figure 5: Mask R-CNN model frame.

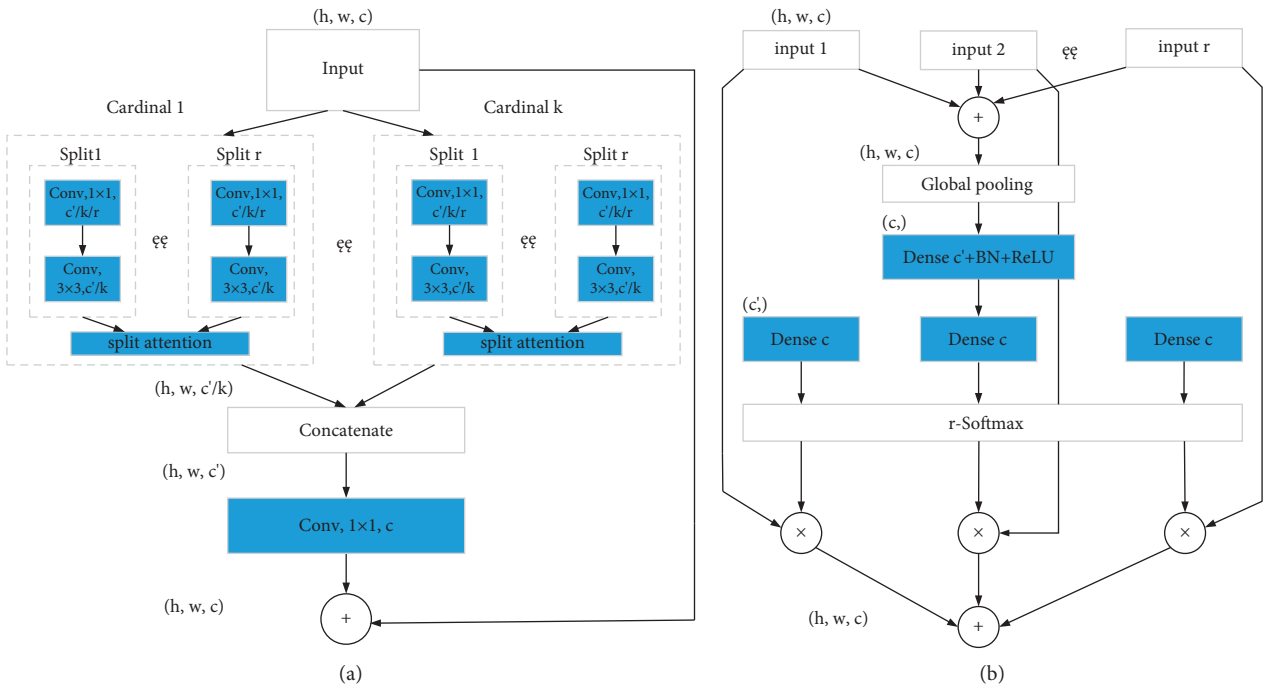

Figure 6: ResNeSt block and split attention module. (a) ResNeSt block. (b) Split attention.

samples predicted to be positive samples; and F_N represents the number of negative samples predicted by positive samples.

4. Calculation Results

4.1. Detection Results of YOLOv4. Figure 7 shows the calculation results based on the YOLOv4. The results show that the overall effect of YOLOv4 algorithm in crack detection is better, and the main reason for higher detection accuracy is that the image interference is low, and the object features are relatively simple. It can be seen from Figure 7(a) that the YOLOv4 model has carried out error detection on jamming objects. One is to detect the jamming items as cracks, and the other is to detect the jamming items as substitute numbers. The same error detection occurs in Figure 7(b), but the detection accuracy of other categories is high, which shows that the model has strong robustness.

Furthermore, the detection accuracy and average accuracy of each category are calculated, and the results are shown in Table 2.

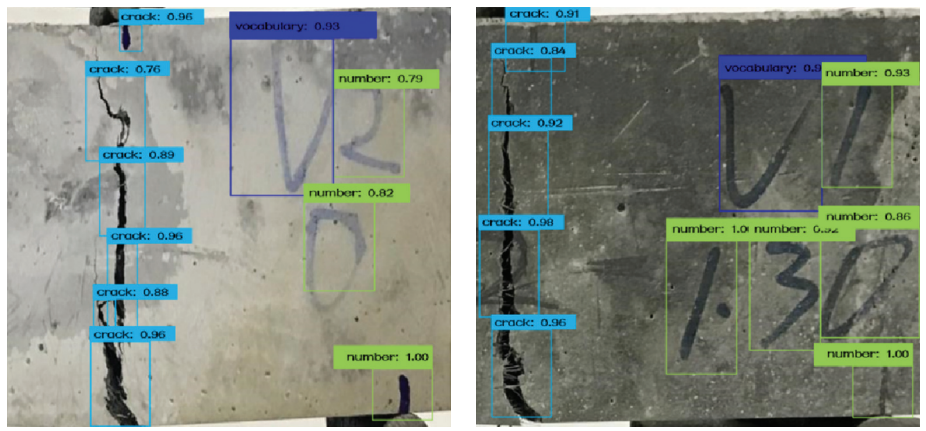

(a) (b)

Figure 7: YOLOv4 results.

Table 2: Detection results of YOLOv4.

Model	Average precision			$F1$ (%)
	Crack AP (%)	Number AP (%)	Vocabulary AP (%)	
YOLOv4	73.81	84.42	87.96	82.60

(a) (b)

Figure 8: Mask R-CNN results.

Table 3: Detection results of Mask R-CNN.

Model	Average precision			$F1$ (%)
	Crack AP (%)	Number AP (%)	Vocabulary AP (%)	
Mask R-CNN	84.32	91.26	95.73	90.44

4.2. Detection Results of Mask R-CNN. Figure 8 shows the calculation results based on Mask R-CNN. Figure 8 shows that the effect of fracture prediction is good, and the accuracy of model detection is still insufficient compared with the other two types. For example, it is difficult to detect and segment the two ends of the crack in the image, which is due to the strong background interference of the predicted image.

Furthermore, the detection accuracy and average accuracy of each category are calculated, and the results are shown in Table 3.

4.3. Detection Results of Improved Mask R-CNN. Figure 9 shows the calculation results based on the improved Mask R-CNN. As can be seen from Figure 9, the improved model

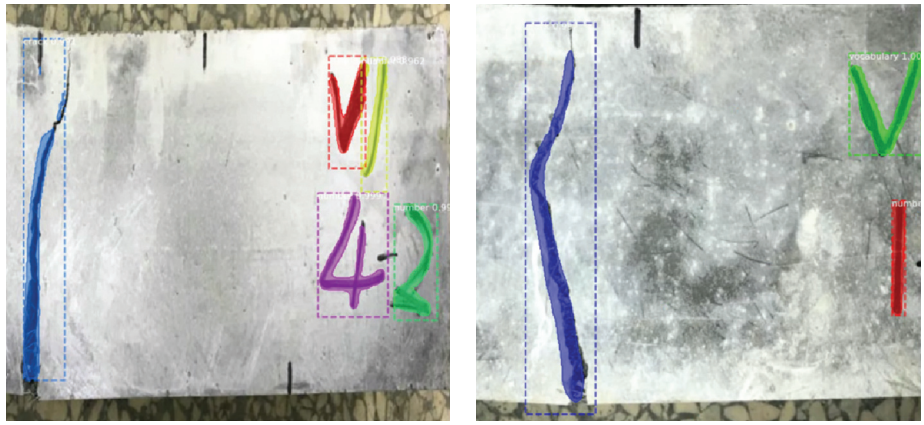

(a) (b)

Figure 9: The test results of improved Mask R-CNN crack detection model.

Table 4: Detection results of improved Mask R-CNN.

Model	Average precision			$F1$ (%)
	Crack AP (%)	Number AP (%)	Vocabulary AP (%)	
Improved Mask R-CNN	92.57	97.63	98.08	96.09

can detect and identify cracks well, and the segmentation of cracks is also more accurate.

Furthermore, the detection accuracy and average accuracy of each category are calculated, and the results are shown in Table 4.

5. Conclusion

In order to realize the intellectualization of concrete crack detection and better prevent the occurrence of accidents, in this paper, a crack recognition model of steel fiber reinforced concrete is established based on computer vision and the deep learning method. Therefore, some conclusions are drawn as follows. (1) In this paper, the crack image is obtained through the steel fiber concrete experiment, and the crack database is expanded by using the deep learning data enhancement method. (2) Based on the network of YOLOv4 and Mask R-CNN, the crack recognition model of steel fiber reinforced concrete is established, and the average recognition accuracy is 82.60% and 90.44%, respectively. (3) Based on the traditional Mask R-CNN network, this paper proposes an improved Mask R-CNN network model, and its average recognition accuracy is 96.09%. However, the environment of concrete is very complex, such as shadows, stains, and so on, which will interfere with the accuracy of crack identification in actual engineering. Therefore, we will consider the crack identification of concrete in complex environment and further identify the length and width of cracks in future research.

Data Availability

The crack database data used to support the findings of this study have been deposited in the Baidu online disk repository (https://pan.baidu.com/s/1ozcIOnY4Yl6RzRrQ-IBXUg (password: 093r)).

Ethical Approval

Ethical review and approval were waived for this study because the institutions of the authors who participated in data collection do not require IRB review and approval.

Consent

Not applicable.

Conflicts of Interest

The authors declare that they have no conflicts of interest.

Authors' Contributions

Yang Ding, Hai-Qiang Yuan, and An-Ming She finished the model. Yang Ding wrote the original manuscript. Tong-Lin Yang and Zhong-Ping Wang supervised the study. Jing-Liang Dong, Yuan Pan, and Shuang-Xi Zhou contributed to manuscript writing. All the authors discussed the results.

Acknowledgments

This study was supported by the National Key R&D Program of China (grant nos. 2019YFC1906203 and 2016YFC0700807), Key R&D Project of Jiangxi Province (grant no. 20171BBG70078), National Natural Science Foundation of China (grant nos. 51108341, 52163034, 51662008, 51968022, and 51708220), and Opening Project of Key Laboratory of Soil and Water Loss Process and Control

in Loess Plateau, Ministry of Water Resources (grant no. 201806).

References

[1] H. Bay, A. Ess, T. Tuytelaars, and L. Gool, "Speeded-up robust features (SURF)," *Computer Vision and Image Understanding*, vol. 110, no. 3, pp. 346–359, 2008.

[2] C. Y. Fu, W. Liu, A. Ranga, A. Tyagi, and A. Berg, "Dssd: deconvolutional single shot detector," arXiv preprint arXiv: 1701.06659, 2017.

[3] R. Girshick, J. Donahue, T. Darrell, and J. Malik, "Rich feature hierarchies for accurate object detection and semantic segmentation," in *Proceedings of the IEEE Conference on Computer Vision and Pattern Recognition*, pp. 580–587, Columbus, OH, USA, June 2014.

[4] T. Aoki, A. Yamada, K. Aoyama et al., "Automatic detection of erosions and ulcerations in wireless capsule endoscopy images based on a deep convolutional neural network," *Gastrointestinal Endoscopy*, vol. 89, no. 2, pp. 357 e2–363. e2, 2019.

[5] N. Dalal and B. Triggs, "Histograms of oriented gradients for human detection,"vol. 1, pp. 886–893, in *Proceedings of the 2005 IEEE Computer Society Conference on Computer Vision and Pattern Recognition (CVPR'05)*, vol. 1, pp. 886–893, IEEE, Washington, DC, USA, June 2005.

[6] Y. Chen, J. Li, H. Xiao, J. Xiaojie, Y. Shuicheng, and F. Jiashi, "Dual path networks," arXiv preprint arXiv:1707.01629, 2017a.

[7] F. Wang, M. Jiang, C. Qian et al., "Residual attention network for image classification," in *Proceedings of the IEEE Conference on Computer Vision and Pattern Recognition*, pp. 3156–3164, Venice, Italy, October 2017.

[8] G. Huang, Z. Liu, L. Van Der Maaten, and K. Weinberger, "Densely connected convolutional networks," in *Proceedings of the IEEE Conference on Computer Vision and Pattern Recognition*, pp. 4700–4708, Honolulu, HI, USA, July 2017.

[9] Y. Chen, C. Zhang, T. Qiao, J. Xiong, and B. Liu, "Ship detection in optical sensing images based on YOLOv5," in *Proceedings of the Twelfth International Conference on Graphics and Image Processing (ICGIP 2020)*, p. 117200E, November 2020.

[10] A. Radford, L. Metz, and S. Chintala, "Unsupervised representation learning with deep convolutional generative adversarial networks," *Computer science*, arXiv: 1511.06434v2, 2015.

[11] Y. Yu, K. Zhang, L. Yang, and D. Zhang, "Fruit detection for strawberry harvesting robot in non-structural environment based on Mask R-CNN," *Computers and Electronics in Agriculture*, vol. 163, Article ID 104846, 2019a.

[12] G. E. Hinton, S. Osindero, and Y. W. Teh, "A fast learning algorithm for deep belief nets," *Neural Computation*, vol. 18, no. 7, pp. 1527–1554, 2006.

[13] A. Krizhevsky, I. Sutskever, and G. E. Hinton, "Imagenet classification with deep convolutional neural networks," in *Proceedings of the Advances in Neural Information Processing Systems*, pp. 1097–1105, Long Beach, CA, USA, December 2012.

[14] R. Girshick, "Fast R-CNN," in *Proceedings of the IEEE International Conference on computer vision*, pp. 1440–1448, Santiago, Chile, December 2015.

[15] S. Ren, K. He, R. Girshick, and J. Sun, "Faster R-CNN: towards real-time object detection with region proposal networks," in *Proceedings of the Advances in Neural Information Processing Systems*, pp. 91–99, Montreal, QC, Canada, December 2015.

[16] T. Y. Lin, P. Dollár, R. Girshick, H. Kaiming, H. Bharath, and B. Serge, "Feature pyramid networks for object detection," in *Proceedings of the IEEE Conference on Computer Vision and Pattern Recognition*, pp. 2117–2125, Venice, Italy, October 2017.

[17] J. Redmon, S. Divvala, R. Girshick, and A. Farhadi, "You only look once: unified, real-time object detection," in *Proceedings of the IEEE Conference on Computer Vision and Pattern Recognition*, pp. 779–788, Las Vegas, NV, USA, June 2016.

[18] S. Du, P. Zhang, B. Zhang, and H. Xu, "Weak and occluded vehicle detection in complex infrared environment based on improved YOLOv4," *IEEE Access*, vol. 9, pp. 25671–25680, 2021.

[19] Y. Yu, C. Wang, X. Gu, and J. Li, "A novel deep learning-based method for damage identification of smart building structures," *Structural Health Monitoring*, vol. 18, no. 1, pp. 143–163, 2019b.

[20] J. Pang, H. Zhang, C. Feng, and L. Li, "Research on crack segmentation method of hydro-junction project based on target detection network," *KSCE Journal of Civil Engineering*, vol. 24, no. 9, pp. 2731–2741, 2020.

[21] Z. Yu, Y. Shen, and C. Shen, "A real-time detection approach for bridge cracks based on YOLOv4-FPM," *Automation in Construction*, vol. 122, Article ID 103514, 2021.

[22] S. Luan, C. Chen, B. Zhang, C. Xianbin, H. Jungong, and L. Jianzhuang, "Gabor convolutional networks," *IEEE Transactions on Image Processing*, vol. 27, no. 9, pp. 4357–4366, 2018.

[23] Y. J. Cha, W. Choi, and O. Büyüköztürk, "Deep learning-based crack damage detection using convolutional neural networks," *Computer-Aided Civil and Infrastructure Engineering*, vol. 32, no. 5, pp. 361–378, 2017.

[24] C. A. Ferreira, T. Melo, P. Sousa, and M. Meyer, "Classification of breast cancer histology images through transfer learning using a pre-trained inception resnet v2," in *Proceedings of the International Conference Image Analysis and Recognition*, pp. 763–770, Springer, Halifax, Canada, July 2018.

[25] A. Bochkovskiy, C. Y. Wang, and H. Y. M. Liao, "Yolov4: optimal speed and accuracy of object detection," arXiv preprint arXiv:2004.10934, 2020.

[26] J. Redmon and A. Farhadi, "YOLO9000: better, faster, stronger," in *Proceedings of the IEEE Conference on Computer Vision and Pattern Recognition*, pp. 7263–7271, Venice, Italy, October 2017.

[27] Z. Zheng, P. Wang, W. Liu, L. Jinze, Y. Rongguang, and R. Dongwei, "Distance-IoU loss: faster and better learning for bounding box regression," *AAAI Conference on Artificial Intelligence*, vol. 34, no. 7, pp. 12993–13000, 2020.

[28] K. He, G. Gkioxari, P. Dollár, and R. Girshick, "Mask R-CNN," in *Proceedings of the IEEE International Conference on Computer Vision*, pp. 2961–2969, Venice, Italy, October 2017.

[29] X. Sun, P. Wu, and S. C. H. Hoi, "Face detection using deep learning: an improved faster R-CNN approach," *Neurocomputing*, vol. 299, pp. 42–50, 2018.

[30] L. C. Chen, G. Papandreou, F. Schroff, and H. Adam, "Rethinking atrous convolution for semantic image segmentation," arXiv preprint arXiv:1706.05587, 2017.

[31] H. Yan, H. Lu, M. Ye, K. Yan, Y. Xu, and Q. Jin, "Improved mask R-CNN for lung nodule segmentation," in *Proceedings of the 2019 10th International Conference on Information Technology in Medicine and Education (ITME)*, pp. 137–141, Qingdao, China, August 2019.

[32] X. Shao, H. Zhu, D. Guo, R. Zheng, and J. Wei, "Research on detection of large coal blockage at the transfer point of belt conveyor based on improved mask R-CNN," *IOP Conference*

Series: Earth and Environmental Science, vol. 440, no. 5, Article ID 052028, 2020.

[33] L. Zuo, P. He, C. Zhang, and Z. Zhang, "A robust approach to reading recognition of pointer meters based on improved mask-RCNN," *Neurocomputing*, vol. 388, pp. 90–101, 2020.

[34] Y. Wang, J. Wu, and H. Li, "Human detection based on improved mask R-CNN," *Journal of Physics: Conference Series*, vol. 1575, Article ID 012067, 2020.

[35] K. He, X. Zhang, S. Ren, and J. Sun, "Deep residual learning for image recognition," in *Proceedings of the IEEE Conference on Computer Vision and Pattern Recognition*, pp. 770–778, Las Vegas, NV, USA, June 2016.

Hindawi
Advances in Materials Science and Engineering
Volume 2021, Article ID 4100896, 9 pages
https://doi.org/10.1155/2021/4100896

Research Article

Research on Intelligent Compaction Technology of Subgrade Based on Regression Analysis

Ziyi Hou,[1] Xiao Dang,[1] Yezhen Yuan,[2] Bo Tian,[3] and Sili Li[3]

[1]*School of Civil Engineering and Transportation, Hebei University of Technology, Tianjin 300401, China*
[2]*Chongqing Jiaotong University, Chongqing 400074, China*
[3]*Research Institute of Highway Ministry of Transport, Beijing 100088, China*

Correspondence should be addressed to Sili Li; decoli27@gmail.com

Received 7 June 2021; Revised 3 August 2021; Accepted 3 August 2021; Published 9 September 2021

Academic Editor: Yongsheng Yao

A remote monitoring system with the intelligent compaction index CMV as the core is designed and developed to address the shortcomings of traditional subgrade compaction quality evaluation methods. Based on the actual project, the correlation between the CMV and conventional compaction indexes of compaction degree K and dynamic resilient modulus E is investigated by applying the one-dimensional linear regression equation for three types of subgrade fillers, clayey gravel, pulverized gravel, and soil-rock mixed fill, and the scheme of fitting CMV to the mean value of conventional indexes is adopted, which is compared with the scheme of fitting CMV to the single point of conventional indexes in the existing specification. The test results show that the correlation between the CMV and conventional indexes of clayey gravel and pulverized gravel is much stronger than that of soil-rock mixed subgrades, and the correlation coefficient can be significantly improved by fitting CMV to the mean of conventional indexes compared with single-point fitting, which can be considered as a new method for intelligent rolling correlation verification.

1. Introduction

Subgrade soil settlement beneath pavements is a major concern for engineers [1]. Compaction plays an important role in improving the strength of the subgrade and pavement [2], and in long-term engineering practice, a variety of compaction quality evaluation indexes have been formed at home and abroad, mainly including two categories of physical testing indexes represented by compaction degree and mechanical indexes represented by elastic modulus [3, 4], although the testing methods and principles of these evaluation indexes are different, but most of them have low testing efficiency, poor representation, lagging results, and other disadvantages. With the continuous development of the engineering industry, there is an urgent need for a device that can test compaction with the vehicle, which can display the compaction test results in real time and guide the operator to operate reasonably. The corresponding detection systems have been developed in Sweden, Germany, USA, Japan, and China, and various compaction control indicators based on the harmonic method have been proposed, such as CMV [5–7] in Sweden and CCV [8–10] in Japan. Intelligent compaction technology can continuously and comprehensively reflect the compaction information of the subgrade, and when using the intelligent compaction system to quantitatively evaluate the compaction quality, the correlation between CMV and conventional indicators needs to be established, but this relationship is not fixed because CMV indicators are affected by multiple factors such as roller type, vibration frequency, and soil type. It is stipulated in JT/T 1127-2017 [11] that, before carrying out intelligent compaction control, the one-dimensional linear regression equation between the intelligent compaction index and the conventional index is established by point-to-point coordinate correspondence, and the correlation coefficient must be ensured to be above 0.7.

The existing intelligent compaction equipment is mainly oriented to the use of compaction operators, and the

secondary development is difficult and expensive to meet the requirements of actual projects. In view of this, this paper designs a subgrade intelligent compaction system with CMV as the core, using GPS technology [12], sensor technology [13], wireless transmission [14], and other key technologies to realize the real-time remote monitoring of compaction quality information.

Because the conventional fitting method does not consider the influence of the two testing methods in the roller wheel width direction on the correlation coefficient, this paper proposes an improved scheme for fitting CMV with the average value of conventional indicators along the wheel width direction, and relying on the Nanning Shajing-Wuxu Expressway project, three filler types of subgrades are selected to fit the relationship between CMV and conventional quality control indexes of compaction K and dynamic resilient modulus E [15–17], respectively.

2. Intelligent Laminating System

2.1. System Architecture. In order to realize the comprehensive real-time control of highway subgrade compaction and meet the integrated management needs of the compactor operator, construction unit, establishment unit, and owner, the design and development of the subgrade intelligent compaction system is carried out with the thinking of Internet of Things [18] as the guide. The overall architecture of the system is shown in Figure 1, which mainly contains the data acquisition layer, compaction data transmission layer, and application layer at the local end of the roller, where the data acquisition layer mainly includes hardware such as piezoelectric vibration sensors, GNSS antennas, 4G/WiFi antennas, data processing units, and intelligent display terminals. In the process of roller rolling, the vibration signal and high-precision positioning coordinate data of the vibrating wheel are unified and summarized with the data processing unit, and after certain algorithms are solved, compaction trajectory, compaction number, compaction thickness, compaction degree, and other compaction quality parameters are formed. The intelligent display terminal will visualize these data and provide key information in the form of images, figures, sounds, etc., to guide the compactor operator to operate reasonably.

The data transmission layer is mainly for 4G signal remote transmission to achieve effective data upload and data sharing among rollers. In view of the weak 4G network in some areas, wireless AP bridging network is used to solve the data transmission problem, and data transmission and sharing are realized through the WiFi module of the vehicle system.

The application layer mainly includes application service, data service, cloud platform access, and key indicator warning. With the background of the raster map [19], computer graphics and numerical values are used to dynamically display roller operation information, and managers can log in to the website to query the real-time dynamics of the roller, historical playback, quality reports, and many other contents, which can effectively improve management efficiency and save management costs, while the early warning system on the cell phone can push the information of the warning unqualified area in real time to achieve early detection of problems and early treatment and improve the process of construction quality control management.

2.2. Core Metrics Algorithm. The basic principle of intelligent compaction is to view the roller as a loading system acting on the subgrade and to reflect the compaction degree of the subgrade by using the spectrum analysis of the dynamic corresponding signal between the vibrating wheel and the soil, so as to realize the compaction quality detection of the whole rolling surface. The intelligent compaction system reflects the compaction degree size by the distortion degree of the acceleration signal, and its key index is the CMV, which is calculated by first collecting the compaction signal into the acceleration signal collector and then using the fast Fourier transform (FFT) [20, 21] technique for spectrum analysis to obtain the amplitude of each frequency component under different force states and find the fundamental frequency signal amplitude and the first harmonic amplitude. The intelligent compaction CMV corresponding to the intelligent compaction system can be expressed by the following equation [22]:

$$\mathrm{CMV} = C\frac{A_1}{A_0}, \tag{1}$$

where A_1 is the first harmonic amplitude, A_0 is the fundamental frequency signal amplitude, and C is a fixed constant.

As the data processing unit for acceleration signal processing, it is not possible to calculate all signals but only selectively intercept one section for calculation and analysis, which requires the use of window functions [23] to achieve; the common window functions are the rectangular window, triangular window, Hanning window, etc. After a comprehensive comparison of the applicability of the window functions, the Hanning window [11] is selected for signal calculation, and its function is

$$f(t) = \begin{cases} \dfrac{1}{T}\left(\dfrac{1}{2} + \dfrac{1}{2}\cos\dfrac{\pi t}{T}\right), & 0 \le |t| \le T, \\ 0, & |t| \ge T. \end{cases} \tag{2}$$

For every 20 cm of roller travel, the intelligent rolling system performs a data calculation, and the CMV over the full width of the roller's vibrating wheel is considered to be the same value.

3. Regression Analysis Field Test Protocol

3.1. Overview of the Test Site. The new project of Nanning Shajing-Wuxu Expressway is 25.8 km long, divided into two sections, most areas are filled with clay gravel and powdery gravel, and a few areas are filled with earth rock mixture; the basic physical properties of the filler are shown in Table 1.

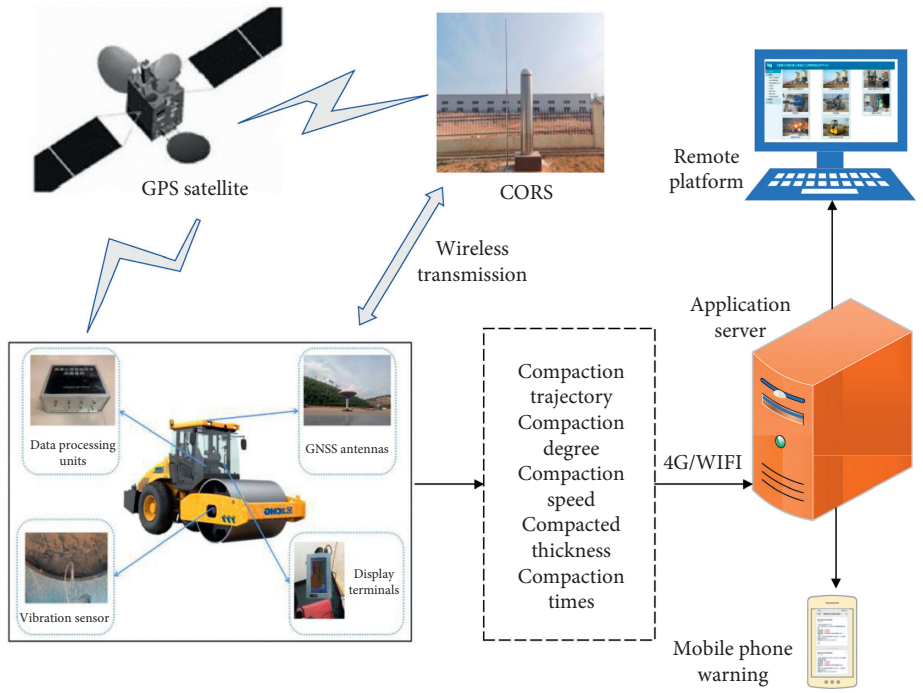

Figure 1: Overall system design diagram.

3.2. Test Equipment. This test involves the data collection of intelligent compaction index CMV and conventional compaction evaluation index, intelligent rolling equipment has been described in the previous section, conventional compaction index using compaction degree and dynamic resilient modulus, of which compaction degree is strictly in accordance with the "Highway Road Base Pavement Field Determination Procedure" JTG E60-2008 [24] requirements using the sand filling method of experimental determination, dynamic resilient modulus using KFD- 100A light falling hammer bending, and sinking instrument (PFWD); the basic parameters of the instrument are shown in Table 2.

Lightweight drop hammer-type bending instrument obtains load by impacting a rigid bearing plate located on the surface of the subgrade with the hammer falling freely, and the impact load and displacement due to the falling hammer are measured by load and acceleration sensors. The displacements are obtained by quadratic integration of the accelerations. In determining the modulus of resilient of the subgrade, the elastic half-space theory model was used for calculation [25, 26]. The dynamic resilient modulus is calculated as

$$E = \frac{\left(1 - v^2\right)p}{2rD}, \tag{3}$$

where E represents the dynamic resilient modulus measured by the system (MPa), P represents the load (N), D represents the displacement (m), r represents the radius of the bearing plate (m), and V represents Poisson's ratio.

Vibratory roller is the material carrier for the realization of intelligent rolling technology. To ensure the reliability of the data, XS263J, a roller model, is used for the whole experiment, and its basic performance parameters are shown in Table 3.

3.3. Test Methodology. The subgrade fill involved three forms of clayey gravel, pulverized gravel, and soil-rock mixed fill, so three test sections were selected to carry out the tests independently, and in order to ensure the comparability of the test results, the roller models, construction techniques, and test methods were identical at the three test sites.

In order to avoid the data collection being too concentrated and affecting the fitting effect, the roller was rolled 3 times and 5 times throughout 7 times along the three paths, and the system automatically generated the CMV of the rolling area during the rolling process. As shown in Figure 2, six inspection points were set up uniformly in each rolling area, and the spacing between adjacent inspection points in the same rolling strip was 10 m. In view of the lossy detection of sand filling, the dynamic resilient modulus E was firstly detected, and then the compaction was detected at the same position.

3.4. Fitting Method. Depending on the number of samples per test point and the fitting method, the correlation calibration can be further refined into the following two schemes.

3.4.1. Scheme 1: CMV and Conventional Index Single-Point Fit. From the perspective of GPS coordinate correspondence, the first scheme uses the point-to-point fitting

Table 1: Physical indicators of the filler.

Embankment type		Maximum dry density (g/cm^3)	Optimum moisture content (%)	Liquid limit (%)	Plastic limit (%)	Curvature factor	Unevenness factor
Earthwork Embankment	Clayey gravel	2.16	6.9	22.9	16.7	—	—
	Pulverized gravel	1.94	10.2	34.1	23.9	—	—
Soil and stone mixed fill		2.35	4.3	—	—	1.8	15.5

Table 2: PFWD performance parameters.

Projects	Performance parameters
Load-bearing plate diameter	100 mm
Falling height	50–530 mm
Load sensors	Rated range 20 kN
Acceleration sensor	Rated range 500 m/s^2
Height	1100 mm
Weight	15 kg

Table 3: Roller parameters.

Projects	Operating weight of the whole machine (kg)	Vibrating wheel width (mm)	Vibration frequency (Hz)	Nominal amplitude (mm)	Excitation force (kg)	Front wheel distribution mass (kg)	Rear wheel distribution mass (kg)	Vibrating wheel diameter (mm)
Parameters	26000	2170	27/32	1.9/0.95	405/290	13000	13000	1600

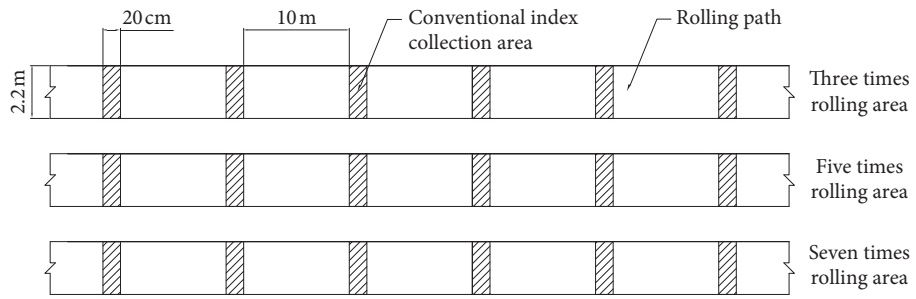

Figure 2: Overall arrangement of sampling points for conventional indicators.

method in JT/T 1127-2017. As shown in Figure 3(a), the compaction area represented by one CMV is a rectangular area of 2.2 m in length and 20 cm in width, and the conventional indexes are tested at the center of this area. In the end, one CMV, one dynamic resilient modulus, and one compaction value are collected at each test point, and a total of 18 test points are collected for the three compaction strips, generating 18 sets of such corresponding data for further fitting analysis.

3.4.2. Scheme 2: CMV and Conventional Index Mean Fit. The compaction value and dynamic resilient modulus reflect the compaction effect of a circular area with a diameter of about 20–30 cm, and the influence area is much smaller than the rectangular area represented by one CMV. Considering that the actual conventional indexes may have some variability along the wheel width direction, in order to reduce the influence of single-point abnormal data on the fitting effect, the test scheme was improved on the basis of scheme 1, and multiple points were carried out along the wheel width direction of the roller. The conventional indexes were collected as shown in Figure 3(b), and the average value of five detection points was used as the conventional indexes in the region and further linearly fitted with the CMVs.

3.5. Correlation Analysis of the CMV and Conventional Indicators

3.5.1. Establishing a Mathematical Model for the Calibration of Intelligent Compaction Indicators and Conventional Indicators. To establish the linear relationship between the CMV and conventional indicators, first, draw a scatter plot in a plane coordinate system with CMV as the x-coordinate and conventional indicators as the y-coordinate, and seek a straight line so that the sum of squares of the vertical

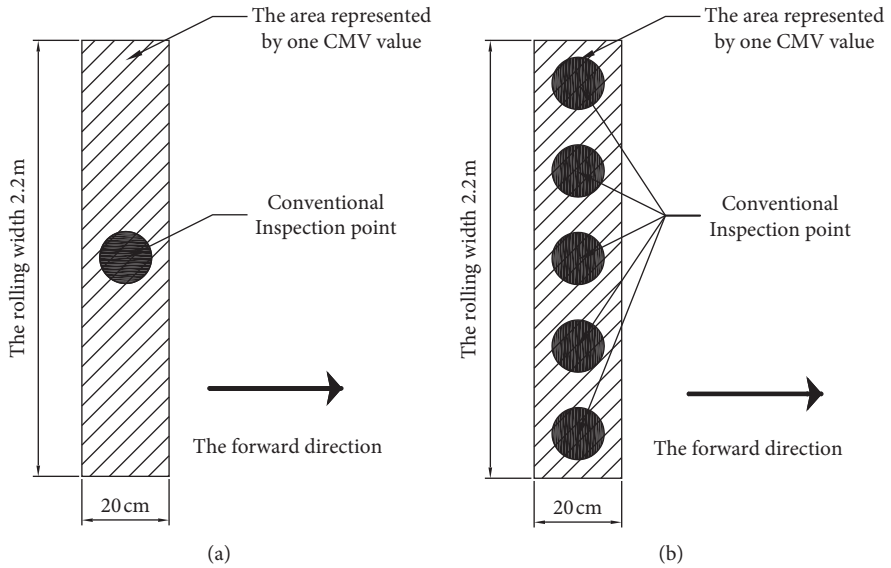

Figure 3: Fitting scheme. (a) Single-point fitting. (b) Multipoint mean fit.

distance from each scatter point to the line is minimized, that is, the minimum value point of the demand function:

$$S(a,b) = \sum_{k=1}^{m} \left[(a + bx_k) - y_k\right]^2. \tag{4}$$

Function (4) finds the first-order partial derivatives of the two variables a and b, respectively, giving

$$\begin{aligned} \frac{\partial S}{\partial a} &= 2\sum_{k=1}^{m}\left[(a + bx_k) - y_k\right], \\ \frac{\partial S}{\partial a} &= 2\sum_{k=1}^{m}\left[(a + bx_k) - y_k\right]x_k. \end{aligned} \tag{5}$$

Letting it to be equal to 0, the regular system of equations is obtained as

$$\begin{bmatrix} \mathrm{ma} + \sum_{k=1}^{m} bx_k = \sum_{k=1}^{m} y_k \\ \sum_{k=1}^{m} ax_k + \sum_{k=1}^{m} bx_k^2 = \sum_{k=1}^{m} x_k y_k \end{bmatrix}. \tag{6}$$

To determine the unknown parameters a and b in the regression equation, it is necessary to solve the regular system of equations:

$$\begin{bmatrix} m & \sum_{k=1}^{m} x_k & \cdots & \sum_{k=1}^{m} x_k^n \\ \sum_{k=1}^{m} x_k & \sum_{k=1}^{m} x_k^2 & \cdots & \sum_{k=1}^{m} x_k^n \\ \vdots & \vdots & \vdots & \vdots \\ \sum_{k=1}^{m} x_k^n & \sum_{k=1}^{m} x_k^{n+1} & \cdots & \sum_{k=1}^{m} x_k^{2n} \end{bmatrix} \begin{bmatrix} a_0 \\ a_1 \\ \vdots \\ a_n \end{bmatrix} = \begin{bmatrix} \sum_{k=1}^{m} y_k \\ \sum_{k=1}^{m} x_k y_k \\ \vdots \\ \sum_{k=1}^{m} x_k^n y_k \end{bmatrix}. \tag{7}$$

For each test in the field, the intelligent compaction value CMV and a single conventional compaction index (compaction or dynamic resilient modulus) comprised 18 sets of one-to-one corresponding two-dimensional data, and regression fitting was performed with the clayey gravel CMV and single-point compaction K. The collected test data are shown in Table 4.

A straight line fit of $y = a + bx$, with a and b being the regression coefficients, is performed on the data in Table 4, and substituting the data into the regular set of equations yields

$$\begin{bmatrix} 18 & 537.6 \\ 537.6 & 18107 \end{bmatrix} \begin{bmatrix} a \\ b \end{bmatrix} = \begin{bmatrix} 1656.5 \\ 50179.5 \end{bmatrix}. \tag{8}$$

The solution yields $a = 81.755$ and $b = 0.344$, so the fitted equation for the clayey gravel CMV and single-point compaction K is $y = 0.344x + 81.755$, i.e., $K = 0.344\mathrm{CMV} + 81.755$. To further verify the reliability of this regression equation fitting the actual data, a correlation test needs to be carried out, and the correlation coefficient is defined as

$$r = \frac{\sum_{k=1}^{m}(x_k - \overline{x})(y_k - \overline{y})}{\sqrt{\sum_{k=1}^{m}(x_k - \overline{x})^2 \sum_{i=1}^{n}(y_k - \overline{y})^2}}. \tag{9}$$

Substituting the data into equation (9), the correlation coefficient $r = 0.81$, and 0.7 is taken as the cutoff point for the strength of correlation in JT/T 1127-2017, which indicates that the clayey gravel CMV has a good correlation with the single-point compaction K and meets the needs of engineering applications.

3.6. CMV and Single-Point Conventional Index Fitting. Figure 4 shows the correlation verification results between the CMV and single-point compactness in the test section of clayey gravel, pulverized gravel, and soil-rock mixed fill. The

Table 4: Statistics of the CMV and single-point compaction of clayey gravel.

Serial number	CMV	Compaction degree K (%)	Serial number	CMV	Compaction degree K (%)
1	18.2	84.7	10	30	93.2
2	12.4	87.1	11	28.6	93.8
3	22.7	86.5	12	30.2	93.8
4	19.6	83.4	13	26	96.4
5	18.5	86.3	14	45.6	96.6
6	11.2	88.2	15	42.1	96.7
7	36.7	93.1	16	39.5	96.5
8	36.5	93.4	17	44.3	96.4
9	42.5	93.7	18	33	96.7

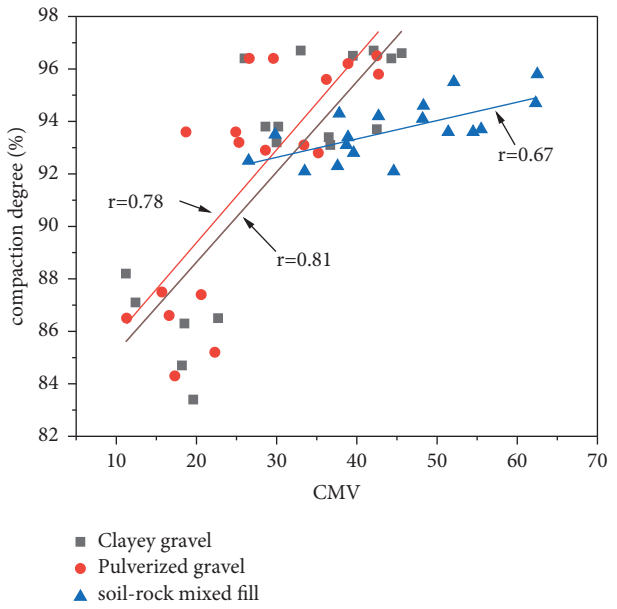

Figure 4: CMV and single-point compaction degree fit.

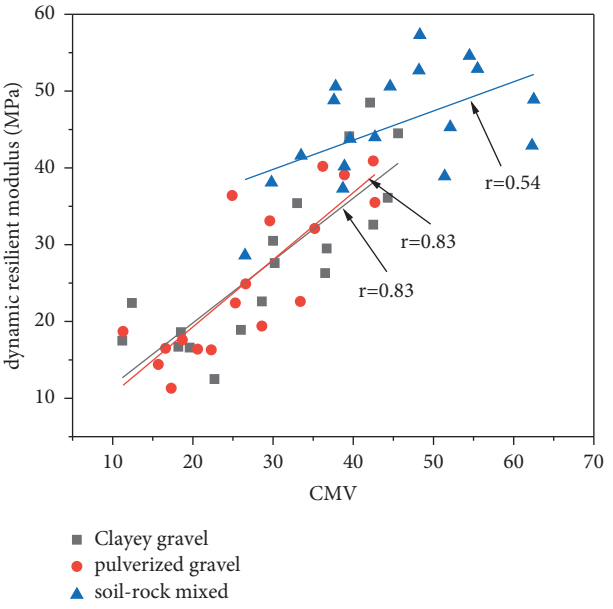

Figure 5: CMV and single-point dynamic resilient modulus fit.

correlation coefficients of the CMV and compaction in these three test sections are 0.81, 0.78, and 0.67, respectively. The correlation between the CMV and compaction is stronger for the clayey gravel and pulverized gravel sections, while the correlation between the CMV and compaction is weaker for the soil-rock mixed section. Figure 5 shows the correlation verification results between the CMV and single-point dynamic resilient modulus in the test section of clayey gravel, pulverized gravel, and soil-rock mixed fill. The correlation coefficients of the CMV and dynamic resilient modulus in these three test sections are 0.83, 0.83, and 0.54, respectively. Similarly, the correlation between the CMV and dynamic resilient modulus is stronger for the clayey gravel and pulverized gravel sections, while the correlation between the CMV and dynamic resilient modulus is weaker for the soil-rock mixed section.

3.7. CMV and Conventional Index Mean Fit. Figure 6 shows the correlation verification results between the CMV and compaction degree mean value, and the correlation coefficients for the clayey gravel, pulverized gravel, and soil-stone

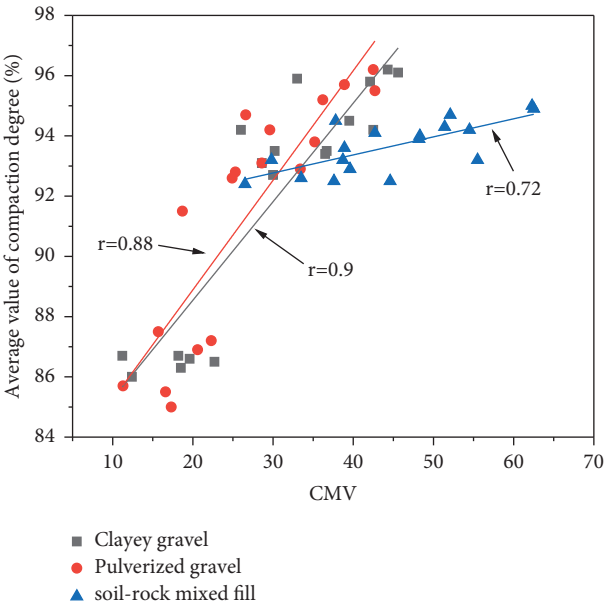

Figure 6: CMV and compaction degree mean value fit.

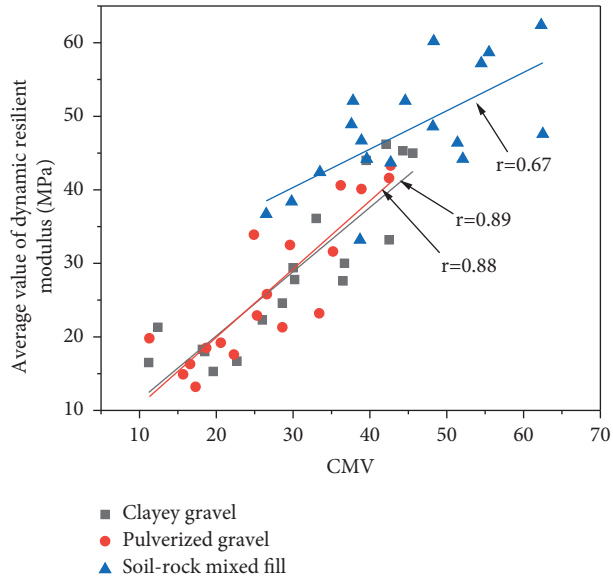

Figure 7: CMV and dynamic resilient modulus mean value fit.

Table 5: Correlations of different fitting schemes.

Fitting scheme	General indicators	Soil type	Regression equation	Correlation coefficient
Single-point fit of the CMV to conventional metrics	Compaction degree (%)	Clayey gravel	$Y = 0.34397x + 81.75453$	0.81
		Pulverized gravel	$Y = 0.35442x + 82.2894$	0.78
		Soil and stone mixed fill	$Y = 0.07004x + 90.53055$	0.67
	Dynamic resilient modulus (MPa)	Clayey gravel	$Y = 0.81216x + 3.57135$	0.83
		Pulverized gravel	$Y = 0.87405x + 1.81463$	0.83
		Soil and stone mixed fill	$Y = 0.38024x + 28.39997$	0.54
CMV and conventional index mean fit	Compaction degree (%)	Clayey gravel	$Y = 0.32728x + 81.99755$	0.9
		Pulverized gravel	$Y = 0.36386x + 81.61207$	0.88
		Soil and stone mixed fill	$Y = 0.05995x + 90.97041$	0.72
	Dynamic resilient modulus (MPa)	Clayey gravel	$Y = 0.87403x + 2.65116$	0.89
		Pulverized gravel	$Y = 0.9277 + 1.39252$	0.88
		Soil and stone mixed fill	$Y = 0.52152 + 24.67414$	0.67

mix sections are 0.9, 0.89, and 0.72, respectively. The correlation between the CMV and compaction degree mean value is relatively weak in the soil-stone mixed section, but it also meets the requirements of use. Figure 7 shows correlation verification results between the CMV and dynamic resilient modulus mean value, and the correlation coefficients for the clayey gravel, pulverized gravel, and soil-stone mix sections are 0.89, 0.88, and 0.67, respectively.

3.8. Comparative Analysis of the Fitting Effect. The correlation between the intelligent compaction index CMV and the conventional index compaction and dynamic resilient modulus under three kinds of subgrade fillers was established through field tests, and the correlation was checked for two fitting methods, point to point and point to average, and the correlation is shown in Table 5.

In order to further compare the differences between the two fitting methods, the correlation coefficients of point-to-point fitting and point-to-mean fitting were compared under different soils with the same conventional indexes, and the results are shown in Figure 8, which shows that the correlation coefficients of both the fitting of CMV and compaction and the fitting of the CMV and dynamic resilient modulus are higher than those of single-point fitting; especially, the mean fitting can improve the correlation coefficient of soil-rock mixed subgrade. The correlation coefficient between CMV and compaction can be improved from 0.67 to 0.72, from a weak correlation to a strong correlation, which is of great significance in practical applications. This indicates that

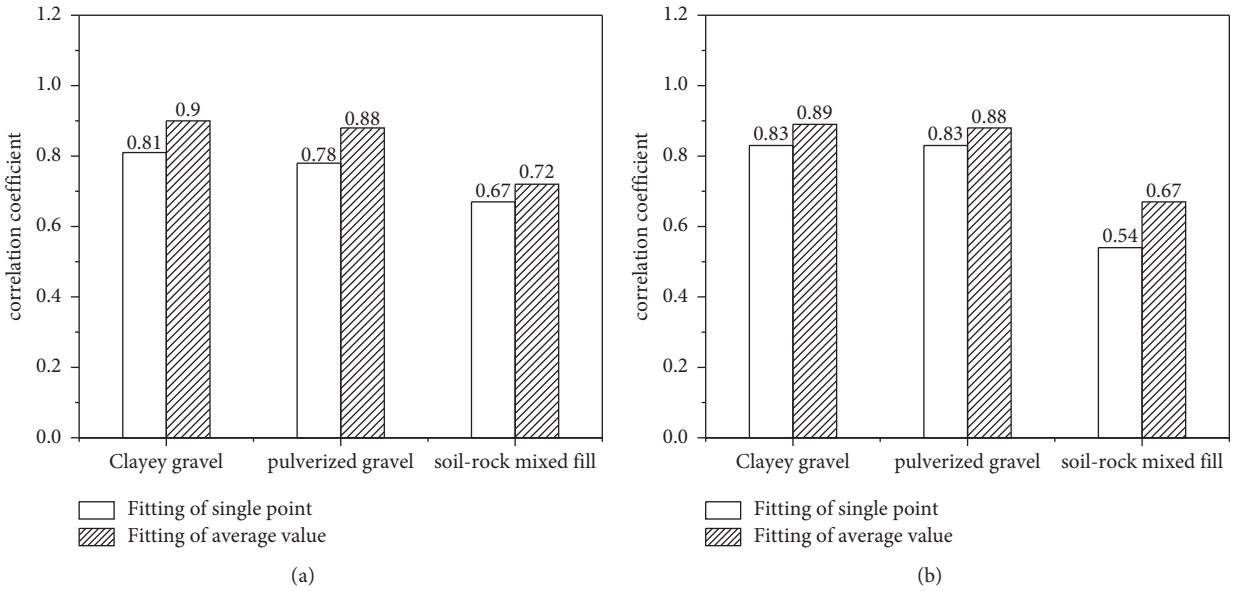

Figure 8: Comparison of correlation coefficients between single-point fit and mean fit. (a) Compaction fitting. (b) Dynamic resilient modulus fitting.

the improved fitting scheme can significantly improve the correlation between the CMV and conventional indexes.

4. Conclusion

(1) CMV of clayey gravel, pulverized gravel, and soil-rock mixed subgrade has a certain positive correlation with the conventional indexes (K and E), in which the correlation coefficients of clayey gravel and pulverized gravel are much higher than those of soil-rock mixed subgrade. It is recommended that the quality control of earth subgrade is carried out by the CMV, and the multi-indicator control method with CMV as the main and compaction number as the supplement is adopted for soil-rock mixed-fill subgrade to ensure the compaction quality meets the standard.

(2) Twelve linear regression equations determined by three filler types, two types of conventional indicators, and two fitting methods can be used as a reference for correlation calibration between the CMV and conventional indicators.

(3) The correlation between the CMV and single-point conventional indicators is weak, and the data are more volatile, while the correlation between the CMV and the mean value of conventional indicators along the wheel width direction is stronger, and the data fluctuate less, so the latter method is better to be fitted when analyzing the correlation between the CMV and conventional indicators.

Data Availability

The data used to support the findings of this study are included within the article.

Conflicts of Interest

The authors declare that they have no conflicts of interest.

References

[1] Y. Yao, J. Ni, and J. Li, "Stress-dependent water retention of granite residual soil and its implications for ground settlement," *Computers and Geotechnics*, vol. 129, Article ID 103835, 2021.

[2] G. Qian, K. Hu, J. Li, X. Bai, and N. Li, "Compaction process tracking for asphalt mixture using discrete element method," *Construction and Building Materials*, vol. 235, Article ID 117478, 2020.

[3] Z. Zhang, Z. Zhou, T. Guo et al., "A measuring method for layered compactness of loess subgrade based on hydraulic compaction," *Measurement Science and Technology*, vol. 32, no. 5, Article ID 055106, 2021.

[4] H. I. Park, G. C. Kweon, and S. R. Lee, "Prediction of resilient modulus of granular subgrade soils and subbase materials using artificial neural network," *Road Materials and Pavement Design*, vol. 10, no. 3, pp. 647–665, 2009.

[5] S. A. Kumar, R. Aldouri, S. Nazarian, and J. Si, "Accelerated assessment of quality of compacted geomaterials with intelligent compaction technology," *Construction and Building Materials*, vol. 113, pp. 824–834, 2016.

[6] C. L. Meehan, D. V. Cacciola, F. S. Tehrani, A. Jamshidi, and A. Doree, "Assessing soil compaction using continuous compaction control and location-specific in situ tests," *Automation in Construction*, vol. 73, pp. 31–44, 2017.

[7] N. W. Facas, R. V. Rinehart, and M. A. Mooney, "Development and evaluation of relative compaction specifications using roller-based measurements," *Geotechnical Testing Journal*, vol. 34, no. 6, pp. 634–642, 2011.

[8] S. Yoon, M. Hastak, and J. Lee, "Suitability of intelligent compaction for asphalt pavement quality control and quality assurance," *Journal of Construction Engineering and Management*, vol. 144, no. 4, Article ID 04018006, 2018.

[9] J. Ling, S. Lin, J. Qian, and J. Zhang, "Continuous compaction control technology for granite residual subgrade compaction," *Journal of Materials in Civil Engineering*, vol. 30, no. 12, Article ID 04018316, 2018.
[10] Q. Xu and G. K. Chang, "Evaluation of intelligent compaction for asphalt materials," *Automation in Construction*, vol. 30, pp. 104–112, 2013.
[11] Ministry of Transport China, "Technical Requirements for Continuous Compaction Control System of Fill Engineering of Subgrade for Highway," Ministry of Transport China, Beijing, China, JT/T 1127-2017, 2017.
[12] M. Castro, L. Iglesias, R. Rodríguez-Solano, and J. A. Sanchez, "Geometric modelling of highways using global positioning system (GPS) data and spline approximation," *Transportation Research Part C: Emerging Technologies*, vol. 14, no. 4, pp. 233–243, 2006.
[13] J. Hu, B. Zheng, C. Wang, C. H. Zhao, Q. Pan, and Z. Xu, "A survey on multi-sensor fusion based obstacle detection for intelligent ground vehicles in off-road environments," *Frontiers of Information Technology & Electronic Engineering*, vol. 21, pp. 675–692, 2020.
[14] O. E. Muogilim, K. K. Loo, and R. Comley, "Wireless mesh network security: a traffic engineering management approach," *Journal of Network and Computer Applications*, vol. 34, no. 2, pp. 478–491, 2011.
[15] A. Kavussi, K. Rafiei, and S. Yasrobi, "Evaluation of PFWD as potential quality control tool of pavement layers," *Journal of Civil Engineering and Management*, vol. 16, no. 1, pp. 123–129, 2010.
[16] V. George and A. Kumar, "Studies on modulus of resilience using cyclic tri-axial test and correlations to PFWD, DCP, and CBR," *International Journal of Pavement Engineering*, vol. 19, no. 11, pp. 976–985, 2018.
[17] J. Qian, Y. Yao, J. Li, H. Xiao, and S. Luo, "Resilient properties of soil-rock mixture materials: preliminary investigation of the effect of composition and structure," *Materials*, vol. 13, no. 7, p. 1658, 2020.
[18] R. Want, B. N. Schilit, and S. Jenson, "Enabling the internet of things," *Computer*, vol. 48, no. 1, pp. 28–35, 2015.
[19] B. Jenny, B. Šavrič, and J. Liem, "Real-time raster projection for web maps," *International Journal of Digital Earth*, vol. 9, no. 3, pp. 215–229, 2016.
[20] J. Hongxia, W. Hongfu, L. Jihong, and P. Ruru, "Development of image pattern for textile based on FFT," *International Journal of Clothing Science & Technology*, vol. 24, 2012.
[21] M. Garrido, "A new representation of FFT algorithms using triangular matrices," *IEEE Transactions on Circuits and Systems I: Regular Papers*, vol. 63, no. 10, pp. 1737–1745, 2016.
[22] W. Hu, X. Shu, B. Huang, and M. E. Woods, "An examination of compaction meter value for asphalt pavement compaction evaluation," *International Journal of Pavement Engineering*, vol. 19, no. 5, pp. 447–455, 2018.
[23] M. Das, R. Kumar, and B. Sahana, "Implementation of effective hybrid window function for ECG signal denoising," *Traitement du Signal*, vol. 37, no. 1, pp. 119–128, 2020.
[24] G. Wang, Z. Wang, and F. Meng, "Vertical vibrations of elastic foundation resting on saturated half-space," *Applied Mathematics and Mechanics*, vol. 28, no. 9, pp. 1199–1207, 2007.
[25] Ministry of Transport of the People's Republic of China, "Field test methods of subgrade and pavement for highway Engineering," MOT, Beijing, China, JTG E60-2008, 2008.
[26] A. N. Guz and T. V. Rudnitskii, "Contact interaction of an elastic punch and an elastic half-space with initial (residual) stresses," *International Applied Mechanics*, vol. 43, no. 12, p. 1325, 2007.

Hindawi
Advances in Materials Science and Engineering
Volume 2021, Article ID 2241351, 14 pages
https://doi.org/10.1155/2021/2241351

Research Article

Quantitative Study on Empirical Strength Parameters of Extremely Fractured Phyllite Based on Fractal Theory

Yongbin Xie, Xiaoyu Yang, Jianhua Dong, and Guosheng Liu

Western Centre of Disaster Mitigation in Civil Engineering, Ministry of Education, Lanzhou University of Technology, Lanzhou 730050, China

Correspondence should be addressed to Jianhua Dong; djhua512@163.com

Received 8 July 2021; Accepted 12 August 2021; Published 18 August 2021

Academic Editor: Bo Li

Extremely broken phyllite is widely distributed and is easily seen in engineering construction. Aiming at the problem that the empirical strength parameters of extremely broken surrounding rock have intense subjectivity and significant difference, based on the characteristics of the existence of particle group state in the highly broken surrounding rock, the fractal theory and large-scale direct shear test are used, the fractal description of polar broken phyllite samples with different pile numbers in fault fracture zone of Qinyu Tunnel is carried out, and the fractal dimensions and empirical strength parameters of each sample are determined. Based on a fractal description and large shear test, the functional relationship between fractal dimension and empirical strength parameter of extremely broken phyllite in fault fracture zone is established, and the quantitative value method of empirical strength parameter determined by fractal dimension of extremely broken phyllite is given, which provides ideas for the quantitative value of empirical strength parameter of the similar extremely broken surrounding rock.

1. Introduction

Rock mass strength criterion is the basis for judging whether it is damaged in theory and an important basis for engineering design. Generally, the accuracy of relevant empirical parameters in the strength criterion is the most important factor to determine whether the rock mass strength criterion is reasonable. Therefore, in engineering design practice, reasonably and accurately determining the relevant empirical parameters of rock mass strength criterion is the basis of its wide application. The Hoek–Brown strength criterion is a combination of rock theoretical research results and many test results statistics. Its simplicity and practicability have been widely accepted by the engineering geological circles. It is the most widely used and influential rock strength criterion so far, and it is also a method recommended by the international society of rock mechanics [1–4]. The envelope of the Hoek–Brown strength criterion is parabola, which can describe the nonlinear failure characteristics of rock mass. The essence of the strength criterion is to attribute all factors affecting the strength characteristics of rock mass to two empirical strength parameters m and s, so the value of empirical parameters m and s of rock mass will play a decisive role in the accuracy of the strength criterion [5, 6]. It is of great scientific value to apply the Hoek–Brown strength criterion to study the quantitative value of rock mass empirical parameters.

The empirical parameters m and s of the Hoek–Brown strength criterion are mainly determined by laboratory test and field estimation [7–9]. The empirical parameters determined by the indoor test method are relatively accurate, but there are some shortcomings, such as long cycle, high cost, and large size effect [10–12]. Field estimation is a method to establish a quantitative relationship between rock mass quality evaluation index and empirical parameters by comprehensively considering many factors affecting rock mass strength. Its process is simple and practical. RMR rock mass scoring system and GSI field rock mass quality classification method have been widely used [13, 14]. However, the RMR rock mass scoring system is not suitable for broken rock mass, so GSI geological strength index is the most widely used empirical strength parameter value method [15].

Sonmez and Ulusay [16] have given the GSI value table, which can consider the distribution of discontinuities, roughness, and filling materials. Cai et al. [17] proposed a method to determine GSI by using the block's volume and the structural surface parameters. Jiang et al. [18] introduced the rock mass fragmentation index to determine the number of rock mass volume joints and rock mass structure grade and used the above parameters to determine the GSI value of rock mass. It can be seen from the above research that there are many factors influencing the GSI value of the geological strength index, which is mainly based on the structural characteristics and structural surface characteristics of the rock mass, and the value is highly subjective. The extremely broken surrounding rock is formed by the continuous expansion and connection of the total rock mass in the random distribution of initial defects under external load, weathering, and other factors. It is mainly in particle group, and it is difficult to determine the above characteristics of the rock mass accurately. Therefore, the value of GSI for the extremely broken surrounding rock has certain randomness. For the same surrounding rock, the values of empirical parameters are quite different.

The extremely broken phyllite in the Qinyu Tunnel is the rock fragment and gravel torn from the phyllite fault wall after the relative movement of the two walls of the fault. Its main mineral combination is sericite, chlorite, and quartz, containing a small amount of feldspar, carbonaceous, and iron, and its engineering properties are very poor. If the strength characteristics of the extremely broken phyllite cannot be accurately evaluated in the tunnel construction, it is very prone to engineering geological disasters. Therefore, in order to accurately give the empirical strength parameters of the Hoek–Brown strength criterion for extremely broken phyllite, based on the theory that broken rock blocks may show fractal distribution characteristics in a statistical sense, the field samples of extremely broken phyllite in different positions of fault fracture zone are taken, the fractal distribution characteristics of highly broken phyllite in fault fracture zone are verified by a screening test, and the fractal dimension quantitative indexes representing the characteristics of extremely broken phyllite in different positions are obtained. Based on the laboratory large-scale shear test, the empirical strength parameters of the highly fractured phyllite at different positions of the fault fracture zone are determined, and the functional relationship between the empirical strength parameters and fractal dimension of the extremely fractured phyllite is established. The empirical strength parameters of the Hoek–Brown strength criterion are determined by using the quantitative parameters in fractal theory, which provides ideas and methods for the quantitative value of the empirical parameters of the extremely fractured phyllite at similar fault fracture zones.

2. Sampling and Fractal Description of Extremely Fractured Phyllite

The test sample comes from the fault fracture zone of ZK345 + 735~ZK346 + 660 section of the Qinyu Tunnel. The sampling point of sample I is near the interface between hanging wall and fracture zone, and the pile number is ZK345 + 740. The sampling point of sample II is near the stake ZK345 + 965. The sampling point of sample III is located in the middle of the fracture zone, and the pile number is ZK346 + 120. The sampling point of sample IV is near ZK346 + 350. The sampling point of sample V is located near the interface between footwall and fracture zone, and the pile number is ZK346 + 650. When sampling on-site, it can be seen that the rock mass in the fracture zone is greyish-black, with loose structure, good grading, and angular shape. The general particle size is 2–4 cm, and the maximum visible particle size is 8–15 cm. The sampling position and extremely broken phyllite on-site are shown in Figure 1.

After sampling, the rock samples are put into plastic bags, wrapped with preservative film, and sealed in prefabricated wooden cases. Labels are pasted on the wooden cases to note the sampling position. Screening tests are carried out for extremely broken phyllite at each sampling point in laboratory. The representative grading of each sampling point is shown in Table 1.

The fractal relation of broken rock is usually defined by particle size and its quantity relationship. However, the number of particles in the broken rock is large, and the distribution range of particle size is vast. It is difficult to establish the fractal model of the particle size by existing test methods. Tyler et al. [19, 20] propose to describe the fractal characteristics of broken rock by the mass distribution of particle size, whose formula is as follows:

$$\frac{M(d \geq d_i)}{M_T} = 1 - \left(\frac{d_i}{\beta}\right)^{3-D}, \tag{1}$$

where d is the particle size of broken particles, d_i is the particle size of a grading particle, $M(d \geq d_i)$ is the mass of particles larger than the particle size d_i in the sample, M_T is the total mass of the sample, β is the coefficient related to the shape and size range of broken particles, and D is the fractal dimension, which is the quantitative parameter of fractal geometry to characterize the properties of broken surrounding rock.

When it is the statistical maximum particle size d_i, i.e., $d_i = d_{\max}$, it is simplified by formula (1), and the correlation coefficient characterizing the size range of broken surrounding rock is

$$\beta = d_{\max}. \tag{2}$$

By taking equation (2) into equation (1), we can get the following results:

$$\left(\frac{d_i}{d_{\max}}\right)^{3-D} = \frac{M(d < d_i)}{M_T}. \tag{3}$$

Take logarithm on both sides of equation (3). If the logarithm $d_i/d_{\max}$ and logarithm $M(d < d_i)/M_T$ of each sample can show an excellent linear relationship, it can be considered that the sample shows exemplary distribution fractal characteristics, and the fractal dimension of the broken surrounding rock sample can be obtained.

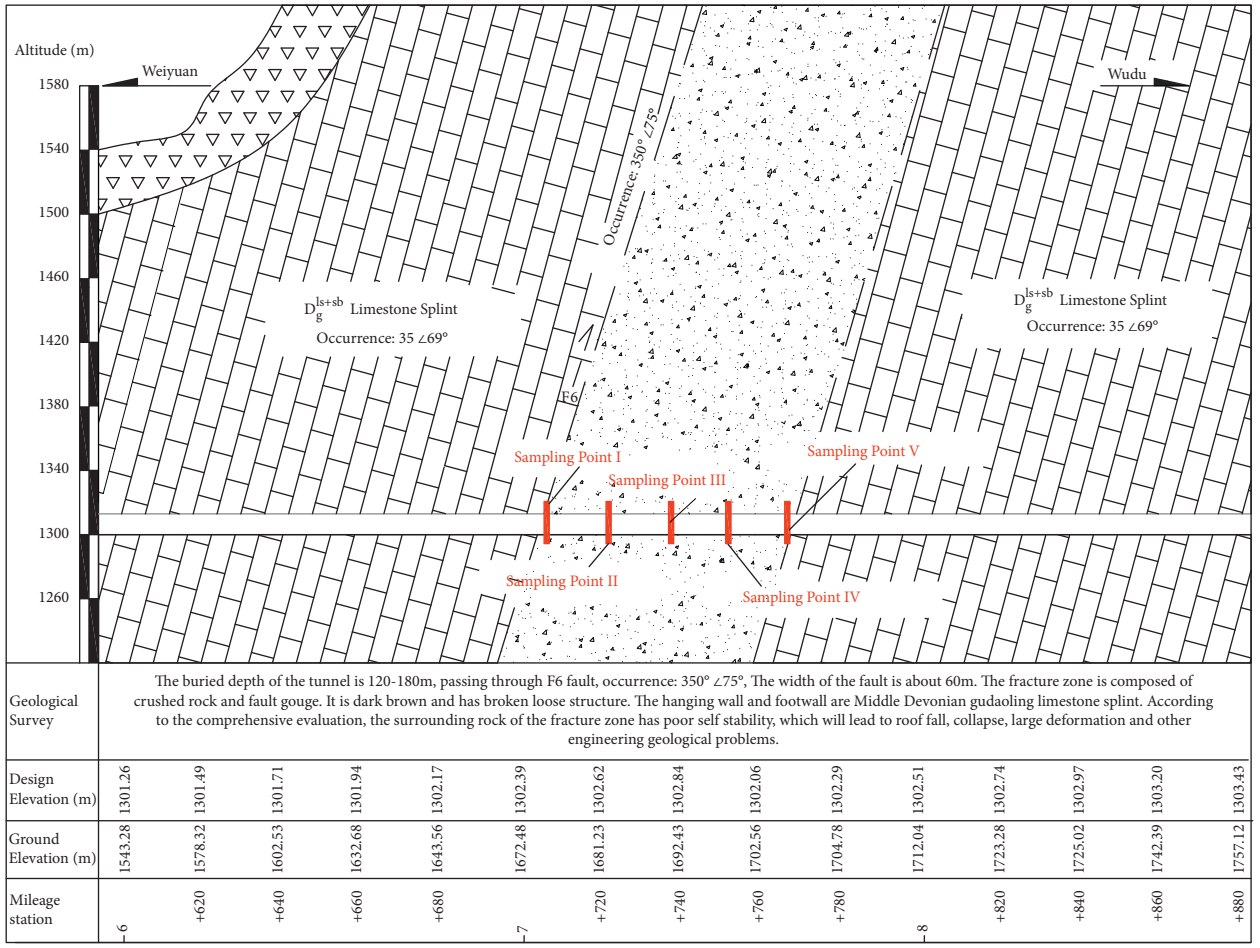

(a)

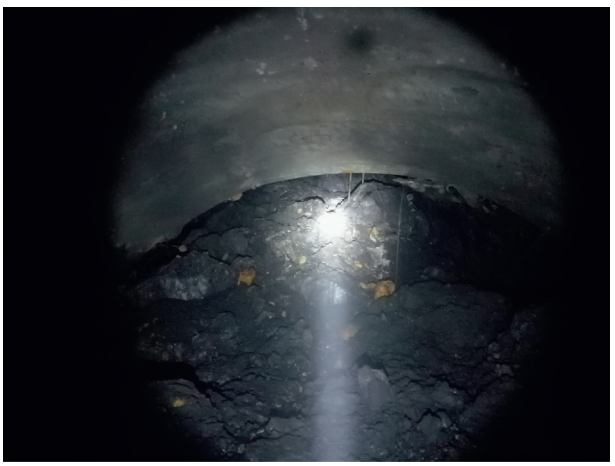

(b)

Figure 1: Location of sampling points and diagram of extremely fractured phyllite. (a) Schematic diagram of sampling point location. (b) Site photos of extremely fractured phyllite.

Table 1: Representative gradation of different sampling points.

Sample	Composition of representative graded particles (%)							
	150~80 mm	80~60 mm	60~40 mm	40~20 mm	20~10 mm	10~5 mm	5~0.1 mm	<0.1 mm
I	0.0	10.2	12.9	27.4	10.8	12.7	16.7	9.3
II	5.1	12.8	23.3	23.4	14.3	5.8	10.9	4.4
III	7.5	13.6	14.1	29.2	18.8	9.7	6.8	0.3
IV	2.0	15.3	17.8	22.7	18.2	8.2	14.3	1.5
V	0.0	5.3	10.9	21.5	24.8	9.5	17.9	10.1

$$D = 3 - k, \tag{4}$$

where k is the slope of curve fitting with the logarithm of $d_i/d_{\max}$ and $M(d < d_i)/M_T$ as abscissa and ordinate.

According to the particle grading table of samples at fault fracture zone of different pile numbers in Table 1, the fractal curve of each sample is drawn, as shown in Figure 2.

It can be seen from the fractal curve of each sample in Figure 2 that the fractal curve of grain size distribution of extremely fractured phyllite samples with different pile numbers in fault fracture zone is approximately a straight line, and the correlation coefficient is more significant than 0.95 after fitting the straight line to each data point. The fractal dimension can be used as a quantitative index to characterize the grain size characteristics of the highly fractured phyllite. It is feasible to evaluate the grain size characteristics of the extremely fractured surrounding rock by using the fractal dimension. The slope of the fitting line is brought into equation (4) to obtain the fractal dimension of samples with different pile numbers in the fault fracture zone, as shown in Table 2.

According to Table 2, the correlation coefficients are close to 1, so the extremely broken surrounding rock in the fault fracture zone can show good fractal characteristics, and its fractal dimension varies from 2.154 to 2.643. The fractal dimension of sample V is the largest. Compared with the sample gradation in Table 1, it is found that the content of fine aggregate with particle size less than 5 mm is the most. The fractal dimension of sample III is the smallest. Comparing with the sample gradation in Table 1, it is found that the content of fine material with particle size less than 5 mm is the least. In addition, by comparing the fractal dimension and acceptable particle content of each sample, it is found that the smaller the fine particle content in the sample, the smaller the fractal dimension of the sample, and the fractal dimension value is closely related to the particle gradation of the sample. For the same kind of broken surrounding rock, the grain gradation is the most critical factor affecting the strength of rock mass, and the fractal dimension can well reflect the grain characteristics of the extremely broken surrounding rock, so it is feasible to establish the relationship between fractal dimension and strength parameters.

3. Determination of Empirical Strength Parameters Based on Large-Scale Shear Test

In order to establish the relationship between fractal dimension of extremely fractured phyllite and empirical strength parameters, it is necessary to determine the empirical strength parameters accurately. The large-scale direct shear test is the most commonly used indoor test method to accurately determine the empirical parameters of rock mass. In this paper, the empirical strength parameters of extremely fractured phyllite at different pile numbers in fault fracture zone are determined by large-scale direct shear tests.

3.1. Shearing Instrument and Sample Handling. The test was performed with a large direct shearing apparatus manufactured by GEOCOMP, USA, as shown in Figure 3. The direct shearing instrument mainly includes displacement sensor, load sensor, loading system, support, shear box, limit switch, intelligent control system, and measuring system. The shearing instrument and measuring system transmit data during the test through the network connection. The loading system is a stepper motor, which is fixed in the vertical and horizontal directions of the support, respectively. The cutting box cavity is cuboid, size 305 mm × 305 mm × 200 mm (long) × wide × high), the upper shear box is fixed, but vertical stress can be applied in the vertical direction, and the lower shear box can move horizontally under thrust. The intelligent control system controls the horizontal movement of the lower shear box at a fixed shear rate while maintaining constant vertical stress at the top of the upper shear box.

When carrying out large-scale indoor shear tests, the size of the shear box is fixed. If the size of the sample directly used in the field is limited by the size, the test data will be distorted. Therefore, the oversize should be treated before the test is carried out. Determine the maximum allowable sample material diameter of 60 mm according to the shear box size. The equivalent substitution method is to distribute the superparticle content in the sample to each gradation with the maximum allowable particle size and the 5 mm particle size utilizing the weighted average method. The superparticle can be processed without changing the coarse particle content. It is suitable for samples with less than or equal to 50% content with the superparticle content [21]. Superparticle sizes of samples I~V can be well treated. The particle size content of each sample after modification of superparticle size is calculated as follows:

$$P_{5i} = \frac{P_5}{P_5 - P_0} P_{05i}, \tag{5}$$

$$P_5 = \sum_1^n P_{5i} = \sum_1^n P_{05i} + P_0, \tag{6}$$

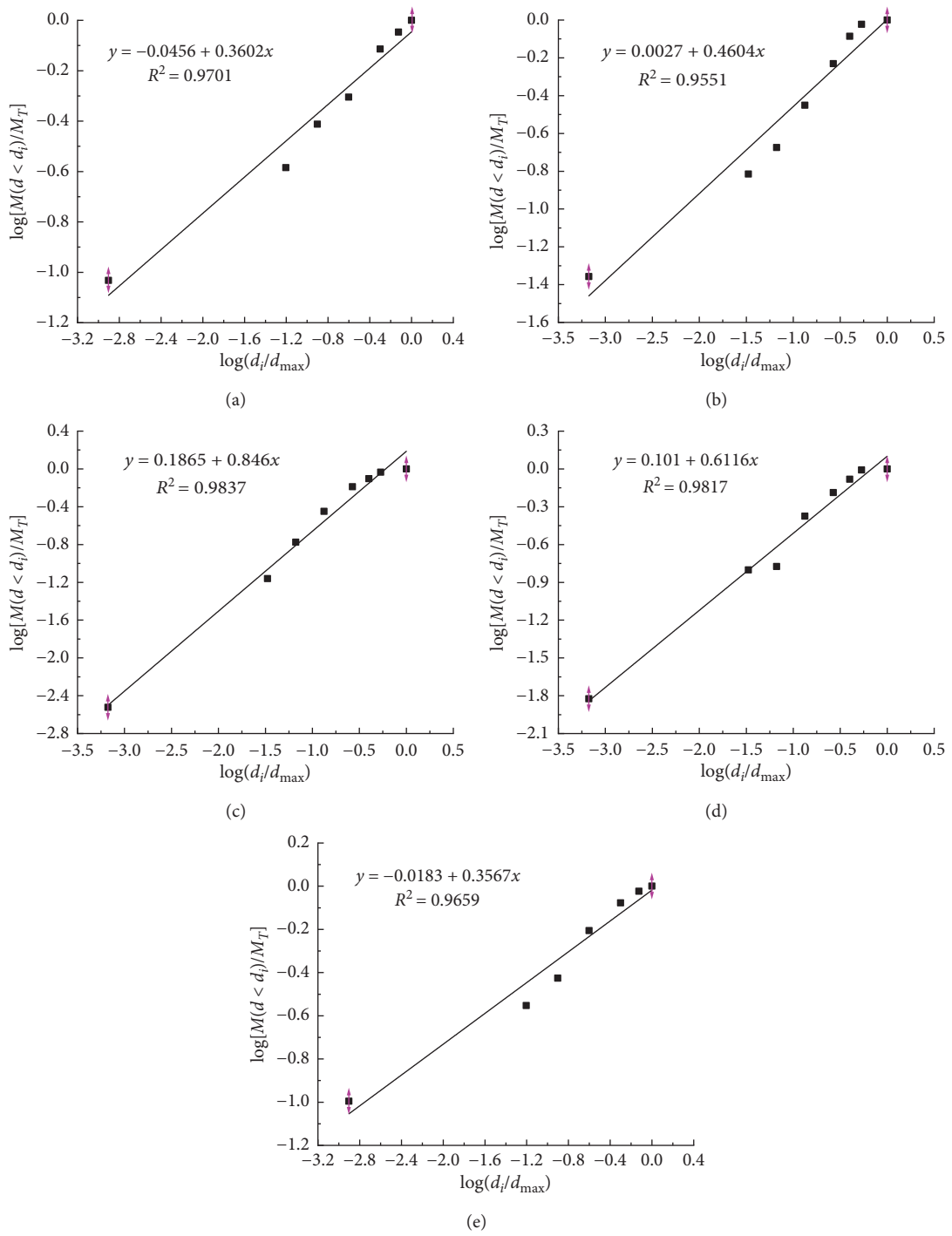

FIGURE 2: Fractal curve of particle size distribution of samples with different pile numbers in fault fracture zone. Fractal curve of particle size distribution of (a) sample I, (b) sample II, (c) sample III, (d) sample IV, and (e) sample V.

where P_0 is the content percentage of sample superparticle size, P_5 is the percentage of sample with particle size larger than 5 mm, P_{5i} is the percentage of particle size greater than 5 mm after distribution by the weighted average method, and P_{05i} is the content percentage of each grade particle size of the original sample.

Based on the grading of each sample in Table 1, formulas (5) and (6) are used to treat the ultraparticle size of extremely fractured phyllite samples of each pile number in the fault fracture zone. The grading of each sample before and after treatment is shown in Figure 4.

3.2. Large Shear Test Process and Results. Prepare the samples according to the grading characteristics after ultraparticle treatment in Figure 4. Remove the upper and lower shear

Table 2: Fractal dimension values and correlation coefficients of different samples.

Sample name	Fractal dimension D	Correlation coefficient R^2
Sample I	2.640	0.9701
Sample II	2.540	0.9551
Sample III	2.154	0.9837
Sample IV	2.338	0.9817
Sample V	2.643	0.9659

(a) (b)

Figure 3: Large direct shearing instrument. (a) Large direct scissor photos. (b) Upper and lower shear boxes.

boxes, place them on the support frame, fix the upper and lower shear boxes, and sample layers by layers. In order to prevent uneven distribution of coarse and fine particles of the sample, rough classification of coarse and fine particles was carried out with 5 mm as the limit before the sample was poured into the shear box. According to the height of the shear box, each sample filling will be completed 3 times, and each filling height is about 60 mm. Fill and divide the coarse and fine particles into three equal parts. First, pour in one coarse particle material, and then pour in another fine particle material. Mix evenly and remove the large particle size on the surface. Then, hammer it down with rubber. Repeat the above steps to start the second filling until the sample filling is complete. After filling the sample, install the shear box, start the loading system of the shearing apparatus, and make sure that the load sensor is cleared without contact with the rest of the shearing apparatus. The normal stress was applied according to the designed load condition. After the numerical value of the normal stress was stabilized, the upper shear box was slightly lifted by the front and rear beams on the shear box, and the bolts fixing the upper and lower shear boxes were removed. The shear test began at a loading rate of 2 mm/min with the normal stress unchanged. Figure 5 shows the filling and shearing process of some specimens.

Figure 6 shows the shear stress and shear displacement curves of each specimen of extremely fractured phyllite at each fault fracture zone under normal stress conditions of 100 kPa, 150 kPa, 200 kPa, 250 kPa, and 300 kPa.

It can be seen from the diagram that, under different normal stress conditions, the shear stress of each sample increases gradually with the increase of shear displacement. When the shear displacement is between 40 mm and 50 mm, the shear stress of each sample starts to reach its peak value. Continue the shear test until the shear displacement reaches 80 mm, and the shear stress of each sample will gradually decrease, which may be the influence of the increase of shear displacement and the decrease of shear area. The particle size distributions of samples 1 and 5 are close, and the maximum shear stress values under different normal stress conditions are close. Particle size distributions of sample 2 and sample 4 are close, and their maximum shear stress values under different normal stresses are also close. The coarse particle content of sample 3 is higher than that of other samples. By comparing the maximum shear stress values under different normal stress conditions, it can be seen that the shear stress of sample 3 is higher than that of other samples under the same normal stress conditions. It shows that particle size is the most important factor affecting the strength of materials in extremely fractured surrounding rocks composed of the same material.

3.3. Determination of Empirical Strength Parameters for Each Sample. The empirical strength criterion of rock mass is formed by statistics of many test data to overcome the defect of the theoretical strength criterion. The empirical strength criterion put forward by E. Hoek and E. T. Brown in 1980 is the most widely used one, which can be applied to complete or broken jointed rock mass [2]. Its expression is

$$\sigma_1 = \sigma_3 + \sigma_c \left(m \frac{\sigma_3}{\sigma_c} + s \right)^{0.5}, \tag{7}$$

where σ_1 is the maximum principal stress of rock mass failure, σ_3 is the minimum principal stress of rock mass failure, σ_c is the uniaxial compressive strength of rock block, m and s are both empirical parameters of rock mass, m mainly reflects the degree of hardness and softness of rock,

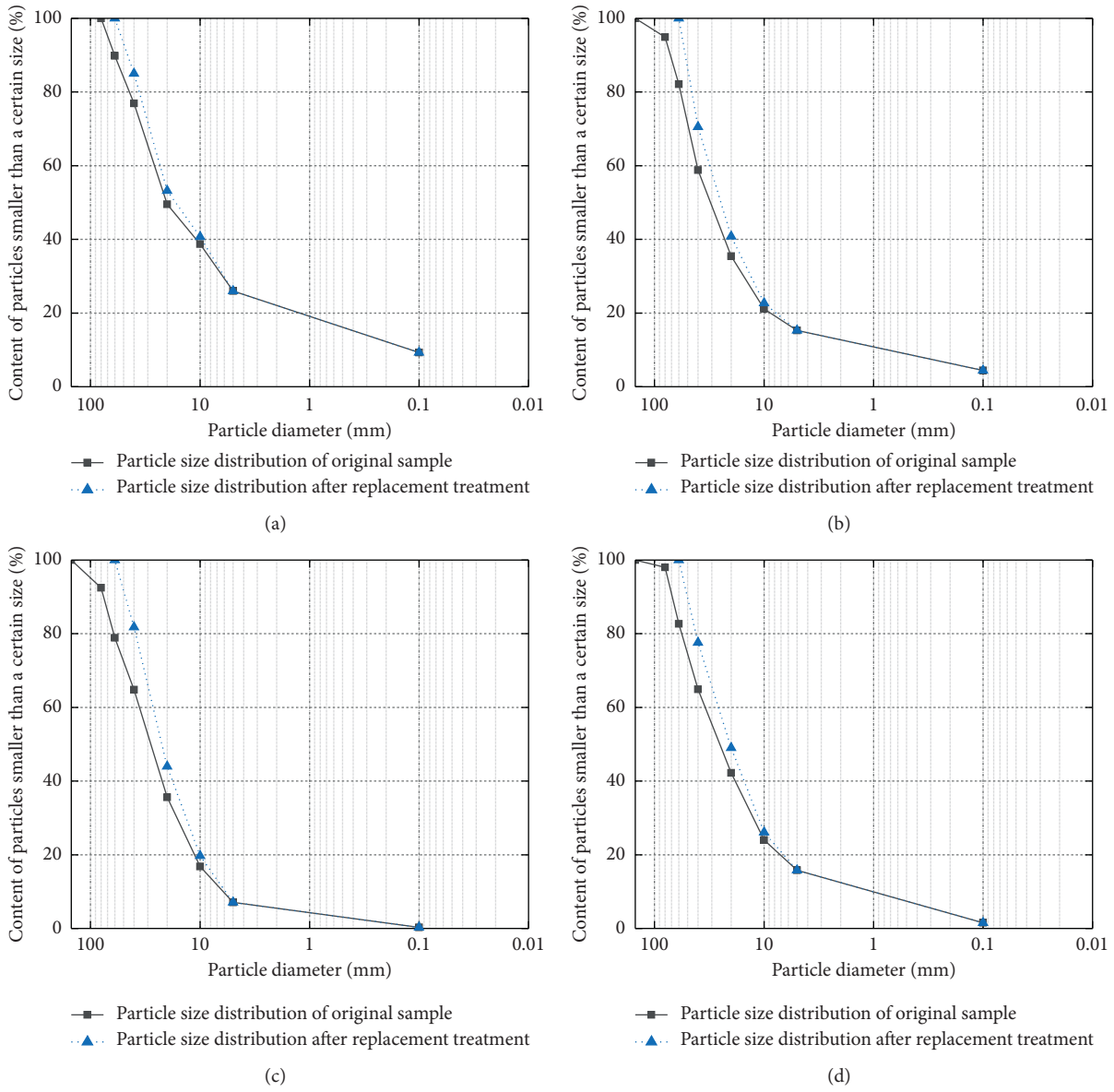

Figure 4: Continued.

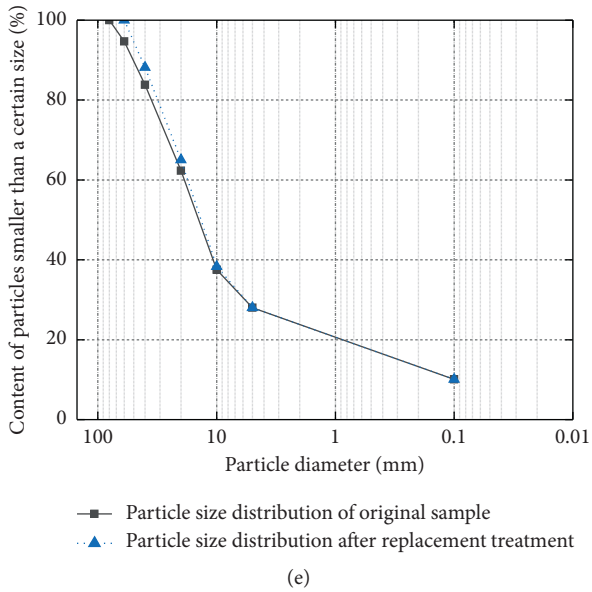

(e)

Figure 4: Gradation curves before and after treatment of superparticle size of piles in fault fracture zone. (a) Gradation curve of sample I before and after superparticle treatment. (b) Gradation curve of sample II before and after superparticle treatment. (c) Gradation curve of sample III before and after superparticle treatment. (d) Gradation curve of sample IV before and after superparticle treatment. (e) Gradation curve of sample V before and after superparticle treatment.

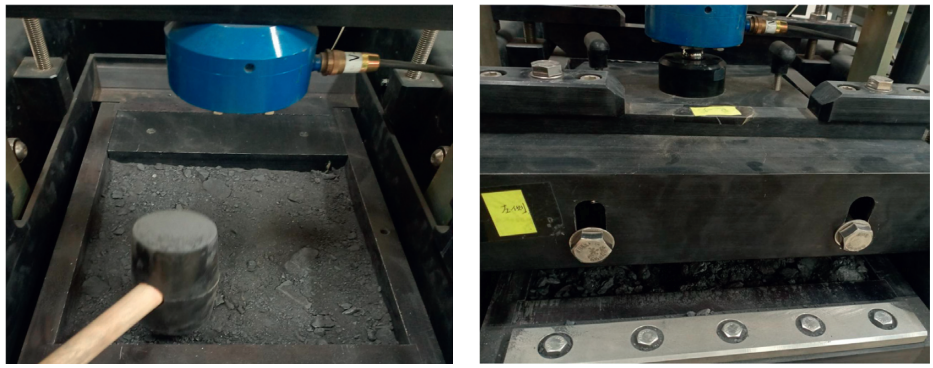

(a) (b)

Figure 5: Filling and shear process photographs of extremely fractured phyllite samples at fault fracture zone. (a) Photos of surface leveling and filling of extremely broken phyllite samples. (b) Photos of shear process of extremely fractured phyllite samples.

and the value range is usually between 0.0000001 and 25, and s reflects the fragmentation degree of rock mass, and the value range is between 0 and 1.

When the empirical parameters m and s are determined by large shear test statistics, the expression of equation (7) is transformed. At this time, the relationship between the empirical parameters and the maximum and minimum principal stresses is as follows:

$$\left(\frac{\sigma_1 - \sigma_3}{\sigma_c}\right)^2 = m\frac{\sigma_3}{\sigma_c} + s. \tag{8}$$

According to Balmer's deduction hypothesis [2], the stress of the material in the limit state satisfies Mohr's circle equation, and the relationship is as follows:

$$\left(\frac{\sigma_1 + \sigma_3}{2} - \sigma\right)^2 + \tau^2 = \left(\frac{\sigma_1 - \sigma_3}{2}\right)^2. \tag{9}$$

The maximum and minimum principal stress, shear stress, internal friction angle, and normal stress are as follows:

$$\begin{aligned} \sigma_1 &= \sigma + \tau\frac{1 - \cos(90 + \phi)}{\sin(90 + \phi)}, \\ \sigma_3 &= \sigma - \tau\frac{1 + \cos(90 + \phi)}{\sin(90 + \phi)}, \end{aligned} \tag{10}$$

where σ and τ are the normal stress and shear stress obtained from the shear test and ϕ is the corresponding internal friction angle.

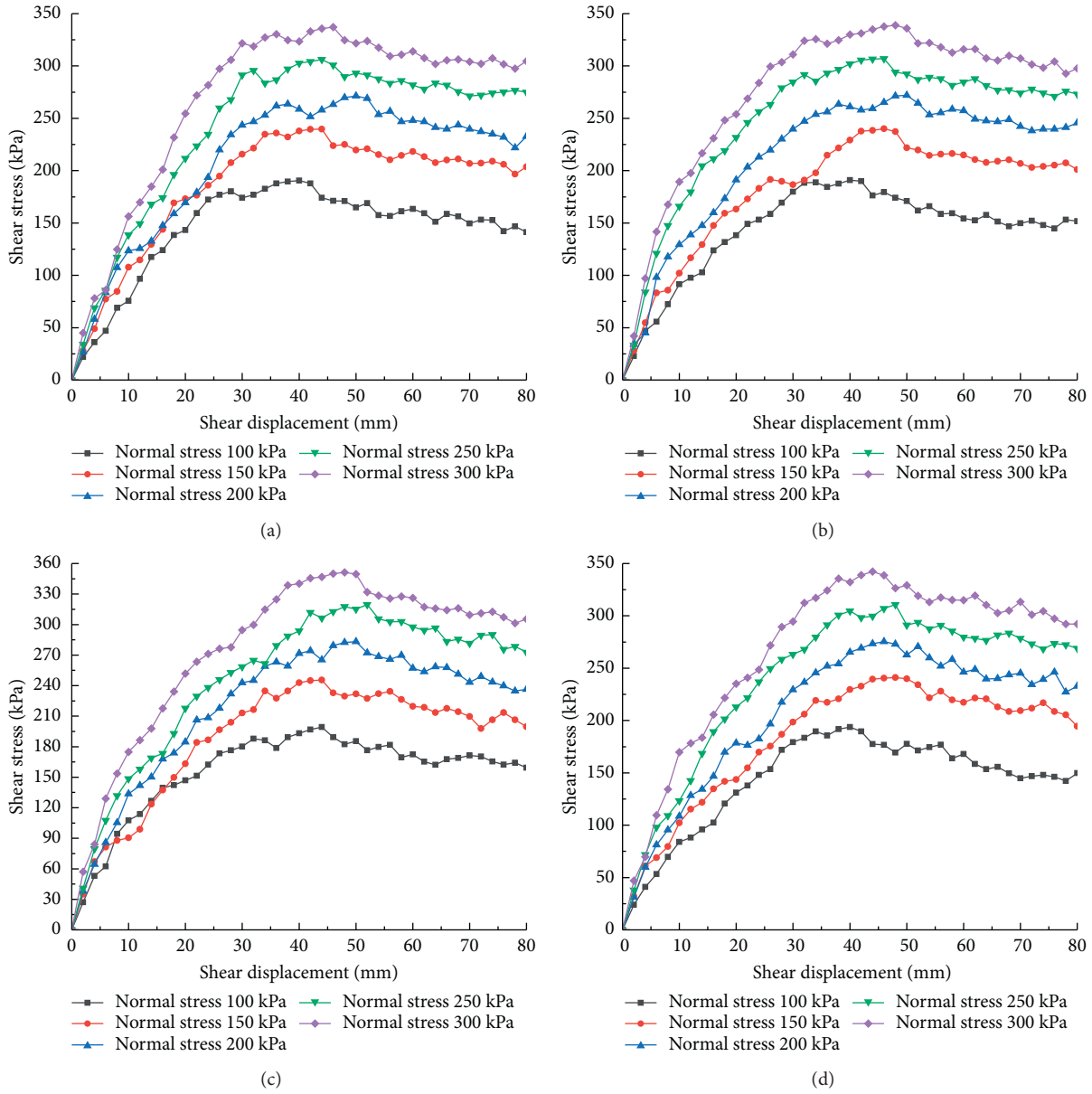

Figure 6: Continued.

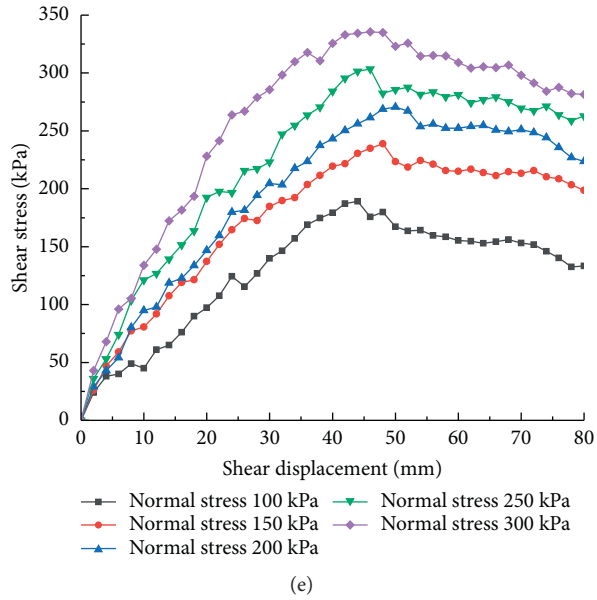

Figure 6: Shear stress-shear displacement curves of each sample under different normal stress conditions. (a) Sample I shear stress-shear displacement curve. (b) Sample II shear stress-shear displacement curve. (c) Sample III shear stress-shear displacement curve. (d) Sample IV shear stress-shear displacement curve. (e) Sample V shear stress-shear displacement curve.

Taking the maximum shear stress during the direct shear test of each sample as the shear strength of each sample, according to the test results in Figure 6, the maximum and minimum principal stresses of each sample under the limit state under different normal forces can be obtained, as shown in Table 3.

For the uniaxial compressive strength σ_c = 21MPa of phyllite blocks, the empirical parameters m and s can be fitted according to the functional relation of equation (8) by calculating the maximum and minimum principal stresses from each sample. The fitting results are shown in Figure 7.

It can be seen from the diagram that the linear function relation of equation (8) can be used to fit the test results obtained from the shear test. The slope of the fitted line is the empirical constant m of each sample, and the constant term of the line is the empirical parameter s, as shown in Table 4.

4. Establishment of Relationship between Fractal Dimension and Strength Empirical Parameters of Extremely Fractured Phyllite

According to the corresponding fractal dimensions and experience parameters of each sample in Tables 2 and 4, the fractal dimensions and experience constants D~m and D~s of each sample are plotted in a rectangular coordinate system, and the relationship fitting is carried out, as shown in Figure 8.

Figure 8 shows the relationship between the fractal dimension D of each sample and the empirical strength parameters m and s. It can be seen from the diagram that the empirical strength parameters m and s decrease with the increase of the fractal dimension of the sample, and there is a significant correlation between the fractal dimension D and the empirical strength parameters. The regression analysis method shows that the linear relationship mainly exists for the empirical parameters s and the fractal dimension D, which can be expressed as

$$s = a_s + b_s D, \tag{11}$$

where D is the fractal dimension of extremely broken surrounding rock and a_s and b_s are the test constants related to the lithology of fractured surrounding rock. For the extremely fractured phyllite in the fault fracture zone of this paper, a_s is taken as 0.00085 and b_s is taken as −0.00013.

For the empirical parameter m and fractal dimension D, they can show exponential correlation, so the empirical parameter m and fractal dimension D can be expressed as follows:

$$m = a_n D^{b_n}, \tag{12}$$

where D is the fractal dimension of extremely broken surrounding rock and a_n and b_n are the test constants related to the grain and lithology of the fractured surrounding rock. For the extremely fractured phyllite in the fracture zone of this paper, a_n is taken as 0.3422 and b_n is taken as −0.712.

In conclusion, the fractal dimension of fractal quantification parameter can be determined for extremely fractured phyllite at fault fracture zone according to screening test and fractal theory. The empirical strength parameters are determined by combining formulas (11) and (12) using the high correlation between fractal dimension and empirical strength parameters. It not only solves the shortcomings of long period and high cost of indoor test but also solves the problem that geological strength index is greatly influenced by human factors, and its value is highly subjective.

Table 3: Maximum and minimum principal stresses of each specimen under different normal stresses (kPa).

Sample name	Normal stress $p = 100$ kPa		Normal stress $p = 150$ kPa		Normal stress $p = 200$ kPa		Normal stress 250 kPa		Normal stress $p = 300$ kPa	
	σ_1	σ_3	σ_1	σ_3	σ_1	σ_3	σ_1	σ_3	σ_1	σ_3
Sample I	470.87	1.42	616.39	26.02	728.44	59.65	845.91	91.60	956.01	125.62
Sample II	473.94	2.34	619.93	27.33	732.64	60.96	850.98	93.50	960.13	127.68
Sample III	500.09	0.91	643.09	27.89	768.84	59.21	891.96	91.01	1005.4	125.30
Sample IV	482.55	1.96	626.30	27.93	743.76	60.64	863.97	92.65	976.05	126.74
Sample V	468.16	2.72	614.66	27.23	726.55	60.87	840.73	93.92	953.13	127.43

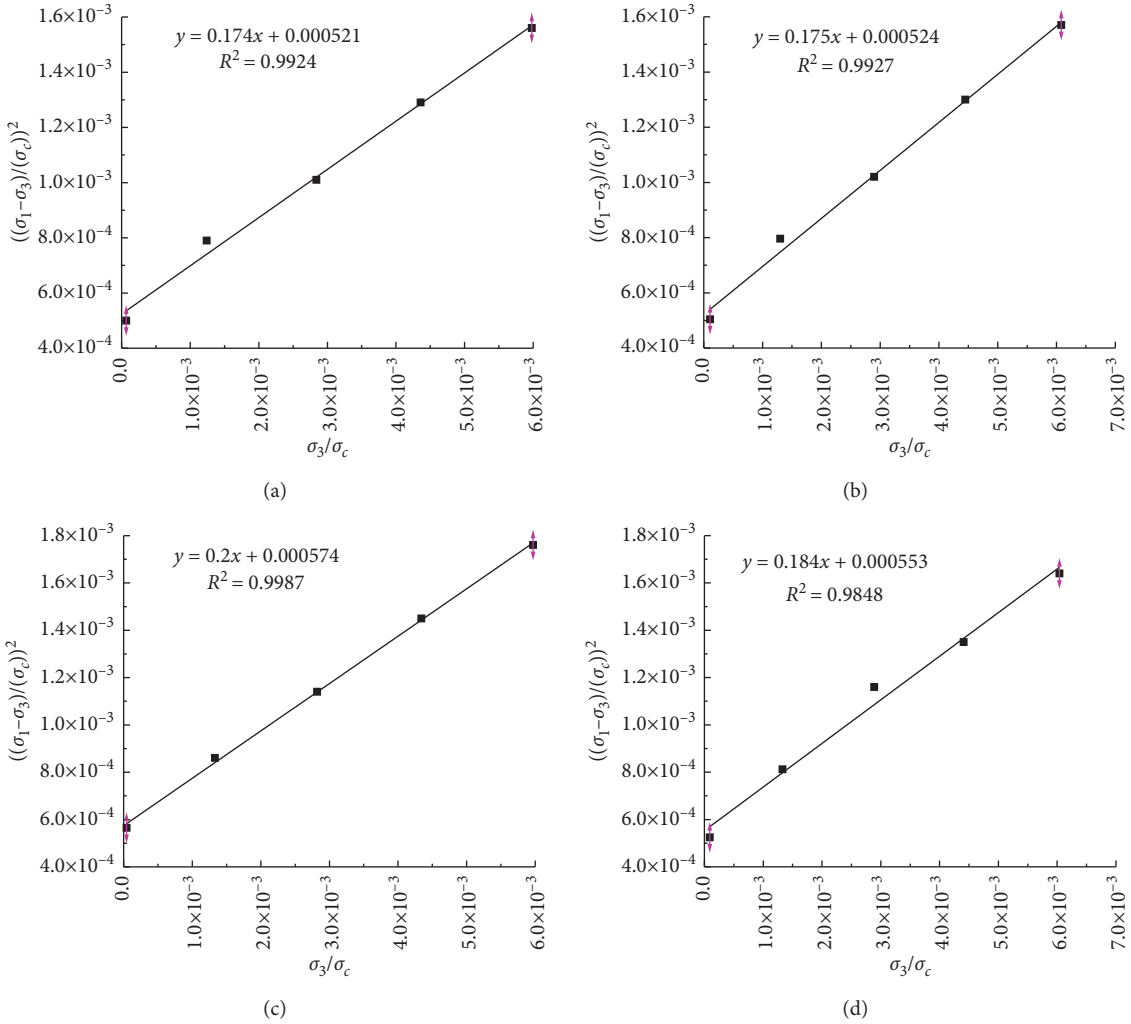

Figure 7: Continued.

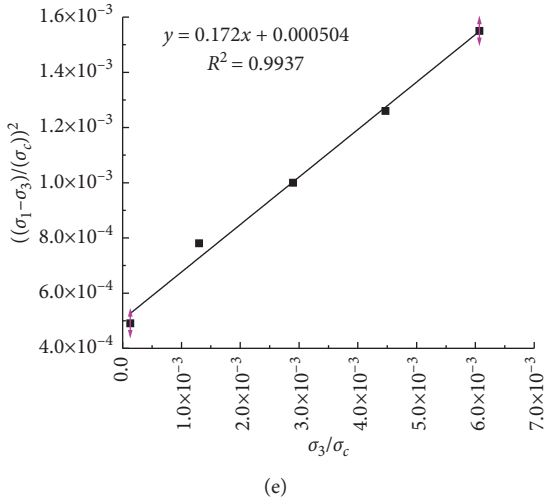

(e)

Figure 7: Determination of empirical parameters m and s for each sample. Empirical parameters m and s of (a) sample I, (b) sample II, (c) sample III, (d) sample IV, and (e) sample V.

Table 4: Experience constants and correlation coefficients for each sample determined by shear test.

Sample name	Empirical constant m	Empirical constant s	Correlation coefficient
Sample I	0.174	0.000521	0.9924
Sample II	0.175	0.000524	0.9927
Sample III	0.200	0.000574	0.9987
Sample IV	0.184	0.000553	0.9848
Sample V	0.172	0.000504	0.9937

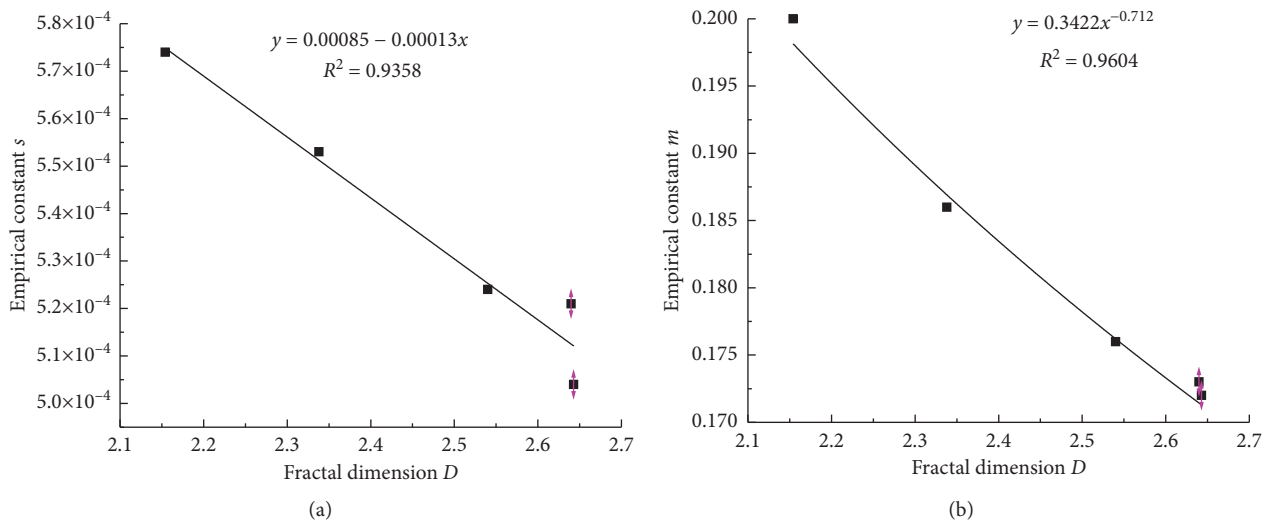

(a) (b)

Figure 8: Fractal dimension and empirical parameter relation curve of extremely fractured phyllite at fault fracture zone. (a) Relationship between fractal dimension D and s of extremely fractured phyllite. (b) Relationship between fractal dimension D and m of extremely fractured phyllite.

5. Conclusions

In this paper, field sampling of polar shattered phyllite of different pile numbers in fault fracture zone of Qinyu Tunnel was carried out, and the fractal characteristics of polar broken phyllite were verified by the screening test. Based on fractal theory and large shear test, a method to quantify the empirical strength parameters of polar broken phyllite was established. The specific conclusions are as follows:

(1) Each sample of extremely fractured phyllite with different pile numbers in the fault fracture zone shows good fractal characteristics. The fractal dimension changes from 2.154 to 2.643. The fractal dimension of different fractal quantification indexes of sample gradation is different, which is manifested as the larger the content of coarse particles, the smaller the fractal dimension.

(2) The closer the gradation of samples is, the smaller the difference of shear strength is. The greater the content of coarse particles, the greater the shear strength of extremely fractured phyllite under the same normal stress condition. The shear strength of extremely fractured surrounding rock is closely related to the grain size characteristics of samples.

(3) The empirical strength parameter m and fractal dimension D of extremely fractured phyllite at fault fracture zone show a good exponential relationship, while the empirical parameter s and fractal dimension D show an excellent linear relationship. Based on the above relationship, the empirical strength parameter can be quantified by the fractal dimension obtained from the field screening test.

(4) In this paper, only the quantitative method for empirical strength parameters of extremely fractured phyllite at fault fracture zone is discussed, the number of samples is limited, and the sampling position is relatively single. Further tests on extremely fractured phyllite at fault fracture zone and analysis of surrounding rocks of different types of fault fracture zone can be carried out, thus expanding the quantitative method for empirical strength parameters of extremely fractured surrounding rocks.

Data Availability

The data used to support the findings of this study are available from the corresponding author upon request.

Conflicts of Interest

The authors declare that they have no conflicts of interest regarding the publication of this study.

Acknowledgments

The project presented in this study was supported by the Natural Science Foundation of China (no. 51778275) and Longyuan Young Innovative and Entrepreneurial Talents (Team Project no. 2020RCXM120).

References

[1] E. Hoek and E. T. Brown, "Empirical strength criterion for rock masses," *Journal of the Geotechnical Engineering Division*, vol. 106, no. 9, pp. 1013–1035, 1980.

[2] E. Hoek and E. T. Brown, *Underground Excavation in rock*, Austin & Sona Ltd, Hertford, UK, 2nd edition, 1988.

[3] E. Hoek, "Strength of rock and rock masses," *International Society for Rock Mechanics News Journal*, vol. 2, no. 2, pp. 4–16, 1994.

[4] E. Hoek, C. Carranze-Toress, and B. Corkum, "Hoek-Brown failure criterion-2002 edition," in *Proceeding of the North American Rock Mechanics Society Meeting*, pp. 267–273, Toronto, July 2002.

[5] T. Maolin, H. Lijun, and M. Qingbin, "Nonlinear regression analysis for deep rock mass parameters of the hoek-brown failure criterion based on the differential evolution," *KSCE Journal of Civil Engineering*, vol. 25, pp. 3160–3171, 2021.

[6] X.-L. Yang, "Seismic displacement of rock slopes with nonlinear Hoek-Brown failure criterion," *International Journal of Rock Mechanics and Mining Sciences*, vol. 44, no. 6, pp. 948–953, 2007.

[7] A. J. Li, R. S. Merifield, and A. V. Lyamin, "Stability charts for rock slopes based on the Hoek-Brown failure criterion," *International Journal of Rock Mechanics and Mining Sciences*, vol. 45, no. 5, pp. 689–700, 2008.

[8] K. Jyant and R. Obaidur, "Lower bound limit analysis of unsupported vertical circular excavations in rocks using Hoek-Brown failure criterion," *International Journal for Numerical and Analytical Methods in Geomechanics*, vol. 44, no. 7, 2020.

[9] Xu Jiang, D. Guoliang, and G. Weiming, "Elastoplastic analysis of normal stiffness of bore wall of the rock-socketed pile based on Hoek-Brown failure criterion and cavity expansion theory," *Japanese Geotechnical Society Special Publication*, vol. 8, no. 7, 2020.

[10] K. W. John, "An approach to rock mechanics," *Journal of the Soil Mechanics and Foundations Division*, vol. 88, no. 4, pp. 1–30, 1962.

[11] E. Hoek, "Strength of jointed rock masses," *Géotechnique*, vol. 33, no. 3, pp. 187–223, 1983.

[12] E. Hoek and E. T. Brown, "Practical estimates of rock mass strength," *International Journal of Rock Mechanics and Mining Sciences*, vol. 34, no. 8, pp. 1165–1186, 1997.

[13] X.-L. Yang and J.-H. Yin, "Slope equivalent mohr-coulomb strength parameters for rock masses satisfying the hoek-Brown criterion," *Rock Mechanics and Rock Engineering*, vol. 43, no. 4, pp. 505–511, 2010.

[14] J. L. Justo, E. Justo, J. M. Azañón, P. Durand, and A. Morales, "The use of rock mass classification systems to estimate the modulus and strength of jointed rock," *Rock Mechanics and Rock Engineering*, vol. 43, no. 3, pp. 287–304, 2010.

[15] E. Eberhardt, "The Hoek-Brown failure criterion," *Rock Mechanics and Rock Engineering*, vol. 45, no. 6, pp. 981–988, 2012.

[16] H. Sonmez and R. Ulusay, "Modifications to the geological strength index (GSI) and their applicability to stability of slopes," *International Journal of Rock Mechanics and Mining Sciences*, vol. 36, no. 6, pp. 743–760, 1999.

[17] M. Cai, P. K. Kaiser, H. Uno, Y. Tasaka, and M. Minami, "Estimation of rock mass deformation modulus and strength

of jointed hard rock masses using the GSI system," *International Journal of Rock Mechanics and Mining Sciences*, vol. 41, no. 1, pp. 3–19, 2004.

[18] G. Jiang, N. Hu, G. Hong, and G. Li, "Determination of rock mass mechanical parameters based on quantification and correction method of GSI value," *Rock and Soil Mechanics*, vol. 39, no. 6, pp. 2211–2218, 2018.

[19] S. W. Tyler and S. W. Wheatcraft, "Fractal scaling of soil particle-size distributions: analysis and limitations," *Soil Science Society of America Journal*, vol. 56, no. 2, pp. 362–369, 1992.

[20] P. Yang, Y. Luo, and Y. Shi, "Fractal characteristics of soil characterized by weight distribution of particle size," *Chinese Science Bulletin*, vol. 38, no. 20, pp. 1896–1899, 1993.

[21] S. Ben, *Specification for Coarse Grained Soil Test of Hydropower and Water Conservancy Projects*, China Electric Power Press, Beijing, China, 2007.

Hindawi
Advances in Materials Science and Engineering
Volume 2021, Article ID 7548996, 9 pages
https://doi.org/10.1155/2021/7548996

Research Article

Multifactor Analysis of Calibration and Service Quality of the Soil Moisture Sensor Applied in Subgrade Engineering

Ke Xiao, Wen-qi Bai, and Si-si Wang

Hunan Institute of Metrology and Test, Changsha 410014, China

Correspondence should be addressed to Ke Xiao; 261758604@qq.com

Received 25 July 2021; Accepted 9 August 2021; Published 12 August 2021

Academic Editor: Yongsheng Yao

The soil is an important natural resource, and its moisture status plays a key role in the strength and stability of the soil structure. In civil industries including the agriculture engineering and the forestry engineering, moisture sensors are widely used to test and monitor the engineering properties and long-term service performance of soil. The influence of multiple factors on the quality and the accuracy of the soil moisture sensor should be taken into account. Both laboratory and field tests were performed by the time-domain reflectometry (TDR) method. The soil dielectric constant and magnetic permeability under different moisture contents, different temperatures, and different dry densities were comprehensively evaluated. At the same time, the sensitive factors in the service performance of the TDR sensor have been revealed by the real state of tested soil samples. Based on the testing principle of TDR, a calibration calculation model has been developed to evaluate accurately the moisture content of the subgrade slope. The results show that both the moisture content and the dry density had a significant influence on the dielectric constant and the magnetic permeability of soil. The developed calculation model has a good fitting effect and stability. Through the model, the influence of moisture content and temperature on the soil dielectric constant has been analyzed, and the fitting goodness is above 90%. After half a year of settlement, the soil was gradually drained and consolidated, and the moisture content of the subgrade section gradually decreased. It verified that the monitoring method determined by the laboratory calibration test was effective and accurate.

1. Introduction

In general, soil structure is a three-phase body consisting of solid, liquid, and gas phases [1]. The water in soil exists in many forms, including bound, unbound, and vaporous water. The moisture status of soil is usually tested and monitored to determine the engineering nature of the soil, control the quality of pressure implementation, verify the early warning of geological hazards, and analyze the fine management of agricultural production [2–4]. Water in soil is usually quantified by water content, which is defined as the ratio of water to soil particles in soil except for structural water. In the nature, soil moisture content changes dynamically over time and environmental factors [5]. Environmental factors such as dry evaporation and precipitation alternately change, causing several wet and dry cycles in slope soil [6]. The soil structure is not fully compacted because of the considerable change of water content, leading to harmful accidents, such as subgrade slip, water damage, and uneven settlement of engineering structures [7]. Therefore, testing and evolution of moisture content have been the focus of research in subgrade engineering for a long time.

The progress of sensor technology and the Internet constantly improves and develops the test methods of moisture content [8]. At present, some interesting topics are given increasing attention, such as in situ nondestructive detection [9], automatic real-time monitoring [10], remote wireless transmission [11], and intelligent health management [12]. Among them, the real-time monitoring of moisture content is widely used in agricultural production, geological forecasting, and road-based engineering [13]. In geological engineering, Yang et al. [14] studied the influence of environmental factors on slope stability by monitoring the change of slope moisture content to prevent geological disasters, such as landslides and mudslides. In the area of relic

protection, Ruiz Valero et al. [15] monitored the existing environment of a building and evaluated its reinforced stability and water damage. In the subgrade project, Ahmed et al. [16] used the change of moisture content to analyze the influence of freezing, rain, soil, and other factors on subgrade performance. Moisture distribution can be monitored through several methods. The time-domain reflectometry (TDR) method, ground detection radar method, soil resistance method, and capacitance method have been used for a single point or small ranges [17]. The distribution and change of soil moisture in large areas of time and space are usually determined using remote sensing technology [18]. However, many problems with the real-time monitoring of soil moisture content still exist. For example, the suitability and accuracy of test methods are susceptible to soil influences and constraints. In addition, measuring instruments, sensors, and other hardware have common disadvantages, including large size, high energy consumption, high cost, and other issues.

As the basis of road surface, the quality (strength and stability) of a subgrade directly affects the service life of pavement structures [19]. Given the lack of carrying capacity, the subgrade is permanently deformed, resulting in various problems on the road surface, such as subsidence and ruts [20]. This kind of engineering problem is closely related to the moisture content and migration law in soil [21]. The researchers aim to solve this engineering problem by performing in situ monitoring and a water migration model test to calibrate the moisture content of subgrade soil and its evolution mechanism evaluation. The relationship between the soil characteristic parameters (i.e., dielectric constant, conductivity, and resistivity) measured by the sensor and the soil moisture content (i.e., the sensor calibration model) must be determined by obtaining the moisture content of the soil through the sensor [22]. The classical Topp model characterizes the relationship between the volume moisture content of the soil body and the dielectric constant with three polynomials [23]. Ledieu et al. [24] used the square root formula to characterize the relationship between volume moisture content and dielectric constants. Cui et al. [25] validated and compared the feasibility of the Topp and Ledieu models through laboratory and in situ tests. The existing calibration model is relatively complex, and the accuracy of the test results is influenced by other components in the soil [26]. Moreover, the moisture of the subgrade soil evaporates violently because of the perennial high temperature and heavy rainfall in southern China [27]. The moisture content of the subgrade changes extensively; thus, the effect of the moisture content on the modulus of the subgrade must be fully considered. Therefore, monitoring the moisture changes of highway foundations during operation is vital to improve the drainage design and maintenance measures of highways in the area.

Careful consideration of the relationship between soil moisture content and dry density can improve the accuracy of the sensor to determine the moisture content. In addition, the simultaneous detection of the compaction and moisture content changes of the subgrade soil has important engineering significance in subgrade engineering. In the present research, a calculation model for moisture content, dielectric constant, and permeability has been established based on the TDR principle. Laboratory calibration tests were performed using PVC pipes to determine the engineering properties of silt. The influencing factors and changing law of the moisture content were compared and analyzed, and the measurement quality of the sensor was verified. The TDR sensor was applied to the southern subgrade slope to verify the monitoring method by observing the moisture content of the slope for half a year.

2. Testing Principle and Factor Analysis

2.1. Time-Domain Reflectometry and Its Principle. The basic principle of TDR involves the propagation of electromagnetic waves at different rates in material medium with different dielectric constants. The dielectric constant in the soil depends mainly on moisture content because the dielectric constant of water is much larger than that of other substances in the soil.

The dielectric constant of the solid-liquid-gas three-phase mixture evidently changes when the proportion of water in a certain volume of soil varies. Therefore, soil moisture content can be calculated by measuring the dielectric constant of soil. Topp et al. [23] first measured the apparent dielectric constant of soil. They then established the empirical relationship between the volume moisture content and the dielectric constant in different types of soil based on a large number of experiments, as shown in equation (1). In each TDR test unit, the relationship similar to equation. (1) must be calibrated separately and built into the chip to convert the field measurement of ε to the volumetric moisture content of the soil w.

$$w = -0.53 \times 10^{-2} + 2.92 \times 10^{-2}\varepsilon - 5.5 \times 10^{-4}\varepsilon^2 + 4.3 \times 10^{-6}\varepsilon^3, \quad (1)$$

where w is the volumetric moisture content; ε is the dielectric constant of the soil.

Reflection and refraction occur when the electromagnetic wave meets the boundary between two kinds of media in the process of propagation. The propagation velocity of the electromagnetic wave in different media is related to the dielectric constant, as shown in equation (2) [28]. In general, the permeability of a nonmagnetic material (μ) is nearly the same as that of a vacuum (μ_0). Therefore, equation (2) shows that the propagation velocity of the electromagnetic wave is mainly affected by the dielectric constant ε.

$$v_p = \frac{1}{\sqrt{\mu\varepsilon}}, \quad (2)$$

where v_p is the propagation rate of electromagnetic wave; μ is the magnetic permeability of the soil.

The TDR sensor has been widely used in measuring soil moisture content, and its measurement results are fast and accurate. However, TDR sensor application also has some drawbacks [29]. The time (t) between two reflections is very short because of the high velocity (v_p) of the electromagnetic wave and the limited length of the probe. The total time

spent on the forward and back propagation of the signal on the probe is greater than the rising edge time of the excitation signal. Realizing ultra-high-speed delay measurement technology is difficult because of the influence of probe length and geometry length.

2.2. Effect Factor Analysis. Based on the abovementioned discussion, TDR calculates the dielectric constant of the propagation medium through the propagation rate of the electromagnetic wave. The dielectric properties of soil are significantly affected by frequency, temperature, and soil dry density.

The existing laboratory experiments showed that the dielectric properties of soil change with frequency potentially because of dielectric polarization. An induced charge generates and weakens the electric field when a dielectric is placed in an applied electric field. The dielectric constant is the ratio of the original applied electric field to the electric field in the final medium. At the micro level, generating an induced charge refers to dielectric polarization, which can be divided into two categories, elastic displacement polarization and relaxation polarization. Elastic displacement polarization is considered an instantaneous polarization; therefore, it is not affected by frequency. For relaxation polarization, the orientation polarization time of the inherent electric distance is between 10^{-2} and 10^{-8}. Thus, if the measurement frequency is within this range or higher than its maximum value, then the dielectric properties inevitably change under the influence of relaxation polarization.

Soil dielectric properties are affected by temperature because temperature plays an essential role in determining relaxation time, as shown in equation (3) [30]. In general, a body is most stable when it has the lowest energy. As the temperature increases, the relaxation time of the medium decreases, as shown in equation (3). Therefore, the dielectric constant increases with the increase of temperature.

$$\tau(T) = \tau_0 e^{(E_a/KT)}, \tag{3}$$

where T is the temperature; K is the Boltzmann constant; and E_a is the effective electric field on the dipole.

The physical explanation is that the energy of the dipole inside the dielectric increases with the increase of temperature, and the dipole changes from relatively stable to active. Macroscopically, the value of dielectric constant increases with the increase of dielectric susceptibility.

The volume of air in soil mainly comes from the contribution of the pores between soil particles. Soil dry density refers to the ratio of the dried soil mass to the original soil volume, as shown in equation (4). Under the same moisture content, the higher the soil dry density, the higher is the mass of soil particles and water in the unit volume. This condition makes the unit volume of soil particles and water increase and the unit volume of natural air decrease. Soil dry density reflects the compactness of the soil and can indirectly reflect air content. Therefore, the higher the soil dry density, the higher is the dielectric constant of the soil. On the contrary, the lower the soil dry density, the lower is the dielectric constant of the soil.

$$\rho_d = \frac{m_d}{V}, \tag{4}$$

where ρ_d is the dry density of soil; m_d is the quality of the dried soil; and V is the volume of soil before drying.

According to domestic and foreign literature, soil moisture content measurement by the TDR method is inevitably restricted by the factors that influence the dielectric properties of soil. In general, the dielectric constant is affected by signal frequency, soil temperature, and soil dry density. However, most TDR sensors on the market do not consider the influence of soil dry density on the results of soil moisture content measurement. This scenario increases the measurement errors of the TDR sensor.

3. Materials and Sensor Calibration

The moisture content of subgrade monitoring is an important means of long-term evaluation of southern humid area subgrade stability. In order to use the TDR sensor to accurately measure the moisture content of subgrade soil change, a laboratory calibration test is one of the essential preparations before on-site monitoring.

3.1. Materials. The soil sample for the test came from the salt soil of a highway subgrade in Guangdong Province. The size gradation is an important parameter to evaluate engineering properties and optimize material properties for soils or mixtures [31]. The particle grading curve is shown in Figure 1. The density of natural soil is 1.21 g/cm^3, and the initial mass moisture content is 4.35%. The liquid limit is 34%, and the plastic limit is 13%. The compaction test determines that the maximum dry density of the soil sample is 1.34 g/cm^3, and the optimum moisture content is 14.6% [32].

3.2. Calibration Method. In this study, a PVC pipe with one end closed was used as a fixed volume container for the moisture content comparison test, and the same soil sample was used for two parallel tests. Under the condition that the initial moisture content and the quality of the soil sample are known, the deionized water that needs to be added is calculated to prepare soil samples with different moisture content. The test soil sample prepared by the wet method is about 8000 g, and the designed moisture content is 7%, 10%, 13%, 16%, and 19%, respectively. The soil samples were sampled to determine the initial mass moisture content after the material was uniformed for 24 hours. In order to simulate the actual compaction state of the subgrade as much as possible, the TDR sensor was placed in the middle of the PVC pipe, and the test soil samples were backfilled and compacted in 10 layers according to the dry density of the construction site, and necessary sealing measures were taken. The schematic diagram of the calibration test device is shown in Figure 2.

The specific evaluation steps are as follows: (a) A thermometer was inserted into the center hole of the probe positioning mold, and the temperature was checked using the thermometer. (b) The thermometer was unplugged. (c)

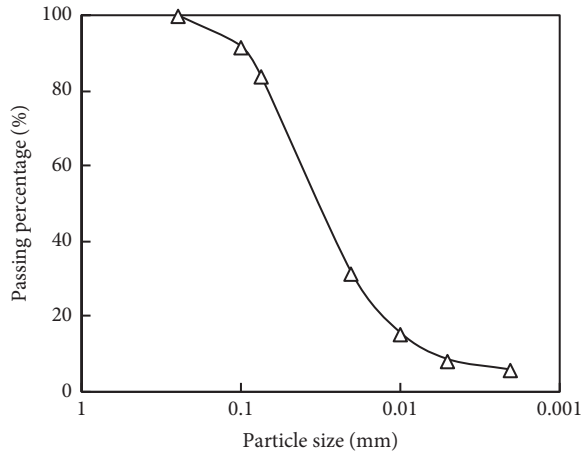

Figure 1: Soil particle sieving result.

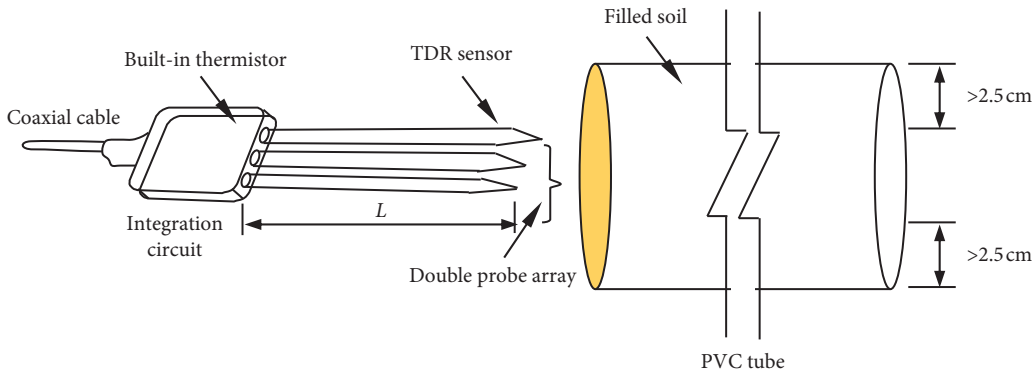

Figure 2: Schematic diagram of the TDR sensor and the calibration test device.

The probe was driven into the soil, the probe positioning mold was removed, and the soil powder at the edge of the PVC pipe was cleaned. (d) The test instruments were connected to determine the dielectric constant and permeability of soil samples through waveform analysis. (e) The soil samples were selected from the upper, middle, and lower parts of PVC pipes, and the average moisture content of soil samples was accurately obtained through the drying method.

The dielectric constant of soil is related to the magnetic conductivity of soil, the proportion of its components, and soil type. Siddiqui et al. established the relationship between the mass moisture content and dry density of soil and the apparent dielectric constant of soil, as shown in equation (5), to consider the influence of dry density. As calibration coefficients, a is related to the dielectric constant of soil particles and the dry density of soil, and b is related to the properties of pure liquid. The calibration of parameters a and b can be obtained using soil samples with different moisture contents and dry densities obtained by the standard compaction test (ASTM D698-2000).

$$\sqrt{\varepsilon} = a\frac{\rho_d}{\rho_w} + bw, \tag{5}$$

where ρ_w represents the density of water; a and b are the calibration coefficients of the dielectric constant.

In general, the soil dielectric constant and magnetic permeability are regarded as two independent parameters. Dielectric constants are used to obtain the soil moisture content, and permeability is used for evaluation. However, these two parameters have an inherent relationship. The soil moisture content can be determined through the test on dielectric constants and magnetic permeability by applying the inner link between them without the density equation. Therefore, considering the soil dielectric constant and magnetic permeability of the influence of soil moisture content, Yu and others proposed the tests of soil moisture content and dry density of the one-step method. First, they set up the dielectric constant of the soil electrical conductivity calibration equation, as shown in equation (6). Then, according to equations (5) and (6), the soil dry density and moisture content can be determined by equations (7) and (8).

$$\sqrt{\mu} = c\frac{\rho_d}{\rho_w} + dw, \tag{6}$$

$$\rho_d = \frac{d\sqrt{\varepsilon} - b\sqrt{\mu}}{ad - cd}\rho_w, \tag{7}$$

$$w = \frac{a\sqrt{\mu} - c\sqrt{\varepsilon}}{ad - cd}, \tag{8}$$

where c and d are the calibration coefficients of the magnetic permittivity.

Moreover, the dielectric constant and conductivity tests are affected by the ambient temperature. The temperature of the field test may not be the same as the temperature of the laboratory calibration. Therefore, temperature compensation is required during field testing. The influence of temperature on the dielectric constant of soil is related to soil type, as shown in equation (9). The test temperature T is generally between 4°C and 40°C.

$$\varepsilon_{20^\circ\mathrm{C}} = \varepsilon_T \times f(T), \tag{9}$$

where $f(T)$ represents the temperature compensation function. For noncohesive soil, $f(T) = 0.97 + 0.0015T$, and for cohesive soil, $f(T) = 1.10–0.004T$.

Therefore, according to the test results and calibration equation, the least square method was used to fit the test curve, and the corresponding calibration coefficients a, b, c, and d can be obtained.

4. Quality Evaluation and Subgrade Application

4.1. Laboratory Results of Sensor Calibration. Figure 3 shows the regression curve of the calibrated parameter results. Figure 3(a) illustrates the relationship between the dielectric constant and the mass moisture content of the soil, thereby obtaining the calibration coefficients a and b of the dielectric constant. Figure 3(b) illustrates the relationship between the magnetic permeability and the mass moisture content of the soil, thereby obtaining the magnetic permeability calibration coefficients c and d. According to the calibration curve in Figure 3, calibration results are in good agreement. The moisture content and dry density can be obtained by a test in the field through calibration coefficients and prediction formulas. In addition, the parameters of different soil samples can be measured through laboratory tests to establish TDR sensors database. According to the established database, the moisture content and dry density of the field soil samples can be easily and quickly obtained. If the subgrade engineering requires high accuracy, then the sensor test should strictly follow the steps in Section 3.2, and the test soil sample must be calibrated before the test.

4.2. Comparison between the Calculated and Actual Moisture Content. Figure 4(a) shows the results of moisture content measurement obtained using the TDR sensor at 25°C. The actual soil mass moisture content ranges from 4.35% to 18.83%. The sensor tests six groups of soil samples under different dry density conditions and outputs the dielectric parameters and permeability. The moisture content calculated according to equation (8) is compared with the actual moisture content obtained through the drying method. Ideally, the calculated moisture content and actual moisture content should fall on the straight line with a slope of 1 in Figure 4. However, in most cases, the experimental results show that the calculated moisture content is greater than the actual moisture content, and the absolute error is between −3.35% and 0.68%. Therefore, this finding shows that the measurement accuracy of the sensor in this experiment is not high, and the consistency check R^2 is 84.64%. The reason is that the TDR sensor is calibrated by the general relationship between volumetric moisture content and dielectric constant. According to domestic and foreign literature, the content of bound water in the soil has a considerable effect on the determination of dielectric constant because the apparent dielectric constant of the soil is affected by factors such as soil quality, dry density, and temperature. In a certain frequency range, the dielectric constant of free water is constant, and the dielectric constant of bound water increases as the content of bound water increases.

The digital temperature sensor is used to verify the temperature of the TDR soil temperature-moisture sensor. Figure 4(b) shows the temperature results of the six soil samples with different bulk densities and moisture contents measured by digital temperature sensors and TDR sensors. Figure 4(b) shows that the calculated temperature and the measured temperature fall on both sides of the 45°C line closely, and the absolute error between them is from −1.7°C to 0.9°C. The temperature measurement result of the TDR sensor is relatively reliable, and the consistency test R^2 is 98.85%.

4.3. Effect of Temperature and Dry Density on Sensor Evaluation. Figure 5 shows the effect of temperature on the output current of the TDR sensor's moisture content port under different compaction conditions when the moisture content is 10.11% and 18.83%. The degree of compaction used in this experiment is 90%, 93%, and 96%, and the corresponding dry densities are 1.21, 1.25, and 1.29 g/cm^3. The test results indicate that the output current of the TDR sensor gradually increases as the temperature increases. When the temperature is less than 10°C, the output current rises slowly; however, it rises rapidly when it is greater than 10°C. This phenomenon is also found in soil samples with other moisture content.

The dielectric properties in matter represent the dynamic balance between molecular polarization and Brownian motion in the electrostatic field. The increase in temperature can accelerate the orientation movement of polar molecules and the Brownian movement of particles in the soil. This situation leads to an increase in the dielectric constant of the soil, which is reflected in the increase in the output current. Figure 5 shows that temperature is one of the main factors affecting the output current of the TDR sensor, and eliminating the influence of temperature is vital to improve the detection accuracy of soil moisture content.

Moreover, the results in Figure 5 show that the output current generally increases with the increase of soil dry density. The output current of the sensor increases rapidly when the soil dry density increases from 1.21 g/cm^3 to 1.29 g/cm^3. With the same moisture content, the soil samples with high soil dry density have larger soil particle content per unit volume and lower air content than the soil samples with low soil dry density. Under the same temperature, the relative permittivity of soil particles is greater than that of air. Thus, the output current increases as the soil dry density

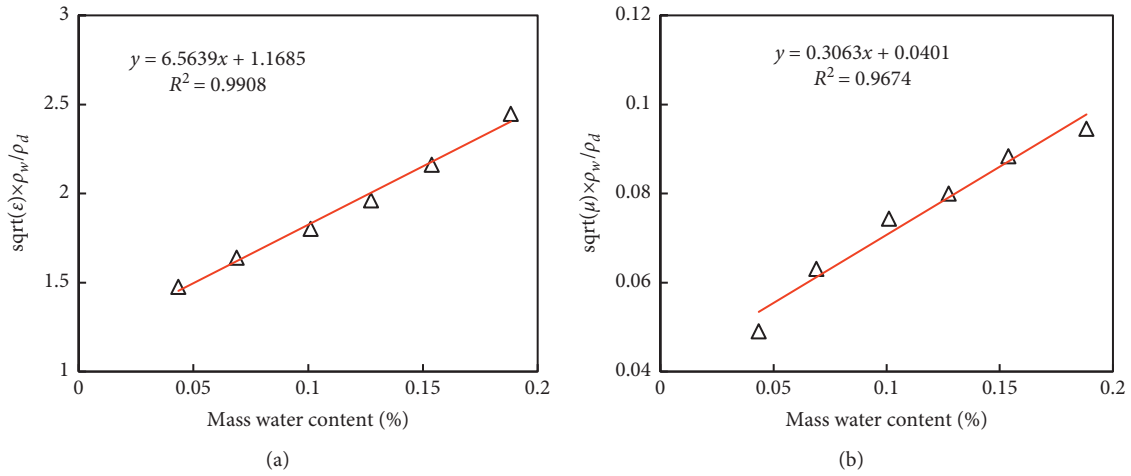

Figure 3: Calibration results of sensor parameters: (a) dielectric constant; (b) magnetic permittivity.

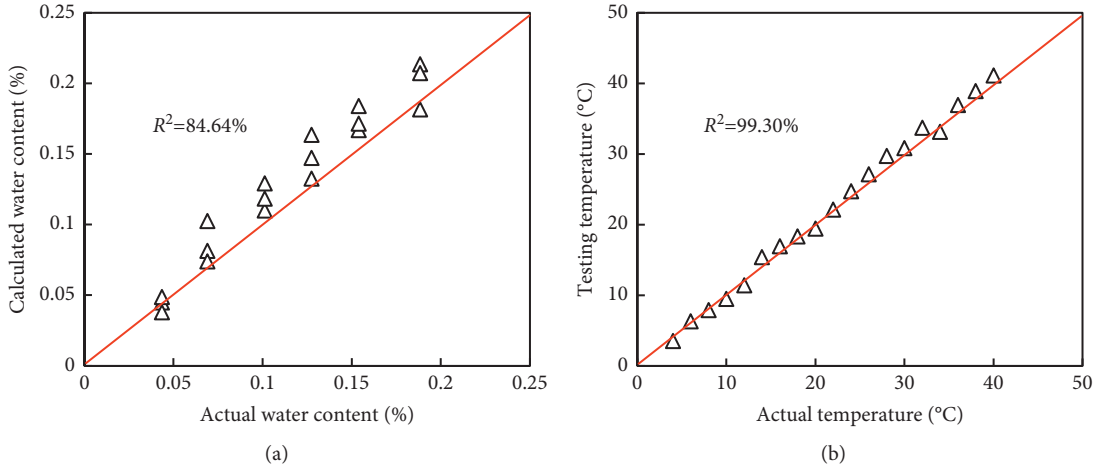

Figure 4: Testing results of (a) moisture content and (b) temperature in the laboratory.

increases. The studies about the samples with the other five moisture contents have similar conclusions. Under the same temperature, the output current increases with the increase of soil dry density.

4.4. Seasonal Variations in Moisture of Subgrade. The laboratory calibration test indicated that the moisture content measured by the TDR sensor has a good linear correlation with the actual one. The relevant parameters should be determined according to the formula of this research before burying the TDR sensor. Then, the actual moisture content of the subgrade structure can be obtained through the TDR sensor.

This test measures the depth of the slope and the top surface of the subgrade affected by precipitation under natural conditions. Two TDR sensors were buried in two layers in the subgrade with a filling height of 15 m, as shown in Figure 6(a). The sensor positions along the direction of the cross section of the subgrade are 1 and 2 m away from the subgrade slope. The initial moisture content of the in situ soil was taken while the two TDR sensors were being buried, and the initial data were taken after the instrument readouts have been stable for 4 hours. During the on-site monitoring, the subgrade structure of the test section has experienced the rainy season from June to August and the dry season from September to November. The moisture content of the subgrade changes with the seasons, as shown in Figure 6(b).

The monitoring data showed that the moisture content of the silt subgrade during the roadbed construction was large. After half a year of settlement, the soil was gradually drained and consolidated, and the moisture content of the subgrade section gradually decreased. The moisture content of observation points at a distance of 1 m from the slope is lower than that of observation points 2 m away from the slope because the soil near the slope surface is much susceptible to external weather conditions. These findings verified that the monitoring method determined by the laboratory calibration test is effective.

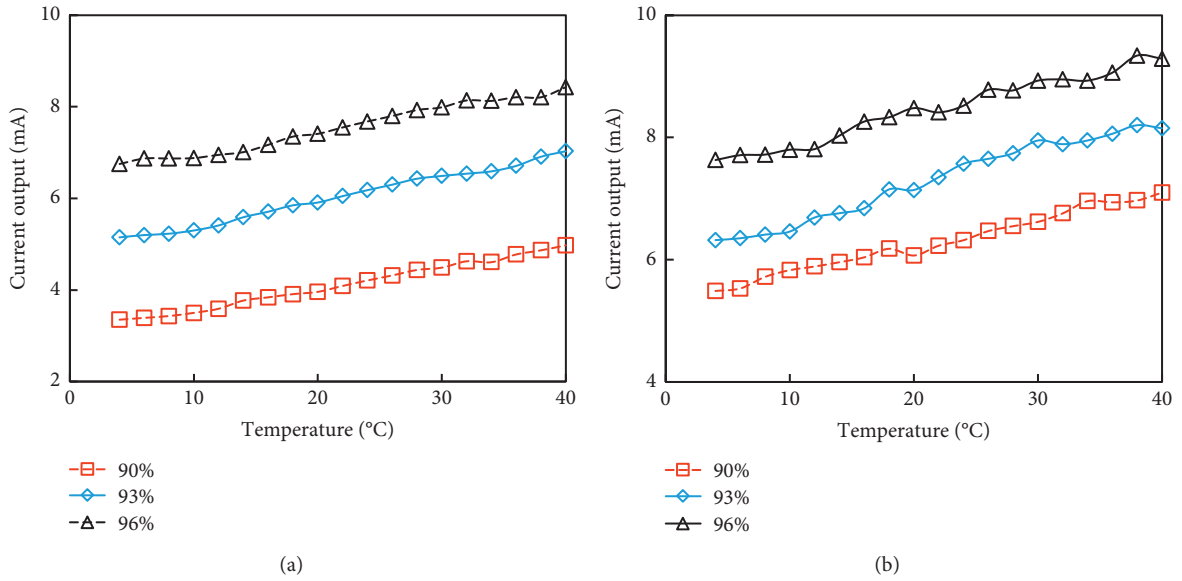

Figure 5: Influence of temperature on TDR sensor test results at the moisture of (a) 10.11%; (b) 18.83%.

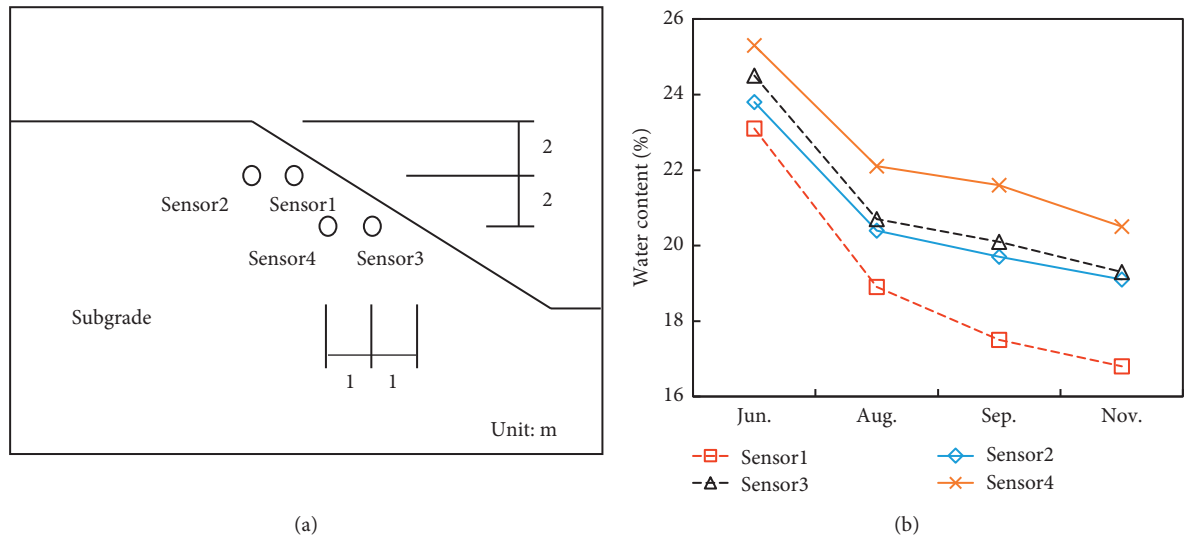

Figure 6: Field (a) sensor layout plot and (b) moisture-time relationship of subgrade.

5. Conclusions

The structural strength and the agricultural productivity of soil are closely related to the moisture content. TDR sensors have been widely used in the agricultural production and service monitoring in the civil engineering. This study analyzed the influence of moisture content and dry density on the quality of testing sensors through laboratory calibration experiments. At the same time, taking a typical slope in the southern China as an example, a field study of the moisture content of the subgrade soil was carried out, and the periodic changes of the moisture content were tracked. The main findings of this paper are as follows:

(a) Changes in soil moisture content or dry density results in significant changes in soil dielectric constant and magnetic permeability. In TDR calibration, the dielectric constant and the electrical conductivity are used as intermediate variables. The results indicated that the coupling effect between the volumetric moisture content and the dry density of soil should be completely considered.

(b) Based on the principle of TDR, a calculation model for dielectric constant and electrical conductivity has been established. The model has a good fit effect and stability by comparing the calculated moisture content and actual results of soil samples.

(c) It provides a feasible means for the real-time monitoring of the moisture content on the side slope of the subgrade and has theoretical and engineering application significance. Through the model calibration, the influence law of moisture content and temperature on soil dielectric constant is analyzed. The quality of the model has been verified with the fitting goodness more than 90%.

(d) After half a year of settlement, since the soil was gradually drained and consolidated, the moisture content of the subgrade section gradually decreased. The test results shows that the soil near the surface of the slope was more susceptible to external weather conditions. It also verifies that the monitoring method determined by the laboratory TDR calibration test was successful.

Data Availability

The testing data used to support the findings of this study are included within the article.

Conflicts of Interest

The authors declare no conflicts of interest.

Acknowledgments

The authors gratefully acknowledge the National Key Research and Development Program of China (2019YFF0216804).

References

[1] J. Jiang, J. Wang, W. Wang, and W. Zhang, "Modeling influence of gas/liquid/solid three-phase boundary zone on cathodic process of soil corrosion," *Electrochimica Acta*, vol. 54, no. 13, pp. 3623–3629, 2009.

[2] J. Zhang, F. Li, L. Zeng, J. Peng, and J. Li, "Numerical simulation of the moisture migration of unsaturated clay embankments in southern China considering stress state," *Bulletin of Engineering Geology and the Environment*, vol. 80, no. 1, pp. 11–24, 2021.

[3] P. R. Ward, K. C. Flower, N. Cordingley, C. Weeks, and S. F. Micin, "Soil water balance with cover crops and conservation agriculture in a mediterranean climate," *Field Crops Research*, vol. 132, pp. 33–39, 2012.

[4] C. F. Chiu, W. M. Yan, and K.-V. Yuen, "Reliability analysis of soil-water characteristics curve and its application to slope stability analysis," *Engineering Geology*, vol. 135-136, pp. 83–91, 2012.

[5] W. Zhang, H. Zheng, F. Jiang, Z. Wang, and Y. Gao, "Stability analysis of soil slope based on a water-soil-coupled and parallelized smoothed particle hydrodynamics model," *Computers and Geotechnics*, vol. 108, pp. 212–225, 2019.

[6] Y. Lu and S. H. Liu, "Cracking in an expansive soil under freeze–thaw cycles," *Sciences in Cold and Arid Regions*, vol. 9, no. 4, pp. 392–397, 2018.

[7] Y. Yao, J. Ni, and J. Li, "Stress-dependent water retention of granite residual soil and its implications for ground settlement," *Computers and Geotechnics*, vol. 129, Article ID 103835, 2021.

[8] Z. Gao, Y. Zhu, C. Liu, H. Qian, W. Cao, and J. Ni, "Design and test of a soil profile moisture sensor based on sensitive soil layers," *Sensors*, vol. 18, no. 5, Article ID 1648, 2018.

[9] Q. Wang, X. e. Liu, S. Yang, M. Jiang, and J. Cao, "Non-destructive detection of density and moisture content of heartwood and sapwood based on X-ray computed tomography (X-CT) technology," *European Journal of Wood and Wood Products*, vol. 77, no. 6, pp. 1053–1062, 2019.

[10] Q. Kong, H. Chen, Y.-l. Mo, and G. Song, "Real-time monitoring of water content in sandy soil using shear mode piezoceramic transducers and active sensing-a feasibility study," *Sensors*, vol. 17, no. 10, Article ID 2395, 2017.

[11] X. Zhang, J. Zhang, L. Li, Y. Zhang, and G. Yang, "Monitoring citrus soil moisture and nutrients using an IoT based system," *Sensors*, vol. 17, no. 3, p. 447, 2017.

[12] K. Chandrasekaran and M. Senthilkumar, "Effect of herbal extract treatment on the moisture management properties of cotton knitted fabrics," *Journal of Natural Fibers*, vol. 17, no. 4, pp. 557–572, 2020.

[13] J. S. Whiteley, J. E. Chambers, S. Uhlemann, P. B. Wilkinson, and J. M. Kendall, "Geophysical monitoring of moisture-induced landslides: a review," *Reviews of Geophysics*, vol. 57, no. 1, pp. 106–145, 2019.

[14] Z. Yang, H. Cai, W. Shao et al., "Clarifying the hydrological mechanisms and thresholds for rainfall-induced landslide: in situ monitoring of big data to unsaturated slope stability analysis," *Bulletin of Engineering Geology and the Environment*, vol. 78, no. 4, pp. 2139–2150, 2019.

[15] L. Ruiz Valero, V. Flores Sasso, and E. Prieto Vicioso, "In situ assessment of superficial moisture condition in façades of historic building using non-destructive techniques," *Case Studies in Construction Materials*, vol. 10, Article ID e00228, 2019.

[16] A. Ahmed, S. Hossain, M. S. Khan, and A. Shishani, "Data-based real-time moisture modeling in unsaturated expansive subgrade in Texas," *Transportation Research Record: Journal of the Transportation Research Board*, vol. 2672, no. 52, pp. 86–95, 2018.

[17] Y.-S. Yao, J.-L. Zheng, Z.-S. Chen, J.-H. Zhang, and Y. Li, "Field measurements and numerical simulations of temperature and moisture in highway engineering using a frequency domain reflectometry sensor," *Sensors*, vol. 16, no. 6, p. 857, 2016.

[18] E. Babaeian, M. Sadeghi, S. B. Jones, C. Montzka, H. Vereecken, and M. Tuller, "Ground, proximal, and satellite remote sensing of soil moisture," *Reviews of Geophysics*, vol. 57, no. 2, pp. 530–616, 2019.

[19] J. Li, J. Zheng, Y. Yao, J. Zhang, and J. Peng, "Numerical method of flexible pavement considering moisture and stress sensitivity of subgrade soils," *Advances in Civil Engineering*, vol. 2019, Article ID 7091210, 2019.

[20] J. Qian, Y. Yao, J. Li, H. Xiao, and S. Luo, "Resilient properties of soil-rock mixture materials: preliminary investigation of the effect of composition and structure," *Materials*, vol. 13, no. 7, p. 1658, 2020.

[21] Y. Yao, S. Luo, J. Qian, J. Li, and H. Xiao, "Soil-water characteristics of the low liquid limit silt considering compaction and freeze-thaw action," *Advances in Civil Engineering*, vol. 2020, Article ID 8823666, 2020.

[22] J. Pytka, P. Budzyński, M. Kamiński, T. Łyszczyk, and J. Józwik, "Application of the TDR soil moisture sensor for terramechanical research," *Sensors*, vol. 19, no. 9, Article ID 2116, 2019.

[23] G. C. Topp, J. L. Davis, and A. P. Annan, "Electromagnetic determination of soil water content: measurements in coaxial transmission lines," *Water Resources Research*, vol. 16, no. 3, pp. 574–582, 1980.

[24] J. Ledieu, P. De Ridder, P. De Clerck, and S. Dautrebande, "A method of measuring soil moisture by time-domain reflectometry," *Journal of Hydrology*, vol. 88, no. 3-4, pp. 319–328, 1986.

[25] F. Cui, Y. Du, J. Ni, Z. Zhao, and S. Peng, "Effect of shallow-buried high-intensity mining on soil water content in ningtiaota minefield," *Water*, vol. 13, no. 3, p. 361, 2021.

[26] J. Zhang, A. Zhang, C. Huang, H. Yu, and C. Zhou, "Characterising the resilient behaviour of pavement subgrade with construction and demolition waste under Freeze-Thaw cycles," *Journal of Cleaner Production*, vol. 300, Article ID 126702, 2021.

[27] J. Zhang, A. Zhang, J. Li, F. Li, and J. Peng, "Gray correlation analysis and prediction on permanent deformation of subgrade filled with construction and demolition materials," *Materials*, vol. 12, no. 18, p. 3035, 2019.

[28] H. Bhuyan, A. Scheuermann, D. Bodin, and R. Becker, "Use of time domain reflectometry to estimate moisture and density of unbound road materials: laboratory calibration and field investigation," *Transportation Research Record: Journal of the Transportation Research Board*, vol. 2655, no. 1, pp. 71–81, 2017.

[29] G. Curioni, D. N. Chapman, A. C. D. Royal et al., "Time domain reflectometry (TDR) potential for soil condition monitoring of geotechnical assets," *Canadian Geotechnical Journal*, vol. 56, no. 7, pp. 942–955, 2019.

[30] Z. Tian, T. Ren, Y. Kojima, Y. Lu, R. Horton, and J. L. Heitman, "An improved thermo-time domain reflectometry method for determination of ice contents in partially frozen soils," *Journal of Hydrology*, vol. 555, pp. 786–796, 2017.

[31] J. Li, J. Zhang, G. Qian et al., "Three-dimensional simulation of aggregate and asphalt mixture using parameterized shape and size gradation," *Journal of Materials in Civil Engineering*, vol. 31, no. 3, Article ID 04019004, 2019.

[32] IHSMT, *Test Methods of Soils for Highway Engineering (JTG 3430-2020)*, Beijing, China, 2021.

Hindawi
Advances in Materials Science and Engineering
Volume 2021, Article ID 9205509, 12 pages
https://doi.org/10.1155/2021/9205509

Research Article

An Advanced Otsu Method Integrated with Edge Detection and Decision Tree for Crack Detection in Highway Transportation Infrastructure

Haihang Han,[1] Hanyu Deng,[2,3] Qiao Dong,[2] Xingyu Gu,[2] Tianjie Zhang,[1] and Yangyang Wang[1]

[1]*Zhejiang Scientific Research Institute of Transport, Zhejiang Provincial Key Lab for Detection and Maintenance Technology of Road and Bridge, Hangzhou, Zhejiang 311305, China*
[2]*School of Transportation, National Demonstration Center for Experimental Road and Traffic Engineering Education, Southeast University, Nanjing, Jiangsu 211189, China*
[3]*Department of Civil and Environmental Engineering, University of California, Davis, Berkeley, CA 95616, USA*

Correspondence should be addressed to Qiao Dong; qiaodong@seu.edu.cn

Received 19 April 2021; Revised 1 July 2021; Accepted 13 July 2021; Published 21 July 2021

Academic Editor: Francisco Javier Fernández Fernández

The detection of various cracks on pavement surfaces has drawn more and more attention from pavement maintenance engineers. In the traditional pavement image segmentation, due to the small area of the pavement cracks, the gray level of crack pixels only accounts for a very small portion in the grayscale histogram, making it difficult to segment. This paper developed an improved Otsu method integrated with edge detection and a decision tree classifier for cracking identification in asphalt pavements. An image preprocessing approach including Gaussian function-based spatial filtering and top-hat transform is firstly proposed to reduce the influence of poor shading and lighting effects significantly. Four edge detection operators including Prewitt, Sobel, Gauss–Laplace (LoG), and Canny are evaluated. The Canny edge detection has demonstrated outstanding performance in crack detection; this algorithm helps to obtain more details of both cracks and noises. The Sobel and LoG operators show similar image segmentation and retain fewer noises. The decision tree classifier based on the ID3 algorithm can effectively classify different types of cracks including transverse, longitudinal, and block ones.

1. Introduction

With the rapid development of the highway transportation infrastructure network and the increase of pavement service life, pavement distress including cracks, potholes, ruts, etc., increase rapidly. The detection and treatment of pavement distress have gradually become an important focus in the field of pavement engineering. As major pavement distress, cracks usually indicate the reduction of pavement performance and risk more serious pavement structural distresses. Therefore, the quick detection and treatment of pavement cracks at an early age is the key to extending the service life of pavements and saving maintenance funds [1]. Traditional crack detection methods rely on manual identification, which is inefficient and subjective. In recent years, a variety of intelligent detection equipment such as multifunctional pavement detection vehicles have been used in pavement distress evaluation, which usually involves an automatic collection of high-quality pavement images without the traffic's influence.

With the development of computer technology and digital image processing technology, digital pavement crack recognition methods began to appear and develop rapidly. Morphological operations like top-hat and bottom-hat are applied for the contrast enhancement of the image, which helps to achieve better efforts of the segmentation of verminous objects like retinal vessels [2]. Multiscale new top-hat transform was also conducted on infrared image

enhancement algorithm through contrast enhancement [3]. Experts and scholars have proposed many automatic crack extraction methods based on pavement surface images. The classical edge detection algorithm is used to obtain the crack edge by extracting the pixels with a larger gradient [4, 5]. Tsai et al. used different edge detection operators including Sobel, LoG, Canny, and Prewitt to detect the crack structure on the original concrete [6]. It was found that the LoG operator is ideal and relatively simple. Canny operator has the best capability to extract weak edges, but it is also more vulnerable to noise. The performance of six edge detectors and the deep convolutional neural networks (DCNN) for concrete crack detection was investigated and compared. A hybrid crack detector by combining the DCNN and the edge detector was proposed, which had 24 times less noise than the least noisy edge detector [7]. Wang et al. proposed an asphalt pavement crack detection algorithm based on multiscale ridge edge [8]. The filter was constructed by Gaussian function, and its first-order and second-order derivatives were used to convolute the rows and columns of the image respectively to determine the ridge edge center and width. Then, the ridge edge detected at each scale was fused to obtain the ridge edge image and finally denoised and connected to detect cracks by the expansion and minimum spanning tree algorithm. Mao-De et al. proposed a pavement crack edge detection algorithm based on the morphology [9]. For the pavement image after median filtering, the gradient operator and closing operator are appropriate for edge extraction and gap closure, which can better extract the skeleton of pavement cracks.

The threshold method segments pavement cracks and background by setting static or dynamic thresholds, realizing the automatic extraction of cracks [10, 11]. In 1979, Otsu proposed a classical threshold segmentation method based on a gray histogram [12]. The maximum value of the variance between classes was used as the criterion to obtain the threshold K, and then the image was binarized. This method is simple and easy to understand and has the potential to be extended to two or even multithreshold segmentation. Li et al. proposed a pavement crack image segmentation method related to the neighborhood difference histogram based on threshold idea, which has better effects for the early development of narrow cracks [13]. The steerable matched filtering and an active contour model [13] firstly enhances the contrast between cracks and surrounding pavement and captures crack discontinuity and curvature and then uses a region-based active contour model for crack segmentation. Ai et al. proposed an automatic image crack segmentation method based on probability and large-scale domain information on the pixel level using threshold segmentation [14]. Lau et al. proposed U-Net-based network architecture for the automated pavement crack segmentation [15]. The traditional convolutional network has a fully connected layer as the final layer, which the U-Net model only contains convolutional layers [15] and therefore is more efficient. The probability generation model and support vector machine were used to calculate the crack probability based on the pixel gray level and the domain information, employing the probability overlay map for crack segmentation and extraction.

After the segmentation results are obtained, the decision tree method is used to eliminate the noise part by further optimizing the segmentation results. Decision tree technology can establish classification models because of its simplicity and proximity like human thinking [16]. ID3 algorithm is one of the most representative decision tree algorithms. It adopts a branch strategy and constructs a decision tree through a selection window [17]. After that, the C4.5 algorithm [18] and SPRINT algorithm [19] were proposed. Qin et al. found that ID3 algorithm can quickly develop an accurate decision tree and is effective with a large number of attribute values [20]. The ID3 decision tree can effectively remove the noise from the segmentation results and improve the segmentation.

The deep learning-based method has achieved remarkable successes in computer vision, especially in the last five years [21–23]. However, it is still hard to interpret the detector based on the convolutional network. In addition, deep learning needs a large amount of high-quality images for training and requires extensive labeling work. Therefore, the traditional image process still has some advantages on pavement crack detection. The edge detection method and threshold method mentioned above are simple and highly efficient, but they are too sensitive to noise and have poor effects when the background is complex or the gray level of the background is close to that of the crack. In order to solve these problems, this study proposes a method combining the edge detection method with the threshold method. An improved Otsu method based on the edge detection algorithm is also proposed. A decision tree was then used to identify the cracks from background noises. Four edge detection methods including the Prewitt operator, Sobel operator, Laplace of Gauss (LoG) method, and Canny were evaluated with the improved optimal global threshold method in segmenting pavement images. The gray images of asphalt pavement surface collected by pavement evaluation vehicles are used for this study. The influences of different edge detection operators and the proposed algorithm on the final segmentation are discussed to validate the proposed method.

2. Methodology

There are several assumptions for crack detection based on image processing [4]. In the gray image of pavement surface including cracks, the gray values of crack pixels are deeper than those of pavement pixels, and the gray distribution of cracks and pavement backgrounds is independent. A crack is a narrow, continuous target and a group of interconnected segments with different directions. The width of a crack is not constant over the entire length. The pixels in the crack can be considered as the optical and/or geometric points of interest. In 1979, Otsu [12] proposed the optical global threshold image segmentation method, namely, the Otsu method. This method is considered to be the best method in global threshold processing under the condition of maximum interclass variance [4]. However, in the crack region segmentation of pavement images, if the crack area only accounts for a small proportion of the whole image, it is

difficult to obtain satisfying results by using the Otsu method. As shown in Figure 1, in this study, the edge detection method is firstly used to identify all edges in the image. The Otsu method is then used to select the optimal threshold value of the edge region in the pavement image for the segmentation, and the decision tree is adopted to further eliminate the noise from cracks.

2.1. Image Preprocessing. The quality of pavement surface images is usually reduced by many reasons including different lighting conditions such as sunny or cloudy, random grainy texture, nonuniform lighting, irregular shadows, pavement markings, watermarks, tire marks, oil stains, etc. These factors have a significant impact on the detection of cracks based on the image processing. The image preprocess mainly includes eliminating or reducing the negative effects of those factors and could significantly improve the image processing effectiveness. In this study, the Gaussian function-based spatial filtering and top-hat transform are utilized to preprocess the collected pavement images.

To filter out the noise to prevent false detection, a Gaussian filter kernel can be convolved with the image to slightly smooth the image to reduce the effects of obvious noise on the edge detector. Spatial domain filtering based on Gaussian function, including using a two-dimensional Gaussian function to construct a filter template in the spatial domain to smooth the image by spatial convolution of the input image, is described as follows:

$$G(x, y) = e\frac{x^2 + y^2}{2\sigma^2}, \tag{1}$$

where σ is the kernel, a distribution parameter, with a default value of 2.5 and x, y are the input values.

In grayscale morphology, the combination of image subtraction and opening and closing operations produces the top-hat transform and bottom-hat transform. The top-hat transform and bottom-hat transformation have generally similar functions, while the difference is the object. The top-hat transform is used for light objects on a dark background, and the bottom-hat transform is used for dark objects on a light background. The top-hat of f is defined as f minus its opening operation:

$$T_{\text{tophat}}(f) = f - (f \circ b). \tag{2}$$

Similarly, the bottom-hat of f is defined as the closing operation minus f:

$$T_{\text{bothat}}(f) = (f \cdot b) - f, \tag{3}$$

where f is the original image and b is a structural element. The size of b is decided mostly based on the conversion relation between the pixel and the realistic scale and the common size of cracks. The default size of b is 150 mm.

2.2. Edge Detection. One drawback of using the Otsu method for pavement crack detection is that crack only accounts for a very small area in the image and is not very prominent in the gray-level histogram of the image. This study adopts edge detection to identify the potential crack edge area first and then uses the Otsu method to only deal with the identified crack edge area to significantly improve the detection efficiency. Traditional edge detection algorithms in image processing include the Prewitt gradient operator, Sobel gradient operator, Gauss–Laplace (LoG) operator, and Canny operator. For edge detection, the edge in the image refers to an abrupt gray-level change. Both first-order and second-order differentiation can be used to detect gray-level change. The derivative of a function at a point can be defined by difference. There are several assumptions of the derivative. The approximation of the first derivative should be zero in the area of unique gray level and should not be zero at the start of gray steps or ramps and within the gray ramp. The approximation of the second derivative should be zero in the area of unique gray level, must not be zero at the start of gray steps or slops, and must be zero within the gray ramp. The derivative is approximated by Taylor expansion to construct the filter template. The approximates of the first and second derivatives of the function are shown as follows:

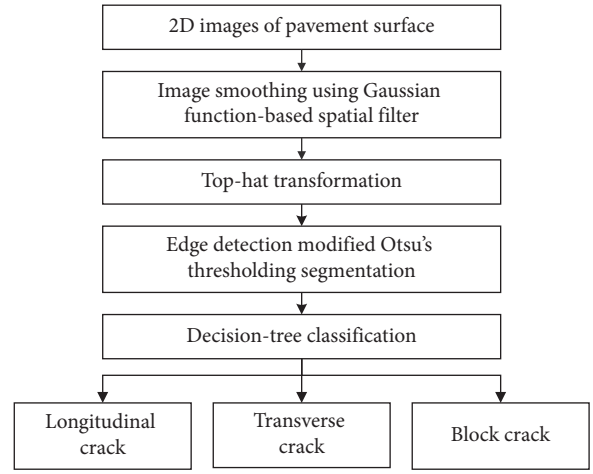

Figure 1: Flowchart of the methodology.

$$\frac{\partial f}{\partial x} = f'(x) = f(x+1) - f(x), \tag{4}$$

$$\frac{\partial^2 f}{\partial^2 x} = f''(x) = f(x+1) + f(x-1) - 2f(x). \tag{5}$$

In edge detection, there are three commonly used edge models: step edge, ramp edge, and roof edge. Figure 2 shows the grayscale curves and the first- and second-order differential curves of the ramp and the roof edge models. As shown in Figure 2(b), in the second derivative, the two extreme points are the maximum and minimum points of the second derivative at the bottom and top of the gray ramp. The intersection of the straight line connecting the maximum and minimum points of the second derivative and the zero gray-level axis is called the zero-crossing point of the second derivative.

2.2.1. Prewitt and Sobel Operator. The intensity and direction of the gray-level gradient in images can be detected based on the first-order difference of the image gray

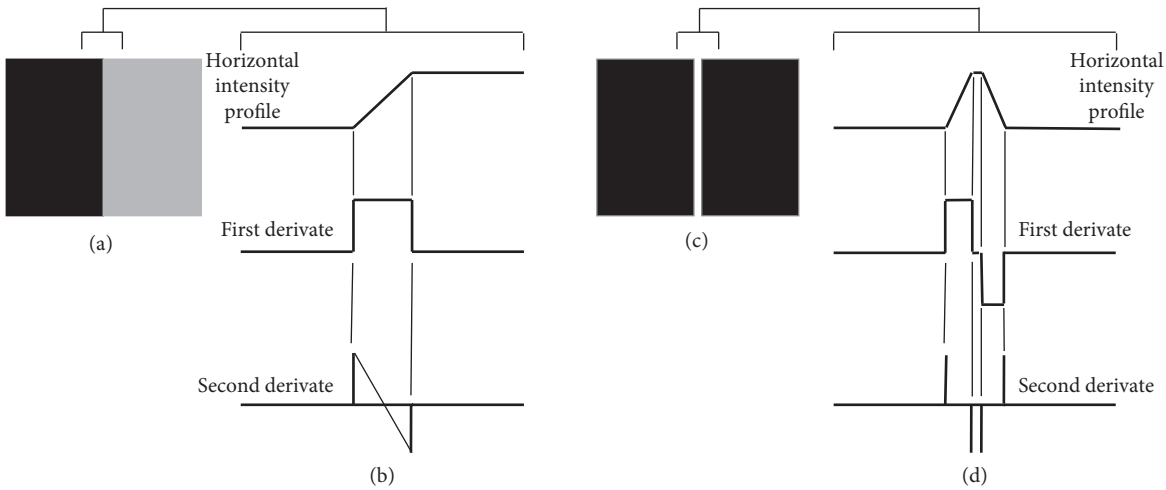

Figure 2: Schematic of the gray model and its first and second derivatives. (a) Ramp edge model. (b) Gray profile of the ramp edge model and its corresponding first and second derivatives. (c) Roof edge model. (d) Gray profile of the roof edge model and its corresponding first- and second-order derivative.

gradient. Both the Prewitt and Sobel operators are discrete differentiation operators for edge detection by gradient transform. Figure 3 shows the templates of the two gradient operators. The operators use two 3×3 kernels which are convolved with the image to calculate approximations of the derivatives—one for horizontal changes, and the other for vertical.

The grayscale gradient of the image can be obtained using the gradient operator shown in Figure 3. Usually, we can use the gradient images g_x and g_y, which at each point contain the horizontal and vertical derivative approximations, respectively, to calculate the gradient intensity at the gradient's direction based on equation (6). $M(x, y)$ is the magnitude of the gradient. To save calculation time, the intensity of the gradient can also be approximated by equation (7).

$$M(x, y) = \operatorname{mag}\begin{pmatrix} \dfrac{\partial f}{\partial x} \\ \dfrac{\partial f}{\partial y} \end{pmatrix} = \sqrt{g_x^2 + g_y^2}, \tag{6}$$

$$M(x, y) = |g_x| + |g_y|. \tag{7}$$

The difference between the Prewitt operator and Sobel operator is that the Sobel operator has a larger coefficient of the center point. The central part of the pixel occupies a greater weight, which can smooth the noise better than the Prewitt operator [24]. The templates in Figure 3 can be revised to make the edge detection more sensitive to the diagonal direction.

2.2.2. Laplace of Gaussian (LoG) Operator. In the gradient operator based on the second derivative, Marr and Hildreth combined the Laplace operator (equation (9)) and the two-dimensional Gaussian function with σ as the standard deviation (equation (1) to form the LoG operator (equation (9)) [25]. Laplacian is also very sensitive to noise as other first-order methods. To reduce the noise effect, the two-step LoG operation is to first smooth the image with a Gaussian filter and then to detect the zero-crossings using Laplacian. After generating the spatial convolution template from equation (9), we can perform spatial convolution on the input image $f(x, y)$ to obtain the result $g(x, y)$ and find the zero-crossing point in $f(x, y)$ to identify the edge in the input image $f(x, y)$.

$$\nabla^2 = \frac{\partial^2}{x^2} + \frac{\partial^2}{y^2}, \tag{8}$$

$$\begin{aligned} \nabla^2 G(x, y) &= \frac{\partial^2 G(x, y)}{x^2} + \frac{\partial^2 G(x, y)}{y^2} \\ &= \left[\frac{\left(x^2 + y^2\right) - 2\sigma^2}{\sigma^4}\right] e^{-\left(\left(x^2+y^2\right)/\left(2\sigma^2\right)\right)}. \end{aligned} \tag{9}$$

The LoG operator uses Gaussian low-pass filtering to smooth the image, effectively reducing noise interference. In addition, the LoG operator has an equal response to the gray change of any template direction in the original image, instead of using multiple templates to calculate the gray gradient in different directions of the image when using the operator based on the first derivative, and therefore is also very efficient.

2.2.3. Canny Operator. The Canny operator uses the first-order directional derivative of the two-dimensional Gaussian function in any direction to reduce noise and compare it with the spatial convolution of the input image $f(x, y)$ to suppress noise and then find the maximum gradient to detect the edge of the image. The Canny operator firstly uses a Gaussian filter to smooth the input image and find the intensity gradients of the image. Then, it applies gradient magnitude thresholding or lower-bound cut-off

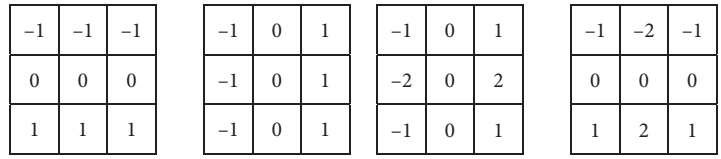

Figure 3: Prewitt and Sobel operator templates. (a) Prewitt operator. (b) Sobel operator.

suppression to get rid of spurious response to edge detection and applies a double threshold to determine potential edges. At last, it finalizes the detection of edges by suppressing all the other edges that are weak and not connected to strong edges. The Canny operator has a low error rate since all edges should be found, and there should be no spurious responses. It can also locate the edge close to the real edge. Therefore, it is one of the most strictly defined methods that provide good and reliable detection.

2.3. Otsu's Thresholding. The result of edge detection is not the crack area itself, but the edge of the crack area. It still needs image segmentation to identify the crack area. The purpose of the improved Otsu method using edge detection is to find the edge in the image and only use the pixels near the edge area to construct a grayscale histogram and use the grayscale histogram as the object of the Otsu method to obtain the segmentation threshold. This can effectively reduce the influence of a relatively large background area on Otsu's best global threshold segmentation.

The basic principle of Otsu's method is to use a threshold to divide the image into two parts, the region, and the background by maximizing the between-class variance. Otsu's method is based on computations performed on the histogram of an image, which is a one-dimensional array. The corresponding threshold gray value for classification is called the optimal threshold. For an image with a total of N pixels, the probability p_i of each gray level in the gray image is calculated by

$$p_i = \frac{n_i}{N}, \quad i = 0, 1, 2 \ldots, L-1, \tag{10}$$

where n_i is the number of pixels whose gray value is i and $L-1$ is the largest gray value.

Let K be the initial value of the threshold; use this threshold to divide all pixels into two parts with gray values from 0 to $K-1$ and from K to $L-1$. The between-class variance σ_B^2 is calculated by equation (11). Generally, the initial value K of the threshold is usually set to 1, and the maximum between-class variance when $K = 1, 2 \ldots, L-2$ is calculated. A gray value K that maximizes σ_B^2 is calculated as the final segmentation threshold.

$$\sigma_B^2 = \omega_0 (\mu_0 - \mu_r)^2 + \omega_1 (\mu_0 - \mu_r)^2, \tag{11}$$

where $\omega_0 = \sum_{i=0}^{k-1} p_i$, $\omega_1 = \sum_{i=k}^{L-1} p_1 = 1 - \omega_0$, $\mu_0 = \sum_{i=0}^{k-1} i p_i / \omega_0$, $\mu_1 = \sum_{i=k}^{L-1} p_i / \omega_1$, and $\mu_r = \sum_{i=0}^{L-1} p_i$.

The improved Otsu method integrating edge detection includes the following steps.

(1) Obtain pavement crack image $f(x, y)$ after preprocessing and edge detection.

(2) Specify a threshold value of gray level T to threshold the image to obtain a binary image $gT(x, y)$.

(3) For the area where $gT(x, y)$ equals to the logical value 1, find the corresponding area in image $f(x, y)$ to calculate the gray-level histogram and use equation (10) to calculate the probability value of each gray level.

(4) For each gray-level probability value obtained in step (3), use equation (11) to calculate the maximum between-class variance σ_B^2 and obtain the best threshold K to segment image $f(x, y)$.

2.4. Decision Tree Classifier. Pavement crack only accounts for a small part in pavement images. After the edge detection and Otsu's thresholding, the detected regions in the image may still include potholes and noises, other than cracks, and need to be further classified. Decision tree is a robust supervised learning classifier for pattern recognition, which relies on a labeled training set. Decision tree has small computation cost and high classification accuracy. It is also very easy to generate classification rules which are accurate and easy to understand.

Decision tree has a tree structure used for classification and prediction [16]. Generally, it consists of root nodes, decision nodes, branches, and leaves. The root node includes the full set of samples. Decision nodes and branches from the root are connected to each leaf. It represents the classification path of a sample. Each decision node represents a classification on a feature. Each branch represents a classification result, and leaves refer to a class or part of a class. Determination of the optimal subfeature is the key to the training of the decision tree.

The ID3 tree uses a greedy search approach to determine decision node selection. It picks an ideal attribute once and does not reconsider or modify its previous choices. ID3 algorithm uses entropy and information gain to determine which attributes best split the data. This algorithm can ensure that a decision tree is developed with the most simple path being found and the smallest number of branches. The expected information or entropy is a measure of uncertainty associated with a random number. Let the training set be X; the total number of samples is N, which contains M different classes w_i. Let N_i be the number of samples belonging to class w_i in $\widetilde{X}$. For a given sample classification, the expected information required is

Table 1: Description of features.

No.	Feature	Description
X1	Ratio of the major axis and the minor axis	The ratio of the length (in pixels) of the major axis to the length (in pixels) of the minor axis of the ellipse that has the same normalized second central moments as the region, returned as a scalar
X2	Angle between the horizontal axis and the major axis of the ellipse	Angle between the horizontal the x-axis and the major axis of the ellipse that has the same normalized second central moments as the region, returned as a scalar
X3	Area of the region	Actual number of pixels in the region
X4	Standard deviation of the gray level in the region	Standard deviation value of the gray histogram of pixels in the region
X5	Mean of the gray level in the region	Mean value of the gray histogram of pixels in the region
X6	Third-order moment of regional grayscale	Third-order moment value of the gray histogram of pixels in the region

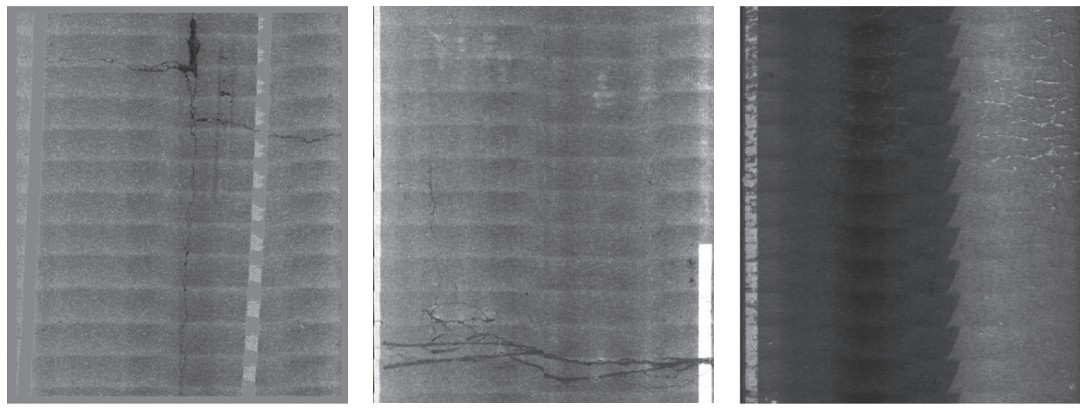

(a) (b) (c)

Figure 4: Samples for each crack class. (a) Longitudinal crack. (b) Transverse crack. (c) Block crack.

$$I(N_1, N_2, \ldots, N_M) = -\sum_{i=1}^{M} p_i \log_2 (p)_i, \tag{12}$$

where p_i is the probability that the sample belongs to class w_i, $p_i = N_i/N$.

In this study, six features are extracted as the predictors to train the decision tree, including the ratio of the major axis and the minor axis of the ellipse with the same second moment as the region; the angle between the horizontal axis and the major axis of the ellipse, the ellipse and the region have the same second moment; area of the region; the standard deviation of the gray level in the region; mean of the gray level in the region; and the third-order moment of regional grayscale. The detailed description of the features is listed in Table 1. A total of 251 pavement crack images including 131 transverse cracks, 92 longitudinal cracks, 45 block cracks, and some noises are labeled as the training set. The images with their original large size of 3.75 m*5 m were used to perform crack classification. Figure 4 shows the sample of each type of crack. The image segments are classified into four groups of transverse cracks, longitudinal cracks, block cracks, and noises. After training the decision tree, the pavement crack image can be reconstructed with only predicted cracks to calculate the location, length, and width of the cracks.

To evaluate the accuracy of pavement classifications, several performance measures including precision, recall, and F-measure as shown in equations (13)–(15) are frequently adopted. Precision is the ratio of the number of positive samples correctly classified as positive over the total number of positive samples. The recall is the ratio of the number of positive samples correctly classified as positive over the total number of positive samples. F-measure combines precision and recall:

$$\text{precision} = \frac{TP}{(TP + FP)}, \tag{13}$$

$$\text{recall} = \frac{TP}{(TP + FN)}, \tag{14}$$

$$F - \text{measure} = \frac{2 * \text{precision} * \text{recall}}{\text{precision} + \text{recall}}. \tag{15}$$

3. Discussion of Results

Pavement crack images were collected and processed with the proposed method including preprocess, edge detection, Otsu's thresholding, and ID3 decision tree classification. Different edge detection operators were evaluated and compared. The code for image preprocess and edge detection is shown in the Appendix section.

3.1. Preprocessing. Figure 5 shows a typical pavement surface image using the top-hat filtering, which is to remove the brightness in the background information from an image

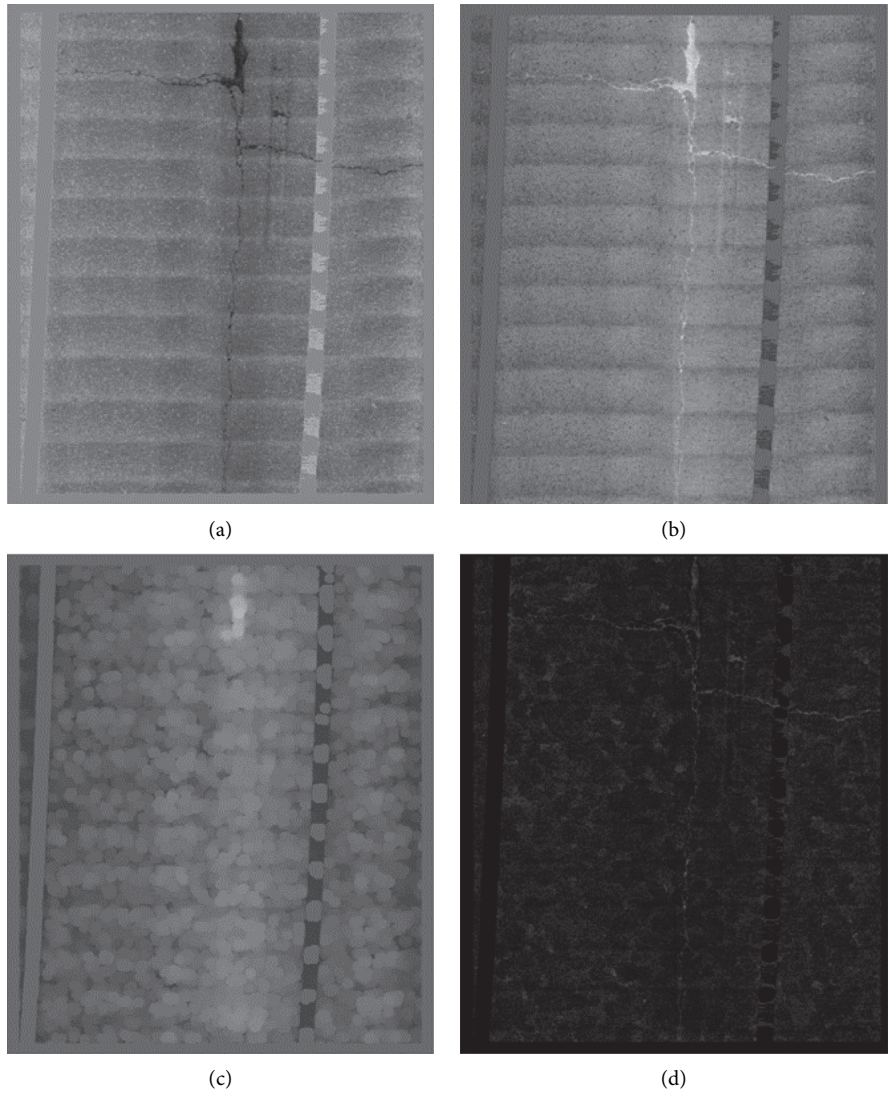

Figure 5: Effect of top-hat conversion. (a) Original image. (b) Image after color reversing. (c) Brighter areas in the image. (d) Result of the top-hat transformation.

through opening operations. The color of the pavement image was reversed, the crack was light, and the background was dark as shown in Figure 5(b). Figure 5(c) shows the brighter area in the image, which could be reduced by the top-hat transform. Figure 5(d) then can be obtained by reducing the brighter area in the original image, and the cracks become clearer.

3.2. Influence of Edge Detections. The original road image and image segmentation with preprocessing, edge detection, and Otsu's thresholding are shown in Figure 6. Figures 6(b)~6(e) clearly show that the developed Otsu's method effectively extracted the main crack area from the background area, showing a good segmentation effect. Generally, different edge detection methods have little effect on image segmentation. To further compare the results of image segmentation in more detail, the number of noise regions of different edge detection is calculated. For the pavement image shown in Figure 6, the numbers of noise regions of the Prewitt, Sobel, LoG, and Canny operators are 143, 111, 123, and 159, respectively. The corresponding numbers of crack regions are 21, 21, 21, and 23, respectively. Generally, the four operators obtained the same crack regions. The Canny edge detection has a better effect on crack detection than the other methods, obtaining more details of the edge and crack area, while retaining more noises. The Sobel and LoG operators show similar image segmentations. The Prewitt and Canny operators have more noise in the image background. This is because the Sobel gradient operator and the spatial domain filter template in the LoG operator could reduce noise. In addition, by comparing Figures 6(a) and 6(f), it can be seen that preprocessing significantly improves segmentation effects. A large amount of noise remains without preprocessing. A good segmentation could not be obtained by solely using edge detection and Otsu's thresholding.

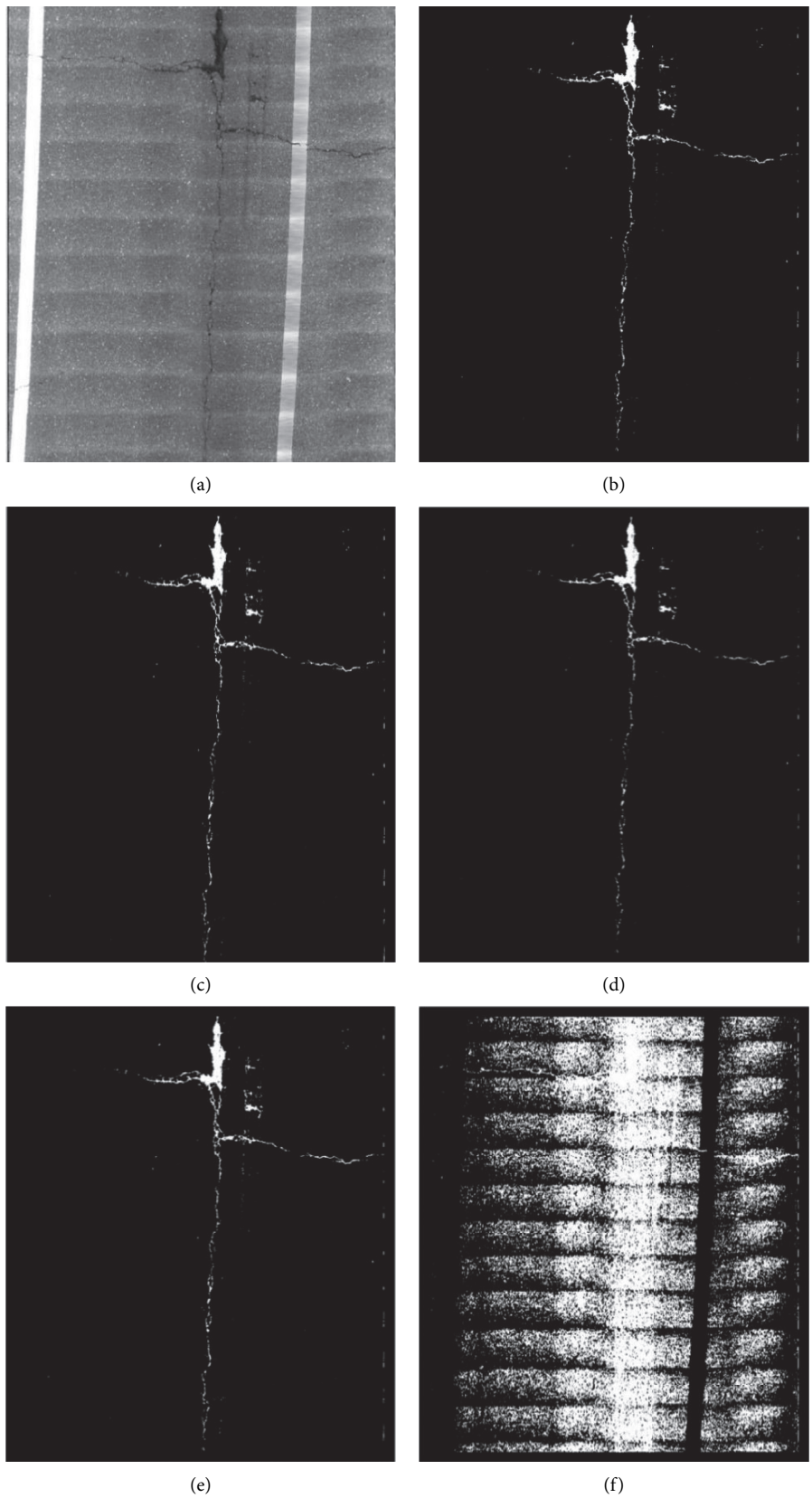

Figure 6: Image segmentation using different operators. (a) Original image. (b) Prewitt operator. (c) Sobel operator. (d) LoG operator. (e) Canny operator. (f) Segmentation without preprocessing.

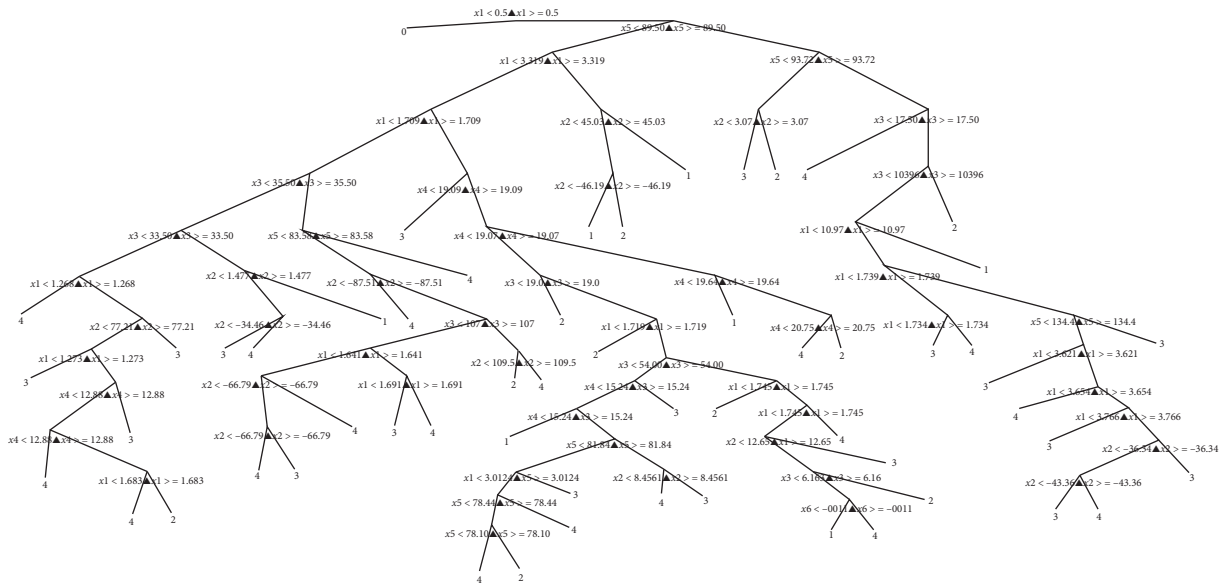

Figure 7: Structure of the decision tree.

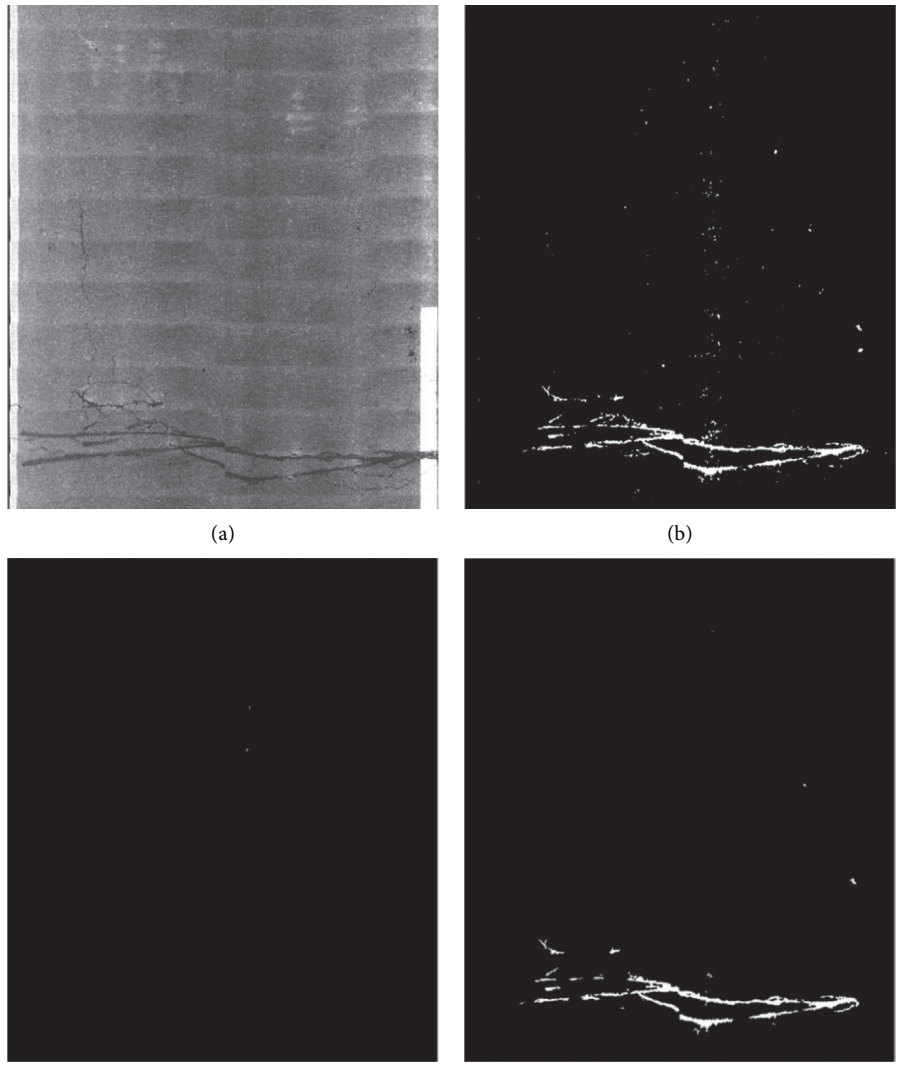

(a) (b)

(c) (d)

Figure 8: Continued.

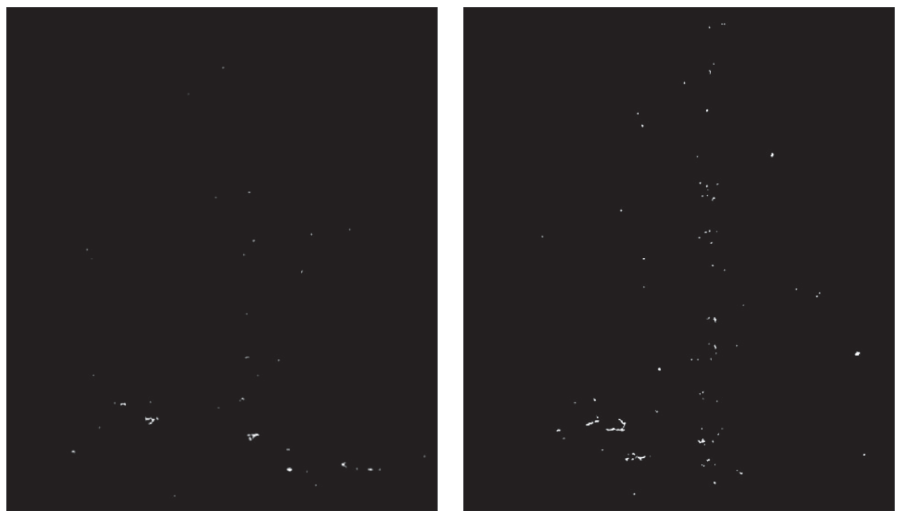

(e) (f)

Figure 8: The effect of decision tree classifier. (a) Original image. (b) Segmentation. (c) Longitudinal crack classification image. (d) Transverse crack classification image. (e) Block crack classification image. (f) Noises.

3.3. Decision Tree Classification. Figure 7 shows the structure of the decision tree model. $x_1, x_2 \ldots, x_6$ are the six features defined above. Figure 8 shows the pattern recognition effect of the decision tree classifier with a pavement crack image containing transverse cracks. It can be seen from Figure 8(d) that the transverse crack regions in the image segmentation results are effectively classified and be separated from other types of cracks and noise. In Figure 8(d), the noises are significantly reduced, which shows that the secondary denoising effect of the decision tree classifier. Generally, different types of cracks and the corresponding regions in the image are successfully extracted, except that part of the branches of the transverse cracks are identified as block cracks, and a very small amount of noise appears in the longitudinal crack classification image. The proposed method achieved a precision of 88.9%, a recall of 82.8%, and an *F*-measure of 85.3%, indicating a comparable performance.

4. Conclusion

Because the area of the pavement crack is too small, comparing with the image background, the crack only accounts for a very small portion in the grayscale histogram and the pixels are highly concentrated, making it difficult to split effectively. This paper developed an improved Otsu method integrated with edge detection and decision tree classifier for cracking identification in asphalt pavements through image segmentation. An image preprocessing approach including Gaussian function-based spatial filtering and top-hat transform is also proposed.

The Gaussian function-based spatial filtering and top-hat transform significantly reduce the influence of poor shading and lighting effects and improve the image segmentation effects. The improved Otsu optimal global threshold segmentation method based on edge detection could effectively segment pavement crack images after valid preprocessing. All the four edge detection operators have similar effects on segmentation. The Canny edge detection has a better effect on crack detection, obtaining more details of the edge and crack area, as well as more noises. The Sobel and LoG operators show similar image segmentation and retain fewer noises. The decision tree classifier based on ID3 algorithm can effectively classify different types of cracks including transverse, longitudinal, and block cracks, which also has high calculation efficiency.

The proposed method achieved a fairly high precision, indicating a comparable performance on the crack detection based on 2D pavement surface images. However, it is still sensitive to the quality of images, especially when the pavement surface image contains extensive dirty spots, water, pavement texture, or shadows. Recently, the high-resolution surface profile of pavement can be obtained with 3D cameras and laser line scanner. Those distress detection algorithms can be potentially directly used to process the data with depth information to evaluate pavement distress or texture. They can also be integrated with the deep learning-based methods to firstly identify the critical region to improve the calculation efficiency. In future studies, more types of cracks and other pavement distress including potholes and raveling could be potentially detected using the proposed methods with more pavement distress images for training the decision tree model.

Appendix

```
"Code for image preprocess and edge detection"
function [I] = autotophat(I, varargin)
%Gaussian filter and Top-hat transformation
if nargin = = 1
   A = 1; cj = 150;
   disp("Default A = 1, cj = 350");
```

```
else
   if nargin = = 2
   A = varargin{1};
   cj = 350;
   disp("A = input value");
   else
      if nargin = = 3
      A = varargin{1};
      cj = varargin{2};
      else
         disp("wrong input");
         return;
      end
   end
end
   ave = fspecial("Gaussian",3);
I = imfilter(I, ave);
[ri,~] = size(I);
se = strel("rectangle", [ri, round(cj*A)]);
w = fspecial("average", [10]);
Ibg = imopen(aveimf(I), se);
%I = medfilt2(I, [9]);
%I = imtophat(I, se);
I = I + mean(mean(Ibg))-Ibg;
%figure, imshow(Ibg);
%figure, imshow(I)
end
function F3 = cannyotsu(F2, n, varargin)
%Canny-revised Otsu
sigma = 2.5;
if nargin = = 3
   sigma = varargin{1};
end
lap = abs(edge(F2, "canny", [], sigma));
lap = lap/max(lap());
h = imhist(lap);
q = percentile2i(h, n);
markerimage = lap > q;
fp = F2.*uint8(markerimage);
hp = imhist(fp); %figure, plot(hp);
hp(1 : 12) = 0; %hp(2) = 0; hp(3) = 0;
%figure, bar(hp, 0)
t = otsuthresh(hp);
%hp(1:round(255*(1−t))) = 0;
%t = otsuthresh(hp);
F3 = imbinarize(F2, t);
end"
```

Data Availability

Access to data is restricted as the dataset is from a third-party company and is under commercial confidentiality.

Conflicts of Interest

The authors declare that they have no conflicts of interest regarding the publication of this paper.

Acknowledgments

This study was sponsored by the Science and Technology Project of Zhejiang Provincial Department of Transport under Grant nos. 2020045 and 2020053, to which the authors are very grateful.

References

[1] M. Huang, Q. Dong, F. Ni, and L. Wang, "LCA and LCCA based multi-objective optimization of pavement maintenance," *Journal of Cleaner Production*, vol. 283, p. 124583, 2021.

[2] R. Kushol, M. H. Kabir, M. S. Salekin, and A. B. M. A. Rahman, "Contrast enhancement by top-hat and bottom-hat transform with optimal structuring element: application to retinal vessel segmentation," in *Image Analysis and Recognition*, F. Karray, A. Campilho, and F. Cheriet, Eds., Springer International Publishing, New York, NY, USA, 2017.

[3] X. Bai, F. Zhou, and B. Xue, "Infrared image enhancement through contrast enhancement by using multiscale new top-hat transform," *Infrared Physics & Technology*, vol. 54, no. 2, pp. 61–69, 2011.

[4] H. Zakeri, F. M. Nejad, and A. Fahimifar, "Image based techniques for crack detection, classification and quantification in asphalt pavement: a review," *Archives of Computational Methods in Engineering*, vol. 24, no. 4, pp. 1–43, 2016.

[5] A. G. Ouyang and Y. P. Wang, "Edge detection in pavement crack image with beamlet transform," in *Proceedings of the 2nd International Conference on Electronic & Mechanical Engineering and Information Technology*, Atlantis press, Beijing, China, December 2012.

[6] Y.-C. Tsai, V. Kaul, and R. M. Mersereau, "Critical assessment of pavement distress segmentation methods," *Journal of Transportation Engineering*, vol. 136, no. 1, pp. 11–19, 2010.

[7] S. Dorafshan, R. J. Thomas, and M. Maguire, "Comparison of deep convolutional neural networks and edge detectors for image-based crack detection in concrete," *Construction and Building Materials*, vol. 186, pp. 1031–1045, 2018.

[8] S. F. Wang, Y. L. Che, N. Li, Z. G. Xu, and Y. S. An, "Asphalt pavement crack detection algorithm based on multi-scale ridges," *Zhongguo Gonglu Xuebao/China Journal of Highway and Transport*, vol. 30, pp. 32–41, 2017.

[9] Y. Mao-De, B. O. Shao-Bo, and H. E. Yu-Yao, "A method of image detection and analysis for pavement crack based on morphology," *Journal of Engineering Graphics*, vol. 28, 2008.

[10] A. Akagic, E. Buza, S. Omanovic et al., "Pavement crack detection using Otsu thresholding for image segmentation," in *Proceedings of the 2018 41st International Convention on Information and Communication Technology*, pp. 1092–1097, Electronics and Microelectronics (MIPRO), OPatija, Croatia, May 2018.

[11] M. Kamaliardakani, L. Sun, and M. K. Ardakani, "Sealed-crack detection algorithm using heuristic thresholding approach," *Journal of Computing in Civil Engineering*, vol. 30, no. 1, p. 10, 2016.
[12] N. Otsu, "A threshold selection method from gray-level histograms," *IEEE Transactions on Systems, Man, and Cybernetics*, vol. 9, no. 1, pp. 62–66, 1979.
[13] S. Li, Y. Cao, and H. Cai, "Automatic pavement-crack detection and segmentation based on steerable matched filtering and an active contour model," *Journal of Computing in Civil Engineering*, vol. 31, no. 5, Article ID 04017045, 2017.
[14] D. Ai, G. Jiang, L. Siew Kei, and C. Li, "Automatic pixel-level pavement crack detection using information of multi-scale neighborhoods," *IEEE Access*, vol. 6, pp. 24452–24463, 2018.
[15] S. L. H. Lau, E. K. P. Chong, X. Yang, and X. Wang, "Automated pavement crack segmentation using U-net-based convolutional neural network," *IEEE Access*, vol. 8, pp. 114892–114899, 2020.
[16] S. B. Kotsiantis, "Decision trees: a recent overview," *Artificial Intelligence Review*, vol. 39, no. 4, pp. 261–283, 2013.
[17] J. R. Quinlan, "Induction of decision trees," *Machine Learning*, vol. 1, no. 1, pp. 81–106, 1986.
[18] S. Ruggieri, "Efficient C4.5 [classification algorithm]," *IEEE Transactions on Knowledge and Data Engineering*, vol. 14, no. 2, pp. 438–444, 2002.
[19] J. C. Shafer, R. Agrawal, and M. Mehta, "SPRINT: a scalable parallel classifier for data mining," in *Proceedings of the VLDB'96, 22th International Conference on Very Large Data Bases*, Mumbai, India, September 1996.
[20] Z. Qin, C. Yu, L. Qingquan, M. Qingzhou, and W. Song, "CrackTree automatic crack detection from pavement images," *Pattern Recognition Letters*, vol. 33, no. 3, pp. 227–238, 2012.
[21] C. P. Wang Kelvin, A. Zhang, Q. Li Joshua, Y. Fei, C. Chen, and B. Li, "Deep learning for asphalt pavement cracking recognition using convolutional neural network," in *Proceedings of the Airfield and Highway Pavements*, pp. 166–177, Philadelphia, PA, USA, August 2017.
[22] A. Zhang, K. C. P. Wang, Y. Fei et al., "Deep learning-based fully automated pavement crack detection on 3D asphalt surfaces with an improved CrackNet," *Journal of Computing in Civil Engineering*, vol. 32, no. 5, Article ID 4018041, 2018.
[23] J. Liu, X. Yang, and S. Lau, "Automated pavement crack detection and segmentation based on two-step convolutional neural network," *Computer-Aided Civil and Infrastructure Engineering*, vol. 35, no. 11, pp. 1291–1305, 2020.
[24] A. Zhang, Q. Li, and K. C. P. Wang, "Matched filtering algorithm for pavement cracking detection," *Transportation Research Record: Journal of the Transportation Research Board*, vol. 2367, no. 1, pp. 30–42, 2013.
[25] R. C. Gonzalez and P. Wintz, *Digital Image Processing*, Addison-Wesley, Boston, MA, USA, 2010.

Hindawi
Advances in Materials Science and Engineering
Volume 2021, Article ID 1055006, 10 pages
https://doi.org/10.1155/2021/1055006

Research Article

Microstructural Mechanical Analysis of Warm-Mixed Reclaimed Semiflexible Pavement Materials with Interfacial Weakening Effect

Hua Tan,[1,2] Weian Xuan,[1,2] and Huang Wenke[3]

[1]*Guangxi Transportation Science and Technology Group Co. Ltd., Nanning 530007, China*
[2]*Guangxi Key Lab of Road Structure and Materials, Nanning 530007, China*
[3]*School of Civil Engineering, Guangzhou University, Guangzhou 510006, China*

Correspondence should be addressed to Huang Wenke; h.wenke@gzhu.edu.cn

Received 15 June 2021; Accepted 13 July 2021; Published 20 July 2021

Academic Editor: Meng Guo

Warm-mixed reclaimed asphalt pavement technology, as an environmental recycling method to reuse waste materials, has been widely investigated around the world. However, the skeleton of the reclaimed asphalt mixture is unstable due to the existence of the reclaimed materials. Semiflexible pavement has been successfully used in heavy traffic area due to its high rutting resistance. For combination with these two methods, a warm-mixed reclaimed semiflexible pavement material was proposed in this study. In order to investigate the interfacial weakening effect of the warm-mixed reclaimed semiflexible pavement material in a microstructural perspective, an image-based two-dimensional microstructural finite element model was presented. Results show that the maximum compressive stress of the new and RAP aggregates and cement mortar with interface is greater than that without interface and the compressive stress of the material increases when considering the interface. Besides, the maximum compressive strain of the material with interface is greater than that without interface and the strain values in the models with interface at all three positions are greater than those without interface.

1. Introduction

Asphalt concrete, which has the advantages of smooth surface, low noise, and convenient maintenance, is one of the most common types of pavement surface materials used in the world. After some years of use, the asphalt binder becomes brittle and cracks due to oxidation of the binder and the load repetition [1]. A large amount of asphalt mixture waste from the maintenance of asphalt pavement has caused great pollution to the environment. So, great efforts have been made to reuse the waste asphalt mixture by researchers [2–8]. Reclaimed asphalt pavement (RAP) technology can not only realize the reuse of waste materials but also reduce the use of new aggregates. The RAP technology is to add appropriate amount of new asphalt binder, new aggregates, and rejuvenation into the waste asphalt material and then remix them to form a new asphalt mixture. The most commonly used way to regenerate the reclaimed asphalt pavement is to mix them at a temperature of 170°C, which leads to the old asphalt binder in the recycle materials to age again. This will greatly weaken the performances of the asphalt mixture. Besides, hot mixing of asphalt mixture consumes a lot of energy, increases carbon dioxide emissions, and produces a lot of exhaust gases that are harmful to the environment [9–11].

In recent years, a new green environmental protection type of asphalt reclaimed material, namely, foamed warm-mixing reclaimed asphalt mixture, has been used because of its low energy consumption, low emission, and decreasing aging of the old asphalt binder [12–14]. The foamed warm-mixing technology of asphalt is to produce foamed asphalt binder by adding a certain proportion of water in the foaming device. When the water meets hot asphalt binder, it evaporates rapidly, and its volume expands rapidly. The

increase of the asphalt working ability enables it to fully encapsulate aggregate at a lower temperature, so as to realize the mixing and compaction of the mixture at a lower temperature. Although the foamed warm-mixing reclaimed asphalt mixture technology can reduce the viscosity of asphalt binder so as to reduce the mixing and compaction temperature, it does not have much advantage in the aspects of high temperature performance, low temperature crack resistance, and water stability compared with the hot-mix asphalt mixture.

Semiflexible pavement, with open-graded matrix asphalt mixture (void ratio is 20–25%) filled with special cement grouting materials, combines some of the best qualities from both flexible and rigid pavements surfaces [15]. These flexible, jointless, and water-proofing properties that characterize asphalt are accompanied by a high static bearing capacity, rutting, and wear resistance, as well as resistance to oil and fuel spillage that are characteristic of conventional concrete surfaces [16,17]. As a part of semiflexible pavement material, the cement grouting materials are able to interlock with the matrix asphalt mixture to form strength and then enhance the performance of the pavement. Motivated by this innovative semiflexible hybrid composite pavement type, warm-mixed reclaimed semiflexible pavement material was proposed in this study in order to improve the road performances of the foamed warm-mixed reclaimed asphalt mixture.

There are three types of interfaces in the warm-mixed reclaimed semiflexible pavement material, which are new aggregate-asphalt mastic interface, RAP aggregate-asphalt mastic interface, and cement mortar-asphalt mastic interface. These interfaces have different adhesion properties which affect the mechanical performances of the mixture. The traditional macroscopic mechanical tests are difficult to investigate the internal mechanical responses due to the interfaces. Thanks to the digital image processing technology and finite element method, researchers can gain insight into the internal structural properties of the materials in a microstructural perspective [18–20]. Many efforts of reconstruction of numerical microstructural model for asphalt mixture based on CT slices or cross-cutting images have been made to conduct virtual tests to predict micromechanical response under different loading conditions [21–23]. However, in these finite element models, interface between aggregate and asphalt mastic is not considered. Instead, the interface is assumed to be completely bound together; that is, the nodes at the interface are shared by aggregate and asphalt mastic. As a result, the mechanical response of the model under loading is different from the reality. So, it is very important to establish a more accurate microstructural numerical model including interfaces in order to accurately analyze the internal mechanical response of asphalt mixture.

In this paper, the warm-mixed reclaimed semiflexible asphalt mixture was prepared and then beam-shape cross session image of the specimen was obtained. Image-based finite element method was applied to reconstruct the microstructural digital samples of the warm-mixed reclaimed semiflexible asphalt mixture including and excluding interfaces. The interfaces properties were obtained through pull-off tests. Then, the digital models were applied to conduct virtual tests in order to investigate the internal mechanical response with and without interfaces.

2. Materials and Methods

2.1. Materials. The raw asphalt with a penetration grade of 60–80 (0.1 mm) provided by Shell Road Solutions Xinyue (Foshan) Co., Ltd. was selected as the asphalt binder in this study. Tests of the engineering properties for asphalt binder were conducted according to the Chinese specifications (JTG E20-2011) and detailed properties are provided in Table 1. Crushed diabase stones were used as coarse and fine aggregates and the mineral filler was limestone powder. Tests of the engineering properties were conducted according to the Chinese specifications (JTG E42-2005). The detailed properties of aggregate and mineral filler are provided in Table 2.

The reclaimed asphalt pavement (RAP) materials provided by Guangzhou Municipal Engineering Maintenance Office Co., Ltd. were tested according to the Chinese specifications (JTG F41-2008) in order to obtain the RAP aggregate properties and retained asphalt content. The RAP materials, which are composed of coarse aggregates, fine aggregates, and asphalt binder, were dried and sieved before testing. In this study, the RAP materials with diameter less than 4.75 mm were removed as shown in Figure 1. The asphalt binder in RAP was extracted by centrifugal separation method and then recovered using Abson method according to the Chinese specifications (JTG F41-2008). The detailed properties of aggregate and retained asphalt binder can be seen in Table 3.

The dry powder mortar provided by Guangdong Longhu Technology Co., Ltd. was chosen in this study, which is made of cement, sand, and other additives. The gradation of cement mortar is shown in Table 4.

2.2. Sample Preparation. In this study, the standard Marshall method was employed to prepare the test specimens. The procedures for preparing test specimen are provided as follows:

(1) 450 mm × 150 mm × 185 mm matrix asphalt mixture slab with target air void of 25% was prepared using standard Marshall method. The specimen was demolded after curing at room temperature for 24 h.

(2) Cement mortar with water-cement ratio of 0.22 and sand content of 30.25% was prepared according to the gradation of dry powder mortar shown in Table 4. Before the filling procedure, bottom and edges of the specimen were enclosed with transparent films to prevent cement mortar from flowing out.

(3) The specimen was placed on the vibration table and filled with the prepared cement mortar until there was no bubble appearing on the surface. Then, scrape off the excess cement mortar on the surface of the specimen with a scraper.

Table 1: Properties of asphalt binder.

Properties	Unit	Test results	Test method
Penetration at 25°C	0.1 mm	71.8	T 0604
R&B softening point	°C	50	T 0606
Ductility at 10°C	cm	49.4	T 0605
Solubility	%	99.7	T 0607
Flash point	°C	328	T 0611
Density at 15°C	g/cm^3	1.040	T 0603

(4) The transparent films shall be removed when the specimen filled with cement mortar was placed for 24 hours, and then the specimen was placed in a curing box with a temperature of 20°C ± 3°C and a humidity of more than 80% for curing.

(5) Beam-shape specimens with dimensions of 380 mm × 50 mm × 63 mm were extracted from the compacted slab.

Brief experimental process is presented in Figure 2. As can be seen from Figure 2(c)), the connectivity voids formed by the aggregates are fully filled by cement mortar, and the materials are in a tight packing state, which shows that the prepared cement mortar has good fluidity, and the design of the matrix asphalt mixture meets the filling requirements.

2.3. Finite Element Modeling. Before reconstructing the finite element model of asphalt mixture based on Figure 2(c), different compositions of the image should be divided first based on segmented method [24]. Basically, the OTSU method was usually utilized for segmentation of the asphalt mixture cross-sectional image. Since warm-mixed reclaimed semiflexible pavement material consists of complex compositions, among which cement mortar and new aggregates are similar in grayscale intensity, it is very difficult to segment the compositions of mixture specimen image by the grayscale-based segmented method. Therefore, the manual method was utilized for segmentation in this study. Segmentation of the cross-sectional image is shown in Figure 3 (new aggregates in red, RAP aggregates in blue, asphalt mastic in yellow, and cement mortar in purple).

In order to obtain the interface zones between different compositions of semiflexible pavement material, the following methods are adopted in this paper: Firstly, individual particles of the same composition were identified and marked, and the binary images of each particle was corroded by the circular shaped structure element of radius 1. Every new binary images of each particle were marked separately. Then, subtraction operations were applied between the new markers and the original markers of the binary images of each particle. The new aggregate-asphalt mastic interface, the RAP aggregate-asphalt mastic interface, and the cement mortar-asphalt mastic interface were obtained according to the subtraction operations results.

A binary image is represented by an $m \times n$ logical matrix, where pixel values are 1 (true) or 0 (false). In order to input the element and node information into the finite element software such as ABAQUS, the node and element numbering rules for generating the pixel-based numerical model are defined as follows: the node and element numbering sequences start from the lower left corner of the matrix and then go to the right side of each line; the last number of each line is followed by the next line. The node and element numbering diagram of the image pixel matrix are shown in Figure 4. The element and node information are generated with the MATLAB programming and written into an input file of ABAQUS for numerical simulations. The 4-node bilinear reduced integration with hourglass control elements (CPS4R) with a unit length was used in constructing the mesh. The finite element model contained a total of 974,298 elements and 976,642 nodes. Consolidation constraint boundary conditions were applied to the bottom of the digital sample, and the load of 0.7 MPa was imposed to the top of the digital specimen. Figure 5 presents the pixel-based numerical model of asphalt mixture.

3. Model Parameters Acquisition

The new aggregates, RAP aggregates, asphalt mastic, and cement mortar used in this study were assumed to be elasticity. The parameters of each composition are shown in Table 5.

In order to analyze the influence of interface weakening on the mechanical properties of the mixed material, the elastic parameters of different interfaces should be obtained. In this paper, the interface parameters of semiflexible materials were obtained by pull-off tests. Details of the pull-off test are as follows: (1) the aggregates were processed into cylindrical specimens with a diameter of 25 mm and a height of 8 mm, and the cylindrical specimens were put into an oven at 120°C and heated for 2 h. (2) The surfaces of different cylindrical specimens were coated with foamed asphalt binder, reclaimed asphalt binder, and foamed asphalt binder + cement mortar, respectively. (3) Two specimens coated with the same binder were installed and the asphalt film thickness was controlled within 15 μm. Excess asphalt or cement mortar on the side wall of the specimen was scraped off. The prepared specimens coated with cement mortar were placed into a curing box with humidity greater than 80% and cured for 28 days. (4) Tensile failure tests were carried out at a tensile velocity of 10 mm/min and the force-displacement curves' results were recorded. Three replicate tests were performed. The interface parameters of the semiflexible material with different boundary were extracted from the force-displacement curves. The flow chart of pull-off test is shown in Figure 6 and the interfacial modulus of warm-mixed reclaimed semiflexible materials is presented in Table 6.

Table 2: Properties of aggregate and mineral filler.

Materials	Physical properties	Unit	Test results	Test method
Coarse aggregate	Relative apparent density	—	2.69	T 0304
	Water absorption	%	0.20	T 0307
	Aggregate crushed value	%	20.0	T 0316
	Abrasion value	%	26	T 0317
	Flat and elongated pieces	%	13	T 0312
Fine aggregate	Relative apparent density	—	2.68	T 0328
	Clay content	%	2.3	T 0333
	Sand equivalent	%	72.8	T 0334
Mineral filler	Relative apparent density	—	2.81	T 0352
	Moisture content	%	0.08	T 0332

Figure 1: RAP material after drying and sieving.

Table 3: Test results of RAP material.

Materials	Physical properties	Unit	Test results	Test method
Asphalt binder in RAP	Penetration at 25°C	0.1 mm	15.1	T 0604
	Ductility at 15°C	cm	57	T 0605
	Ductility at 25°C	cm	106	T 0605
	R&B softening point	°C	71.9	T 0606
	Dosage	%	4.4	—
Coarse aggregate in RAP	Flat and elongated pieces	%	3.4	T 0312
	Aggregate crushed value	%	11.57	T 0316
Fine aggregate in RAP	Angularity	%	21.14	T 0344

4. Results and Discussion

In this study, two kinds of two-dimensional microstructural numerical models with and without interfaces were established, and a uniform load was applied to the top of the specimen to investigate the distribution of stress and strain in the material.

4.1. Stress Distribution Analysis. The stress nephograms of the two models are shown in Figure 7. As can be seen from the figures, the red to orange colors in the stress nephogram represent tensile stresses, and the yellow to purple colors in the stress nephogram represent compressive stress. According to the stress distribution nephograms of the two models, it was found that the new and RAP aggregates and cement mortar mostly located in the green area (shown in Figures 7(a)–7(d)), while the asphalt mastic basically located in the yellow area (shown in Figures 7(e) and 7(f)), which indicates that the new and RAP aggregates and cement mortar were subjected to most of the compressive stress, while the asphalt mortar was subjected to most of the tensile stress. In practice, the strength of the warm-mixed reclaimed semiflexible materials is mainly provided by aggregate and cement mortar. So, the stress distributions in the nephograms are consistent with the actual loading distribution in the material.

According to the stress distribution nephogram of the two models, the maximum compressive stress of the new and RAP aggregates and cement mortar with interface is greater than that without interface. As can be seen from the stress nephogram, the areas of new and RAP aggregates, cement mortar, and asphalt mastic in green are larger than those without interface, which indicates that the compressive stress of the material increases when considering the interface.

Table 4: Gradation of dry powder mortar.

Components	Cement	Sand	Fly ash	Heavy calcium	Additive
Dosage (%)	35	30.25	10	15	9.75

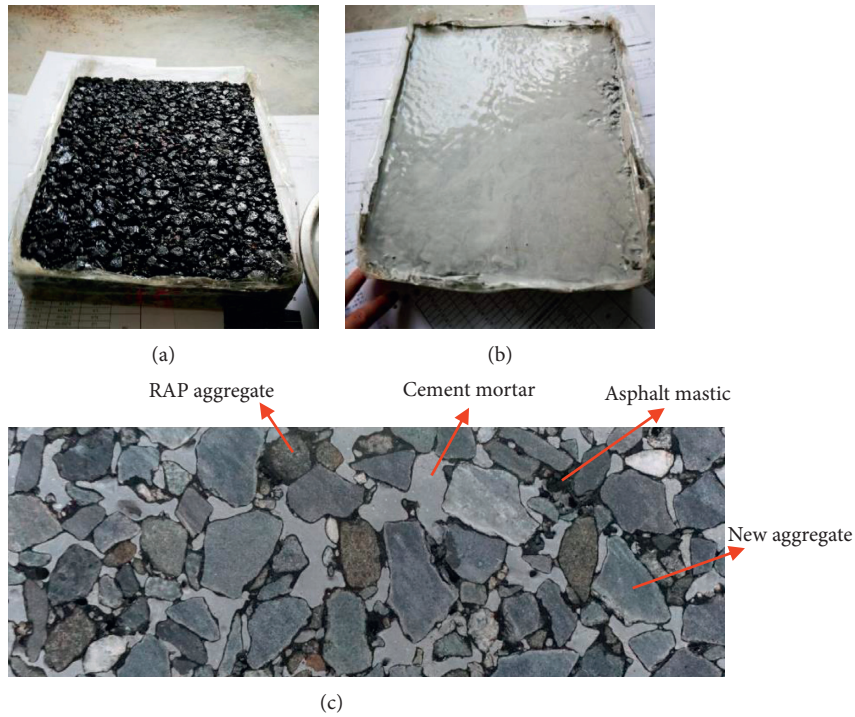

Figure 2: Brief experimental process of the semiflexible pavement materials: (a) matrix asphalt mixture slabs; (b) slab sample filled with cement mortar; (c) cross section of the semiflexible material.

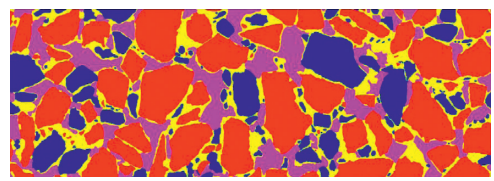

Figure 3: Segmentation of the cross-sectional image.

Three positions shown in Figures 7(a) and 7(b) were selected to investigate the differences of stress in detail. The stresses at three key positions for the two models are presented in Figure 8. As can be seen from Figure 8, the stress values of the microstructural model with interface at positions 1 and 2 are both smaller than those without interface, but the stress values at position 3 are larger than those without interface. The main reason is that the interface area of the warm-mixed reclaimed semiflexible material can absorb part of the stress, which reduces the stress around the interface.

4.2. Strain Distribution Analysis. The strain nephograms of the two models are shown in Figure 9. As can be seen from the figures, the dark red to orange colors in the strain nephogram represent tensile strain, and the orange to purple colors in the strain nephogram represent compressive strain. According to the strain distribution nephogram of the two cases, it is found that the strain is mainly distributed in the cement mortar and asphalt mastic, while small strain occurs only in the local part of aggregate. This is because the aggregates have higher elastic modulus and are much larger than other materials. So the strain on aggregates is minimal, while the strain of materials with low modulus will be slightly larger. In practice, aggregates in the warm-mixed reclaimed semiflexible materials have a large degree of impingement and form a tight skeleton. In addition, the grouting material fills most of the voids, and the cement mortar provides part of the strength after curing. So, the semiflexible material has a strong antideformation ability, and the overall strain distribution is in line with the actual situation.

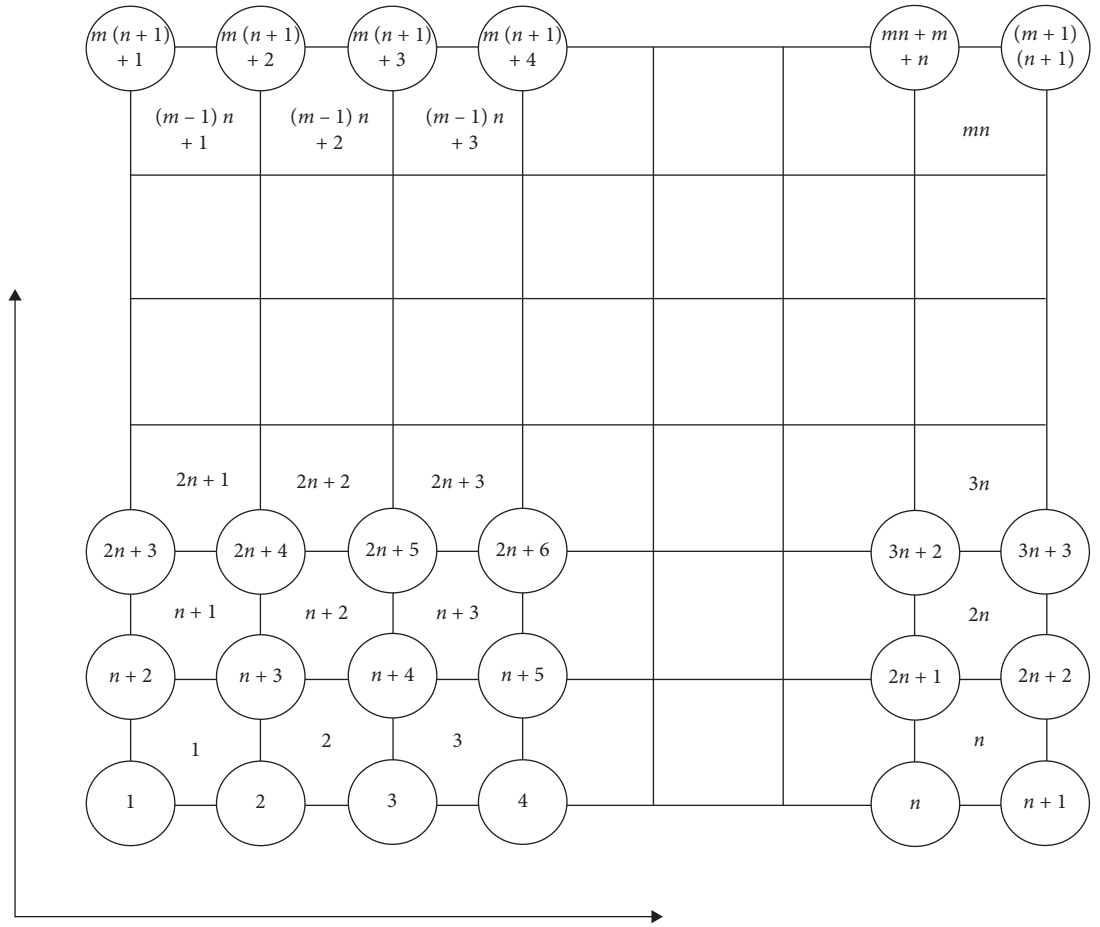

Figure 4: Sketch map of elements and nodes label for the image pixel matrix.

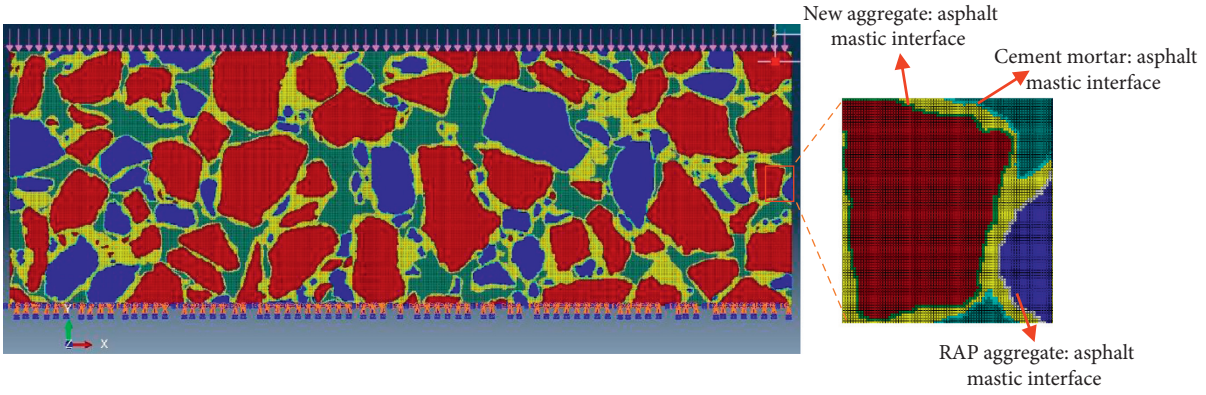

Figure 5: Reconstruction of semiflexible pavement material using the finite element method: (a) model with interface; (b) model without interface.

Table 5: Parameters of warm-mixed reclaimed semiflexible pavement.

Materials	Temperature (°C)	Modulus (MPa)	Poisson's ratio
New aggregate (diabase)	—	70000	0.25
RAP (granite)	—	50000	0.28
Asphalt mastic	25	1250	0.35
Cement mortar	—	15000	0.30

Figure 6: Flow chart of pull-off test.

Table 6: Interfacial modulus of warm-mixed reclaimed semiflexible materials.

Types of interface	Temperature (°C)	Interface modulus (MPa)	Poisson's ratio
New aggregate-asphalt mastic interface	25	212	0.4
RAP aggregate-asphalt mastic interface	25	305	0.4
Cement mortar-asphalt mastic interface	25	82	0.4

According to the strain distribution nephogram of the two models, the maximum compressive strain of the material with interface is greater than that without interface. Three positions shown in Figure 9 were selected to investigate the differences of strain in detail. The strains at three key positions for the two models are presented in Figure 10.

As can be seen from Figure 10, the strain values in the models with interface at all three positions are greater than those without interface. The strain values in the models with interface at positions 1 and 2 are much larger than those without interface and the strain values at positions 3 are close to each other. The main reason is that the aggregates and the asphalt mastic coated with cement mortar form a network structure, and the load needs to destroy the interface structure before it can be further transferred. In the laboratory experiment, we found that the cracking of warm-mixed reclaimed semiflexible material also developed at the interface. Therefore, the interface structure was subjected to the greatest strain degree, while the area with relatively dispersed interface structure is less affected.

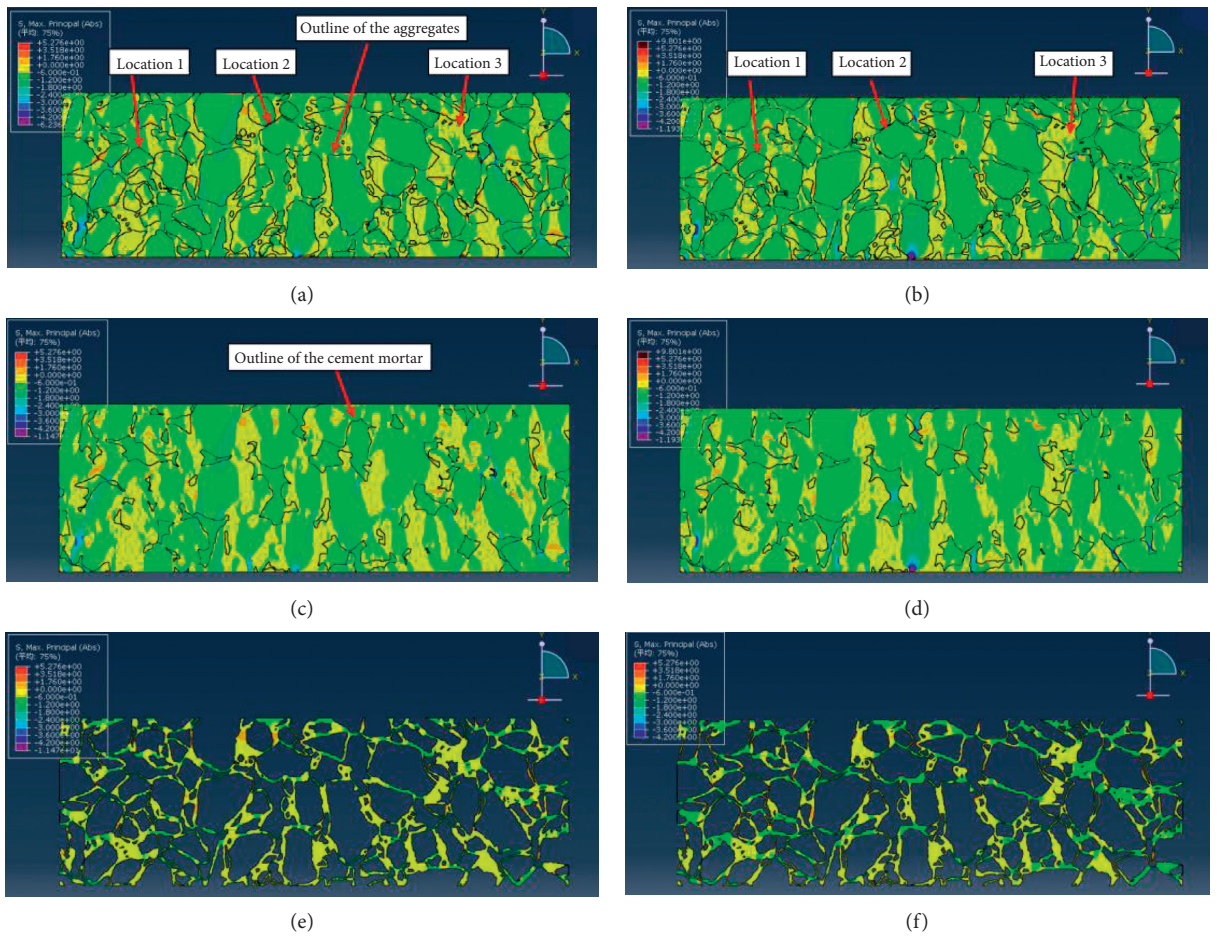

Figure 7: Stress nephogram: (a) aggregates outline with interface; (b) aggregates outline without interface; (c) cement mortar outline with interface; (d) cement mortar outline without interface; (e) asphalt mastic with interface; (f) asphalt mastic without interface.

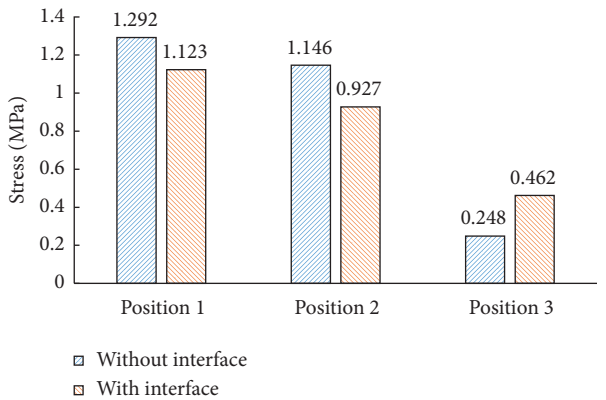

Figure 8: Histogram of stress at three key positions.

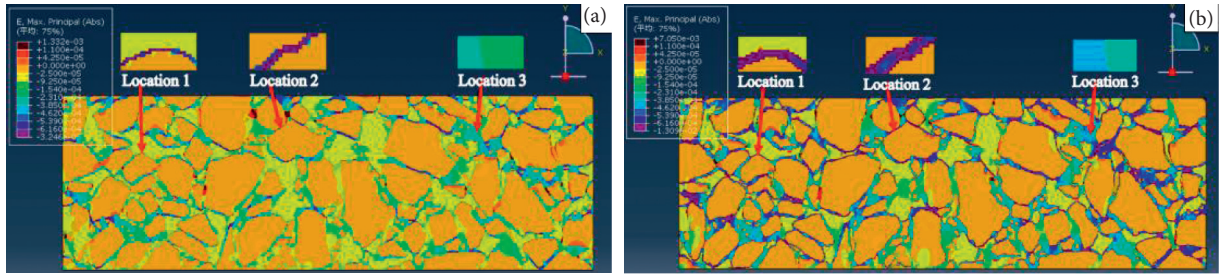

Figure 9: Strain distribution diagram of internal structure: (a) with interface; (b) without interface.

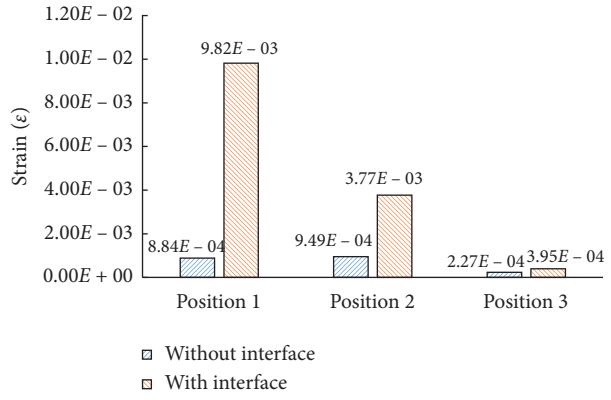

Figure 10: Histogram of strain at three key positions.

5. Conclusions

In this paper, the influence of interface weakening of warm-mixed reclaimed semiflexible materials on the internal force distribution was investigated through two-dimensional microstructural finite element modeling. Two kinds of two-dimensional microstructural numerical models with and without interfaces were reconstructed from digital image slice, and a uniform load was applied to the top of the models to investigate the distribution of stress and strain in the material. The following conclusions were drawn:

(1) The manual method was utilized to separate the different compositions of the asphalt mixture in the image, and pixel-based finite element method was proposed to reconstruct the digital samples. Microstructural finite element models including and excluding interfaces were successfully established.

(2) The maximum compressive stress of the new and RAP aggregates and cement mortar with interface is greater than that without interface, and the compressive stress of the material increases when considering the interface.

(3) Stress values of the microstructural model with interface at positions 1 and 2 are both smaller than those without interface, but the stress values at positions 3 are larger than those without interface. The main reason is that the interface area of the warm-mixed reclaimed semiflexible material can absorb part of the stress, which reduces the stress around the interface.

(4) The maximum compressive strain of the material with interface is greater than that without interface and the strain values in the models with interface at all three positions are greater than those without interface.

(5) Strain values in the models with interface at all three positions are greater than those without interface. The main reason is that the aggregates and the asphalt mastic coated with cement mortar form a network structure, and the load needs to destroy the interface structure before it can be further transferred.

Data Availability

The data used to support the findings of this study are included within the article.

Conflicts of Interest

The authors declare that there are no conflicts of interest regarding the publication of this paper.

Acknowledgments

This work was supported by the Science and Technology Program of Nanning (no. 20193129), Key Research and Development Plan of Guangxi (no. AB19245019), and Open Project of Guangxi Key Lab of Road Structure and Materials (no. 2018gxgclkf003). The authors thank all those who contributed to the image technique and the experimental

part of this study. In addition, the authors acknowledge the National Supercomputer Center (NSCC) in Guangzhou for providing computing resources useful in conducting the research reported in this paper.

References

[1] J.-F. Su, E. Schlangen, and J. Qiu, "Design and construction of microcapsules containing rejuvenator for asphalt," *Powder Technology*, vol. 235, pp. 563–571, 2013.

[2] A. M. Tahir, K. Khailesh, R. Vishnu, and C. Venkaiah, "Performance evaluation of rejuvenated recycled asphalt blends at high and intermediate pavement temperatures," *International Journal of Pavement Engineering*, pp. 1–13, 2021.

[3] D. Li, L. Zhen, F. Zou, and H. Yu, "Effects of rubber absorption on the aging resistance of hot and warm asphalt rubber binders prepared with waste tire rubber," *Journal of Cleaner Production*, vol. 303, Article ID 127082, 2021.

[4] P. Guo, S. Chen, F. Xie et al., "Influence of coarse aggregate morphological properties on the performances of warm-mix asphalt containing recycled asphalt pavement," *Journal of Materials in Civil Engineering*, vol. 33, no. 5, Article ID 04021081, 2021.

[5] J. Wang, N. Su, F. Xiao, and N. Amirkhanian Serji, "Dynamic modulus characteristics of mixtures containing recycled asphalt pavements, warm mix additives, and antistrip agents," *Journal of Testing and Evaluation*, vol. 49, no. 3, Article ID 20200006, 2021.

[6] M. Guo, M. Liang, S. Anand, B. Amit, and D. Luo, "Characterization of rejuvenation of various modified asphalt binders based on simplified chromatographic techniques," *International Journal of Pavement Engineering*, pp. 1–11, 2021.

[7] M. Guo, X. Liu, Y. Jiao, Y. Tan, and D. Luo, "Rheological characterization of reversibility between aging and rejuvenation of common modified asphalt binders," *Construction and Building Materials*, vol. 301, Article ID 124077, 2021.

[8] M. Guo, M. Liang, Y. Fu, S. Anand, and B. Amit, *Average Molecular Structure Models of Unaged Asphalt Binder Fractions*, Materials and Structures, Springer Nature, Basingstoke, UK, 2021.

[9] S. Mo, Y. Wang, F. Xiong, C. Ai, D. Wang, and T. G. Y. Amy, "Changes of asphalt fumes in hot-mix asphalt pavement recycling," *Journal of Cleaner Production*, vol. 258, Article ID 120586, 2020.

[10] H. Chamod, X. Hou, J. Wang, and F. Xiao, "A comprehensive review on the utilization of reclaimed asphalt material with warm mix asphalt technology," *Construction and Building Materials*, vol. 227, Article ID 117096, 2019.

[11] L. Qiang, G. Sun, Y. Lu, Y. Meng, S. Luo, and L. Gao, "Effects of warm-mix asphalt technologies and modifiers on pavement performance of recycled asphalt binders," *Journal of Cleaner Production*, vol. 282, Article ID 125435, 2020.

[12] S. Liu, S. Zhou, and A. Peng, "Laboratory evaluation of foamed warm mix binders and mixtures containing reclaimed asphalt pavements," *Construction and Building Materials*, vol. 258, Article ID 119773, 2020.

[13] K. Amir and M. Seyed Mohsen, "Fracture and mechanical properties of water-based foam warm mix asphalt containing reclaimed asphalt pavement," *Construction and Building Materials*, vol. 269, Article ID 121332, 2021.

[14] P. F. Abreu Liliana, R. M. Oliveira Joel, M. R. D. Silva Hugo, P. Daniela, and V. Fonseca Paulo, "Suitability of different foamed bitumens for warm mix asphalts with increasing recycling rates," *Construction and Building Materials*, vol. 142, pp. 342–353, 2017.

[15] J. Pei, J. Cai, D. Zou et al., "Design and performance validation of high-performance cement paste as a grouting material for semi-flexible pavement," *Construction and Building Materials*, vol. 126, pp. 206–217, 2016.

[16] J. Cai, J. Pei, Q. Luo, J. Zhang, L. Rui, and X. Chen, "Comprehensive service properties evaluation of composite grouting materials with high-performance cement paste for semi-flexible pavement," *Construction and Building Materials*, vol. 153, pp. 544–556, 2017.

[17] M. Gong, Z. Xiong, H. Chen et al., "Evaluation on the cracking resistance of semi-flexible pavement mixture by laboratory research and field validation," *Construction and Building Materials*, vol. 207, pp. 387–395, 2019.

[18] Y. Gong, H. Bi, C. Liang, and S. Wang, "Microstructure analysis of modified asphalt mixtures under freeze-thaw cycles based on CT scanning technology," *Applied Sciences*, vol. 8, no. 11, pp. 1–14, 2018.

[19] W. Huang, X. Cai, L. Xiang, and K. Wu, "Influence of nominal maximum aggregate size and aggregate gradation on pore characteristics of porous asphalt concrete," *Materials*, vol. 13, p. 1355, 2020.

[20] J. Hu, P. Liu, D. Wang, and M. Oeser, "Influence of aggregates' spatial characteristics on air-voids in asphalt mixture," *Road Materials and Pavement Design*, vol. 19, no. 4, pp. 837–855, 2017.

[21] T. Schüler, R. Jänicke, and H. Steeb, "Nonlinear modeling and computational homogenization of asphalt concrete on the basis of XRCT scans," *Construction and Building Materials*, vol. 109, pp. 96–108, 2016.

[22] W. Huang, H. Wang, Y. Yin, X. Zhang, and J. Yuan, "Microstructural modeling of rheological mechanical response for asphalt mixture using an image-based finite element approach," *Materials*, vol. 12, no. 13, p. 2041, 2019.

[23] W. Huang, Z. Ren, X. Zhang, and J. Yu, "Investigation on microstructural damage properties of asphalt mixture using linear and damage-coupled viscoelastic model," *Applied Sciences*, vol. 9, no. 2, pp. 1–19, 2019.

[24] W. Huang and X. Zhang, "Segmentation of coarse aggregate adhesion images using morphological multiscale algorithm," *Journal of Harbin Institute of Technology*, vol. 48, no. 3, pp. 125–130, 2016.